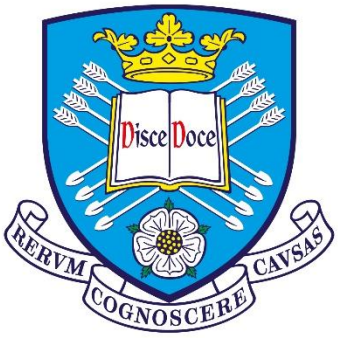

The University Of Sheffield.

Structural Degradation Studies of High Voltage Lithium Ion Battery Materials

Laura Wheatcroft

A thesis submitted in partial fulfilment of the degree of Doctor of Philosophy

Supervisors: Professor Beverley J. Inkson
Dr Doğan Özkaya, Johnson Matthey
Dr James Cookson, Johnson Matthey

The University of Sheffield
Faculty of Engineering
Department of Materials Science and Engineering

September 2020

Abstract

High voltage Li-ion battery materials are being developed for high energy density applications, such as electric vehicles, and grid scale storage [1], [2]. However, high voltage cathode materials, such as $LiCoPO_4$, typically undergo severe capacity loss during cycling [3]–[5], preventing commercialisation.

Degradation within high voltage cathode electrodes can occur due to parasitic surface reactions with the electrolyte at the electrode/ electrolyte interface [4], [6], and via structural degradation within individual cathode particles. Parasitic reactions at the electrode/ electrolyte interface can result from a lack of passivation by a cathode electrolyte interphase (CEI) layer [6] when operating outside the electrolyte stability window. Structural degradation within individual primary particles can occur due to defect formation, or unstable phase formation [5], [7]. If unstable phases form near the electrode/ electrolyte interface degradation can be accelerated by parasitic reactions from the electrolyte.

Improving the electrochemical properties of high voltage cathodes requires detailed understanding of the underlying degradation mechanisms. However, characterising degradation in Li-ion cathode materials is difficult because Li is hard to detect, and complex local environments exist within a single electrode. Ideally, techniques used to characterise degradation should correlate the underlying electrode microstructure with degradation induced chemical and structural changes.

Here, novel electron and ion microscopy techniques are developed to study degradation phenomena at the electrode surface, within individual primary particles, and during cycling. The techniques aim to correlate chemistry and microstructure, and enable understanding of the role of local environment in degradation behaviour. The techniques are validated by conducting a comprehensive study of degradation in high voltage Li-ion battery material $LiCoPO_4$.

The CEI layer is challenging to image and characterise because the CEI layer is thinner (10-20 nm) than the anode equivalent SEI layer (up to 1 μm), and CEI layers typically contain Li. He-ion microscopy (HIM) and secondary ion mass spectrometry (SIMS), a mass spectrometry technique integrated into some helium ion microscopes, are suited to CEI layer studies because HIM is a highly surface sensitive imaging technique, and SIMS is capable of detecting Li. Here, He-ion microscopy (HIM) and *in-situ* Ne-ion time-of-flight secondary ion mass spectrometry (SIMS) has been used for the first time to study CEI formation resulting from electrolyte oxidation on the cathode.

HIM is used to image the CEI layer on $LiCoPO_4$ at length scales enabling the thickness and morphology of the CEI to be related to the underlying microstructure. HIM imaging showed that the CEI forms on $LiCoPO_4$ agglomerates. SIMS mapping and depth profiling characterisation identified that the CEI layers are composed of oxyfluorophosphates, and a layer of uncycled Li exists on the surface of charged electrodes. Using HIM SIMS to analyse cathodes at different states of charge and after different cycle numbers, enabled direct imaging of the partial dissolution of the CEI layers across the electrode. Partial CEI dissolution is most significant on larger $LiCoPO_4$ agglomerates. The HIM SIMS technique provides new opportunities for correlating underlying electrode microstructure with heterogeneous CEI formation.

Li is hard to detect with most chemical spectroscopy techniques. Co in $LiCoPO_4$ oxidised from Co(II)-Co(III) as Li is removed. Electron Energy Loss Spectroscopy has been previously used to

measure the change in Fe valence state in $LiFePO_4$ to study lithiation mechanisms [8]. Here, the de-lithiation mechanisms of $LiCoPO_4$ are visualised post-mortem using an electron energy loss spectroscopy (EELS) technique to map changes in the valence state of Co across the electrode.

Using Co valence state EELS, the shrinking-core de-lithiation mechanism of $LiCoPO_4$ was directly visualised. The unstable $CoPO_4$ phase forms on the outside of $LiCoPO_4$ particles, leaving it susceptible to damage from the electrolyte. Damage from the electrolyte is observed as a layer of Co(II) on the outside of particles, along with a region of trapped Li on the surface of electrodes charged to 5.1 V vs. Li/ Li^+. Results from valence state EELS characterisation, in conjunction with the HIM SIMS results indicate that the cyclability of $LiCoPO_4$ could be improved by improving the stability of $CoPO_4$, or developing methods to shield $CoPO_4$ from electrolyte degradation.

To prevent the impact of sample damage, and ensure transient states during charging could be characterised, an *in-operando* TEM technique was investigated to image changes in primary particle microstructure during cycling of active materials. The initial set-up aimed to create a Li-ion half-cell in the TEM. $LiCoPO_4$ was successfully isolated on the nano-cell working electrode, however, plating of Li from the electrolyte onto the reference electrode was unsuccessful. The results presented suggest a pseudo-reference electrode cell, using Pt as the reference electrode, would be a better set-up for *in-operando* TEM.

As part of the *in-operando* TEM set-up, the electrolyte was irradiated with the electron beam. It was found that the electrolyte formed a series of precipitates with increasing electron dose, which post-mortem energy dispersive X-ray spectroscopy identified as consisting of carbon, fluorine, oxygen, and phosphorous. The precipitates formed as a result of electrolyte reduction from the electron beam. The results present an opportunity to use a closed liquid cell set-up in the TEM to study reduction mechanisms of different lithium ion battery electrolytes.

The novel electron microscopy techniques presented in this thesis offer future routes to characterising complex degradation mechanisms in high voltage Li-ion battery materials. The methods enable correlation of chemical and structural changes with electrochemical history, whilst maintaining an understanding of the complex local environment.

References

[1] A. Kraytsberg and Y. Ein-Eli, “Higher, Stronger, Better… A Review of 5 Volt Cathode Materials for Advanced Lithium-Ion Batteries,” *Adv. Energy Mater.*, vol. 2, no. 8, pp. 922–939, 2012.

[2] “High-energy battery technologies,” Faraday Institution, 2020.

[3] M. Zhang, N. Garcia-Araez, and A. L. Hector, “Understanding and development of olivine $LiCoPO_4$ cathode materials for lithium-ion batteries,” *J. Mater. Chem. A*, vol. 6, no. 30. pp. 14483–14517, 2018.

[4] E. Markevich, R. Sharabi, H. Gottlieb, V. Borgel, K. Fridman, G. Salitra, D. Aurbach, G. Semrau, M. A. Schmidt, N. Schall, and C. Bruenig, “Reasons for capacity fading of $LiCoPO_4$ cathodes in $LiPF_6$ containing electrolyte solutions,” *Electrochem. commun.*, vol. 15, no. 1, pp. 22–25, 2012.

[5] Y. H. Ikuhara, X. Gao, C. A. J. Fisher, A. Kuwabara, H. Moriwake, K. Kohama, H. Iba, and Y. Ikuhara, “Atomic level changes during capacity fade in highly oriented thin films of cathode material $LiCoPO_4$,” *J. Mater. Chem. A*, vol. 5, no. 19, pp. 9329–9338, 2017.

[6] J. Manzi and S. Brutti, “Surface chemistry on $LiCoPO_4$ electrodes in lithium cells: SEI

formation and self-discharge," *Electrochim. Acta*, vol. 222, pp. 1839–1846, 2016.

[7] F. C. Strobridge. R. J. Clément, M. Leskes, D. S. Middlemiss, O. J. Borkiewicz, K. M. Wiaderek, K. W. Chapman, P. J. Chupas, and C. P. Grey, "Identifying the Structure of the Intermediate, $Li_{2/3}CoPO_4$, Formed during Electrochemical Cycling of $LiCoPO_4$," *Chem. Mater.*, vol. 26, no. 21, pp. 6193–6205, 2014.

[8] X. Mu, S. Muto, K. Tatsumi, H. Kondo, K. Horibuchi, T. Kobayashi, and T. Sasaki, "Comprehensive analysis of TEM methods for $LiFePO_4$/$FePO_4$ phase mapping: spectroscopic techniques (EFTEM, STEM-EELS) and STEM diffraction techniques (ACOM-TEM)," *Ultramicroscopy*, vol. 170, pp. 10–18, 2016.

Acknowledgements

I would like to thank my supervisor, Prof. Beverley J. Inkson. I am very grateful for the opportunities she has created (including trips to JM, Germany, and Sweden) and for her support and advice throughout the project. I would like to thank Dr Doğan Özkaya, from Johnson Matthey, for his support throughout the project. Thank you for organising regular trips to the Johnson Matthey microscopes, visits to JM and Liverpool, and for providing help and advice throughout the project. I would also like to thank Dr James Cookson for his support throughout the project. In particular, thank you for providing materials, advice, and organising visits to the JM battery materials department for much appreciated advice from Dr Jamie Stephens, and Dr Noelia Cabello.

I would like to thank some individuals who provided invaluable help and support throughout the project. Firstly, thank you to Dr Trung Dung Tran, Johnson Matthey, for helping with all the EELS collection, providing fantastic advice on processing all the data, and being willing to teach me about the technique. Thank you to Dr Gregor Hlawacek, and his group from the Helmholtz Zentrum Dresden Rossendorf for organising the trips to HZDR for HIM SIMS, and providing advice on the technique. Thank you to Dr Nico Klingner, HZDR, for welcoming me to Dresden, helping me conduct the HIM SIMS experiments, and for the help processing all the data! Thank you to Dr Layla Mehdi, and Dr Juhan Lee from the University of Liverpool for demonstrating their *in-operando* TEM methods. Thank you also to Dr Manfred Schuster, Johnson Matthey, for organising visits to the JM microscope at Harwell.

Thank you to a number of individuals from the University of Sheffield for their help and support. Thank you to the staff and post-docs at the Sorby Centre for their help teaching me electron microscopy, and for always being willing to provide help. Special thanks is given to Dr John Nutter for his help with electron diffraction, and always being willing to help out with the F200. Thank you to Chris Hill from the Biomedical department for all the microtoming training, help, and support. Thank you to Dr Nik Reeves McLaren, and Dr Rob Moorehead for all their help and advice with XRD. Finally, a huge thank you to the staff and students in the Sheffield Kroto battery lab, and the Energy Storage CDT for all their help, advice, support, and jokes throughout the project. I hope we all keep in touch!

I would like to acknowledge the Engineering and Physical Sciences Research Council, and Johnson Matthey for funding my PhD, and the Leverhulme Trust for funding the visits to the Helium ion microscope.

Finally, a huge thank you to my Mum and Dad for their love and support throughout the highs and lows of the PhD journey!

Contents

1 INTRODUCTION

1.1 MOTIVATIONS AND AIMS

For a more sustainable future there has recently been a drive to develop electric vehicles and grid-scale energy storage, with the government pledging to fully decarbonise transport by 2050 [1], [2]. Li-ion batteries are currently being used and are being developed for electric vehicles, however, for sufficient driving ranges to compete with petrol vehicles, high energy density Li-ion battery materials are required [1], [3].

A method of increasing the energy density of a Li-ion battery is to increase the operating potential of the cathode material, leading to the development of high voltage Li-ion cathode materials (cathodes where redox occurs over 4.5 V vs. Li/ Li^+) [4]. However, high voltage cathode materials, such as $LiCoPO_4$ undergo severe degradation during cycling [5], preventing commercialisation.

At high potentials, standard electrolytes oxidise causing electrode-electrolyte interface degradation [6]–[8]. At anode operating potentials, electrolyte reduction forms a passivating solid electrolyte interphase (SEI), which protects the anode from further degradation from the electrolyte. However, the equivalent film in cathodes, the cathode electrolyte interphase (CEI), can be unstable preventing electrode passivation [6]–[8]. Structural degradation within cathode particles can also occur through the formation of anti-site defects, and unstable de-lithiated phases which can be particularly susceptible to electrolyte attack [9]–[11].

Understanding of degradation processes is further complicated by the complexity of environments within Li-ion battery electrodes. The composite nature of binder, active material, conductive additive, and electrolyte within electrodes, together with variations in potential, stress and temperature, leads to multiple degradation environments.

Characterisation of degradation within Li-ion batteries is challenging. Li is difficult to detect with most spectroscopies due to its low binding energies. The complex environments present within Li-ion batteries also make a comprehensive picture of degradation difficult to obtain. The majority of techniques used to characterise Li-ion battery degradation are bulk averaging techniques, such as X-ray diffraction, and spectroscopies, missing understanding of heterogeneous local microstructure, and correlation of local chemical environment with microstructure.

Recently new X-ray microscopy techniques have been developed, such as X-ray computed tomography, in combination with X-ray diffraction [12], and scanning transmission X-ray microscopy in combination with X-ray absorption spectroscopy to correlate microstructure with local chemistry [13]. X-ray techniques are useful for probing micron-size local environments; however, electron microscopies are better suited to probe nano to atomic-scale phenomena.

CEI layers, and lithiation mechanisms are particularly difficult to characterise because both are nano-scale phenomena, and require detection of Li for full characterisation. Microscopy techniques, such as Helium ion microscopy, and secondary ion mass spectrometry [14], [15], and scanning transmission electron microscopy and electron energy loss spectroscopy [16] have the potential to correlate microstructures with chemistry, and provide an understanding of local environment.

The aim of this project is to develop different advanced microscopy techniques to characterise degradation in high voltage Li-ion battery materials. The techniques should be able to allow the user to understand how electrochemical cycling leads to microstructural evolution of electrodes,

including changes in local chemistry, phases, electrode structure and distribution/mobility of Li ions.

Another aim of the project is to apply the techniques developed to the high voltage battery material $LiCoPO_4$, in order to identify reasons for its known severe degradation so the performance can be improved. Applying the techniques to $LiCoPO_4$ will also validate the techniques so they could be applied to other Li-ion battery materials with similar degradation issues.

1.2 THESIS NOVELTY

High voltage cathode materials undergo both surface degradation from degradation of the electrolyte at the electrode-electrolyte interface, forming cathode electrolyte interphase [7], [6], and structural degradation within the individual cathode particles [9], [10], [17]. The techniques demonstrated in this thesis characterise (1) poor formation of passivating cathode electrolyte interphase (CEI) layers, and (2) chemical and crystallographic structural degradation within individual $LiCoPO_4$ particles. A technique which could characterise degradation within primary particles *in-operando* was also developed using *in-operando* TEM.

Helium ion microscopy (HIM) and *in-situ* Ne-ion secondary ion mass spectrometry (SIMS) is developed, for the first time, as a methodology to directly image, and chemically characterise CEI layers on $LiCoPO_4$. He-ion microscopy enables highly surface sensitive secondary electron imaging. The He^+ beam interaction with the surface produces improved surface resolution compared with scanning electron microscopy. HIM imaging is compared with SEM imaging to confirm improved surface resolution. SIMS is one of the few chemical characterisation techniques which can directly detect Li so is used within the He-ion microscope as a chemical characterisation technique for CEI layers.

An electron energy loss spectroscopy (EELS) Co L-edge mapping technique is developed as a method to map the Co(II), and Co(III)-rich regions of $LiCoPO_4$. As Co is redox active during de-lithiation of $LiCoPO_4$, mapping the Co(II), and Co(III) valence states is analogous to mapping the lithiated, and de-lithiated regions within individual $LiCoPO_4$ particles, allowing the de-lithiation mechanisms to be investigated with the STEM-EELS technique. Sample preparation using microtome sectioning is also shown to improve the resolution of lithiated and de-lithiated phases within $LiCoPO_4$ samples.

Both the HIM-SIMS, and EELS techniques are performed *ex-situ*. *Ex-situ* techniques can result in sample damage from transfer into microscopes, and can miss transient processes which occur during cycling. To counter this and potentially enable CEI layer, and structural characterisation of $LiCoPO_4$ during cycling, an *in-operando* TEM technique was developed. Unfortunately, a number of obstacles were experienced during set-up of the *in-operando* TEM technique, so the strategy used to set-up the technique is shown, and methods of improvement on the strategy used here suggested.

1.3 THESIS STRUCTURE

This thesis is presented using the self-contained results chapter structure, with the aims, objectives, introduction, experimental, results, discussion, and conclusions relevant to each

results chapter being presented within a single chapter rather than in the traditional thesis format. A general literature review is presented at the start of the thesis to introduce and discuss literature relevant to all chapters. As all the chapters required electrode manufacturing as part of the methods, a standalone electrode, and cell manufacturing experimental chapter is presented prior to the results chapters. The main findings of all chapters are summarised in the conclusions chapter, and the further work chapter proposes future work which can be built on the work presented in all chapters.

The results of the thesis work are split into four distinct Chapters as listed below:

Chapter 4 introduces He-ion microscopy (HIM), and *in-situ* time of flight secondary ion mass spectrometry (ToF SIMS) as new techniques to image and chemically characterise nano-scale cathode electrolyte interphase (CEI) formation and its distribution across the electrode at the macro-scale. The Chapter discusses why HIM-SIMS is useful for characterising CEI layers by comparing the HIM technique to SEM, and identifies CEI layer formation mechanisms on $LiCoPO_4$ during cycling. The HIM-SIMS technique is used to correlate CEI formation with underlying microstructure for the first time. Work presented in this chapter has been accepted by ACS Applied Energy Materials (*ACS Appl. Energy Mater.* 2020, 3, 9, 8822-8832).

Chapter 5, and Chapter 6 are partner chapters where an EELS Co L-edge oxidation state mapping technique is developed, and used to identify the lithiated, and de-lithiated regions within individual $LiCoPO_4$ particles and understand the evolving chemical structure of $LiCoPO_4$. The EELS oxidation technique development is presented in Chapter 5, and the technique is used to directly image the de-lithiation mechanisms of $LiCoPO_4$ in Chapter 6.

Chapter 5 presents the development of the EELS Co L-edge oxidation state mapping technique. The chapter discusses how EELS Co L-edge mapping standards were extracted, and uses diffraction techniques to identify the standards. O K-edge extractions were also performed to identify regions of Co-O hybridisation. The significance of the shapes of the extracted Co L-edge, and O K-edge EELS spectra are discussed. The importance of sample preparation is explained by comparing sectioned, and non-sectioned samples.

Chapter 6 uses the EELS Co L-edge mapping technique developed in Chapter 5 to spatially resolve the lithiated and de-lithiated regions within individual $LiCoPO_4$ particles. The technique was applied to the first cycle at different states of charge on the first cycle to image the de-lithiation mechanism. The technique was also applied to later cycles to understand how the de-lithiation mechanism varies as $LiCoPO_4$ degrades. The later cycles work is discussed in context with the HIM-SIMS results to have a comprehensive understanding of degradation with $LiCoPO_4$.

Chapter 7 presents work performed to develop an *in-operando* TEM technique to characterise Li-ion battery materials. Unfortunately, equipment issues were experienced during the course of the project so the technique was not developed to completion. Chapter 7 presents the work performed towards developing the *in-operando* TEM technique, including understanding the effects of the electron beam on electrolytes, and setting up the *in-operando* cell as a half-cell in the TEM. The chapter presents an extensive literature review on previous *in-operando* TEM methods, and perspectives on *in-operando* TEM as a technique based on experiences in this project.

1.4 CONTRIBUTIONS AND ACKNOWLEDGEMENTS

A number of people made invaluable contributions to the work presented in this thesis. My thanks are given to all for their help and advice throughout the PhD. The contributions are split by results chapter.

$LiCoPO_4$ powder used in this thesis was supplied by Dr James Cookson's group at Johnson Matthey. Advice on the preparation of electrodes was given by Dr James Stevens, and Dr Noelia Cabello, Johnson Matthey. The work in this project was also funded by a Johnson Matthey CASE award.

Chapter 4

Major contributors were made by Dr Nico Klingner, Dr René Heller, and Dr Gregor Hlawacek, Helmholtz Zentrum Dresden- Rossendorf (HZDR), Germany. This work was funded by the PicoFIB Network (Leverhulme PI Inkson) and HZDR, Germany.

Experimental design was performed by L. Wheatcroft, with advice from N. Klingner, and B.J. Inkson. Sample preparation, and electrochemical testing was performed by L. Wheatcroft. He-ion imaging, and secondary ion mass spectrometry (SIMS) were performed by N. Klingner, in collaboration with L. Wheatcroft. The ToF SIMS for the HIM as a spectroscopic technique was developed by N. Klingner, R. Heller, G. Hlawacek, and collaborators at HZDR [14], [15]. Depth profiling presented in this work was made possible by work by R. Heller. He-ion image, and SIMS data analysis, and image interpretation was performed by L. Wheatcroft, with help and advice from N. Klingner, and G. Hlawacek. SEM, and STEM imaging was performed by L. Wheatcroft, and advice on image interpretation given by B.J. Inkson.

Chapter 5 and Chapter 6
Major contributors were: Dr Trung Dung Tran, and Dr Doğan Özkaya, Johnson Matthey, and Chris Hill, University of Sheffield.

Experimental design was performed by L. Wheatcroft, with help and advice from T. D. Tran, D. Özkaya, and B.J. Inkson. Electrode manufacture, and electrochemical experiments were performed by L. Wheatcroft. Microtome sample preparation was performed by L. Wheatcroft and C. Hill. C. Hill performed microtoming on the first cycle samples presented in Figure 6.3. L. Wheatcroft performed microtoming on all other samples, with advice from C. Hill. EELS and STEM imaging was performed by T. Tran, in collaboration with L. Wheatcroft. EELS data analysis, and image interpretation was performed by L. Wheatcroft with advice from T. Tran, D. Özkaya, and B.J. Inkson. XRD, TEM imaging, and SAED (selected area electron diffraction) were performed by L. Wheatcroft. Data analysis for XRD, TEM, and SAED was also performed by L. Wheatcroft.

Chapter 7

Major contributors were: Dr Muhammed Sajid Ali Asghar, University of Sheffield, Dr Vitor Leite Martins, University of Sheffield, Dr Doğan Özkaya, Dr Beata Layla Mehdi, and Dr Juhan Lee, University of Liverpool.

Electrolyte irradiation experiments were performed by L. Wheatcroft, and M. S. A. Asghar. Electrolyte Li deposition experiments in the *in-situ* holder were performed by L. Wheatcroft, with advice from V. L. Martins. Post-mortem SEM experiments were performed by L. Wheatcroft. Microtome and electrode position experiments were performed by D. Özkaya, and L. Wheatcroft. Help and advice on the best use of the *in-operando* TEM set-up was given by B. L. Mehdi, and J.

Lee. Although not presented here, further *ex-situ* electrolyte cycling experiments were performed at the University of Liverpool by L. Wheatcroft, and J. Lee, with help and advice from B. L. Mehdi.

1.5 REFERENCES

[1] M. Ue, K. Sakaushi, and K. Uosaki, "Basic knowledge in battery research bridging the gap between academia and industry," *Mater. Horizons.*, vol. 7, pp. 1937-1954 2020.

[2] "Government launches Road to Zero Strategy to lead the world in zero emission vehicle technology - GOV.UK." [Online]. Available: https://www.gov.uk/government/news/government-launches-road-to-zero-strategy-to-lead-the-world-in-zero-emission-vehicle-technology. [Accessed: 04-Jul-2020].

[3] Faraday Report "UK electric vehicle and battery production potential to 2040," Faraday Insitution, 2020. Available: https://faraday.ac.uk/wp-content/uploads/2020/03/2040_Gigafactory_Report_FINAL.pdf. [Accessed: 03-Dec-2020]

[4] A. Kraytsberg and Y. Ein-Eli, "Higher, Stronger, Better… A Review of 5 Volt Cathode Materials for Advanced Lithium-Ion Batteries," *Adv. Energy Mater.*, vol. 2, no. 8, pp. 922–939, 2012.

[5] M. Zhang, N. Garcia-Araez, and A. L. Hector, "Understanding and development of olivine $LiCoPO_4$ cathode materials for lithium-ion batteries," *J. Mater. Chem. A,* vol. 6, pp. 14483-14517, 2018.

[6] W. Li, A. Dolocan, P. Oh, H. Celio, S. Park, J. Cho, and A. Manthiram, "Dynamic behaviour of interphases and its implication on high-energy-density cathode materials in lithium-ion batteries," *Nat. Commun.*, vol. 8, pp. 14589, 2017.

[7] J. Manzi and S. Brutti, "Surface chemistry on $LiCoPO_4$ electrodes in lithium cells: SEI formation and self-discharge," *Electrochim. Acta*, vol. 222, pp. 1839–1846, 2016.

[8] E. Markevich, R. Sharabi, H. Gottlieb, V. Borgel, K. Fridman, G. Salitra, D. Aurbach, G. Semrau, M. A. Schmidt, N. Schall, and C. Bruenig, "Reasons for capacity fading of $LiCoPO_4$ cathodes in $LiPF_6$ containing electrolyte solutions," *Electrochem. commun.*, vol. 15, no. 1, pp. 22–25, 2012.

[9] Y. H. Ikuhara, X. Gao, C. A. J. Fisher, A. Kuwabara, H. Moriwake, K. Kohama, H. Iba, and Y. Ikuhara, "Atomic level changes during capacity fade in highly oriented thin films of cathode material $LiCoPO_4$," *J. Mater. Chem. A*, vol. 5, no. 19, pp. 9329–9338, 2017.

[10] F. C. Strobridge, H. Liu, M. Leskes, O. J. Borkiewicz, K. M. Wiaderek, P. J. Chupas, K. W. Chapman, and C. P. Grey, "Unraveling the Complex Delithiation Mechanisms of Olivine-Type Cathode Materials, $LiFe_xCo_{1-x}PO_4$," *Chem. Mater.*, vol. 28, no. 11, pp. 3676–3690, 2016.

[11] M. Kaus, I. Issac, R. Heinzmann, S. Doyle, S. Mangold, H. Hahn, V. S. K. Chakravadhanula, C. Kübel, H. Ehrenberg, and S. Indris, "Electrochemical delithiation/relithiation of $LiCoPO_4$: A two-step reaction mechanism investigated by in situ X-ray diffraction, in situ X-ray absorption spectroscopy, and ex situ $^{7}Li/31^{P}$ NMR spectroscopy," *J. Phys. Chem. C*, vol. 118, no. 31, pp. 17279–17290, 2014.

[12] D. P. Finegan, A. Vamvakeros, L. Cao, C. Tan, T. M. M. Heenan, S. R. Daemi, S. D. M. Jacques, A. M. Beale, M. Di Michiel, K. Smith, D. J. L. Brett, P. R. Shearing, and C. Ban, "Spatially Resolving Lithiation in Silicon-Graphite Composite Electrodes via in Situ High-Energy X-ray Diffraction Computed Tomography," *Nano Lett.*, vol. 19, no. 6, pp. 3811–

3820, 2019.

[13] J. D. Sugar, F. El Gabaly, W. C. Chueh, K. R. Fenton, T. Tyliszczak, P. G. Kotula, and N. C. Bartelt, "High-resolution chemical analysis on cycled $LiFePO_4$ battery electrodes using energy-filtered transmission electron microscopy," *J. Power Sources*, vol. 246, pp. 512–521, 2014.

[14] N. Klingner, R. Heller, G. Hlawacek, J. von Borany, J. Notte, J. Huang, and S. Facsko, "Nanometer scale elemental analysis in the helium ion microscope using time of flight spectrometry," *Ultramicroscopy*, vol. 162, pp. 91–97, 2016.

[15] N. Klingner, R. Heller, G. Hlawacek, S. Facsko, and J. von Borany, "Time-of-flight secondary ion mass spectrometry in the helium ion microscope," *Ultramicroscopy*, vol. 198, pp. 10–17, 2019.

[16] Z. Wang, D. Santhanagopalan, W. Zhang, F. Wang, H. L. Xin, K. He, J. Li, N. Dudney, and Y. S. Meng, "In situ STEM-EELS observation of nanoscale interfacial phenomena in all-solid-state batteries," *Nano Lett.*, vol. 16, no. 6, pp. 3760–3767, 2016.

[17] J. G. Lapping, S. A. Delp, J. L. Allen, J. L. Allen, J. W. Freeland, M. D. Johannes, L. Hu, D. T. Tran, T. R. Jow, and J. Cabana, "Changes in Electronic Structure upon Li Deintercalation from $LiCoPO_4$ Derivatives," *Chem. Mater.*, vol. 30, no. 6, pp. 1898–1906, 2018.

2 LITERATURE REVIEW

2.1 INTRODUCTION TO LITHIUM ION BATTERIES

Batteries are devices made up of a connected series of electrochemical cells which store chemical energy and release electrical energy [1]. All electrochemical cells are based on redox reactions where electrons are transferred between species resulting in the reduction (gain of electrons) and oxidation (loss of electrons) of the reactants and products. Energy in electrochemical cells is stored by spatially separating the oxidation and reduction processes allowing them to occur on electrodes (the anode and cathode) (see Figure 2.1) [1]. On discharge the two electrodes are electrically connected allowing the redox reaction to occur spontaneously. Electrons can be collected and used for useful work whilst ions are transferred across a liquid electrolyte. In lithium ion batteries the charge carrying species are Li^+ ions [1].

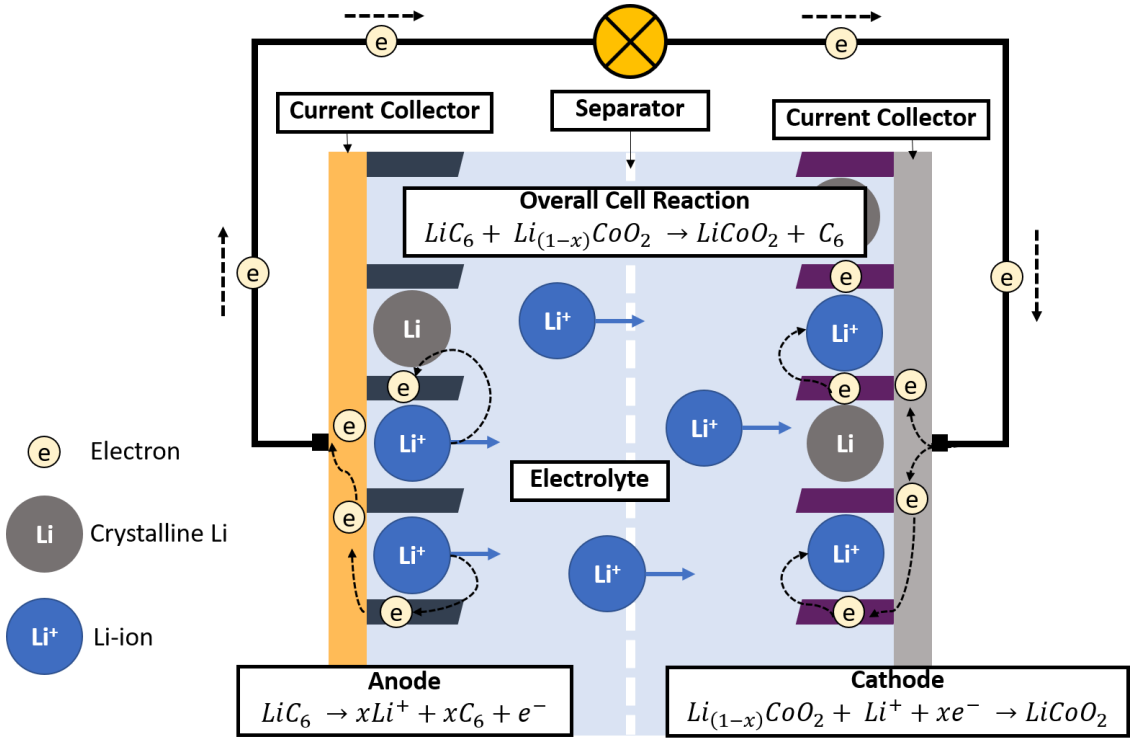

Figure 2.1: Diagram showing the operating principle of a Li-ion battery. The redox equations shown are reactions which occur in a $LiCoO_2$/ graphite Li-ion cell during discharge. During discharge oxidation occurs at the anode (dark grey), releasing electrons which flow around the circuit to perform useful work. Oxidised Li at the anode forms Li^+ ions which migrate across the electrolyte towards the cathode (purple) to balance the charge difference. The reaction completes via reduction of Li^+ ions at the cathode. The overall cell reaction equation (the overall redox equation) is also shown.

For the discharge reaction to occur spontaneously, the reaction chemical potential on the cathode side must be less than the reaction chemical potential on the anode side [2]–[4]. In practical terms the chemical potential requirement results in anodes having a redox potential closer to Li/ Li^+ vs. SHE (standard hydrogen potential), than cathodes [2].

The main components of a Li-ion cell are the electrodes (the anode and the cathode), the electrolyte, the separator, and the current collectors (see Figure 2.1 and Figure 2.2).

The electrolyte is a medium which allows Li^+ ions to be transferred from one electrode to the other. The electrolyte can be a liquid (Li salt dissolved in a solvent), or a solid (polymer or Li-ion conducting ceramic) [5]. All the cells in this thesis use liquid electrolytes.

The separator is an electrically insulating physical barrier that prevents the anode and cathode from touching but allows transfer of Li^+ ions through it. Separators are typically polymer membranes, such as microporous polyolefin materials, or fibre glass [5].

The electrodes are where the Li oxidation and reduction reactions occur to produce current. The principle components of the electrode are shown in Figure 2.2. The principle components are the active material, where the Li oxidation and reduction reactions occur (see Figure 2.1), the conductive additive which provides an electronic conduction pathway from the current collector to the active material, binder which holds the particles together into a composite porous structure, and finally the current collector which acts as a conductor for electrons in and out of the electrode [6]. As the electrical conductivity of the carbon additive is higher than the cathode particles [6], electron conduction to different parts of the cathode film can vary based on the coverage of conductive additive around electrode components, and the size of cathode agglomerates. As electrons are required for oxidation and reduction, variations in electrical conductivity through the film can alter the lithiation and de-lithiation of cathode particles.

Electrodes are designed to optimise the surface area of active material which touches electrolyte, but still provide a conduction pathway for electrons to the current collector. Therefore, they are designed to be porous architectures [5], [6]. Increased resistance can occur if areas are not porous enough for electrolyte ion penetration and/ or flow.

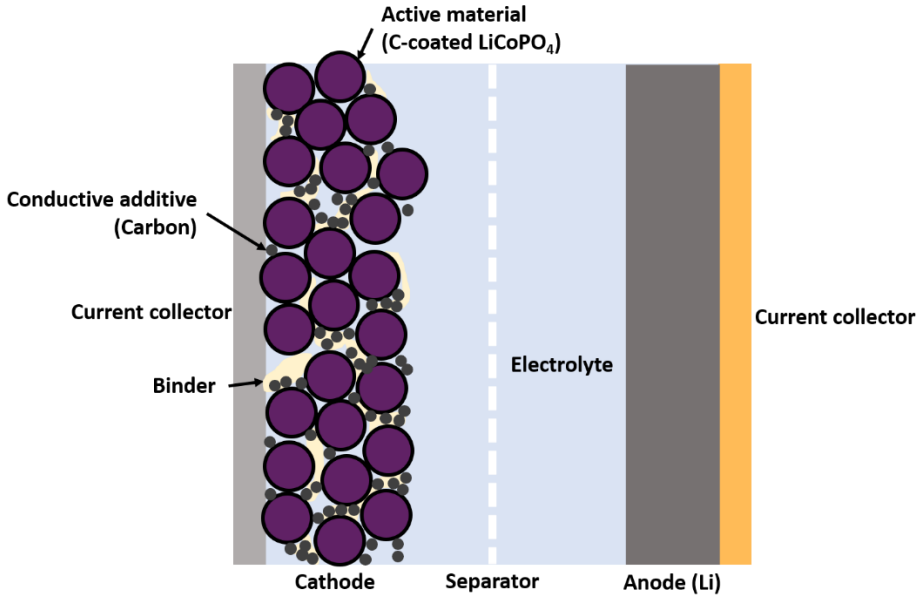

Figure 2.2: Schematic of a typical Li-ion half-cell. The electrode is a composite of active material, conductive additive and binder. The electrode is porous to allow electrolyte to make contact with active material.

2.1.1 Lithium Ion Battery Metrics

One of the potential applications for high energy lithium ion batteries is electric vehicles. The US advance battery consortium (USABC) listed the ideal requirements, at cell level, of a battery for an electric vehicle [7]:

Useable specific energy at C/3 rate: 350 Wh kg^{-1}

Useable energy density at C/3 rate: 750 Wh l^{-1}

Peak specific discharge power (80 % depth of discharge over 30 s): 700 W kg^{-1}

Peak power density (80 % depth of discharge over 30 s): 1500 W l^{-1}

Cycle life: 1000 cycles

Calendar life: 15 years

Cost: \$100 kW^{-1} h^{-1}

The **C-rate** (specified as C/3 rate in the ideal requirements list) is a measure of the rate a battery is discharged relative to its maximum capacity. C/3 indicates the battery is discharged using a current which causes full discharge in 3 hours [8].

Cycle life: The number of charge and discharge cycles a battery can undergo before it fails to meet performance criteria [8]

Specific energy: nominal energy per unit mass of the cell. Often in lab based scenarios, gravimetric, or specific energy and capacity is defined per unit mass of active material in the electrode of interest (eg. the cathode) [8], [9].

Energy density: nominal energy per unit volume of the cell [8].

Depth of discharge: the proportion of battery capacity which has been discharged expressed as a percentage of the maximum capacity [8]

Peak specific discharge power/ density: the peak power (energy/ time) experienced when the cell is discharged to 80 % depth of discharge over 30 s per unit mass or per unit volume respectively [8].

Calendar life: number of years the cell operates within its requirements [8]

Another metric regularly used in lab-based environments is the **specific capacity**, defined as the total Amp-hours available per mass of the cell (in industry typically), or active material (in laboratories) when the battery is discharged at a specified C-rate from 100 % state of charge to a specified cut-off voltage [8]. Practically this specific capacity is measured as the product of the discharge current and discharge time divided by the mass of active material in the electrode [3]. The specific energy is the product of the cell voltage and the specific capacity [3].

To date, no lithium ion battery chemistry has met the electric vehicle requirements outlined by the USABC [7]. For example, a comparison of cell energy density achieved by a number of commercial Li-ion batteries, showed the Samsung Galaxy S Li-ion battery cell had the highest energy density, with an energy density of ~290 Wh kg^{-1} [9].

The electric vehicle requirements demonstrate a few challenges for Li-ion battery development: (1) increasing the overall cell specific capacity, (2) increasing the energy, and power density, (3) developing materials that do not severely degrade at high C-rates for fast charging, and (4) balancing the anode and cathode capacities. Therefore, there is currently a research focus on improving the 3 challenges. It should be noted a number of these criteria are being solved by

beyond Li-ion battery technologies, such as solid state batteries, and Li-metal anodes [4], [7], [9]. This review covers Li-ion battery technology, as the primary focus of this thesis is on advanced characterisation methods to determine degradation mechanisms, rather than developing the best battery material.

Battery energy and power densities are typically improved by manipulating the thickness of the electrode [9]. This is beyond the scope of this review, but mentioned for completeness.

Anode and cathode chemistries can be grouped depending on their redox reaction mechanisms into conversion electrodes, and intercalation electrodes [2]. Intercalation electrodes, such as graphite anodes, layered structured cathodes such as lithium nickel manganese cobalt oxide, and polyanions cathodes, such as $LiFePO_4$, and $LiCoPO_4$, can store guest ions within the lattice (eg. Li^+) [2]. In contrast, conversion electrodes, such as Si anodes, and BiF_2 cathodes, undergo a solid state redox reaction during discharge where a crystal structure change occurs, accompanied by breaking and recombination of bonds [2].

Figure 2.3 shows the potential vs. specific capacity trends for intercalation, and conversion materials. For materials with a high specific energy density, ideally a high specific capacity would be required (such as a conversion cathode and anode) [2].

Figure 2.3 demonstrates that typically anode specific capacities, in particular conversion anodes, such as Si, have higher specific capacities than most cathode materials. Part of the challenge in Li-ion battery design is load balancing, where enough active cathode mass is added to the cell to intercalate all the Li^+ released from the anode [9]. If load balancing is not achieved, the excess material adds to the weight of the cell, decreasing the specific energy and power density. Figure 2.3 demonstrates part of the challenge for lithium ion batteries is to develop higher capacity cathode materials [2], [9].

High energy densities, and in particular high power densities, require an increased potential difference between the anode and the cathode, so an intercalation cathode with a high nominal voltage, paired with a conversion anode would be useful (see Figure 2.3). To date the majority of commercialised cathode materials, such as $LiCoO_2$, and $LiFePO_4$ operate with an operating potential of 3.5- 4.0 V vs. Li/ Li^+ [2]. Therefore, to achieve a higher potential difference between the anode and cathode for high energy, and power density applications, higher redox potentials are required.

High voltage cathode materials have a number of degradation challenges, leading to low cycle life due to rapid capacity loss. This thesis, and review, focusses on characterising degradation of cathode microstructures, and determining the underlying degradation mechanisms in high voltage lithium ion cathode materials.

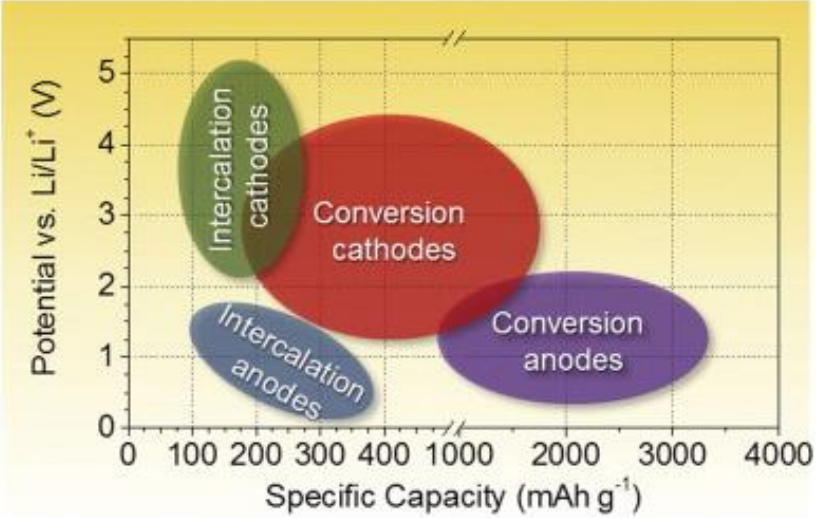

Figure 2.3: Potential vs. Li/ Li⁺ against specific capacity of intercalation, and conversion anode and cathode materials. Republished with permission from Materials Today, 18, 5 (2015) 252-264 [2]*. Copyright Elsevier.*

2.2 High Voltage Cathode Materials

The operating principle of a Li-ion battery can also be viewed in terms of an open circuit energy level diagram (see Figure 2.4) [10], [11]. Differences in the chemical potential (μ_C- cathode chemical potential, μ_A- anode chemical potential) of redox processes occurring on either side of the electrochemical cell produce a cell voltage, V_{cell} as shown in Equation 1. F is the Faraday constant.

$$V_{cell} = \frac{\mu_C - \mu_A}{F}$$

Equation 1 [12]

There is currently a drive to increase the energy density stored in Li-ion cells for high energy devices such as electric vehicles (as discussed in 2.1.1). The total stored energy (E_{stored}) is defined by the Equation 2, where Q_{cell} is the cell charge capacity and V_{cell} is the cell voltage defined in Equation 1.

$$E_{stored} = Q_{cell} \times V_{cell}$$

Equation 2 [12]

Equation 2 highlights two methods to increase the energy stored by a Li-ion cell: (1) by increasing the cell charge capacity or (2) by increasing the overall cell voltage [2], [12]. Increasing the cell charge capacity can be achieved by choosing anode and cathode materials which allow more Li to be inserted and removed on charge and discharge per mass of material. An example of using a material with a greater gravimetric capacity would be to replace graphite (carbon) anodes (372 mAh g^{-1}) with a material with a higher theoretical capacity, such as Si (3579 mAh g^{-1}) [2]. However, as stated above in 2.1.1, increasing the anode capacity would also require balancing with increased mass of cathode material. Increasing the cathode mass could decrease the gravimetric energy density of the whole cell, and increase the cost per energy as the cathode is the most expensive component [13].

Equation 1 suggests that increasing V_{cell} can be achieved by increasing the chemical potential difference between μ_C and μ_A. There is a requirement that $\mu_A > \mu_{metal}^{Li}$ in order to prevent Li plating and dangerous short circuiting of the cell leading to thermal runaway [12], hence most commercial Li-ion cells use carbonaceous materials as anodes which have an anode potential (V_{Li}^{anode}/Li^+) of ~0 V vs. Li/Li^+ [12].

Another method of increasing V_{Cell} is to increase μ_C, leading to the development of high voltage cathode materials [12], [14], where redox occurs at potentials greater than 4.5 V vs. Li/ Li^+.

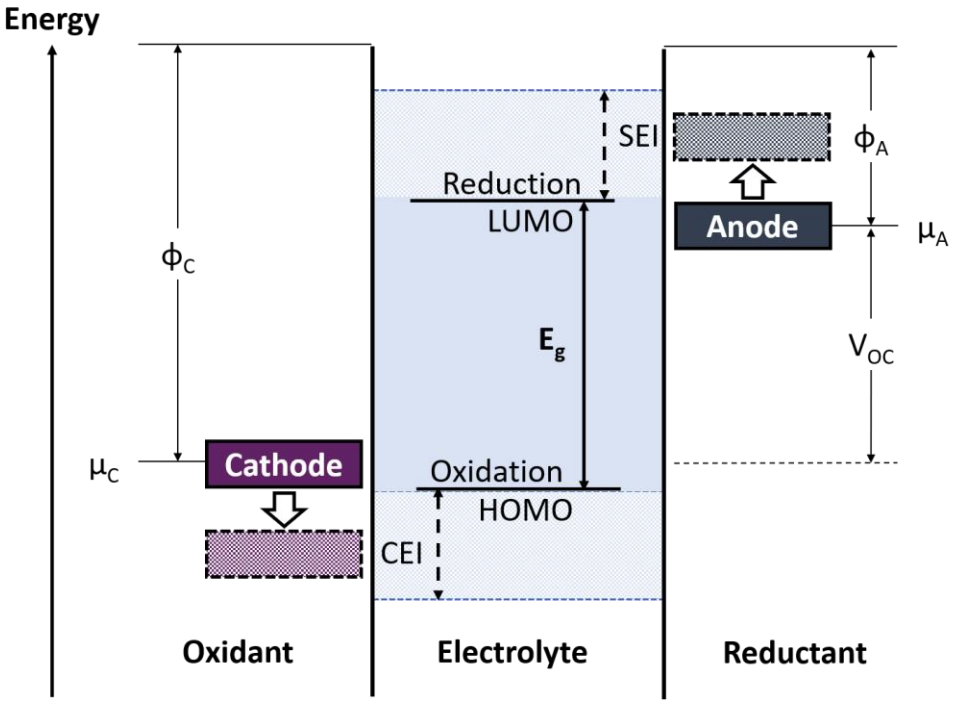

Figure 2.4: Schematic of an open-circuit energy level diagram of a Li-ion battery cell. Φ_C and Φ_A – Work functions of the cathode and anode respectively. μ_C and μ_A- electrochemical potentials of the cathode and anode respectively. LUMO- lowest unoccupied molecular orbital of the anode. HOMO- highest unoccupied molecular orbital of the cathode. E_g- electrolyte energy separation window required for thermodynamic stability of the electrolyte. V_{OC}- open circuit potential. If μ_A is greater than LUMO and μ_C is less than HOMO, reduction and oxidation of the electrolyte will occur respectively. The oxidation and reduction reactions can be kinetically stabilised if a passivation layer is formed on the electrode surfaces. The passivation layer is called the solid electrolyte interphase (SEI) at the anode and the cathode electrolyte interphase (CEI) at the cathode. Adapted with permission from Chem. Mater., 22, 3, 2010, 587-603 [10]*. Copyright 2010 the American Chemical Society.*

High voltage lithium ion battery cathodes are defined as cathodes with a nominal operating potential greater than 4.5 V vs. Li/ Li^+ [12], [15]. The 3 main classes of cathodes are defined by their crystal structure: layered oxides, spinels, and polyanion materials with the olivine structure [2], [12], [15]. One strategy of increasing the redox potential, and hence μ_C, of a cathode is to substitute the transition metal ions for ions which have higher redox potentials vs. Li/ Li^+ [15]. For example $LiFePO_4$ operates at 3.5 V vs. Li/ Li^+, whereas the redox potentials for Mn, Co, and Ni are 4.1, 4.8, and 5.1 V vs. Li/ Li^+ respectively [16]. Mn, Co, and Ni have greater filling of d-orbital states and more protons than Fe, thus the energy cost required to remove an electron from Mn, Co, and Ni is greater due to an increased force of attraction between the nucleus and the d-shell electrons resulting in a higher redox potential [16].

Although high voltage cathodes offer higher operating potentials, and hence higher energy densities, to date none have been successfully commercialised. High voltage cathodes suffer from severe degradation processes, often related to the electrolyte. Electrolyte induced dissolution of high voltage cathodes has been reported, particularly in lithium-manganese-oxide spinels [15].

Figure 2.4 shows that if the cathode operates outside of the electrolyte window, cathode electrolyte interphase (CEI) layers can begin to form [15]. CEI layers have been reported on high voltage cathode materials in $LiPF_6$ electrolytes in ethylene carbonate, and dimethyl carbonate [17]–[19]. CEI layers can act like a solid electrolyte interphase (SEI) layer (which form on anodes), and be passivating, but in cathodes they are typically reported as unstable and not passivating [17]–[19], [20].

Overall, high voltage cathode materials have promise for high energy density applications, however, they present added degradation challenges.

2.3 $LiCoPO_4$

The increased demand for high Li-ion batteries in high power, and high energy applications, such as electric vehicles, has led to the development of high voltage cathode materials [12]. $LiFePO_4$ (LFP) is an olivine-structured lithium transition –metal orthophosphate material which has been successfully commercialised due to high cycling performance, and safety characteristics, and relative cheapness [21], [22]. $LiFePO_4$ has a theoretical capacity of 170 mAh g^{-1}, however redox potential (3.45 V vs. Li/ Li^+) is comparatively low compared to other cathodes (see Figure 2.5), leading to lower gravimetric energy densities.

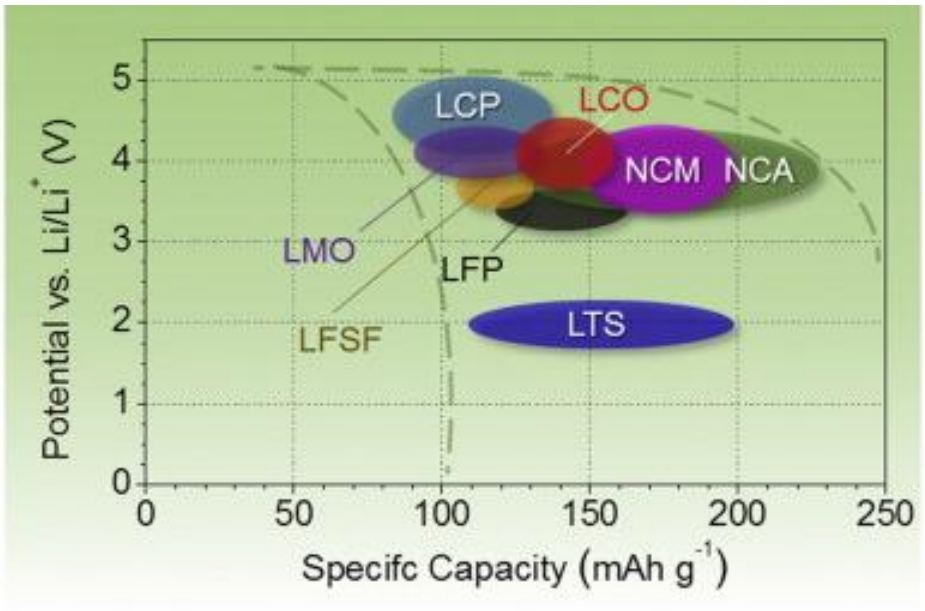

Figure 2.5: Average discharge potential vs. Li/ Li^+ verses specific capacity of different cathode materials: LCP- lithium cobalt phosphate, LMO- lithium manganese oxide, LCO- lithium cobalt oxide, NCM- nickel manganese cobalt oxide, LFSF- lithium iron fluorosulfate, LTS- lithium titanium sulphide, NCA- nickel cobalt aluminium oxide. Reprinted with permission from Materials Today, 18, 5, 2015 252-264 [2]*. Copyright 2015 Elsevier.*

For olivine materials, a method of increasing the redox potential is to change the M in $LiMPO_4$ to transition metals which have a redox couple at higher potentials (M= Mn, Co, or Ni) [14], [23].

$LiCoPO_4$ was first synthesised by Amine et al. in 2000 [24], substituting Fe for Co in the olivine crystal structure. $LiCoPO_4$ has a theoretical capacity of 167 mAh g^{-1}, and a redox potential of 4.8 V vs. Li/ Li^+ [23], [24], hence compared to $LiFePO_4$, the specific capacity is similar, but the redox potential is higher (see Figure 2.5).

Despite Co being more expensive than other transition metals [25], some research suggests the higher energy density of $LiCoPO_4$ compared with $LiFePO_4$ results in a lower cost per energy (142 vs. 158 \$ kW^{-1} hr^{-1} respectively) [26], [27], heading towards the ideal cost per energy listed in 2.1.1. It should be noted the particular research papers referenced are relatively old (2007, and 2018), and the price of Co has since increased so this may not be accurate anymore [2]. The cost per energy is mentioned as a driver for the initial development of $LiCoPO_4$. $LiCoPO_4$ was chosen to be studied in this thesis for reasons other than cost (discussed later in this section).

Figure 2.6 shows the unit cell of $LiCoPO_4$. $LiCoPO_4$ has an orthorhombic Pnma crystal structure consisting of CoO_6 octahedra, LiO_6 octrahedra, and PO_4 tetrahedra. The structure forms 1-dimensional channels Li along the [0 1 0] direction, along which Li migration occurs preferentially [28]–[30]. On de-lithiation, $LiCoPO_4$ maintains Pnma symmetry [31]–[34], in the form of $CoPO_4$ (cobalt (III) phosphate). Specific lithiation mechanisms and structure changes are discussed in detail in 2.3.1.

The $(PO_4)^{3-}$ polyanion network helps to stabilise oxygen at full charge (full de-lithiation) in $LiFePO_4$ due to the strong covalent P-O bonds, limiting O_2 release [23], [35]. However in $LiCoPO_4$ oxygen release has been reported at full charge [36], [37], although this is mitigated by the presence of carbon coatings [36].

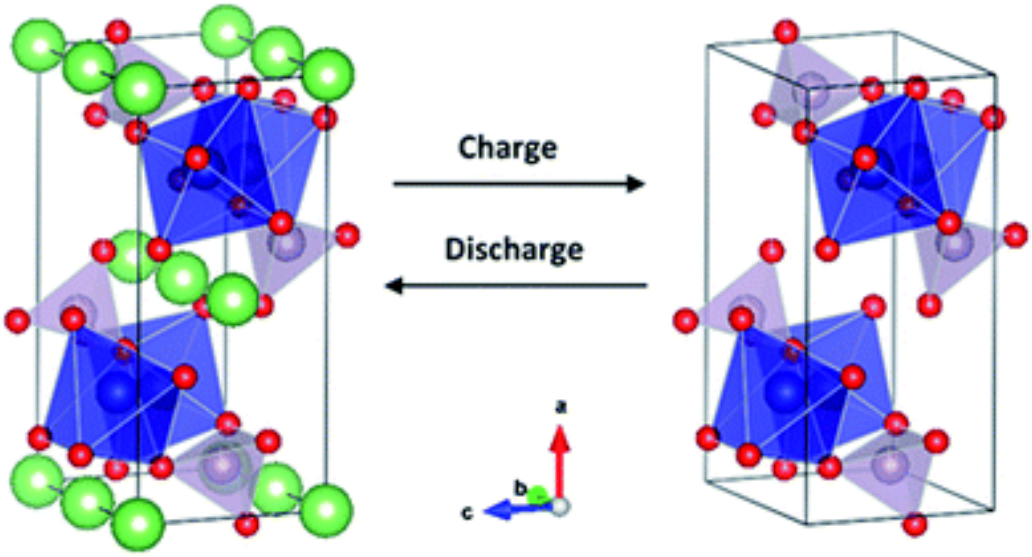

Figure 2.6: $LiCoPO_4$ unit cell (green- Li), Red- oxygen, linked to CoO_6 octahedra (blue), and PO_4 tetrahedra (purple). $CoPO_4$ maintains the Pnma structure on de-lithiation. Reproduced from J. Mater. Chem. A, 2018, 6, 14483-14517 [23] *with permission from The Royal Society of Chemistry (2018).*

Despite its initial promise, $LiCoPO_4$ suffers from a number of challenges [23], in part resulting from its crystal structure. Firstly, the corner shared CoO_6 octahedra are separated by oxygen atoms of the PO_4 tetrahedra (see Figure 2.6), hence the CoO_6 network cannot form a continuous network. Electron delocalisation is therefore difficult, resulting in poor electronic conductivity [35] (10^{-9} S

cm^{-1} [38], [39], compared with 10^{-3} S cm^{-1} for $LiCoO_2$ [23]). Other than ion doping [23], some strategies for improving the poor electronic conductivity have included carbon coating the $LiCoPO_4$ particles [38], [40], [41], and decreasing the size of the $LiCoPO_4$ particles to nm-particles [23], [40], [41].

One of the principle reasons $LiCoPO_4$ has not been commercialised is that it suffers from poor cycling stability [23], [34], [42], which is a significant hindrance given the ideal battery characteristics listed in 2.1.1. Fully de-lithiated $LiCoPO_4$ ($CoPO_4$ in Figure 2.6) is unstable as the octahedrally co-ordinated Co^{3+} is in high spin state and thus is unstable in contact with air and moisture leading $CoPO_4$ to amorphise [32], [43]. As Li migrates along the [010] direction, $LiCoPO_4$ is susceptible to defects blocking the lithiation channels, such as anti-site defects [29], [44]. The high operating voltages also leave the material vulnerable to electrolyte-electrode interface instability [19], [45]–[47]. Moreover, cracking has been previously observed in $LiCoPO_4$, allowing fresh surface to be exposed to electrolyte for further degradation [19]. The degradation, and lithiation mechanisms are discussed in full in 2.3.1, and 2.3.2.

$LiCoPO_4$ was selected as the material of interest for this thesis because it undergoes severe degradation. One of the primary aims of the thesis is to demonstrate new methods of characterising Li-ion battery materials, therefore a material which degrades so the differences between pristine, partial lifetime degradation, and 'dead' within a week or two was preferential to one which would take months of cycling to image phenomena. Moreover, as a high voltage battery material, it is likely some of the degradation imaging would be applicable to other high voltage battery materials, which are a current major research focus [12].

$LiCoPO_4$ was also chosen because material was available where the active particle size is small (to counter the poor electronic conductivity). In the chosen material the $LiCoPO_4$ particles were between 200 and 300 nm (see Chapter 3). Therefore, the $LiCoPO_4$ could fit into the *in-situ* transmission electron microscopy (TEM) holder, which forms part of the research presented in this thesis (see Chapter 7).

2.3.1 Lithiation Mechanisms and Structural Degradation

The galvanostatic charging curve of $LiCoPO_4$ contains 2 plateaus (see Figure 2.7), which have been linked to 2 phase transitions during charge by a number of research papers [31]–[34], [43], [48].

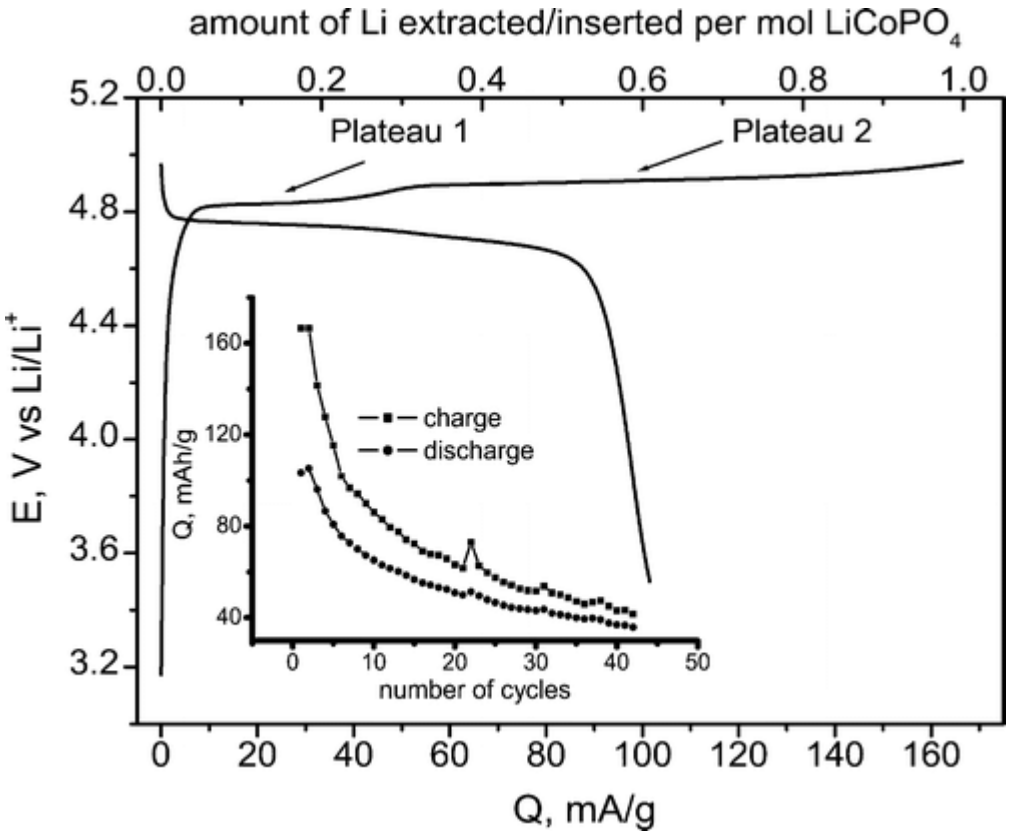

Figure 2.7: First charge and discharge galvanostatic charging profile at C/6 of a $LiCoPO_4$ cell, and (the insert) the gravimetric capacity (Q) decay on cycling. Reprinted with permission from Chem. Mater. 2007, 19, 4, 908-915 [31]. *Copyright 2007 the American Chemical Society.*

Potentiostatic, and galvanostatic intermittent titration techniques (GITT, and PITT) performed by [31] suggested the two plateaus in Figure 2.7 were likely the equilibrium potentials of two, 2-phase regions. *In-situ* neutron diffraction confirmed that $LiCoPO_4$ retains Pnma symmetry throughout charging, but the 2-pateaus result from changes in unit cell parameters (shrinking during charge), and Li content decreasing during charge [23]. The unit cell parameter changes during de-lithiation result in an overall ~7 % volume shrinkage based on XRD calculated unit cell parameters [23]. The phase regions were identified as $LiCoPO_4 \rightarrow Li_xCoPO_4$ for plateau 1, and $Li_xCoPO_4 \rightarrow CoPO_4$ for plateau 2 [31].

Most literature studies agree that the charging end phase is $CoPO_4$, with a Pnma space group [31]–[34], [43], [48]. However, as will be discussed later in this section, there is discrepancy about the identity of the end phase due to its instability [33], and X-ray absorption results which dispute complete oxidation of Co(II) in $LiCoPO_4$ to Co(III) in $CoPO_4$ [49], [50].

Considering the intermediate phase Li_xCoPO_4, an initial estimate of x in Li_xCoPO_4 used Vegard's law (the linear relationship between Li content and unit cell size), and determined x to be 0.7 [31]. However, Ehrenberg et al. suggested x to be 0.6, using neutron diffraction to calculate Li content [32]. A later study involving *ex-situ* ^{31}P, and ^{7}Li nuclear magnetic resonance imaging to investigate the local Li and P environments, along with X-ray absorption near-edge structure (XANES), and *in-situ* XRD suggested a composition of $Li_{2/3}CoPO_4$ as the mid-phase [50]. $Li_{2/3}CoPO_4$ was later confirmed using similar techniques [43]. Thus, to date the best understanding of the phase

transitions which occur upon de-lithiation of $LiCoPO_4$ is: $LiCoPO_4 \rightarrow Li_{2/3}CoPO_4 \rightarrow CoPO_4$ [33], [34], [43], [50].

Strobridge *et al.* conducted a detailed study of the structure of $Li_{2/3}CoPO_4$, and found Li was distributed around a superlattice (a x 3b x c) [43]. Li in $Li_{2/3}CoPO_4$ was distributed between two types of Li sites in the superlattice, 4 Liα sites are surrounded by 6 Co^{2+} ions, and 8 Liβ sites are surrounded by 3 Co^{2+}, and 3 Co^{3+} ions [43]. Vacancies (6 possible vacancy combinations) within the Li superlattice form a disordered superlattice leading overall to $Li_{2/3}CoPO_4$ stoichiometry [43].

Despite $CoPO_4$ being confirmed as the end phase by a number structural of studies (using neutron, and X-ray diffraction) [33], [34], [43], [50], [51], electronic structure studies using electron energy loss spectroscopy (EELS), and X-ray absorption spectroscopy (XAS) suggest Co(II) does not fully oxidise to Co(III) during charging of $LiCoPO_4$ [49], [50]. X-ray absorption spectroscopy (XAS) studies by Lapping et al. have previously found that the oxidation state of Co will not shift completely to Co(III), but residual Co(II) remains, indicated by the existence of Co(II) multiplicities on the Co L-edge XAS spectrum [49].

XAS is a bulk technique, and the studies using XAS, under Ar to prevent contamination from air, to investigate Co-edges did not determine the spatial origin of the spectra [49], [50]. Lapping et al. also used both surface sensitive XAS (total electron yield- TEY), and bulk sensitive XAS (total fluorescence yield- TFY) in their XAS studies [49]. TEY is more surface sensitive as it detects ejected photoelectrons from the X-ray absorption process, whilst TFY detects radiated photons due to fluorescence processes [49]. Lapping found using TEY XAS that the surface of charged $LiCoPO_4$ was Co(II)-rich, which may explain the lack of Co(III) signal [49]. Other studies ([19], [33], [43], [52]) suggested partial self-discharge, and spontaneous electron re-incorporation into the lattice from the electrolyte, which would result in a Co(II)-rich surface. To date nobody has spatially resolved the Co valence states in partially de-lithiated $LiCoPO_4$ to confirm if Co(III) from $CoPO_4$ forms in the centre of particles, with a Co(II) edge from either Li re-incorporation into the lattice, or electron re-incorporation.

The structure of $CoPO_4$ is unstable as Co(III) is octahedrally co-ordinated and in a high spin configuration [33], [43]. Some research papers have suggested detailed refinements when $LiCoPO_4$ is in the $CoPO_4$ state are difficult because of failure of the material to achieve long-range order [33], [43]. To date nobody has successfully synthesised $CoPO_4$ via a route other than electrochemically de-lithiating $LiCoPO_4$. Wolfenstine *et al.* attempted chemical de-lithiation, but was unsuccessful in complete de-lithiation [53]. Therefore, it is likely some Li remains intercalated in the lattice, even when the material is 'fully charged'.

The phase transition mechanism: $LiCoPO_4 \rightarrow Li_{2/3}CoPO_4 \rightarrow CoPO_4$ suggests that as Li is removed from the lattice, the $LiCoPO_4$ structure charge compensates for Li removal by increasing the oxidation state of Co. As discussed, Co XAS studies have found that across the whole sample Co(II) does not fully oxidise to Co(III). However, further studies considering the O K-edge have also noticed a pre-edge feature on XAS O K-edge spectra consistent with Co-O hybridisation [49]. O K-edge hybridisation results from O 2p hybridisation with Co 3d states due to an increase in the unoccupied density of states in the uncharged electrode above the fermi level (compared to the uncycled electrode) [49], [54]. The potential for O hybridisation suggests O is also redox active.

Lapping et al. also combined XAS studies with density functional theory (DFT) of the oxygen states, and found increased oxygen charge compensation in the charged state of $LiCoPO_4$ which suggested depletion of O at high potentials [49]. Oxygen loss has been directly imaged using HRTEM (high resolution TEM) by Ikuhara et al. [29]. Loss of oxygen induced structural deformation which could be a contributing factor to the severe capacity loss observed during cycling of $LiCoPO_4$ (see Figure 2.7 in-set). However, it is unclear if the oxygen loss is intrinsic to $LiCoPO_4$ to $CoPO_4$ structural transformation or if it results from electrolyte surface reactions.

Despite the O K-edge discrepancy and the uncertainty about complete de-lithiation of $LiCoPO_4$, the Co oxidation state changes as Li is extracted from $LiCoPO_4$. Therefore, it should be possible to track Co oxidation state changes using spectrum imaging techniques to enable spatial resolution of the oxidation states as a function of cycling and local microstructure. A study such as this may aid understanding of the formation of $CoPO_4$, and the efficacy of phase changes as a function of cycling of $LiCoPO_4$. Spatial resolution of spectrum data is discussed further in 2.4.

A second mechanism for capacity loss in $LiCoPO_4$ discussed in literature is anti-site defect formation [29], [44], [55]. Anti-site defects in $LiCoPO_4$ are Co^{3+} (in the unstable octahedrally co-ordinated state in the M2 position) moving to Li (M1) positions in the lattice, causing blockage of the 1-dimension Li^+ diffusion pathways (see Figure 2.6) [29]. Ikuhara proposed that the anti-site defect formation occurred most easily at the surface region due to greater depletion of Li at the surface [29], however, this and the $LiCoPO_4$ lithiation mechanism have yet to be confirmed.

For anti-site defects to occur near the surface, Li depletion must occur near the surface. A number of lithiation mechanisms exist in literature, however, the two dominant models for olivine materials such as $LiCoPO_4$, and $LiFePO_4$ are domino cascade, and shrinking-core [33], [34], [56], [57]. In the domino-cascade model the $LiMPO_4$- MPO_4 reaction (where M is a transition metal) occurs particle by particle rapidly, where Li is removed almost instantaneously across a single particle [33], [56]. Thus, the XRD patterns can look like a solid solution, due to $LiMPO_4$, and MPO_4 particles co-existing in a single electrode. In the shrinking-core model, Li is extracted from the edge of the particle, resulting in 2 phases within the same particle. The core is described as the Li-rich, or Li poor zone in the centre of the particle [33].

Strobridge et al. identified using *in-situ* XRD that $LiCoPO_4$ did not undergo domino cascade, but de-lithiation was more likely to proceed via a shrinking-core type model, with a coherent phase boundary between the $LiCoPO_4$ phases [33]. Palmer et al. found a similar de-lithiation mechanism, also using *in-situ* XRD, proposing $CoPO_4$ nucleates in the centre of the $LiCoPO_4$ particles (see Figure 2.8) [34].

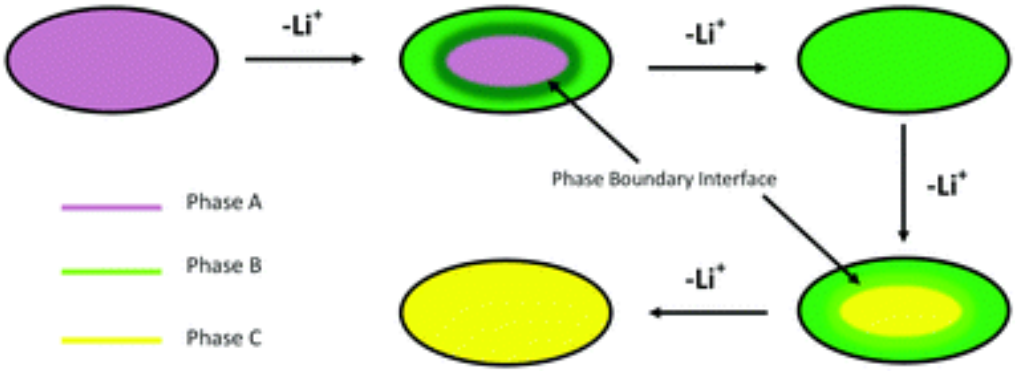

Figure 2.8: Shrinking-core de-lithiation mechanism of $LiCoPO_4$ proposed by Palmer et al. Phase A- $LiCoPO_4$, Phase B- $Li_{2/3}CoPO_4$, Phase C- $CoPO_4$. Reprinted from Chem. Commun., 2016, 52, 14169-14172 [34] *with permission from the Royal Society of Chemistry (2016).*

Neither the Strobridge study, or the Palmer study spatially resolved the phases. If $CoPO_4$ first forms in the centre of the particle, as suggested by [34], this would influence where anti-site defects are more likely to form. $LiCoPO_4$ would be subject to both electrolyte-based degradation [46] (discussed in 2.3.2) on the outside, and anti-site defect formation from within [29]. Greater understanding of the lithiation mechanisms, and phase formations would thus aid cathode designs to improve the cyclability of $LiCoPO_4$.

Overall, detailed studies on the structural degradation of $LiCoPO_4$ have been performed, but studies which spatially resolve phases enabling imaging of de-lithiation mechanisms are limited.

2.3.2 Electrolyte Induced Challenges

Surface degradation and passivation layer formation was previously a phenomenon studied in anode materials, as the redox potentials of anode materials lie above the electrolyte reduction potential for most common Li-ion battery materials [10], [11]. Recently, surface degradation and SEI/ CEI (cathode electrolyte interphase) formation has been widely reported in high voltage Li-ion batteries [17]–[19], [46], [47], [52], [58], [59] due to high voltage cathode materials operating above the electrolyte oxidation potential [11] of most standard electrolytes, such as $LiPF_6$ in ethylene carbonate and dimethyl carbonate.

Surface degradation of electrode materials and SEI/ CEI film formation can lead to battery capacity and performance loss for a number of reasons. Surface degradation can consume Li by dissolution into the electrolyte, resulting in capacity loss [46], whilst SEI formation can lead to capacity loss from Li consumption into un-mobile state, and an increase in overall cell impedance (particularly if the SEI thickens) [60]. SEI formation is typically considered a good thing in anode materials, as the layer acts as a passivation layer to further attack from the electrolyte [10]. However, if the passivation layer is unstable, either by dissolution or cracking during cycling, fresh active material can be exposed to electrolyte resulting in increased degradation [17], [59], [61], [62].

Electrolyte induced surface degradation has been previously reported for $LiCoPO_4$ using $LiPF_6$ in ethylene carbonate (EC) and dimethyl carbonate (DMC) electrolytes [46], [47], [58]. Upon de-lithiation, $LiCoPO_4$ forms the less stable $CoPO_4$ phase [33], [34], [43], [63]. Markevich et al. determined that HF formation in $LiPF_6$, formed from trace presence of water in $LiPF_6$ electrolytes [64], resulted in nucleophilic attack of F^- on the P-O bonds in the PO_4^{3-} tetrahedra of near-surface $CoPO_4$ (see Figure 2.6) via the following proposed mechanism:

$PO_4^{3-} + HF + H^+ \leftrightarrow PO_3F^{2-} + H_2O$

$PO_3F^{2-} + HF + H^+ \leftrightarrow PO_2F_2^- + H_2O$

$PO_2F_2^- + HF + H^+ \leftrightarrow POF_3 + H_2O$

POF_3 and Li salts of the fluorophosphates ions ($LiPO_2F_2$, and Li_2PO_3F) are known to be soluble in electrolyte solutions [65], resulting in mass dissolution of charged $LiCoPO_4$ [46]. Similar HF attack mechanisms have been proposed by [19], [47] for $LiCoPO_4$, and high voltage lithium nickel manganese cobalt oxide materials [18].

A second surface degradation mechanism noted in literature is spontaneous transfer of electrons from the electrolyte to the unstable octahedrally co-ordinated Co^{3+} in $CoPO_4$ [19], [33]. It is unclear if the spontaneous re-incorporation of electrons is accompanied by re-intercalation of Li on the surface of the particles or due to Co incorporation into the CEI, as some papers report detecting less Co^{3+} on the surface [19], whilst others report spontaneous self-discharge, implying Li re-incorporation into the lattice [52].

Finally, CO_2 gas formation has also been reported as a result of accumulation of electrolyte decomposition-by-products on the $LiCoPO_4$ surface, and oxidation of electrolyte solvents [52]. Gas formation has been previously reported in high voltage $LiNi_{0.5}Mn_{1.5}O_4$ [66]. Gassing can cause further degradation of electrode materials, including dissolution of metal ions, and growth of resistive SEI layers [67] (neither phenomena have been deeply studied for $LiCoPO_4$).

CEI layers have also been reported to form on $LiCoPO_4$, resulting from oxidation of electrolyte species, detected using TEM imaging [19], and electrochemical impedance studies [68]. Given the severe capacity fading which occurs on cycling in $LiCoPO_4$, it is unlikely the CEI layer is passivating [23]. [68] reported CEI formation resulted in an increased cell impedance, whilst [61] suggested dissolution of the CEI on discharge which would allow increased electrolyte attack on the surface (although dissolution was not imaged in this case). Moreover, [19] suggested the porous, and partially reactive nature of the CEI on $LiCoPO_4$ aided Co^{2+} formation by spontaneous reincorporation of electrons from the electrolyte on the surface of $LiCoPO_4$ particles.

If the CEI layer continues to thicken, increasing Li consumption can result in reduced capacity [18]. CEI thickening has been observed in $LiCoPO_4$ by post-mortem transmission electron microscopy analysis [69]. If the CEI layer becomes too thick, it can become detrimental to battery performance due to the need for lithium ions to diffuse through the layer resulting in increased cell resistance. Thickening also indicates an inability to easily stabilise the CEI layer.

A number of papers have studied the surface chemistry using techniques such as X-ray photoelectron spectroscopy (XPS) and Raman spectroscopy [19], [46], [47], [58]. Typical components found on the surface of $LiCoPO_4$ post-cycling in $LiPF_6$ in EC and DMC have included Li_2CO_3, HC-F, CF_2 [19], oxyfluorophosphates, such as PO_2F_y [46], and other organics.

To date, the structure, and morphology of the $LiCoPO_4$ CEI has not been discussed in literature. [19], [52] reported a porous CEI structure, suggesting this aided Co^{3+} reaction with the electrolyte, and self-discharge. A mosaic CEI structure has previously been proposed for lithium nickel manganese cobalt oxides (NMC) (see Figure 2.9) [18]. Multiple CEI compounds form a mosaic structure in the NMC CEI, with organic, and fluoro- phosphate compounds (similar to those found

on $LiCoPO_4$ surfaces [19], [46], [47]) on the top-surface, and metal fluoride compounds, where the CEI has reacted with the cathode, towards the cathode surface [17], [18].

The structure, and chemistry of the CEI are important because they influence the stability of the CEI, and therefore the ability of the CEI to passivate the electrode. For example, the polycarbonate, and fluoro-phosphate compounds found on the surface of the NMC CEI in Figure 2.9, are more susceptible to dissolution [65]. Similar electron Co(III) disproportionation to $LiCoPO_4$ [19] has been reported in $LiCoO_2$, however, once a stable passivating CEI forms, the disproportionation stops [70], suggesting a structural difference between the passivating layers in $LiCoPO_4$, and $LiCoO_2$.

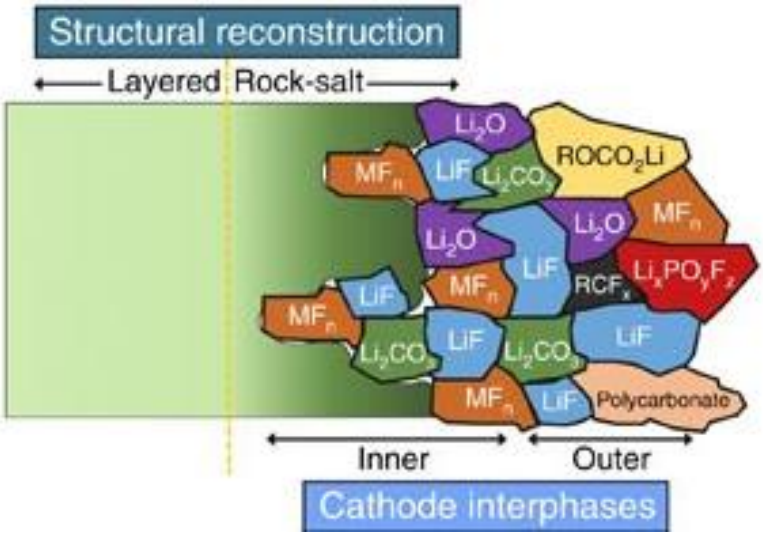

Figure 2.9: Composite mosaic CEI structure of high voltage NMC. Reprinted from Nature Communications, 8, 2017, 14589 [18] *with permission from the Nature Publishing Group (2017).*

There has also been debate on which parts of the electrode are effected by CEI formation in $LiCoPO_4$. [19] reported CEI formation on both the $LiCoPO_4$ particles, and the conductive additive, suggesting the conductive additive could influence CEI formation. However, [69] found CEI layer only on $LiCoPO_4$.

A number of strategies have been employed to improve the cyclability, and stability of $LiCoPO_4$ in the electrolyte. Some strategies have involved using different electrolyte additives which form stable CEI layers on $LiCoPO_4$ by oxidising at lower potentials [58], [69], [71]. For example, thiophene (TPN) oxidises at 4.4 V vs. Li/ Li^+, lower than the oxidation onset of $LiPF_6$ in EC/ DMC (~4.9 V vs. Li/ Li^+), hence TPN can form a passivating polymer film on $LiCoPO_4$ [71].

Most of the strategies involve increased HF scavenging. Sharabi et al. reported the use of fibre glass silica separators improved the cyclability of $LiCoPO_4$ as silica is a better HF scavenger than polypropylene [47]. Similarly, Kim et al. reported the use of HF scavenging binders, such as sodium carboxymethyl cellulose (CMC) rather than typical polyvinylidine fluoride (PVDF), aided the cyclability of $LiCoPO_4$ [72]. The influence of the binder coverage has also previously been reported to influence the surface chemistry of high voltage NMC cathodes [73].

Overall, the literature shows a detailed understanding of the chemistry, and degradation mechanisms which occur on $LiCoPO_4$ particles. However, phenomena, such as CEI layer

dissolution, has only previously been suggested to explain EIS data [61] without direct microscopy-based evidence. Moreover, the influence of electrode components on CEI formation has been alluded to [72], [73], but not previously studied in detail, likely due to difficulties imaging CEI layer morphology changes at fields of view which would allow conclusions comparing CEI formation with underlying electrode morphology to be drawn. CEI characterisation techniques are discussed in detail in 2.4.

2.4 Characterisation of Lithium Ion Battery Degradation Mechanisms

2.4.1 Need for Correlative, and Multiscale Characterisation Techniques for Lithium Ion Batteries

The move towards high voltage cathodes for high energy applications, such as electric vehicles, has required the development of materials which exhibit more complex degradation processes. Electrodes consist of a range of complex interfaces, such as conductive additive/ electrolyte, active material/ electrolyte, and active material/ binder, which can lead to different degradation mechanisms so degradation in Li-ion batteries happens in a number of different complex environments (see Figure 2.10). For example, CEI layer formation on $LiCoPO_4$ particles has been reported by Manzi et al. [19], but Kim et al. have noted the binder type can influence the stability of the CEI layer [72], therefore the proximity of the binder to the particle may influence the CEI formation.

Further complex environments exist within the entire 3D electrode array. Figure 2.10 illustrates the system complexity of two primary particles of $LiCoPO_4$. $LiCoPO_4$ electrodes consist of a 3D array of particles, primary particles, or secondary agglomerates of primary particles, electrically connected by conductive additive particles, and glued together using binder (see Figure 2.2).

So far the majority of degradation studies have used a range of different *ex-situ* techniques to study the different phenomena, usually in conjunction with electrochemical techniques [12], [19], [58], [72], [74], [75], [23], [33], [34], [44]–[47], [52], and some techniques used in $LiCoPO_4$ research are listed in Figure 2.10. Electrochemical techniques can provide quantify battery performance, as well as track changes in distinct degradation mechanisms across multiple length scales [74], [76], although other techniques are required to confirm observations.

The degradation mechanisms illustrated in Figure 2.10 have been colour coded based on the primary characterisation technique used to investigate the mechanism in the research articles referenced. The techniques have been split into categories based on the physical aspect the techniques probe: spectroscopy techniques, structural investigations, and electron-based microscopy techniques.

Spectroscopy techniques probe the local chemistry, and techniques such as X-ray photoelectron spectroscopy (XPS), Raman spectroscopy, fast-fourier transform infrared spectroscopy (FTIR), and X-ray absorption spectroscopy (XAS) have been used to probe various $LiCoPO_4$ degradation mechanisms in literature [19], [45]–[47], [52], [58], [69]. Structural investigation techniques, such as X-ray diffraction (XRD), and neutron diffraction, have been used to probe crystal structure changes such as phase change mechanisms [31], [33], [34], [43]. Microscopy techniques have been used to study morphological changes in $LiCoPO_4$, such as transmission electron microscopy (TEM) [19], or scanning electron microscopy (SEM) for CEI layer growth [58]. Other techniques, such as

secondary ion mass spectrometry [18] have also been used to probe CEI layers, however the focus of Figure 2.10 is to demonstrate the techniques used for $LiCoPO_4$ research.

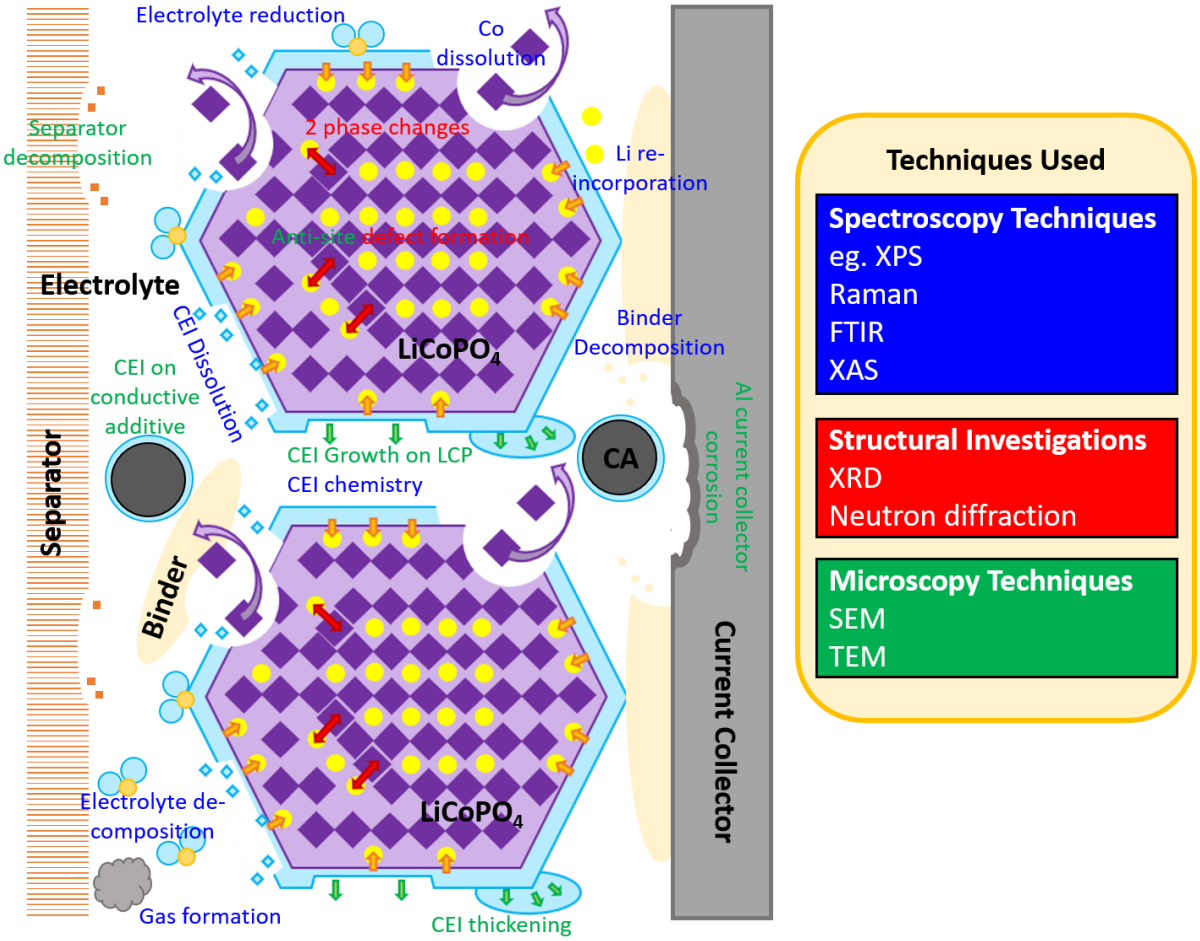

Figure 2.10: Summary of some of the degradation mechanisms of $LiCoPO_4$ reported in literature [12], [19], [58], [72], [74], [75], [23], [33], [34], [44]–[47], [52]. *The different degradation mechanisms have been colour coded based on the type of characterisation method primarily used to investigate the phenomenon in the research articles referenced. Grey circles (CA)- conductive additive. Yellow circles- Li, Purple diamonds- Co, light blue coating- CEI layer, purple hexagons- $LiCoPO_4$ particles.*

The complexity of the electrode environment makes full characterisation and understanding of the consequences of the degradation mechanisms challenging. The use of the techniques shown in Figure 2.10 can often only tell part of the story. For example, XPS has been used by a range of studies to characterise the local chemistry of CEI layers in $LiCoPO_4$ [46], [58], and SEI layers on other materials [77]–[79]. Although XPS is useful for providing information on the local chemistry, it does not provide information on the CEI morphology [79], so information on aspects such as the thickness, and porosity is missed.

Mapping of spectroscopic data can provide some information on the distribution of chemical species across the electrode [78]. However, without correlating spectroscopic date with microscopy data, the impact of morphology, and the local environment can still be difficult to define.

The complexity issue can be overcome by correlating multiple techniques looking at the same area, although re-finding a 1 µm feature on a 1 cm^2 sample can be challenging, and moving battery materials between different instruments can potentially damage features [80].

Exposure to air for $LiCoPO_4$ can be detrimental to characterisation. Malmgren et al. reported changes to both the morphology, and chemistry of SEI layers on graphite anodes [80]. Given $LiCoPO_4$ CEI layers consist of similar lithium, and fluoro-phosphate species (depending on the electrolyte) to SEI on graphite [19], [45], it is highly likely $LiCoPO_4$ CEI layers will undergo similar degradation on air exposure. The charged state phase $CoPO_4$, has also been reported to amorphise as a consequence of air exposure [33], [43]. It is therefore important to minimise air exposure, preferably to no air exposure, during characterisation.

Due to the need to understand degradation processes in next generation battery materials, and the issues caused by traditional *ex-situ* characterisation techniques, there has been a drive to develop correlative microscopies for Li-ion battery characterisation. Correlative microscopies are techniques which apply different characterisations to the same area of sample [81]–[83]. For lithium ion battery research, preferably the techniques should be contained within the same instrument to minimise sample damage [80].

Correlative microscopy has been used for a number of years in biological applications which involve complex reactions across a variety of different environments, similar to batteries [83]–[85]. Correlative microscopies have four aims: (1) identify the specific region of interest (eg. the CEI layer), (2) put the feature in the context of the larger region (eg. does the CEI form on $LiCoPO_4$ only, and does the electrode microstructure play a role), (3) identify information using different methodologies (eg. investigate CEI layer chemistry with XPS, and morphology with AFM), and (4) improve the resolution using higher resolution techniques (such as TEM) [83].

Examples of correlative microscopy for lithium ion batteries exist in literature which have correlated SEI chemistry with morphology. Lee et al. combined low acceleration voltage, extreme high resolution scanning electron microscopy, and XPS to investigate the SEI surface morphology and chemistry on graphite anodes , finding that it consisted of both dense films and fine particles [86]. Similarly, AFM and Raman spectroscopy have been combined to investigate surface layers on $LiCoO_2$ [87]. Manzi et al. investigated CEI formation using TEM, and XPS [19].

The majority of techniques used for CEI investigations have correlated imaging the CEI feature (aim (1)), with methods which can detect chemistry (aim (3)). However, for $LiCoPO_4$ CEI layers a number of key questions exist, as discussed in 2.3.2.; (1) does the CEI layer only form on $LiCoPO_4$ [19], [69], (2) does the CEI remain stable [46], [61], and (3) given potential contributions from the binder [72] and separator [45], does the electrode microstructure influence CEI layer formation.

In part, CEI layer formation questions exist because the majority of the techniques used have been constrained to certain length scales, such as TEM for nm-scale (1 $LiCoPO_4$ particle) analysis [52], or bulk surface techniques such as XPS, which don't link to phase morphology [46]. Techniques which could investigate CEI layers across multiple length scales would be beneficial, bringing in aim (2), and (4).

A similar visualisation, and length scale problem exists for lithiation mechanism studies. So far the majority of lithiation mechanism discussions for $LiCoPO_4$ have involved using *in-situ* or *ex-situ* XRD

techniques [33], [34], [43]. XRD is excellent at providing averaged structural information about the crystal, however, it is difficult to draw conclusions about the spatial distribution of the phases formed which is very important. For example, if the unstable $CoPO_4$ phase forms on the outside of $LiCoPO_4$ particles during charging, rather than nucleating on the inside, as suggested by [34] using XRD, strategies for mitigating electrolyte degradation of the $CoPO_4$ phase, reported by [43], [46], may change.

Moreover, the XRD studies [31], [33], [34], [43], and TEM studies [44], [49] do not provide information on the impact of the electrode 3D microstructure, and the relation of other components of the cell (electrolyte, binder, conductive additive, and current collector) on the primary/ secondary particle phase changes.

A problem with commonly used characterisation techniques for lithium ion batteries is that very few chemical, and morphological investigative techniques are able to observe phenomena over multiple different length scales. For example, a method of detecting anti-site defects in $LiCoPO_4$ is STEM [44], [55]. The STEM method can detect anti-site defect clustering within individual primary particles [44], however, it is more difficult to do this on larger length scales (such as electrode scale), as STEM techniques can measure features from nm-µm length scales.

As shown in Figure 2.10, the ability to correlate morphology and chemistry across multiple length scales is critical for understanding degradation mechanisms, as the electrode components produce different local environments. Currently, modelling and electrochemical characterisation techniques are capable of measuring degradation process over multiple length scales [76]. However, currently there are very few microscopy techniques capable of multi-scale, correlative microscopy using the same instrument. The ability to observe phenomena across different length scales would aid the development of future methods to prevent degradation, as it would enable further correlation with models and electrochemical techniques.

The length scale characterisation issue is further exacerbated by the difficulties detecting Li. Li is difficult to detect as most elemental spectroscopies, such as energy dispersive X-ray spectroscopy (EDS), rely on characteristic X-ray energies or inelastic scattering energies (eg. EELS). The Li K-edge occurs at 55 eV, and the low energy X-rays generated have a high absorption probability [88]. Mass spectrometries, such as secondary ion mass spectrometry (SIMS) can detect sputtered Li ions as they rely on the separation of masses for elemental detection [18], [89]. Previously SIMS has been used in SEI layer studies [18]. Given Li-ion battery chemistry is centred around Li, difficulties detecting Li creates a characterisation challenge.

This thesis specifically focusses on electron and ion microscopy characterisation methods which can aid understanding of lithiation mechanisms, and CEI layers in $LiCoPO_4$ by enabling correlating morphological, and chemical characterisation methods across different length scales. The developed methods should be able to be expanded to other materials. The following sections discuss characterisation methods currently used for characterisation of the SEI/ CEI, and lithiation/ de-lithiation mechanisms.

2.4.2 Characterisation of CEI Layers

CEI/ SEI layer morphology characterisation has typically focussed on characterisation at the nm length scale as this is the length scale of the SEI feature [79]. Theoretically, CEI layers form on all

particles, but as shown by Figure 2.10, the growth may differ across the electrode due to different environments, so visualisation of the CEI/ SEI on the µm scale would be beneficial.

Currently there are very few methods which can image CEI layers on the µm-scale, unless CEI layers are thick (~1 µm). Theoretically AFM could measure CEI layers across a wide surface area, however a long measurement time would be required, and images are impacted by the surface roughness of the electrode surface [79]. SEM is the most user accessible technique for C/SEI visualisation over multiple length scales, as SEM is a common instrument in most research facilities, and can image surfaces from the mm length scale to the nm length scale [90]. Moreover, unlike transmission electron microscopy, relatively little sample preparation is required for surface imaging [90].

A detailed discussion of the contrast mechanisms and operating principles of SEM is presented in section 4.3.1. A brief discussion is presented here to aid the literature discussion of electron microscopy as a technique for S/CEI layer characterisation.

SEM produces images by rastering an electron beam across a surface causing the incident electron beam to interact with atoms on the surface [90], and down into the sample to a depth dependent on the incident beam energy and sample material. The incident beam interactions produce secondary electrons (SE), via inelastic scattering of the incident electron beam, and secondary electrons generated near the surface (typically <20 nm depth) can escape the sample and reach a detector [90].

Contrast (C) is defined as:

$$Contrast = \frac{\Delta S}{S}$$

Where ΔS is the change in signal collected at a point in the image, and S is the maximum signal collected in the imaged area. Signal in electron microscopy images is typically measured as greyscale [90], [91]. Secondary electrons typically generate topographical contrast [90]. Backscattered electrons (BSE) can also be produced when incident electrons are scattered through high angles by coulombic interactions with atomic nuclei, and re-emerge at the surface [91]. Backscattered electrons provide compositional contrast [90], [91].

SEM secondary electron imaging has been previously used to image S/CEI layers [86], [92]–[96]. An issue with SEM imaging of the SEI layer is the surface contrast can be minimal [79], [94]–[96] due to the thinness of the surface film, particularly on cathodes the CEI layer can be very thin (0.3-4 nm for layered oxide cathodes [18], [59]). Therefore, the secondary electron SEM images can often indicate the SEI layer exists, but provide no further information on the morphology, chemistry, or location.

Several imaging strategies have been employed to circumvent the thickness issue. SEI layer images can be obtained by taking cross-sections of the electrode, using broad beam (Ar^+) ion-milling, or focussed ion beam (FIB) sectioning [79], [86], [94], [97], [98]. The cross-section technique has a particular advantage of enabling thickness measurement, and morphology observation [86]. However, the field of view is limited, and ion implantation/ sputtering has the potential to damage the surface film.

Staining using osmium tetroxide, to enhance the contrast of the organic component, has allowed µm length scale surface imaging of the SEI [92]. Staining has an advantage of enhancing the chemical composition differences of the surface of the electrode, enabling the SEI to be visualised. However, analysing the chemical composition with other techniques would be difficult post-staining.

To avoid sample damage through staining methods, previous studies have used low dosage secondary electron SEM (low voltage), in order to reduce the depth of the electron interaction volume allowing more surface sensitive imaging [86], [93]. The electron interaction volume is the volume in which electron scattering events happen within the sample [90]. Lowering the beam energy reduces the penetration depth of the incident electrons (depth of the interaction volume), increasing the surface yield of SE, and causing the images to have increased surface contrast (as shown by the monte-carlo simulations in Figure 2.11 (a-c)). The SEI produces enhanced contrast in secondary electron images when the beam voltage is lowered from 10 kV to 1 kV (Figure 2.11), however ion milling is required for SEI thickness analysis [86], and chemical characterisation is not possible in the SEM.

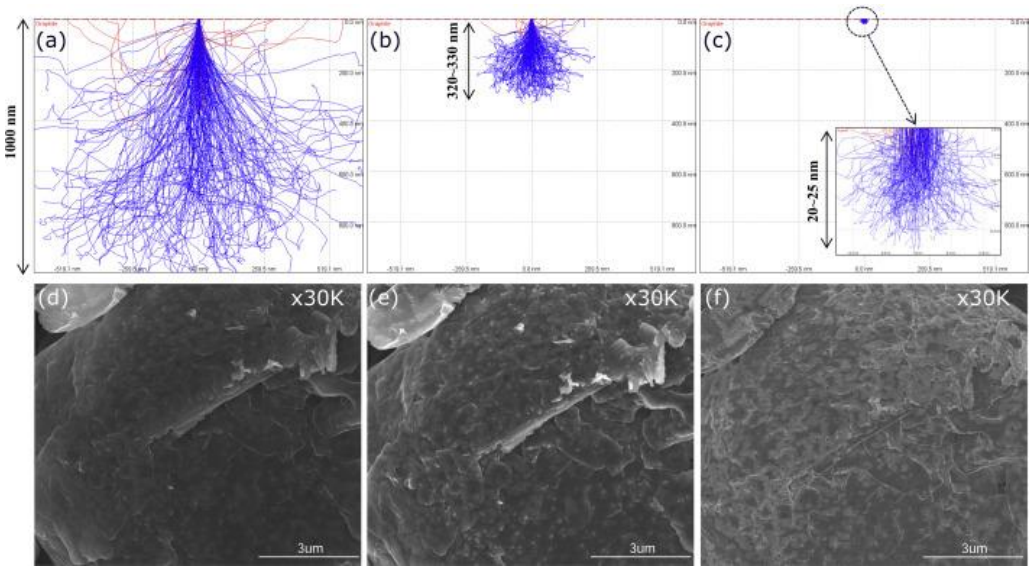

Figure 2.11: (a-c) Monte-carlo simulations of the electron interaction volume in graphite using (a) 10, (b) 5, and (c) 1 kV incident electron beams. (d-f) secondary electron images at (1) 10, (b) 5, and (c) 1 kV beam voltages of the graphite surface containing SEI layers. The SEI layer in (f) is visible by the lighter contrast. The layers are 25-30 nm thick. Reprinted with permission from J. Power Sources, 247, 2014, 307-313 [86]. *Copyright (2014) Elsevier.*

Lowering the beam voltage is a useful method of reducing the electron interaction volume, enhancing surface contrast. However, as reported by [86], lowering the beam voltage may decrease the electron dose reaching the detector, making focussing difficult. Another strategy to increase the surface sensitivity of an SEM image, which to the best of the author's knowledge has so far not been widely reported in the battery research field, is to use different SEM detectors [90], [99]. An in-lens detector (ILD) (where the secondary electron detector is positioned in the electron beam source column) collects a different angular distribution of SE compared to a typical Everhart-Thornley detector (positioned to the side of the beam source) [90]. In-lens detectors detect more 'SE1' electrons which originate from the surface interaction zone of the incident primary electrons, whereas the Everhart-Thornley detector collects both SE1 and SE2 electrons. SE2 electrons originate around the point of exit of BSE electrons, which can be some distance from

the incident beam spot, and therefore decreasing the surface resolution. A full explanation of In-lens detector vs. Everhart-Thornley detector SEM contrast is discussed in 4.3.1.

A further method to enhance the surface sensitivity of secondary electron images is to use different incident beam sources. Focussed ion beam microscopy (FIB) can produce highly surface sensitive ion-induced secondary electron (iSE) or secondary ion (iSI) images, and as a result has been widely employed in the semi-conductor industry [100], [101]. It should be noted that FIB iSE or iSI imaging may result in significant specimen damage from the incident ions compared to SEM SE imaging, dependant on ion species, energy, dose, and sample material. Figure 2.12 shows the simulated sputter yield, and implantation paths of different 30 keV ion species used in FIB microscopes. The Helium source produces the lowest sputter yield (0.01 atoms), so would produce the least sample sputtering damage in the SEI context. Figure 2.12 also shows the lateral width of the ion interaction volume at the surface (near the red line) is the smallest for He^+ ions. Therefore, the escape region for He^+ induced secondary electrons is the smallest out of the FIB ion sources, leading to the most surface sensitive imaging [102].

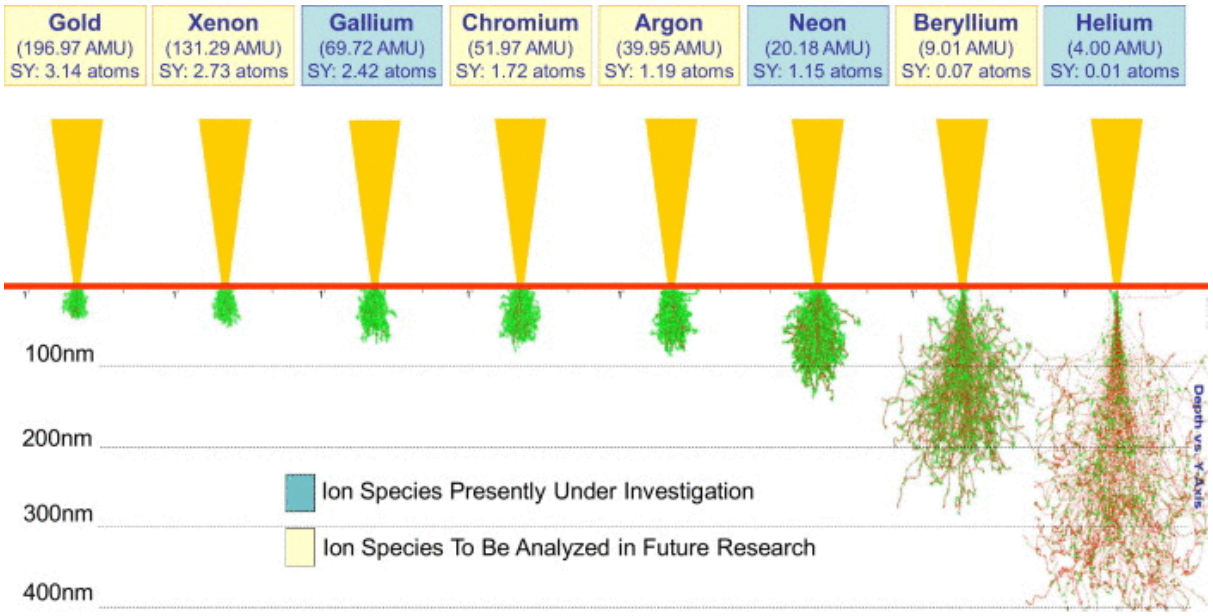

Figure 2.12: Simulated sputter yield (SY) and implantation paths of different ion sources at 30 keV beam energies. Reprinted with permission from J. Vacuum Science and Technology B, 26, 6, 2010, C6F15 [103]. *Copyright (2010) the American Vacuum Society.*

Microscopy which uses a He^+ gas field ion source for secondary electron generation is called Helium ion microscopy (HIM) [102]. Compared to SEM, the lateral width of the SE escape volume (leading to increased surface resolution), is smaller for the HIM [104]. A full discussion on the contrast mechanisms, and operational principles of HIM is in section 4.3.2. Despite its potential advantage for surface sensitive imaging, currently the He-ion microscope has not been used for C/SEI studies on battery materials.

Chemical analysis of SEI layers is difficult in the SEM as SEM relies predominantly on energy dispersive X-ray spectroscopy (EDS) for chemical analysis. EDS has a couple of disadvantages for SEI layer characterisation (1) Li is very difficult to detect with EDS due to the low K-edge absorption energy (55 eV) [88], and (2) higher beam energies (generally >10 kV) are required to excite all the X-ray lines of interest, limiting the surface sensitivity of the technique [105]. To circumvent the

EDS issue, authors often use other techniques, such as XPS, or FTIR, in combination with SEM for full characterisation of the SEI layer. As described above, transfer to different instruments risks sample damage, although new vacuum transfer chambers are recently becoming available.

Gas field ion microscopy offers the potential to use secondary ion mass spectrometry (SIMS) as a chemical characterisation technique using the gas-field ion source produced focussed ion beam as the incident beam [102], [106]–[108]. SIMS is a technique which bombards a sample with primary ions (eg. Ar^+, Ga^+, or Cs^+), sputtering secondary particles from the surface [109]. Particles which ionise during sputtering can be detected and analysed using a mass spectrometer [109].

SIMS has previously been widely used for chemical characterisation of SEI layers in lithium ion batteries, and has an advantage of being able to detect Li [18], [80], [89], [110]. Cs^+ SIMS mapping, and depth profiling (where the ion beam is used to mill through the sample whilst collecting mass spectra) has generated 3-dimensional chemical imaging of nickel-rich layered titanium oxide. The technique offers multi-scale chemical mapping of the electrode, however imaging morphology can be difficult as historically SIMS instruments have had high current sources which have not been optimised for focussed ion beam imaging.

It should be noted that unlike XPS or FTIR, SIMS does not offer information on bonding states, and hence is limited to elemental mapping [79]. This is a disadvantage of the SIMS technique as the chemical bonding states within SEI layers can provide information about whether the layer is an organic layer formed on the surface, or if it is causing destruction to the sub-surface electrode [79].

Combining FIB microscopy with SIMS offers interesting prospects for surface sensitive, imaging combined with chemical composition mapping. The earliest FIB machines all used Ga^+ ion sources and enabled the first FIB-SEM analysis. Sui *et al.* [111] mapped the lithium distribution in charged NMC electrodes using a gallium ion source FIB-SEM with an installed TOF-SIMS system.

Figure 2.12 illustrates that He^+ ions are likely to produce the most surface sensitive imaging of current gas-field ion microscopy systems, however for effective SIMS analysis the ion yield can be too low and other ion sources may be more effective (see Chapter 4). Recently SIMS systems have been added to He-ion microscopes to enable chemical characterisation in the HIM using Ne^+-ions [106], [107], [112], [113]. For battery research a HIM SIMS set-up has produced high resolution lithium maps of lithium titanate [113], however, so far there is no reported literature on SEI layer studies in the HIM.

Overall, the complex environment of a lithium ion electrode, and the potential for sample damage when transferring samples for correlative imaging, demonstrates a need for a technique capable of imaging SEI layers at multiple scales which can correlate *in-situ* the images with chemical characterisation. A HIM SIMS set-up offers prospects for both multiscale imaging and chemical characterisation. However, as SIMS is a mass spectrometry technique, the chemical correlation would be limited to ion fragment mapping (elemental mapping) rather than a detailed map of the bonding states provided by complementary techniques such as FTIR, or XPS.

2.4.3 Characterisation of Lithiation Mechanisms

For $LiCoPO_4$ research to date, the majority of research into lithiation mechanisms has involved XRD for phase analysis [31]–[34], [43], XAS [49], [50], and NMR [33], [43], [50] for electronic

structure analysis, and S/TEM [29], [44], and detailed XRD refinements [51] for crystal structure defect analysis. Apart from S/TEM, the majority of the techniques used have been 'bulk' analysis techniques, where the phases, or electronic structure features have not been spatially resolved.

Non-spatially resolved XAS studies on the Co K-edge, and L-edge by [49], [50] suggest Co(II) does not oxidise completely to Co(III). However, XRD studies by [31]–[34], [48] shows the $CoPO_4$ phase nucleates in $Li_{2/3}CoPO_4$ particles, with [34] suggesting the nucleation of $CoPO_4$ occurs at the centre of the particle. A spatially resolved study would aid understanding in this area.

Spatially resolved studies have proved invaluable for understanding the de/lithiation mechanisms in $LiFePO_4$. Initially, the shrinking-core model was used to describe the de/lithiation mechanisms of $LiFePO_4$ based on electrochemical results, in combination with *in-situ* XRD [114]–[116], proposing that a core of $LiFePO_4$ forms as Li exits the particle. However, phase mapping using TEM showed the analysed particles were all either $LiFePO_4$, or $FePO_4$, suggesting a domino-cascade de/lithiation model [57].

A few methods exist for spatially resolving phases within active material particles. Scanning Transmission X-ray microscopy in combination with fluorescence yield XAS can spatially resolve oxidation states [117]. Electron microscopy techniques have also previously been used for spatial mapping of phases in $LiFePO_4$. The electron microscopy techniques can be split into spectral techniques, where mapping is performed based on chemical information from energy spectra, such as electron energy loss spectroscopy (EELS) [118], [119], or energy filtered TEM (EFTEM) [119], [120], or diffraction based techniques, such as automated crystal orientation mapping (ACOM)-TEM [57], [119]. Spectrum imaging (a spectra collected at each pixel), allows 2-Dimensional mapping of spectroscopic data [118], [119] (see Figure 2.13).

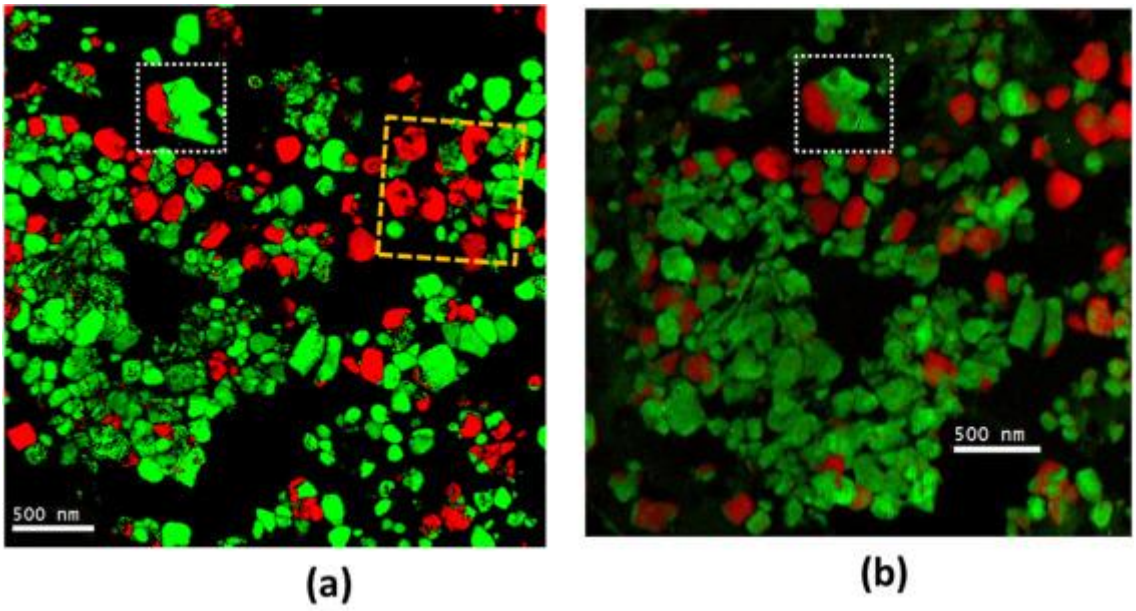

Figure 2.13: Comparison between an ACOM-TEM phase map of $LiFePO_4$ (green), and $FePO_4$ (red) (a), and an EFTEM-spectrum image of the Fe-$L_{3,2}$ edge (b). Reprinted with permission from Ultramicroscopy, 170, 2016, 10-18 [119]. *Copyright (2016) Elsevier.*

EFTEM spectrum collection uses a parallel beam, whilst EELS collection typically uses a convergent beam in scanning transmission electron microscopy mode (STEM). To generate spectra in EFTEM,

the energy-selecting slit is moved by an energy ΔE until the whole required energy range is collected. In STEM-EELS the beam scans across the sample, collecting spectra at each pixel [120]. EFTEM is beneficial as the collected signal can be less noisy than EELS. However, EFTEM data collection is subject to more data artefacts than EELS, such as dark current drift, ghosting on the CCD, spatial drift, and energy drift, which will affect the acquired spectra [120]. Moreover, specimen thickness can cause issues with both EFTEM, and EELS data acquisition due to increased likelihood of multiple inelastic scattering events and electron absorption, with EFTEM imaging being more effected by thickness than EELS [119].

ACOM diffraction mapping is less affected by thickness, but data acquisition currently takes longer (eg. 45 mins for ACOM, compared with 13 mins for Li-K edge, and Fe-M edge EFTEM [119]). Given Li-ion battery materials are susceptible to electron beam damage (discussed in detail in 7.2.2) the potential for high electron beam dosages from long acquisition times could be detrimental.

In 2.4.1 the need for multi-scale imaging, in combination with correlative microscopy, and spectroscopy was discussed. Recently, techniques have been developed which are capable of characterising features across different length scales. X-ray computed tomography (XCT) has been combined with XRD to provide phase analysis throughout the 3D network of an electrode [121]. Energy dispersive X-ray spectroscopy (EDS) in cross-sectional SEM has been combined with XCT to observe chemical changes throughout the electrode [122]. However, XCT has a lower resolution for sub-micron features than S/TEM techniques, so drawing conclusions about intra-particle phases is difficult.

TEM sample preparation, and the requirement that TEM samples must be < 1 μm thick to be electron transparent, can limit understanding of the position of analysed particles within the electrode, compared to XCT methods. A common method of TEM Li-ion battery sample preparation is to scrape electrode particles from the electrode directly onto the TEM support grid [119], [120]. This limits air exposure sample damage, as sample preparation can be performed in a glove box, however, the particles are no longer in their original positions in the electrode. Moreover, particle thickness can cause issues with EFTEM and EELS due the thickness effect on plural scattering, particularly in the centre of particles.

[119], [120] used ultramicrotomy to preserve the position of particles in the electrode during S/TEM analyses. Ultramicrotomy is a specimen preparation technique which uses a sharp blade to cut ultra-thin slices of a sample. The benefits of mechanically sectioning the sample are that specimen thickness uniformity is improved, and the original position of electrode particles within the electrode is preserved for TEM imaging. Therefore, conclusions can be drawn about the position of the particles relative to the current collector, aiding understanding of the impact of local environment. However, ultramicrotomy specimens may exhibit mechanical deformation. Additionally, a large limitation of imaging in the TEM is that only 2-Dimensional projection imaging can be produced, without TEM tomography (imaging at multiple tilt angles) which can require large electron doses [123] potentially damaging the active material.

Overall, S/TEM based spectroscopies show promise for correlating chemistry with morphology in lithium-ion battery materials. The techniques have been used extensively for $LiFePO_4$, but have not so far been used for $LiCoPO_4$. A portion of the thesis focusses on STEM-EELS for $LiCoPO_4$. A further literature review discussing the technique is presented in 5.2.

2.4.4 *In-situ* Techniques for Li-ion Battery Characterisation

So far only *ex-situ* techniques have been discussed, where samples are removed from cells and then characterised post-mortem. The *ex-situ* approach creates a number of problems (1) exposure of electrodes to air, or other atmospheres, may cause changes to the surface, valence states, and interfacial reactions [80], [124], and (2) batteries are dynamic systems, so by studying systems *ex-situ* detailed structural changes and intermediate stages of charge and discharge can be lost. For example, metastable phases have been observed during the de-lithiation of $LiFePO_4$ using *in-operando* XRD, which have not been previously observed using *ex-situ* techniques [125], [126].

Moving away towards *in-situ/ in-operando* techniques for characterisation is important for correlating theoretical models with electrochemical technique observations [76], aiming to evaluate dynamic processes in much more detail than the current state-of-the-art.

Alternatives to *ex-situ* techniques are *in-situ*, or *in-operando* techniques [124], [127]. *In-situ* techniques describe techniques 'in the natural or original position or place' [124]; for example, this would entail characterising $LiCoPO_4$ in the presence of electrolyte. *In-operando* implies the material is behaving as it would in the device [124]; for a battery this would require charging and discharging of the material in a half or full-cell configuration [128], [129].

For $LiCoPO_4$ studies specifically, there have been a few *in-operando* studies considering the lithiation mechanisms using XRD or operating cells, but minimal *in-operando* studies to evaluate CEI layer formation and electrolyte degradation. The majority of the *in-operando* de-lithiation mechanism studies have employed *in-operando* X-ray diffraction [31], [33], [34], [43], [50]. I*n-situ* XAS has also been used for lithiation mechanism studies [50]. The *in-operando* XRD studies have enabled observation of the intermediate $Li_{2/3}CoPO_4$ phase [31], [33], [34], [43], [50] which may be more difficult to observe using *ex-situ* techniques given the partial self-discharge reported by [52]. *In-situ* XAS results have enabled observation of incomplete oxidation of Co [50], indicating the electrode is not completely charging during the charge cycle, and similar to *ex-situ* XAS results [49].

So far none of the *in-operando* studies on the de-lithiation mechanisms of $LiCoPO_4$ have allowed spatial resolution of the results as they have employed bulk techniques, such as XRD, or XAS [31], [33], [34], [43], [50]. As stated above in 2.4.3 a lack of spatial resolution risks incomplete understanding of the mechanism.

A few *in-operando* techniques exist which can spatially resolve phases during charge and discharge. Synchrotron *in-operando* liquid fluorescence yield X-ray microscopy, in combination with fluorescence yield XAS has been used to spatially resolve the oxidation state changes of Fe in $LiFePO_4$ to enable spatial mapping of the charged and discharged states of $LiFePO_4$ [117]. Spatial resolution enabled the differences in the lithiation mechanisms of ellipsoidal, and platelet nano particles to be observed [117]. Open cell *In-situ* TEM has also allowed spatial resolution of the phases, as well as the development of mid phases during lithiation of spinel Fe_2O_4 [130].

So far the studies on electrolyte induced degradation of $LiCoPO_4$ have employed *ex-situ* techniques [19], [45], [52], [58]. *Ex-situ* studies risk not observing the nature of the instability of the electrolyte/ electrode interface and CEI layer, suggested by [46], [61]. Moreover, the S/CEI layer on battery materials in general is known to be sensitive to atmosphere change which occurs

on removal from the cell, particularly if air exposure occurs [80]. Consequently, *in-situ* or *in-operando* characterisation of the S/CEI layer would be beneficial.

A number of different techniques have been employed in literature to observe SEI formation *in-situ*. SEI growth has previously been observed using sealed liquid cell *in-situ* TEM [131], [132], and liquid cell *in-situ* SEM [133].

As high voltage battery materials, such as $LiCoPO_4$, undergo degradation both within the material, and as a result of exposure to unstable electrolytes at high voltages [19], [44], [46], [59], a technique which can observe changes in both regions of interest would be beneficial. *In-situ* TEM is unique as it has previously been used for both SEI growth formation studies [131], [132], and for structural change studies of electrode particles during charge and discharge [130]. *In-situ* TEM is able to make use of the many structural and chemical imaging modes of S/TEM microscopes to provide local information on SEI, and structural change mechanisms, as the mechanisms occur on the nanoscale.

So far the review has discussed the benefits of *in-situ* and *in-operando* techniques for Li-ion battery research. However, there are a number of challenges, unique to each technique, involved in collecting the data, setting up an *in-situ*, or *in-operando* cell, and being able to correlate the results to a cell in normal operation [124]. Many challenges exist in particular for *in-situ* TEM, where the significant size limitation of specimens, and high energy incident electron beam, can cause significant deviations from representative battery environments. This thesis focusses on the development of an *in-situ* liquid TEM technique for Li-ion battery research (Chapter 7). The full review on the development of *in-situ* TEM techniques, and the challenges associated with the techniques is presented in section 7.2.

2.5 SUMMARY

Overall, a number of challenges exist for the use of $LiCoPO_4$ cathodes in Li-ion batteries, due to microstructural changes during use which result in severe degradation of $LiCoPO_4$. The challenges include understanding of the phases which form during cycling, and the interplay of electrolyte degradation and the intrinsic $LiCoPO_4$ degradation mechanisms resulting from an unstable charged state. These challenges are enhanced by the use of $LiCoPO_4$ in complex electrode environments, which change the reaction conditions across the whole electrode.

To date, most studies have considered a small portion of electrodes, such as single particles, or bulk surface studies, without considering the underlying heterogeneous electrode microstructures. This is likely due to a lack of techniques for studying degradation of electrodes at different length-scales (eg. multiple fields of view in a microscope), whilst correlating chemical, and structural changes. Moreover, lithium ion battery reaction mechanisms are time-dependent, so all characterisation ideally needs to be carried out at different states of charge and cycle number.

Therefore, there is room for the development of new characterisation techniques which can meet these challenges. This thesis aims to demonstrate this by using $LiCoPO_4$ as the material of interest to prove new insights can be made with novel techniques. The specific techniques developed in the thesis are He-ion microscopy and *in-situ* HIM-SIMS for CEI layer detection, STEM-EELS to study the lithiation mechanisms of $LiCoPO_4$, and the development of an *in-operando* TEM technique.

As discussed in 2.4.2 He-ion microscopy is highly surface sensitive, high resolution imaging technique, and in this thesis it will be combined with SIMS, a chemical characterisation technique which can detect Li. Despite the advantages for CEI layer characterisation HIM-SIMS could provide, to date no detailed study of CEI formation has been performed using a HIM-SIMS instrument.

STEM-EELS has previously been used to successfully map the Fe(II), and Fe(III) regions of $LiFePO_4$ to aid understanding of the de-lithiation mechanisms [118], [119]. No detailed study de-lithiation study for $LiCoPO_4$ has been performed using the STEM EELS techniques, so this thesis presents an adaptation of the LFP STEM-EELS technique. Microtoming has also been investigated as a method to improve knowledge of the original location of analysed particles and hence understanding of the local environment on de-lithiation, and to improve the resolution of the STEM-EELS mapping.

Both the HIM SIMS and STEM-EELS techniques provide *ex-situ* analysis of cathodes. *In-operando* studies offer major benefits reducing sample damage, and allowing intermediate changes to be observed. Therefore, an *in-operando* TEM technique was also developed.

2.6 REFERENCES

[1] J. B. Goodenough, "Changing Outlook for Rechargeable Batteries," *ACS Catalysis*, vol. 7, no. 2. American Chemical Society, pp. 1132–1135, 2017.

[2] N. Nitta, F. X. Wu, J. T. Lee, and G. Yushin, "Li-ion battery materials: present and future," *Mater. Today*, vol. 18, no. 5, pp. 252–264, 2015.

[3] J. B. Goodenough and K. S. Park, "The Li-ion rechargeable battery: A perspective," *Journal of the American Chemical Society*, vol. 135, no. 4. American Chemical Society, pp. 1167–1176, 2013.

[4] A. Manthiram, "A reflection on lithium-ion battery cathode chemistry," *Nature Communications*, vol. 11, no. 1. Nature Research, pp. 1–9, 2020.

[5] D. Deng, "Li-ion batteries: basics, progress, and challenges," *Energy Sci. Eng.*, vol. 3, no. 5, pp. 385–418, 2015.

[6] A. Kraytsberg and Y. Ein-Eli, "Conveying Advanced Li-ion Battery Materials into Practice the Impact of Electrode Slurry Preparation Skills," *Adv. Energy Mater.*, vol. 6, no. 21 2016.

[7] "High-energy battery technologies," Faraday Institution, 2020.

[8] MIT Electric Vehicle Team, "A Guide to Understanding Battery Specifications." [Online]. Available: https://web.mit.edu/evt/summary_battery_specifications.pdf. [Accessed: 27-Apr-2020].

[9] M. Ue, K. Sakaushi, and K. Uosaki, "Basic knowledge in battery research bridging the gap between academia and industry," *Mater. Horizons*, 2020.

[10] J. B. Goodenough and Y. Kim, "Challenges for Rechargeable Li Batteries," *Chem. Mater.*, vol. 22, no. 3, pp. 587–603, 2010.

[11] P. Peljo and H. H. Girault, "Electrochemical potential window of battery electrolytes: The HOMO-LUMO misconception," *Energy Environ. Sci.*, vol. 11, no. 9, pp. 2306–2309, 2018.

[12] A. Kraytsberg and Y. Ein-Eli, "Higher, Stronger, Better… A Review of 5 Volt Cathode Materials for Advanced Lithium-Ion Batteries," *Adv. Energy Mater.*, vol. 2, no. 8, pp. 922–939, Aug. 2012.

[13] "UK electric vehicle and battery production potential to 2040," Faraday Institution, 2020.

[14] C. Liu, Z. G. Neale, and G. Cao, "Understanding electrochemical potentials of cathode materials in rechargeable batteries," *Materials Today*, vol. 19, no. 2. Elsevier B.V., pp. 109–123, 2016.

[15] M. Hu, X. Pang, and Z. Zhou, "Review Recent progress in high-voltage lithium ion batteries," *Journal of Power Sources*, vol. 237. pp. 229–242, 2013.

[16] F. Zhou, M. Cococcioni, K. Kang, and G. Ceder, "The Li intercalation potential of $LiMPO_4$ and $LiMSiO_4$ olivines with M = Fe, Mn, Co, Ni," *Electrochem. commun.*, vol. 6, no. 11, pp. 1144–1148, 2004.

[17] E. M. Erickson, W. Li, A. Dolocan, and A. Manthiram, "Insights into the Cathode–Electrolyte Interphases of High-Energy-Density Cathodes in Lithium-Ion Batteries," *ACS Appl. Mater. Interfaces*, vol. 12, no. 14, 2020.

[18] W. Li, A. Dolocan, P. Oh, H. Celio, S. Park, J. Cho, and A. Manthiram, "Dynamic behaviour of interphases and its implication on high-energy-density cathode materials in lithium-ion batteries," *Nat. Commun.*, vol. 8, p. 14589, 2017.

[19] J. Manzi and S. Brutti, "Surface chemistry on $LiCoPO_4$ electrodes in lithium cells: SEI formation and self-discharge," *Electrochim. Acta*, vol. 222, pp. 1839–1846, 2016.

[20] E. M. Erickson, E. Markevich, G. Salitra, D. Sharon, D. Hirshberg, E. de la Llave, I. Shterenberg, A. Rosenman, A. Frimer, and D. Aurbach, "Review-Development of Advanced Rechargeable Batteries: A Continuous Challenge in the Choice of Suitable Electrolyte Solutions," *J. Electrochem. Soc.*, vol. 162, no. 14, pp. A2424–A2438, 2015.

[21] J. Wang and X. Sun, "Olivine $LiFePO_4$: The remaining challenges for future energy storage," *Energy and Environmental Science*, vol. 8, no. 4. Royal Society of Chemistry, pp. 1110–1138, 2015.

[22] Z. Bi, X. Zhang, W. He, D. Min, and W. Zhang, "Recent advances in $LiFePO_4$ nanoparticles with different morphology for high-performance lithium-ion batteries," *RSC Advances*, vol. 3, no. 43, pp. 19744–19751, 2013.

[23] M. Zhang, N. Garcia-Araez, and A. L. Hector, "Understanding and development of olivine $LiCoPO_4$ cathode materials for lithium-ion batteries," *J. Mater. Chem A,* vol. 6, no. 30, pp. 14483-14517, *2018*.

[24] K. Amine, H. Yasuda, and M. Yamachi, "Olivine $LiCoPO_4$ as 4.8 V electrode material for lithium batteries," *Electrochem. Solid-State Lett.*, vol. 3, no. 4, pp. 178–179, 2000.

[25] "London Metal Exchange: Home." [Online]. Available: https://www.lme.com/. [Accessed: 26-Apr-2020].

[26] W. F. Howard and R. M. Spotnitz, "Theoretical evaluation of high-energy lithium metal phosphate cathode materials in Li-ion batteries," *J. Power Sources*, vol. 165, no. 2, pp. 887–891, 2007.

[27] D. Liu, W. Zhu, C. Kim, M. Cho, A. Guerfi, S. A. Delp, J. L. Allen, T. R. Jow, and K. Zaghib, "High-energy lithium-ion battery using substituted $LiCoPO_4$: From coin type to 1 Ah cell," *J. Power Sources*, vol. 388, pp. 52–56, 2018.

[28] D. Morgan, A. Van der Ven, and G. Ceder, "Li Conductivity in Li_xMPO_4 (M = Mn, Fe, Co, Ni) Olivine Materials," *Electrochem. Solid-State Lett.*, vol. 7, no. 2, p. A30, 2004.

[29] Y. H. Ikuhara, X. Gao, C. A. J. Fisher, A. Kuwabara, H. Moriwake, K. Kohama, H. Iba, and Y. Ikuhara, "Atomic level changes during capacity fade in highly oriented thin films of cathode material $LiCoPO_4$," *J. Mater. Chem. A*, vol. 5, no. 19, pp. 9329–9338, 2017.

[30] C. A. J. Fisher, V. M. H. Prieto, and M. S. Islam, "Lithium battery materials $LiMPO_4$ (M = Mn, Fe, Co, and Ni): Insights into defect association, transport mechanisms, and doping behavior," *Chem. Mater.*, vol. 20, no. 18, pp. 5907–5915, 2008.

[31] N. N. Bramnik, K. Nikolowski, C. Baehtz, K. G. Bramnik, and H. Ehrenberg, "Phase transitions occurring upon lithium insertion-extraction of $LiCoPO_4$," *Chem. Mater.*, vol. 19, no. 4, pp. 908–915, 2007.

[32] H. Ehrenberg, N. N. Bramnik, A. Senyshyn, and H. Fuess, "Crystal and magnetic structures of electrochemically delithiated $Li_{1-x}CoPO_4$ phases," *Solid State Sci.*, vol. 11, no. 1, pp. 18–23, 2009.

[33] F. C. Strobridge, H. Liu, M. Leskes, O. J. Borkiewicz, K. M. Wiaderek, P. J. Chupas, K. W. Chapman, and C. P. Grey, "Unraveling the Complex Delithiation Mechanisms of Olivine-Type Cathode Materials, $LiFe_xCo_{1-x}PO_4$," *Chem. Mater.*, vol. 28, no. 11, pp. 3676–3690, 2016.

[34] M. G. Palmer, J. T. Frith, A. L. Hector, A. W. Lodge, J. R. Owen, C. Nicklin, and J. Rawle, "In situ phase behaviour of a high capacity $LiCoPO_4$ electrode during constant or pulsed charge of a lithium cell," *Chem. Commun. Chem. Commun*, vol. 52, no. 52, pp. 14169–14172, 2016.

[35] J. Wang and X. Sun, "Understanding and recent development of carbon coating on $LiFePO_4$ cathode materials for lithium-ion batteries," *Energy and Environmental Science*, vol. 5, no. 1. Royal Society of Chemistry, pp. 5163–5185, 2012.

[36] S. Theil, M. Fleischhammer, P. Axmann, and M. Wohlfahrt-Mehrens, "Experimental investigations on the electrochemical and thermal behaviour of $LiCoPO_4$-based cathode," *J. Power Sources*, vol. 222, pp. 72–78, 2013.

[37] N. N. Bramnik, K. Nikolowski, D. M. Trots, and H. Ehrenberg, "Thermal stability of $LiCoPO_4$ cathodes," *Electrochem. Solid-State Lett.*, vol. 11, no. 6, p. A89, 2008.

[38] J. Wolfenstine, J. Read, and J. L. Allen, "Effect of carbon on the electronic conductivity and discharge capacity $LiCoPO_4$," *J. Power Sources*, vol. 163, no. 2, pp. 1070–1073, 2007.

[39] J. Wolfenstine, U. Lee, B. Poese, and J. L. Allen, "Effect of oxygen partial pressure on the discharge capacity of $LiCoPO_4$," *J. Power Sources*, vol. 144, no. 1, pp. 226–230, 2005.

[40] M. Prabu, S. Selvasekarapandian, M. V. Reddy, and B. V. R. Chowdari, "Impedance studies on the 5-V cathode material, $LiCoPO_4$," *J. Solid State Electrochemistry*, 2012, vol. 16, no. 5, pp. 1833–1839, 2012.

[41] J. M. Lloris, C. Pérez Vicente, and J. L. Tirado, "Improvement of the electrochemical performance of $LiCoPO_4$ 5 V material using a novel synthesis procedure," *Electrochem. Solid-State Lett.*, vol. 5, no. 10, p. A234, 2002.

[42] F. Wang, J. Yang, Y. Nuli, and J. Wang, "Novel hedgehog-like 5 V $LiCoPO_4$ positive electrode material for rechargeable lithium battery," *J. Power Sources*, vol. 196, no. 10, pp. 4806–4810, 2011.

[43] F. C. Strobridge, R. J. Clément, M. Leskes, D. S. Middlemiss, O. J. Borkiewicz, K. M. Wiaderek, K. W. Chapman, P. J. Chupas, and C. P. Grey, "Identifying the Structure of the

Intermediate, $Li_{2/3}CoPO_4$, Formed during Electrochemical Cycling of $LiCoPO_4$," *Chem. Mater.*, vol. 26, no. 21, pp. 6193–6205, 2014.

[44] A. Boulineau and T. Gutel, "Revealing Electrochemically Induced Antisite Defects in $LiCoPO_4$: Evolution upon Cycling," *Chem. Mater.*, vol. 27, no. 3, pp. 802–807, 2015.

[45] R. Sharabi, E. Markevich, V. Borgel, F. Salitra, D. Aurbach, G. Semrau, M. A. Schmidt, N. Schall, and C. Stinner, "Significantly improved cycling performance of $LiCoPO_4$ cathodes," *Electrochem. commun.*, vol. 13, no. 8, pp. 800–802, 2011.

[46] E. Markevich, R. Sharabi, H. Gotttlieb, V. Borgel, K. Fridman, G. Salitra, D. Aurbach, G. Semrau, M. A. Schmidt, N. Schall, and C. Bruenig, "Reasons for capacity fading of $LiCoPO_4$ cathodes in $LiPF_6$ containing electrolyte solutions," *Electrochem. commun.*, vol. 15, no. 1, pp. 22–25, 2012.

[47] R. Sharabi, E. Markevich, V. Borgel, G. Salitra, G. Gershinsky, D. Aurbach, G. Semrau, M. A. Schmidt, N. Schall, and C. Stinner, "Raman study of structural stability of $LiCoPO_4$ cathodes in $LiPF_6$ containing electrolytes," *J. Power Sources*, vol. 203, pp. 109–114, 2012.

[48] N. Bramnik, K. Bramnik, T. Buhrmester, C. Baehtz, H. Ehrenberg, and H. Fuess, "Electrochemical and structural study of LiCoPO4-based electrodes," *J. Solid State Electrochem.*, vol. 8, no. 8, pp. 558–564, 2004.

[49] J. G. Lapping, S. A. Delp, J. L. Allen, J. L. Allen, J. W. Freeland, M. D. Johannes, L. Hu, D. T. Tran, T. R. Jow, and J. Cabana, "Changes in Electronic Structure upon Li Deintercalation from $LiCoPO_4$ Derivatives," *Chem. Mater.*, vol. 30, no. 6, pp. 1898–1906, 2018.

[50] M. Kaus, I. Issac, R. Heinzmann, S. Doyle, S. Mangold, H. Hahn, V. S. K. Chakravadhanula, C. Kübel, H. Ehrenberg, and S. Indris, "Electrochemical delithiation/relithiation of $LiCoPO_4$: A two-step reaction mechanism investigated by in situ X-ray diffraction, in situ X-ray absorption spectroscopy, and ex situ $^{7}Li/^{31}P$ NMR spectroscopy," *J. Phys. Chem. C*, vol. 118, no. 31, pp. 17279–17290, 2014.

[51] S. Brutti, J. Manzi, D. Meggiolaro, F. M. Vitucci, F. Trequattrini, A. Paolone, and O. Palumbo, "Interplay between local structure and transport properties in iron-doped $LiCoPO_4$ olivines," *J. Mater. Chem. A*, vol. 5, no. 27, pp. 14020–14030, 2017.

[52] J. Manzi, F. M. Vitucci, A. Paolone, F. Trequattrini, D. Di Lecce, S. Panero, and S. Brutti, "Analysis of the self-discharge process in $LiCoPO_4$ electrodes: bulks," *Electrochim. Acta*, vol. 179, pp. 604–610, 2015.

[53] J. Wolfenstine, B. Poese, and J. L. Allen, "Chemical oxidation of $LiCoPO_4$," *J. Power Sources*, vol. 138, no. 1–2, pp. 281–282, 2004.

[54] J. Suntivich, W. T. Hong, Y-L. Lee, J. M. Rondinelli, W. Yang, J. B. Goodenough, B. Dabrowski, J. W. Freelang, and Y. Shao-Horn, "Estimating hybridization of transition metal and oxygen states in perovskites from O K-edge X-ray absorption spectroscopy," *J. Phys. Chem. C*, vol. 118, no. 4, pp. 1856–1863, 2014.

[55] Q. D. Truong, M. K. Devaraju, T. Tomai, and I. Honma, "Direct Observation of Antisite Defects in $LiCoPO_4$ Cathode Materials by Annular Dark- and Bright-Field Electron Microscopy," *ACS Appl. Mater. Interfaces*, vol. 5, no. 20, pp. 9926–9932, 2013.

[56] C. Delmas, M. Maccario, L. Croguennec, F. Le Cras, and F. Weill, "Lithium deintercalation in $LiFePO_4$ nanoparticles via a domino-cascade model," *Nat. Mater.*, vol. 7, no. 8, pp. 665–671, 2008.

[57] G. Brunetti, D. Robert, P. Bayle-Guillemaud, J. L. Rouvière, E. F. Rauch, J. F. Martin, J. F. Colin, F. Bertin, and C. Caryron, "Confirmation of the domino-cascade model by $LiFePO_4/FePO_4$ precession electron diffraction," *Chem. Mater.*, vol. 23, no. 20, pp. 4515–4524, 2011.

[58] E. Markevich, G. Salitra, K. Fridman, R. Sharabi, G. Gershinsky, A. Garsuch, G. Semrau, M. A. Schmidt, and D. Aurbach, "Fluoroethylene Carbonate as an Important Component in Electrolyte Solutions for High-Voltage Lithium Batteries: Role of Surface Chemistry on the Cathode," *Langmuir*, vol. 30, no. 25, pp. 7414–7424, 2014.

[59] W. Li, B. Song, and A. Manthiram, "High-voltage positive electrode materials for lithium-ion batteries," *Chemical Society Reviews*, vol. 46, no. 10. Royal Society of Chemistry, pp. 3006–3059, 2017.

[60] M. M. Kabir and D. E. Demirocak, "Degradation mechanisms in Li-ion batteries: a state-of-the-art review," *Int. J. Energy Res.*, vol. 41, no. 14, pp. 1963–1986, 2017.

[61] N. Okita, K. Kisu, E. Iwama, Y. Sakai, Y. Lim, Y. Takami, M. T. Sougrati, T. Brousse, P. Rozier, P. Simon, W. Naoi, and K. Naoi, "Stabilizing the Structure of $LiCoPO_4$ Nanocrystals via Addition of Fe^{3+}: Formation of Fe^{3+} Surface Layer, Creation of Diffusion-Enhancing Vacancies, and Enabling High-Voltage Battery Operation," *Chem. Mater.*, vol. 30, no. 19, pp. 6675–6683, 2018.

[62] A. Mukhopadhyay and B. W. Sheldon, "Deformation and stress in electrode materials for Li-ion batteries," *Progress in Materials Science*, vol. 63., pp. 58–116, 2014.

[63] N. N. Bramnik, K. G. Bramnik, C. Baehtz, and H. Ehrenberg, "Study of the effect of different synthesis routes on Li extraction-insertion from $LiCoPO_4$.", *J. Power Sources*, vol. 145, no. 1, pp. 74-81, 2005.

[64] S. F. Lux, I. T. Lucas, E. Pollak, S. Passerini, M. Winter, and R. Kostecki, "The mechanism of HF formation in $LiPF_6$ based organic carbonate electrolytes," *Electrochem. commun.*, vol. 14, no. 1, pp. 47–50, 2012.

[65] A. V. Plakhotnyk, L. Ernst, and R. Schmutzler, "Hydrolysis in the system $LiPF_6$ - Propylene carbonate - Dimethyl carbonate - H_2O," *J. Fluor. Chem.*, vol. 126, no. 1, pp. 27–31, 2005.

[66] B. Michalak, H. Sommer, D. Mannes, A. Kaestner, T. Brezesinski, and J. Janek, "Gas Evolution in Operating Lithium-Ion Batteries Studied in Situ by Neutron Imaging," *Sci. Rep.*, vol. 5, pp. 15627, 2015.

[67] S. S. Zhang, "Insight into the Gassing Problem of Li-ion Battery," *Front. Energy Res.*, vol. 2, p. 59, 2014.

[68] L. Dimesso, C. Spanheimer, D. Becker, and W. Jaegermann, "Properties of $LiCoPO_4$-non-graphitic carbon foam composites," *J. Eur. Ceram. Soc.*, vol. 34, no. 4, pp. 933–941, 2014.

[69] Y. Wang, H. Ming, J. Qiu, Z. Yu, M. Li, S. Zhang, and Y. Yang, "Improving cycling performance of $LiCoPO_4$ cathode material by adding tris(trimethylsilyl) borate as electrolyte additive," *J. Electroanal. Chem.*, vol. 802, pp. 8–14, 2017.

[70] E. Markevich, G. Salitra, and D. Aurbach, "Influence of the PVdF binder on the stability of $LiCoO_2$ electrodes," *Electrochem. commun.*, vol. 7, no. 12, pp. 1298–1304, 2005.

[71] L. Y. Xing, M. Hu, Q. Tang, J. P. Wei, X. Qin, and Z. Zhou, "Improved cyclic performances of $LiCoPO_4$/C cathode materials for high-cell-potential lithium-ion batteries with thiophene as an electrolyte additive," *Electrochim. Acta*, vol. 59, pp. 172–178, 2012.

[72] E. J. Kim, X. Yue, J. T. S. Irvine, and A. R. Armstrong, "Improved electrochemical performance of $LiCoPO_4$ using eco-friendly aqueous binders," *J. Power Sources,* vol. 403, pp. 11-19, 2018.

[73] J. Fondard, E. Irisarri, C. Courrèges, M. R. Palacin, A. Ponrouch, and R. Dedryvère, "SEI Composition on Hard Carbon in Na-ion Batteries After Long Cycling: Influence of Salts ($NaPF_6$, NaTFSI) and Additives (FEC, DMCF)," *J. Electrochem. Soc.*, vol. 167, no. 7, p. 070526, 2020.

[74] C. Pastor-Fernández, K. Uddin, G. H. Chouchelamane, W. D. Widanage, and J. Marco, "A Comparison between Electrochemical Impedance Spectroscopy and Incremental Capacity-Differential Voltage as Li-ion Diagnostic Techniques to Identify and Quantify the Effects of Degradation Modes within Battery Management Systems," *J. Power Sources*, vol. 360, pp. 301–318, 2017.

[75] X. Zhang, J. Zhu, and E. Sahraei, "Degradation of battery separators under charge-discharge cycles," *RSC Adv.*, vol. 7, no. 88, pp. 56099–56107, 2017.

[76] A. Wang, S. Kadam, H. Li, S. Shi, and Y. Qi, "Review on modeling of the anode solid electrolyte interphase (SEI) for lithium-ion batteries," *npj Computational Materials*, vol. 4, no. 1., pp. 1–26, 2018.

[77] V. Shutthanandan, M. Nandasiri, J. Zheng, M. H. Engelhard, W. Xu, S. Thevuthasan, and V. Murugesan, "Applications of XPS in the characterization of Battery materials," *J. of Electron Spectroscopy and Related Phenomena*, vol. 231, pp. 2–10, 2019.

[78] R. Grissa, V. Fernandez, N. Fairley, J. Hamon, N. Stephant, J. Rolland, R. Bouchet, M. Lecuyer, M. Deschamps, D. Guyomard, and P. Moreau, "XPS and SEM-EDX Study of Electrolyte Nature Effect on Li Electrode in Lithium Metal Batteries," *ACS Appl. Energy Mater.*, vol. 1, no. 10, pp. 5694–5702, 2018.

[79] X.-B. Cheng, R. Zhang, C.-Z. Zhao, F. Wei, J.-G. Zhang, and Q. Zhang, "A Review of Solid Electrolyte Interphases on Lithium Metal Anode," *Adv. Sci.*, vol. 3, no. 3, p. 1500213, 2016.

[80] S. Malmgren, K. Ciosek, R. Lindblad, S. Plogmaker, J. Kühn, H. Rensmo, K. Erdström, and M. Hahlin, "Consequences of air exposure on the lithiated graphite SEI," *Electrochim. Acta*, vol. 105, pp. 83–91, 2013.

[81] R. Moroni, M. Börner, L. Zielke, M. Schroeder, S. Nowak, M. Winter, I. Manke, R. Zengerle, and S. Thiele, "Multi-Scale Correlative Tomography of a Li-Ion Battery Composite Cathode," *Sci. Rep.*, vol. 6, no. 1, pp. 1–9, Jul. 2016.

[82] J. Wu, M. Fenech, R. F. Webster, R. D. Tilley, and N. Sharma, "Electron microscopy and its role in advanced lithium-ion battery research," *Sustainable Energy and Fuels*, vol. 3, no. 7, pp. 1623–1646, 2019.

[83] J. Caplan, M. Niethammer, R. M. Taylor, and K. J. Czymmek, "The power of correlative microscopy: Multi-modal, multi-scale, multi-dimensional," *Current Opinion in Structural Biology*, vol. 21, no. 5, pp. 686–693, 2011.

[84] A. A. Mironov and G. V. Beznoussenko, "Correlative microscopy: A potent tool for the study of rare or unique cellular and tissue events," *Journal of Microscopy*, vol. 235, no. 3. pp. 308–321, 2009.

[85] T. Cao, C. Zach, S. Modla, D. Powell, K. Czymmek, and M. Niethammer, "Multi-modal registration for correlative microscopy using image analogies," *Med. Image Anal.*, vol. 18,

no. 6, pp. 914–926, 2014.

[86] S. H. Lee, H. G. You, K. S. Han, J. Kim, I. H. Jung, and J. H. Song, “A new approach to surface properties of solid electrolyte interphase on a graphite negative electrode,” *J. Power Sources*, vol. 247, pp. 307–313, 2014.

[87] “Analyzing Li-ion Batteries Using Combined AFM and Raman Microscopy.” [Online]. Available: https://www.azonano.com/article.aspx?ArticleID=3053. [Accessed: 17-Apr-2020].

[88] P. Hovington, V. Timoshevskii, S. Burgess, H. Demers, P. Statham, R. Gauvin, and K. Zaghib, “Can we detect Li K X-ray in lithium compounds using energy dispersive spectroscopy?,” *Scanning*, vol. 38, no. 6, pp. 571–578, 2016.

[89] I. V. Veryovkin, C. E. Tripa, A. V. Zinovev, S. V. Baryshev, Y. Li, and D. P. Abraham, “TOF SIMS characterization of SEI layer on battery electrodes,” *Nucl. Instruments Methods Phys. Res. Sect. B Beam Interact. with Mater. Atoms*, vol. 332, pp. 368–372, 2014.

[90] M. Suga, S. Asahina, Y. Sakuda, H. Kazumori, H. Nishiyama, T. Nokuo, V. Alfredsson, T. Kjellman, S. M. Stevens, H. S. Cho, M. Cho, L. Han, S. Che, M. W. Anderson, F. Schüth, H. Deng, O. M. Yaghi, Z. Liu, H. Y. Jeong, A. Stein, K. Sakamoto, R. Ryoo, and O. Terasaki, “Recent progress in scanning electron microscopy for the characterization of fine structural details of nano materials,” *Progress in Solid State Chemistry*, vol. 42, no. 1–2, pp. 1–21, 2014.

[91] E. L. Joseph Goldstein, Dale Newbury, Patrick Echlin, David C. Joy, Alton D. Romig Jr., Charles E. Lyman, and Charles Fiori, *Scanning Electron Microscopy and X-Ray Microanalysis: A Text for Biologists, Materials Scientists, and Geologists*, Second Edi. New York: Plenum Press, 1992.

[92] M. Zier, F. Scheiba, S. Oswald, J. Thomas, D. Goers, T. Scherer, M. Klose, H. Ehrenberg, and J. Eckert, “Lithium dendrite and solid electrolyte interphase investigation using OsO_4,” *J. Power Sources*, vol. 266, pp. 198–207, 2014.

[93] J. T. Lee, N. Nitta, J. Benson, A. Magasinski, T. F. Fuller, and G. Yushin, “Comparative study of the solid electrolyte interphase on graphite in full Li-ion battery cells using X-ray photoelectron spectroscopy, secondary ion mass spectrometry, and electron microscopy,” *Carbon N. Y.*, vol. 52, pp. 388–397, 2013.

[94] S. Bhattacharya, A. R. Riahi, and A. T. Alpas, “Thermal cycling induced capacity enhancement of graphite anodes in lithium-ion cells,” *Carbon N. Y.*, vol. 67, pp. 592–606, 2014.

[95] N. L. Hamidah, F. M. Wang, and G. Nugroho, “The understanding of solid electrolyte interface (SEI) formation and mechanism as the effect of flouro-o-phenylenedimaleimaide (F-MI) additive on lithium-ion battery,” *Surf. Interface Anal.*, vol. 51, no. 3, pp. 345–352, 2019.

[96] C. K. Chan, R. Ruffo, S. S. Hong, and Y. Cui, “Surface chemistry and morphology of the solid electrolyte interphase on silicon nanowire lithium-ion battery anodes,” *J. Power Sources*, vol. 189, no. 2, pp. 1132–1140, 2009.

[97] N. Pavlin, S. Hribernik, G. Kapun, S. D. Talian, C. Njel, R. Dedryvère, and R. Dominko, “The Role of Cellulose Based Separator in Lithium Sulfur Batteries,” *J. Electrochem. Soc.*, vol. 166, no. 3, pp. A5237–A5243, Dec. 2019.

[98] R. Pathak, K. Chen, A. Gurung, K. M. Reza, B. Bahrami, J. Pokharel, A. Baniya, W. He, F.

Wu, Y. Zhou, K. Xu, and Q. Qiao, “Fluorinated hybrid solid-electrolyte-interphase for dendrite-free lithium deposition,” *Nat. Commun.*, vol. 11, no. 1, pp. 1–10, 2020.

[99] B. J. Griffin, “A comparison of conventional Everhart-Thornley style and in-lens secondary electron detectors-a further variable in scanning electron microscopy,” *Scanning*, vol. 33, no. 3, pp. 162–173, 2011.

[100] R. H. Livengood, Y. Greenzweig, T. Liang, and M. Grumski, “Helium ion microscope invasiveness and imaging study for semiconductor applications,” *J. Vac. Sci. Technol. B Microelectron. Nanom. Struct.*, vol. 25, no. 6, pp. 2547–2552, 2007.

[101] L. E. Ocola, C. Rue, and D. Maas, “High-resolution direct-write patterning using focused ion beams,” *MRS Bull.*, vol. 39, no. 4, pp. 336–341, 2014.

[102] T. Wirtz, O. De Castro, J.-N. Audinot, and P. Philipp, “Imaging and Analytics on the Helium Ion Microscope,” *Annu. Rev. Anal. Chem.*, vol. 12, no. 1, pp. 523–543, 2019.

[103] S. Tan, R. Livengood, D. Shima, J. Notte, and S. McVey, “Gas field ion source and liquid metal ion source charged particle material interaction study for semiconductor nanomachining applications,” *J. Vac. Sci. Technol. B, Nanotechnol. Microelectron. Mater. Process. Meas. Phenom.*, vol. 28, no. 6, p. C6F15-C6F21, 2010.

[104] M. T. Postek, A. Vladár, C. Archie, and B. Ming, “Review of current progress in nanometrology with the helium ion microscope,” *Measurement Science and Technology*, vol. 22, no. 2, 2011.

[105] P. Burdet, S. A. Croxall, and P. A. Midgley, “Enhanced quantification for 3D SEM-EDS: Using the full set of available X-ray lines,” *Ultramicroscopy*, vol. 148, pp. 158–167, 2015.

[106] N. Klingner, R. Heller, G. Hlawacek, J. von Borany, J. Notte, J. Huang, and S. Facsko, “Nanometer scale elemental analysis in the helium ion microscope using time of flight spectrometry,” *Ultramicroscopy*, vol. 162, pp. 91–97, 2016.

[107] N. Klingner, R. Heller, G. Hlawacek, S. Facsko, and J. von Borany, “Time-of-flight secondary ion mass spectrometry in the helium ion microscope,” *Ultramicroscopy*, vol. 198, pp. 10–17, 2019.

[108] B. Song, T. Sui, S. Ying, L. Li, L. Lu, and A. M. Korsunsky, “Nano-structural changes in Li-ion battery cathodes during cycling revealed by FIB-SEM serial sectioning tomography,” *J. Mater. Chem. A*, vol. 3, no. 35, pp. 18171–18179, 2015.

[109] Schwarz S.A., “Secondary Ion Mass Spectroscopy,” in *Encyclopedia of Materials: Science and Technology*, 2nd ed., Elsevier, 2001, pp. 8283–8290.

[110] H. Ota, T. Akai, H. Namita, S. Yamaguchi, and M. Nomura, “XAFS and TOF-SIMS analysis of SEI layers on electrodes,” *J. Power Sources*, vol. 119–121, pp. 567–571, 2003.

[111] T. Sui, B. Song, J. Dluhos, L. Lu, and A. M. Korsunsky, “Nanoscale chemical mapping of Li-ion battery cathode material by FIB-SEM and TOF-SIMS multi-modal microscopy,” *Nano Energy*, vol. 17, pp. 254–260, 2015.

[112] T. Wirtz, N. Vanhove, L. Pillatsch, D. Dowsett, S. Sijbrandij, and J. Notte, “Towards secondary ion mass spectrometry on the helium ion microscope: An experimental and simulation based feasibility study with He^+ and Ne^+ bombardment,” *Appl. Phys. Lett.*, vol. 101, no. 4, p. 041601, 2012.

[113] D. Dowsett and T. Wirtz, “Co-Registered In Situ Secondary Electron and Mass Spectral Imaging on the Helium Ion Microscope Demonstrated Using Lithium Titanate and

Magnesium Oxide Nanoparticles," *Anal. Chem.*, vol. 89, no. 17, pp. 8957–8965, 2017.

[114] H. C. Shin, K. Y. Chung, W. S. Min, D. J. Byun, H. Jang, and B. W. Cho, "Asymmetry between charge and discharge during high rate cycling in $LiFePO_4$ - In Situ X-ray diffraction study," *Electrochem. commun.*, vol. 10, no. 4, pp. 536–540, 2008.

[115] V. Srinivasan and J. Newman, "Existence of path-dependence in the $LiFePO_4$ electrode," *Electrochem. Solid-State Lett.*, vol. 9, no. 3, p. A110, 2006.

[116] A. K. Padhi, K. S. Nanjundaswamy, and J. B. Goodenough, "Phospho-olivines as Positive-Electrode Materials for Rechargeable Lithium Batteries," *J. Electrochem. Soc.*, vol. 144, no. 4, p. 1188, 1997.

[117] Y. Li, J. N. Weker, W. E. Gent, D. N. Mueller, J. Lim, D. A. Cogswell, T. Tyliszczak, and W. C. Chueh, "Dichotomy in the Lithiation Pathway of Ellipsoidal and Platelet $LiFePO_4$ Particles Revealed through Nanoscale Operando State-of-Charge Imaging," *Adv. Funct. Mater.*, vol. 25, no. 24, pp. 3677–3687, 2015.

[118] Y. Honda *et al.*, "Microscopic mechanism of path-dependence on charge–discharge history in lithium iron phosphate cathode analysis using scanning transmission electron microscopy and electron energy-loss spectroscopy spectral imaging," *J. Power Sources*, vol. 291, pp. 85–94, 2015.

[119] X. Mu, S. Muto, K. Tatsumi, H. Kondo, K. Horibuchi, T. Kobayashi, and T. Sasaki, "Comprehensive analysis of TEM methods for $LiFePO_4$/$FePO_4$ phase mapping: spectroscopic techniques (EFTEM, STEM-EELS) and STEM diffraction techniques (ACOM-TEM)," *Ultramicroscopy*, vol. 170, pp. 10–18, 2016.

[120] J. D. Sugar, F. El Gabaly, W. C. Chueh, K. R. Fenton, R. Tyliszczak, P. G. Kotula, and N. C. Bartelt, "High-resolution chemical analysis on cycled LiFePO4 battery electrodes using energy-filtered transmission electron microscopy," *J. Power Sources*, vol. 246, pp. 512–521, 2014.

[121] D. P. Finegan, A. Vamvakeros, L. Cao, C. Tan, T. M. M. Heenan, S. R. Daemi, S. D. M. Jacques, A. M. Beale, M. Di Michiel, K. Smith, D. J. L. Brett, P. R. Shearing, and C. Ban, "Spatially Resolving Lithiation in Silicon-Graphite Composite Electrodes via in Situ High-Energy X-ray Diffraction Computed Tomography," *Nano Lett.*, vol. 19, no. 6, pp. 3811–3820, 2019.

[122] A. Poozhikunnath, J. Favata, B. Ahmadi, J. Xiong, L. Bonville, S. Shahbazmohamadi, J. Jankovic, and R. Maric, "Correlative Microscopy-Based Approach for Analyzing Microscopic Impurities in Carbon Black for Lithium-Ion Battery Applications," *J. Electrochem. Soc.*, vol. 166, no. 14, pp. A3335–A3341, 2019.

[123] P. Ercius, O. Alaidi, M. J. Rames, and G. Ren, "Electron Tomography: A Three-Dimensional Analytic Tool for Hard and Soft Materials Research," *Advanced Materials*, vol. 27, no. 38. Wiley-VCH Verlag, pp. 5638–5663, 2015.

[124] D. Liu, Z. Shadike, R. Lin, K. Qian, H. Li, K. Li, S. Wang, Q. Yu, M. Liu, S. Ganapathy, X. Qin, Q-H. Yang, M. Wagemaker, F. Kang, X-Q. Yang, and B. Li, "Review of Recent Development of In Situ/Operando Characterization Techniques for Lithium Battery Research," *Advanced Materials*, vol. 31, no. 28. Wiley-VCH Verlag, p. 1806620, 2019.

[125] Y. Orikasa, Y. Gogyo, H. Yamashige, M. Katayama, K. Chen, T. Mori, K. Yamamoto, T. Masese, Y. Inada, T. Ohta, Z. Siroma, S. Kato, H. Kinoshita, H. Arai, Z. Ogumi, and Y. Uchimoto, "Ionic Conduction in Lithium Ion Battery Composite Electrode Governs Cross-

sectional Reaction Distribution," *Sci. Rep.*, vol. 6, no. 1, p. 26382, 2016.

[126] Y. Koyama, T. Uyama, Y. Orikasa, T. Naka, H. Komatsu, K. Shimoda, H. Murayama, J. Fukuda, H. Arai, E. Matsubara, Y. Uchimoto, and Z. Ogumi, "Hidden Two-Step Phase Transition and Competing Reaction Pathways in $LiFePO_4$," *Chem. Mater.*, vol. 29, no. 7, pp. 2855–2863, 2017.

[127] P. Harks, F. M. Mulder, and P. H. L. Notten, "In situ methods for Li-ion battery research: A review of recent developments," *J. Power Sources*, vol. 288, pp. 92–105, 2015.

[128] W. R. Brant, D. Li, Q. Gu, and S. Schmid, "Comparative analysis of ex-situ and operando X-ray diffraction experiments for lithium insertion materials," *J. Power Sources*, vol. 302, pp. 126–134, 2016.

[129] F. Rosciano, M. Holzapfel, H. Kaiser, W. Scheifele, P. Ruch, M. Hahn, R. Kötz, and P. Novák, "A multi-sample automatic system for in situ electrochemical X-ray diffraction synchrotron measurements," *J. Synchrotron Radiat.*, vol. 14, no. 6, pp. 487–491, 2007.

[130] T. Shang, Y. Wen, D. Xiao, L. Gu, Y.-S. Hu, and H. Li, "Atomic-Scale Monitoring of Electrode Materials in Lithium-Ion Batteries using In Situ Transmission Electron Microscopy," *Adv. Energy Mater.*, vol. 7, no. 23, p. 1700709, 2017.

[131] Z. Zeng, W.-I. Liang, H.-G. Liao, H. L. Xin, Y.-H. Chu, and H. Zheng, "Visualization of Electrode–Electrolyte Interfaces in $LiPF_6$ /EC/DEC Electrolyte for Lithium Ion Batteries via in Situ TEM," *Nano Lett.*, vol. 14, no. 4, pp. 1745–1750, 2014.

[132] R. R. Unocic, X-G. Sun, R. L. Sacci, L. A. Adamczyk, D. H. Alsem, S. Dai, N. J. Dudney, and K. L. More, "Direct Visualization of Solid Electrolyte Interphase Formation in Lithium-Ion Batteries with In Situ Electrochemical Transmission Electron Microscopy," *Microsc. Microanal.*, vol. 20, no. 4, pp. 1029–1037, 2014.

[133] M. Golozar, A. Paolella, H. Demers, S. Bessette, M. Lagacé, P. Bouchard, A. Guerfi, R. Gauvin, and K. Zaghib, "In situ observation of solid electrolyte interphase evolution in a lithium metal battery," *Commun. Chem.*, vol. 2, no. 1, pp. 1–9, 2019.

3 EXPERIMENTAL: MANUFACTURE OF ELECTRODES AND CELLS

3.1 MATERIAL CHOICE

3.1.1 Electrode Materials

Carbon coated $LiCoPO_4$ (C-$LiCoPO_4$) was used as the active material in this work. The C-$LiCoPO_4$ powder (Johnson Matthey) consisted of 200- 300 nm $LiCoPO_4$ particles (as measured by SEM and TEM), with an amorphous carbon coating. The carbon coating was 3-8 nm thick (as measured by TEM). $LiCoPO_4$ is often coated with carbon to increase the electrical conductivity of $LiCoPO_4$ electrodes and to act as a barrier to further electrolyte degradation [1], [2].

Nano particle C-$LiCoPO_4$ was chosen for two reasons, (1) nano-sized particles helps improve electrical conductivity [1], and (2) the *in-situ* TEM holder, used in this thesis, had a maximum particle size limit of 500 nm. Thinner materials are also better for imaging in TEM.

Polyvinylidene fluoride (MTI) (PVDF) was used as the binder for the electrodes. The purpose of the binder is to hold the electrode components together. PVDF was selected as the binder as it is a common binder used in battery electrodes, and is inert to reaction in most electrolyte solutions [3]. N-methyl 2-pyrrolidone (NMP) (Sigma Aldrich) was chosen as the solvent for the slurry as it is capable of dissolving NMP, and regularly used in battery slurry making [3].

Carbon black, super C65 (C.Nergy TIMCAL) was chosen as the conductive additive. The Super C65 consisted 65 nm carbon black nanoparticles. $LiCoPO_4$ has poor electronic conductivity, so nanoparticle carbon black was added to aid conductivity [3].

The electrodes were coated onto carbon coated Al foil (MTI) as the current collector. Al was chosen as it is electrochemically inert at high potentials [4]. Both non- coated and C-coated Al foil were used as current collectors during the project. However, it was found that electrode adhesion improved using C-coated Al, particularly post-calendaring. C-coated Al foil was used as the current collector for the results presented in this thesis.

3.1.2 Electrolyte

1.0 M $LiPF_6$ in a 50/ 50 volume ratio of dimethyl carbonate (DMC), and ethylene carbonate (EC) (LP-30) (Sigma-Aldrich) was used as the electrolyte. The trace H_2O content was 5 ppm, and the trace HF content was 14 ppm [5]. LP-30 has been previously used by other authors for $LiCoPO_4$ [6]–[8], so the use in this work makes the results comparable. Cycling with LP-30 is known to present poor cyclability in $LiCoPO_4$ [9]. Other electrolytes, such as those with additives such as fluoro-ethylene carbonate (FEC) are known to improve the cyclability of $LiCoPO_4$ [9]. The purpose of the thesis is to present novel methods of characterising degradation, so the priority was to choose an electrolyte more widely studied with $LiCoPO_4$, than an electrolyte which would improve the cyclability.

1.0 M $LiPF_6$ in 100 % DMC (Sigma Aldrich) was also used in order to confirm the CEI layer was not being influenced by the presence of ethylene carbonate [10]. The electrolyte is stated where 1.0 M $LiPF_6$ in 100 % DMC was used, otherwise all the cells in this thesis used 1.0 M $LiPF_6$ in a 50/ 50 volume ratio of DMC and EC.

3.1.3 Separators

Whatman GF/ F fibre glass separators were used to ensure sufficient pressure in the cell for cycling. Fibreglass has also previously been shown to aid cyclability of $LiCoPO_4$ [8]. Celgard 2325

was also used to prevent fibre glass from attaching to the electrode, which could have made electron microscopy of the electrodes more difficult as fibre glass is insulating.

Celgard 2325 is a porous polymer separator film consisting of 3 layers: polypropylene-polyethylene-polypropylene (PP-PE-PP). Whatman GF/F fibre glass separators are a type of fibre glass filter paper. Both separators are miscible to LP-30.

To ensure the results were not influenced by the separator choice, cells containing Celgard 2325, and Whatman GF/F separators, and just Whatman GF/F separators were cycled and imaged post-mortem. All the cells in the thesis used both the fibreglass, and PP-PE-PP separators unless stated otherwise where only the fibre glass separator was used.

3.1.4 Coin Cell Components

A half-cell set-up was used with Li foil (Sigma-Aldrich), rather than using a full-cell with graphite. A half-cell set-up was used to ensure an infinite supply of Li for cycling, so theoretically degradation would not be further enhanced by chemistry beyond the cathode.

The results presented used Cambridge Energy Solutions CR2016 304 stainless steel coin cells, with a 0.5 mm 304 stainless steel spacer. 2016 refers to the coin cell dimensions- 20 mm diameter, and 16 mm thickness.

It has been previously reported that stainless steel coin cells can degrade at high potentials [4]. Al coated MTI CR2032 (20 mm diameter, 32 mm thickness) coin cells were tested to confirm if an improvement in cyclability occurred. To ensure the cell pressure was maintained, an MTI Al wavy spring, and 2 0.5 mm spacers were used for 2032 coin cells.

No notable improvement was noticed when using Al coated coin cells against stainless steel coin cells so stainless steel coin cells were used for the results presented in the thesis for availability and ease of assembly.

3.2 Electrode Manufacture

3.2.1 Electrode Slurry

Composite electrodes with a composition of 90 wt. % C-$LiCoPO_4$ (Johnson Matthey), 5 wt. % polyvinylidene fluoride (PVDF) binder (MTI) and 5 wt. % Super C65 conductive additive (C.Nergy TIMCAL) were manufactured using a tape casting method. 90 wt. % active material was used to maximise the amount of active material in the electrode.

A slurry of C-$LiCoPO_4$, PVDF and C65 with N-methyl-2-Pyrrolidone (Sigma Aldrich) as a solvent was mixed with an orbital mixer (Thinky). A number of mixing steps were used to prevent the formation of large agglomerates which could otherwise increase the resistance as less $LiCoPO_4$ would be connected to the conductive carbon network [3]. De-bubbling is a setting on the orbital mixer which helps prevent bubble formation. The mixing steps are outlined below.

- 10 wt. % PVDF in NMP solution was made prior to mixing the slurry to prevent clumps of unmixed binder forming in the slurry, and to aid dissolution of the PVDF.
- C65 was mixed with NMP at 500 rpm for 30 s, 2000 rpm for 2 mins and 2200 rpm de-bubbling for 2 mins. The mixing process was performed twice.
- C-$LiCoPO_4$ and NMP were added to the C65 and NMP slurry and mixed at 500 rpm for 30 s, 2000 rpm for 2 mins and 2200 rpm de-bubbling for 2 mins. The mixing process was performed twice. The purpose of adding C-$LiCoPO_4$ at this step was to ensure the C65

coated the C-$LiCoPO_4$ particles. NMP was added to help prevent the formation of agglomerates.

- The 10 wt. % PVDF/ NMP solution was added to the slurry mix with extra NMP, and the slurry mixed at 500 rpm for 30 s, 2000 rpm for 2 mins, and 2200 rpm de-bubbling for 2 mins. The mixing process was performed twice. Extra NMP was added to help the PVDF solution fully coat the particles.
- NMP was added to the slurry and the slurry mixed at 2000 rpm for 2 mins, and 2200 rpm for 30 s twice to ensure the slurry was viscous enough to self-level when spread, but not run off the doctor blade table.

The slurry was spread to a nominal 200 µm thickness using a doctor blade on carbon coated Al (MTI) (see Figure 3.1) and dried at 80 °C.

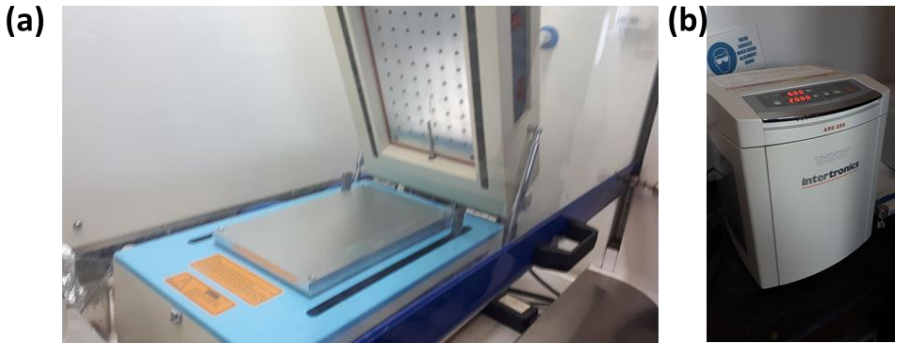

Figure 3.1: (a) Thinky orbital mixer, and (b) doctor blade and spreader

3.2.2 Calendaring

The electrode sheets were calendared using a hot roller (MTI) sandwiched between 2 stainless steel sheets and Al foil (Al foil touching the electrode surface) at room temperature to obtain electrode densities between 1.7 g cm^{-3} and 1.9 g cm^{-3}.

The electrode densities were chosen based on calendaring tests performed early in the project, which showed 1.7 g cm^{-3} to 1.9 g cm^{-3} to be the optimal electrode density (see Figure 3.2) as the initial specific capacity increased, and the electrode degradation was less severe over 10 cycles. Calendaring also improved the overall cell resistance.

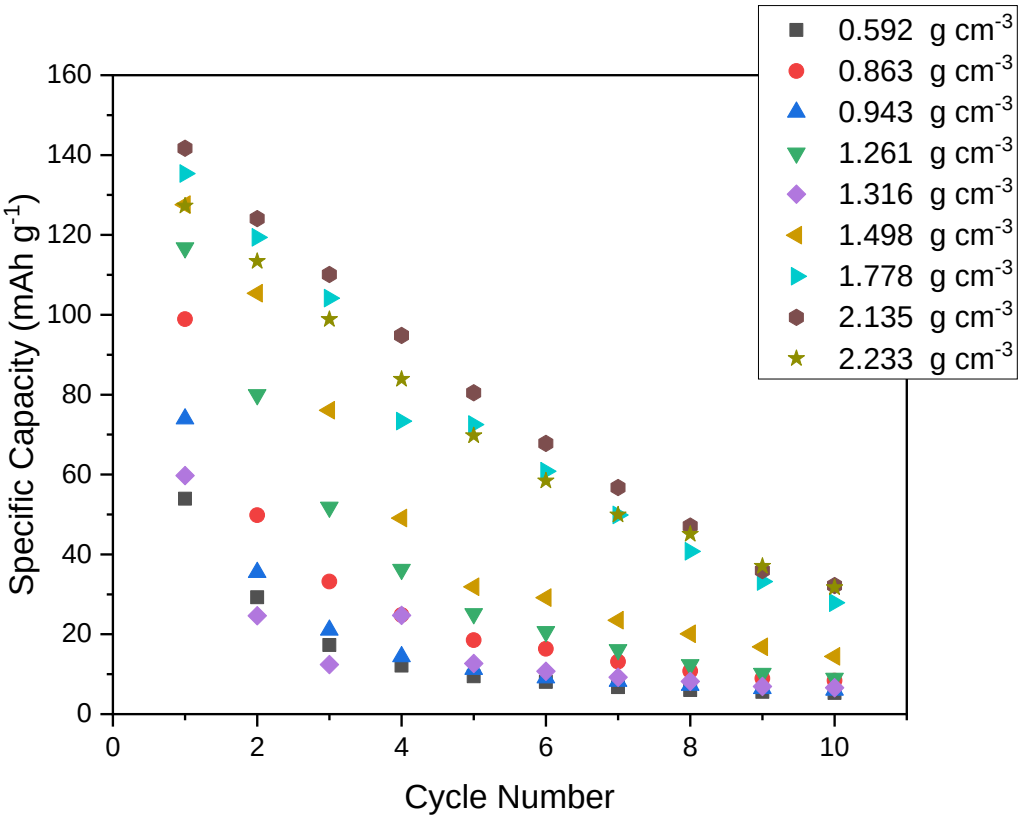

Figure 3.2: Specific capacity against cycle number for cells cycled at 0.1C for 10 cycles between 2.5 V vs. Li/ Li⁺, and 5.1 V vs. Li/ Li⁺. The cells were calendared to different densities.

The electrodes were punched into 12 mm diameter discs ready for assembly into cells.

3.3 Cell Manufacture

The electrodes were assembled into half cells using Li metal (0.38 mm thickness) (Sigma Aldrich) as a counter electrode with a Whatman GF/F separator and Celgard 2325 separator, or just a GF/ F separator with 160 µL of $LiPF_6$ in 50/ 50 volume ratio of ethylene carbonate and dimethyl carbonate (Sigma Aldrich) electrolyte. The cells were sealed in CR2016 coin-cells (Cambridge Energy Solutions) in an argon filled glove box. The atmosphere was controlled to contain <0.1 ppm O_2 and H_2O. Prior to cycling the cells were rested for 12 hours to ensure the electrolyte fully wetted the separators and electrode.

A diagram showing the coin cell assembly is shown in Figure 3.3.

(a) Polypropylene and Fibre Glass Separators

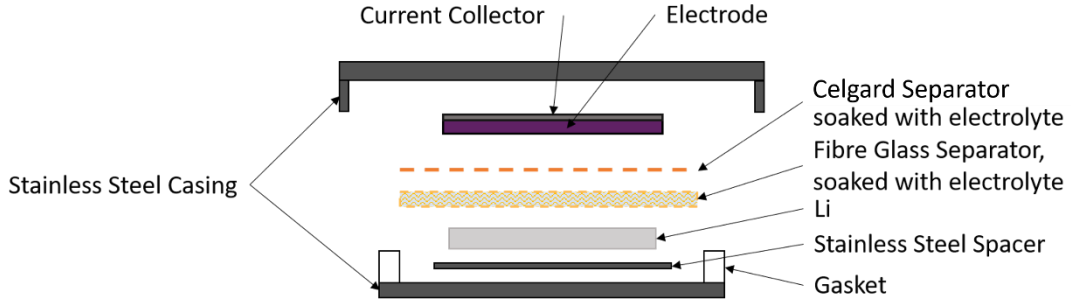

(b) Fibre Glass Separator Only

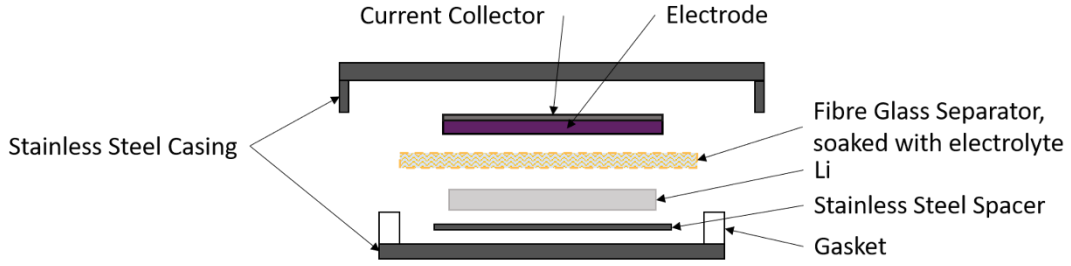

Figure 3.3: Schematic of the coin cell assembly using (a) Celgard, and fibreglass separator, and (b) only a fibreglass separator.

3.4 SUMMARY

The experimental presented here is the coin cell manufacturing process. Where coin cell cycling results are presented in the thesis, the manufacturing process described here was used. The specific cycling conditions, and post-mortem analysis sample preparation, and techniques are described in the relevant chapters.

3.5 REFERENCES

[1] M. Zhang, N. Garcia-Araez, and A. L. Hector, "Understanding and development of olivine $LiCoPO_4$ cathode materials for lithium-ion batteries," *J. Mater. Chem.,* vol. 6, pp. 14483-14517 2018.

[2] J. Wolfenstine, J. Read, and J. L. Allen, "Effect of carbon on the electronic conductivity and discharge capacity $LiCoPO_4$," *J. Power Sources*, vol. 163, no. 2, pp. 1070–1073, 2007.

[3] A. Kraytsberg, and Y. Ein-Eli, "Conveying Advanced Li-ion Battery Materials into Practice The Impact of Electrode Slurry Preparation Skills," *Adv. Energy Mater.*, vol. 6, no. 21, p. 1600655, 2016.

[4] A. Kraytsberg, and Y. Ein-Eli, "Higher, Stronger, Better ... A Review of 5 Volt Cathode Materials for Advanced Lithium-Ion Batteries," *Adv. Energy Mater.*, vol. 2, no. 8, pp. 922–939, 2012.

[5] Sigma Aldrich, "$LiPF_6$ in ethylene carbonate and dimethyl carbonate: Certificate of Analysis," 2020. Available https://www.sigmaaldrich.com/catalog/product/aldrich/809357?lang=en&region=GB#productDetailSafetyRelatedDocs. Accessed: [03-Dec-2020]

[6] E. Markevich, R. Sharabi, H. Gottlieb, V. Borgel, K. Fridman, G. Salitra, D. Aurbach, G. Semrau, M. A. Schmidt, N. Schall, and C. Bruenig, “Reasons for capacity fading of $LiCoPO_4$ cathodes in $LiPF_6$ containing electrolyte solutions,” *Electrochem. commun.*, vol. 15, no. 1, pp. 22–25, 2012.

[7] J. Manzi, and S. Brutti, “Surface chemistry on $LiCoPO_4$ electrodes in lithium cells: SEI formation and self-discharge,” *Electrochim. Acta*, vol. 222, pp. 1839–1846, 2016.

[8] R. Sharabi, E. Markevich, V. Borgel, G. Salitra, G. Gershinsky, D. Aurbach, G. Semrau, M. A. Schmidt, N. Schall, and C. Stinner, “Raman study of structural stability of $LiCoPO_4$ cathodes in LiPF6 containing electrolytes,” *J. Power Sources*, vol. 203, pp. 109–114, 2012.

[9] E. Markevich, G. Salitra, K. Fridman, R. Sharabi, G. Gershinsky, A. Garsuch, G. Semrau, M. A. Schmidt, and D. Aurbach, “Fluoroethylene carbonate as an important component in electrolyte solutions for high-voltage lithium batteries: Role of surface chemistry on the cathode,” *Langmuir*, vol. 30, no. 25, pp. 7414–7424, 2014.

[10] J. B. Goodenough, and Y. Kim, “Challenges for Rechargeable Li Batteries,” *Chem. Mater.*, vol. 22, no. 3, pp. 587–603, 2010.

4 DEGRADATION AT THE ELECTRODE SURFACE: NEW METHODS TO UNDERSTAND THE FORMATION OF CATHODE ELECTROLYTE INTERPHASE

4.1 INTRODUCTION

Development of high voltage Li-ion battery materials has been hindered by undesired reactions at the electrolyte-electrode interface. The undesired reactions can result in the formation of cathode electrolyte interphase layers on the surface of cathodes due to oxidation of the electrolyte under high voltages [1].

Very few techniques are capable of combining microstructural characterisation of the whole electrode (included both primary particles, and agglomerates), with *in-situ* chemical characterisation to correlate morphology of CEI layers with chemistry. This is likely due to the difficulty imaging thin films and characterising species containing lithium.

For $LiCoPO_4$, there is currently debate about where the CEI layers form on the cathode; either solely on $LiCoPO_4$ [2], or also involving the conductive additive [3]. Despite the acknowledgement of a link between microstructure and local CEI layer occurrence on $LiCoPO_4$ electrodes due to different local environments, to date, most cathode electrolyte interphase studies of $LiCoPO_4$ have focussed on bulk chemical characterisation of the CEI layer [3]–[5]. Common techniques used to study CEI layer chemistry are X-ray photoelectron spectroscopy, and Raman spectroscopy [3]–[5].

Helium ion microscopy (HIM) is a recently introduced type of gas-ion focussed ion beam (FIB) microscopy which produces images via He^+ or Ne^+ ion induced secondary electrons (He/ Ne-iSE). Other types of FIB imaging include Gallium, and Xenon ion beams [6]. Helium ion microscopy can provide more surface sensitive imaging with higher spatial resolution compared to SEM [7], [8], [9], and other types of ion beam source [6], as a result of a reduced electron escape volume and higher secondary electron yield. In this thesis HIM is used for the first time to attempt to image CEI due to its increased surface sensitivity over other microscopies.

Time-of-flight secondary ion mass spectrometry (ToF-SIMS) for HIM, using an incident He^+ or Ne^+ beam, has been developed by Klingner and co-workers [10], [11], which allows surface sensitive chemical characterisation, including the detection of high spatial resolution Li^+, ideal for battery electrode and CEI research. The combination of high-resolution surface imaging and Li detection is ideal for CEI layer characterisation.

4.2 AIMS AND OBJECTIVES

One of the aims of the thesis was to find a technique which could image CEI layer formation on $LiCoPO_4$ with high resolution, and chemically characterise the layer, as a function of electrochemical history, in order to identify degradation mechanisms. The combination of high-resolution imaging and chemical characterisation, provided by a HIM-SIMS technique, is used to correlate the morphology and chemistry of the CEI layer on $LiCoPO_4$ with local cathode microstructure.

Here, the process of cathode electrolyte interphase (CEI) formation in $LiCoPO_4$, is investigated for the first-time using Helium Ion Microscopy (HIM), and *in-situ* secondary ion mass spectrometry (SIMS). Imaging with helium ion microscopy is compared with more common scanning electron

microscopy techniques to confirm if similar imaging could be achieved with more readily available imaging techniques. Chemical characterisation with Ne-ion secondary ion mass spectrometry is performed with mass spectra mapping, to correlate the helium ion imaging with local chemistry, and via depth profiling to understand the formation of CEI layers on the electrode surface.

4.3 INTRODUCTION TO TECHNIQUES USED

4.3.1 Scanning Electron Microscopy

Scanning electron microscopy is a technique which uses electrons, originating from a primary electron beam scanned across the sample, which have interacted with the sample surface, by being scattered by the surface or ejecting a sample electron, to form an image. The use of electrons for image formation results in high spatial resolution images. The high resolution and surface sensitivity has meant SEM is a popular technique for material science applications [12].

4.3.1.1 Sample-Electron Interactions: Contrast Formation

The operating principle of a scanning electron microscope is dependent on electron interactions with the sample. The two most commonly detected types of electron are backscattered electrons and secondary electrons. The primary electron beam, from the electron gun impacts the sample. Scattered primary electrons which return to a detector are called backscattered electrons (BSE), and sample electrons which are ejected from the surface by the primary beam are called secondary electrons (SE) [12].

Backscattered electrons are electrons from the incident beam (the electron beam which hits the sample) which have been predominantly elastically scattered by the sample. Elastic scattering occurs due to coulombic interaction of the incident electrons with the charged nucleus (Rutherford scattering) of atoms in the sample [13]. This type of scattering causes the electron to deviate from its initial path. As Rutherford scattering occurs due to interactions with the nucleus, the atomic number influences the scattering probability. Therefore, backscattered electrons provide compositional contrast in SEM imaging, higher atomic numbers yielding greater BSE emission intensity [12].

Secondary electrons are specimen electrons which form when an incident beam is inelastically scattered by the material transferring some of its energy to the electrons in the sample. If the electrons, which have gained energy, gain enough energy to escape the sample, they are termed secondary electrons [12]. Detected secondary electrons can be split into 3 categories depending on the origin of the incident beam.

- SE1- secondary electrons which are formed by inelastic scattering of the incident beam. As they form from the incident beam, the escape area is mainly spatially localised to the incident beam, leading to high spatial resolution (Figure 4.1) [12].
- SE2- secondary electrons which are formed from backscattered electrons inelastically scattering with the sample as they escape the sample surface. As the scattered electrons originate, in this case, from a backscattered electrons from deeper within the sample, the escape area is not as localised as SE1 electrons, leading to lower spatial resolution (Figure 4.1) [12].
- SE3- secondary electrons formed from backscattered electrons which hit and inelastically scatter with the chamber (such as the objective lens). As SE3 electrons are also formed

from backscattered electrons, the spatial information is as broad as SE2 electrons (Figure 4.1) [12].

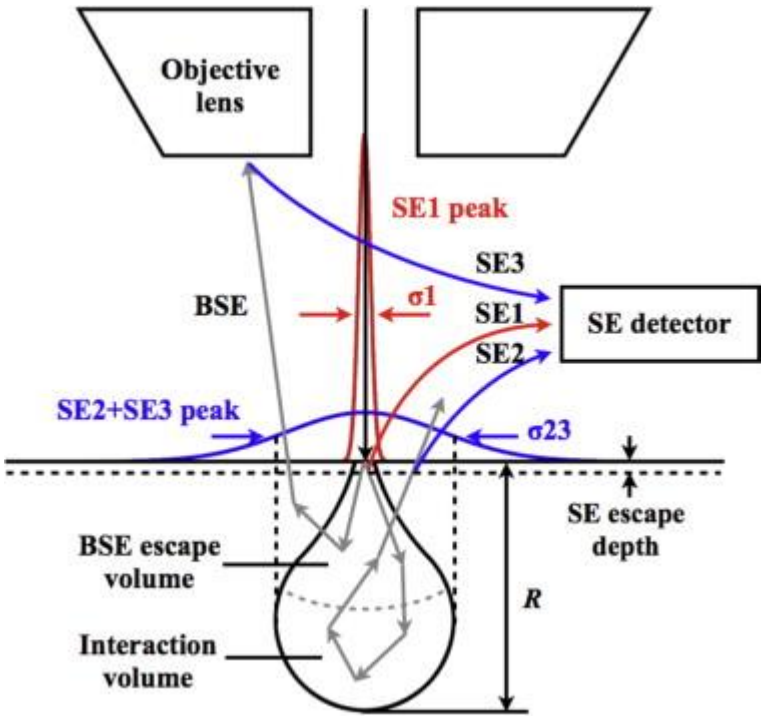

Figure 4.1: Schematic showing the electron-sample interactions which occur at an interaction distance, R, below the sample surface and the possible paths to a chamber secondary electron detector upon escape from the surface. SE1, SE2 and SE3 are the different types of detected secondary electron. SE1 electron provide more spatially localised information (σ1) than SE2 and SE3 electrons (σ23). BSE denotes backscattered electrons which escape from deeper within the sample than secondary electrons (SE). Republished with permission from Elsevier [12].

Secondary electrons produce predominantly topographical contrast as secondary electron emission is proportional to the surface tilt [12], and enhance by edge-contrast.

Resolution in an SEM is dependent on the escape area of electrons from the sample. This can be influenced by a number of factors such as the landing energy of the incident beam, the incident beam diameter, the beam shape, and the size of the interaction volume [12].

The size of the interaction volume is dependent on the beam energy, which is influenced by the incident beam voltage. Decreasing the beam voltage and current decreases the size of the interaction volume, increasing the surface resolution. However, lowering the landing energy also lowers the yield of secondary and backscattered electrons, decreasing the signal intensity. A compromise must be found between resolution and intensity [12].

4.3.1.2 SEM Detectors

SE1 electrons are the optimal secondary electrons to detect for topographic analysis as they have only interacted with the surface of the sample and have the highest spatial resolution. The most common type of secondary electron detector used commercially is the Everhart-Thornley detector and is typically placed at an angle to the sample (Figure 4.2). However, it is not possible for an Everhart-Thornley detector to distinguish between SE1, SE2 and SE3 electrons [12].

Decreasing the working distance should theoretically increase the resolution of the image as smaller spot sizes are possible at lower working distances. However, with a typical Everhart-

Thornley set-up decreasing the working distance would increase the ratio of detected SE3s to SE1 and SE2s, hence this type of set-up is unable to access the high resolution advantages of smaller probe sizes [12].

A solution to the working distance problem is to put the detector within the objective lens (Figure 4.2). This type of detector is called an In-lens detector (ILD). As the detector is within the lens it reduces the SE3 issue described above and takes advantage of being where the highest yield of SE1 electrons occurs (see Figure 4.1). Therefore ILDs have much greater resolution than Everhart-Thornley based systems [12].

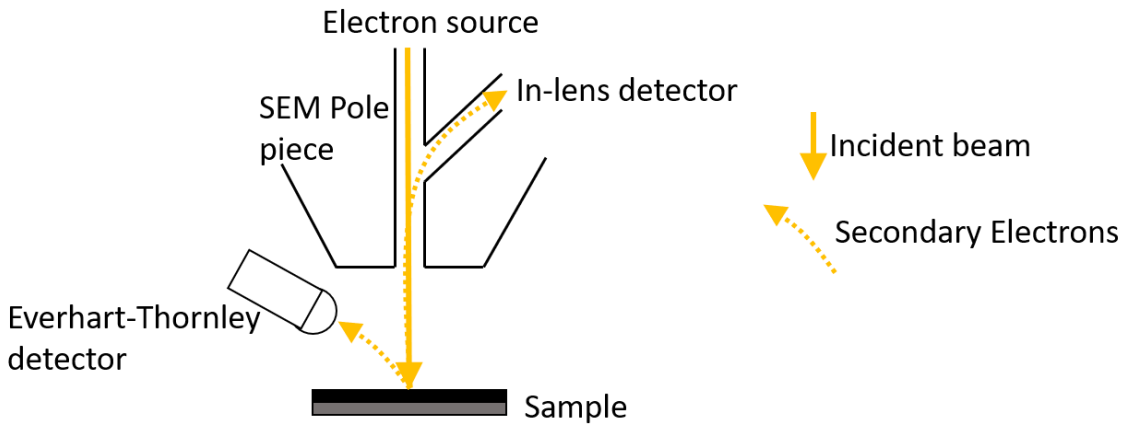

Figure 4.2: Schematic of the detector set-up in an SEM.

4.3.2 Helium Ion Microscopy

Helium ion microscopy (HIM) is a type of focussed ion beam microscopy which produces images via He^+ or Ne^+ ion induced secondary electrons (He-iSE). HIM was developed in order to take advantage of an ion beam source with a high brightness, and low energy spread, allowing ion beams to be focussed to a small probe size, and negligible sputtering effect on the sample [14].

4.3.2.1 Sample-Ion beam Interactions, and Secondary Electron Generation: Contrast Formation

Contrast in HIM is generated from a number of different mechanisms. Compared to SEM the contrast mechanisms in HIM result in (i) more surface sensitive imaging, (ii) higher resolution imaging of insulating samples, and (iii) composition contrast with secondary electrons, and (iv) voltage contrast resulting from sub-surface features (static capacitive contrast) [8] [7].

HIM images are more surface sensitive than SEM images because the yield of SE1 is relatively much greater than SE2 electrons [14], [8], [15]. The secondary electron escape volume is laterally much smaller in HIM than in SEM because the ion beam entering the surface scatters fewer electrons than an electron beam entering the surface (see Figure 4.3) [15]. A low population of SE2 electrons is generated due to the small secondary electron escape volume. No backscattered electrons are generated, as the incident beam is a He^+ ion beam. Some backscattered ions can occur, leading to the formation of a low yield of SE2 electrons, however the majority of the secondary electron population produced by He^+ ion beam scattering are SE1 electrons [8].

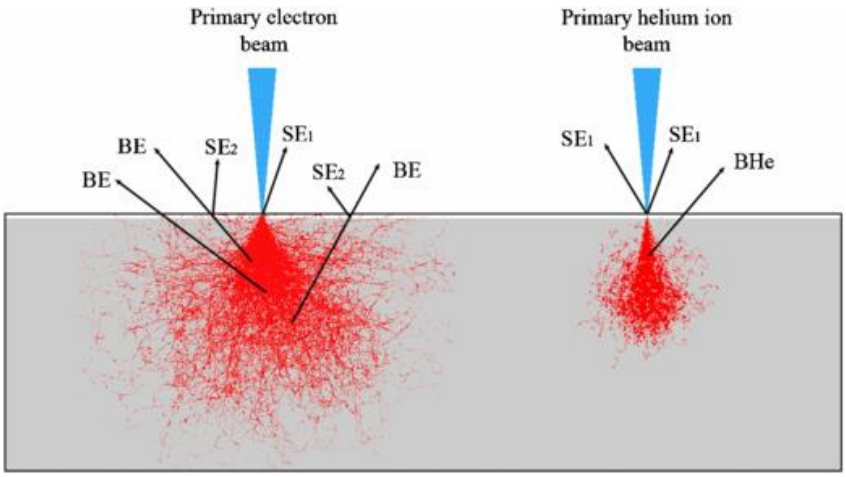

Figure 4.3: Schematic of the electron interactions in an SEM (primary electron beam) and a HIM (primary helium ion beam). Republished with permission from IOP Publishing, Ltd [15].

HIM is capable of high resolution imaging insulating samples if a low energy electron flood gun is used to suppress positive charge build-up on the surface [8]. HIM uses a beam of positively charged He^+ ions (or Ne^+ ions) as the incident beam. A positively charged incident beam results in a build-up of positive charge on the surface of an insulating sample, suppressing the yield of secondary electrons. The result of secondary electron yield suppression is charging samples will appear dark in a HIM, in contrast to SEM where charging samples appear brighter [8]. Use of an electron flood gun during imaging can suppress positive charge build-up, increasing the yield of secondary electrons [8].

Compositional contrast in SEM is maximised when using back-scattered electrons. However, in HIM secondary electrons have been found to produce measurable compositional contrast [8], [16], [7]. Compositional contrast extends to sub-surface contrast (if an insulating film is on the surface) as charging effects (the surface field) generated by insulating samples can be reduced by a conducting sub-surface, leading to a higher secondary electron yield [7].

Ne^+ ions can also be used as an incident beam in most helium ion microscopes. Ne^+ ions are heavier than He^+ ions so generate a higher sputtering yield (up to 30 % at the same energy) than He^+ ions [17]. The increased sputtering rate of Ne^+ makes it the preferred ion in the HIM for milling applications [17]. However, typically variable incident beam intensity occurs in Ne^+ ion induced secondary electron images due to current fluctuations in the gas field ionization source which can create variable intensity across a raster scan, and the surface imaging resolution can therefore be lower when using a Ne^+ ion incident beam [18].

4.3.2.2 Operating Principles: He^+ gas field ionization source

A brief discussion about the gas field ionization source (GFIS) is presented here as the set-up impacts the capabilities of SIMS depth profiling work presented.

In a helium ion microscope, a He^+ or Ne^+ ion beam is raster scanned across the sample. Ion beam interactions with the sample can produce secondary electrons. The electrons are extracted, and detected by an Everhart-Thornley Detector (ETD) to produce a grey-scale image [14].

The He^+ and Ne^+ beam is generated by a gas field ionization source (GFIS). The GFIS consists of a cryogenically cooled tip, with a tip radius of 100 nm. The tip is positively biased so that He or Ne gas injected in the vicinity of the tip is ionised by the strong electric field around the sharp tip. At the optimal sharpness, the 3-atom trimer tip can produce very high brightness. The resulting

ionisation of gas ions by the tip produces 3 beamlets known as a trimer. One atom from the trimer is selected as the primary emitter producing a high brightness GFIS (4×10^9 A cm^{-2} sr^{-1}) [7], [9].

If the trimer is 'lost' due to atom rearrangement the brightness of the incident beam reduces, decreasing image quality. The use of heavier gas elements, such as Ne^+ can reduce the lifetime of the trimer due to effects such as adatoms (where atoms are affixed to the trimer) [17]. The instability of the trimer for heavier elements limits the Ne^+ ion milling duration in the HIM.

4.3.3 Secondary Ion Mass Spectrometry

Secondary ion mass spectrometry (SIMS) is a technique which can be used to investigate the chemistry of a surface. SIMS instruments use a primary ion beam to sputter the surface of a sample. Sputtering of the sample surface produces secondary ions which can be extracted and run through a mass spectrometer to determine sputtered ion number and mass.

The yield of negative or positive ion fragments can be enhanced by changing the primary ion beam source. In the case of conventional SIMS, an O_2^+ beam increases the yield of positive ions and a Cs^+ beam increases the yield of negative ions. The difference occurs due to changes in ionisation efficiency due to the electronegativity of the primary ion beam.

Relative sensitivity factors (RSF) are a measure of the likelihood of a particular ion being sputtered from a surface. The tables in Figure 4.4 and Figure 4.5 show the relative sensitivity factors of secondary ions sputtered from a silicon matrix. The RSF factors are important to consider when evaluating SIMS spectra.

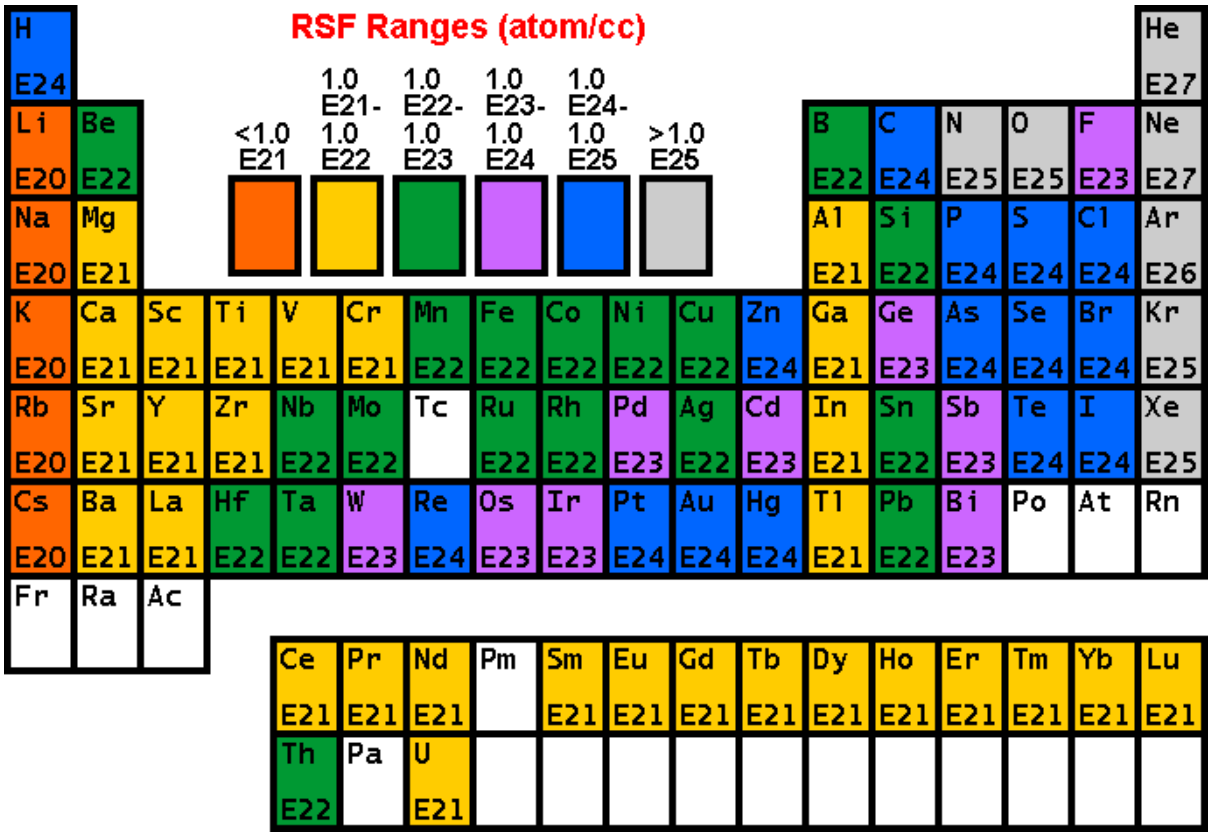

Figure 4.4: RSF factors of positive ions with an O_2^+ primary bombardment beam from a silicon matrix. Ions at the orange end of the spectrum have higher RSF factors, and hence the yield will be increased. Atom/ cc- atoms per cubic centimetre, E21- 10^{21} atom/cc Figure from [19]*, made using tables from* [20] *Data republished with permission from Elesevier.*

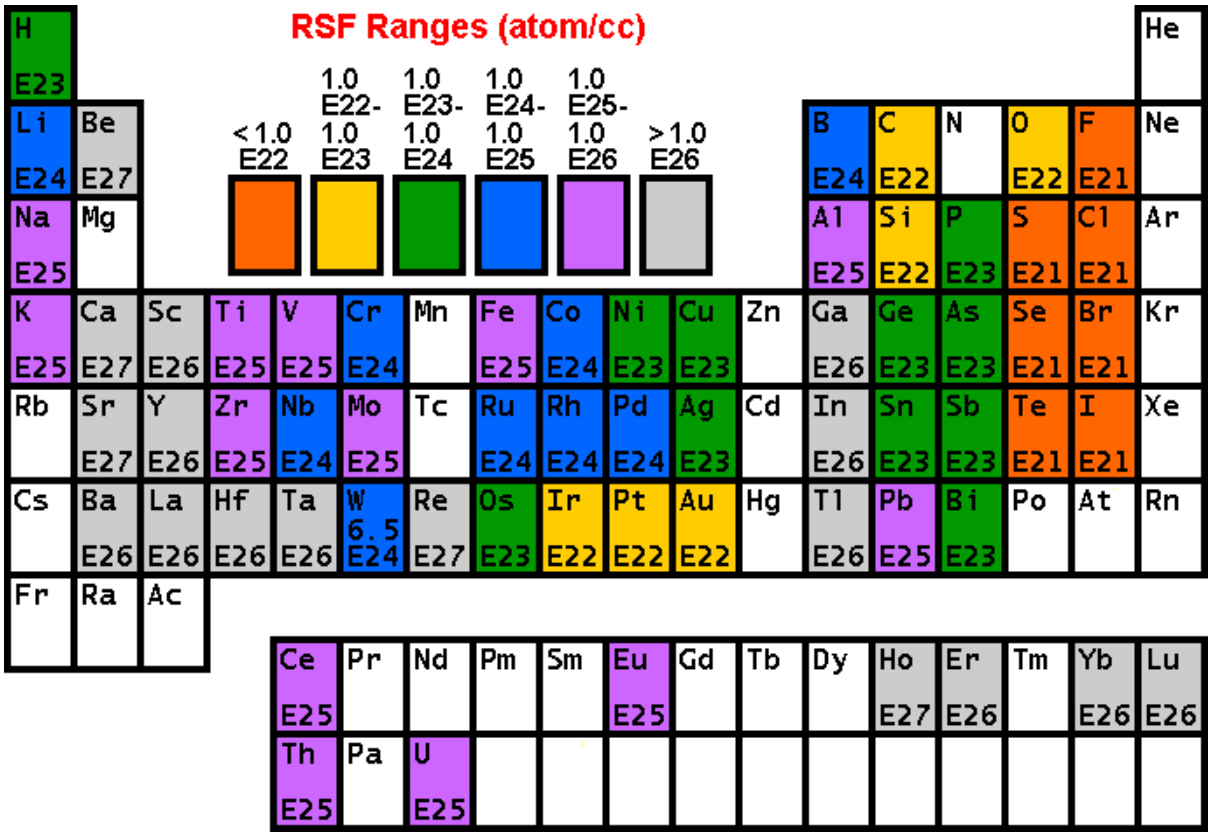

Figure 4.5: RSF factors of negative ions with an Cs^+ primary bombardment beam from a silicon matrix. Ions at the orange end of the spectrum have higher RSF factors, and hence the yield will be increased. Atom/ cc- atoms/ cubic centimetre, 1.0E22- 1.0 × 10^{22} atom/ cc. Figure from [19]*, made using tables from* [20]*. Data republished with permission from Elsevier.*

4.3.3.1 Time of Flight Secondary Ion Mass Spectrometry for the Helium Ion Microscope

Chemical analysis in the HIM can be challenging as the low velocity of the low energy incident ions is too low to produce the X-rays required for energy dispersive X-ray spectroscopy [21]. As a result, alternative methods have been pursued to enable chemical characterisation, such as secondary ion mass spectrometry (SIMS) [7], [21], [11], [10], [22].

SIMS in the HIM uses He^+ or Ne^+ beams as a primary ion beam which penetrates the sample, creating collision cascades which lead to the sputtering of sample atoms and molecules. The sputtered material can ionise during the sputtering process producing secondary ions [11]. Ne^+ is often used for SIMS in the HIM as the sputtering yield from He^+ is much smaller. The secondary ions can be separated and detected using a time-of-flight [11], [10], or magnetic mass spectrometer [7], [22]. Mass spectra can be collected to generate lateral distribution maps, or depth profiles can be measured [10].

As the HIM typically only has He^+ and Ne^+ as ion sources for SIMS, it is not possible to use the electropositive advantages of Cs^+ or electronegative advantages of O_2^+ to enhance negative and positive secondary ion yield respectively. In the HIM, stage biasing is used to increase the yield of positive secondary ions, or negative secondary ions at the detector [10].

4.4 EXPERIMENTAL

4.4.1 Electrochemical Testing

90wt. % $LiCoPO_4$, 5 wt. % C65, and 5 wt. % PVDF electrodes were manufactured into coin cells as described in the 'Experimental: Electrode and Cell Manufacture' chapter. Galvanostatic cycling up to 10 cycles, at 0.1C between 2.5 and 5.1 V vs. Li/ Li^+ was performed using a Maccor galvanostat. After each Galvanostatic charge step, the cell was charged potentiostatically at 5.1 V vs. Li/ Li^+ to ensure complete charging. After each discharge the cell was left to rest for 1 hour.

After cycling the coin cells were disassembled in an argon filled glove box using an MTI de-crimping machine. The electrodes were rinsed with dimethyl carbonate (DMC- Sigma Aldrich) to remove liquid electrolyte, and were mounted onto SEM stubs in the glove box. The samples were sealed into mylar bags for transport to the HIM in Germany. On transfer into the HIM the electrodes were briefly exposed to air (~ 1 min) as there was no access to a vacuum transfer chamber.

4.4.2 HIM-SIMS Analysis of the CEI Layer

HIM analysis of cycled electrodes was performed in a Zeiss Orion NanoFab Helium Ion Microscope at the Helmholtz-Zentrum Dresden-Rossendorf. Imaging was performed with a He^+ beam at 25 keV as the incident focussed ion beam, and the ion-induced secondary electrons (iSE) detected with an Everhart-Thornley Detector (ETD).

In-situ ToF-SIMS measurements were performed with a ToF-SIMS detector (ToF-SIMS for the HIM) designed and built by Klingner et al. [11], [10]. Secondary ions were sputtered using 25 keV Ne^+ ions as the incident ion beam. Site-specific mass spectra, lateral ion distribution maps and depth profiles of both positive and negative secondary ions were collected on different areas of the cycled electrodes.

ToF-SIMS measurements were enabled by pulsing the primary ion beam, biasing the sample to either plus or minus 500 V for positive and negative SIMS, respectively. The stage was tilted by 54 ° to position the sample surface perpendicular to the extraction optics, therefore all Ne^+ ion images appear tilted compared to He^+ images. Sputtered ions with the same polarity as the bias voltage are accelerated into the ToF SIMS spectrometer, where they were separated due to differing mass to charge ratios, and velocities allowing [10]. Ions were detected on a multichannel plate (MCP). Spectra were collected by applying 30 pulses per pixel with a pulse length of 50 to 150 ns. For SIMS depth profiling the measured area was over-scanned by 100 % with an un-blanked beam for ~100 µs per pixel. The depth profiling region of interest field of views were between 0.5 and 1.5 µm depending on the feature size.

The raw SIMS data was collected as counts against channel number (where channel number referred to different parts of the detector). Depending on the exact set-up of the extraction optics relative to the sample, different m/z ratios can be represented by counts on different channels. The SIMS spectra were calibrated using software developed by Klingner et al. [10] to identify the the m/z ratio represented by ion counts on the detector channels. Calibration was performed so each peak correlated to within 0.2 u of an integer (as mass/ charge ratios must be integers, 0.5, or 0.33 depending on the ion charge). To identify the m/z ion fragments, the SIMS spectra were compared with previous Cs^+ SIMS by Manthiram *et al.* on high voltage Li-ion battery electrodes using the same electrolyte (LP-30) [23]. The results were also compared with previous XPS studies on C-$LiCoPO_4$ to help identify the composition of the CEI layer [4], [24].

4.4.3 SEM and TEM Microstructural Analysis

The samples were prepared for SEM by mounting the washed electrodes to an SEM stub using carbon tape. SEM images of the cycled electrodes were taken with a FEI Helios NanoLab G3 UC using the in-lens detector (ILD) and ETD for electron induced secondary electron imaging (eSE), and a backscattered electron (BSE) detector. The images were detected at different beam currents and voltages.

Scanning Transmission Electron Microscopy (STEM) High Angle Annular Dark Field (HAADF) and Bright Field (BF) images were taken with a JEOL JEM F200 at 200 kV using Gatan HAADF and JEOL BF detectors. Samples were prepared by scraping and grinding dried electrode onto a TEM grid, in an Ar filled glove box, and transferring into the microscope. The samples were briefly exposed to air on transfer to the microscope (~ 2 mins). This chapter contains 1 example of a micro-tomed electrode. The process for micro-toming is described in the 'Degredation within $LiCoPO_4$ particles' chapter.

4.5 RESULTS

4.5.1 Experiments Presented

To confirm the $LiCoPO_4$ electrodes cycled experienced degradation, likely to result from electrolyte degradation, the specific capacity drop, cell resistance, and coulombic efficiency changes were measured. The cycling results are presented in section 1.1.1.

One of the objectives of this chapter was to identify if HIM was capable of imaging CEI layers. To confirm if HIM was capable of imaging CEI layers the results must prove, (1) HIM can image a surface film which extends through the electrode cross-section, and (2) the surface film chemistry must differ from the uncycled electrode surface chemistry, and regions where the surface film is not present.

An uncycled electrode, and 10^{th} cycle discharged electrode were imaged using HIM to confirm if CEI layers were visible using HIM. The electrode was imaged from the top surface (the electrode-electrolyte-separator interface), and on the cross-section by imaging cracks generated by tearing the electrode prior to imaging to ensure surface features existed throughout the electrode structure. The initial HIM imaging results are presented in section 4.5.3.

In order to confirm the thickness of surface features imaged using HIM, Stopping Range of Motion in Matter monte-carlo simulations were carried out. The model details are presented in section 4.5.3.1.1.

To show the capabilities of surface imaging and chemical characterisation of a helium ion microscope, compared with standard scanning electron microscopy, electrodes were imaged using the HIM, and SEM under different imaging conditions. SEM imaging was performed using the Everhart Thornley, and In-lens detector at different voltages, and beam currents to simulate the surface sensitivity achieved using HIM. The SEM imaging results are presented in section 4.5.3.2.

Ne^+-ion ToF SIMS spectra, and lateral mapping were performed on cycled, and uncycled electrodes to confirm differences in chemistry between imaged surface films, and regions without the film. Initial chemical characterisation using SIMS is presented in section 4.5.4.

The second objective was to use HIM-SIMS to investigate surface degradation phenomena in $LiCoPO_4$ by correlating microstructural changes imaged using HIM, with chemical changes investigated with SIMS. To investigate degradation phenomena in $LiCoPO_4$, HIM imaging, and SIMS depth profiling were performed on cells cycled for different cycle numbers, and to different states of charge. In order to confirm the macro-scale changes observed using HIM resulted from nano-scale features, STEM imaging was also performed. The cycle-life induced degradation results are presented in section 4.5.5.

As the binder/ conductive additive rich- regions, and $LiCoPO_4$-rich regions potentially behaved differently, HIM, SIMS depth profiling, and STEM imaging were performed on both regions. HIM, SIMS depth profiling, and STEM imaging were performed on binder, conductive additive-rich regions, and on $LiCoPO_4$-rich regions to determine if the surface chemistry varied with local chemistry. The cycle-life induced degradation results in section 4.5.5 are split into observations from $LiCoPO_4$-rich regions (4.5.5.1), and observations from binder/ conductive additive-rich regions (4.5.5.3).

To ensure surface features were not a result of cathode and separator interactions, the separators, and electrodes were also imaged post-mortem using SEM. The separator difference results are presented in section 4.5.5.5.

Table 4.1 shows the cell cycling conditions, and post-mortem characterisation techniques used for the experiments.

Table 4.1: $LiCoPO_4$ half-cell cycling conditions for the electrodes analysed post-mortem in this chapter, and the post-mortem analysis performed. SIMS analysis is split into spectra, mapping, and depth profiling (DP). Y- experiment performed.

Experi-ment	Electrode Cycle History	Separator	HIM	SIMS			S/ TEM	SEM	Sec-tion
				Spectra	Map	DP			
Imaging the surface using HIM	Uncycled	-	Y						4.5.3
	10 full cycles (2.5-5.1 V)	Fibreglass + Celgard	Y						
Surface imaging with different techniques	Uncycled	-	Y					Y	4.5.3.2
	10 full cycles (2.5-5.1 V)	Fibreglass + Celgard	Y					Y	
Surface chemical characterisation	Uncycled	Fibreglass + Celgard	Y	Y	Y				4.5.4
	10 full cycles (2.5-5.1 V)	Fibreglass + Celgard	Y	Y	Y				
Effect of Cycle life	Uncycled	-	Y			Y	Y		4.5.5
	1 full cycle (2.5-5.1 V) 1 charge (2.5- 5.1 V)	Fibreglass + Celgard	Y			Y			
	2 full cycles (2.5-5.1 V)	Fibreglass + Celgard	Y			Y			
	4 full cycles (2.5-5.1 V) 1 charge (2.5-5.1 V)	Fibreglass + Celgard	Y						
	5 full cycles (2.5-5.1 V)	Fibreglass + Celgard	Y						
	9 full cycles (2.5-5.1 V) 1 full charge (2.5-5.1 V)	Fibreglass + Celgard	Y			Y			
	10 full cycles (2.5-5.1 V)	Fibreglass + Celgard	Y			Y	Y		
Separator Effect	10 full cycles (2.5-5.1 V)	Fibreglass + Celgard	Y					Y	4.5.5.5
	10 full cycles (2.5-5.1 V)	Fibreglass	Y						

4.5.2 Electrochemical Testing

Typical electrochemical characteristics of a C-$LiCoPO_4$ half-cell are shown in Figure 4.6. The calculated electrochemical property values are averages for all the cells measured in the SIMS experiments. The errors reported are the standard deviation of the property for all the cells measured. Specific capacity was calculated using:

$$Specific\ Capacity = \frac{Charge\ or\ Discharge\ time\ \times Charge\ or\ Discharge\ Current}{Mass\ of\ C - LiCoPO_4}$$

Coulombic efficiency for each cycle was calculated using:

$$Coulombic\ efficiency = \frac{Discharge\ Specific\ Capacity}{Charge\ Specific\ Capacity}$$

The overall cell resistance was calculated by multiplying the current by the initial voltage drop when the cell finished charging and began discharging.

All cells tested and analysed *ex-situ* displayed similar characteristics. The average initial specific discharge capacity of the electrodes imaged post-mortem in this chapter was 118 ± 3.8 mAh g^{-1}; lower than the theoretical capacity of C-$LiCoPO_4$ (167 mAh g^{-1}) [25]. 3.8 mAh g^{-1} is the standard deviation of the initial discharge specific capacities. By the 10th cycle the cells had on average lost 79 % of their initial capacity (Figure 4.6 (a)), indicating severe degradation similar to previous studies on C-$LiCoPO_4$ in $LiPF_6$ EC/ DMC electrolytes [4].

Cell resistance was measured from the voltage drop in the Galvanostatic cycling curves. Overall cell resistance increased as the capacity dropped but stabilised at cycle 8 (Figure 4.6 (a) and (b)). A low initial coulombic efficiency (64 %) was observed on the first cycle indicating Li consumption. This behaviour has been previously attributed to the formation of CEI layer on the first cycle ([3]). Coulombic efficiency stabilised to 96 %, lower than needed for a commercial cell and a further indicator of degradation processes which prevent Li insertion and de-insertion in the electrode occurring.

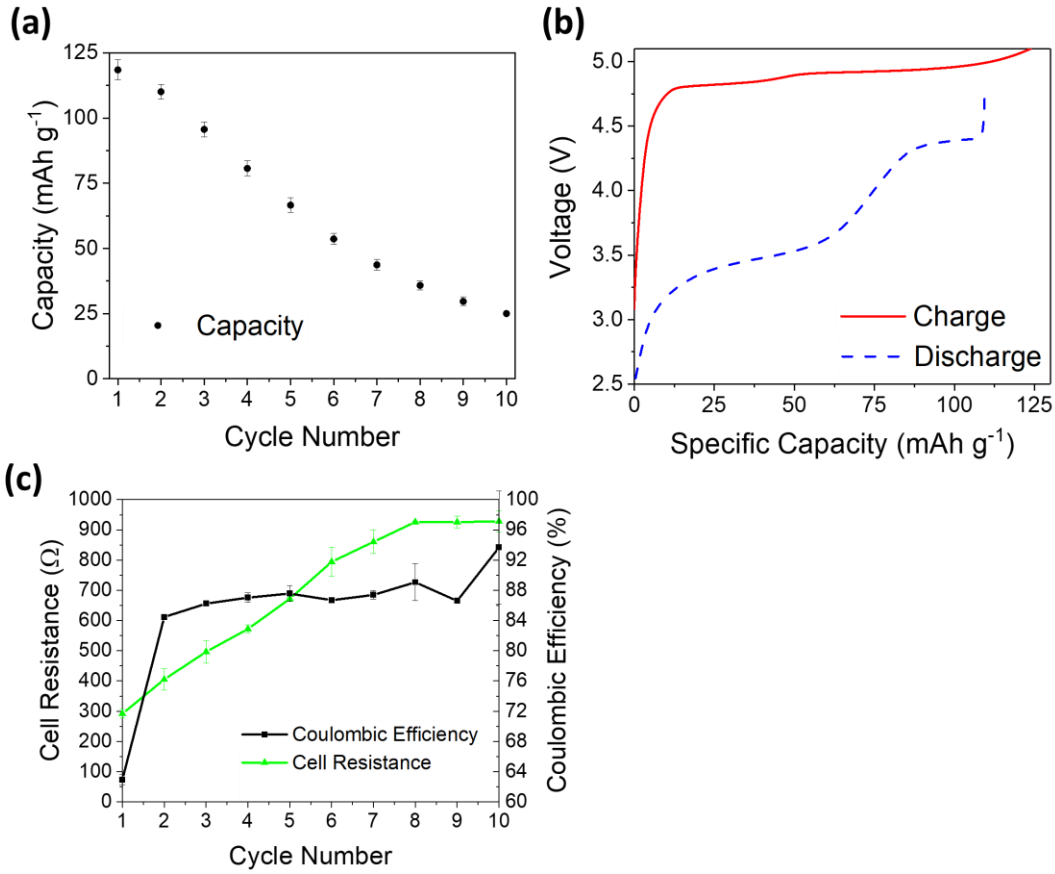

Figure 4.6: Representative electrochemical behaviour of C-LiCoPO$_4$ electrodes at 0.1C. (a)- variation of specific capacity with cycle number, (b)- Galvanostatic charge and discharge curve on the second cycle, (c)- coulombic efficiency and overall cell resistance calculated from the voltage drop on the galvanostatic charge and discharge curves. Reproduced with permission from [26]*. Copyright 2020, the American Chemical Society.*

4.5.3 Microstructural Characterisation with HIM

4.5.3.1 Imaging electrodes using HIM

To confirm whether degradation induced surface features, such as CEI films, could be imaged using HIM, an uncycled electrode, and an electrode cycled for 10 cycles were imaged using HIM.

The uncycled electrode (Figure 4.7 (a)) exhibited two types of morphology, smooth round regions with rougher regions in-between, corresponding to C-LiCoPO$_4$ agglomerates and C65, and binder-rich regions respectively.

Changes to the surface microstructure were observed after 10 complete cycles using HIM (Figure 4.7 (b), (c) and (d)). Distinct regions of dark contrast were observed, indicating regions of low He^+-ion induced secondary electron yield (He-iSE) (Figure 4.7 (b)). The low He-iSE yield regions were not present on the surface of uncycled electrodes using comparable incident He^+-ion beam conditions (Figure 4.7 (a)).

Higher magnification imaging (Figure 4.7 (d)) shows that the particles in the dark contrast region are less well defined. Lower particle definition potentially indicates the presence of a film on the electrode surface results in low He-iSE yield. To confirm the low He-iSE yield regions resulted from surface films, the He^+ beam was used to mill through the layer for 45 s. The area contrast changed from dark at the start of milling (Figure 4.7 (e)), to similar contrast to the LCP agglomerates in

Figure 4.7 (a) after milling for 45 s (Figure 4.7 (f)), confirming the low He-iSE yield resulted from the presence of a surface film.

Figure 4.7 (c) is an image of a crack on the electrode surface, showing a cross-section through the electrode. The large crack formed as a result of tearing the electrode after de-crimping. Patches of dark contrast, low He-iSE yield film extend through the cross-section of the electrode (Figure 4.7 (c)), as well as the top surface.

Low contrast regions, similar to those seen on the He-iSE images (Figure 4.7 (b)), are also visible through detection of electron induced secondary electrons (eSE) with an In-lens detector (ILD) in an SEM (Figure 4.7 (f)). ILD images are eSE images with a majority yield of SE1 electrons; He-iSE images are also majority SE1 yield images which explains the contrast similarity [12] (see 4.3.1.2).

Using SEM backscattered electron (BSE) imaging (Figure 4.7 (g)) C-$LiCoPO_4$ agglomerates can be clearly distinguished from binder-rich regions as C-$LiCoPO_4$ appears bright on BSE images. BSE images provide compositional contrast, hence as Co in $LiCoPO_4$ is a heavier element than C, and F in the binder, $LiCoPO_4$ agglomerates appear brighter. The C65 particles are not clearly visible on the backscattered image (Figure 4.7 (g)), but are visible on the secondary electron ILD, eSE SEM image (Figure 4.7 (h)). C65 is more clearly visible on the ILD image (Figure 4.7 (h)) because edge contrast is stronger from secondary electrons than backscattered electrons [12].

Figure 4.7 (b) and (c) show the low He-iSE yield film coverage is heterogeneous across the electrode surface. The low He-iSE yield film is also present in mostly circular regions (Figure 4.7 (b) and (c)). Using thresholding analysis in Image J, the average area of the low He-iSE yield regions on the 10^{th} cycle discharged electrode was calculated as 5.7 ± 34. 8 μm^2. The areas of the low He-iSE yield regions ranged from 321 μm^2 to 0.2 μm^2.

Comparison between the eSE ILD image (Figure 4.7 (h)) with the BSE image of the same region (Figure 4.7 (g)) shows that the low secondary electron yield film forms on C-$LiCoPO_4$ agglomerates. C-$LiCoPO_4$ agglomerates are also round (as shown in (Figure 4.7 (g)), which explains the shape of the low He-iSE yield regions in the He-iSE image (Figure 4.7 (b)) and the SEM ILD image (Figure 4.7 (h)).

Comparison between BSE and ILD eSE electrode imaging (Figure 4.7 (h) and (g)) also shows that that the secondary electron yield is not consistent across all the C-$LiCoPO_4$ agglomerate. The large ~20 µm C-$LiCoPO_4$ agglomerate in Figure 4.7 (h) exhibits regions of both low and high eSE yield. The mottled eSE contrast in the predominantly bright contrast outer edge of the large agglomerate in Figure 4.7 (h) may indicate the low eSE yield film is thinner in this region. The differences in electron yield suggest heterogeneous formation of the low secondary electron yield surface film.

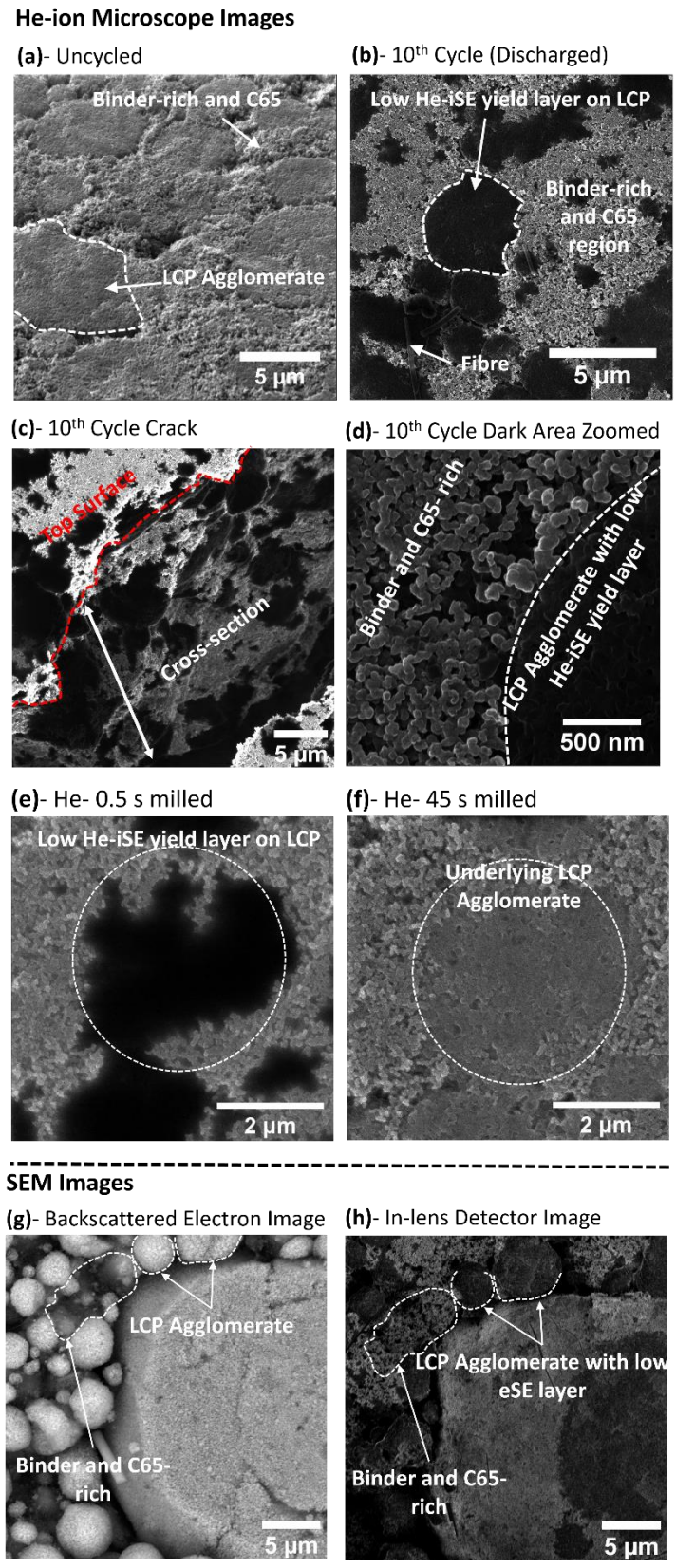

Figure 4.7: HIM He-iSE images of (a) uncycled electrode surface tilted to 54 °, (b) electrode surface of a 10th cycle discharged electrode, (c) a crack in the surface of the 10th cycle discharged electrode, showing the cross-section through the electrode, and (d) a higher magnification image of the top surface of the 10th cycle discharged electrode. (e), (f)- He-iSE images of the surface after 0.5 s He+ milling (e), and 45 s He+ milling (f). SEM images of the top surface of a 10th cycle discharged electrode using (g) a backscattered electron image and (h) in-lens secondary electron image.

The fibre in (b) originates from the fibre-glass separator. Adapted with permission from [26]*. Copyright 2020, the American Chemical Society.*

4.5.3.1.1 Estimating the Thickness of the low He-iSE yield film

A surface film was detected on cycled electrodes by both He-iSE imaging, (Figure 4.7 (b), (c), and (d)), and SEM ILD-eSE imaging (Figure 4.7 (h)). For the 10th cycle discharged electrode, the thickness of the low He-iSE yield layer was estimated by milling through the low He-iSE yield layer until bright contrast was found. The milling was performed by imaging the area with a dwell time of 2 µs per pixel and a He^+ beam energy of 25 keV. For each image the beam current was recorded.

Images of the low He-iSE yield layer at the start of milling, after 18 s milling and at the end of milling are shown in Figure 4.8. At the start of milling Figure 4.8 (a), the film on the surface has low He^+-iSE yield. After milling for 18 s (Figure 4.8 (b), edges of the film have lighter contrast than the centre, indicating the film is thinner. After milling for 45 s the low He^+-iSE yield film has been removed Figure 4.8 (c), revealing the underlying $LiCoPO_4$ agglomerate.

The He^+ beam mill calculation presented here aims to estimate the thickness of the low He^+-ISE yield region.

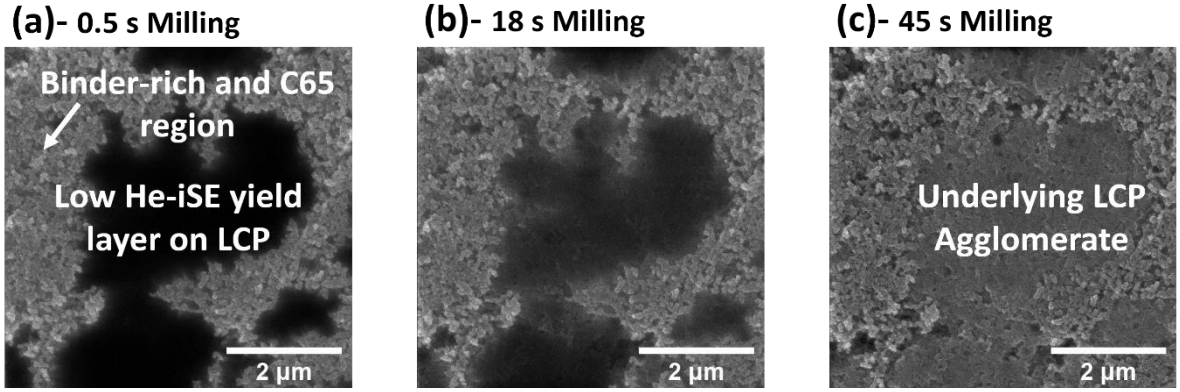

Figure 4.8: Images of the electrode surface after different He^+ ion milling time. The times shown are the total He^+ ion milling time for the whole image (product of the dwell time and number of pixels). The images show the surface after (a) 0.5 s milling, (b) 18 s milling, and (c) 45 s milling. Adapted with permission from [26]*. Copyright 2020, the American Chemical Society.*

For each frame the total ion fluence (the number of He^+ ions received by the area milled per second) was calculated using:

$$Ion\ Fluence = \frac{Beam\ current\ \times Dwell\ Time\ \times Number\ of\ pixels}{Image\ Area\ \times Charge\ on\ 1\ He^+\ ion\ (1.6\ \times 10^{-19}\ C)}$$

For a frame of 36 µm^2 area, with 262144 pixels, 2 µs beam dwell time per pixel, and a beam current of 34.3 pA, the ion fluence was calculated as 3.12×10^{14} ions cm^{-2}.

In order to calculate the milling depth, the sputter fluence (atoms removed per area by the incident He^+ ion beam) was calculated. Sputter fluence was calculated using:

$$Sputter\ fluence = Sputtering\ Yield\ \times Ion\ Fluence$$

The sputtering yield was calculated using Stopping and Range of Ions in Matter (SRIM) software by J. F. Ziegler [27]. SRIM is based on the Monte Carlo simulation method and can calculate the sputter yield (number of atoms ejected from a surface by an ion hitting the surface with a certain energy). The software requires (1) the incident beam ion, (2) the incident beam energy, (3) the ion

angle, and (4) the sputtering target material. For the estimation of the thickness of the low He-iSE yield film the following parameters were used:

(1) The incident beam ion: He^+
(2) The incident beam energy: 25 keV
(3) The ion angle: 0 ° (perpendicular to the surface)
(4) Sputtering target material: SRIM in-built amorphous carbon on ionic-bonded $LiCoPO_4$. The low He-iSE yield region was assumed to be amorphous carbon-rich as subsequent depth profiling in presented in 4.5.5 showed a high yield of C_2^- and C^+ at the surface of the electrode. It is also known that carbon containing compounds which form as a result of electrolyte degradation are typically amorphous [23]. As the chemistry of the electrode surface is more complex, the thickness value calculated using the SRIM method is an estimate.

SRIM modelling estimated the sputtering yield of amorphous carbon on $LiCoPO_4$ as 0.0497 atoms/ ion. From this the sputter fluence for the example frame described above was found to be 1.55×10^{13} atoms cm^{-2}

The depth sputtered could be estimated using:

$$Depth\ Sputtered = \frac{Sputter\ Fluence}{Atomic\ Density\ of\ Amorphous\ Carbon}$$

The atomic density of amorphous carbon was 5.03×10^{22} atoms cm^{-3}, which was calculated assuming the density of amorphous carbon was 1 g cm^{-3}.

The total depth sputtered was calculated using:

$$Total\ depth\ Sputtered = \frac{Sputter\ fluence}{Atomic\ Density\ of\ Amorphous\ Carbon} \times number\ of\ frames$$

For the example frame, the depth sputtered was 0.003 nm. The total depth sputtered was calculated over 130 frames imaged and found to be 0.2 nm.

0.2 nm suggests the film was 1 atomic layer thick. As the contrast of the film varies, but does not reveal the microstructure underneath with increasing milling time (Figure 4.8 (b)), this estimate is incorrect as 1 atomic layer thickness is unlikely to result in contrast differences in HIM and ILD SEM (Figure 4.7 (b) and (f)). The error most likely occurred because the system is more complicated than amorphous carbon on top of $LiCoPO_4$ using SRIM. As will be shown in 4.5.4, the layer does not only consist of carbon, and the SRIM used here assumes only single ions are sputtered, negating the possibility of sputtering clusters of ions.

The film is visible on in-lens eSE detector images (Figure 4.9). The resolution limit of an SEM is 2 nm [12], suggesting the film is at least greater than 2 nm thick.

4.5.3.2 Influence of Microscope Type and Beam Conditions on Microstructure Characterisation

Imaging of electrodes cycled for 10 complete cycles was performed in an SEM with ILD and ETD detectors to compare the detection of the low He-iSE yield layer when imaging with an incident He^+, and electron beam. The same area of electrode was imaged using He^+-iSE signals using an ETD detector, and SEM eSE signals using ETD and ILD detectors (Figure 4.9).

Figure 4.9 (b) shows that the surface film has low secondary electron yield using an ILD detector, similar to HIM imaging in Figure 4.9 (c). However, the edges of the film are sharper using higher resolution He-iSE imaging compared with ILD electron induced secondary electron (eSE) imaging. The film has similar contrast to the binder- C65- rich regions when using an ETD (Figure 4.9 (a)), making it more difficult to distinguish.

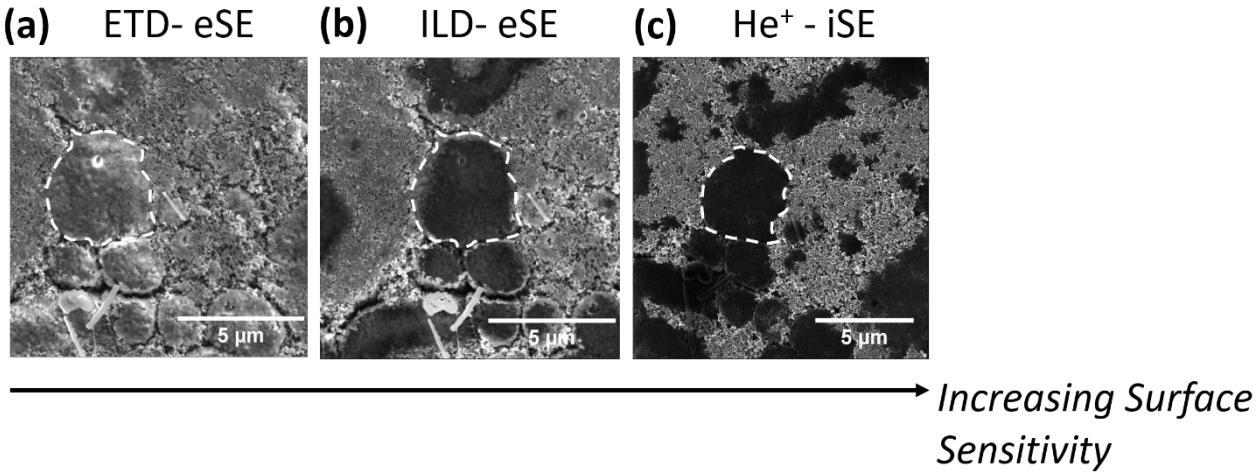

Figure 4.9: Images of the top surface of a 10th cycle discharged C-$LiCoPO_4$ electrode taken with different incident beam and electron detectors; (a)- ETD-eSE- Everhart Thornley detector electron induced secondary electron image, (b)- ILD-eSE- In-lens detector electron induced secondary electron image, (c)- He^+- iSE- Helium ion induced secondary electron image with a negative stage bias. Reproduced with permission from [26]*. Copyright 2020, the American Chemical Society.*

It should be noted that the ETD and ILD images in Figure 4.9 (a) and (b) were taken after the HIM resulting in 1 week of air exposure due to travel from Germany, and a lack of access to glove boxes for sample storage.

Figure 4.10 shows an SEM ETD eSE image, and an SEM ILD eSE image of the same area of a 10^{th} cycle discharged electrode taken with 1 min of electrode air exposure. The ILD eSE image clearly shows a low electron induced secondary electron yield film, similar to Figure 4.9 (b), however, a film is not visible on the electrode surface when using ETD eSE imaging. By contrast, the ETD image of the electrode exposed to air for 1 week in Figure 4.9 (a) shows evidence of a clear surface film. The air exposure likely caused the low He-iSE film to oxidise, causing the film to appear thicker in the images. Therefore, the film imaged in Figure 4.9 (a) did not result from electrochemical cycling.

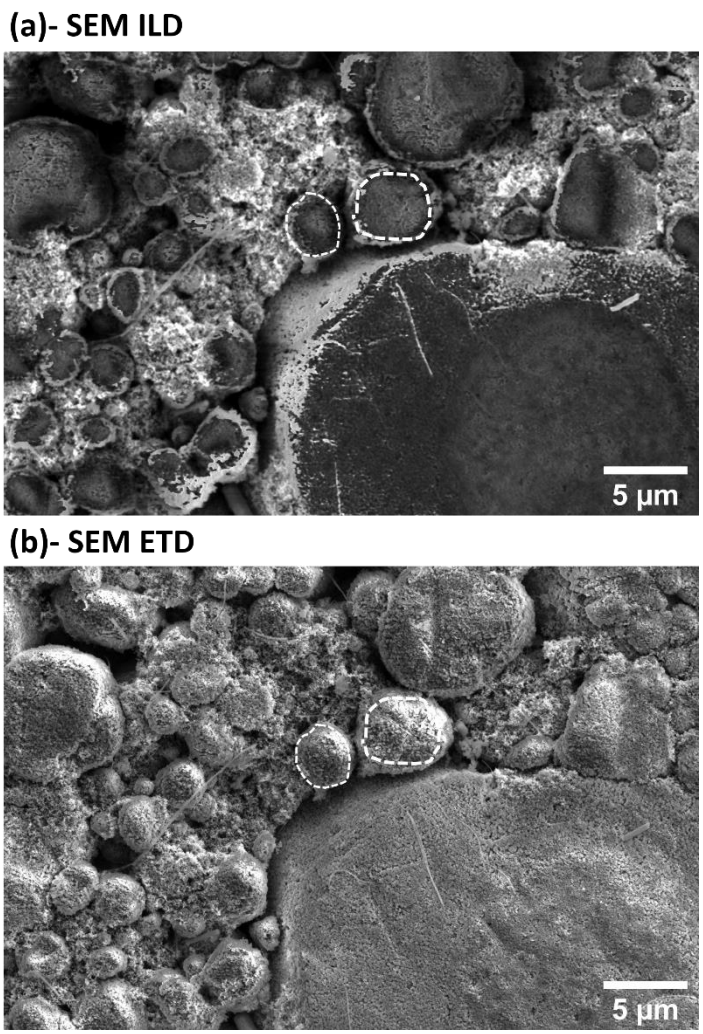

Figure 4.10: SEM eSE images of a 10th cycle discharged electrode exposed to air for 1 min, taken using at 5 kV, and 0.4 nA beam current with (a) and in-lens detector, and (b) an Everhart Thornley Detector. The circled regions represent the same region on each micrograph. Adapted with permission from [26]*. Copyright 2020, the American Chemical Society.*

Figure 4.11 shows SEM ILD eSE images at different beam currents and incident beam voltages. As stated in 4.3.1.1, increasing the beam voltage, increases the electron penetration depth and electron interaction volume.

The images in Figure 4.11 are of the same area on the 10th cycle discharged electrode as the BSE, and ILD eSE in Figure 4.7 (g), and (h), and the ILD, and ETD eSE images in Figure 4.10 (a), and (b). The region consists of a large, ~ 20 µm diameter C-$LiCoPO_4$ in the bottom right hand corner of the images. The large C-$LiCoPO_4$ agglomerate is surrounded by smaller C-$LiCoPO_4$ agglomerates (1- 10 µm in diameter). C65 and binder-rich clusters exist in-between the C-$LiCoPO_4$ agglomerates. Low eSE yield films are present on the C-$LiCoPO_4$ agglomerates. However, on the large C-$LiCoPO_4$ agglomerate, the film is concentrated at the centre of the agglomerate, with mottled contrast on the outside of the particle.

Comparing the ILD eSE image of the large agglomerate in the bottom right hand corner in Figure 4.10 (a), with the ILD eSE images of the same agglomerate in the bottom right hand corner in Figure 4.11 shows initially the low eSE film covered the whole agglomerate. The image in Figure 4.10 was taken prior to the images in Figure 4.11. The disappearance of the layer implies the

electron beam damaged the layer. The remaining low eSE region on the large agglomerate in the images in Figure 4.11 was likely thicker than the layer on the outside of the agglomerate.

The image of the low eSE layers on all the agglomerates is crispest at 1 kV beam voltage and 50 pA beam current (Figure 4.11 (f)). At 1 kV, and 50 pA detail can be observed in the low eSE yield region on the large agglomerate. Lowering the beam voltage reduced the penetration depth, making imaging more surface sensitive, whilst lowering the beam current reduced charging effects as fewer eSEs are generated.

At higher beam currents (100- 200 pA) at 1 kV the surface layer contrast difference is less pronounced and the images are brighter (Figure 4.11 (d) and (e)). The higher electron beam current SEM images appear brighter due to more incident electrons resulting in a higher eSE yield.

For a given beam current at 5 kV beam voltage (Figure 4.11 (a), (b) and (c)), the film eSE yield is lower than the 1 kV images (Figure 4.11 (d), (e), and (f)). However, due to a deeper electron escape depth the edges of the dark regions are not well defined, and also appear streaky, blurring the edges of the surface layer (Figure 4.11 (a), (b) and (c)). The streakiness of the low secondary electron yield regions layer is a charging effect and implies the surface layer is in the positive charging regime, potentially because the layer is insulating. The presence of an insulating surface layer may help explain the rise in overall cell resistance shown in Figure 4.6 (c).

The HIM imaging and ILD voltage variations presented demonstrate the importance of optimising microscope settings to study microstructure of the electrode and CEI layer.

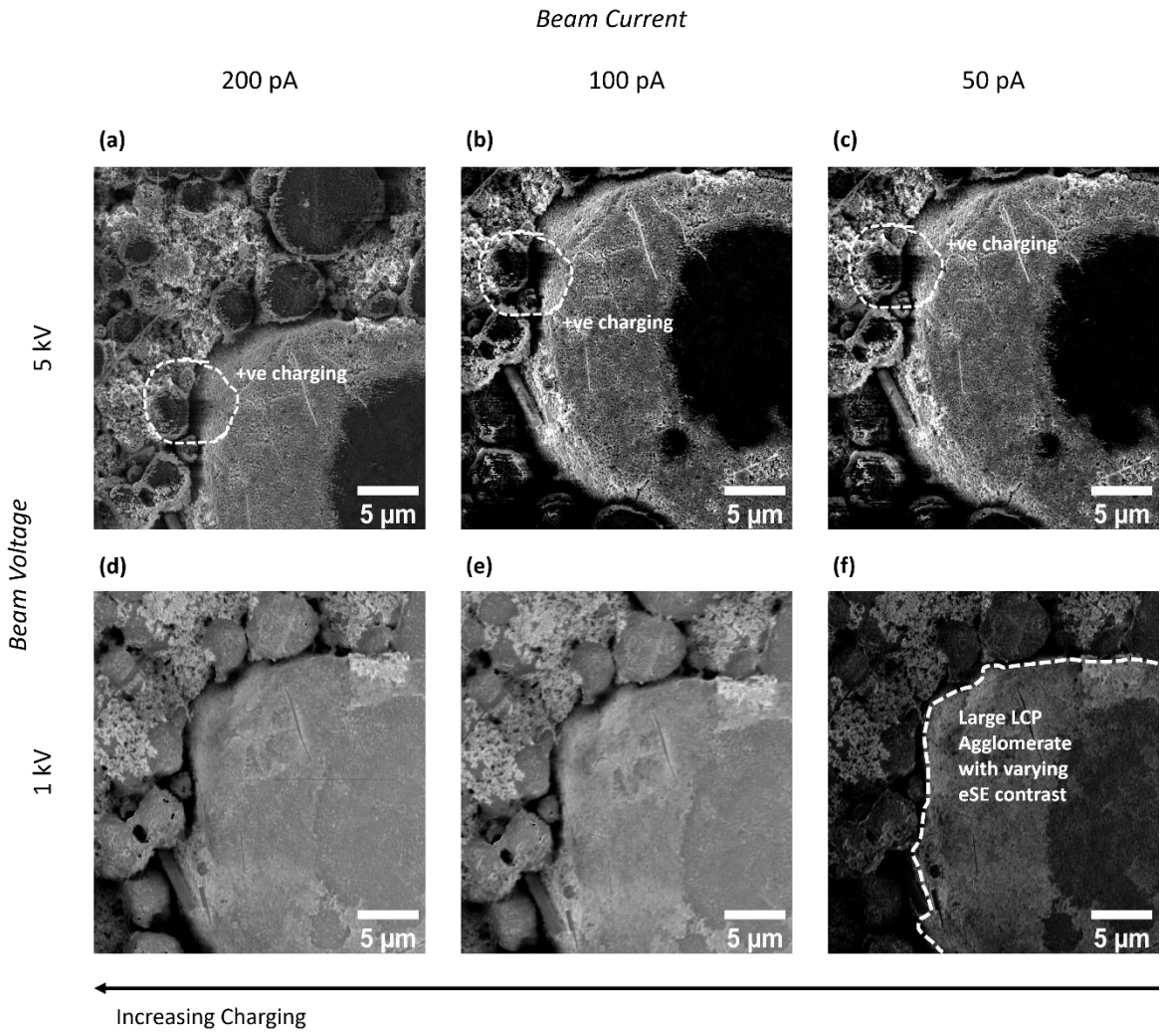

Figure 4.11: SEM ILD-eSE images of the same region of a 10th cycle discharged C-LiCoPO$_4$ electrode top surface using different incident electron beam currents (200 pA, 100 pA and 50 pA) and voltages (5 kV and 1 kV).

4.5.4 Chemical Characterisation with Ne$^+$ ion ToF SIMS

Ne-ion ToF SIMS is used here as a new method to enable site-specific chemical characterisation of the electrode surface in the HIM. Calibration of the SIMS spectra is described in 4.5.4.1. The ToF SIMS, positive and negative mode spectra of uncycled and cycled electrodes are presented in 4.5.4.2. and justification for identification of the ion fragments is detailed in 4.5.4.3.

4.5.4.1 Calibration of the SIMS spectra

Ne$^+$ ion ToF SIMS spectra collected from the HIM are recorded as ion counts against channel number. The channel number refers to the channel on the microchannel plate (MCP) at the end of the extraction which the ions impact. The set-up is detailed in [10], [11], and shown in Figure 4.10. Due to ion separation resulting from different relative velocities, heavier ions will hit different channels on the MCP than lighter ions. Calibration of the channel number with the mass to charge ratio of some known ions allows the mass to charge ratios of other ions detected by the MCP to be know, provided the milling rate is uniform and the sample is homogeneous. Given that the electrodes weren't polished of the sample, and the milling rates vary depending on whether the region is binder or agglomerate rich, the intensity counts from the ToF-SIMS spectra are not used as precise measures of ion fragment concentration in these experiments.

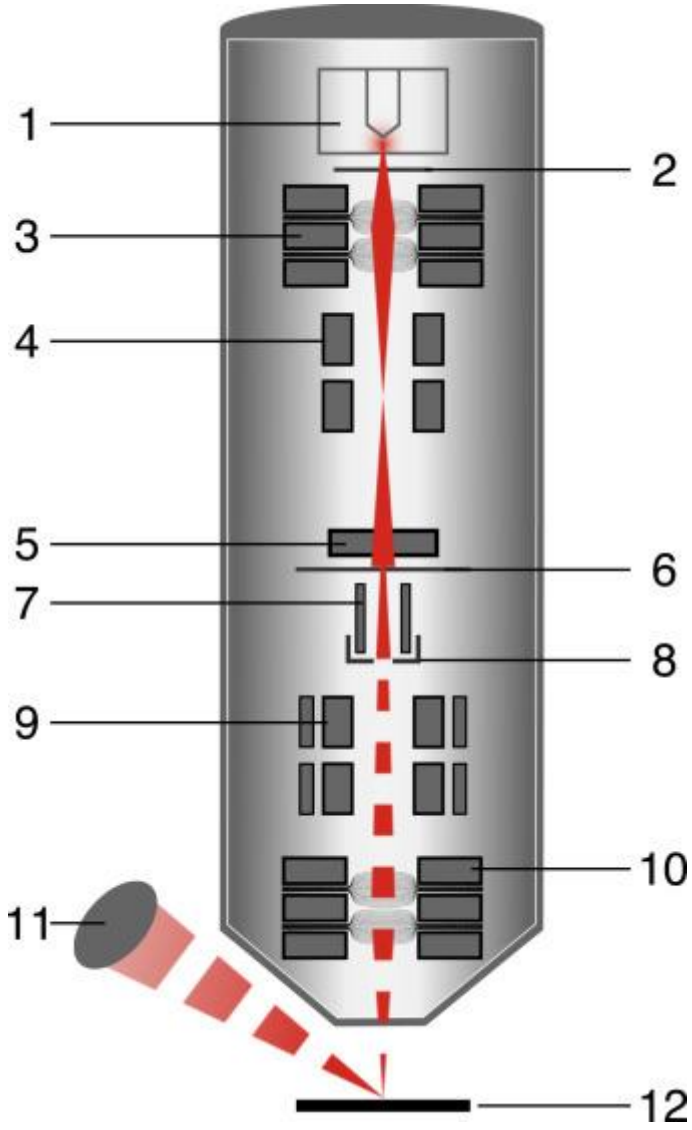

Figure 4.12: Schematic of a helium ion microscope showing 1. The source and gas chamber, 2. Extractor, 3. Einzel lens I, 4. Quadrupole, 5. Column isolation valve, 6. Aperture, 7. Blanking unit, 8. Faraday cup, 9. Octopole, 10. Einzel lens II, 11. The micro-channel plate (MCP) at the end of the ToF SIMS extraction tube, and 12. The sample holder. Red indicates the beam path. The ions from the sample holder (12) to the MCP plate at (11) are the sputtered secondary ions. Reprinted with permission Ultramicroscopy, 162, 2016, 91-97. Copyright (2016) Elsevier, [11].

A negative and positive SIMS spectra of ion yield against channel number for the uncycled electrode is shown in Figure 4.13. The ion counts per channel were an order of 10 greater for the positive SIMS spectrum, compared with the negative SIMS spectrum (Figure 4.13 (a), and (b)). The positive SIMS collection area was 375 μm^2. The spectrum collection area was not recorded for the negative SIMS spectrum. Given the ion counts are similar to the ion counts per channel of the depth profiles, it is likely the sample area was ~ 1 μm^2. The purpose of this section of the thesis is to demonstrate calibration of the SIMS spectra. The impact of the collection area error will be discussed in 4.5.4.2, and 4.5.4.3.

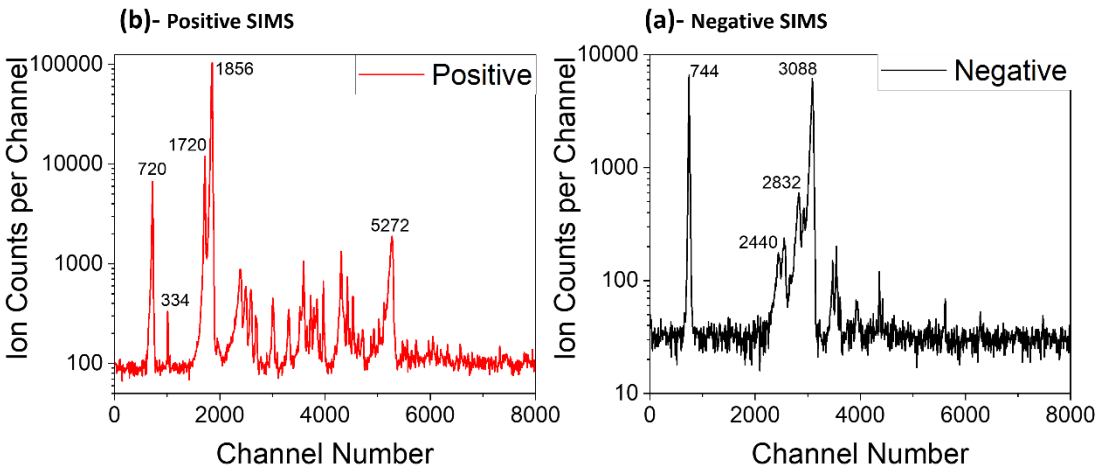

Figure 4.13: ToF SIMS Spectra showing Ion Counts per Channel against Channel number for (a) negative SIMS, and (b) positive SIMS. The Channel numbers of peaks used in calibration are displayed.

In order to identify the ion fragments, channel number must be converted to mass to charge ratio by calibrating each spectra to peaks with known mass to charge ratios. In this work, the identity of each peak was deduced based on knowledge of what elements were contained within the uncycled electrode and what elements are likely to appear in positive or negative mode SIMS given the relative sensitivity factors of each element (Figure 4.4 and Figure 4.5).

It is known that uncycled cell components contain the following species:

- Active material: $LiCoPO_4$
- Active material carbon coating: C
- Conductive additive: (Carbon black) C
- Binder: $-(C_2H_2F_2)_n-$

Table 4.2 details the cell components, the associated single element ion components which may form and whether they will be more likely detected in positive or negative SIMS mode based on the RSF values in Figure 4.4 and Figure 4.5.

Table 4.2: Cell components, the associated single element ion fragment, the mass to charge ratio of the fragment, whether the fragment is most likely to occur in positive or negative SIMS mode and the peak guess channel number.

Component	Ion	Mass to Charge (m/z) ratio (u)	Positive or Negative SIMS	Peak guess Channel Number
$LiCoPO_4$	Li^+	6 or 7	Positive	Li-7: 1720, Li-6: 1856
	O^-	16 or 18	Negative	O-16: 2832
	P^-	31	Negative	
	Co^+	59	Positive	
Conductive Additive	C^-	12 or 14	Negative	C-12: 2440
	C^-	12 or 14	Negative	
Binder	H^+ or H^-	1 or 2	Positive or Negative	H-1: 720,
	F^-	19	Negative	F-19: 3088

Single element ion fragments were considered because lower channel counts result from lower mass to charge ratio fragments. The RSF values shown in Figure 4.4 and Figure 4.5 show that Li^+ ions will occur in positive SIMS spectra, and O^-, and F^- ions will occur in negative SIMS spectra (see Table 4.2). Therefore, as the majority of the elements present in $LiCoPO_4$ electrodes occur within the first 20 elements of the periodic table, the potential identities of the lower channel number peaks were limited, allowing their identities to be deduced. For example, on both the positive and negative SIMS spectra (Figure 4.13 (a) and (b)), the first peak which occurs is a high intensity peak at 720 and 744 in the positive and negative spectra respectively. The lowest mass to charge ratio which could be present is for H^+ and H^- (1 u). Therefore, the first peak is identified as to be 1 u.

Different mass guesses for the peaks were attempted until the peak channel numbers in the spectra calibrated to within ± 0.2 u of an integer mass to charge ratio (m/z). The accuracy of within ± 0.25 u of an integer was chosen because ion fragments must have an integer value due to mass number being based on the number of protons and neutrons in the nucleus (unless the ion fragments have a +2 or +3 charge, when the value will be .5 or .3333). The ± 0.25 u value was chosen as an accuracy marker based on previous calibration work by Klingner et al. [11].

Figure 4.14 shows Δm/z against channel number for the positive and negative SIMS 10^{th} cycle discharged spectra in Figure 4.13. Δm/z is the difference between the calculated m/z ratio and the integer m/z ratio of each peak. Figure 4.14 shows that for all the peaks (except one peak in the positive SIMS spectrum at channel number 4447 (41 u), the peak fitting errors were within the

acceptable error limits (± 0.2 u). It is possible the channel number 4447 peak in the positive SIMS spectra is an ion with a m/z ratio of 41.5 u.

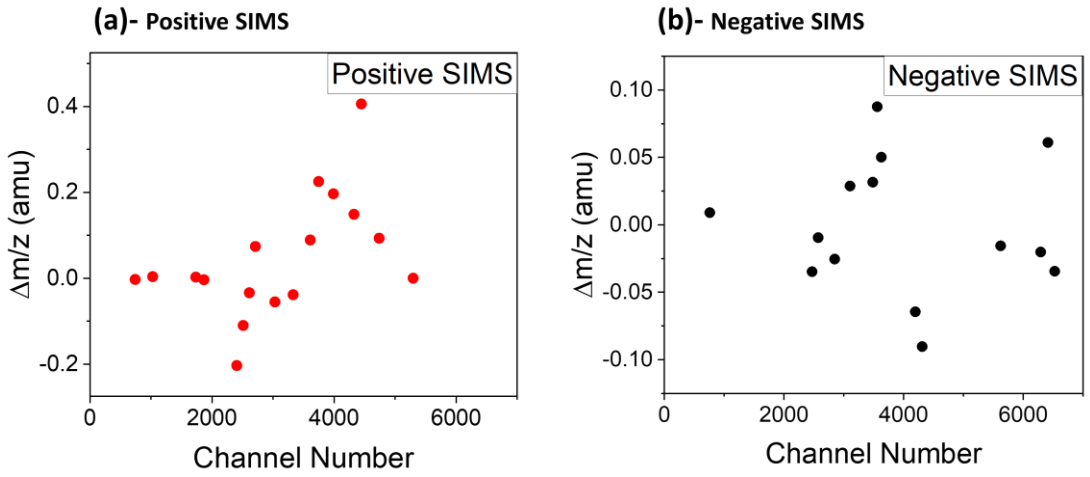

Figure 4.14: m/z charge ratio error (Δm/z) against the channel number for (a) the positive, and (b) the negative SIMS spectra in Figure 4.13.

For calibration, the calibration software developed by Klingner et al. [11] required the identity of at least 4 of the peaks to be deduced, and the maximum of the peak to be known. Maxima were calculated by fitting each peak to a Gaussian curve for each peak in the calibration software. As demonstrated by the broadness of the peaks in Figure 4.13, calibration was less accurate for broader peaks.

Another error which affected calibration included peak doublets, caused by poor alignment of the spectrometer with the sample, hence ions of the same mass to charge ratio took slightly different time to reach the MCP. Doublets occurred on the low m/z ratio fragments of some of the spectra. The occurrence of doublets caused the true maxima to be inaccurate.

The doublet error on some of the SIMS spectra resulted in the calibration of the lower m/z ratio ion (up to 19 u) to have a calibration with an error of ±0.5 u. As not all the spectra contained doublets, and no extra peaks occurred on spectra containing doublets, the identities of the peaks could be deduced from mass spectra which did not have the doublet error.

4.5.4.2 Ne-ion ToF SIMS spectra and mapping of cycled and uncycled electrodes

Figure 4.15 shows the positive (a) and negative (b) Ne^+ ion SIMS spectra of an uncycled C-$LiCoPO_4$ electrode, and an electrode at the 10^{th} cycle in the discharged state.

The concentrations of the ions sputtered have not been calculated because the beam conditions varied (the current dropped) when acquiring the spectra. Moreover, the electrode surface was rough which may have influenced sputtering yield of some ions. As the conditions were not identical when collecting the spectra, it is difficult to attribute small changes in peak intensity to phenomena such as absolute concentration. The analysis of the SIMS spectra will therefore be qualitative.

The positive spectra in Figure 4.15 (b) show that no new mass to charge ratio peaks appear on the surface of the cycled electrode compared to the uncycled electrode. On both the uncycled and the 10^{th} cycle discharged SIMS spectra, the most intense peaks occur at 6 u, 7u and 59 u. The 59 u peak shape is broader than the 6 u and 7 u peaks.

The negative spectra in Figure 4.15 (a) shows that a number of new mass to charge ratio peaks appeared on the cycled electrode, compared to the uncycled electrode. Both the uncycled and cycled electrode surfaces had peaks at 12 u, 16 u, 19 u, 24 u, 31 u, 63 u and 79 u. However, the peaks at 63 u and 79 u were more intense on the cycled electrode SIMS spectra compared to the uncycled spectra. A series of new peaks formed on the cycled electrode, the most intense being at 35 u, 37 u, 45 u, 82 u and 85 u.

The overall ion count of the uncycled C-$LiCoPO_4$ negative spectrum is an order of magnitude lower than the other SIMS spectrum in Figure 4.15. As stated in 4.5.4.1 the lower ion counts on the uncycled SIMS spectrum likely occurred because the collection area was smaller than the collection area of the other SIMS spectra (375 μm^2). The uncycled SIMS collection area was not recorded, but estimated as ~1 μm^2.

The area difference error may result in some peaks not occurring because the signal is contained within the background noise, making the qualitative observations invalid. Higher sampling areas result in a higher secondary ion yield, and hence less noise, so for lower secondary ion yield peaks, such as 82 u, and 85 u, the peaks may have occurred within the noise of the uncycled SIMS spectra.

However, comparison with other SIMS spectra collected show that the yield of 82 u, and 85 u significantly increased on cycling. The depth profiles presented in subsequent chapters were also checked for 82 u, and 85 u peaks. Depth profiles were taken over 0.5- 1.5 μm^2 sample (depending on the feature size). 82 u, and 85 u did not occur in the uncycled depth profile spectra, but did occur on cycled spectra taken closer to the surface of cycled electrodes.

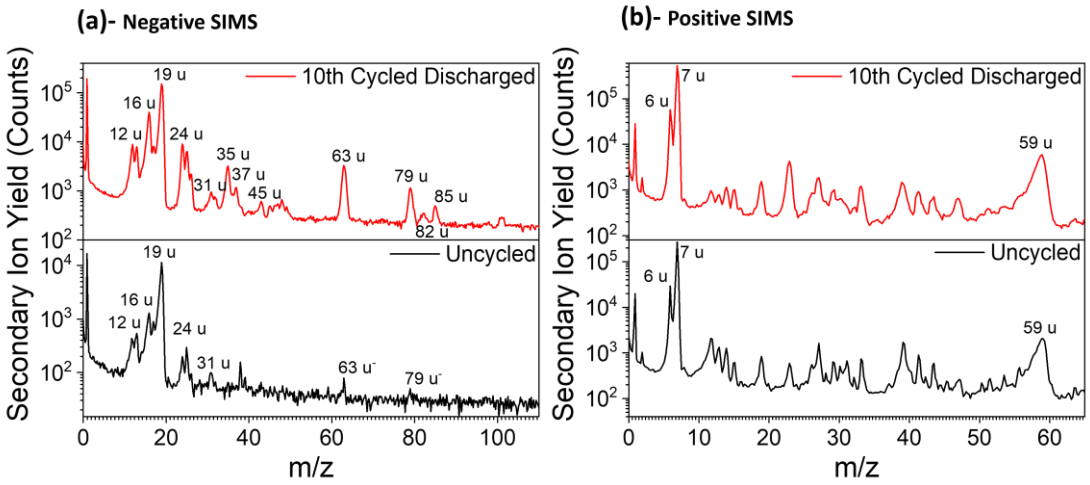

Figure 4.15: Ne-ion secondary ion mass spectra of the top surface of an uncycled electrode and the 10th cycled electrode in (a) negative and (b) positive mode. SIMS spectra are an average over 375 μm^2 for the positive SIMS spectra (b), and the Negative cycled spectra (a), and hence encompass the low He-iSE yield layer, C-$LiCoPO_4$ agglomerates and binder/ C65. The area of the uncycled negative SIMS collection area is unknown. The m/z ratios for peaks used in the discussion are identified. Reproduced with permission from [26]*. Copyright 2020, the American Chemical Society.*

The unique advantage of using ToF-SIMS in the HIM for chemically characterising the electrode surface is the direct high spatial resolution correlation of microstructure changes with chemistry using ToF SIMS mapping, including detection of Li (Figure 4.16). The SIMS maps in Figure 4.16 (a-f) are of the same region as the He-iSE image in Figure 4.16 (g), and the Ne-iSE image in Figure 4.16 (h) on a 10th cycle discharged electrode. It should be noted the contrast inverts for the Ne-iSE image, so the low surface film appears lighter than the surrounding areas.

The maps in Figure 4.16 were constructed by plotting the total yield intensity of the area under the peaks in Figure 4.15. The peak minimum and maximum m/z values were defined by the intersections of the fitted Gaussian curve with the m/z axis. If it was obvious the program defined maximum included a neighbouring peak, the minima and maxima were manually adjusted so the counts included in the map did not include neighbouring peaks. As a result, the channel widths defining the peaks varied depending on the broadness of the peak in the total SIMS spectra.

The maps show that the low He-iSE yield layer regions are rich in 59 u, 63 u, 7 u and 16 u ions compared to the binder and C65-rich regions. Ion fragments with 19 u m/z are more concentrated in the binder-rich regions compared to the low He-iSE yield layer, but are still present in the low He-iSE yield layer. Ion fragments with 12 u m/z ratio appear marginally more concentrated on the low He-iSE yield layer regions than in the binder- C65-rich regions.

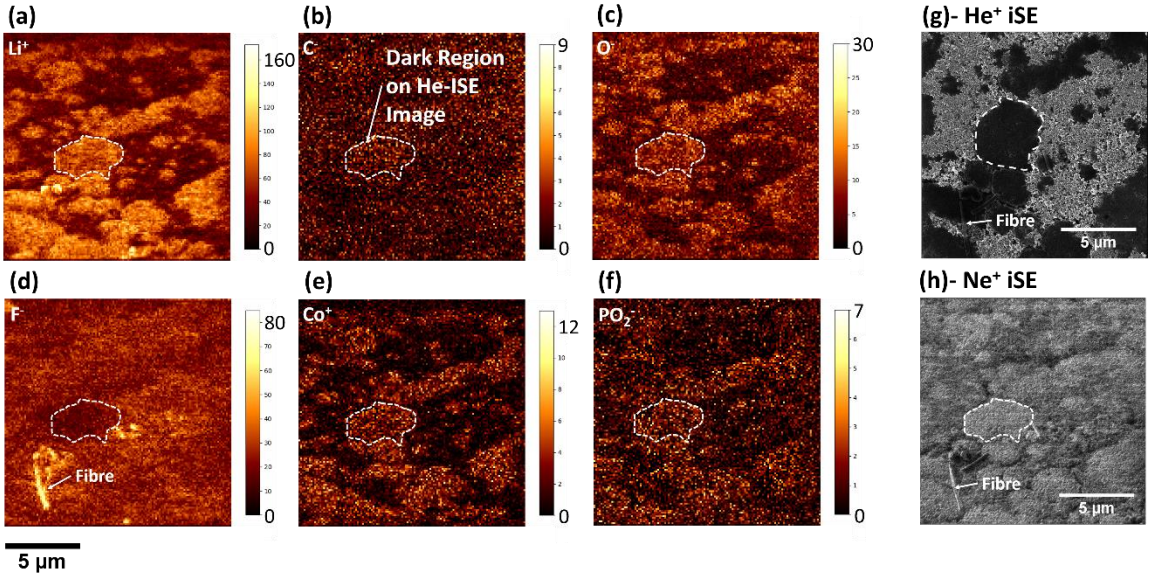

Figure 4.16: SIMS maps of the electrode top surface of a 10th cycle discharged C-$LiCoPO_4$ electrode imaged at a tilt angle of 54 °. The colour gradient scales are secondary ion counts per pixel. The maps presented are (a) 7 u (Li^+), (b) 12 u (C^-), (c) 16 u (O^-), (d) 19 u (F^-), (e) 59 u (Co^+), (f) 63 u (PO_2^-). The white dotted circle represents the low He-iSE yield layer region circled on the He-iSE image in (g), and the Ne-iSE image in (h). Reproduced with permission from [26]*. Copyright 2020, the American Chemical Society.*

4.5.4.3 Identification of the mass fragments

Comparing the spatial distribution maps in Figure 4.16 to the spectra in Figure 4.15 allows the ion fragments to be identified. For multiple element fragments, the SIMS spectra were also compared to previous work using SIMS on cycled electrodes. As this is the first example of Ne^+ ion ToF-SIMS on $LiCoPO_4$ electrodes, the results were also compared to Cs^+ ion SIMS work on high voltage electrodes using the same electrolyte [23]

The identities of the peaks which change significantly in the spectra, or are an area of interest for depth profiling are detailed in Table 4.3. Table 4.3 also shows the supporting evidence for the identity of the ions resulting in the peaks in Figure 4.15.

Table 4.3: Table showing the mass to charge (m/z) ratio, the identified ion fragment, origin of fragment and the supporting evidence for the ion fragment of the peaks labelled in Figure 4.15

Mode	m/z (u)	Ion	Identified ion fragment	Supporting Evidence for Ion Identification
-ve	12	C^-	C-coating or Binder	C expected on the surface as part of carbon coating, and binder. 12 u is present across the whole surface (Figure 4.16 (b))
	16	O^-	$LiCoPO_4$	O expected from $LiCoPO_4$. 16 u found on the $LiCoPO_4$ agglomerates (Figure 4.16 (c))
	19	F^-	Binder	F expected from binder areas. 19 u found on binder rich regions of the electrode (Figure 4.16 (d)).
	24	C_2^-	C-coating or binder	Previously found from carbon additive and binder components with Cs^+ SIMS [23].
	31	P^-	$LiCoPO_4$	P expected on the surface from $LiCoPO_4$. Peak was too weak to confirm via mapping. Presence on uncycled electrodes means it is unlikely to be electrolyte degradation fragments, such as CH_3O^- [23].
	35	OF^-	Degradation product	35 u is only found on cycled electrodes so is a fragment from degradation on the surface. Similar fragments were found by Manthiram et al. [28]. Mass fragment at 37 u, likely to be O^{18} isotope of OF^-.
	37	$O^{18}F^-$	Degradation product	O-18 is an isotope of O [29]. Product is similarly only found on surface of cycled electrodes.
	45	LiF_2^-	Degradation product	A typical fragment found on high voltage electrodes cycled with $LiPF_6$ electrolytes. Forms from $Li_xPO_7F_z$, or LiF [23].
	63	PO_2^-	$LiCoPO_4$/ Degradation product	Could originate from PO_4 tetrahedra in $LiCoPO_4$, or from $Li_xPO_yF_z$ components. Previously found on $LiPF_6$ electrolyte high voltage cathodes using Cs^+ SIMS [23].
	79	PO_3^-	$LiCoPO_4$/ Degradation product	Could originate from PO_4 tetrahedra in $LiCoPO_4$, or from $Li_xPO_yF_z$ components. Previously found on $LiPF_6$ electrolyte high voltage cathodes using Cs^+ SIMS [23]. Depth profiles in Figure 4.19 (a, b, and c) show 79 u follows 63 u trend, so likely both are likely to be similar products.
	85	POF_2^-	Degradation product	Could originate from $Li_xPO_yF_z$ components. Previously found on $LiPF_6$ electrolyte high voltage cathodes using Cs^+ SIMS [23]. Similarities with F^- trend in the negative

				depth profiles imply the fragment contains F Figure 4.19 (b, and c).
+ve	6	$Li(6)^+$	$LiCoPO_4$	Li-6 is an isotope of Li with an isotopic abundance (mole fraction) of 0.019- 0.078 [29]. Lowest mass number expected (aside from H-1, and H-2). Expected on SIMS spectra, but with less intensity than Li-7.
	7	$Li(7)^+$	$LiCoPO_4$	Li-7 is an isotope of Li with an isotopic abundance of 0.922-0.981 [29]. Expected on SIMS spectra, but with greater intensity than Li-6.
	59	Co^+	$LiCoPO_4$	59 u is the only stable isotope of Co [29]. Co^+ could originate from $LiCoPO_4$. The broadness of the Co^+ peak in Figure 4.15, suggests the ion originates from the bulk due to the broad energy distribution of ions sputtered from a bulk material. Co^+ is less mobile than Li^+, so it is Surprising Co^+ is visible on the surface of electrodes when mapping (Figure 4.16 (e)), through a 2- 8 nm carbon layer on the electrodes, unless it is in the layer.
	59	$Li_3F_2^+$	Degradation Product	Previous Bi^+ SIMS analysis of high voltage materials cycled with $LiPF_6$ in EC/ DMC identified 59 u as $Li_3F_2^+$ [30]. $Li_3F_2^+$ fragments form cathode electrolyte interphase (CEI) components [30]. 59 u peak in Figure 4.15 (a) is broad, possibly due to Li-7 and Li-6 isotopes present in $Li_3F_2^+$ ($^6Li_2{}^7LiF_2^+$, $^6Li^7Li_2F_2^+$, and $^7Li_3F_2^+$) [30], although no other significant Li and F containing fragments were identified. If 59 u is $Li_3F_2^+$, it is surprising it is present on uncycled electrodes (Figure 4.15 (b)) as $Li_3F_2^+$ forms as a fragment of CEI layer species which form when the electrode is cycled [30].

4.5.5 Cycling Behaviour of the Electrodes

He-iSE images of the C-$LiCoPO_4$ electrode surfaces were taken under comparable imaging conditions at different cycle numbers to assess how the electrode microstructure varies with cycle

life (Figure 4.17). After being charged to 5.1 V vs. Li/ Li^+ on the 2nd, 5th and 10th cycles a low He-iSE yield layer is present (Figure 4.17 (a), (b) and (c)), indicating that the layer forms at high voltages.

There are no low He-iSE yield regions (dark contrast regions) on the surface of the discharged electrode after the second cycle (Figure 4.17 (d)), indicating the layer is either not present or very thin. Given all the electrodes in Figure 4.17 had the same pre-imaging treatment, the lack of layer on the 2nd cycle discharged electrode (Figure 4.17 (d)) implies dissolution of the layer during cycling.

After the 5th cycle, the low He-iSE yield layer is visible in the discharged state (Figure 4.17 (e)), however regions of variable contrast indicate the thickness of the layer is in-homogeneous. In-homogenous thickness suggests partial dissolution of the low He-iSE layer dissolution on discharge.

On the 10th cycle electrode, in the discharge state (Figure 4.17 (f)), there is less contrast variability of the low He-iSE yield regions compared with the 5th cycle discharged cycle electrode (Figure 4.17 (e)). Increased homogeneity of the low He-iSE layer at later cycles correlates with the increase in resistance and loss of capacity in Figure 4.6.

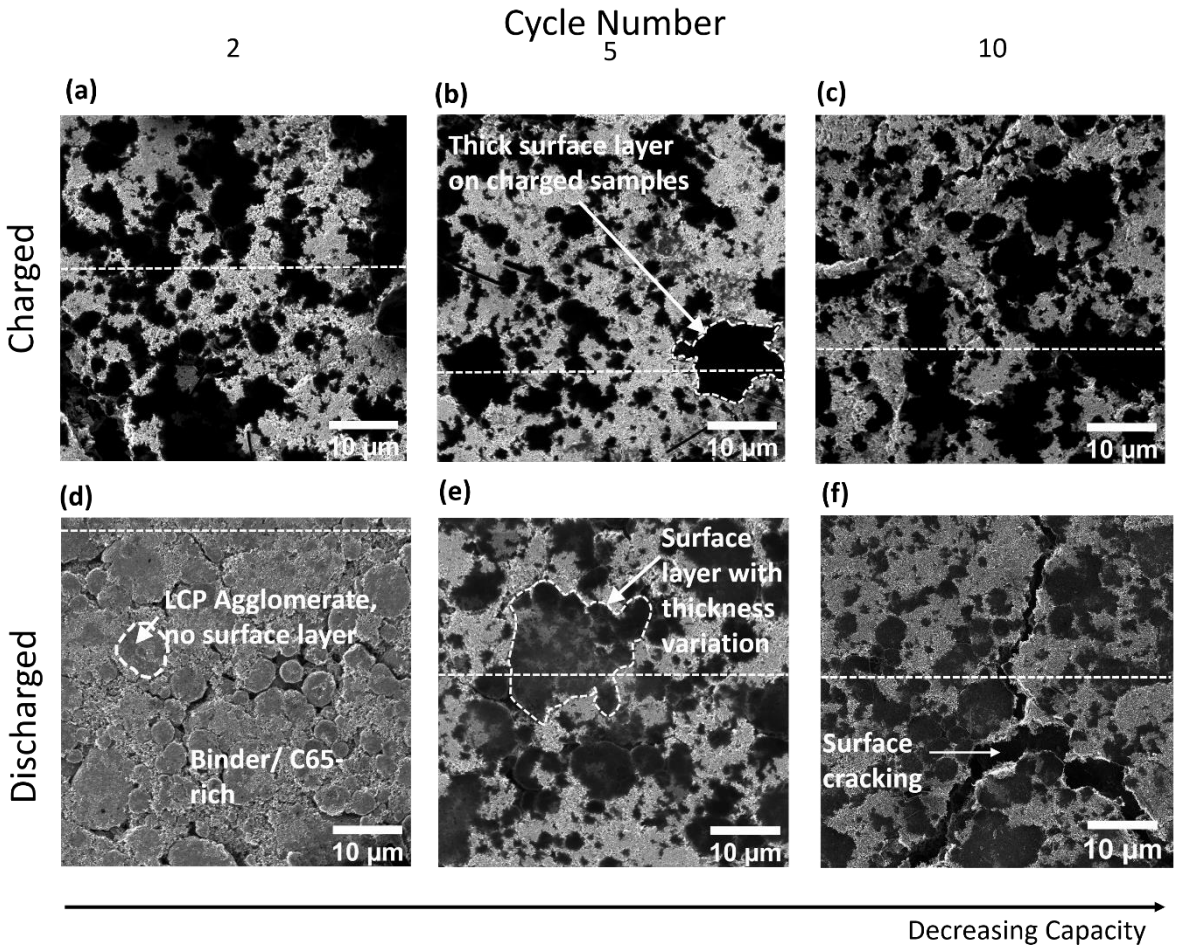

Figure 4.17: He^+-iSE images of the top surface of cycled electrodes showing the variation in microstructure with cycle number and state of charge. Dark contrast corresponds to the low He-iSE yield surface layer and light contrast corresponds to binder/ C65- rich regions. 'Charged' samples (a-c) were charged to 5.1 V vs. Li/ Li^+ and de-crimped on the cycle number shown. Similarly, 'Discharged' samples (d-f) were discharged to 2.5 V vs. Li/ Li^+ on the cycle number shown. The white dotted line on the images represents the line used to quantify the contrast differences in Figure 4.18. Reproduced with permission from [26]. *Copyright 2020, the American Chemical Society.*

In order to quantify the changes in signal collected from low He-iSE yield regions, and high He-iSE yield regions, the normalised signal collected across a single image was collected (Figure 4.18). The normalised grey scale represents the signal (measured in grey scale) at a point in the image, divided by the highest grey scale signal measured on that image. For the charged samples, the low He-iSE yield layer regions have 0 grey scale signal, indicating no detectable helium ion induced secondary electron emission. For the discharged samples, the signal does not drop to zero. The results may indicate secondary electron emission from the low He-iSE regions results from the underlying C-$LiCoPO_4$ due to a thinner surface layer.

The regions showing inhomogeneous He-iSE yield in Figure 4.17 (e) and (f) (the discharged samples) are predominantly on larger agglomerates, consistent with the presence of residual CEI at the centre of the large agglomerate in Figure 4.11.

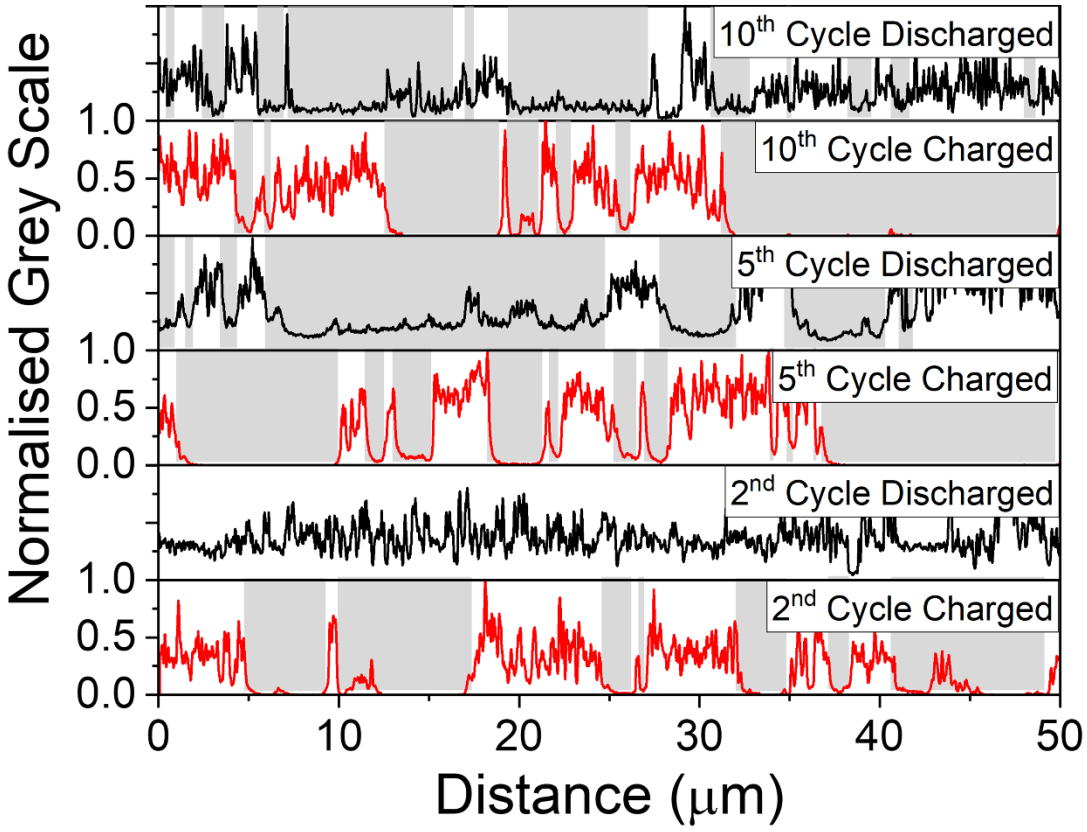

Figure 4.18: Normalised grey scale signal line profiles of the images in Figure 4.17. The white dotted line on the images in Figure 4.17 indicate the regions the line profiles were taken from. The grey scale has been normalised to the maximum value for each image. The grey boxes indicate low He-iSE surface layer regions on the image. Reproduced with perimission from [26]. *Copyright 2020, the American Chemical Society.*

4.5.5.1 Ne-SIMS Depth Profiles of the C-$LiCoPO_4$ Agglomerates

Ne-SIMS chemical depth profiling (Figure 4.20) was performed on cycled C-$LiCoPO_4$ primary particle agglomerates with a low He-iSE yield surface layer present (see Figure 4.17) to investigate the variation in surface chemistry with cycling [26]. A schematic of the microstructure of the cycled C-$LiCoPO_4$ agglomerate electrode surface is shown in Figure 4.19. Cycled electrode agglomerates consist of 300 nm carbon coated $LiCoPO_4$ primary particles, binder, and CEI layer. Ne-SIMS depth profiles of the C-$LiCoPO_4$ agglomerates contain sputtered ion fragments originating from all three

components throughout milling (Figure 4.19). The lateral width of the scanned areas was larger than one $LiCoPO_4$ primary particle (between 0.5 and 1.5 µm field of view, depending on the region of interest), hence up to 3 regions were sampled on each sample. The trends discussed in this section were consistent between different regions of the same sample.

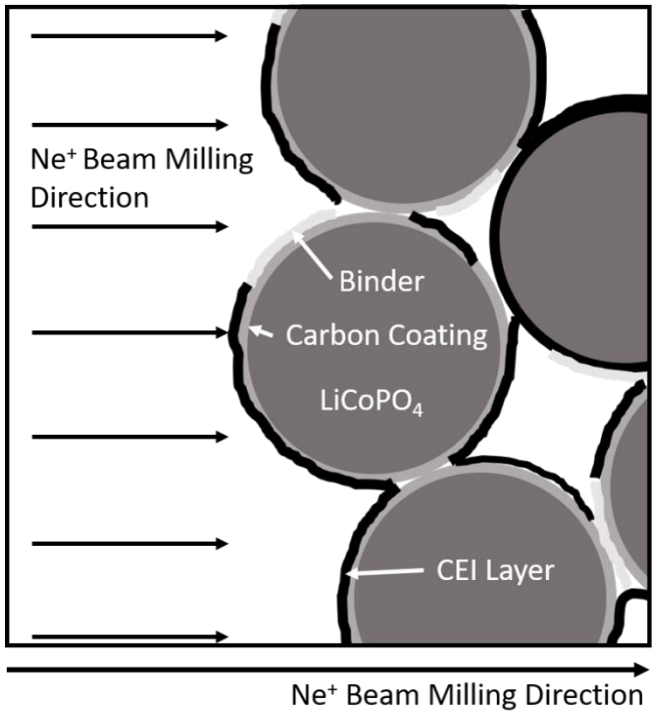

Figure 4.19: Schematic of a C-$LiCoPO_4$ agglomerate as the Ne^+ ion beam mills through the sample. The arrow indicates the milling direction. As the ion milling area is larger than a single C-$LiCoPO_4$ particle, multiple components are scanned during a SIMS depth profile as the ion beam mills through the sample. Reproduced with permission from [26]*. Copyright 2020, the American Chemical Society.*

The SIMS depth profiles in Figure 4.20 are presented as measured ion intensities normalised to the maximum count measured for the individual fragment to qualitatively compare changes in surface layer chemistry between different cycle numbers post-mortem [26]. It was not possible to quantify the sputtered ion yield as sample concentration because the cathode surface is too complex to be modelled with SRIM due to surface roughness and the presence of multiple different components with different sputtering yields. Standard depth profiles were not taken as in [31].

The normalised ion yields are plotted against Ne^+ ion fluence in Figure 4.20. Ne^+ ion fluence is the product of the beam current and milling time, divided by the milling area [26]. The ion yields are not plotted against depth as quantifying the Ne-SIMS sputtering depth and sputtering rate is difficult for an electrode. Sputtering depth can be calculated by measuring the depth of the sputtering crater and calculating a sputtering rate. Surface roughness makes post-measurement optical profiling to measure the sputter crater depth difficult. A crater deep enough to be measured with post-milling optical profiling could be created using long milling times [23]. However, in Ne-SIMS in the HIM long milling times are difficult due to the instability of the Ne-FIB trimer, as discussed in 4.3.2.2.

The ions analysed in the negative SIMS depth profiles in Figure 4.20 (a), (b), and (c) are 16 u (O^-), 19 u (F^-), 24 u (C_2^-), 63 u (PO_2^-), 79 u (PO_3^-) and 85 u (POF_2^-) [26]. Table 4.4 identifies where the fragments originate. O^-, and F^- were chosen as these are the most intense peaks on the spectra in Figure 4.15 (a). C_2^- was chosen to represent carbon as the O^- peak overlapped with the C^- peak when the O^- peak intensity increased during depth profiling, resulting in an inaccurate depth profile for the 12 u ion. PO_2^-, PO_3^-, and POF_2^- were chosen as their ion yields were significantly higher on cycled electrode surfaces compared to the uncycled electrode (see Figure 4.15 (a)).

On the cycled electrodes, a surface layer is present on the C-$LiCoPO_4$ agglomerates (as identified in the He^+ iSE images, Figure 4.17 (a, b, and c)). The Ne-SIMS depth profiles of the 20th cycle discharged electrodes (Figure 4.20 (b) and (c)) show POF_2^- on the surface. POF_2^- was not present on the surface (or through the depth profile) of the uncycled electrode (Figure 4.20 (a)), consistent with the results in Figure 4.15 (a). A 85 u (POF_2^-) peak was also detected on the second cycle charged electrodes. The depth profile is not plotted in Figure 4.20 (b) because the relative intensity of the 85 u peak for the second cycle charged electrode was small.

The yield of F^- and POF_2^- follow similar trends on the 10th cycle discharged electrode depth profiles (Figure 4.20 (b), and (c)), with both fragments exhibiting relatively constant concentrations throughout the milling. The presence of POF_2^- at the surface of cycled electrodes is consistent with the layer forming as a result of electrolyte oxidation.

Ne-SIMS depth profiling shows the transitions between different components of the $LiCoPO_4$ agglomerates (detailed in Figure 4.20 (g)) based on the appearance of maximum counts from different fragments during milling. Sputtering into the uncycled electrode (Figure 4.20 (a), initially F^- is high, indicating a thin layer of surface binder. The C_2^- yield remains high as the F^- yield drops indicating milling progress into the carbon coating layer on the $LiCoPO_4$ particles. O^-, PO_2^- and PO_3^- have the highest yield towards the end of the depth profile, representing milling into the $LiCoPO_4$-rich region bulk. The yields of the ion fragments of binder and carbon layer do not drop to zero as the agglomerates are porous, and particles randomly distributed within the milling area (see Figure 4.19).

In the depth profile of the 2nd cycle charged electrodes, the Ne-SIMS depth profiles (Figure 4.20 (b)) show that the highest yields of F^-, C_2^-, and O^-, PO_2^- and PO_3^- occur in a similar sequence to the uncycled electrode. However, the yields of O^-, PO_2^-, and PO_3^- increase, and C_2^- yield decreases, after less Ne^+ ion fluence (after less depth) during depth profiling on the second cycle charged sample (Figure 4.20 (b)) compared to the uncycled electrode (Figure 4.20 (a)). The increase in O^-, PO_2^-, and PO_3^-, and decrease in C_2^- yield after less Ne^+ ion fluence implies changes (potentially chemical intermixing) to the carbon coating layer during cycling.

The transition between the highest yield of O^-, PO_2^-, and PO_3^- and the lowest C_2^- yield occurs after more Ne^+ ion fluence on the 2nd cycle charged electrode (Figure 4.20 (b)) compared with the 10th cycle discharged electrode (4.20 (c)). The occurance of the transition after less milling implies further chemical changes to the carbon coating, and a shifting of interfaces with increased cycling.

The ions analysed in the positive Ne-SIMS depth profiles of the C-$LiCoPO_4$ agglomerates (Figure 4.20 (d), (e), (f)) are 7 u (Li^+), 12 u (C^+) and 59 u (Co^+) (see Table 4.4). Li^+ was analysed to confirm Li presence in the CEI layer. C^+ was measured to represent the carbon-coating layer. The ionisation efficiency of C in positive SIMS is less than in negative SIMS, so the C^+ trends in the positive SIMS depth profiles (Figure 4.20 (d), (e), and (f)) do not match the C_2^- trends in the negative depth

profiles (Figure 4.20 (a), (b), and (c)). As discussed previously in 4.5.4.3, 59 u ion fragments could originate from either Co^+, or $Li_3F_2^+$, or be a contribution from both.

Lithium is expected near the surface of uncycled electrodes and any discharged electrodes because the discharged state of $LiCoPO_4$ is $LiCoPO_4$ [32]. Ne-SIMS depth profiling of the uncycled C-$LiCoPO_4$ agglomerate shows that initially the Li^+ yield increases (Figure 4.20 (d)). The depth profile of the 10th cycle discharged electrode, known to have a surface layer, also exhibits an initial increase in Li^+ yield, but the maximum yield of Li^+ occurs deeper into the agglomerate (Figure 4.20 (f)).

Sputtered Li^+ ions are detected at all sputtered depths, corresponding to both the carbon-coating in the uncycled electrode, and the surface layer in the 10th cycle discharged electrode (Figure 4.20 (d), (e), and (f)).

If the electrode was fully charged, lithium is not expected to be present on the charged electrodes (Figure 4.20 (e), and (f)), as the charged state of $LiCoPO_4$ is $CoPO_4$ [32]. However, a Li^+-rich region is present on the surface of the 2nd cycle charged electrode, as shown by an increase in Li^+ yield with depth, reaching a maximum after milling with 3.59×10^9 ions μm^{-2} (Figure 4.20 (e)). The Li^+ yield then steadily decreases with depth away from the surface, indicating a layer of uncycled Li.

Lithium was also detected on the surface of the 10th cycle charge electrode (Figure 4.20 (f)). The increase to the maximum yield of Li occurred after further ion milling (1.0×10^{10} ions μm^{-2}) compared with the 2nd cycle charged electrode (3.59×10^9 ions μm^{-2}). The maximum Li^+ yield occurred after an initial spike in 59 u yield after an ion fluence of 1.35×10^9 ions μm^{-2}.

Considering the positive Ne-SIMS depth profiles of the 59 u ion fragments (Co^+ or $Li_3F_2^+$), the 59 u yield steadily increases with Ne^+ ion fluence/depth in both the uncycled electrode (Figure 4.20 (d)) and the 10th cycle discharged electrode (Figure 4.20 (f)). However, the 59 u maximum occurs after more Ne^+ ion fluence in the 10th cycle discharged electrode (Figure 4.20 (g)). The gradual increase in the yield of 59 u is consistent with 59 u representing Co^+ ions, as $LiCoPO_4$ represents the bulk (as shown on Figure 4.19).

The Ne-SIMS depth profile from the 2nd cycle charged electrodes both has the maximum yield of 59 u at the outer surface of the electrode (Figure 4.20 (e)). The yield of 59 u decreases after milling further into the electrode surface. A similar trend was observed in the 10th cycle charged electrode (Figure 4.20 (f). The high yield of 59 u at the surface of charged samples is surprising if the 59 u signal originates solely from Co^+, ions, since the Co^+ yield should increase to a maximum when ion milling reaches the $LiCoPO_4$-rich and $CoPO_4$-rich bulk regions in the discharged and charged samples respectively. The high yield of 59 u at the outer surface of the charged electrodes could arise from the additional contribution of $Li_3F_2^+$ ions arising from electrolyte oxidation.

Table 4.4: Table showing the m/z ratios, the associated ions, and their origin for the ions tracked in the depth profiles in Figure 4.20.

Negative SIMS Depth Profiles		
m/z	**Ion**	**Origin**
16 u	O^-	$LiCoPO_4$
19 u	F^-	Binder/ Surface Layer
24 u	C_2^-	C65/ Binder/ Surface Layer/ C-coating
63 u	PO_2^-	$LiCoPO_4$/ Surface Layer
79 u	PO_3^-	$LiCoPO_4$/ Surface Layer
85 u	POF_2^-	Surface Layer
Positive SIMS Depth Profiles		
7 u	Li^+	
12 u	C^+	
59 u	Co^+/ $Li_3F_2^+$	

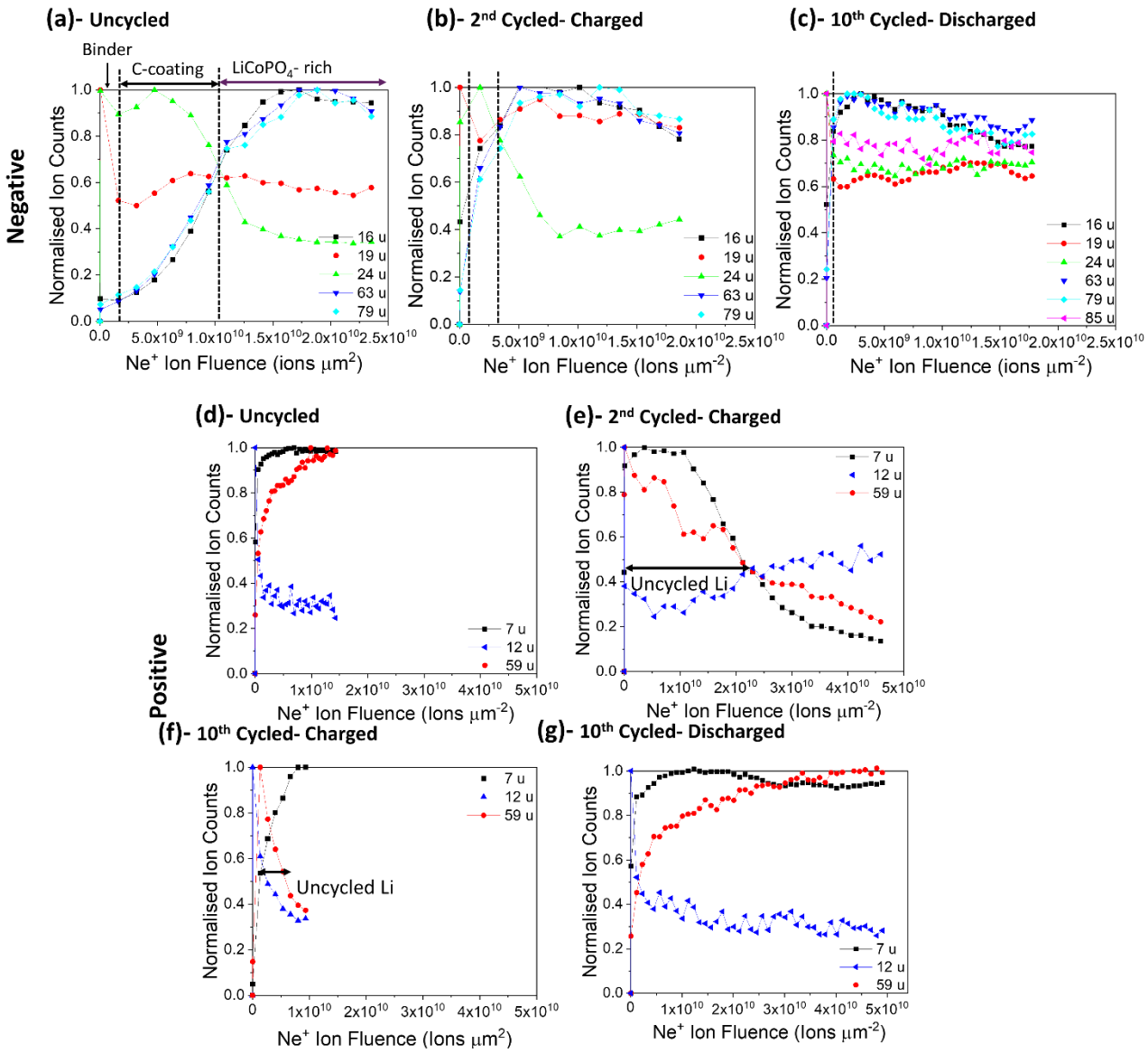

Figure 4.20: Depth profiles of C-$LiCoPO_4$ agglomerates. (a), (b) and (c)- negative SIMS depth profiles of an uncycled, a second cycle, charged and a 10th cycle, discharged respectively. (d), (e), (f) and (g)- positive SIMS depth profiles of an uncycled, a second cycle, charged, a 10th cycle, charged and a 10th cycle, discharged electrode respectively. Positive and negative SIMS were not performed at the same point. The ion fragment intensities have been normalised to the highest intensity of each ion fragment in the depth profile. The ion fragments are: 16 u- O^-, 19 u- F^-, 24 u- C_2^-, 63 u- PO_2^-, 79 u- PO_3^-, 85 u- POF_2^-, 7 u- Li^+, 59 u- Co^+/ $Li_3F_2^+$. Reproduced with permission from [26]. *Copyright 2020, the American Chemical Society.*

4.5.5.2 S/TEM imaging of the C-$LiCoPO_4$ Agglomerates

To establish if the composition of the carbon layer had changed, STEM high angle annular dark field (HAADF) and bright-field (BF) imaging was performed (Figure 4.21).

$LiCoPO_4$ appears bright in the HAADF images (Figure 4.21 (c), (e), (g), and (i)), and dark in the bright field images (Figure 4.21 (b), (d), (f), and (h)). Carbon coating is visible on all the uncycled electrode TEM and STEM images (Figure 4.21 (a), (b), (c), (d), (e), and (f)). In the HAADF images the carbon coating has darker contrast than $LiCoPO_4$, but brighter in the HAADF images. However, there is variation in thickness and contrast of the carbon coating between the images.

TEM imaging of the uncycled electrode (Figure 4.21 (a)) shows the carbon coating (as an amorphous region) on the surface of the crystalline $LiCoPO_4$. The electrode in this sample had

been micro-tomed so the image is of a cross-section of the particle. The carbon coating ranges from 5 nm to 8 nm thickness.

The STEM images in Figure 4.21 are of non-micro-tomed electrode particles; the electrodes were prepared as described in 4.4.3. The carbon coating on the uncycled particles in Figure 4.21 (b) and (c) shows uniform contrast and is 2- 5 nm thick. The carbon coating on the uncycled particles Figure 4.21 (d), and (e) is also 2- 3 nm thick, however, a bright band of contrast is visible at the boundary between $LiCoPO_4$ and the carbon coating.

The variation in thickness of the carbon coating between the uncycled electrode TEM images and STEM images in Figure 4.21 is possibly due to the TEM image in Figure 4.21 (a) being of a cross-section, and the images in Figure 4.21 (b), and (c) being of whole particles. The images are taken in transmission mode, so variations in sample thickness could confuse the thickness of a coating on the edges of the particles.

The STEM images of the 10^{th} cycle discharged electrode (Figure 4.21 (f), (g), (h), and (i)) show a coating on the edge of $LiCoPO_4$. The coating in Figure 4.21 (f), and (g) is 6 nm, whilst in Figure 4.21 (h), (i) the coating is 8 nm thick. 6- 8 nm is thicker than the carbon coating thickness measured for the uncycled electrode particles in Figure 4.21 (b), (c), (d), and (e) (2-3 nm), but similar to the carbon coating thickness measured in the TEM image in Figure 4.21 (a) (5- 8 nm). It is therefore difficult to determine if the coating is the carbon coating or a cycling effect, like the low He-iSE yield layer in Figure 4.17.

A bright band of contrast is visible at the interface between the coating and $LiCoPO_4$ on the 10^{th} cycle discharged electrode HAADF image in Figure 4.21 (g), similar to the bright contrast visible on the uncycled electrode in Figure 4.21 (e). These contrast changes are consistent with local variations in composition, composed of a higher concentration of heavy element (Co dissolved from the adjacent $LiCoPO_4$) consistent with the surface Co detected in the Ne-SIMS (Figure 4.20 (d), (e), (f), and (g)). In addition, the local variations in coating thickness may also contribute to increased local scattering.

On the BF and HAADF images of the cycled electrode in Figure 4.21 (f), and (g) darker regions (~ 2 nm in diameter) on the BF image, and a corresponding bright region in the HAADF image, is visible at the coating/ $LiCoPO_4$ interface and at the edge of the coating. As the contrast differences are visible on both the BF and HAADF images, it is likely this is a region of different composition, composed of a higher concentration of heavy element. This may imply heavy element, such as Co, dissolution. No evidence of similar behaviour was seen on the uncycled electrode images (Figure 4.21 (b), (c), (d), and (e).

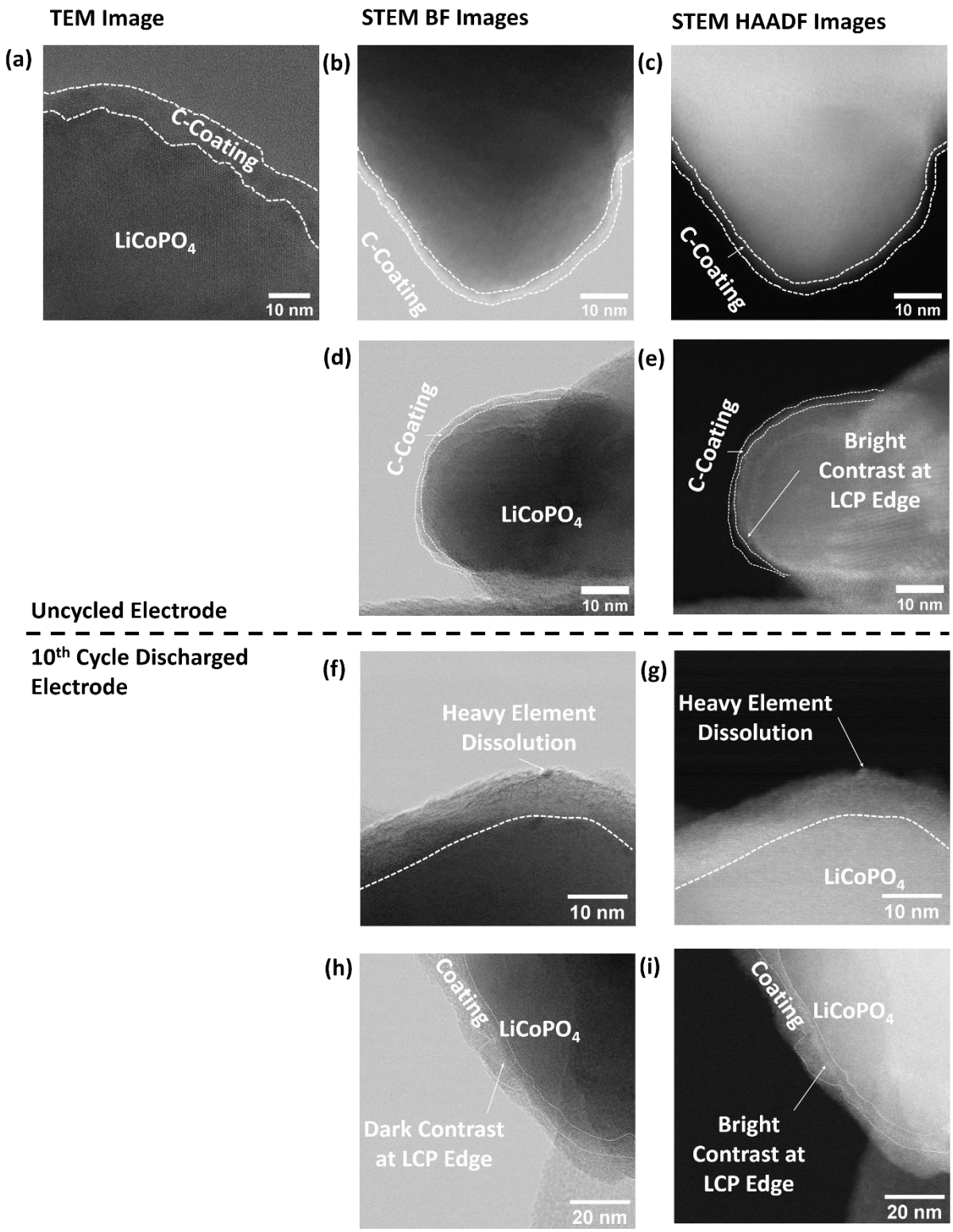

Figure 4.21: TEM (a), STEM Bright Field (BF) (c, d, f, and h), and High Angle Annular Dark Field (HAADF) images (b, e, g, and i) of the uncycled electrode (a, b, c, d, and e), and 10th cycle discharged electrode (f, g, h, and i). Adapted with permission from [26]. *Copyright 2020, the American Chemical Society.*

4.5.5.3 Depth profiling of the binder and conductive additive-rich regions in $LiCoPO_4$ electrodes

The He-iSE images in Figure 4.17 indicate that the binder and C65 rich regions do not form a low He-iSE yield layer when cycled. In order to understand if the binder and C65 regions are affected

chemically when cycled, SIMS spectra (Figure 4.22) (Ne-SIMS depth profiling (Figure 4.23) and STEM imaging (Figure 4.24) of the C65 and binder-rich regions were performed.

Comparing the negative SIMS spectra in Figure 4.22 (a), on cycling for 10 complete cycles PO_2^-, PO_3^-, and POF_2^- peaks increase in intensity. A peak at 101 u also occurred, but was not identified. The intensity of the O^- peak relative to the F^- peak also increased. The presence of PO_2^-, PO_3^-, and POF_2^- on cycled electrodes is similar to the electrode SIMS spectra in Figure 4.15 (a).

Comparing the positive SIMS spectra in Figure 4.22 (b), on cycling for 10 complete cycles the spectra did not change significantly. The relative intensity of the 7 u (Li^+) increased compared to the 12 u (C^+) peak after cycling for 10 cycles, suggesting an increased Li^+ surface concentration.

The presence of 59 u (Co^+) on both the positive uncycled, and cycled spectra in Figure 4.22 (b) is surprising as Co originates from $LiCoPO_4$. The presence of Co suggests the spectra areas may have included $LiCoPO_4$ primary particles. The He-iSE image in Figure 4.7 (d) shows some $LiCoPO_4$ just below the Conductive additive-binder-rich layer, hence taking SIMS spectra of the area likely included $LiCoPO_4$ particles. Observations on the negative SIMS spectra in Figure 4.22 (a) were also likely contaminated by contribution from the C-$LiCoPO_4$ primary particles.

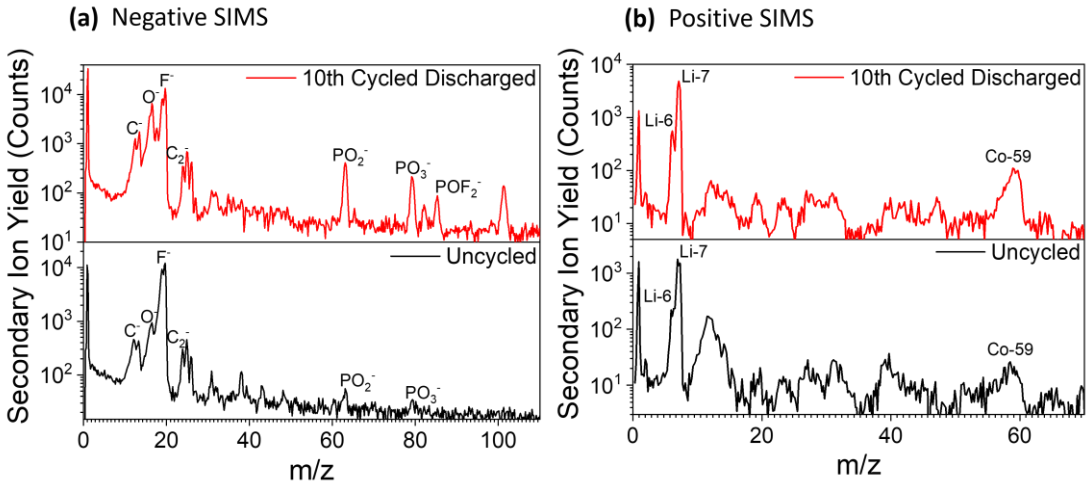

Figure 4.22: Negative (a) and positive (b) SIMS spectra of binder and C65-rich regions of a 10th cycle discharged electrode (red), and an uncycled electrode (black). The positive SIMS spectra were taken over a 2.25 µm² (10th cycle discharged electrode), and 0.25 µm² area (uncycled electrode), and the negative SIMS spectra were taken over a 0.25 µm² (10th cycle discharged electrode), and 100 µm² area (uncycled electrode).

Similar to the C-$LiCoPO_4$ agglomerate depth profiles in Figure 4.20, the depth profiles of the binder- C65- rich regions have been plotted as normalised ion counts against Ne^+ ion fluence (Figure 4.23). The results are therefore described qualitatively and the trends compared. The ion fragments analysed in the depth profiles in Figure 4.23 are identified in Table 4.5.

24 u in Figure 4.23 is representative of C_2^- which can originate from C65 or binder. The 24 u trend is similar for the uncycled (Figure 4.23 (a)) and 2nd cycle discharged sample (Figure 4.23 (b)). The lowest yield of C_2^- occurs at the start, but remains relatively constant throughout the milling period. 24 u on the 10th cycle discharged cycle is also low at the start of milling (Figure 4.23 (c)), but gradually increases over the milling period.

The F^- trend is similar across all the samples (Figure 4.23 (a), (b), and (c)). The yield of F^- is highest at the surface and drops to a relatively constant yield after 1.38×10^9 ions µm² of Ne^+ ion fluence

for the uncycled, 2nd cycle charged, and 10th cycle discharged samples. F^- typically originates from the binder, implying a coating of binder around the C65 particles.

O^-, PO_2^-, and PO_3^- are present in the uncycled, and cycled SIMS depth profiles (Figure 4.23 (a), (b), and (c). The presence of O^-, PO_2^-, and PO_3^- can be attributed to either cycling effects or $LiCoPO_4$ (as shown in Figure 4.13 and Table 4.3). The presence of O^-, PO_2^-, and PO_3^- in the uncycled binder-C65- rich region is surprising, as in the uncycled electrodes these components originate from $LiCoPO_4$. It is possible the area depth profiled had some C-$LiCoPO_4$ is present under the C65 and binder. The binder-rich region circled on backscattered electron SEM image Figure 4.7 (e) had some bright regions in the binder-rich area, implying the presence of C-$LiCoPO_4$ under the binder and C65.

O^-, PO_2^-, and PO_3^- have their highest yield on the surface of the cycled electrodes (23004, 1941, 576 ions per channel respectively) (Figure 4.23 (b), and (c)) which drops after 1.37×10^9 Ne^+ ions μm^{-2}. In contrast the highest yield of O^-, PO_2^-, and PO_3^- on the uncycled electrode occurs after 1.89×10^{10} Ne^+ ions μm^{-2}. The high yield of O^-, PO_2^-, and PO_3^- on the cycled electrodes is unlikely to be from $LiCoPO_4$ as the yield should have increased as milling moved into more concentrated regions of $LiCoPO_4$ deeper in the surface. However, if $LiCoPO_4$ particles, and the associated surface layer are exposed to the beam by gaps in the conductive additive particles, O^-, PO_2^-, and PO_3^- yield would be high at the start. The high yield on the surface of O^-, PO_2^-, and PO_3^- of the cycled electrodes may be the result of cycling effects.

85 u (POF_2^-) was not present on the uncycled electrode depth profile (Figure 4.23 (a), but present on the cycled electrode depth profiles (Figure 4.23 (b), and (c)). This trend is similar to the surface SIMS spectra in Figure 4.22. For the cycled samples (Figure 4.23 (b), and (c)), the POF_2^- depth profile yield is highest at the surface and drops after 1.37×10^9 Ne^+ ions μm^{-2}, similar to the O^-, PO_2^-, and PO_3^- trends.

However, the yield of 85 u (POF_2^-) is more scattered than O^-, PO_2^-, and PO_3^-, potentially because the ion count is much lower for POF_2^- compared with O^-, PO_2^-, and PO_3^-. For the 10th cycle discharged electrode, the initial ion yield of O^-, PO_2^-, and PO_3^- was 23,004, 1941, and 1156 ions per channel respectively, whilst the initial yield of POF_2^- was 576 ions per channel.

Table 4.5: m/z ratios and the associated ion for the depth profiles in Figure 4.23.

m/z	Ion
16 u	O^-
19 u	F^-
24 u	C_2^-
63 u	PO_2^-
79 u	PO_3^-
85 u	POF_2^-

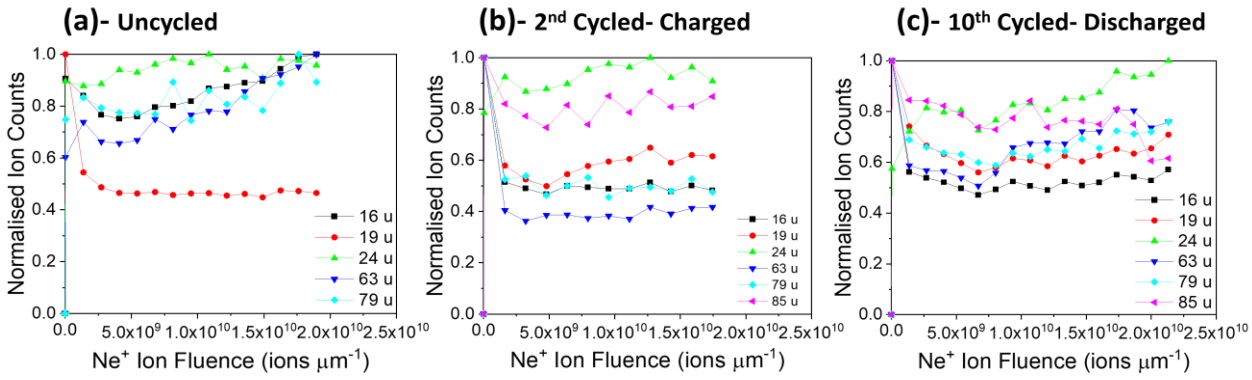

Figure 4.23: Negative SIMS depth profiles of the binder-rich regions (high He-iSE yield regions on the HIM images), within the C-$LiCoPO_4$ electrodes. (a)- Uncycled electrode, (b)- 2nd cycle electrode charged to 5.1 V vs. Li/ Li^+, (c)- 10th cycle electrode discharged to 2.5 V vs. Li/ Li^+.

4.5.5.4 S/TEM of the binder and conductive additive-rich regions

Due to the possible presence of small amounts of $LiCoPO_4$ in the C65- and binder- rich regions indicated by Figure 4.7 (e) and Figure 4.23 (a), it is not possible to determine if the presence of POF_2^- is not forming due to the presence of $LiCoPO_4$. To understand if any surface layers are forming on the C65-, and binder-rich regions, STEM BF and HAADF images of C65 binder were taken before and after cycling (Figure 4.24). The samples in Figure 4.24 were prepared as described in 4.4.3 (they were not micro-tomed).

The STEM BF images in Figure 4.24 (a), (c), and (e) show that C65 is a crystalline solid, with concentric fringe contrast arising from a graphitic onion structure. Bright regions on the HAADF images (Figure 4.24 (b), (d), and (f)) are present within the C65 particles. The bright HAADF regions correspond to dark regions on the BF image (Figure 4.24 (a), (c), and (e)). The bright regions on the HAADF indicated composition differences in the C65, and may result from trace amounts of Iron 2 ppm, Nickel 1 ppm, Vanadium (<1 ppm), Chromium (<1 ppm) and Copper (<1 ppm) in the initial carbon black powder [33]. Binder is also present as an amorphous layer adhering the C65 particles (Figure 4.24 (c)).

The microstructure of the C65 particles from the uncycled electrode (Figure 4.24 (a) and (b)) and the 10th cycle discharged particle in Figure 4.24 (c), and (d) is similar, with no discernible surface films other than binder. However, the C65 particle in Figure 4.24 (e), and (f) has a crystalline film with a similar crystal structure to the C65 particles. The HAADF image of the film in Figure 4.24 (f) has similar contrast differences to the uncycled C65 in Figure 4.24 (b), so the film is likely to be an overlapping C65 particle.

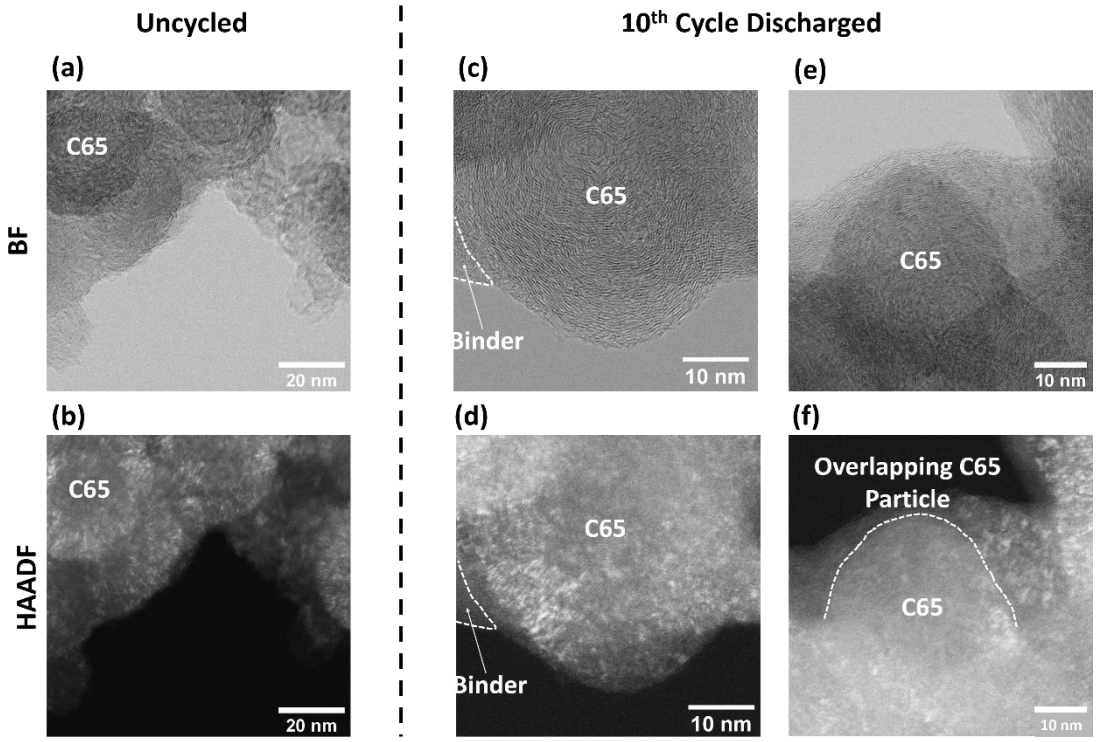

Figure 4.24: STEM BF (a), (c), and (e) and STEM HAADF (b), (d), and (f) of uncycled C65 electrode components (a), and (b), and 10th cycle C65 electrode components discharged to 2.5 V vs. Li/ Li^+ (c), (d), (e) and (f).

4.5.5.5 Influence of other cell components on surface film formation

In order to understand if other cell components could have an influence on the formation of the low He-iSE yield regions in Figure 4.17, the coin cells were cycled using different separators and with $LiPF_6$ electrolytes with a different solvent mix.

The results presented in 1.1.1, 4.5.3, 4.5.4, 4.5.5.1, and 4.5.5.3 used both a Celgard 2325 separator (polypropylene, polyethylene, polypropylene separator) and a Whatman GF/F glass fibre separator for cycling, with the face of the celgard separator in contact with the electrode (as shown in Figure 4.25 (a)). A polypropylene separator was inserted in order to prevent fibre glass contamination on the surface causing charging issues during imaging. However, to confirm the surface film present on cycled electrodes in Figure 4.17, was not caused by the degradation of the separator, cells with a fibre glass only separator (as shown in Figure 4.25 (b)) were also cycled and imaged using He-iSE imaging (Figure 4.26). 10th cycle charged electrodes were imaged (Figure 4.26 (a), and (c)), as 10th cycle charged electrodes had the starkest contrast changes between the low He-iSE yield films and the C65- binder-rich regions (Figure 4.18).

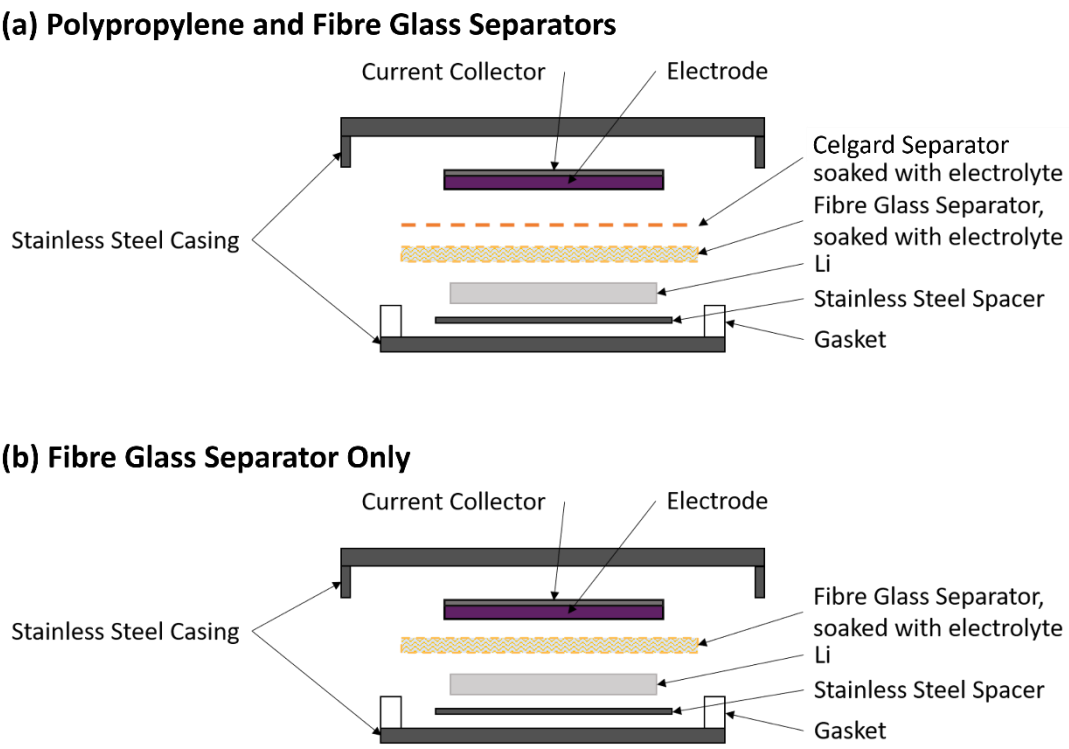

Figure 4.25: Schematics of the 2016 coin-cell set-up with (a) both Celgard 2325 (PP-PE-PP), and Whatman GF/F fibreglass separators, and (b) with just a fibre glass separator (b). In both cases, the separators are soaked with electrolyte.

Low He-iSE yield films were found on the electrode surfaces of electrodes cycled with both a polypropylene-polyethylene-polypropylene separator and a fibre glass separator (Figure 4.26 (a), and (c)) when cycled with $LiPF_6$ in a 50/50 volume ratio of DMC and EC. The low He-iSE film is forming on C-$LiCoPO_4$ agglomerates, given the circular shape of the low He-iSE yield regions in (Figure 4.26 (a), and (c)).

Despite both electrodes forming low He-iSE yield surface layers, there are some differences between the low He-iSE films in Figure 4.26 (a) and (c). The low He-iSE surface layers formed on the surface of 10th cycle charged electrodes in contact with a PP-PE-PP separator (Figure 4.26 (a)) have homogenous, dark contrast in this region, however, some larger agglomerates have heterogenous contrast (see Figure 4.17).

The low He-iSE yield films on the electrode surface in contact with fibreglass separator (Figure 4.26 (c)) have mostly heterogeneous contrast, similar to the heterogeneous contrast on the discharged electrodes in Figure 4.17 (e), and (f). The heterogeneous contrast also occurs on larger single agglomerates on the charged electrode in contact with fibreglass separator in Figure 4.26 (c).

Given the differences between the low He-iSE regions on 10th cycle charged electrodes shown in Figure 4.26 (a), and (c), the surface of the polypropylene, polyethylene, polypropylene separator in contact with the electrode during cycling was imaged using SEM ILD imaging (Figure 4.26 (b)). Prior to imaging the separator was washed with DMC (as described in 4.4.2 and 4.4.3), and a gold coating applied to limit charging effects during SEM imaging.

Pores are visible on the surface of the cycled electrode (Figure 4.26 (b)). The pores are present as part of the separator design and allow electrolyte to flow through the separator [34]. However, a

region with less signal with a linear shape is visible on the surface of the separator (Figure 4.26 (b)). The lower signal region does not contain pores and has evidence of micro-cracking Figure 4.26 (b). It is likely the region is a film on the separator surface, however, it is not the same shape as the low He-iSE regions in Figure 4.26 (a), so is unlikely to be the same film. The film on the separator is either an electrolyte degradation film, or thicker regions of gold coating. Particles from the electrode are visible on the surface of the separator Figure 4.26 (b). Overall, there is evidence of degradation on the separator surface, but it is different from the electrode surface.

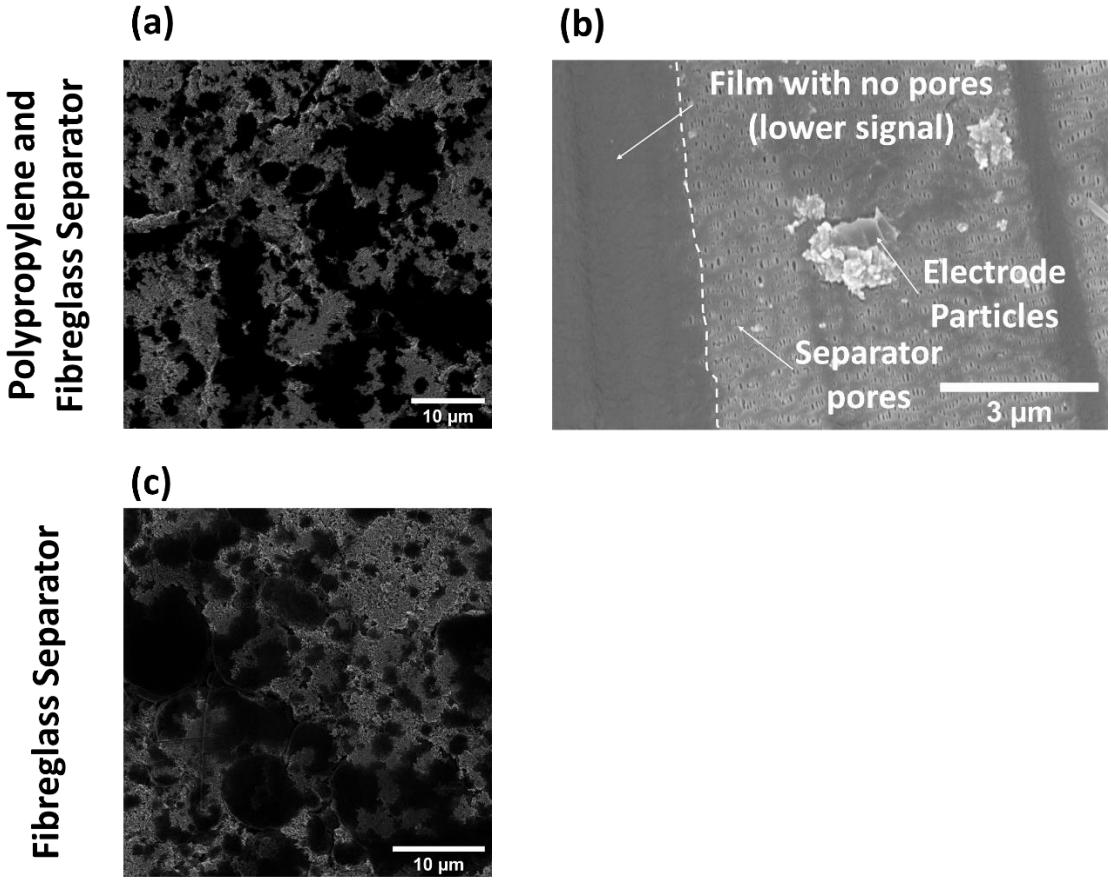

Figure 4.26: He-iSE images of the top surface of 10th cycle electrodes charged to 5.1 V vs. Li/ Li+ using (a) a PP-PE-PP and a fibreglass separator (as in Figure 4.25 (a)) and (c) only a fibreglass separator (c) (as in Figure 4.25 (b)). An SEM ILD image of the electrode surface of a polypropylene separator which had contact with the electrode during cycling (b). The separator in (b) was gold coated prior to imaging.

The results shown in sections 1.1.1, 4.5.3, 4.5.4, 4.5.5.1, 4.5.5.3, and Figure 4.26 used $LiPF_6$ in a 50/ 50 volume ratio of ethylene carbonate (EC) and dimethyl carbonate (DMC). To confirm that the electrolyte solvents used did not influence the formation of the low He-iSE yield surface film, He-iSE images were taken of the electrode surface of electrodes cycled 10 times and discharged to 2.5 V vs. Li/ Li^+ using $LiPF_6$ in 100 % DMC, and 50/50 volume ratio of EC and DMC solvents (Figure 4.27 (a), and (b)).

Low He-iSE yield regions are present on the surface of electrodes cycled with $LiPF_6$ in 100 % DMC, and 50/50 volume ratio of EC and DMC solvents (Figure 4.27 (a), and (b)). The regions are circular on both electrodes (Figure 4.27 (a), and (b)), corresponding to the morphology of the C-$LiCoPO_4$ agglomerates.

The contrast of the low He-iSE yield films on the $LiPF_6$ in 50/50 volume ratio of EC and DMC cycled electrode (Figure 4.27 (b)) is lighter than the low He-iSE yield films in Figure 4.27 (a) because the image in Figure 4.27 (b) is tilted. The tilt angle is unknown as the image is on the edge of a flake in the electrode surface caused by pre-imaging scratching of the electrode surface to aid location finding.

Comparing Figure 4.27 (a), and (b), the surface of both electrodes in Figure 4.27 ((a), and (b)), show lighter contrast within the low He-iSE yield regions, indicating heterogeneous film coverage on the C-$LiCoPO_4$ with and without ethylene carbonate.

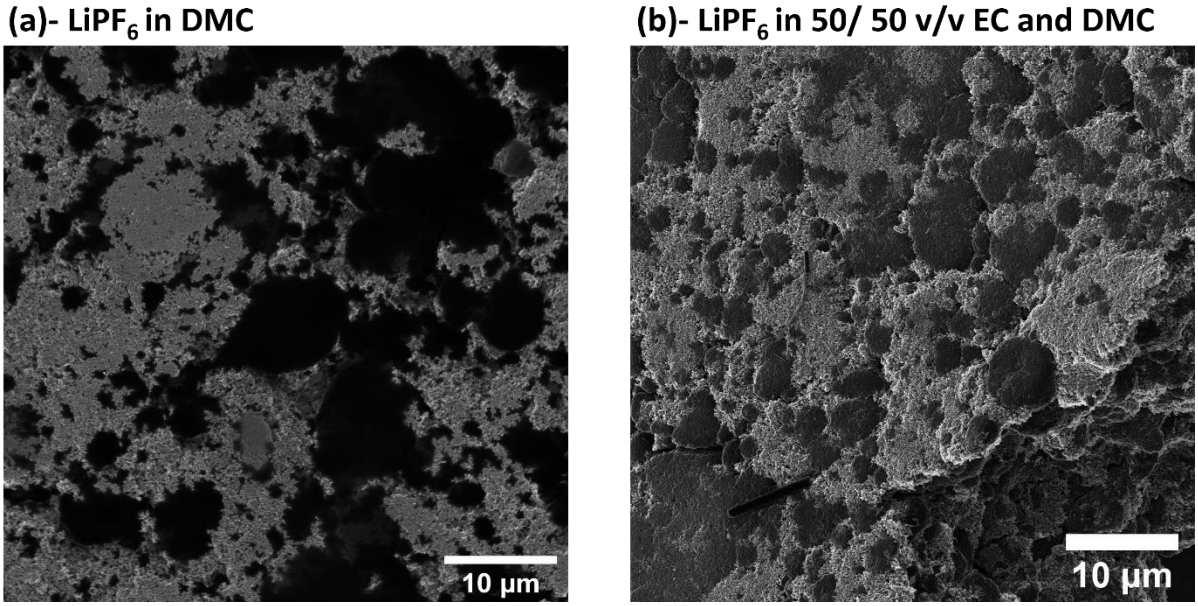

Figure 4.27: He-iSE imaging of the electrode surface of electrodes cycled for 10 times and discharged to 2.5 V vs. Li/Li^+ using $LiPF_6$ electrolytes with just dimethyl carbonate (DMC) (a) or a 50/ 50 volume mix of ethylene carbon (EC), and DMC) (b). The cells contained used both Celgard and fibre glass separators. The electrode surface image in (b) is taken on the edge of a flake in the surface, so the surface is tilted relative to the He ion probe.

4.6 DISCUSSION

4.6.1 Origin of the low He-iSE yield layer

Helium ion imaging and scanning electron microscopy using an in-lens detector revealed a low He^+- and e^-- iSE yield layer on the surface of $LiCoPO_4$ agglomerates on cycled electrodes (Figure 4.7, and Figure 4.11). There are a few possibilities for the origin of the low He^+-iSE film:

(1) A film formed as a result of surface reaction of the separator with electrolyte. Pore blocking films were observed on the surface of cycled polypropylene-polyethylene separators (Figure 4.26 (b)). Due to the compression of the electrode against the separator in the cell, the film may also have deposited on the electrode. Trace amounts of HF can cause degradation on the surface of polypropylene separators, forming pore blocking films [35].

(2) A film formed as a result of air exposure of the electrode prior to microscopy. Comparison between samples exposed to air for 1 week and 1 minute indicate the layer becomes thicker as a result of air exposure (Figure 4.10). It is known that exposure to air can affect the morphology and composition of cycled Li-ion battery electrodes [36], [37].

(3) Cathode electrolyte interphase (CEI) layers formed due to electrolyte reactions with the $LiCoPO_4$. Figure 4.17 indicates that the presence of low He-iSE yield layers is dependent on the cycle number. Cathode electrolyte interphases are known to form on $LiCoPO_4$ after prolonged cycling [4], [3].

The low He-iSE yield layers are most likely to be cathode electrolyte interphase layers as they form on regions in contact with electrolyte, and when the potential is outside the electrolyte window for thermodynamic stability of $LiPF_6$ in EC and DMC (4.8 V vs. Li/ Li^+) [1]. The layers form on $LiCoPO_4$ agglomerates (Figure 4.7 and Figure 4.8), and are present both on the electrode surface and within electrode cross-sections exposed by cracks in the electrode surface (Figure 4.7 (d)). Therefore, the film formed on regions which likely had contact with electrolyte, as the porous structure of the electrode allows electrolyte to penetrate the electrode. Figure 4.17 (a), (b), and (c) show that the film forms after the electrode is charged to 5.1 V vs. Li/ Li^+, which is greater than the upper potential limit for thermodynamic stability of $LiPF_6$ in EC and DMC (4.8 V vs. Li/ Li^+) [1].

Comparing separators suggest that the separator type may have impacted the morphology of the low He-iSE yield layer, as the presence of glass fibre separators resulted in greater thickness inhomogeneity of the low He-iSE yield region (Figure 4.26 (c)). However, the separator type is likely an effect limiting the formation and growth of a CEI layer rather than deposition of separator reaction layers onto the electrode, as the layers found on the electrode are a different shape (round- Figure 4.26 (a)) compared to the layers found on the separator (striped- Figure 4.26 (b)), and the low He-iSE yield layers are found on regions not in contact with separator (Figure 4.7 (d)). The effect of the separator type is discussed in greater detail in 4.6.4.

Figure 4.10 clearly indicates air exposure causes the low He-iSE yield layers to thicken, likely due to oxidation of the layer. As the samples were all exposed to air, albeit for a minimum of 1 min, it is not possible to definitively conclude that the low He-ISE yield regions would be visible if the samples had been handled without air exposure. However, the occurrence of the low He-iSE yield layer is strongly dependent on the cycle life, and state of charge (Figure 4.17). The results therefore indicate the layers are a cycling effect (CEI layers), although the air exposure may have impacted the morphology slightly.

Overall, the results demonstrate the first use of He-ion microscopy as a technique for imaging CEI layers on $LiCoPO_4$.

4.6.2 HIM Imaging of electrodes

He and Ne-gas ion microscopy offers a new route to imaging of CEI layers in battery electrodes, both by high spatial resolution helium ion imaging and neon ion SIMS analysis of the surface chemistry. He-iSE imaging provides clearer imaging of the electrode surface microstructure than ILD or ETD SEM imaging (Figure 4.7, and Figure 4.9). This is because He-iSE images are formed mostly of SE1 electrons which are generated by direct interaction of the ion beam with the electrode surface, and the incident He^+ beam has a smaller spot size than an incident e^- beam [7].

In general, the CEI layer on He-iSE images had low He-iSE yield, appearing dark compared to non-CEI covered areas (Figure 4.7). The CEI layer on charged electrodes was found to have a secondary electron yield low enough that it was undetectable by the detector, resulting in black contrast on the image (Figure 4.18). In general, thicker regions of the CEI appear darker on He-iSE imaging compared with thinner regions- as demonstrated by the lightening contrast as the layer was milled with the He^+ beam (Figure 4.8). Very thin CEI layers enable some SE1 electrons to escape from the underlying material, resulting in lighter contrast (Figure 4.8 (b)).

There are a several of possibilities why the CEI layer has darker contrast compared with uncycled $LiCoPO_4$ agglomerates (Figure 4.7).

Firstly, the CEI layer, being composed of mostly organic compounds (Table 4.3) is likely to be a poor electronic conductor, given the overall cell resistance increases with increasing cycle life as the CEI thickens (Figure 4.6 (c)) [4], [3]. In HIM, charging during imaging results in dark contrast as the build-up of He^+ ions on the surface attracts the secondary electrons which would otherwise escape to the detector [7]. In regions where the CEI is thinner, the charging effect would be less as the underlying $LiCoPO_4$, although a poor conductor [38], is potentially more conductive than the organic CEI layer, resulting in a higher He-iSE yield from these regions. Secondly, the darker contrast could result from compositional contrast which can occur when using secondary electron imaging in a helium ion microscope, as the top surface is rich in Li (Figure 4.15). Modelling would be required to confirm this.

SEM-ILD and He-iSE imaging are both capable of imaging the CEI on the surface of $LiCoPO_4$ electrodes, and in both cases the CEI layer is imaged as low secondary electron yield regions (Figure 4.9). However, imaging of the CEI layer is crisper in the He-iSE images compared with the SEM ILD images (Figure 4.7, and Figure 4.9), due to the very small He-ion spot size and highly localised SEI escape volume resulting in highly surface sensitive imaging.

ILD SEM imaging of CEI layers can be improved by reducing the incident e^- beam voltage using an in-lens detector making the CEI layer sharper (Figure 4.11). Reducing the incident e^- beam voltage causes the interaction volume depth to decrease [12], hence the yield of surface SE1 electrons increasing causing the surface sensitivity of the image to increase.

Increasing the beam current in SEM ILD imaging, increases the electron dose causing the image to appear brighter, but risks damaging the CEI layer faster (Figure 4.10, and Figure 4.11). However, the surface feature resolution also decreases with increased beam current. A compromise must be found between surface resolution, by decreasing the beam voltage, and brightness of the image without rapidly damaging the sample.

SEM backscattered electron imaging was used to identify that the CEI layers were forming on C-$LiCoPO_4$ agglomerates (Figure 4.7 (e)). Backscattered electrons have a deeper interaction volume than SE1 electrons (Figure 4.1), and produce Z-contrast [12], allowing $LiCoPO_4$ to be identified under the CEI layer. Unlike the SEM-ILD images, backscattered electron imaging was not effective in imaging C65 in the binder as BSE imaging has Z contrast, and minimal topographic contrast (Figure 4.7 (e) and (f)), therefore correlation between the imaging techniques is required for full understanding of the system.

In this study, the SEM Everhart-Thornley detector was capable of imaging the CEI layer which formed after 10 cycles after the electrode had undergone air exposure for 1 week (Figure 4.9 (a)). Air exposure of only 1 minute meant the CEI could not be resolved using an ETD (Figure 4.10 (b)), but could be with an eSE ILD which collects a higher ratio of SE1 electrons (Figure 4.10 (a)). Air exposure caused the CEI layer to oxidise and thicken, allowing imaging with less surface sensitive SE2 electrons, otherwise the CEI layer after 10 cycle was too thin to be imaged with an ETD.

Previous studies have been able to image the CEI on $LiCoPO_4$ agglomerates using SEM ETD imaging after 50 cycles [2]. This study demonstrates that low-voltage SEM-ILD and He-iSE imaging were capable of imaging the layer at earlier cycles, after two cycles when the layer was forming (Figure 4.17). This demonstrates the need to optimise imaging conditions to enhance the surface sensitive properties imaging with SE1 electrons could provide.

Overall the results demonstrate that HIM is an optimal technique for imaging CEI layers with improved surface sensitivity over SEM. Similar CEI imaging is possible using, more common, low-voltage SEM-ILD detection, but optimising the imaging conditions by using low-voltage SEM-ILD detection is essential to study CEI layers on C-$LiCoPO_4$.

4.6.3 Chemical Composition of the CEI Layer

The use of Ne-SIMS in the HIM here enables direct correlation of local chemistry with the observed microstructural changes on cycling (Figure 4.16). Negative Ne-ion SIMS on cycled electrodes indicated an increased yield of C_2^-, PO_2^-, PO_3^-, and POF_2^-, compared to the uncycled electrode (Figure 4.15 (a)). Mapping of the electrode indicated that PO_2^- was most concentrated on the CEI layer regions (Figure 4.16 (f)). These findings are consistent with the formation of surface PO_2F_y oxyfluorophosphates as a CEI component found by [3], and [4]. Oxyfluorophosphates result from nucleophilic attack of F^- anions from degraded electrolyte on the P atoms of $LiCoPO_4$, resulting in the breaking of P-O bonds and formation of oxyfluorophosphates and $LiPO_2F_2$ [4]. The presence of CEI layer on electrodes cycled with $LiPF_6$ in DMC only indicates the formation of the CEI results from $LiPF_6$ and DMC, rather than EC (Figure 4.27), supporting the premise that the layer contains oxyfluorophosphates from nucleophilic attack by F^- ions in the electrolyte.

For $LiCoPO_4$ agglomerates, Figure 4.20 (d), (e), (f), and (g) show that the top surface of the agglomerates (the CEI layer) is rich in Li^+, C^+ and C_2^-. Li^+ and C^+ on the surface of the cathode could be ascribed to R-OCO_2Li, or Li_2CO_3, or organic components resulting from the degradation of electrolyte solvent [23]. Li_2CO_3 was found on the surface of $LiCoPO_4$ after prolonged self-discharge by [39], whilst R-OCO_2Li is a typical degradation product of high voltage degradation of $LiPF_6$ in EC and DMC electrolytes [23]. SIMS does not provide information about the bonding states of the mass fragments, limiting the ability to identify the originating CEI component. For information on bonding states, other techniques such as X-ray photoelectron spectroscopy [24], or fast-Fourier transform infrared spectroscopy (FTIR) analysis [39] would be required. However, the formation of Li_2CO_3, $ROCO_2Li$ or organic components are all consistent with the oxidation of electrolyte in high voltage environments [23], and would be expected on the top surface of the CEI layer after cycling (Figure 4.20).

It should be noted that the samples were exposed to air for up to 2 mins before loading into the microscope. There is a strong likelihood that the surface chemistry will have been impacted by the exposure to air, hence most studies employ transfer chambers to mitigate this [23], [36]. For this study, a transfer chamber facility was not available so the samples were briefly air exposed prior to loading into the chamber. The impact of air exposure will be discussed qualitatively as the effect on chemistry depends on how dry the electrode was, and if residual electrolyte salts were present [36]- neither of which were measured prior to SIMS.

For SIMS depth profiling, air exposure affects the outer layer the most. The effect on the sample is strongly dependent on the pre-treatment of the sample prior to air exposure [36]. Chemistry on the surface can change as a result of residual $LiPF_6$ salt on the sample surface decomposing to form HF gas. Malmgren et al. found that on graphite samples this caused Li_2CO_3, lithium alkyl carbonate, lithium oxide, and lithium alkoxide components in the SEI to convert to LiF. Further attack can break ether linkages forming POF_3 gas which hydrolyses to form OPF_2OH and $OPF(OH)_2$ [36]. However, the effect is likely limited as the process is relatively slow and can take up to a few days to equilibrate. P and F containing fragments in the SIMS spectra (Figure 4.15) could have been affected by the $LiPF_6$ break down process, but as the samples were exposed for up to 2 mins, this effect was likely limited.

Volatile components on the surface of the electrode can cause more severe SEI layer contamination on graphite [36], compared to $LiPF_6$ breakdown. In particular water contamination (from moisture in the air) of residual ethylene carbonate on the surface can react with the SEI layer to form LiOH and Li_2O. In this case, air exposure could have increased the secondary ion yields of fragments containing O, C and H [37].

The volatile component effect, and $LiPF_6$ breakdown effect can be limited if the electrode is completely washed and dried prior to analysis [36]. In this case the samples were dried for 4 days under argon, prior to loading into the SIMS instrument which may have limited the effects of air exposure. However, further work would be to repeat the SIMS analysis with a sealed transfer chamber set-up to mitigate the air exposure error completely.

Overall SIMS analysis of the $LiCoPO_4$ CEI layer chemistry identified similar oxyfluorophosphate components to other researchers, however, the results would be improved if air exposure could be mitigated.

4.6.4 Cycling Behaviour of the C-$LiCoPO_4$ Half Cells using $LiPF_6$ in EC and DMC Electrolyte

Considering the 3D spatial distribution of CEI growth on the $LiCoPO_4$ electrodes, imaging of the CEI layer with helium ion microscopy has identified that the CEI forms on C-$LiCoPO_4$ agglomerates exposed to the electrolyte, including penetration into the porous channels and cracks (Figure 4.7). CEI formation on the $LiCoPO_4$ particles is in agreement with [3], and [2], and is consistent with the HF attack on P-O bonds in $LiCoPO_4$ mechanism proposed by [4]. Manzi et al. [3] have previously observed that the CEI layer can form on the carbon conductive additives.

Here, no evidence of a detectable CEI layer forming on the conductive additive, and binder-rich region has been observed through imaging with HIM, SEM or STEM in this instance (Figure 4.7, and Figure 4.24). This is in contrast to work by Manzi et al. who imaged CEI developing on conductive additive regions using post-mortem TEM [3].

Depth profiling of the binder-rich areas found some chemical changes similar to those found on $LiCoPO_4$ agglomerates on cycling (Figure 4.20, and Figure 4.23). POF_2^-, PO_2^-, and PO_3^- was found on the surface of the binder-rich area of the electrodes on cycling (Figure 4.20 (b), and (c)). However, the presence of PO_2^-, and PO_3^- detected within the uncycled electrode indicates that non-agglomerated $LiCoPO_4$ may be within the binder rich regions.

The backscattered electron image in Figure 4.8 (e) shows that $LiCoPO_4$ can be present just under the surface of the binder-rich zones, which wasn't identified on the in-lens detector image Figure 4.7 (h) in the same location as ILD imaging contrast results from near surface topographical surface features. He-iSE imaging is highly surface sensitive, so may not identify the presence of $LiCoPO_4$ under the binder/ C65-rich regions. The presence of CEI layer and $LiCoPO_4$ ion fragments in the depth profiles may have occurred due to unidentified $LiCoPO_4$ in the binder and C65-rich regions.

Using Ne-SIMS depth profiling on the surface of C-$LiCoPO_4$ agglomerates, the surface of charged electrodes was found to be rich in Li^+ (Figure 4.20 (e)). The mill time to complete the mill through the Li^+-rich region was 120 s, which was longer than the mill-time required to mill through the carbon coating, and into $LiCoPO_4$ on the uncycled electrode in Figure 4.20 (a) (65 s). The Li^+ region on the charged samples is therefore likely to be uncycled Li within the $LiCoPO_4$ particle and carbon layer, as well as the CEI layer. The region of 'dead' uncycled lithium would result in capacity loss observed in Figure 4.6 (a).

The presence of Li on the surface of charged electrodes is surprising as the charged state of $LiCoPO_4$ is $CoPO_4$, so there should not have been Li present. However, Manzi et al. previously found evidence for spontaneous reincorporation of Li into the lattice as a result of the instability of an octahedrally co-ordinated Co^{3+} ion in the lattice [3].

Alternatively, the Li could be a Li-rich layer on the surface of the electrode. Li is likely to have a different sputtering rate compared to other ions sputtered from the electrodes. Normalised yield of ions is being used here as an indicator of Li concentration (ie. greater normalised yield, more concentrated Li), as sputtering yield is correlated to the concentration of a component in the matrix. However, sputtering yield is also correlated to the angle of escape incidence, so the roughness of the sample surface may cause Li (or other ions) to have a higher yield than they should, leading to edge effect errors [31]. Figure 4.19 demonstrates that depth profiling was performed on regions with edges of $LiCoPO_4$ particles present, leading to this potential error in these samples. Other researchers have avoided the edge effect error by disregarding edges in the analysis by correlating images with confocal microscopy [31]. In this instance, the edge effect may have caused the Li yield to appear artificially high for longer, but given the Ne^+ ion fluence taken for Li to drop to zero, and the fact that theoretically there should not be Li on the surface of charged $LiCoPO_4$ particles, qualitatively it is likely that uncycled Li is present on the surface of $LiCoPO_4$.

There is some uncertainty regarding the identity of 59 u. 59 u could either be Co^+ from $LiCoPO_4$, or $Li_3F_2^+$, an ion fragment previously reported in Bi^+ ToF SIMS analysis of high voltage cathode materials [30]. Depth profiles on $LiCoPO_4$ agglomerates Figure 4.20 (d), (e), (f) and (g), and positive SIMS spectra (Figure 4.15 (b)) showed the presence of 59 u which could be identified as Co^+. The presence of 59 u on the uncycled electrode makes Co^+ the likely candidate and it follows depth profiling pattern on the expected pattern for the uncycled and discharged electrodes (greater yield deeper in the sample) (Figure 4.20 (d)).

The greater yield of Co^+ deeper in the sample would also account for the bright contrast HAADF images observed on the $LiCoPO_4$/ layer interface in Figure 4.21 (f), and (g) which may indicate Co dissolution. Co dissolution in other high voltage cathode materials is usually identified with ToF SIMS by finding CoF_3^+ fragments due to reaction of Co with the electrolyte, [23]. CoF_3^+ was not found in this instance (Figure 4.15 (b)). However, it has been previously reported that Co dissolution in $LiCoPO_4$, can result from the formation of $Co_2P_2O_7$ (cobalt pyrophosphate), which occurs due to the breakdown of the olivine $LiCoPO_4$ structure [5]. CoF_3^+ fragments would not form from $Co_2P_2O_7$, but PO^- fragments found on the negative SIMS spectra in Figure 4.15 (a) are possible.

Alternatively, 59 u could also be $Li_3F_2^+$ from $LiPO_2F_2$ [30]. On the positive depth profiles in Figure 4.20 (d), (e), and (g), the 59 u trend followed the 7 u (Li^+) trend. However, the 59 u peak is broad, suggesting the 59 u ion results from a bulk ion fragment rather than a surface ion fragment as broad peaks can result from the broad energy distribution of ions sputtered from a bulk material. Co^+ would be a bulk material ion fragment originating from $LiCoPO_4$. A scan with a greater mass resolution ($M/\Delta M \sim 1000$) would help differentiate the 59.93 u fragment contribution from Co^+, from the potential 58.82 $Li_3F_2^+$ fragment, or the use of another technique, such as XPS.

The C-$LiCoPO_4$ agglomerate negative depth profiles in Figure 4.20 (a), (b), and (c), and STEM images in Figure 4.21 (f), (g), (h), and (i) also suggest composition and/ or morphology changes to the carbon layer on the $LiCoPO_4$ particles. The depth profiles show PO_2^-, and PO_3^- fragments occurring with less Ne^+ ion fluence on charged electrodes, whilst the C_2^- signal, an indicator of the

carbon layer, yield drops with less Ne^+ ion fluence with increased cycling Figure 4.20 (b), and (c). A layer is also present on the $LiCoPO_4$ after cycling for 10 times, which is either CEI layer or carbon coating or a mixture. There could be 3 possible scenarios which could cause the PO_2^-, PO_3^-, and C_2^- yield drops observed in Figure 4.20 (a), (b), (c). These are detailed in Figure 4.28.

(i) The CEI layer grows on the carbon coating. In this scenario the earlier occurrence of PO_2^-, and PO_3^- would result from the formation of CEI components, such as oxyfluorophosphates [4].

(ii) The carbon layer is exfoliated and the CEI layer grows on top of the carbon coating. The earlier drop in C_2^- yield would be due to a thinner C-coating, whilst the PO_2^-, and PO_3^- ions would occur due to milling into $LiCoPO_4$. Exfoliation of the C-coating has been previously proposed by Manzi et al. [3].

(iii) Ion migration of Co^+, and PO_2^- ions into the carbon coating and growth of a CEI layer. This scenario would support the bright contrast observed on the STEM HAADF image in Figure 4.21 (g).

Further work is needed to confirm the scenario occurring on the samples studied.

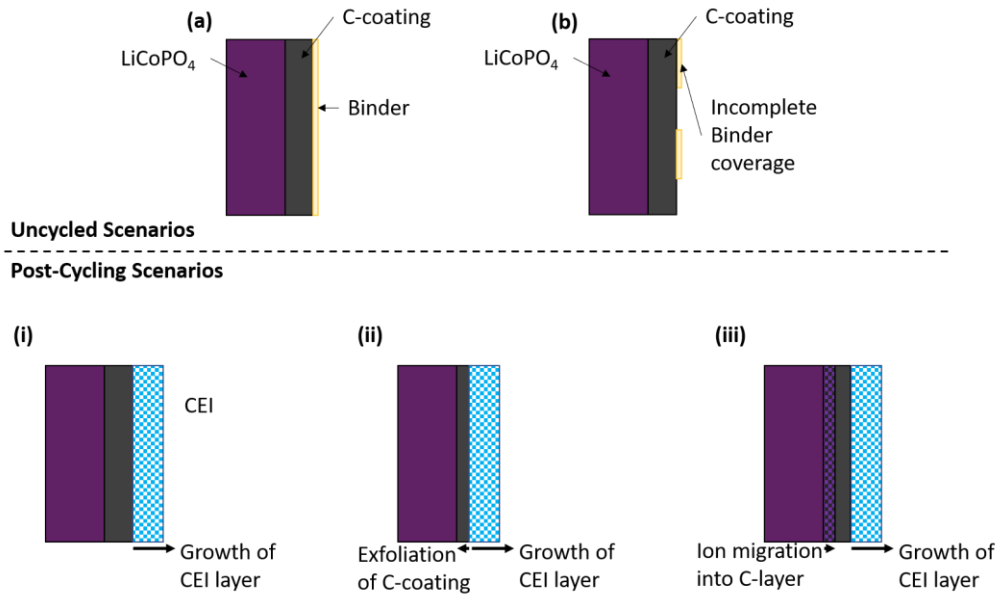

Figure 4.28: Schematic showing the possible scenarios the carbon coating undergoes during cycling. The uncycled scenarios are drawn as binder on coating (a), and incomplete binder coverage on carbon coating (b) as binder fragments were found on sample surface in the uncycled negative depth profile Figure 4.20 (a). The layer is likely to be very thin as binder was not identified on the He-ion images of SEM images (Figure 4.8)

Work presented imaging electrodes cycled with different separators (Figure 4.26) was performed to confirm the low He-ISE layer on the images did not originate from the separator, discussed in 4.6.1. It is worth noting briefly that there are minor differences in the morphology of the layer after cycling with a fibre glass separator, verses a polypropylene, polyethylene, polypropylene separator (Figure 4.26 (a), and (c)). The layer on a charged $LiCoPO_4$ electrode cycled with a fibre glass separator showed mottled contrast, compared to the Celgard separator, indicating the layer is likely thinner when using a fibre glass separator. It has been previously reported that separators can influence the cycle life of $LiCoPO_4$ [40]. Sharabi et al. found that the use of HF scavenging materials as a separator limited the nucleophilic attack by F^- ions by the electrolyte [40]. The CEI

layer may be thinner on the fibre glass separator sample in the zone adjacent to the separator because limited nucleophilic attack by F^- may have resulted in a more stable CEI, compared to the Celgard separator, hence the layer is thinner. Further work would be required to confirm the mechanisms of this.

Considering the dependence of the CEI layer on electrochemical history, the CEI layer was found consistently on the charged electrode samples, but is found to dissolve on discharge (Figure 4.17). CEI formation is expected at high potentials (where electrolyte breakdown occurs). The dissolution of the CEI layer observed on discharge is likely the dissolution of soluble $LiPO_2F_2$ discussed in [4], [40], and [24]. Dissolution of CEI layer would result in fresh $LiCoPO_4$ being exposed to further breakdown from parasitic reactions due to a lack of passivating layer. Exposed $LiCoPO_4$ at high potentials could lead to consumption of $LiCoPO_4$ by the electrolyte leading to capacity drop (observed in Figure 4.6).

An important result of the high spatial resolution He-ion imaging of the CEI layers is the determination that the CEI dissolution is not consistent across the electrode, resulting in variations in the thickness of the CEI layer (Figure 4.17). A porous and unstable CEI layer was reported by Manzi et al. using TEM [3]. However here, high resolution imaging of the CEI has idenitified an inhomogenous CEI across the whole electrode. Inhomogeneous formation of CEI layers has been proposed for other cathode materials using techniques such as EIS [41], but He-ion microscopy allows direct imaging of the inhomogeneous CEI layer.

The He-ion imaging results have shown that there can be disparity between the CEI thickness on larger and smaller $LiCoPO_4$ agglomerates (Figure 4.17). This has not been previously reported, likely due to the difficulty observing CEI layers clearly at field of view which can image electrode microstructure. A possible reason may be faster action by F^- anions in the local presence of more $LiCoPO_4$. It has been previously observed that binder materials can act as an HF scavenger [42], which could help prevent further attack, although the PVDF used here is inefficient at this.

Overall, the results demonstrate a requirement for high resolution imaging of CEI layers and local microstructure, coupled with chemical correlation, using techniques such as helium ion microscopy and *in-situ* Ne-ion ToF-SIMS, to fully understand degradation mechanisms and hence optimise electrode design.

4.7 CONCLUSIONS

This study used Helium ion microscopy for the first time to achieve high resolution images of CEI layers on $LiCoPO_4$ at a field of view which allows comparison with the electrode microstructure. CEI layers were imaged as low SE-yield regions on He-ISE images. Similar contrast was found when using SEM-ILD imaging, however, the resolution of the CEI layer is better using He-ISE imaging as the smaller spot size and high SE1 yield allows for greater surface sensitivity.

In-situ Ne-ion ToF SIMS analysis in the HIM allowed site-specific chemical characterisation, allowing coupling of the observed morphological changes with chemical changes. Using *in-situ* Ne-ion ToF SIMS mapping, the CEI layers were found to be rich in C^-, PO_2^-, and Li^+ compared to surrounding areas.

The Helium ion imaging and *in*-situ Ne-ion SIMS demonstrated that the degradation of C-$LiCoPO_4$ is partly caused by the formation of an unstable CEI layer on C-$LiCoPO_4$ agglomerates. Ne-ion ToF SIMS analysis found the CEI layer is rich in oxyfluorophosphates, in agreement with literature sources [3], [4].

Ne-ion SIMS depth profiling highlighted changes in the 59 u peak ion yield. This may result from Co dissolution into the CEI layer or $LiCoPO_4$ structure degradation into CoP_2O_7. Alternatively, 59 u could be $Li_3F_2^+$ from $LiPO_2F_2$, a typical high voltage CEI layer component. Further work is required to confirm if one or both of the mechanisms is occurring.

Ne-ion SIMS depth profiling also highlighted changes to the carbon layer surrounding the primary $LiCoPO_4$ particles. Reduction in the Ne^+ ion fluence required to reach $LiCoPO_4$-rich regions, and the presence of PO_2^-, and PO_3^- ion fragments in the carbon layer of cycled electrodes implied changes to the carbon layer resulting from cycling. Potential mechanisms of surface evolution include, exfoliation of the C-layer, ion migration from the $LiCoPO_4$ occurring into the carbon layer, or the CEI layer thickening with increased cycling.

Ne-ion ToF SIMS and He-ISE HIM imaging is one of the few techniques enabling chemical characterisation and imaging of CEI layers on a scale that allows full characterisation of the electrode microstructure. Using this advantage, helium ion imaging of electrodes at different points in the cycle life, showed for the first time that the CEI layer is unstable, forming on charge and partially dissolves on discharge. Moreover, it was found that the CEI layer forms in-homogenously across larger electrodes, and shows evidence of thinning.

The in-homogenous formation of the CEI layer, and partial dissolution on discharge could help account for the severe degradation experienced by $LiCoPO_4$ cells. Partial dissolution of the CEI layer would expose fresh $LiCoPO_4$ to further electrolyte degradation, whilst in-homogenous formation of the CEI may imply poor passivation of the electrode by the CEI. The increased inhomogeneity of CEI formation on larger agglomerates highlights a need to control the electrode microstructure to help decrease electrode degradation.

Overall, the results highlight the importance of understanding how the electrode microstructure affects degradation, and the need for techniques which are capable of high resolution imaging and chemical characterisation of electrode surface degradation phenomena.

4.8 FURTHER WORK

Further work is generally split into methods to improve the accuracy, reliability, and information gained from the current, and potential future research avenues which could be explored using the HIM SIMS technique.

All the samples analysed were briefly exposed to air as transfer chamber facilities were not available. As discussed in 4.6.3 this could have impacted the results, in particular, the CEI layer could appear thicker than it would be post-cycling, and the SIMS chemical analysis of compounds containing P-O bonds, C, O, and H could have been effected. Further work would be to repeat the study using a transfer chamber to allow samples to be protected from air exposure prior to analysis.

The depth profiles in Figure 4.20, and Figure 4.23 were plotted against Ne^+ ion fluence rather than correlating to a depth. Ideally the depth profiles would be plotted against depth, which would help confirm the thickness of the CEI layer. As discussed in 4.6.4, milling time could not be correlated to milling depth as the conventional methods of achieving this were not possible. One potential method to measure the depth of the Ne sputter crater (and hence correlate milling time to depth) may have been to Ga mill the Ne sputter crater and measure the crater depth using SEM. This does not account for potential further sputtering by the Ga beam. A method would need to be developed to correlate milling time to sputtering depth.

The 59 u fragment should be identified. This is either Co^+, or $Li_3F_2^+$, or a mixture of both (as discussed in 4.6.4). X-ray photoelectron spectroscopy (XPS) may have helped to identify the 59 u fragment as this is a surface sensitive technique capable of looking at bond structures. If Co was present due to CoP_2O_7, Co-P band should be present on the surface, and measurable with XPS. Alternatively, if 59u was $Li_2F_2^+$ an Li-F signal would be present.

The results identified that changes to the carbon coating occurred as a result of cycling (Figure 4.28). The three scenarios suggested in 4.6.4, were thickening CEI growth on the carbon coating, exfoliation of the carbon coating, and ion migration of Co, and PO_2 into the carbon coating. It was difficult to distinguish between the carbon coating and CEI layer on the STEM images in Figure 4.21 (g, and i) so post-mortem S/TEM was not reliable for establishing if exfoliation or chemical changes had occurred. However, if EELS could be performed at the magnification where the layer is visible, without damaging the sample, understanding if one of the scenarios had occurred may be possible. X-ray photoelectron spectroscopy may also be able to distinguish between carbon bonding present in the carbon coating layer and carbon from the CEI layer, enabling better understanding.

The He-ISE imaging identified that local microstructure played a key part in the CEI morphology- larger agglomerates having greater variation in CEI thickness. This suggests further research avenues considering different agglomerate sizes, or ratios of $LiCoPO_4$, C65, and binder and the influence of CEI formation and cycle life.

Finally, the results presented show a method of high resolution imaging and chemical characterisation of the CEI on $LiCoPO_4$ using helium ion microscopy, and Ne-ion SIMS. As a potential mechanism for the CEI layer appearing dark on He-ISE images is due to contributions from the sub-surface $LiCoPO_4$ (static capacitive contrast), it would be interesting to understand the influence of other materials. For example, the technique could be repeated on SEI forming materials, such as C, or Si, to understand the influence of local microstructure on SEI formation.

4.9 REFERENCES

[1] J. B. Goodenough and Y. Kim, “Challenges for Rechargeable Li Batteries,” *Chem. Mater.*, vol. 22, no. 3, pp. 587–603, 2010.

[2] Y. Wang, H. Ming, J. Qiu, Z. Yu, M. Li, S. Zhang, and Y. Yang, “Improving cycling performance of $LiCoPO_4$ cathode material by adding tris(trimethylsilyl) borate as electrolyte additive,” *J. Electroanal. Chem.*, vol. 802, pp. 8–14, 2017.

[3] J. Manzi and S. Brutti, “Surface chemistry on $LiCoPO_4$ electrodes in lithium cells: SEI formation and self-discharge,” *Electrochim. Acta*, vol. 222, pp. 1839–1846, 2016.

[4] E. Markevich, R. Sharabi, H. Gottlieb, V. Borgel, K. Fridman, G. Salitra, D. Aurbach, G. Semrau, M.A. Schmidt, and N. Schall, C. Bruenig, “Reasons for capacity fading of $LiCoPO_4$ cathodes in $LiPF_6$ containing electrolyte solutions,” *Electrochem. commun.*, vol. 15, no. 1, pp. 22–25, 2012.

[5] R. Sharabi, E. Markevich, V. Borgel, G. Salitra, G. Gershinsky, D. Aurbach, G. Semrau, M.A. Schmidt, N. Schall, and C. Stinner, “Raman study of structural stability of $LiCoPO_4$ cathodes in $LiPF_6$ containing electrolytes,” *J. Power Sources*, vol. 203, pp. 109–114, 2012.

[6] S. Tan, R. Livengood, D. Shima, J. Notte, and S. McVey, “Gas field ion source and liquid metal ion source charged particle material interaction study for semiconductor nanomachining applications,” *J. Vac. Sci. Technol. B, Nanotechnol. Microelectron. Mater.*

Process. Meas. Phenom., vol. 28, no. 6, p. C6F15-C6F21, 2010.

[7] T. Wirtz, O. De Castro, J.-N. Audinot, and P. Philipp, "Imaging and Analytics on the Helium Ion Microscope," *Annu. Rev. Anal. Chem.*, vol. 12, no. 1, pp. 523–543, 2019.

[8] L. Scipioni, C. A. Sanford, J. Notte, B. Thompson, and S. McVey, "Understanding imaging modes in the helium ion microscope," *Journal of Vacuum Science and Technology B: Microelectronics and Nanometer Structures*, vol. 27, no. 6, pp. 3250–3255, 2009.

[9] G. Hlawacek, V. Veligura, R. Van Gastel, and B. Poelsema, "Helium Ion Microscopy." Springer International Publishing, Springer International Publishing Switzerland, 2016.

[10] N. Klingner, R. Heller, G. Hlawacek, S. Facsko, and J. von Borany, "Time-of-flight secondary ion mass spectrometry in the helium ion microscope," *Ultramicroscopy*, vol. 198, pp. 10–17, 2019.

[11] N. Klingner, R. Heller, G. Hlawacek, J. von Borany, J. Notte, J. Huang, and S. Facsko, "Nanometer scale elemental analysis in the helium ion microscope using time of flight spectrometry," *Ultramicroscopy*, vol. 162, pp. 91–97, 2016.

[12] M. Suga, S. Asahina, Y. Sakuda, H. Kazumori, H. Nishiyama, T. Nokuo, V. Alfredsson, T. Kjellman, S. M. Stevens, H. S. Cho, M. Cho, L. Han, S. Che, M. W. Anderson, F. Schüth, H. Deng, O. M. Yaghi, Z. Liu, Z. Liu, H. Young Jeong, A. Stein, K. Sakamoto, R. Ryoo, and O. Terasaki, "Recent progress in scanning electron microscopy for the characterization of fine structural details of nano materials," *Progress in Solid State Chemistry*, vol. 42, no. 1–2., pp. 1–21, 2014.

[13] E. L. Joseph Goldstein, D. Newbury, P. Echlin, D. C. Joy, A. D. Romig Jr., C. E. Lyman, and C. Fiori, *Scanning Electron Microscopy and X-Ray Microanalysis: A Text for Biologists, Materials Scientists, and Geologists*, Second Edi. New York: Plenum Press, 1992.

[14] B. W. Ward, J. A. Notte, and N. P. Economou, "Helium ion microscope: A new tool for nanoscale microscopy and metrology," *J. Vac. Sci. Technol. B Microelectron. Nanom. Struct.*, vol. 24, no. 6, pp. 2871–2874, 2006.

[15] M. T. Postek, A. Vladár, C. Archie, and B. Ming, "Review of current progress in nanometrology with the helium ion microscope," *Measurement Science and Technology*, vol. 22, no. 2. Institute of Physics Publishing, 2011.

[16] B. J. Griffin and D. Joy, "Variation of Rutherford Backscattered Ion and ion-induced secondary electron yield with atomic number in the 'Orion' scanning helium ion microscope," *Microscopy and Microanalysis*, vol. 14, no. SUPPL. 2, pp. 1190–1191, 2008.

[17] F. H. M. Rahman, S. McVey, L. Farkas, J. A. Notte, S. Tan, and R. H. Livengood, "The Prospects of a Subnanometer Focused Neon Ion Beam," *Scanning*, vol. 34, no. 2, pp. 129–134, 2012.

[18] A. Baggott, M. Mazaheri, Y. Zhou, H. Zhang, and B. J. Inkson, "A comparison of He and Ne FIB imaging of cracks in microindented silicon nitride," *Mater. Charact.*, vol. 141, pp. 362–369, 2018.

[19] "Secondary Ion Mass Spectrometry Theory Tutorial." [Online]. Available: http://pprco.tripod.com/SIMS/Theory.htm. [Accessed: 25-Nov-2019].

[20] R. G. Wilson, "SIMS quantification in Si, GaAs, and diamond - an update," *Int. J. Mass Spectrom. Ion Process.*, vol. 143, no. C, pp. 43–49, 1995.

[21] T. Wirtz, D. Dowsett, and P. Philipp, "SIMS on the Helium Ion Microscope: A Powerful

Tool for High-Resolution High-Sensitivity Nano-Analytics," Springer, Cham, 2016, pp. 297–323.

[22] D. Dowsett and T. Wirtz, "Co-Registered In Situ Secondary Electron and Mass Spectral Imaging on the Helium Ion Microscope Demonstrated Using Lithium Titanate and Magnesium Oxide Nanoparticles," *Anal. Chem.*, vol. 89, no. 17, pp. 8957–8965, 2017.

[23] W. Li, A. Dolocan, P. Oh, H. Celio, S. Park, J. Cho, and A. Manthiram, "Dynamic behaviour of interphases and its implication on high-energy-density cathode materials in lithium-ion batteries," *Nat. Commun.*, vol. 8, p. 14589, 2017.

[24] E. Markevich, G. Salitra, K. Fridman, R. Sharabi, G. Gershinsky, A. Garsuch, G. Semrau, M. A. Schmidt, and D. Aurbach, "Fluoroethylene Carbonate as an Important Component in Electrolyte Solutions for High-Voltage Lithium Batteries: Role of Surface Chemistry on the Cathode," *Langmuir*, vol. 30, no. 25, pp. 7414–7424, 2014.

[25] K. Amine, H. Yasuda, and M. Yamachi, "Olivine $LiCoPO_4$ as 4.8 V electrode material for lithium batteries," *Electrochem. Solid State Lett.*, vol. 3, no. 4, pp. 178–179, 2000.

[26] L. Wheatcroft, N. Klingner, R. Heller, G. Hlawacek, J. Cookson, and B. J. Inkson, "Visualisation and Chemical Characterisation of the Cathode Electrolyte Interphase in High Voltage Li-ion Battery Material $LiCoPO_4$ using He-ion Microscopy and in-situ Time-of-Flight Secondary Ion Mass Spectroscopy," *Appl. Energy Materials*, 2020.

[27] J. F. Ziegler, M. D. Ziegler, and J. P. Biersack, "SRIM - The stopping and range of ions in matter (2010)," *Nucl. Instruments Methods Phys. Res. Sect. B Beam Interact. with Mater. Atoms*, vol. 268, no. 11–12, pp. 1818–1823, 2010.

[28] W. D. Li, B. H. Song, and A. Manthiram, "High-voltage positive electrode materials for lithium-ion batteries," *Chem. Soc. Rev.*, vol. 46, no. 10, pp. 3006–3059, 2017.

[29] N. E. Holden, T. B. Coplan, J. K. Böhlke, L. V. Tarbox, J. Benefield, J. R. de Laeter, P. G. Mahaffy, G. O'Connor, E. Roth, D. H. Tepper, T. Walczyk, M. E. Wieser, and S. Yoneda, "IUPAC Periodic Table of the Elements and Isotopes (IPTEI) for the Education Community-Update 2019 (IUPAC Technical Report)."*Pure and Applied Chemistry,* vol. 90, no. 12, pp. 1833-2092, 2019.

[30] J. Vidal Laveda, J. E. Low, F. Pagani, E. Stilp, S. Dilger, V. Baran, M. Heere, and C. Battaglia, "Stabilizing Capacity Retention in NMC811/Graphite Full Cells via TMSPi Electrolyte Additives," *ACS Appl. Energy Mater.*, vol. 2, no. 10, pp. 7036–7044, 2019.

[31] S. Bessette, A. Paolella, C. Kim, W. Zhi, P. Hovington, R. Gauvin, and K. Zaghib, "Nanoscale Lithium Quantification in $Li_XNi_YCo_wMn_ZO_2$ as Cathode for Rechargeable Batteries," *Sci. Rep.*, vol. 8, no. 1, 2018.

[32] F. C. Strobridge, R. J. Clément, M. Leskes, D. S. Middlemiss, O. J. Borkiewicz, K. M. Wiaderek, K. W. Chapman, P. J. Chupas, and C. P. Grey, "Identifying the Structure of the Intermediate, $Li_{2/3}CoPO_4$, Formed during Electrochemical Cycling of $LiCoPO_4$," *Chem. Mater.*, vol. 26, no. 21, pp. 6193–6205, 2014.

[33] "Timical SUPER C65 Conductive Carbon Black as Conductive Additive for Lithium-Ion Batteries 80g/bag - EQ-Lib-SuperC65." [Online]. Available: https://www.mtixtl.com/TimicalSUPERC65forLithium-IonBatteries80g/bag-EQ-Lib-SuperC65.aspx. [Accessed: 29-Nov-2019].

[34] "Battery Separator Products & Literature | Celgard." [Online]. Available: https://www.celgard.com/literature/. [Accessed: 01-Dec-2019].

[35] X. Li, J. Tao, D. Hu, M. H. Engelhard, W. Zhao, J-G Zhang, and W. Xu, "Stability of polymeric separators in lithium metal batteries in a low voltage environment," *J. Mater. Chem. A*, vol. 6, no. 12, pp. 5006–5015, 2018.

[36] S. Malmgren, K. Ciosek, R. Lindblad, S. Plogmake, J. Kühn, H. Rensmo, K. Edström, M. Hahlin, "Consequences of air exposure on the lithiated graphite SEI," *Electrochim. Acta*, vol. 105, pp. 83–91, 2013.

[37] I. V. Veryovkin, C. E. Tripa, A. V. Zinovev, S. V. Baryshev, Y. Li, and D. P. Abraham, "TOF SIMS characterization of SEI layer on battery electrodes," *Nucl. Instruments Methods Phys. Res. Sect. B Beam Interact. with Mater. Atoms*, vol. 332, pp. 368–372, 2014.

[38] M. Zhang, N. Garcia-Araez, and A. L. Hector, "Understanding and development of olivine $LiCoPO_4$ cathode materials for lithium-ion batteries," *Journal of Materials Chemistry A*, vol. 6, no. 30. Royal Society of Chemistry, pp. 14483–14517, 2018.

[39] J. Manzi, F. M. Vitucci, A. Paolone, F. Trequattrini, D. D. Leece, S. Panero, S. Brutti, "Analysis of the self-discharge process in $LiCoPO_4$ electrodes: Bulks," *Electrochim. Acta*, vol. 179, pp. 604–610, 2015.

[40] R. Sharabi, E. Markevich, V. Borgel, G. Salitra, D. Aurbach, G. Semrau, M. A. Schmidt, N. Schall, and C. Stinner, "Significantly improved cycling performance of $LiCoPO_4$ cathodes," *Electrochem. commun.*, vol. 13, no. 8, pp. 800–802, 2011.

[41] N. Dupré, J-F. Martin, J. Oliveri, P. Soudan, D. Guyomard, A. Yamada, and R. Kanno, "Aging of the $LiNi_{1/2}Mn_{1/2}O_2$ positive electrode interface in electrolyte," *J. Electrochem. Soc.*, vol. 156, no. 5, 2009.

[42] E. J. Kim, X. Yue, J. T. S. Irvine, and A. R. Armstrong, "Improved electrochemical performance of $LiCoPO_4$ using eco-friendly aqueous binders," *J. Power Sources*, vol. 403, pp. 11–19, 2018.

5 DEGRADATION WITHIN $LiCoPO_4$ PARTICLES: DEVELOPMENT OF THE EELS OXIDATION STATE MAPPING TECHNIQUE

5.1 AIMS AND OBJECTIVES

The aim of this section of the thesis was to develop a technique which could map the lithiated and de-lithiated regions within individual $LiCoPO_4$ particles. Mapping the lithiated regions could help identify the lithiation mechanisms, and subsequently aid understanding of capacity fade in $LiCoPO_4$ electrodes.

Transmission electron microscopy, and the associated chemical characterisation technique electron energy loss spectroscopy (EELS) are useful for probing features on the nm scale (the scale of $LiCoPO_4$ particles). Unfortunately, Li is difficult to detect using EELS. However, as Li is extracted from $LiCoPO_4$, the oxidation state of Co also changes as a charge compensating mechanism. Co oxidation states can be detected using EELS.

Here an EELS-based lithiation mapping technique was developed by using changes in the Co oxidation state to detect localised changes in lithiation. The Co oxidation states were mapped by MLLS fitting of EELS spectra to Co(II), and Co(III)-rich Co L-edge standards.

The Co(II), and Co(III)-rich EELS L-edge standards were collected from uncycled $LiCoPO_4$, and $CoPO_4$ made by charging $LiCoPO_4$ to 5.1 V vs. Li/ Li^+. X-Ray Diffraction (XRD), and selected area electron diffraction (SAED) were used to confirm the presence of $CoPO_4$.

The O K-edge was also extracted, and changes mapped in order to identify potential Co-O hybridisation [1].

The effects of sample preparation on the effectiveness of EELS mapping are also demonstrated by microtoming and imaging whole particles.

Once the lithiation mapping technique was developed, it was used to understand the de-lithiation mechanisms of $LiCoPO_4$ on the first cycle, and to understand differences in lithiation content in the charged state of later cycles.

5.2 INTRODUCTION

5.2.1 Electron Energy Loss Spectroscopy and Oxidation State Mapping Techniques for Li-ion Battery Research

Transmission electron microscopy (TEM) is a technique in which an electron transparent material is imaged by transmitting an electron beam through the sample. TEM allows high resolution microstructural imaging, electron diffraction, crystallographic analysis, and chemical spectroscopy to be carried out and correlated on the same volume of material.

Scanning transmission electron microscopy (S/TEM) is a transmission electron microscopy technique where the electron beam is focussed into a probe and rastered across the sample. Different imaging modes are achievable due to the smaller probe size than TEM. Electrons which are scattered through the material produce contrast in bright field images. Electrons which are scattered strongly from interactions with high Z-number components can be collected to generate high angle annular dark field (HAADF) images.

Electron energy loss spectroscopy (EELS) is a chemical characterisation technique used in STEM mode. EELS spectrometers analyse electrons that are inelastically scattered by the sample when passing through. Most of the electrons are elastically scattered due to coulomb interactions with atomic nuclei, generating a large peak in EELS spectra at 0 eV energy loss, called the zero loss peak [2]. Some electrons undergoing transmission through a material lose energy due to inelastic scattering, where the incident electrons are scattered due to coulomb interactions with the atomic electrons. Core-loss excitations (where energy of incident primary electrons is transferred to electrons in the material to change energy level) allow for chemical characterisation with EELS [2].

EELS is one of the few chemical characterisation techniques capable of detecting Li. However, most battery electrodes have other components, such as carbon additive and binder materials, which generate enough inelastic energy loss (background signal) to mask the Li signal which occurs at a low energy (Li K-edge at 55 eV) [3]. It is therefore very difficult to directly detect Li using EELS in battery electrodes.

As detection of lithium is difficult, a number of studies on battery materials such as $LiFePO_4$ (analogous to $LiCoPO_4$) have focussed on observing changes in the oxidation state of the transition metal ion and oxygen [4] [5] [6] to fully understand the redox process occurring in the cell. It is possible to use EELS to detect changes in transition metal oxidation states by analysing the energy loss near edge structure (ELNES) of the energy loss spectrum [7].

Transition metals in EELS spectra typically appear as 2 peaks known as the $L_{2,3}$ white lines (see Figure 5.1). The white lines originate from the dipole allowed 2p → 3d band transitions in transition metals. The separation of the 2 lines occur due to spin-orbit splitting from ground states of the transition ($2p_{3/2}$ → 3d and $2p_{1/2}$ → 3d) [8], [1].

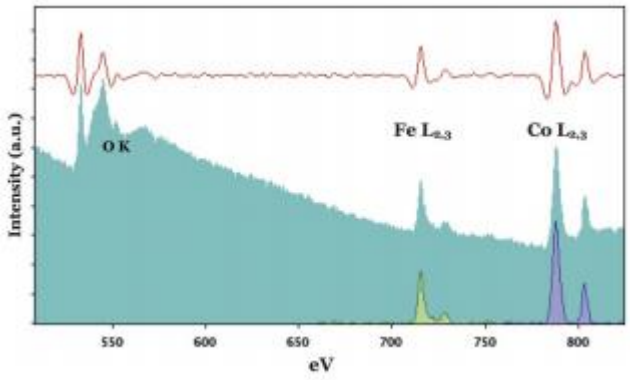

Figure 5.1: Transition metal $L_{2,3}$ white lines (Fe and Co), L_2 is the first peak and L_3 the second, and the oxygen K-edge. Reused with permission from Cambridge University Press [8]

There are a number of different methods to determine transition metal oxidation states from EELS spectra, including the white line ratio (the ratio in height between the 2 white lines), or the O- K edge onset and the energy distance from the L-edge onset and the O- K onset [8]. An alternative method involves using standards and fitting the spectra to the standards of known oxidation states using multiple linear least squares fitting (MLLS) [9].

Accurate oxidation state quantification relies on good signal to noise signal from the EELS spectrum when using methods which require measuring peak height ratios and distances between edge onsets. In cycled electrodes conductive additives and binder materials are present, which

can diminish the signal to noise ratio of the EELS transition metal signal, and mask higher energy loss peaks (such as the M-edges) [4] [5].

To avoid interference from binder and conductive additives, previous studies have chemically de-lithiated $LiFePO_4$, using reagents such as NO_2BF_4 in acetonitrile to study changes in the oxidation state of Fe as $LiFePO_4$ is de-lithiated [4] [5]. Chemical de-lithiation allowed Kobayashi et al. to observe the Li K-edge, which is usually masked by carbon background [5].

Chemical de-lithiation also offers control of the degree of de-lithiation, allowing the oxidation state of Fe to be directly compared with the degree of delithiation. Chemical delithiation of $LiFePO_4$ allowed Sigle et al. to quantify oxidation states using the O K-edge method [4], and allowed

However, chemical de-lithiation does not occur in real cells. A more realistic method to understand the redox processes in Li-ion cells would be to study transition metal oxidation changes using electrochemical delithiation. Laffont et al. performed valence state EELS analysis on electrochemically de-lithiated $LiFePO_4$ [6]. Quantification difficulties due to the lower signal-to-noise ratios were overcome by synthesising end group standards ($LiFePO_4$ and $FePO_4$) and comparing these to the electrochemically de-lithiated samples. This study found similar results to a chemical de-lithiation study by Sigle et al. [4], where fully electrochemically de-lithiated $LiFePO_4$ consists of a core of $FePO_4$ surrounded by a shell of $LiFePO_4$- contrary to bulk studies on $LiFePO_4$ at the time [6].

EELS spectra from known standards can be used to quantify the oxidation state of transition metal L-edges by using multiple linear least squares (MLLS) fitting analysis to fit the standards to the measured transition metal L-edge [6], [9]. MLLS fitting takes known standards and fits acquired spectra, F(E), to a linear combination of their standards, where $S_a(E)$, and $S_b(E)$ are reference models with respect to energy loss E, and B_a, and B_b are scaling coefficients [10].

$$F(E) = AE^{-r} + B_a S_a(E) + B_b S_b(E) + \ldots$$

The principle of MLLS fitting is shown in Figure 5.2.

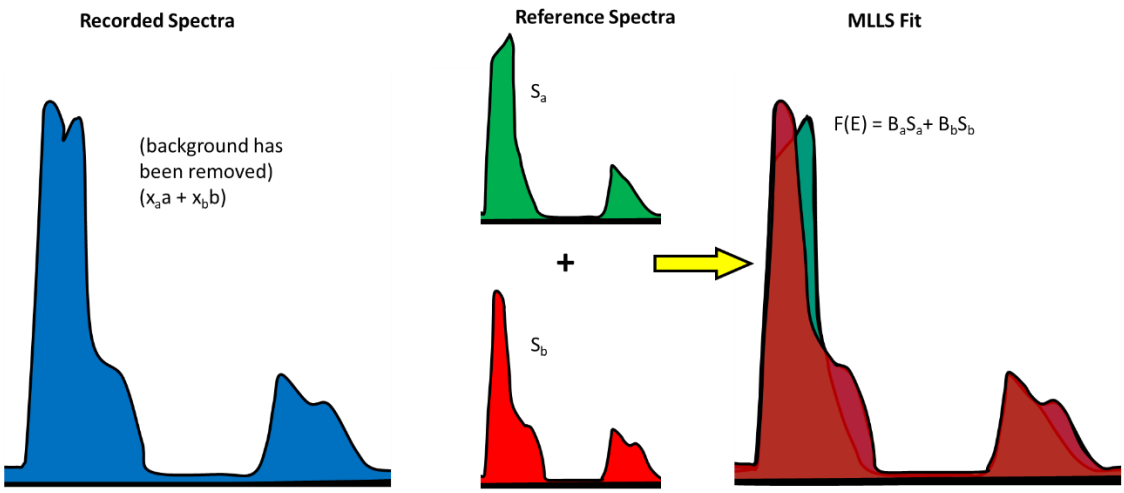

Figure 5.2: Principle of MLLS fitting [10]

Similar to $LiFePO_4$, as $LiCoPO_4$ charges, theoretically the oxidation state of Co changes from Co(II) to 2/3 Co(II), 1/3 Co(III), and finally Co(III) due to phase changes as the material de-lithiates (charges):

$LiCoPO_4$ (Co(II)) → $Li_{2/3}CoPO_4$ (2/3 Co(II), 1/3 Co(III)) → $CoPO_4$ (Co(III)) [11].

The changing Co oxidation state experienced by $LiCoPO_4$ as it delithiates suggests it is possible to understand lithiation mechanisms by measuring oxidation state changes of Co using EELS.

For oxidation state quantification with MLLS fitting, standards with known oxidation states are required. For $LiCoPO_4$, the ideal standards are Co(II)- $LiCoPO_4$, 2/3 Co(II) and 1/3 Co(III)- $Li_{2/3}CoPO_4$, and Co(III)- $CoPO_4$. As variation in the degree of de-lithiation across $LiCoPO_4$ particles is expected on charging, ideally the standards should be synthesised using chemical de-lithiation, and the standards subsequently compared with electrochemically de-lithiated samples. Due to the unstable octahedrally co-ordinated $CoPO_4$ [11], it is difficult to synthesis the end group standards as done for $LiFePO_4$ studies [6]. Work by Wolfenstine et al. found that chemical oxidation of $LiCoPO_4$ (extraction of Li using a strong oxidizing agent- NO_2BF_4 in acetonitrile) did not completely de-lithiate $LiCoPO_4$ to form $CoPO_4$, whereas chemical oxidation of $LiFePO_4$ resulted in only $FePO_4$ [12]. Therefore, the $CoPO_4$ standard in this study is synthesised electrochemically in this study.

X-ray absorption spectroscopy (XAS) studies by Lapping et al. have previously found that the oxidation state of Co will not shift completely to Co(III), but residual Co(II) remains particularly on the surface of the electrode on charging [1]. The partial oxidation of Co on charging has been attributed to a stronger contribution from the O electronic states in $LiCoPO_4$ towards oxidation of the Li, compared with contribution from the Co electronic states [1]. Despite the discrepancy, the oxidation state of Co changes with respect to lithiation content, so tracking changes in Co oxidation state could yield information about the lithiation mechanisms. However, the difficulty in fully achieving Co(II) → Co(III) may impede quantification when using the MLLS fitting approach as the Co(III) standard may be extracted from a region which is still partially lithiated (a Co(III) majority, Co(III)/ Co(II) mixture).

So far most studies have focussed on either quantifying and making observations of the electronic structure [1], or making bulk oxidation state and phase change observations using methods such as nuclear magnetic resonance imaging (NMR) [11], or X-ray diffraction (XRD) [13]. If MLLS fitting is applied across a spectrum image of $LiCoPO_4$, a spatial map showing Li-rich verses Li-poor areas could be generated, allowing better understanding of the lithiation mechanisms.

5.3 EXPERIMENTAL

5.3.1 Cell Testing

In order to study the structural degradation using EELS and XRD, $LiCoPO_4$ half cells were galvanostatically cycled to different potentials on the 1st cycle, 5th cycle, and 10th cycle.

Coin cells were assembled in an Ar filled glove box with the O_2, and H_2O levels at <0.1 ppm. 12 mm diameter, 90 wt. % C-$LiCoPO_4$, 5 wt. % C65 conductive additive, and 5 wt. % PVDF electrode discs were assembled into 2016 stainless steel coin cells (Cambridge Energy Solutions), using Li metal (Sigma Aldrich) as the anode. 16 mm diameter, Whatman GF/F fibre glass filter paper, and 16 mm diameter Celgard 2325, polypropylene-polyethylene-polypropylene (PP-PE-PP) were used as separators. A 0.5 mm stainless steel spacer was inserted to increase the internal cell pressure.

$LiPF_6$ in a 50/ 50 volume ratio of ethylene carbonate (EC), and dimethyl carbonate (DMC), also known as LP-30 (Sigma Aldrich), was used as the electrolyte. Figure 5.3 shows the coin cell set up.

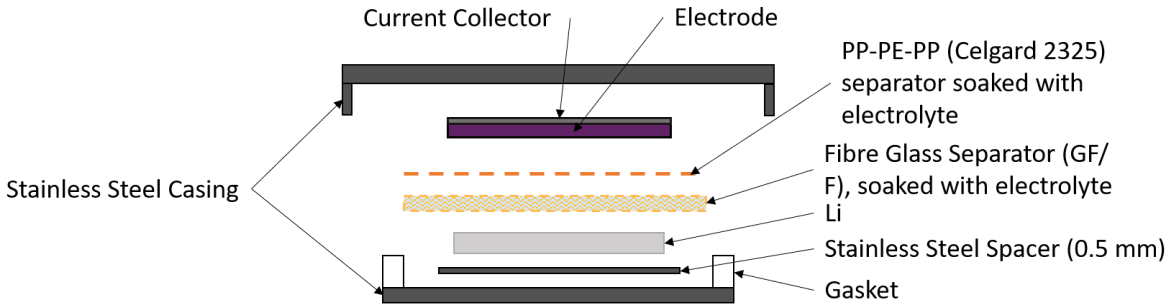

Figure 5.3: Schematic of the 2016 coin cell set up.

Prior to cycling, the half-cells were rested at open circuit potential for 12 hours in order to allow electrolyte to fully penetrate the pores in the electrode. The coin cells were galvanostically cycled at 0.1C. A single, complete, cycle consisted of cycling between 2.5 V vs. Li/ Li^+, and 5.1 V vs. Li/ Li^+, with a 30 min constant voltage step at the highest potential on each charge step and an hour rest after discharge. Details on specific cycling of cells for the experiments are presented in 5.4.1**.**

5.3.2 S/TEM Sample Preparation

After cycling, the coin cells were de-crimped and washed with 1 ml of DMC (Sigma Aldrich), and allowed to dry. De-crimping and drying were performed in an Ar filled glove box, with the O_2, and H_2O levels <0.1 ppm, in order to prevent oxidation of the cycled electrodes. $CoPO_4$ (the charged state of $LiCoPO_4$), is particularly susceptible to oxidation due to air exposure due to the instability of the octahedrally co-ordinated Co^{3+} [11].

Samples were prepared for S/TEM using one of two methods; (1) scraping, or (2) microtoming.

(1) Electrode material (C-$LiCoPO_4$, C65, and PVDF) was scraped from the aluminium current collector and ground in a mortar and pestle in an argon filled glove box. For samples described as air exposed in the results section, the resulting ground powder was suspended in ethanol and sonicated. The suspension was pipetted onto holey carbon copper TEM grids (EM Resolutions), and allowed to dry. Sonication was performed in order to prevent large clusters of particles on the TEM grid. For all other scraped samples, the ground powder was dry mounted onto copper, holey carbon grids by brushing powder onto the grid in an Ar filled glove box. The electrodes were transported to the microscope, sealed in bags in an Ar atmosphere.
In the case of the dry mounted samples, air exposure occurred for a maximum of 2 mins (the time taken to mount the grid onto the TEM holder and insert into the microscope vacuum).

(2) Electrodes were prepared for microtoming by being cut into strips in an Ar filled glove box, and sealed into Al coated bags (Mylar) under Ar. A resin was prepared using 5 ml dodecenyl succinic anhydride (DDSA), 5 ml of araldite resin (CY212), and 5 drops of benzyldimethyl amine (BDMA) (TAAB). The strips were deposited into the resin, and the resin cured at 65 °C for 3 days. The resin mounted electrodes were microtomed using a Reichert-Jung Ultracut E ultromicrotome with a diamond blade. The electrodes were microtomed to 80 nm thickness into water. The microtomed electrodes were mounted onto copper, lacey carbon TEM grids (EM resolutions). After microtoming, the electrodes

were dried, put back into the Ar filled glove box, and transported to the microscope in Al-coated, Mylar bags under Ar. Air exposure to the electrodes occurred for 30 s when being positioned in the resin, and parts of the sample cut by the microtome are exposed to air during the microtoming process if they are not shielded by residual resin.

All electrodes prepared for high resolution imaging and electron diffraction were prepared using the microtoming method. The method used for the EELS samples is stated in the results section.

5.3.3 STEM-EELS Oxidation State and Elemental Characterisation

STEM-EELS characterisation was performed at 200 kV with a JEM ARM200F TEM and EELS spectra were collected using a Gatan Model 965 GIF Quantum ER spectrometer. High and low energy loss EELS spectra were collected simultaneously using DualEELS to allow energy drift to be corrected by aligning the spectrum images to the zero loss peak. The total measurement time was between 5 and 10 mins depending on the measurement area.

Co valence states were measured with EELS by maximising the energy resolution of the Co $L_{2,3}$ edges. Spectra were obtained between 765 and 811 eV with an energy dispersion of 0.025 eV using a collection semi-angle between 42 mrad and 55 mrad. The spot size, and dwell time per pixel were selected by scanning the $LiCoPO_4$ samples, and ensuring the Co $L_{2,3}$ edge remained at a constant energy loss throughout the scan (once the zero-loss was aligned), whilst maintaining a good signal-to-noise ratio.

O K-edge spectra were obtained using a 0.025 eV, or 0.01 eV dispersion.

5.3.4 STEM-EELS Oxidation State and Elemental Characterisation Data Processing

All EELS and EDS results were analysed using Gatan Microscopy Suite 3 (GMS3, Digital Micrograph). Co valence state maps were created, and quantification of the proportion of Co(II) and Co(III)-rich phases was performed from EELS spectrum images using multiple linear least squares (MLLS) fitting between the extracted signal and reference standards for Co(II) and Co(III)-rich areas.

To correct the energy drift as the spectrum was corrected, and allow comparison of the Co-$L_{2,3}$ edges with standards, the spectrum images were calibrated to the zero-loss peak (ZLP) by shifting the ZLP at each pixel to 0 eV. This was possible as the low- and high-loss EELS spectra were collected simultaneously for each image using DualEELS. The calibration method is shown in Figure 5.4 (a).

The background signal was removed from the spectrum image and the summation signal used for quantification to allow comparison with Co(II), and Co(III)-rich standards. The inbuilt GMS3 background removal function was used to extract the signal using the power law background function (as shown in Figure 5.4 (b). The background removal was applied to the summed spectra of the whole spectrum image, and subsequently applied to each pixel on the spectrum image to produce a ‘signal only’ spectrum image.

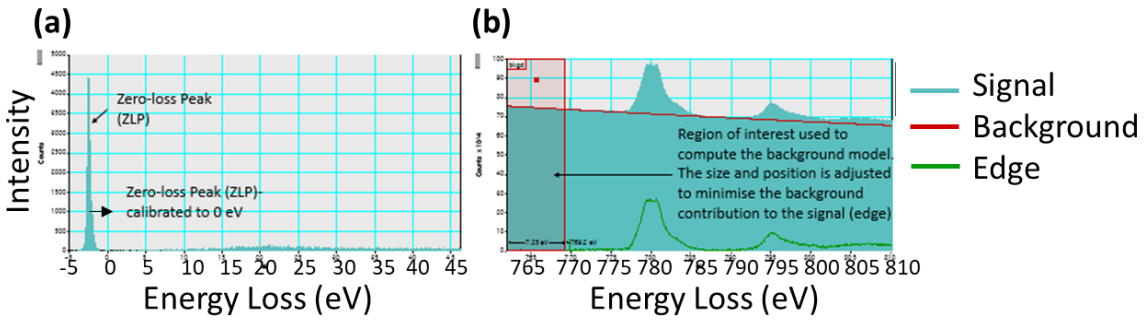

Figure 5.4: (a) Example zero-loss peak showing the need for calibration as the ZLP is not at 0 eV. (b) Co $L_{2,3}$ edges showing the background extraction (red) using the power law function and the subsequent Co $L_{2,3}$ signal (green)

The reference standard for Co(II) was uncycled $LiCoPO_4$, whilst the Co(III)-rich reference standard was a charged region from a $LiCoPO_4$ electrode charged to 5.1 V vs. Li/ Li^+. The ideal reference standard for Co(III) would have been $CoPO_4$ (the end phase when $LiCoPO_4$ is charged [11]), however, this does not exist outside of a $LiCoPO_4$ cell. Therefore, MLLS fitting was initially performed between the spectrum images and Co(II)O and Co_3O_4 to identify the Co(III)-rich regions. The Co(III)-rich signal was extracted from these regions on the charged 5.1 V vs. Li/ Li^+ sample to provide the Co(III)-rich reference. The results for this are described in 5.4.2.

For quantification of the proportion of Co(II), and Co(III)-rich phases present in the spectrum image, MLLS fitting was performed on the background subtracted summed spectrum from the spectrum image. The summed spectrum was used to maximise the signal to noise ratio. MLLS fitting was performed across the entire energy range of the summed signal between the acquired standards using the signal integral function method. The MLLS fit signal integral function returns the integral of the MLLS fit fitted using the Co(II), or the Co(III)-rich standard. The proportion of Co(II) and Co(III)-rich phases present were calculated using:

$$Co(II)/\,Co(III)-rich\,\% = \frac{Co(II)/\,Co(III)-rich\;MLLS\;fit\;integral}{Total\;MLLS\;fit\;integral}$$

The residual represents the proportion of unfitted signal (proportion of the collected signal which was not fitted to either reference). Residual signal could either be entirely Co(II), entirely Co(III), or a mixture of the two, thus representing the fitting error. Other fitting errors were not calculated, as the proportion of unfitted signal was considered to be the largest error. The residual was calculated using:

$$Residual = \frac{MLLS\;fit\;integral - Signal\;integral}{Signal\;integral}$$

To map the Co(II) and Co(III)-rich regions, MLLS fitting was performed on the spectrum image across the entire energy range collected. The output of the mapping were maps where the intensity of each pixel correlated to the integral of the MLLS fit fitted using the Co(II), the Co(III)-rich standard, or residual (misfit) signal.

To produce a map containing the Co(II), and Co(III)-rich regions, the Co(II), and Co(III)-rich maps were overlaid. The EELS spectra were collected on sample areas which were over holes in the TEM grid. However, on some images some of the spectra were collected where some TEM grid was present and on most of the images, background signal was detected in areas which were at

vacuum (regions with no specimen). It is unknown why signal was detected in vacuum, however, detector chip noise and energy spread in the beam may contribute to the presence of background in the vacuum. Resin may also have been present in these areas. The MLLS fitting algorithm in GMS3 version used does not remove negative fitting coefficient results, so the program will assign any area with an EELS signal detected a Co(II), or Co(III)-rich colour, including the vacuum which should not be fitted to either Co(II), or Co(III)-rich standards (as shown in Figure 5.5). To correct this error in the mapping, the brightness and contrast of the combined image were adjusted to ensure the background vacuum regions were black.

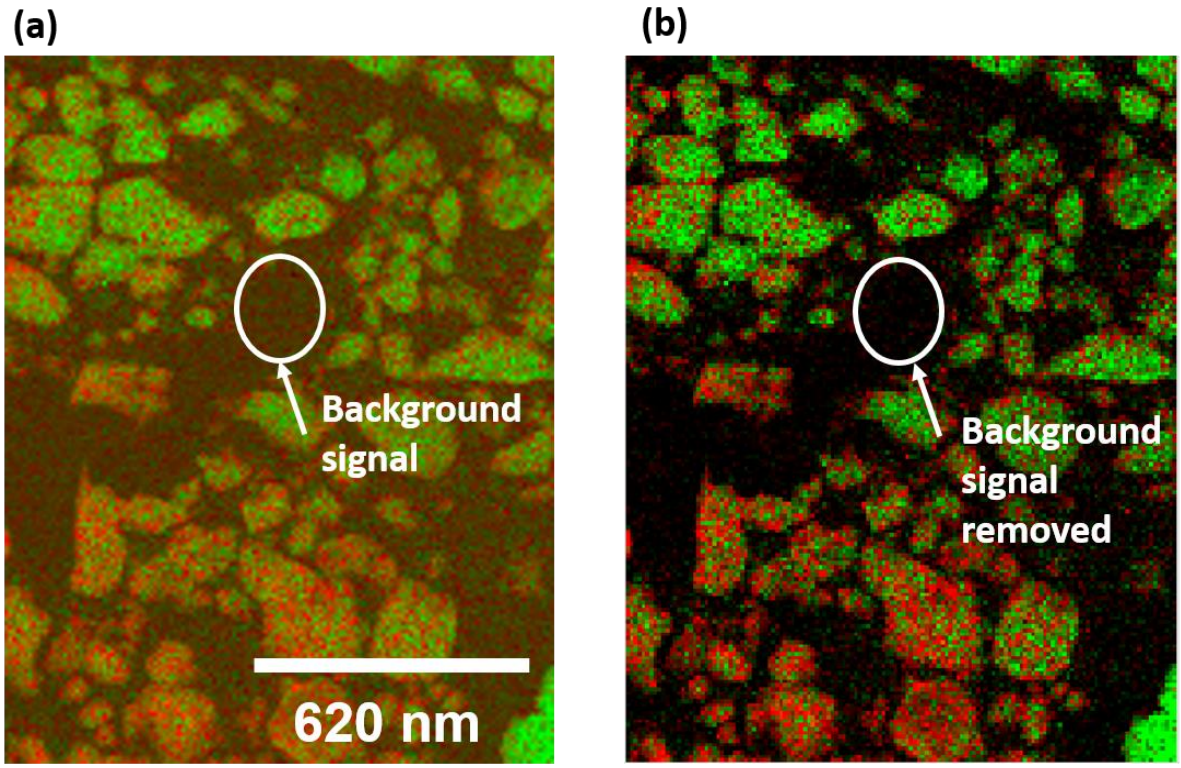

Figure 5.5: (a) Overlaid Co(II) and Co(III)-rich signal integral maps showing Co(II), and Co(III)-rich standard fitting in the background (vacuum) areas of the sample. (b) Contrast corrected map of the area in (a) where the background is black.

Elemental mapping EELS processing was also performed using GMS3. As with the Co valence state maps, the spectrum images were aligned using the zero loss peak. The background after each peak was removed by selecting the appropriate background function for each peak, so the signal was maximised. As the signal-to-noise ratio of the fluorine K-edge was very small, the spectra were deconvolved with the zero-loss peak, using the built-in deconvolution function, in order to identify the F K-edge peak.

5.3.5 S/TEM high resolution imaging and diffraction

TEM high resolution imaging was performed on microtomed samples using a JEOL JEM F200 at 200 kV with a OneView camera. The samples were tilted towards a zone axis by using the objective aperture in bright field mode to find the highly diffracting grains/ particles (dark contrast particles). The microscope was switched into diffraction mode and the sample tilted until the diffraction pattern indicated a zone-axis. Diffraction patterns were taken at this point. The microscope was switched back into TEM imaging mode, and the objective aperture removed, for high resolution imaging of the particles on the zone axis.

5.3.6 X-ray Diffraction Characterisation

Samples were prepared for XRD by scraping the electrode off the current collector, grinding with a mortar and pestle, and loading into glass capillary tubes in an Ar filled glove box. The capillaries were sealed with wax to prevent air exposure during XRD pattern collection. 3 electrodes were mounted per capillary as the capillaries were too long to be filled with 1 electrode.

XRD was performed using a Panalytical Empyrean diffractometer, with a GalliPIX3D X-ray detector, using Ag Kα radiation in transmission, capillary spinner mode. Initially XRD was attempted with Cu Kα radiation, but the signal-to-noise ratio was found to be too low due to fluorescence. Mo Kα radiation was also attempted, but issues with the Mo X-ray mirror impacted the reliability of the results.

XRD results were refined using the Rietveld method using Highscore software.

5.4 Results: Development of the oxidation state mapping technique

5.4.1 Experiments presented

The scope of this section is to demonstrate the development of the oxidation state mapping technique used to identify lithiation mechanisms in $LiCoPO_4$. To ensure oxidation state mapping could be accurately used to study lithiation mechanisms in $LiCoPO_4$ the following steps were taken:

(1) Identification and extraction of appropriate EELS Co L-edge, and O K-edge standards for $LiCoPO_4$, $Li_{2/3}CoPO_4$, and $CoPO_4$.
(2) Confirmation that the sample preparation method, and any potential air exposure, caused minimal damage to the sample.

$LiCoPO_4$ as-received powder was used as the Co(II) standard. The standards for $Li_{2/3}CoPO_4$, and $CoPO_4$ were synthesised electrochemically, therefore appropriate charging potentials to form the standards were selected based on the presence of plateaus in the galvanostatic charging curve. Structural characterisation using SAED, and XRD was performed to confirm the presence of the standard phases in samples charged to the potentials chosen to extract Co L-edge standards.

Exposure to air is known to amorphises $CoPO_4$ (the charged state of $LiCoPO_4$), but the effect on the Co L-edge is unknown. Therefore, the Co L-edge of samples containing $CoPO_4$ exposed to air for 3 days, and 2 mins were compared. 3 days was the longest transit time between Sheffield and Harwell for microscopy, and 2 mins was the time required to remove samples from sealed bags and insert them into the microscope.

Microtoming, as described in section 5.3.2, requires mounting and curing the electrodes in resin. To confirm the microtoming process did not cause changes in the Co L-edge, Co L-edges were extracted from both microtomed, and non-microtomed samples.

The experiments detailed in this chapter are outlined in Table 5.1.

Table 5.1: Table outlining the experiments presented in this chapter, and the sections where they are detailed

Experiment	Electrode cycling history	EELS Co L-edge	SAED	XRD	Section	Notes
Identification + extraction of $LiCoPO_4$ standard	Uncycled	Y	Y	Y	5.4.2	
Identification +extraction of $CoPO_4$ standard	Charged to 5.1 V vs. Li/ Li^+ on the first cycle	Y	Y	Y	5.4.2	
Identification + extraction of $Li_{2/3}CoPO_4$	Charged to 5.1 V vs. Li/ Li^+, and 4.89 V vs. Li/ Li^+ on the first cycle	Y	Y	Y	5.4.2.4	
Identification + extraction of O K-edge standards	Uncycled electrode, and an electrode charged to 5.1 V vs. Li/ Li^+	Y			5.4.2.5	
Effect of air exposure on the Co L-edge	Charged to 5.1 V vs. Li/ Li^+ on the first cycle	Y			5.4.3	Samples were exposed for 3 days, and 2 mins
Effect of microtoming on the Co L-edge	Charged to 5.1 V vs. Li/ Li^+ on the first cycle	Y			5.5.4	Non-microtomed, and microtomed samples were compared

5.4.2 Identifying Appropriate Standards

5.4.2.1 Selecting potentials to collect standards

The ideal standards for EELS spectra analysis using MLLS fitting would be pure samples of the phases which form during cycling, $LiCo(II)PO_4$, $Li_{2/3}Co(II,III)PO_4$, and $Co(III)PO_4$. In order to identify the Co L-edge standards, the galvanostatic charging characteristics were observed to identify the potentials when phase changes were occurring. Ideally the phase changes would be matched with a specific capacity in order to maintain consistency between samples, however, likely due to contributions from the electrolyte, the cell capacities were not consistent enough for this.

Figure 5.6 shows representative 0.1C galvanostatic charge and discharge curves, and the differential capacity curve of the first cycle of a lithium ion half-cell. The differential capacity (Q) in Figure 5.6 (b) was calculated as the integral of the time vs. current curve divided by the active mass of $LiCoPO_4$.

The galvanostatic charge curve in Figure 5.6 (a) shows the presence of 2 voltage plateaus at 4.8 V and 4.9 V vs. Li/ Li^+. On discharge there at 2 plateaus are 4.7 V vs. Li/ Li^+ and at 3.5 V vs. Li/Li^+. The total charging capacity is 223 mAh g^{-1} which is greater than the theoretical capacity of $LiCoPO_4$

(167 mAh g^{-1} [11]), potentially due to contributions from the electrolyte forming CEI layers on charge (discussed in the degradation at the electrode surface chapter).

The differential capacity is the first order differential of capacity (Q) against voltage (V) curve (dQ/dV). Peaks in a differential capacity curves correspond to physical processes occurring in the cell. In Figure 5.6 (b) there are 2 large peaks during charge, corresponding to the voltage plateau potentials on the galvanostatic cycling curve (at 4.84 V vs. Li/Li^+ and 4.91 V vs. Li/Li^+). These peaks are both above the electrolyte break-down potential of $LiPF_6$ in 50/50 vol. EC/ DMC (4.5- 5.0 V vs. Li/Li^+ [14]). The integral of a differential capacity peak gives the capacity gained during the physical process represented by the peak. The specific capacity represented by total integral under the 2 peaks is 154 mAh g^{-1}, less than the theoretical maximum of $LiCoPO_4$ (167 mAh g^{-1}). As the specific capacity resulting from the peaks is less than the theoretical maximum, the peaks are likely a result of material processes within the $LiCoPO_4$ particles, hence reference standards are needed at potentials after the peaks (uncharged, 4.89 V vs. Li/ Li^+ and, 5.1 V vs. Li/ Li^+).

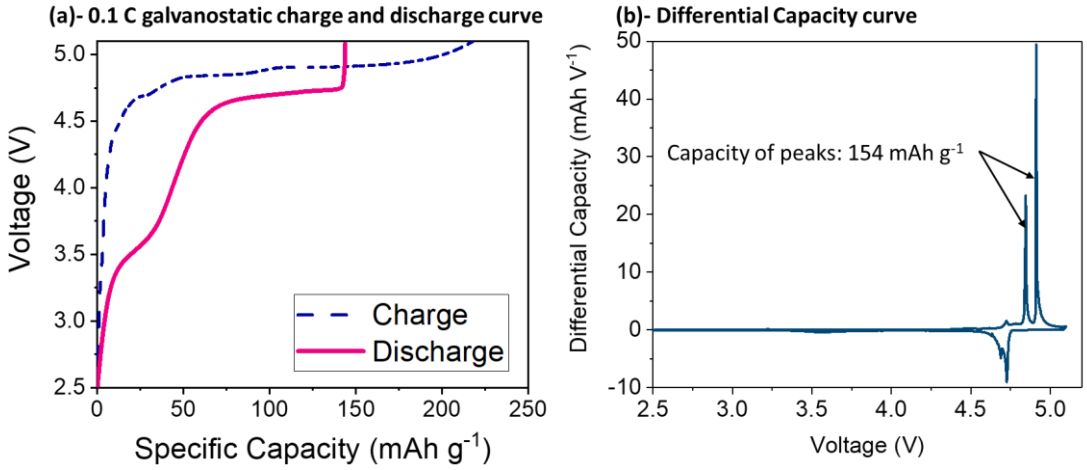

Figure 5.6: Representative 0.1C (a)- galvanostatic charge (blue dashes) and discharge curves (pink solid), and (b)- differential capacity curves of a $LiCoPO_4$ half-cell. Q- specific capacity. dQ/dV = differential capacity

5.4.2.2 Extracting the Co L-edge standards from collected EELS spectrum images

MLLS fitting methodology requires standards to act as a model to fit to the EELS signal. The ideal standards to study lithiation mechanisms in $LiCoPO_4$ would be Co(II), 2/3 Co(II) + 1/3 Co(III) and Co(III) $L_{2,3}$ edges extracted from LiCo(II)PO_4, $Li_{2/3}$Co(II, III)PO_4 and Co(III)PO_4 respectively. Uncycled $LiCoPO_4$ was used as a standard for Co(II)-rich regions. However for Co(III), $CoPO_4$ amorphises on contact with air [11] and does not exist outside of a charged $LiCoPO_4$ cell.

The Co(III) standard was extracted from a 5.1 V vs. Li/ Li^+ sample (fully charged as per the differential capacity curve in Figure 5.6 (b). The Co L-edge Co(III)-rich standard was extracted by MLLS fitting a 5.1 V vs. Li/ Li^+ charged $LiCoPO_4$ sample to Co(II)O, and Co_3(II, III)O_4 Co L-edge standards to identify which regions were Co(II)-rich, and which regions were Co(III)-rich. The Co(III)-rich reference standard was extracted from regions identified as Co(III)-rich after mapping with Co(II)O and Co_3(II, III)O_4. $Li_{2/3}CoPO_4$ will be discussed in a later section.

CoO and Co_3O_4 are common oxides with different oxidation states (Co(II) for CoO and 2/3 Co(III), 1/3 Co(II) for Co_3O_4). The $L_{2,3}$ edge spectra of Co(II)O and Co_3(II, III)O_4 are shown in Figure 5.7. The shape of the $L_{2,3}$ edges for CoO and Co_3O_4 are different, consistent with Co in different oxidation states. There is a shift in the peak and edge onset of the L_2 edge from Co(II) to Co(III) by 1.475 eV

and the ratio between the peak heights of the L_2 and L_3 edges is greater for CoO than Co_3O_4, consistent with literature on transition metal oxide $L_{2,3}$ edge shapes [8].

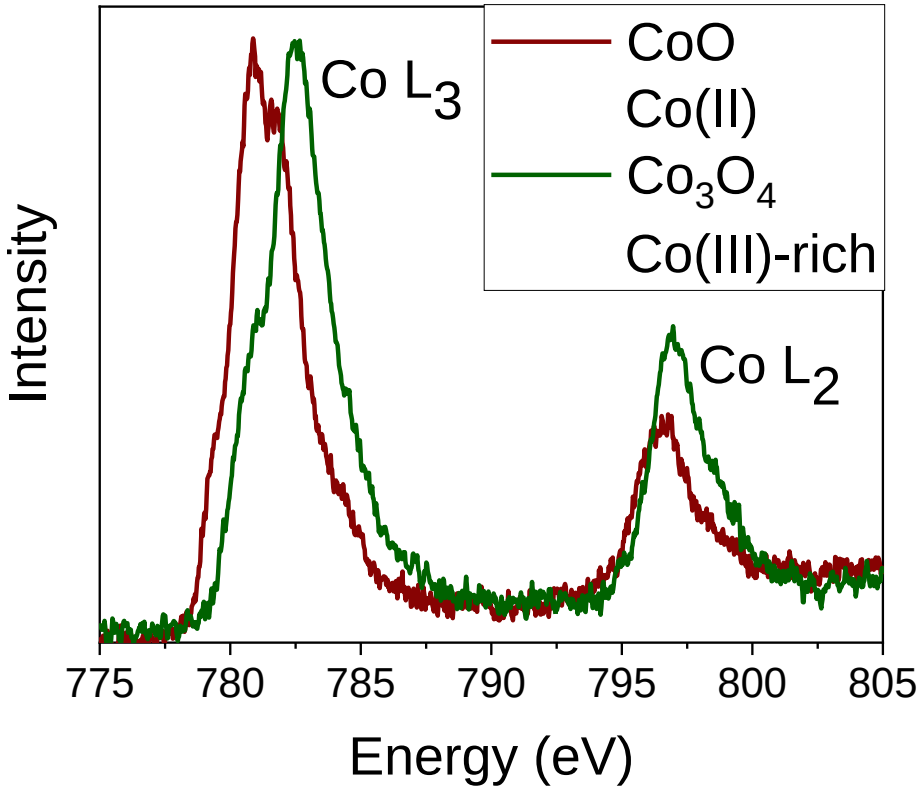

Figure 5.7: Co(II) and Co(III)-rich L-edge EELS signals extracted from Co(II)O (dark red) and Co_3(II,III)O_4 (dark green) respectively. Co L_3-edge is the first peak, Co L_2-edge is the second peak.

The Co(III)-rich EELS signal was extracted from Co(II, III)-rich regions of the 5.1 V vs. Li/ Li^+ sample (as indicated by the yellow box in Figure 5.8 (b)). The Co(II)O and Co_3O_4 Co L-edge signals were also fitted to an uncycled $LiCoPO_4$ electrode to confirm the presence of Co(II) (Figure 5.8 (a)).

Figure 5.8 (a) shows that fitting the Co(II)O to an uncharged $LiCoPO_4$ EELS spectrum image causes the MLLS fit result to be Co(II) (red) for most of the particle area. A region of the particles near the top of Figure 5.8 (a) is slightly green, this was due to thickness complications described in 5.4.4. The region chosen for extraction was completely red, indicating that the resulting $LiCoPO_4$ Co L-edge signal would be mostly Co(II).

Figure 5.8 (b) shows a 5.1 V vs. Li/ Li^+ charged electrode spectrum image fitted to the Co(II)O, and Co_3(II, III)O_4 EELS spectra in Figure 5.7. Regions which fitted to the Co_3(II, III)O_4 reference signal better than to the Co(II)O reference signal are more Co(III)-rich (indicated by mostly green regions of Figure 5.8 (b)). The Co(III)-rich reference signal for de-lithiated $LiCoPO_4$ was extracted from a mostly green region of Figure 5.8 (b), as indicated by the yellow box in Figure 5.8 (b). The extracted Co(III)-rich edge from the 5.1 V vs. Li/ Li^+ electrode is shown in Figure 5.9. In order to confirm this was the most 'Co(III)-rich' region, signals were extracted from other green mixed regions. The same edge shape as the Co(III)-rich edge in Figure 5.9 was found from other mixed red and green areas.

Figure 5.8 (b) shows that the Co_3O_4 reference signal did not map well to a 5.1 V vs. Li/ Li^+ as the map is a mixture of red and green across the whole sample. The poor mapping of the charged sample with the cobalt oxide references in Figure 5.8 (b) is likely because Co(III) bonded to a PO_4 group has a different Co L-edge shape to a Co(III) bonded to a O group. Co in Co_3O_4 consists of tetrahedrally co-ordinated Co(II), and octahedrally co-ordinated Co(III) [15], whereas Co in $CoPO_4$ is octahedrally co-ordinated [11], hence the electron densities are likely to be different.

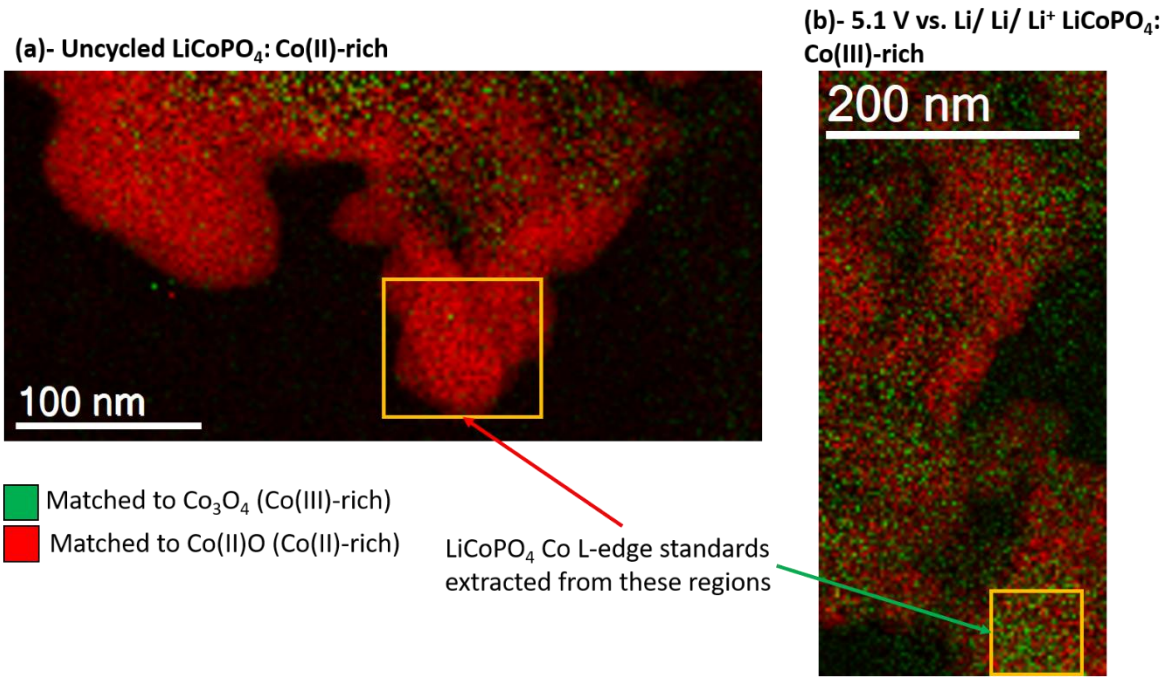

Figure 5.8: EELS maps of (a)- uncycled $LiCoPO_4$, and (b)- 5.1 V vs. Li/ Li^+ charged $LiCoPO_4$ created by MLLS fitting the acquired spectrum image to: green regions- Co_3O_4 Co(III)-rich, and red- Co(II)O Co(II)-rich L edge signals shown in Figure 5.7.

The extracted EELS reference signals from the yellow box regions of the charged $LiCoPO_4$ sample in Figure 5.8 are shown in Figure 5.9 (red- Co(II)-rich, green- Co(III)-rich). As the 5.1 V vs. Li/ Li^+ signal was matched to a mixed oxidation-state oxide, the standard is referred to as Co(III)-rich.

The extracted $LiCoPO_4$ electrode Co(III)-rich and Co(II)-rich signals in Figure 5.9 have distinctly different shapes. The peak on the L_2 edge for the Co(III)- rich sample (green line) has a higher energy loss than the Co(II)-rich L_2 edge (780.7 eV vs. 779.4 eV respectively). There is a hip on the L_3 edge at 782.6 eV, and on the L_2 edge at 797.2 eV on the Co(II)-rich signal (red line), but not on the Co(III)-rich signal. The different edge shapes indicate the presence of different Co oxidation states so the Co(II) and Co(III)-rich references could be used as reference signals for further MLLS fitting.

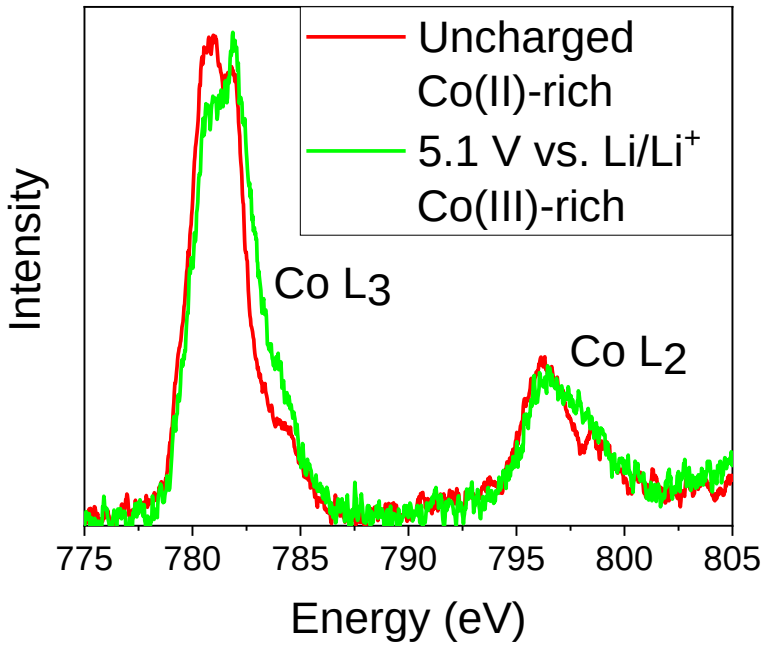

Figure 5.9: Extracted Co L-edge EELS standards: red- Co(II) standard extracted from uncycled $LiCoPO_4$, green- Co(III)-rich standard extracted from $LiCoPO_4$ charged to 5.1 V vs. Li/ Li^+ as shown in Figure 5.8.

Figure 5.10 shows a comparison of the Co L-edges extracted from the $LiCoPO_4$ samples, and Co L-edges extracted from the cobalt oxide samples. The shape the Co(II) edges are similar for both the oxide, and phosphate compounds, however the Co(III)-rich $LiCoPO_4$ Co L-edges are different to the equivalent oxide Co L-edges. The ratio between the L_2 and L_3 edges heights (intensities) of the Co(III) extracted (red) and Co(III)-rich extracted signals (green) in Figure 5.10 are smaller (Co(II)- 2.9, Co(III)- 3.4) compared with CoO and Co_3O_4 (CoO- 2.8, Co_3O_4- 1.9) in Figure 5.10. The comparatively small height ratio would make the L-edge height ratio method of quantifying oxidation state more difficult for $LiCoPO_4$ samples.

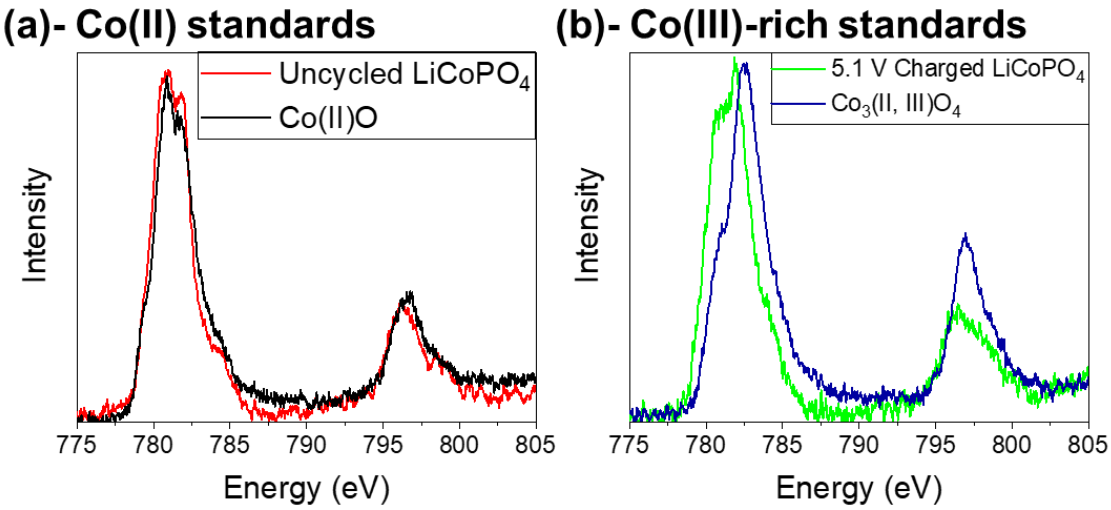

Figure 5.10: Comparison of the cobalt oxide and lithium cobalt phosphate (a) Co(II)-rich, and (b) Co(III)-rich EELS edges. In (a) the Co(II)-rich oxide edge (black) was extracted from Co(II)O, and the Co(II)-rich $LiCoPO_4$ edge (red) was extracted from uncycled $LiCoPO_4$. In (b) the Co(III)-rich oxide edge was extracted from $Co_3(II, III)O_4$ (blue), and the Co(III)-rich $LiCoPO_4$ edge was extracted from a $LiCoPO_4$ electrode charged to 5.1 V vs. Li/ Li^+ (green).

The Co(III) reference should represent fully de-lithiated regions of $LiCoPO_4$ ($CoPO_4$). However, the extracted Co(III)-rich phosphate reference can only be called Co(III)-rich and not Co(III) as the Co(III)-rich signal was extracted from an area selected on the basis the EELS signal from this region fitted better to mixed Co valence state $Co_3(II, III)O_4$ than Co(II)O.

Figure 5.6 (b) shows the specific capacity resulting from the redox peaks was 154 mAh g^{-1}, less than the theoretical capacity of $LiCoPO_4$ (167 mAh g^{-1}), suggesting the 5.1 V vs. Li/ Li^+ charged sample was not be fully de-lithiated. Therefore, the Co(III)-rich standard could be a Co L-edge from a partially de-lithiated region of sample, rather than a fully de-lithiated region of sample.

To confirm that the Co(III)-rich reference is pure Co(III) and not a mixed 2/3 Co(III), 1/3 Co(II), the $L_{2,3}$ edge shape was compared to the $L_{2,3}$ edge from $Co_3(PO_4)_2$ (Figure 5.11). Co in $Co_3(PO_4)_2$ is in a Co(II) oxidation state in the presence of phosphate groups, but without the presence of Li. The shape of the $Co_3(PO_4)_2$ $L_{2,3}$ edge (purple) matches the Co(II) $LiCoPO_4$ edge.

As the $Co_3(PO_4)_2$ edge matches the Co(II)-rich signal, this confirms the Co(II)-rich signal is Co(II). If the shape of the $Co_3(PO_4)_2$ had been a mix between the Co(III)-rich reference and Co(II)-rich reference, this would imply partial filling of electron states due to the presence of Li is having an impact on the shape of the $L_{2,3}$ edge. As this is not the case, the shape of the $L_{2,3}$ edge is more likely to be due to the oxidation state of the Co. At 5.1 V vs. Li/Li^+ the only Co(III)-rich phase that should be present is $CoPO_4$ (pure Co(III)). As the $Co_3(PO_4)_2$ matches the Co(II) reference, by process of elimination the Co(III)-rich reference must represent Co(III)-rich areas.

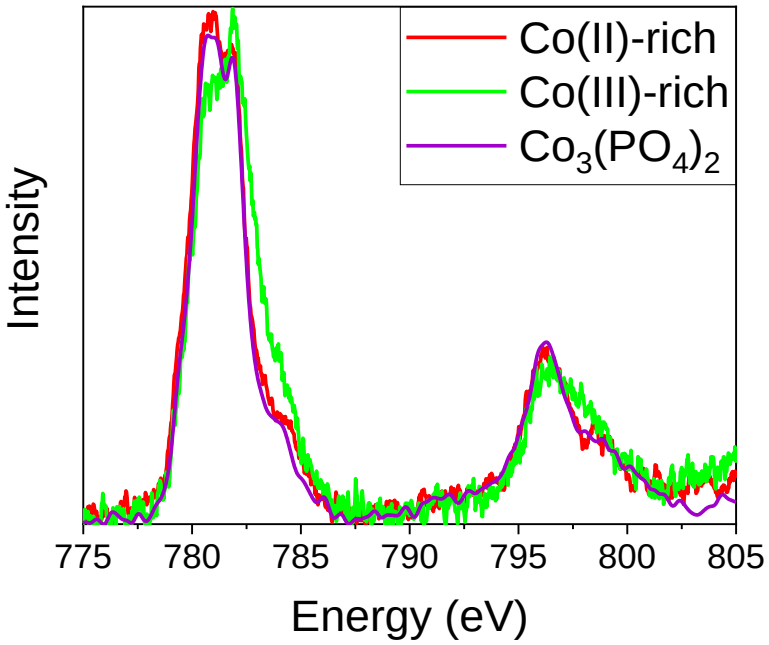

Figure 5.11: Purple- Co L-edge EELS signal extracted from $Co_3(PO_4)_2$ (Co(II) cobalt attached to phosphate groups) compared to extracted Co L-edge standards: red- Co(II) standard extracted from uncycled $LiCoPO_4$, green- Co(III)-rich standard extracted from 5.1 V vs. Li/ Li^+ as shown in Figure 5.8.

The $Co_3(PO_4)_2$ argument ignores the potential for O-Co bond hybridisation effects on the Co(III)-rich edge [1]. To confirm the identity of the Co(III)-rich edge, X-ray diffraction, and electron diffraction were performed.

5.4.2.3 Confirming the phases using XRD and selected area electron diffraction (SAED)

The EELS analysis confirms a difference in the Co L-edge shape between charged and discharged regions of $LiCoPO_4$ electrodes but does not prove the identity of the phases detected. XRD was performed on uncycled electrodes, and electrodes charged to 5.1 V vs. Li/ Li^+ to confirm the identity of the Co(II), and Co(III)-rich regions (Figure 5.12, Figure 5.13, and Figure 5.14).

The acquired XRD pattern for the uncycled electrode is shown in Figure 5.12. An amorphous hump is observed at 8 ° 2θ, which results from the glass capillary tube used to collect the XRD pattern. The refinement results are shown in Figure 5.12. To correct for the amorphous component of the background, the pattern was refined with a Chebychev background model.

Due to the use of hard Ag radiation, the lower angle peaks have a pre-peak sloping asymmetry associated with axial divergence. The patterns were collected using the smallest possible soller slit configuration (0.02 °) to minimise the axial divergence error. To correct for the asymmetry, the pseudo-voigt peak shape components were refined with a split peak shape, width and height. The difference plot shows large fitting errors on the more intense peaks ((111), and (311)).

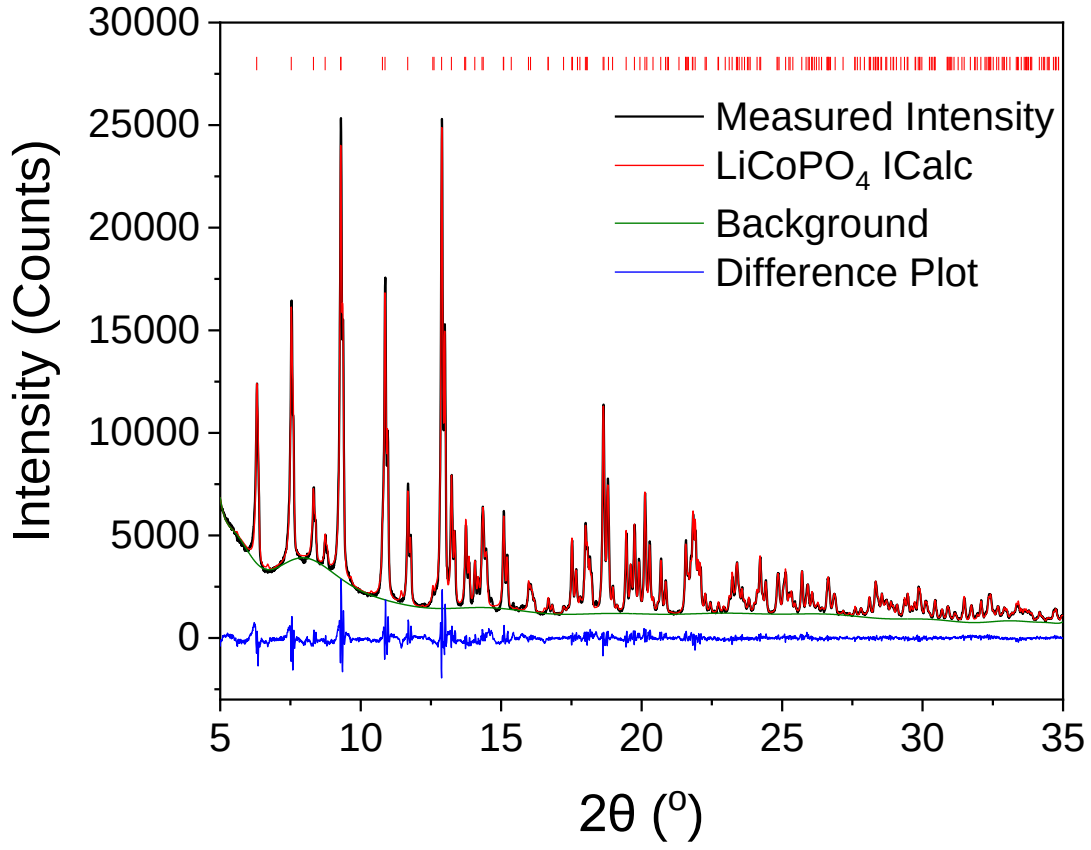

Figure 5.12: Collected XRD pattern (black), calculated intensity profile (red), calculated background using the Chebychev model (green), and the difference plot (blue) of rietveld refined uncycled electrodes. The red dashes indicate peak positions for $LiCoPO_4$. Reproduced with permission from [16]*. Copyright 2020, the American Chemical Society.*

The acquired XRD pattern and rietveld refinement for $LiCoPO_4$ electrodes charged to 5.1 V vs. Li/ Li^+ is shown in Figure 5.13. The refinement fitting was performed using $CoPO_4$, and $Li_{2/3}CoPO_4$ phases due to the presence of peaks attributed to both phases (shown in Figure 5.14). The refinement was performed by fitting the unit cell of both $CoPO_4$, and $Li_{2/3}CoPO_4$ to the measured peak positions, and then refining the atomic co-ordinates and the atomic displacement, B_{iso} values. The occupancy factor of the atomic positions was not refined.

The overall measured intensity of the 5.1 V vs. Li/ Li^+ pattern (Figure 5.13) is less than the measured intensity for the uncycled electrode in Figure 5.12 because less electrode powder used to collect the pattern.

Due to the lower overall intensity of the 5.1 V vs. Li/ Li^+ pattern (Figure 5.13), there is a higher contribution of background towards the intensity of the pattern. An amorphous hump at 7 ° 2θ is observable and results from the use of glass capillaries as a sample holder, similar to the uncycled electrode in Figure 5.12. The background was modelled using user defined basepoints, as the Chebychev background model was unable to accurately model the background for the pattern in Figure 5.13.

Another possibility for the amorphous hump in Figure 5.13 is partial amorphisation of $CoPO_4$, due to accidental air exposure. It was still possible to ascertain the unit cell values of $CoPO_4$ from the pattern (shown in Table 5.2), required to calculate d-spacings for phase identification with SAED.

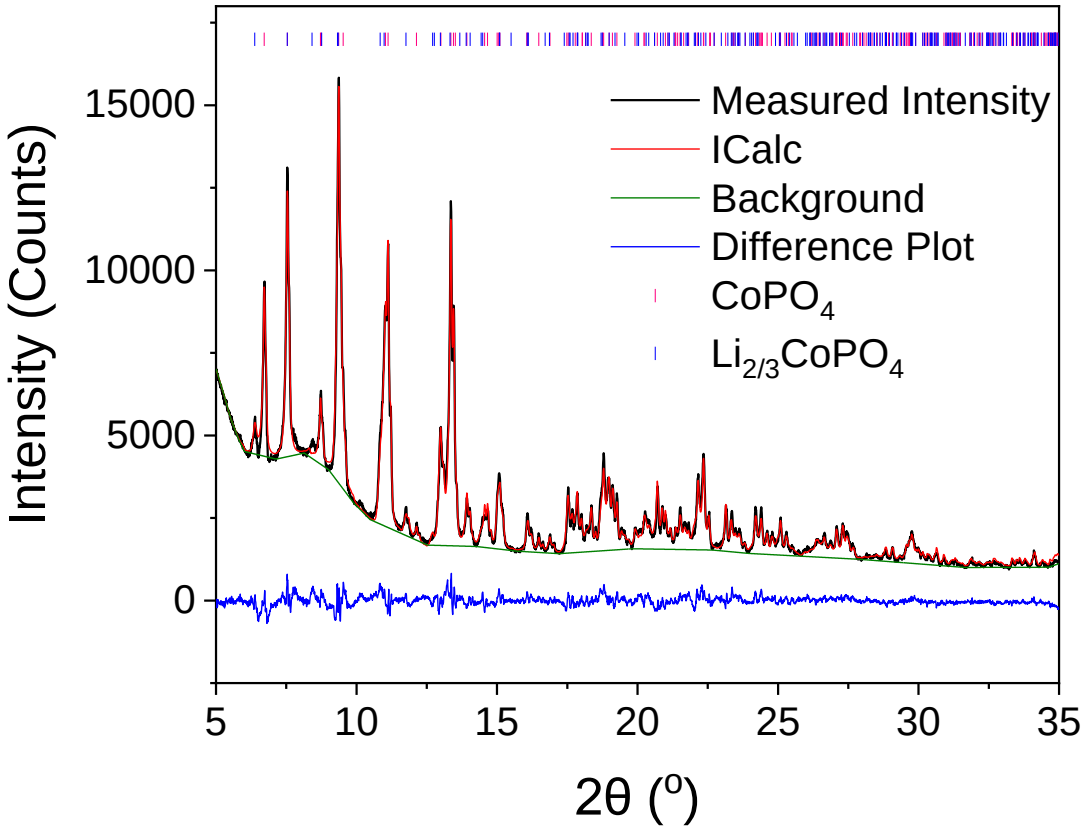

Figure 5.13: Collected XRD pattern (black), calculated intensity profile (red), calculated background using user defined points (green), and the difference plot (blue) of rietveld refined 5.1 V vs. Li/ Li^+ charged electrodes. The blue dashes indicate peak positions for $CoPO_4$, and the pink dashes indicate the peak positions for $Li_{2/3}CoPO_4$.

The XRD patterns in Figure 5.14 have had the background removed in order to analyse the peak positions. The patterns for both the 5.1 V vs. Li/ Li^+ charged electrodes, and the uncycled electrodes were normalised by the (111) plane, as this reflection had the highest intensity regardless of the phase present. The phase percentages (weight fractions) shown on Figure 5.14 were calculated using Highscore plus after rietveld using

$$W_p = \frac{(SZMV)_P}{\sum_i (SZMV)_i}$$

W_p- weight fraction of phase p, S- scale factor, Z- number of formula units per unit cell, M- molecular weight of the formula unit, V- unit cell volume, i- index running over all phases.

The error on the weight fraction was calculated based on:

$$\Delta W_p = \chi W_p \sqrt{\frac{\Delta V^2}{V} + \frac{\Delta S^2}{S}}$$

ΔW_P- error on weight fraction, W_P- weight fraction, ΔV- estimated standard deviation of the unit cell volume, ΔS- estimated standard deviation of the phase scale factor, S- scale factor, and V- unit cell volume, χ- goodness of fit parameter.

The peak reflections for high intensity peaks, and those which vary between phases are labelled to aid discussion. The space group of all 3 phases ($LiCoPO_4$, $Li_{2/3}CoPO_4$, and $CoPO_4$) was found to be P n m a.

The uncycled XRD pattern of $LiCoPO_4$ electrodes was found to contain 100 % $LiCoPO_4$ (Figure 5.14). Therefore the Co(II) EELS signal extracted from the uncycled electrode shown in Figure 5.9 is $LiCoPO_4$.

The 5.1 V vs. Li/ Li^+ electrodes were found to be a mix of $Li_{2/3}CoPO_4$, and $CoPO_4$ (Figure 5.14). As the electrode was charged the (200) reflection shifted to higher 2θ values (6.3 ° for $LiCoPO_4$, for 6.4 ° $Li_{2/3}CoPO_4$, and 6.7 ° for $CoPO_4$). A shift also occurred for the (210) reflection, the (301) reflection, and the (311) reflection. The peak shifts occurred due to the removal of Li causing unit cell volume shrinkage due to a decrease in a the 'a' unit cell parameter (defined in Figure 2.6). Removal of Li^+ allows attraction between transition metal and polyanions layers in the structure, causing shrinkage. A broad shoulder was detected on the 020 reflection (as the reflection shifted to lower 2θ values) associated with the presence of $Li_{2/3}CoPO_4$, in agreement with work by Palmer et al. [13].

Phase analysis found that the electrodes charged to 5.1 V vs. Li/ Li^+ contained 28.6 % $Li_{2/3}CoPO_4$, and 71.4 % $CoPO_4$. Therefore, from bulk analysis of the electrodes using XRD there is some uncertainty in the identity of the Co(III)-rich standard in Figure 5.9 as the distribution of the 28.6 % $Li_{2/3}CoPO_4$ within the bulk sample is unknown.

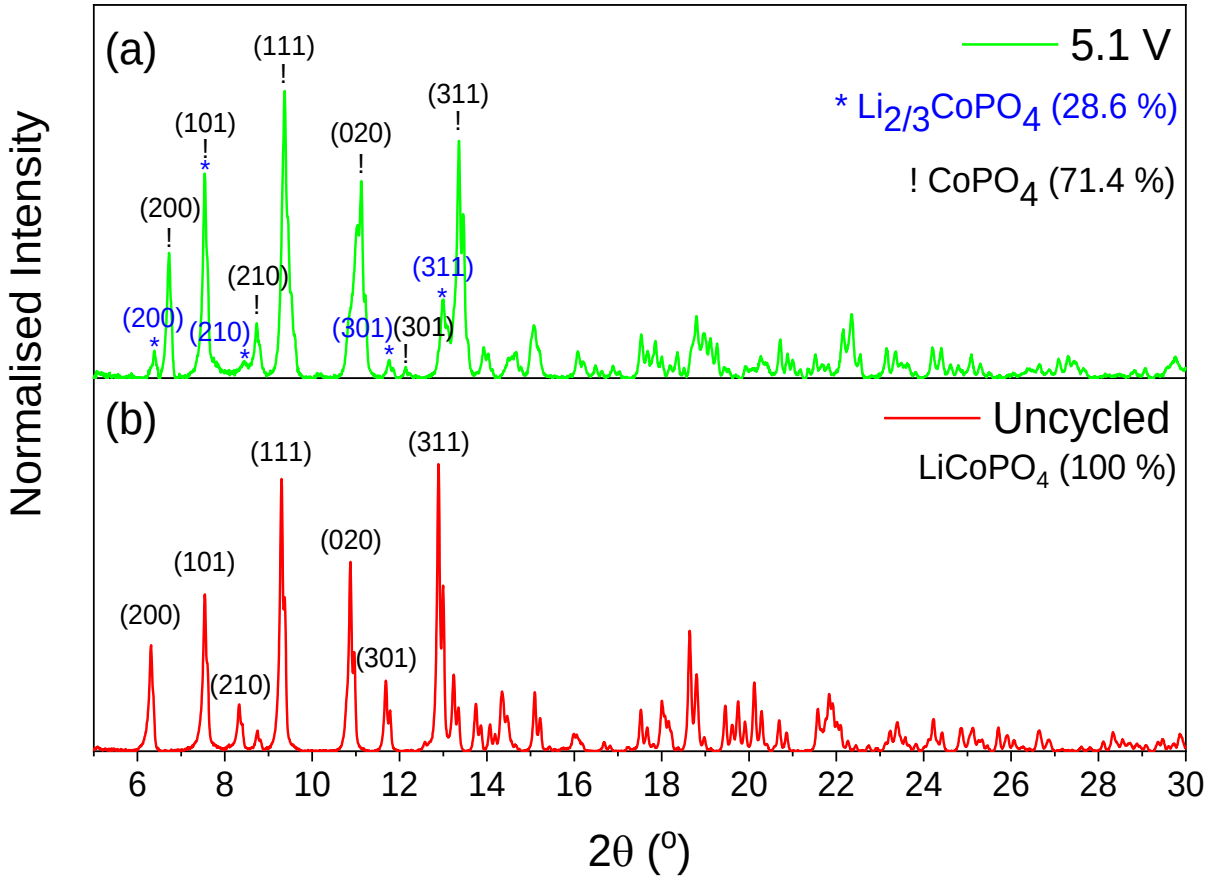

*Figure 5.14: Ag kα XRD patterns of (b) Uncycled (red), and (a) 5.1 V vs. Li/ Li⁺ (green) electrodes. Each pattern was collected using with 3 electrodes mounted in capillaries. The intensities have been normalised by the (111) plane. The crystallographic planes associated with selected reflections are labelled. The peaks on the uncycled pattern are $LiCoPO_4$. On the 5.1 V vs. Li/ Li⁺ pattern, $Li_{2/3}CoPO_4$ reflections are labelled with a blue *, and $CoPO_4$ reflections are labelled with a black !. The proportion of $Li_{2/3}CoPO_4$ proportion was found to be 28.6 %, and the proportion of $CoPO_4$ was 71.4 %. The PDF cards used for refinements were: $LiCoPO_4$- 01-089-6192, $Li_{2/3}CoPO_4$- 04-014-7340, and $CoPO_4$- 04-014-7341. Reproduced with permission from [16]. Copyright 2020, the American Chemical Society.*

The results of the refinements shown in Figure 5.12 and Figure 5.13 are shown in Table 5.2. R_{wp} is the weighted R-value (fitting parameter) defined by:

$$R_{wp} = \sqrt{\left(\frac{\sum w_i(y_{io} - y_{ic})^2}{\sum w i y_{io}^2}\right)}$$

Y_{io}- original pattern intensity at position i 2θ

Y_{ic}- calculated pattern intensity at position i 2θ

w_i- weighted factor defined by $1/ESD^2$, where ESD is the estimated standard deviation at position i

The results in Table 5.2 show a decrease in the overall unit cell volume as Li is removed, with the lattice parameter decreasing in a and b. The lattice parameter increases in direction c as de-lithiation occurs.

The weighted R-value fitting parameters indicate a reasonable fit between the calculated model, and the original parameters. As the main purpose of XRD was to find the lattice parameters to calculate the d-spacings for SAED indexing, the accuracy of the lattice parameters was the most

important aspect, which could be observed by checking the calculated peak positions against the original peak positions.

The numbers in brackets in the unit cell parameters reported in Table 5.2 represent the estimated standard deviation multiplied by the χ (goodness of fit) value for the lattice parameter. The estimated standard deviation and goodness of fit parameter (χ) were calulcated using Highscore Plus. χ is given by (R_{wp}/R_{exp}). R_{wp} is as defined above, and R_{exp} is the expected R-factor, representing the best possible R_{wp}. Since the χ parameter for both the uncycled, and 5.1 V vs. Li/ Li^+ was greater than 1 (2.62 and 2.46 respectively), the estimated standard deviations are an underestimate of the true error, so they were multiplied by χ as a correction. For a more accurate error estimation, multiple samples should have been scanned and refined. The unit cell error estimation method described was performed for all other XRD refinement results presented in this thesis. Some unit cell values do not have a quoted error as the error calculated lay outside the significant figures.

Table 5.2: Refinement results for the rietveld refinements shown in Figure 5.12 and Figure 5.13

Sample	Phase	Unit Cell			R_{wp}
		a (Å)	b (Å)	c (Å)	%
Uncycled	$LiCoPO_4$	10.203(1)	5.9205	4.6985	5.049
5.1 V	$Li_{2/3}CoPO_4$ $CoPO_4$	10.07(1) 9.565(3)	5.853(7) 5.778(2)	4.704(6) 4.7597	4.81

5.4.2.3.1 Indexing SAED Patterns

As the 5.1 V vs. Li/ Li^+ electrode was found to contain a phase mix of $CoPO_4$, and $Li_{2/3}CoPO_4$ via XRD (Figure 5.14), selected area electron diffraction (SAED) was required to identify phases within the particles. However, as the space group does not change between the 3 phases, the electron diffraction patterns will not be significantly different. However, the unit cell volume decreases, hence the d-spacing changes between the 3 phases. Therefore, the SAED patterns were indexed and the closest matching d-spacing to the respective phases used to identify the phase present.

To index the SAED patterns the d-spacings were measured by measuring the reciprocal lattice distances on the diffraction patterns across multiple spots (at least 4), and finding the inverse of the average reciprocal lattice distance. The measurement was averaged to minimise the centre spot distance error, particularly between larger spots in the diffraction patterns. d-spacings were calculated for allowed reflections of a P n m a lattice using:

$$\frac{1}{d} = \frac{1}{\sqrt{\frac{h^2}{a^2} + \frac{k^2}{b^2} + \frac{l^2}{c^2}}}$$

h, k, l- miller indices

a, b, c- lattice parameters

The errors for measured d-spacing for each diffraction spot are shown in Table 5.4. As the d-spacings were calculated by measuring distances between diffraction spots, the width of the diffraction spots was the largest source of error when indexing. Therefore, the d-spacing error (Δd) was calculated as:

$$\Delta d = measured\ d\ spacing\ \times \left(\frac{average\ diffraction\ spot\ width}{measured\ distance\ from\ 000\ to\ diffraction\ spot}\right)$$

The measured d-spacings were matched to calculated d-spacings, by matching the ratio of neighbouring measured d-spacings to ratios between the calculated d-spacings for each hkl miller index.

To phase identify the diffraction patterns a few assumptions were made:

(1) The SAED patterns collected were orientated along a high order zone axis, therefore only planes (1 0 0) to (2 2 4) were checked. The zone axis sites were found using the objective aperture, picking out grains with high levels of elastic scattering, and hence are likely close to the zone axis.

(2) The only phases considered were $CoPO_4$, $Li_{2/3}CoPO_4$, and $LiCoPO_4$ with the same lattice parameters as those measured by XRD. This discounts the possibility of further partial de-lithiation as the Li occupancy was not refined. Therefore, the analysis only confirms the presence of a phase with a similar unit cell to the phases found using XRD refinement (Figure 5.12 and Figure 5.13).

(3) Only allowed reflections of P n m a lattices occurred:

0kl: k + l = 2n
hk0: h = 2n
h00: h = 2n
0k0: k = 2n
00l: l = 2n [17]

The reflection index did not vary with phase. Therefore, if a spot had been identified as 2 0 0, the spot could be 2 0 0 for $LiCoPO_4$, $Li_{2/3}CoPO_4$, and $CoPO_4$. The phase was identified based on the lowest average difference between the calculated d-spacing of $LiCoPO_4$, $Li_{2/3}CoPO_4$, and $CoPO_4$, and the measured d-spacing. The reflection index not varying assumption was made because no extra reflections occurring on modelled SAED patterns in Crystal Maker software, and in the XRD patterns in Figure 5.12, Figure 5.13, and Figure 5.14. The difference in d-spacing value at a given reflection for each phase was smaller than the difference between the d-spacing values for the next reflection (see Table 5.3), so d-spacing differences were more likely due to lattice parameter shift rather than re-labelling of the diffraction spot.

Calculated d-spacing errors shown in Table 5.3, and Table 5.4 were calculated using:

$$d\ spacing\ error = d\ spacing \sqrt{\left(\frac{2\Delta a}{a}\right)^2 + \left(\frac{2\Delta b}{b}\right)^2 + \left(\frac{2\Delta c}{c}\right)^2}$$

Where a, b, and c are the lattice parameters for $LiCoPO_4$, $Li_{2/3}CoPO_4$, and $CoPO_4$ calculated from XRD patterns (see Table 5.2). Δa, Δb, and Δc are the estimated standard deviations multiplied by χ shown in Table 5.2.

Table 5.3: Comparison of calculated miller indices for allowed reflections for $LiCoPO_4$, $Li_{2/3}CoPO_4$, and $CoPO_4$. The d-spacings were calculated using the d-spacing formula, and the lattice constants calculated from XRD in Table 5.2.

Reflection	Calculated d-spacing (nm)		
	$LiCoPO_4$	$Li_{2/3}CoPO_4$	$CoPO_4$
2 0 0	$0.510 \pm 1.80 \times 10^{-5}$	$0.504 \pm 2.02 \times 10^{-4}$	$0.478 \pm 4.47 \times 10^{-5}$
1 0 1	$0.427 \pm 1.51 \times 10^{-5}$	$0.426 \pm 1.71\times 10^{-4}$	$0.426 \pm 3.98 \times 10^{-5}$
2 1 0	$0.387 \pm 1.37 \times 10^{-5}$	$0.382 \pm 1.53 \times 10^{-4}$	$0.368 \pm 3.44 \times 10^{-5}$
0 1 1	$0.368 \pm 1.30 \times 10^{-5}$	$0.367 \pm 1.47 \times 10^{-4}$	$0.367 \pm 3.44 \times 10^{-5}$
2 0 1	$0.346 \pm 1.22 \times 10^{-5}$	$0.343 \pm 1.38 \times 10^{-4}$	$0.337 \pm 3.16 \times 10^{-5}$

As the XRD patterns in Figure 5.14 indicate that electrodes charged to 5.1 V vs. Li/ Li^+ contain $CoPO_4$, and $Li_{2/3}CoPO_4$, the patterns were indexed using different unit cell values for different phases to calculate the d-spacings. Table 5.4 shows the average differences found between 3 measured d-spacings and calculated d-spacings of each possible phase for the diffraction patterns collected. The smallest average d-spacing was used to identify the phase present (see Table 5.4).

Average d-spacing differences were calculated using:

$$Average\ d\ spacing\ difference = \frac{|Calculated\ d1 - measured\ d1| + |Calculated\ d2 - measured\ d2| + |Calculated\ d3 - measured\ d3|}{3}$$

The average differences error was calculated as:

$$Avg\ d\ diff\ error = Avg\ d\ diff\ \times \sqrt{(\sum(\frac{meas\ d\ error_{spot\ i}}{meas\ d_{spot\ i}})^2 + \sum(\frac{calc\ d\ error_{spot\ i}}{calc\ d_{spot\ i}})^2)}$$

Avg d difference - average d spacing difference, spot i- all the indexed diffraction spots in a given diffraction pattern, calc/ meas d $error_{spot\ I}$- calculated/ measured d spacing error for diffraction spot I, calc/ meas $d_{spot\ I}$ – calculated/ measured d spacing for diffraction spot i.

The average differences presented in Table 5.4 show that the regions SAED patterns were collected for the 5.1 V vs. Li/ Li^+ charged particles were identified as $CoPO_4$, and $Li_{2/3}CoPO_4$, in agreement with the XRD patterns in Figure 5.14. $LiCoPO_4$ was found in the uncycled electrodes (Table 5.4), although for the [2 1 -1] zone axis, the $LiCoPO_4$, and $Li_{2/3}CoPO_4$ average differences were the same. The phase is identified as $LiCoPO_4$ as no $Li_{2/3}CoPO_4$ was found in the XRD patterns, and $LiCoPO_4$ should not have de-lithiated without cycling.

Table 5.4 shows the measured and calculated d-spacings were not a perfect match for all the phases. This was likely due measurement error when measuring between diffraction spots. The accuracy of the phase ID could be improved by measuring and comparing more diffraction spots. Given the results matched the XRD pattern results in Figure 5.14, it was assumed the indexing phase identification was correct with 3 measured spots.

However, the Lithium occupancy was not refined from the XRD patterns in Figure 5.13 so it is not possible to confirm that the electrode was fully de-lithiated using SAED as the phase identification process was based on lattice parameter changes. The charged standard will continue to be referred to as Co(III)-rich.

Table 5.4: Comparison between calculated d-spacings, measured d-spacings, and average d-spacings across the measured reflections for the different regions SAED patterns were collected, and the identified phase.

Sample	Zone axis	Plane	Measured d-spacing (nm)	Calculated d-spacing (nm)			Average d-spacing difference for all planes (nm)			Phase
				$LiCoPO_4$	$Li_{2/3}CoPO_4$	$CoPO_4$	$LiCoPO_4$	$Li_{2/3}CoPO_4$	$CoPO_4$	
Uncycled	[-1 2 -1]	(-2 -1 0)	0.385 ± 0.054	$0.386 \pm 1.36 \times 10^{-5}$	$0.382 \pm 1.54 \times 10^{-4}$	$0.368 \pm 3.44 \times 10^{-5}$	$2.67 \times 10^{-3} \pm 6.44 \times 10^{-4}$	$4.00 \times 10^{-3} \pm 9.64 \times 10^{-4}$	$9.33 \times 10^{-3} \pm 2.25 \times 10^{-3}$	$LiCoPO_4$
		(-1 0 1)	0.432 ± 0.060	$0.427 \pm 1.51 \times 10^{-5}$	$0.426 \pm 1.71 \times 10^{-4}$	$0.426 \pm 3.98 \times 10^{-5}$				
		(1 1 1)	0.348 ± 0.049	$0.346 \pm 1.22 \times 10^{-5}$	$0.345 \pm 1.38 \times 10^{-4}$	$0.343 \pm 3.21 \times 10^{-5}$				
	[2 1 -1]	(0 1 -1)	0.367 ± 0.053	$0.368 \pm 1.30 \times 10^{-5}$	$0.367 \pm 1.48 \times 10^{-4}$	$0.367 \pm 3.43 \times 10^{-5}$	$1.67 \times 10^{-3} \pm 3.06 \times 10^{-4}$	$1.67 \times 10^{-3} \pm 3.06 \times 10^{-4}$	$3.00 \times 10^{-3} \pm 5.49 \times 10^{-4}$	$LiCoPO_4$
		(1 0 2)	0.226 ± 0.016	$0.229 \pm 8.09 \times 10^{-6}$	$0.229 \pm 9.21 \times 10^{-5}$	$0.231 \pm 2.16 \times 10^{-5}$				
		(1 -1 1)	0.347 ± 0.029	$0.346 \pm 1.22 \times 10^{-5}$	$0.345 \pm 1.39 \times 10^{-4}$	$0.343 \pm 3.20 \times 10^{-5}$				
5.1 V charged	[-2 0 4]	(0 2 0)	0.291 ± 0.029	$0.296 \pm 1.05 \times 10^{-5}$	$0.293 \pm 1.17 \times 10^{-4}$	$0.289 \pm 2.70 \times 10^{-5}$	$4.85 \times 10^{-3} \pm 7.09 \times 10^{-4}$	$3.37 \times 10^{-3} \pm 4.93 \times 10^{-4}$	$2.62 \times 10^{-3} \pm 3.83 \times 10^{-4}$	$CoPO_4$
		(2 2 1)	0.224 ± 0.015	$0.225 \pm 7.95 \times 10^{-6}$	$0.223 \pm 8.96 \times 10^{-5}$	$0.220 \pm 2.06 \times 10^{-5}$				
		(-2 0 -1)	0.337 ± 0.030	$0.346 \pm 1.22 \times 10^{-5}$	$0.344 \pm 1.38 \times 10^{-4}$	$0.337 \pm 3.15 \times 10^{-5}$				
	[1 -2 3]	(-1 1 1)	0.341 ± 0.049	$0.346 \pm 1.22 \times 10^{-5}$	$0.345 \pm 1.39 \times 10^{-4}$	$0.343 \pm 3.20 \times 10^{-5}$	$3.35 \times 10^{-3} \pm 8.94 \times 10^{-4}$	$2.23 \times 10^{-3} \pm 5.95 \times 10^{-4}$	$6.72 \times 10^{-3} \pm 1.79 \times 10^{-3}$	$Li_{2/3}CoPO_4$
		(1 2 1)	0.241 ± 0.026	$0.243 \pm 8.58 \times 10^{-6}$	$0.241 \pm 9.69 \times 10^{-5}$	$0.239 \pm 2.23 \times 10^{-5}$				
		(2 -1 0)	0.384 ± 0.075	$0.386 \pm 1.36 \times 10^{-5}$	$0.382 \pm 1.54 \times 10^{-4}$	$0.368 \pm 3.44 \times 10^{-5}$				
	[2 1 -1]	(0 1 1)	0.360 ± 0.039	$0.368 \pm 1.30 \times 10^{-5}$	$0.367 \pm 1.46 \times 10^{-4}$	$0.367 \pm 3.43 \times 10^{-5}$	$5.69 \times 10^{-3} \pm 1.25 \times 10^{-3}$	$4.73 \times 10^{-3} \pm 1.04 \times 10^{-4}$	$5.07 \times 10^{-3} \pm 1.12 \times 10^{-3}$	$Li_{2/3}CoPO_4$
		(1 0 2)	0.226 ± 0.015	$0.229 \pm 8.09 \times 10^{-6}$	$0.229 \pm 9.21 \times 10^{-5}$	$0.231 \pm 2.16 \times 10^{-5}$				
		(1 -1 1)	0.340 ± 0.061	$0.346 \pm 1.22 \times 10^{-5}$	$0.345 \pm 1.39 \times 10^{-4}$	$0.343 \pm 3.20 \times 10^{-5}$				

Figure 5.15 shows a TEM image (a), and 2 indexed diffraction patterns taken from uncycled $LiCoPO_4$ particles. The TEM studies, for example the image in Figure 5.15 (a), indicate that the uncycled $LiCoPO_4$ particles are crystalline with an amorphous C coating surrounding the particles. The diffraction patterns, such as examples in Figure 5.15 (b), and (c), confirm the lattice is crystalline $LiCoPO_4$.

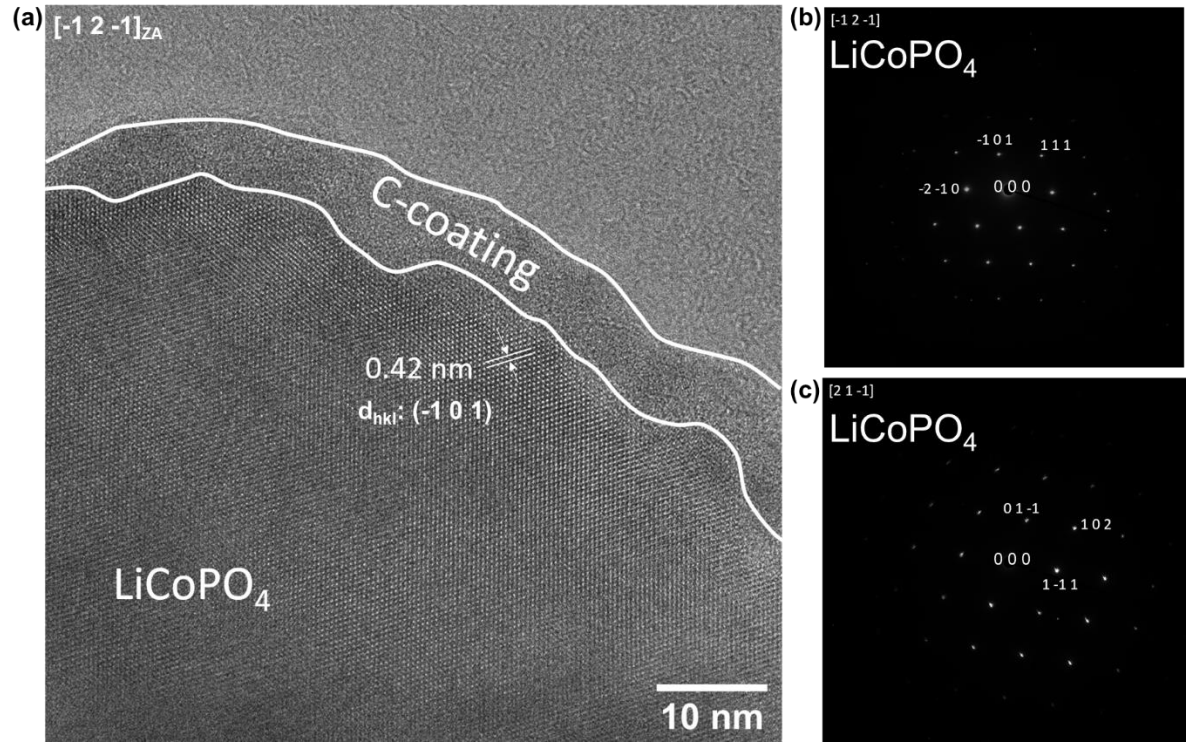

Figure 5.15: (a) TEM image of an uncycled $LiCoPO_4$ particle, and indexed diffraction patterns taken from different particles (b) $[-1\ 2\ -1]_{ZA}$, and (c) $[2\ 1\ -1]_{ZA}$. (b) is the diffraction pattern of the area in TEM image (a). The zone axis direction and phase identified is indicated in the top left hand corner of the diffraction patterns. Reproduced with permission from [16]. Copyright 2020, the American Chemical Society.

The sample SAED patterns of the 5.1 V vs. Li/ Li^+ electrode in Figure 5.16 (a, and b) were indexed to $CoPO_4$, and $Li_{2/3}CoPO_4$ respectively, indicating a mix of $Li_{2/3}CoPO_4$ and $CoPO_4$, consistent with the XRD pattern in Figure 5.14.

Figure 5.16 (a) shows a TEM image of a 5.1 V vs. Li/ Li^+ charged electrode particle identified as $CoPO_4$ with SAED. The plane labelled corresponds to the $CoPO_4$ (-2 0 -1) plane. The (-2 0 -1) plane had the same d-spacing across the whole lattice in the region of particle imaged in Figure 5.16 (a), indicating the particle was $CoPO_4$ across the imaged region. The presence of $CoPO_4$ across a wide area suggests the Co(III)-rich EELS spectra in Figure 5.9, collected from the most Co(III)-rich regions of the 5.1 V vs. Li/ Li^+ electrode originated from $CoPO_4$.

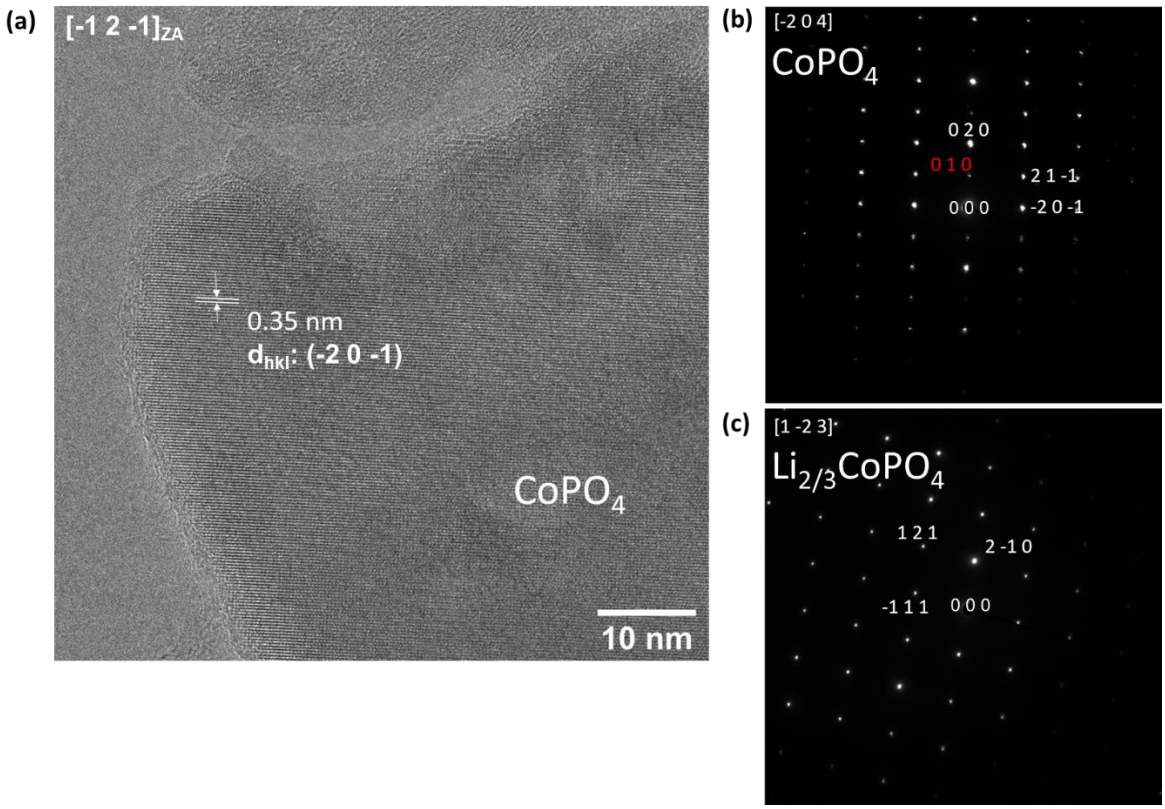

Figure 5.16: TEM image of a 5.1 V vs. Li/ Li^+ charged $LiCoPO_4$ particle, and indexed diffraction patterns taken from different particles (b), and (c). (b) is the diffraction pattern of the area in TEM image (a). The zone axis direction and phase identified is indicated in the top left hand corner of the diffraction patterns.

5.4.2.4 Mapping the third phase: $Li_{2/3}CoPO_4$

Electrochemical cycling Figure 5.6, and XRD patterns in Figure 5.14 indicate that a third phase $Li_{2/3}CoPO_4$ (referred to as phase B) should be present. So far EELS spectra standards have only been collected from an uncycled electrode, for Co(II) ($LiCoPO_4$), and an electrode charged to 5.1 V vs. Li/ Li^+ ($CoPO_4$). To fully understand the lithiation mechanisms and structural changes occurring in $LiCoPO_4$ during cycling, ideally an EELS standard for $Li_{2/3}CoPO_4$ should be collected.

A couple of strategies were employed to extract the phase B EELS standard:

(1) Extraction from red Co(II) areas of the 5.1 V vs. Li/ Li^+ map. $Li_{2/3}CoPO_4$ is 2/3 Co(II), and 1/3 Co(III), therefore the corresponding Co-L edge signal is likely to be fitted to the Co(II) signal during the MLLS fitting procedure. The 5.1 V vs. Li/ Li^+ XRD pattern in Figure 5.14 suggests that the only Co(II)-rich component present is $Li_{2/3}CoPO_4$.

(2) Extraction from a 4.89 V vs. Li/ Li^+ charged sample. Assuming that the two larger peaks in the galvanostatic discharge curve in Figure 5.6 correspond to the $LiCoPO_4$ -> $Li_{2/3}CoPO_4$, and $Li_{2/3}CoPO_4$-> $CoPO_4$ phase transitions, the electrode should consist of $Li_{2/3}CoPO_4$ after charging to 4.89 V vs. Li/ Li^+.

This section demonstrates the phase B EELS standard extraction using the above methods, and the EELS mapping capability using the standard. The extracted $Li_{2/3}CoPO_4$ standard in the extraction results and discussion is referred to as $Li_{2/3}CoPO_4$, however, SAED was not performed in the area where the extractions were performed.

Figure 5.17 shows a $Li_{2/3}CoPO_4$ standard extracted from red regions of a 5.1 V vs. Li/ Li^+ sample (ie. Co(II)-rich regions of the 5.1 V vs. Li/ Li^+ electrode). The extracted $L_{2/3}CoPO_4$ edge is a mix between

the $LiCoPO_4$ (Co(II)-rich) standard, and the $CoPO_4$ (Co(III)-rich) standard. The $Li_{2/3}CoPO_4$ contains maxima on the Co-L_3 edge at 782 eV, and 781 eV. The $CoPO_4$ maxima is at 782 eV, and the $LiCoPO_4$ maxima is at 781 eV. The Co L-edge onset of the $Li_{2/3}CoPO_4$ edge occurs at the same energy loss as the $LiCoPO_4$ (Co(II)-rich) edge (779 eV). The shape of the $Li_{2/3}CoPO_4$ Co L_2 edge is a similar shape to the $LiCoPO_4$ Co(II)-rich L-edge.

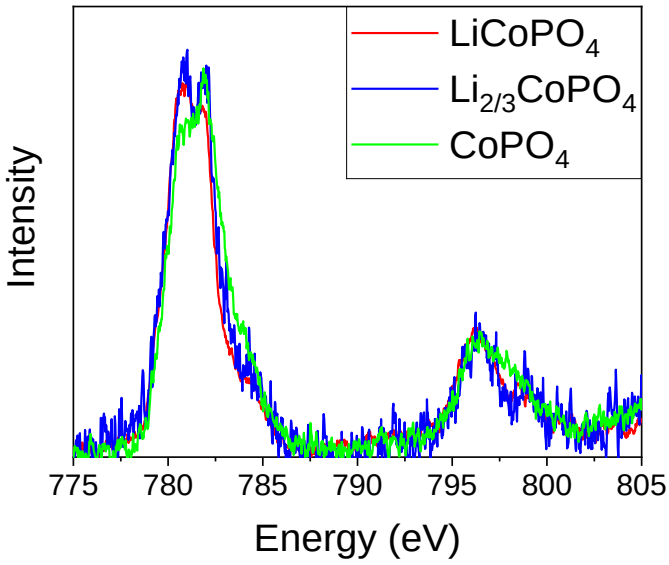

Figure 5.17: EELS standards: blue- $Li_{2/3}CoPO_4$ Co L-edge extracted from the red regions of the 5.1 V vs. Li/ Li^+ microtomed sample in Figure 5.35. Red- Co(II) standard representing $LiCoPO_4$, Green- Co(III) standard representing $CoPO_4$ from Figure 5.9. The structures have been labelled as the assumed structures based on the XRD and SAED patterns presented in 5.4.2.3.

The EELS $Li_{2/3}CoPO_4$ Co L-edge shown in Figure 5.17 is noisier than the $CoPO_4$, and $Li_{2/3}CoPO_4$ Co L-edges because it was extracted from a smaller region of sample due to limited red regions on 5.1 V vs. Li/ Li^+ charged $LiCoPO_4$ samples. Ideally the edge should have been extracted from a purer sample of $Li_{2/3}CoPO_4$. Therefore, a Co L-edge extraction from mixed green and red regions (a mix of Co(II)-rich, and Co(III)-rich sample) on spectrum image maps of the 4.89 V vs. Li/ Li^+ charged $LiCoPO_4$ MLLS fitted with the Co(II), and Co(III)-rich standards in Figure 5.9 for reasons outlined above.

Figure 5.18 shows a comparison between the 5.1 V vs. Li/ Li^+ extracted and the 4.89 V vs. Li/ Li^+ extracted Co L-edge for $Li_{2/3}CoPO_4$. Figure 5.18 shows that the edges are nearly identical regardless of the voltage the electrode was charged to, indicating the Co-L edge likely originated from a similar phase. A notable difference is a slight shift in the first maxima on the Co L_3 edge from 780.6 eV on the 4.89 V sample to 781.0 eV on the 5.1 V sample.

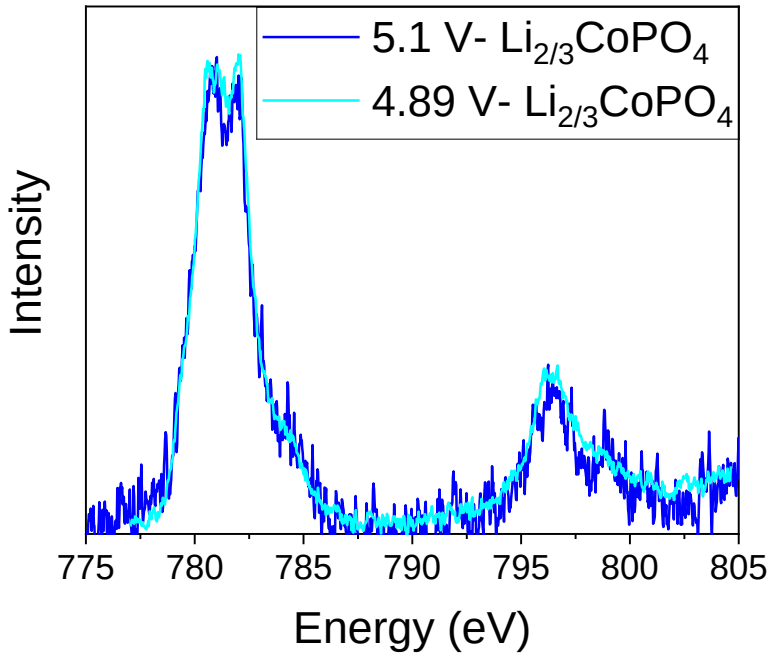

Figure 5.18: $Li_{2/3}CoPO_4$ potential EELS Co L-edge spectra extracted from a 5.1 V vs. Li/ Li^+ sample (dark blue), and a 4.89 V vs. Li/ Li^+ sample (light blue).

Figure 5.19 shows a Mo Kα XRD pattern of electrodes charged to 4.89 V vs. Li/ Li^+. The XRD pattern matches to $LiCoPO_4$, with no $Li_{2/3}CoPO_4$ present. The lattice volume change from $LiCoPO_4$ to $Li_{2/3}CoPO_4$ was a shrinkage of 2.27 % which should result in peak shifts, as indicated by the XRD patterns in Figure 5.14. The dominant change in lattice parameter is in a for $LiCoPO_4$ as it de-lithiates, therefore the (2 0 0), (2 1 0), (3 0 1), and (3 1 1) reflections should shift if the phase has shifted from $LiCoPO_4$ to $Li_{2/3}CoPO_4$. In this case, no shift was detected. This is discussed in full in the lithiation mechanisms of $LiCoPO_4$ chapter.

The lack of SAED collected at the extraction regions makes it difficult to confirm whether the extracted patterns are $Li_{2/3}CoPO_4$, or are regions of uncycled $LiCoPO_4$. However, given that the 5.1 V vs. Li/ Li^+ XRD pattern in Figure 5.14 shows the presence of $Li_{2/3}CoPO_4$ and $LiCoPO_4$ only, it is unlikely this is the case for the 5.1 V vs. Li/ Li^+ sample.

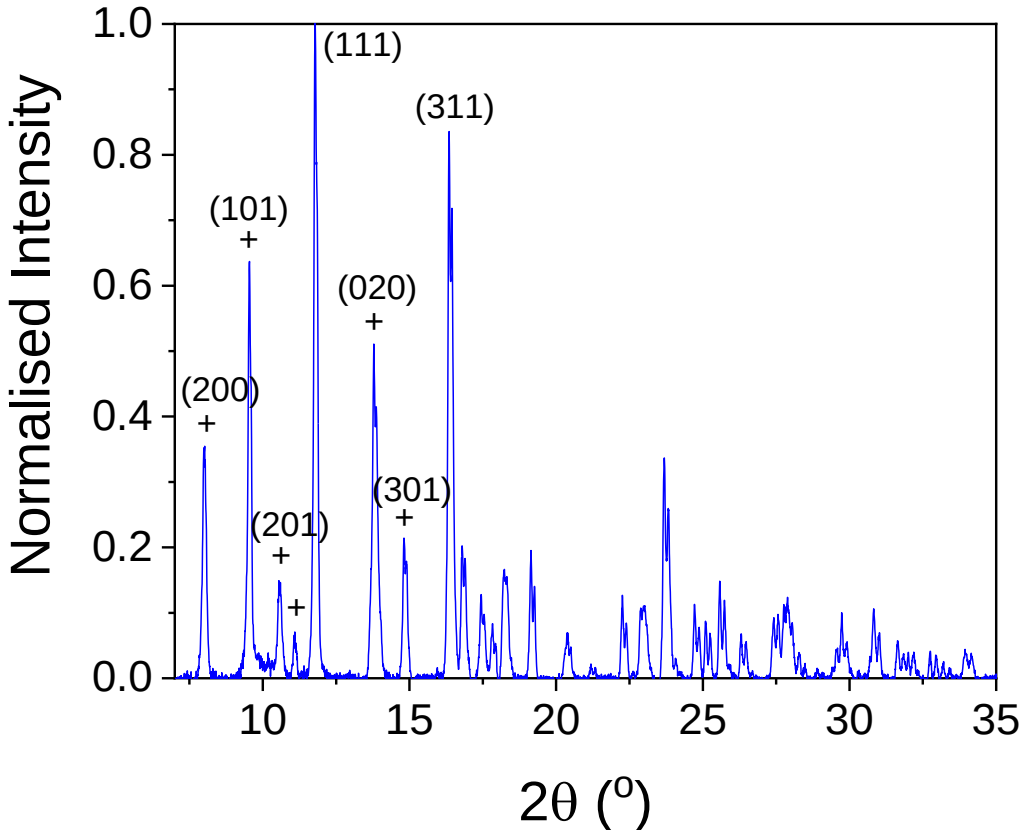

Figure 5.19: Mo K-α XRD pattern of 4.89 V vs. Li/ Li^+ electrodes. The pattern shows 100 % $LiCoPO_4$.

The purpose of collecting the $Li_{2/3}CoPO_4$ standard is to use it to map the presence of $Li_{2/3}CoPO_4$ using MLLS fitting of collected spectra to understand the lithiation mechanisms in $LiCoPO_4$. Figure 5.20 shows a comparison between MLLS fitting of EELS mapping performed using the Co(II)-rich, and Co(III)-rich standards in Figure 5.9, and the $Li_{2/3}CoPO_4$ standards Figure 5.17.

The maps in Figure 5.20 show that $Li_{2/3}CoPO_4$ (blue) is spatially distinguishable from $CoPO_4$ (green), however, it is not possible to spatially distinguish $LiCoPO_4$ from $Li_{2/3}CoPO_4$ in Figure 5.20 (a), and (d), as blue $Li_{2/3}CoPO_4$ regions are mixed with red $LiCoPO_4$ regions in a similar way to the Co(II), and Co(III)-rich regions in Figure 5.20 (b), and (e). This is likely due to the similarity between the $Li_{2/3}CoPO_4$ and $LiCoPO_4$ L_2 edges causing the MLLS fitting to over-fit to $Li_{2/3}CoPO_4$.

The lattice parameter shift from $LiCoPO_4$ to $Li_{2/3}CoPO_4$ (-2.27 %) was smaller than the shift from $Li_{2/3}CoPO_4$ to $CoPO_4$ (-5.14 %) (Table 5.2), suggesting a larger bond length shift from $Li_{2/3}CoPO_4$ to $CoPO_4$ as well as reduced Li content. The small change in lattice parameter may explain the similarity between the $LiCoPO_4$ (Figure 5.17), and $Li_{2/3}CoPO_4$ EELS edges, and subsequent overfitting of $Li_{2/3}CoPO_4$ when performing mapping (Figure 5.20).

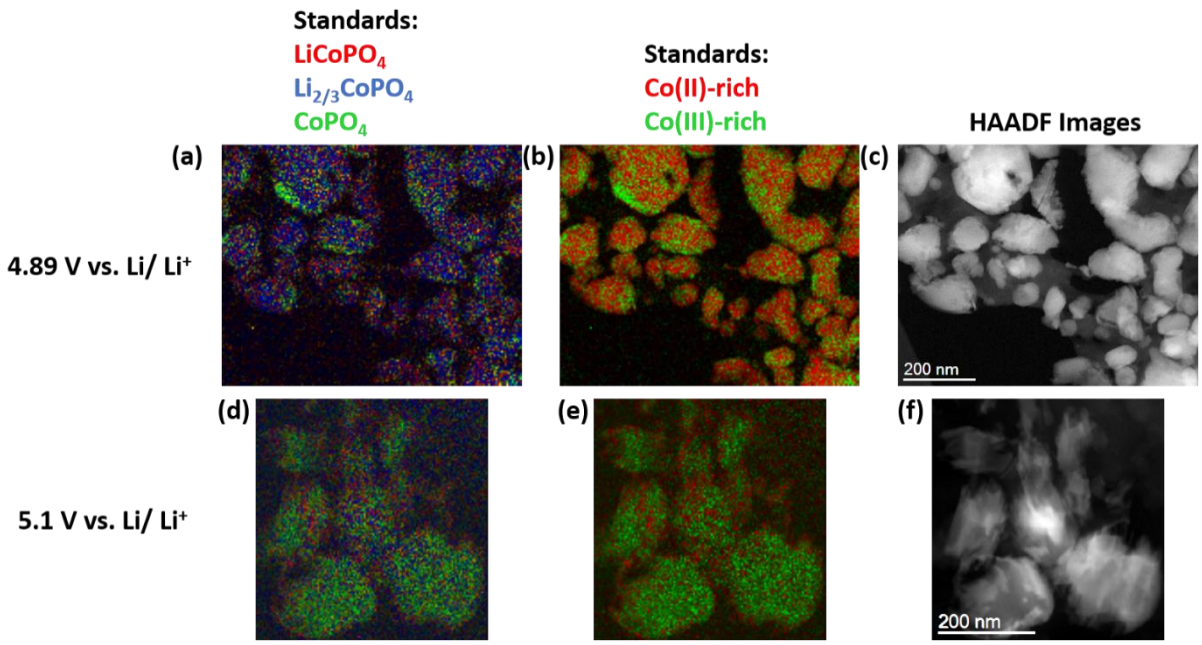

Figure 5.20: Comparison between MLLS fitting Co L-edge maps using $LiCoPO_4$, $Li_{2/3}CoPO_4$, and $CoPO_4$ standards shown in Figure 5.17 and Figure 5.18, Co(II)-rich and Co(III)-rich standards shown in Figure 5.9, and the corresponding HAADF images for an electrode charged to 4.89 V vs. Li/ Li^+ (a, b, and c respectively), and an electrode charged to 5.1 V vs. Li/ Li^+ (d, e, and f).

As fitting could not be meaningfully performed with a $Li_{2/3}CoPO_4$ standard, the rest of the MLLS fitting is performed using the Co(II)-rich and Co(III)-rich standards only. Co(II)-rich represent more lithiated regions, and Co(III)-rich regions represent less lithiated regions. It is likely that the $Li_{2/3}CoPO_4$ phase would be MLLS fit to red Co(II) due to the similarity between the EELS $LiCoPO_4$ Co L-edge, and the Co L-edge $Li_{2/3}CoPO_4$ edge shown in Figure 5.17.

5.4.2.5 The EELS O-K Edge

The O-K edge was mapped to check for Co-O bond hybridisation [1]. O-K edge standards were collected from Co(III)-rich and Co(II)-rich areas in order to perform O-K edge mapping in a similar way to the Co-L edge mapping.

The effects of sample thickness on the EELS O-K edge were analysed as the O-K edge is more prone to changes due to sample thickness due to occurring at a lower energy loss (532 eV) than Co (779 eV). Figure 5.21 shows the variation in the O-K edge signal with t/λ on an uncycled sample where t is sample thickness, and λ is the local electron inelastic mean free path. t/λ is a relative measure of specimen thickness and is calculated using:

$$\frac{t}{\lambda} = -\ln\left(\frac{I_o}{I_t}\right)$$

I_o is the total transmitted zero-loss (elastically scattered) electrons, and I_t is the total transmitted intensity (inelastically scattered electron intensity). t/λ is the mean number of scattering events per incident electron, therefore the thicker the sample, the higher t/λ. Figure 5.21 (a) shows three different regions of a microtomed uncycled electrode sample, and their associated t/λ, from which the O-K edge spectra were extracted.

A method of removing the effects of plural scattering (scattering events enhanced due to sample thickness as incident electrons are inelastically scattered more than once) is fourier-ratio

deconvolution [18]. Fourier-ratio deconvolution of high loss spectra requires a low loss zero loss peak acquired via DualEELS, and can be run as a sub-routine in digital micrograph software.

In order to understand the effects of plural scattering on the O-K edge, the extracted O-K edges were taken from signal extracted spectrum images (where the background had been removed using the power law background function), and from spectrum images which had been deconvolved. Figure 5.21 (b) shows the extracted signal O-K edges. This is the non-deconvolved O-K edge signal. There is little variation in the peak position and shape of the O-K edge peak at 538 eV. However, a shoulder on the O-K edge occurs at 542 eV on the t/λ= 0.86, and t/λ = 0.50 samples. The shoulder is more prominent on the t/λ= 0.86 sample, than the t/λ= 0.50 sample.

For the deconvolved standards in Figure 5.21 (c) the first peak at 538 eV appears identical to the signal only standards in Figure 5.21 (b). Therefore, deconvolution cannot be used to remove the extra shoulder feature on the thicker samples.

The second peak in Figure 5.21 (b) t/λ at 565 eV increases with intensity with increasing t/λ. However, on the deconvolved spectrum in Figure 5.21 (c) the spectra are identical regardless of the t/λ value. As the spectra appear identical after deconvolution (apart from the shoulder at 541 eV), all O K-edge processing is performed on deconvolved spectrum images.

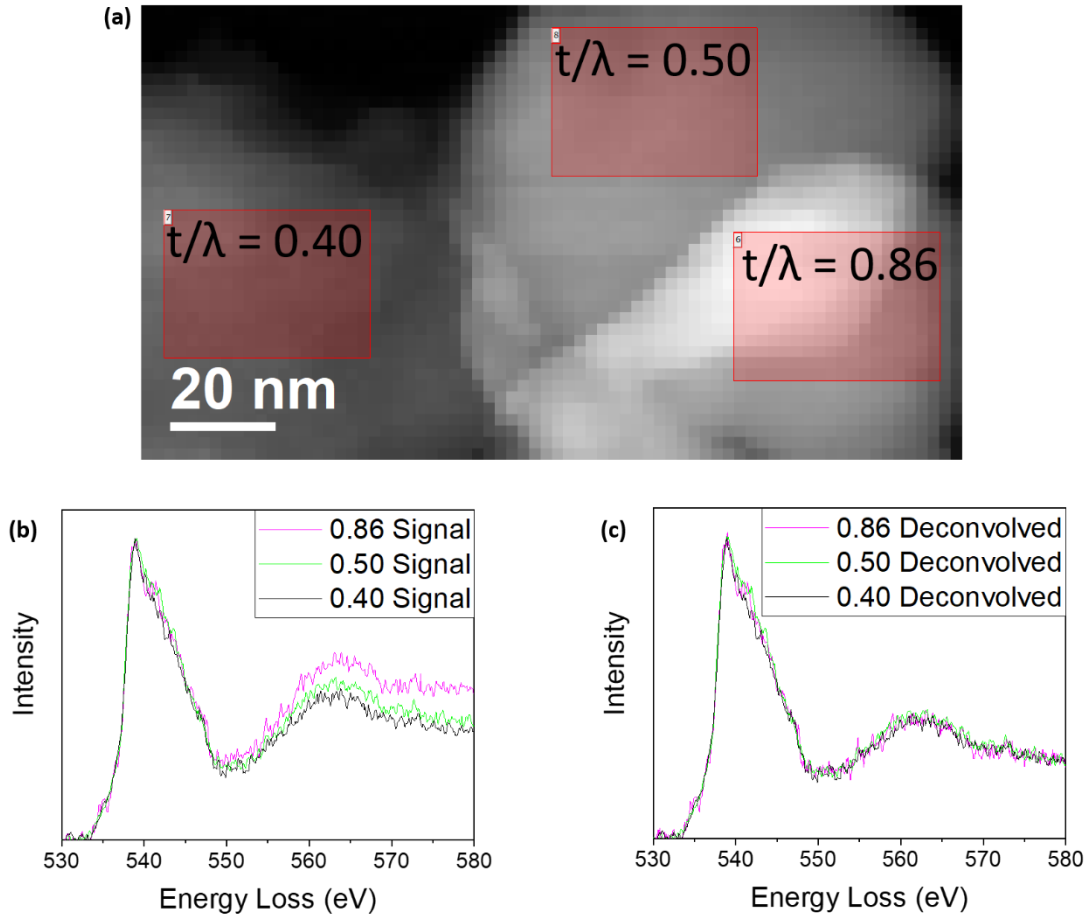

Figure 5.21: (a) HAADF image showing the O-K edge extraction regions of the uncycled sample at t/λ = 0.40, 0.50, and 0.86. (b) EELS O-K edge signals extracted from the t/λ = 0.40, 0.50, and 0.86 regions in (a). (c) Deconvolved O-K edge signals extracted from the t/λ = 0.40, 0.50, and 0.86 regions in (a). The t/λ = 0.86 region represents two overlapping particles.

The sample in Figure 5.21, and Figure 5.22 was prepared using the microtoming method described in 5.3.2. Microtoming requires the sample to be mounted in resin, and sectioned. EELS spectra were taken of the resin and of a $LiCoPO_4$ particle in the resin to determine if the resin has any effect on the shape of the O K-edge. Figure 5.22 (b) shows deconvolved O K-edge spectra of the resin region, and a $LiCoPO_4$ and resin region shown in Figure 5.22 (a). The resin spectrum in Figure 5.22 (b) is mostly noise, whilst the $LiCoPO_4$ and resin spectra clearly shows the O K-edge similar to Figure 5.21 (c). Therefore, the resin is unlikely to affect the shape of the O K-edge.

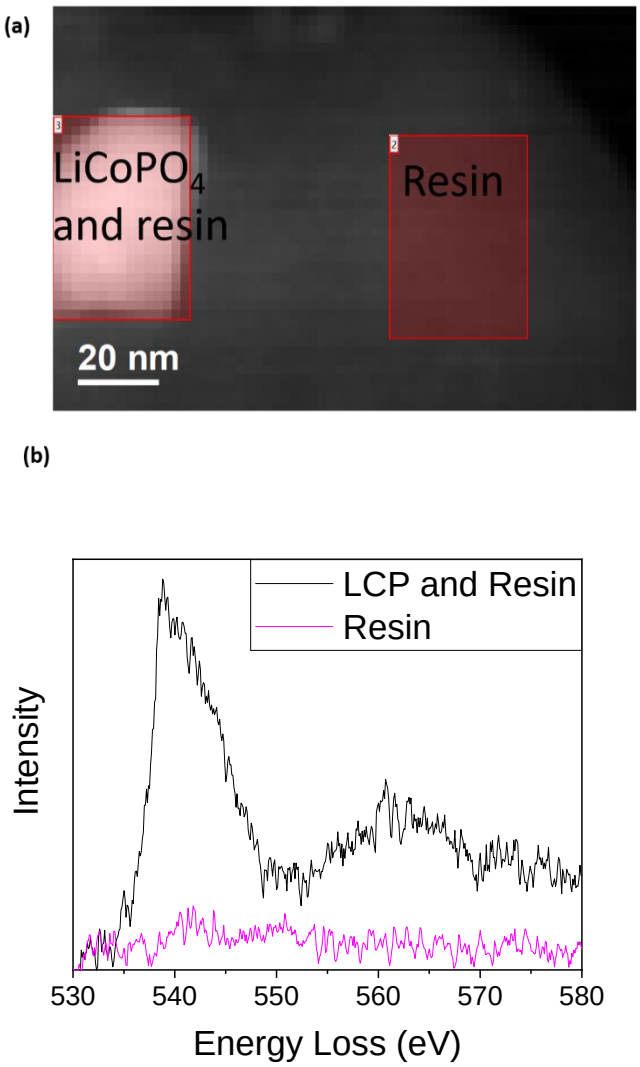

Figure 5.22: (a) HAADF image showing the resin and $LiCoPO_4$ + resin only regions chosen for O-K edge extraction. (b) EELS O-K edge extractions from the resin region (pink), and $LiCoPO_4$ + resin extraction regions (black)

O K-edge standards were acquired for Co(II)-rich regions from an uncycled sample (Figure 5.23), and for Co(III)-rich regions from a 5.1 V vs. Li/ Li^+ sample (Figure 5.25). In order to map the O K-edge, Co L-edge mapping was performed on the area using the standards in Figure 5.9 (Figure 5.23). The Co(II)-rich O K-edge was extracted from a Co(II)-rich (red) region on the uncycled sample, indicated by the red box in Figure 5.23 (b).

Regions of mixed green (Co(III)-rich) and red (Co(II)-rich) are visible on the uncycled map in Figure 5.23 (b), however comparison with the corresponding HAADF image in Figure 5.23 (a) shows that

the mixed regions correspond to thicker sample areas. The effect of thickness on Co-oxidation state mapping is discussed further in 5.4.4.

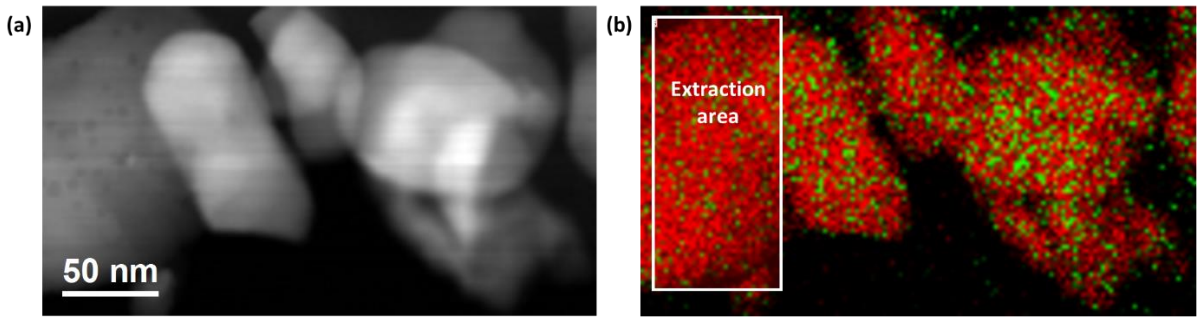

Figure 5.23: (a) HAADF image of an uncycled $LiCoPO_4$ sample, and (b) corresponding EELS Co-L edge map of the area used to extract the Co(II) O-K edge standard. Red- Co(II)-rich, Green- Co(III)-rich.

The EELS Co L-edge was also extracted from the same sample region where the O K-edge was extracted in Figure 5.23 (b) to ensure the edge has not changed compared to previous samples. Figure 5.24 shows a comparison between the Co(II) L-edge shown in Figure 5.9 (Co(II) Old), and the Co(II) L-edge extracted from Figure 5.23 (Co(II) aged). The Co(II) Co L-edge in Figure 5.24 was collected 2 years prior to the Co(II) new edge, but from the same $LiCoPO_4$ material. Fresh electrodes were made for the collection of both edges, and the $LiCoPO_4$ was stored throughout in an argon filled glove box to protect the material.

The Co(II)-rich Co L-edges in Figure 5.24 are almost identical. However, the edge onset for the Co(II) aged sample occurs at 778.8 eV, whilst the edge onset of the Co(II) sample occurs at 779 eV. It is not clear if this is a material difference, a zero-loss alignment issue, or a statistical spread issue. At the point of measurement, only one Co L-edge map was collected of the uncycled sample as it was assumed the uncycled Co L-edge would not shift, so the statistical spread could not be examined.

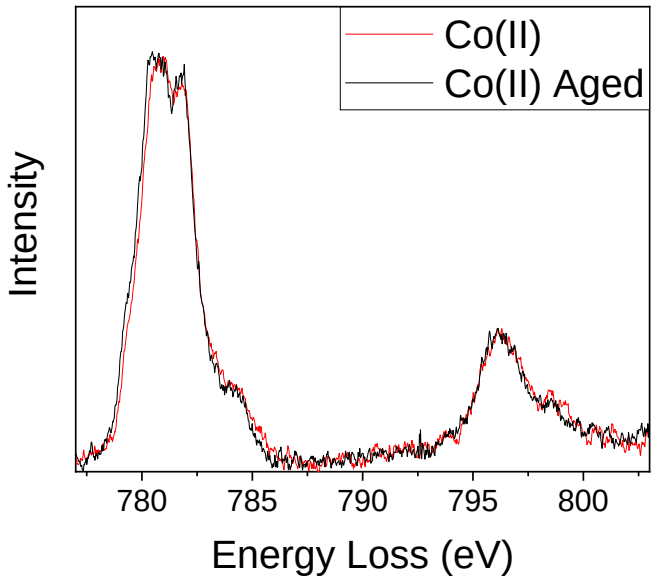

Figure 5.24: Comparison of Co(II) standard extracted from the fresher $LiCoPO_4$ samples in Figure 5.9 (ed), and Co(II) standard extracted from the older sample in Figure 5.23 used for O-K edge extraction (black).

The Co(III)-rich O K-edge spectrum was extracted from a green, Co(III)-rich, region on a Co oxidation state map of a 5.1 V vs. Li/ Li^+ charged electrode made using the aged $LiCoPO_4$ powder (Figure 5.25 (b)). The Co oxidation state map in Figure 5.25 (b) was fitted using the standards in Figure 5.9. The map shows the chosen particle is mostly Co(III)-rich (green), with Co(II)-rich regions on the edge, similar to the specimen maps in Figure 5.20.

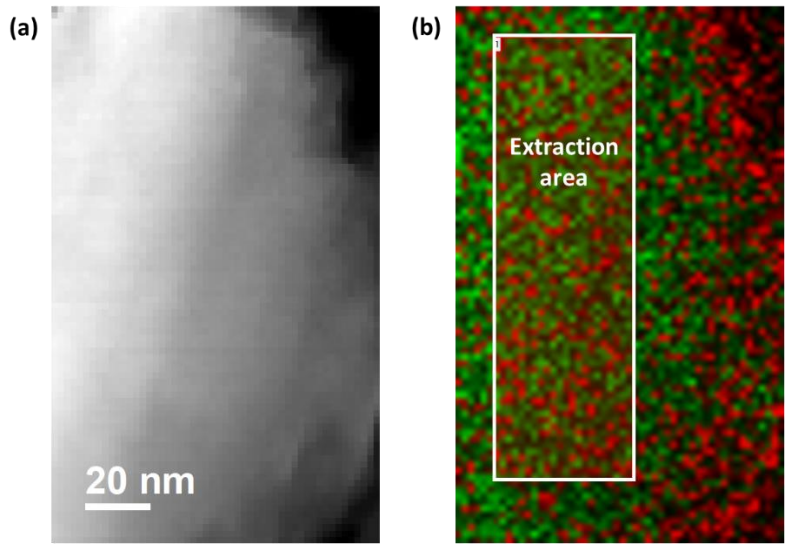

Figure 5.25: (a) HAADF image of a 5.1 V vs. Li/ Li^+ electrode, and (b) corresponding Co-L edge map of the area used to extract the Co(III) O-K edge standard. Red- Co(II)-rich, Green- Co(III)-rich.

Comparison of the Co(III) edges extracted from $LiCoPO_4$ electrodes charged to 5.1 V vs. Li/ Li^+ made using fresh $LiCoPO_4$ powder, and aged powder (Figure 5.26) shows that the Co(III) rich standard has changed. Similar to Figure 5.24, Co(III) aged is the sample the O K-edge is extracted from, and Co(III)-rich is the Co(III)-rich standard in Figure 5.9. The Co(III) aged was made 2 years after Co(III) old from $LiCoPO_4$ stored in an argon glove box.

The Co L_2 edges for the Co(III) aged and Co(III)-rich samples are the same in Figure 5.26. However, the Co L_3 edges have different shapes. The Co L_3 edge onset occurs at 778.9 eV for both samples, and the maximum occurs at 781.8 eV for both samples. However, the edge tapers to the maximum more gradually for the Co(III) aged sample, than the Co(III) old sample. It is unclear why a change in the Co L-edge was seen.

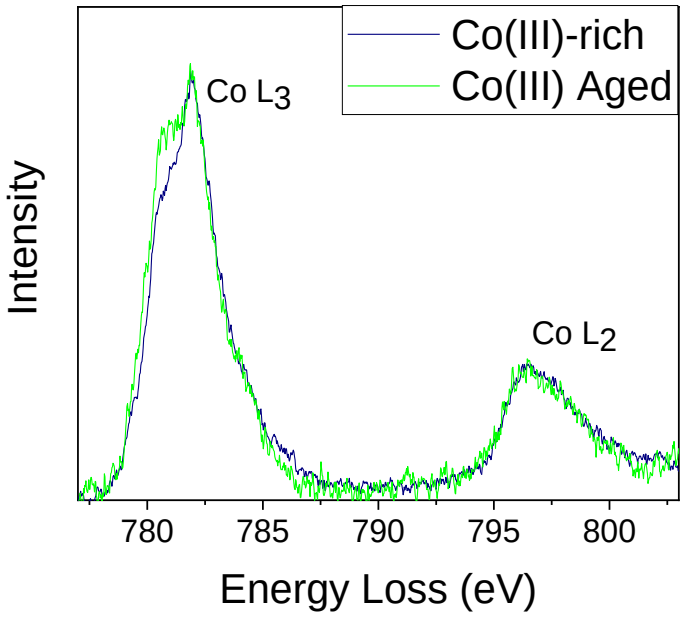

Figure 5.26: Comparison of the original Co(III)-rich standard (green), and the new Co(III)-rich standard extracted from the O-K edge standard sample made with aged $LiCoPO_4$ powder (navy). Both edges were extracted from electrodes charged to 5.1 V vs. Li/ Li^+.

To attempt to explain the difference in the Co L-edge signal between the aged Co(III) standard, and the old Co(III) standard in Figure 5.26, the 1st cycle differential capacity curves of the two electrodes were compared (Figure 5.27). Figure 5.27 shows that the aged Co(III) differential capacity curve contained 3 peaks, present in the original Co(III) differential capacity curve, however, the second peak was broader, and the second peak occurred at a higher potential (4.95 V vs. Li/ Li^+ compared to 4. 91 V vs. Li/ Li^+). The overall specific capacity was also less for the aged sample, compared with the fresher sample (Figure 5.27).

The first peak at 4.6 V vs. Li/ Li^+ has previously been reported in literature [11], and attributed to reactions with the electrolyte. The shift in the third redox peak from 4.91 V vs. Li/ Li^+ to 4.95 V vs. Li/ Li^+ may explain the shift in the Co(III) L-edge, and implies further de-lithiation occurred in parts of the material compared to the fresher sample. It is unclear why the shift in redox peak occurred in the aged sample.

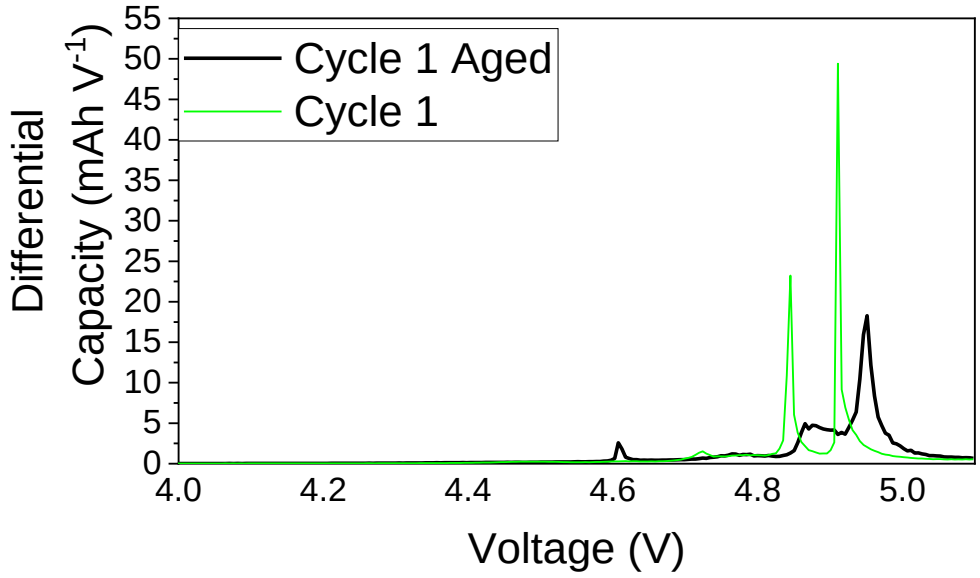

Figure 5.27: Comparison between the differential capacity curves for the electrodes which the aged Co(III) standard (cycle 1 aged- black), and the original Co(III) standard Co L-edges in Figure 5.26 were collected (cycle 1- green).

Figure 5.28 shows the O K-edge spectra extracted from the uncycled (Figure 5.23) and 5.1 V vs. Li/ Li^+ charged electrode (Figure 5.25). The large O K-edge peak has an edge onset at 535.6 eV, and a maximum at 539.0 eV for both the Co(II)-rich, and Co(III)-rich.

However, there are a few distinctive features of the Co(III)-rich O K-edge compared with the Co(II)-rich O K-edge. A pre-edge peak occurs at 532.3 eV on the Co(III)-rich O K-edge which is not present on the Co(II)-rich O K-edge. The pre-edge feature is not purely Gaussian as it has a shoulder at 530.4 eV. The peak 539.0 eV maximum is broader for the Co(III) O K-edge compared to the Co(II) O K-edge. It is unclear why the pre-edge is not purely Gaussian.

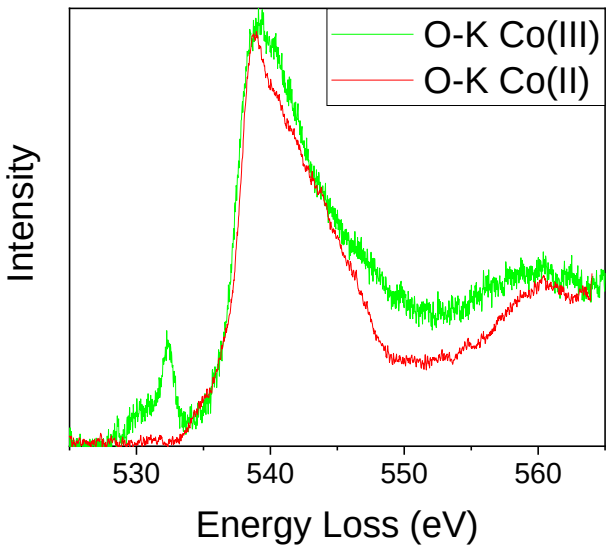

Figure 5.28: Green- EELS O-K edge standard extracted from a Co(III)-rich area, and red- O-K edge standard extracted from a Co(II)-rich area.

Overall, the O K-edge extraction shows there is a difference in the O K-edge on charging. However, as this is an aged LiCoPO4 specimen where the Co L_2-edge are had a modified shape, it is not clear if the difference would have arisen on samples analysed prior to the O K-edge study. The O K-edge was not collected in the original study.

5.4.3 Investigating the Effects of Air Exposure

It is known that $CoPO_4$ amorphises on contact with air due to the instability of the octahedally co-ordinated Co^{3+} in the structure [11]. However, there is no literature on the expected oxidation state of Co post-amorphisation of $CoPO_4$. To test the impact of air exposure on the samples, samples charged to 5.1 V vs. Li/Li^+ were exposed to air for 3 days (representing transfer from Sheffield to Harwell without air protection), and 3 mins (a sample opened from air-proof packaging and transferred directly into the microscope).

The experiments in this section, and the following sample preparation section were performed on electrodes made from the non-aged $LiCoPO_4$ powder.

The EELS Co L_2 and L_3 edges of an uncharged Co(II)-rich sample, a sample charged to 5.1 V vs. Li/Li^+ and exposed to air for 3 mins, and a sample charged to 5.1 V vs. Li/Li^+ and exposed to air for 3 days are shown in Figure 5.29. The samples charged to 5.1 V vs. Li/Li^+ have a similar shaped Co L_2 and L_3 edges. The peak on the Co L_3 edge appears on the higher energy loss edge on both the 5.1 V vs. Li/Li^+ samples, whilst the peak appears on the lower edge on the Co(II)-rich sample. As previously observed, there are 2 peaks on the Co(II)-rich Co L_2 edge collected from the uncycled sample, whereas there is only 1 peak on the 5.1 V vs. Li/Li^+ samples.

Despite the similarity in edge shape between the Co(III)-rich 5.1 V vs. Li/Li^+ charged samples, the Co-L edge of the 3 mins air exposed sample occurs at a higher energy loss (779.1 eV), compared to the 3 mins air exposed sample (778.8 eV). The L_3 edge peak is also shifted to higher energy losses on the 3-day air exposed sample compared to the 3 min air exposed sample (782.3 eV and 781.9 eV respectively). The shifts to higher energy loss indicate oxidation of the sample due to exposure to air.

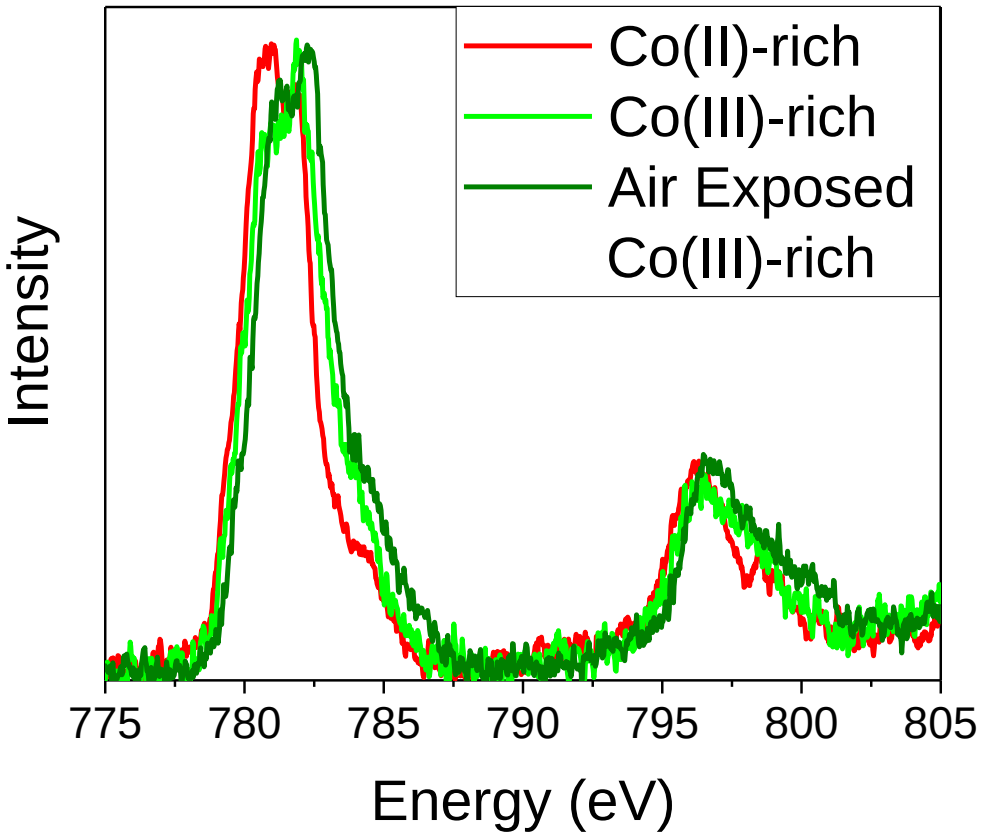

Figure 5.29: EELS Co-L edge spectra of red: Co(II)-rich region from an uncharged sample, light green: Co(III)-rich region from a dry mounted sample (preparation described in 5.3.2), charged to 5.1 v vs. Li/ Li^+, exposed to air when loaded into the microscope (~3 mins), dark green Co(III)-rich region from a 5.1 V vs. Li/ Li^+ sample exposed to air for 3 days after it was de-crimped and taken to atmosphere for sample preparation.

0.4 eV is a small energy loss shift. However, in terms of how well the MLLS fit fitted the original signal, using the 3 days air exposed Co(III)-rich signal in place of the 3 mins significantly improved the MLLS fitting. The MLLS fitting spectra using the 3 mins air exposed spectrum caused the fit to shift to 0.3 eV lower energy losses (see Figure 5.30), thus the contribution from Co(II) is over-fit using the original 3 mins air exposed reference.

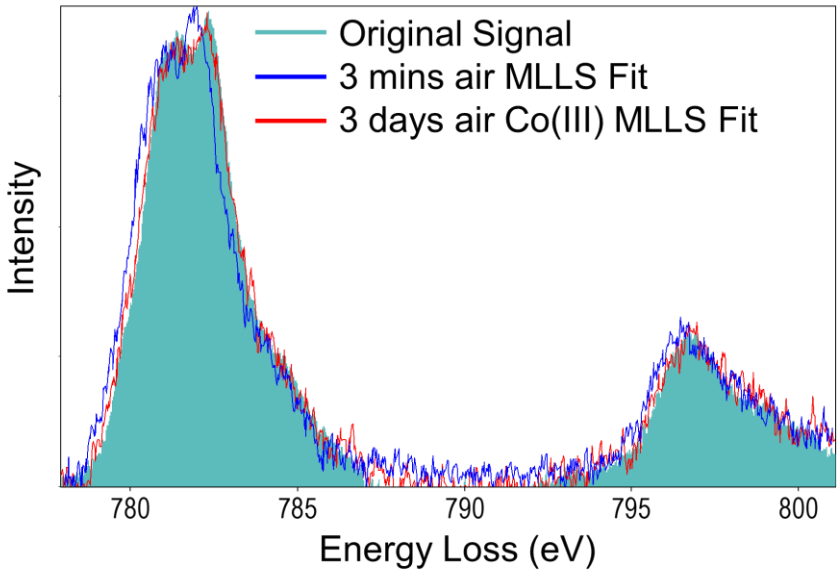

Figure 5.30: Comparison between MLLS fitting using the oxidised Co(III)-rich standard (red), and the 3 mins air exposed Co(III)-rich standard (blue). The MLLS fitting sum spectra are overlaid on the original extracted signal from the region mapped.

To examine the changes to Co(III)-rich oxidation state distribution within the sample due to exposure to air, oxidation state maps of the 3 day air exposed sample, and 3 min air exposed sample charged to 5.1 V vs. Li/ Li^+ were produced (Figure 5.31). For the examined regions, the 3 days air exposed sample showed more green Co(III) rich regions than the 3 min air exposed sample charged (Figure 5.31 (a) and (b) respectively).

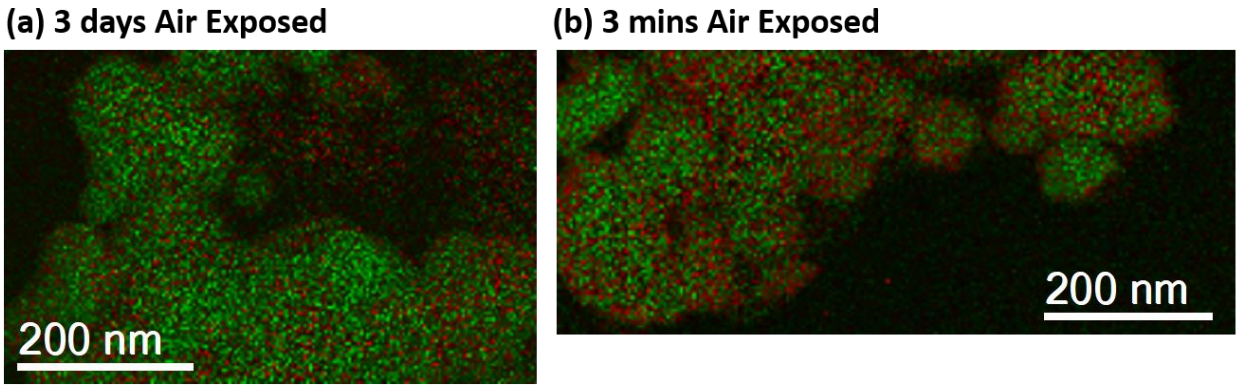

Figure 5.31: Oxidation state maps of (a) a sample charged to 5.1 V vs. Li/ Li^+ and exposed to air for 3 days after de-crimping, and (b) a sample charged to 5.1 V vs. Li/ Li^+ prepared by dry mounting and exposed to air for 3 mins whilst loading into the microscope.

Overall a shift in the electron energy loss of the Co(III)-rich regions were observed when the samples were exposed to air for longer periods of time. The results imply that the samples must be kept as air proof as possible in order to make accurate observations of Co oxidation state changes across the electrode.

5.4.4 Optimising Sample Preparation

Initially the $LiCoPO_4$ samples were prepared using the glove box dry mounting method described in 5.3.2. The advantage of this was that it limited the air exposure experienced by the particles

before transfer into the microscope and the consequences of air exposure described in 5.4.2.5. However, there were problems with the dry mounting sample preparation method.

Figure 5.32 (a) shows a STEM HAADF image of dry mounted particles charged to 4.98 V vs. Li/ Li^+. The bright particles visible in the image are C-$LiCoPO_4$ particles. Variation in the image brightness of the particles indicates thicker regions of the particles along the incident electron beam direction, due to imaging through the centre of particles, or from multiple particles overlapping (the regions ringed in gold in Figure 5.32).

Figure 5.32 (b) shows an oxidation state map of the area represented by the HAADF image in Figure 5.32 (a). Single particles on the edge of the agglomerate appear green (Co(III)-rich), with local Co(II)-rich regions on the edge. Mixed oxidation states are present in the regions circled in gold, where the corresponding HAADF image in Figure 5.32 (a) shows overlapping of C-$LiCoPO_4$ particles, and increased thickness making it is difficult to distinguish one particle from another on the oxidation state map in Figure 5.32 (b).

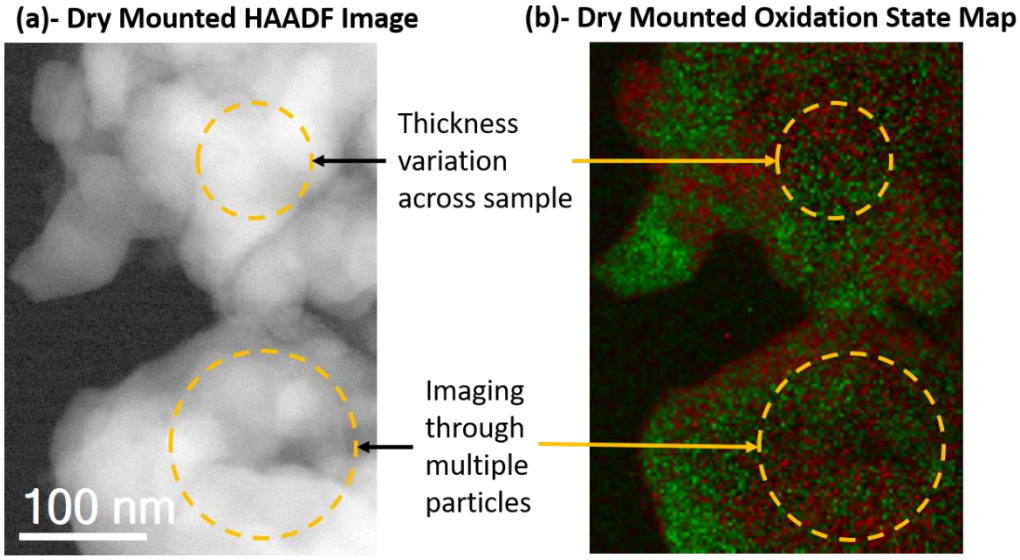

Figure 5.32: (a) HAADF image of dry mounted $LiCoPO_4$ charged to 4.98 V vs. Li/ Li^+, and (b) the oxidation state map corresponding to the HAADF image in (a).

In order to counter the particle thickness, and particle overlap effects apparent in the EELS maps, sample microtoming was attempted in order to keep the sample thickness approximately constant and prevent overlapping of particles (see 5.3.2). A HAADF image of microtomed electrode particles charged to 5.1 V vs. Li/ Li^+ and the corresponding oxidation state map are shown in Figure 5.33 (b).

A representative microtomed section of an electrode charged to 5.1 V vs. Li/ Li^+ is shown in Figure 5.33. Compared to the HAADF image in Figure 5.32 (a), the contrast across the particles in Figure 5.33 (a) is more uniform, indicating greater thickness uniformity. In Figure 5.33 (a), the particles on the right side of the image in Figure 5.33 (b) are brighter than those on the left, indicating they are thicker. This may have resulted from slicing through an agglomerate.

Blurring across the particles is also evident in the image of the microtomed particles (Figure 5.33 (a)), along with fragments of particles on the outside of the main particles due to brittle fracture. This indicates damage to the edges of the C-$LiCoPO_4$ particles caused by microtoming.

The oxidation state mapping of the microtomed particles (Figure 5.33 (b)) shows that the microtoming allows individual particles to be distinguished. Moreover, clearly defined regions of green Co(III)-rich and Co(II)-rich areas are also present, making it easier to identify lithiation mechanisms compared to the dry mounted particle method in Figure 5.32 (b).

Where the particles are thicker in the HAADF image (Figure 5.33 (a)), mixed oxidation states are also observed in the oxidation state map as a mixed green and red region (Figure 5.33 (b)). On the smaller particles, however, mixed oxidation states may have occurred as the sectioning is cutting off the edge of a C-$LiCoPO_4$ particle. This is discussed further in 5.5.4. In order to appropriately analyse microtomed sample oxidation state maps, the particle diameters should be between 100-200 nm (the diameter of the non-microtomed particles), in order to avoid the particle shaving error.

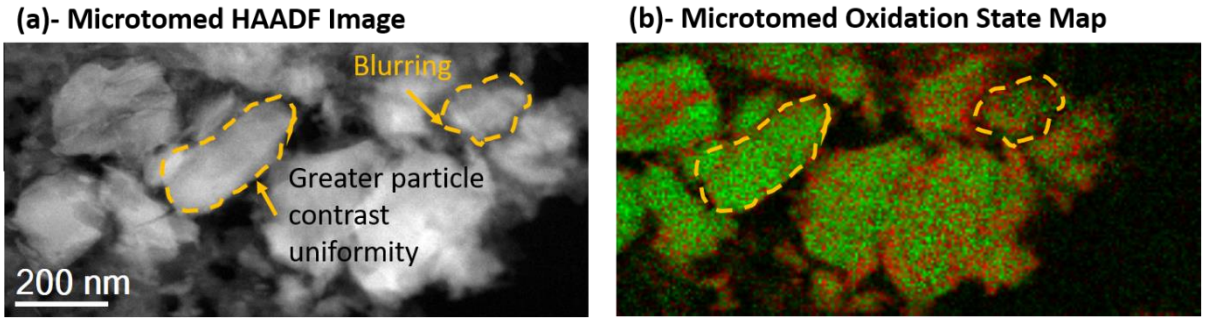

Figure 5.33: (a) HAADF image of microtomed $LiCoPO_4$ electrode particles, and (b) Corresponding oxidation state map of the t area in (a) (red- Co(II)-rich, green- Co(III)- rich).

As shown in 5.4.3, exposure to air can cause the EELS Co L-edge to shift. When microtoming the samples were exposed to air for 30 s when placing into resin for curing, and for an hour during sectioning before being stored in an Ar filled glove box, and for 3 mins prior to loading into the microscope vacuum. To ensure the exposure to air during the microtoming sample preparation did not affect the samples, the Co L_2 and L_3 edges of Co(III)-rich areas of 5.1 V vs. Li/ Li^+ samples which had been microtomed, dry mounted and exposed to air for 3 mins, and dry mounted and exposed to air for 3 days were compared (Figure 5.34).

Figure 5.34 shows the shape of the EELS Co L-edge on charged samples exposed to air for 3 mins, for an hour when microtomed, and for 3 days had similar Co L-edge shapes. However, the Co L_2-edge onsets differ. The Co L_3 edge onset increases to slightly higher energy losses with increased air exposure (779.0 eV for the 3 mins air exposed sample, 778.8 eV for the 1-hour air exposed, microtomed sample, and 779.1 eV for the 3 days' air exposed sample). The peak of the Co L_3 edge does not shift from 781.9 eV after exposure air exposure for an hour during microtoming, but shifts to 782.3 eV after air exposure for 3 days.

The results indicate the air exposure during the microtoming process caused a shift in the Co L-edge, but the shift was not as significant as 3-days air exposure. In terms of using MLLS fitting, the small shifts were found to be significant for incorrect fitting of the spectra if a 3 mins air exposed standard was used as the Co(III)-standard for microtomed samples exposed to air for 1 hour. Minimal differences were noted in the mapping results between the 3 mins air exposed samples,

and 1-hour air exposed samples. Therefore, Co(III)-rich standards collected from micro-tomed samples should be used with micro-tomed samples.

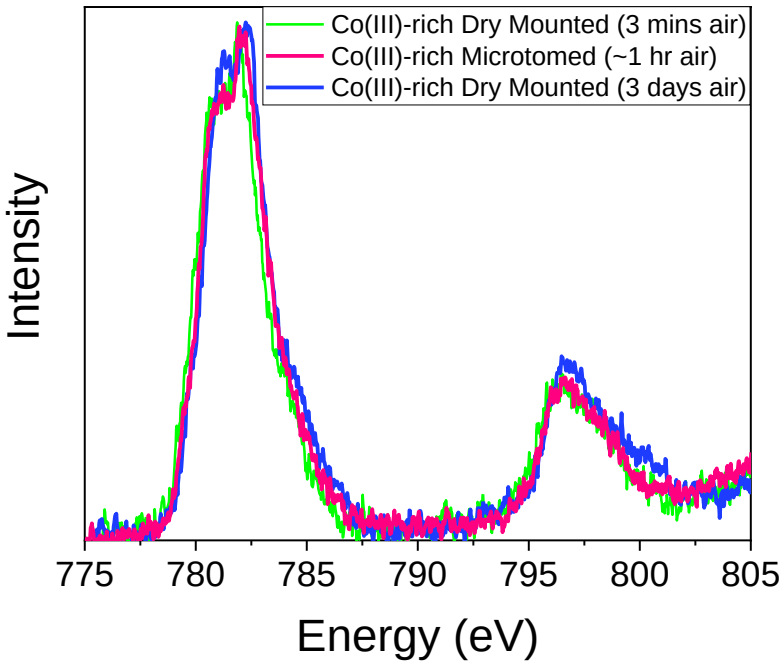

Figure 5.34: EELS Co L-edge of 5.1 V vs. Li/ Li^+ charged electrodes prepared via: Co(III)-rich Old- particles scraped onto TEM grids with 2 mins air exposure, Co(III)-rich New- microtomed electrodes, Air exposed Co(III)-rich-

An advantage of microtoming samples is that the lithiation of particles closer and further away from the aluminium foil current collector could be compared (Figure 5.35). Care must be taken when measuring distances in micro-tomed samples as sample buckling and compression can occur. The HAADF images do not show any evidence of sample buckling, and compression deformation, however there are pores present which could have been compressed. It is possible to say certain regions are relatively closer to the Al current collector than others, but difficult to quantify distances. The distances are described qualitatively as the distance from the image region to the Al foil was not measured when taking the image, and finding the Al foil relies on the Al foil not delaminating from the electrode during microtoming (which occurs frequently).

The HAADF and oxidation state map images of in Figure 5.35 (e), (f), (g), and (h) correspond to regions highlighted on the lower magnification HAADF image in Figure 5.35 (b). Figure 5.35 (c), and (d) were taken further from the Al foil. The oxidation state mapping images in Figure 5.35, and the quantification shown in Figure 5.35 (a) indicate that the particles become more Co(III)-rich as the position is further from the Al foil (ie. closer to the separator facing edge of the electrode and electrolyte source). However, the Co(II)-rich particles in Figure 5.35 (f), and (h) are ~50 nm wide. The Co(II)-rich areas may have occurred due to the particle grazing effect.

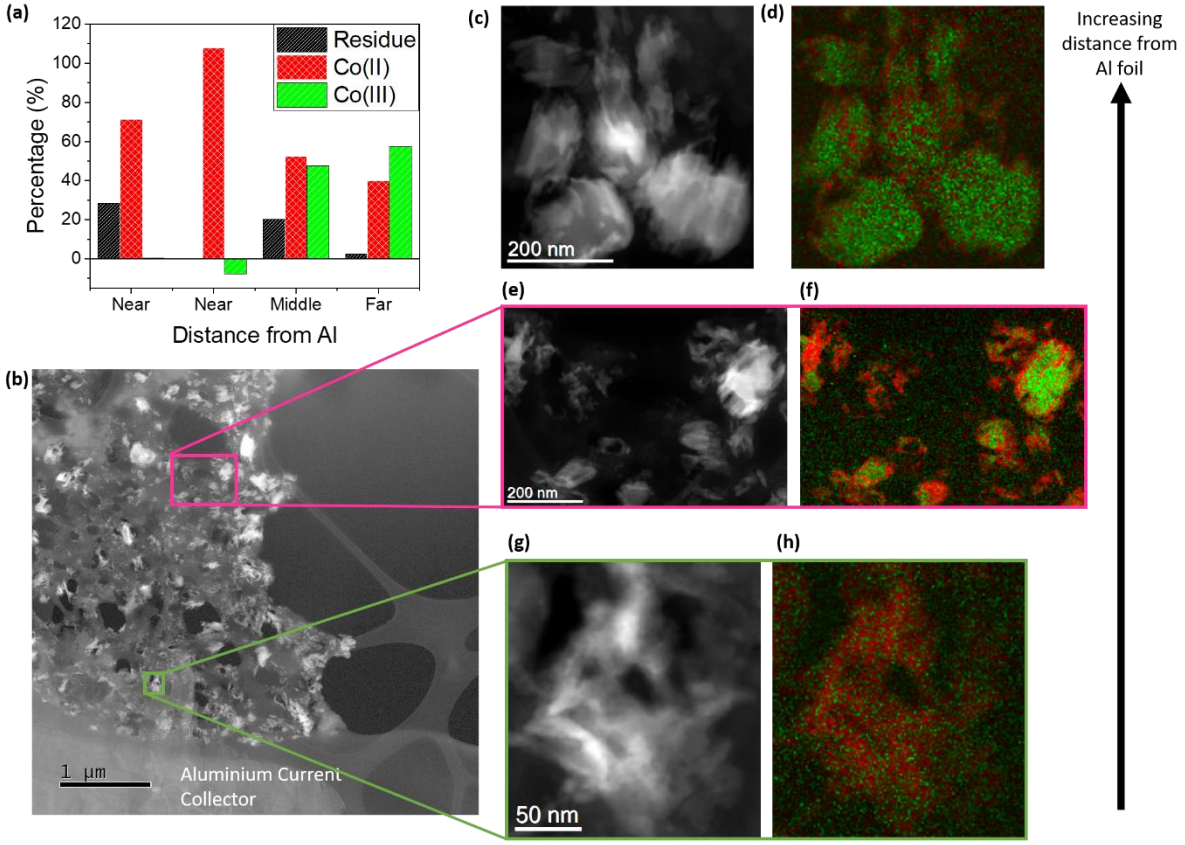

Figure 5.35: (a) Quantification of Co(II), and Co(III) proportions taken from regions on a micro-tomed electrode charged to 5.1 V vs. Li/ Li⁺. The distance of the analysed regions from the Al current collector are described qualitatively as they weren't measured when imaging. (b)- HAADF image overview of the microtomed electrode showing the electrode and aluminium foil current collector. (c), (e), and (g) HAADF images taken at increasing distances away from the HAADF current collector, and (d), (f), and (h) the corresponding oxidation state maps. Green- Co(III)-rich, Red- Co(II)-rich.

Overall, specimen preparation using microtoming has the potential to identify the relationship between 3D particle position and lithiation behaviour, although further work is required to determine this. As there was limited effect from air exposure, and an improvement in particle definition using oxidation state mapping on microtomed particles, the electrode sample preparation method was changed to microtoming for all subsequent samples.

5.5 Discussion: Development of the Oxidation State Mapping Technique

The $LiCoPO_4$ oxidation state mapping technique was developed to use changes in Co oxidation state as a fingerprint for lithiation and de-lithiation, in a similar manner to work previously performed for $LiFePO_4$ [4], [6]. This section assesses the pros and cons of the developed technique, and how they will affect the lithiation mechanisms study. Details on the shape of the EELS edges, and the interpretation of the lithiation mechanisms are the lithiation mechanisms chapter.

5.5.1 Co L-edge EELS standards

It is important to confirm that the EELS Co L-edge standards collected in Figure 5.9 are representative of octahedrally co-ordinated Co(II) in $LiCoPO_4$, and octahedrally co-ordinated Co(III) in $CoPO_4$, so the lithiation mechanisms can be accurately studied from the fitted EELS maps.

The Co(II) standard in Figure 5.9 had similar features to Co(II) L-edge standards collected on uncycled samples in literature for $LiCoPO_4$ [1], with a hip present on the Co L_2 and L_3 edges. The XRD pattern of the uncycled sample was refined to 100 % $LiCoPO_4$ (Figure 5.14), and SAED patterns

were indexed to $LiCoPO_4$ (Figure 5.15). Overall the Co(II) EELS edge in Figure 5.9 is likely to represent octahedrally co-ordinated Co^{2+}.

The Co(II) spectra collected from $LiCoPO_4$ powder of different ages (Figure 5.24) differ slightly, with the sample collected most recently having an edge onset at 781 eV, rather than 782 eV for the original standard. The $LiCoPO_4$ powder was stored in an Ar filled glove box so should not have undergone atmospheric degradation. It is possible the microscope alignment was slightly different, implying that a Co(II) and Co(III)-rich standard would need to be collected prior to each experiment.

The Co(III)-rich standard is different to the Co(II)-rich standard (Figure 5.9), making oxidation state mapping possible (Figure 5.20). The Co(III)-rich standard does not contain any shoulder features present on the Co(II)-rich standards, and the maximum peak occurs at a higher energy loss (781 eV for Co(III) and 779 eV for Co(II)). An EELS literature example of the Co(III) Co L-edge could not be found for comparison.

The shape of the EELS Co(III)-rich L_3 edge contains similar features to the X-ray absorption spectrum (XAS) collected L_3 edge by Lapping et al. [1] (Figure 5.36). However, the charged $LiCoPO_4$ XAS spectrum in [1] contains a multiplet (shoulder) feature on the side of the L_3 edge, which is present on the EELS Co(II) L_3 edge in this study, but not the Co(III)-rich L_3 edge (Figure 5.36). [1] attributed the shape of the charged $LiCoPO_4$ edge to Co^{3+} with some Co^{2+} character due to the existence of some multiplet features (shoulders on the side of the L_3 edge) (Figure 5.36). As the XAS multiplet feature is not present on the EELS Co(III)-rich Co L-edge standard in Figure 5.9, this suggests the edge has more Co^{3+} character, than Co^{2+} character. The XAS technique is not site specific, so the Co^{2+} character could arise from signal contamination with $Li_{2/3}CoPO_4$ in Lapping et al.'s study, which may explain the discrepancy.

Lapping et al. also presented a XAS spectra of doped $LiCoPO_4$ which did not contain the shoulder multiplet feature, leading to the conclusion that the Co had oxidised to Co^{3+} for this compound. The lack of multiplet features on the Co(III)-rich signal in Figure 5.9 suggests that it is Co^{3+}. The site specific nature of EELS analysis allowed for the observation of Co^{3+} regions in $LiCoPO_4$.

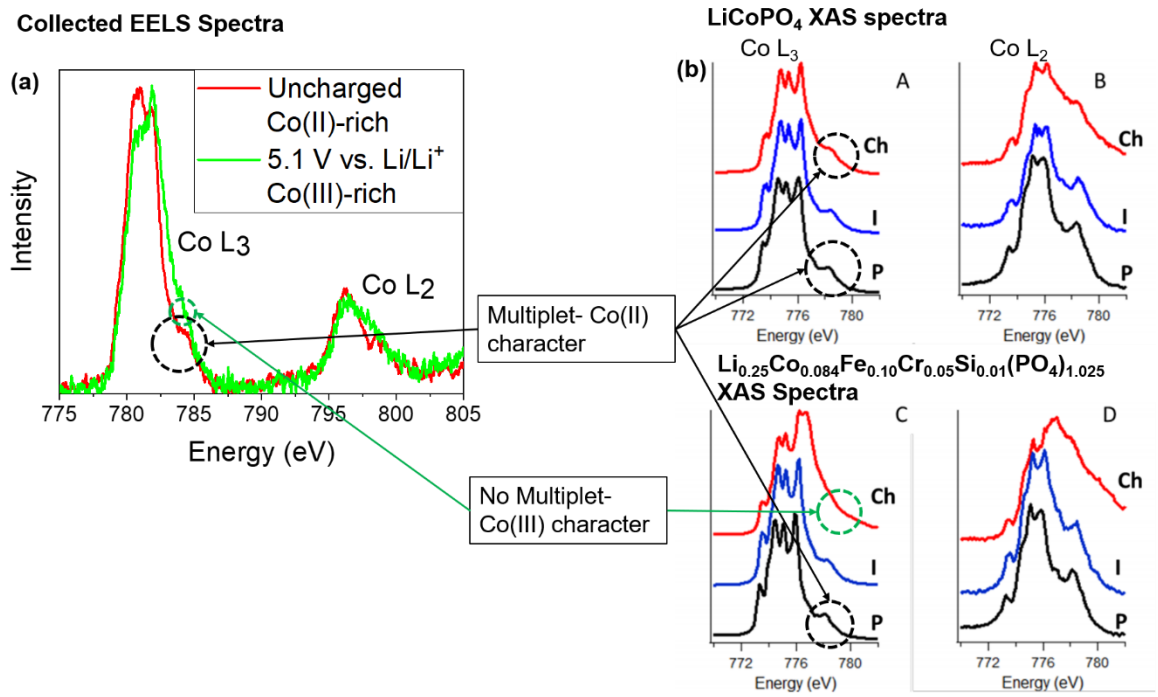

Figure 5.36: Comparison between collected Co L-edge EELS spectra (a), and $LiCoPO_4$, and $Li_{0.25}Co_{0.084}Fe_{0.10}Cr_{0.05}Si_{0.01}(PO_4)_{1.025}$ XAS spectra from [1] *P- pristine (uncycled), I- intermediate charged, Ch- fully charged to 5.3 V vs. Li/ Li^+ for $LiCoPO_4$, and 5.0 V vs. Li/ Li^+ for $Li_{0.25}Co_{0.084}Fe_{0.10}Cr_{0.05}Si_{0.01}(PO_4)_{1.025}$ adapted with permission from Chem. Mater. 2018, 30, 6, 1898-1906. Copyright (2018) American Chemical Society.*

In order to prove the Co(III)-rich EELS standard originated from octahedrally co-ordinated Co^{3+} in $CoPO_4$, XRD and SAED were performed on 5.1 V vs. Li/ Li^+ electrodes (Figure 5.14 and Figure 5.16). XRD and SAED patterns were refined and indexed to $CoPO_4$ implying that the Co(III)-rich standard was Co^{3+}. However, the lithium occupancy was not refined as Li does not interact with X-rays in XRD easily, hence the Li lattice positions and occupancy is not calculated. It is known Li occupancy changes the lattice parameter (Table 5.2), but the degree of Li occupancy associated with the lattice parameter changes could only be estimated from the reference standards used in the refinements.

The SAED patterns were indexed by comparing the d-spacing values for each phase, which rely on variations in the unit cell parameters as the lithium occupancy changes for discrete phases, $LiCoPO_4$, $Li_{2/3}CoPO_4$, and $CoPO_4$. The assumption that only $LiCoPO_4$, $Li_{2/3}CoPO_4$, and $CoPO_4$ form during de-lithiation of $LiCoPO_4$ ignores the possibility of partial lithiation within single particles between these phases (for example, $Li_{0.01}CoPO_4$). Therefore, although the Co(III)-rich standard collected in Figure 5.9 was the edge most shifted to higher energy losses (implying a higher oxidation state) it cannot be confirmed that the edge represents octahedrally co-ordinated Co^{3+} from $CoPO_4$.

Similar lithium occupancy issues when identifying the $Li_{2/3}CoPO_4$ phase standard were also experienced. $Li_{2/3}CoPO_4$ phase standards were extracted from Co(II)-rich areas of a 5.1 V vs. Li/ Li^+ electrode as XRD showed that $Li_{2/3}CoPO_4$ was found in 5.1 V vs. Li/ Li^+ electrodes (Figure 5.14), and also from a 4.89 V vs. Li/ Li^+ charged sample as this voltage occurred after the first large peak in the galvanostatic charge curve (Figure 5.6 (b)). Li occupancy was not refined in Figure 5.14 so it is not certain the phase is $Li_{2/3}CoPO_4$.

XRD of the 4.89 V vs. Li/ Li^+ electrodes showed the sample was 100 % $LiCoPO_4$ (Figure 5.19). This was surprising given 4.89 V vs. Li/ Li^+ occurred after the first red-ox peak at 4.8 V vs. Li/ Li^+ (Figure

5.6), and $Li_{2/3}CoPO_4$ was expected to from after this peak [11], [13]. The error is discussed in the lithiation mechanisms chapter discussion as the comprehensive EELS analysis during the first charge of $LiCoPO_4$ aids the discussion.

Despite the uncertainty in the identity of the $Li_{2/3}CoPO_4$ standard, mapping was attempted. It was found that Co(III)-rich regions could be separated from $Li_{2/3}CoPO_4$, but $Li_{2/3}CoPO_4$ could not be separated from Co(II) $LiCoPO_4$ (Figure 5.20). Principal component analysis may have aided the separation of the $Li_{2/3}CoPO_4$ from $LiCoPO_4$ signals, however this was not performed here. Therefore, mapping will be performed using the Co(III)-rich and Co(II)-rich standards.

Overall, the uncertainty of the identity of the EELS Co L-edge being used as a standard was caused by an inability to quantify the lithium occupancy using XRD or SAED to confirm the extracted EELS edge correlated with $CoPO_4$, and not partially de-lithiated $LiCoPO_4$. A better technique may have been X-ray absorption spectroscopy (XAS), which has been used to quantify oxidation in $LiCoPO_4$ previously [1], although XAS is not site-specific. Neutron diffraction could also have been used to refine the Li occupancy.

The unknown identity of the Co(III)-rich standard makes analysis of the different Co(III) edge shape in Figure 5.26 difficult. Given Co L-edge shifts towards higher energy losses typically results from higher oxidation states, it is likely the Co(III)-rich Co L-edge in Figure 5.26 was collected from a more de-lithiated region of sample than the Co(III)-rich Co L-edge in Figure 5.9. It is possible other influence on the electron density of states, such as Co-O hybridisation also effects the shape of the Co L-edge. Without knowing the Li occupancy of the regions of sample the Co L-edge standards were collected it is not possible to fully interpret the differences in the Co(III)-rich EELS Co L-edge spectra.

As discussed in the introduction, previous studies on $LiFePO_4$ have used chemically delithiated $LiFePO_4$ to form $FePO_4$ to collect the end group standard [6], which enabled a more comprehensive analysis of the EELS Fe L-edges than presented here for Co L-edges. A controlled method of de-lithiating $LiCoPO_4$ could aid understanding of the Co L-edges collected in this study.

Electrochemical de-lithiation here was controlled using galvanostatic charge and discharge, stopping at particular voltages where the $Li_{2/3}CoPO_4$, or $CoPO_4$ phases should have formed due to the completion of the phase change peaks in the differential capacity curve. However, using voltage as a stopping method does not confirm the same amount of lithium has entered the cell as voltage can be varied by other influences. A better method would have been to charge the cells to different specific capacities as theoretically this would have ensured similar lithium occupancy in the electrodes.

A technique such as cyclic voltammetry (CV) may be a better technique for a voltage control experiment, as voltage in CV testing is the independent variable. Moreover, peaks in CV curves are known to correspond to oxidation state changes.

Overall, the Co(II) standard is reliably Co^{2+} from $LiCoPO_4$. The charged standard is likely to be Co(III), however there is uncertainty regarding the identity of the Co(III) standard. Therefore, the standards collected can be used to demonstrate where de-lithiation has occurred in the sample, rather than quantifying the de-lithiation, and it is referred to as Co(III)-rich.

5.5.2 The EELS O K-edge standards

For uncycled $LiCoPO_4$, the O K-edge is affected by the thickness of the sample (Figure 5.21). Fourier-ratio deconvolution was performed on all O K-edge spectrum images to enable improved

mapping. In particular, fourier-ratio deconvolution caused the edge (at maximum 564 eV) to occur at the same intensity regardless of the t/λ ratio, suggesting the maximum at 564 eV is affected as a result of plural scattering.

For regions with a t/λ ratio greater than 0.40, a small shoulder at 541 eV was observed on the O K-edge on uncycled electrodes. Fourier-ratio deconvolution did not remove the shoulder feature at 541 eV. There is no correlation between the presence of the shoulder and whether the region is Co(II), or Co(III)-rich. It is not clear what causes the shoulder feature at 541 eV. The lack of deconvolution influence suggests the shoulder feature does not result from plural scattering. Density functional theory (DFT) modelling would be required to fully understand the shape of the O K-edge.

The resin used for preparing microtome specimens did not contribute to the O K-edge signal (Figure 5.22), so the signal contribution did not need to be removed.

When the electrode is charged to 5.1 V vs. Li/ Li^+ the pre-edge feature at 532 eV in Figure 5.29 occurs, and is also visible on O K-edge XAS spectra collected by Lapping et al. from charged electrodes [1]. Lapping et al. suggested the pre-edge feature occurred due to O 2p hybridisation with Co 3d states [1].

Several studies on $LiFePO_4$ also observed the O K-edge pre-edge feature at 532 eV in the charged state of $LiFePO_4$ ($FePO_4$) [19]–[21]. Suntivich et al. performed a comparison of DFT modelled, and EELS collected O K-edges for $LiFePO_4$ [19]. Suntivich interpreted the pre-edge as the transition from O 1s to the O2p component of the Fe 3d-O2p states in the conduction band of $LiFePO_4$ (Fe-O hybridisation) [19]. Hybridisation is only observed in the charged state (when Co is in the Co(III) oxidation state) as the oxidation of the transition metal (either Fe, or Co) on charging, results in an increase in the density of unoccupied states in the O-2p band above the Fermi level, allowing promotion of transition metal 3d electrons to the O-2p band [1], [19]. Given the similarities between the $LiCoPO_4$, and $LiFePO_4$ systems, and Lapping et al. finding the O K-edge on charged $LiCoPO_4$ using XAS, it is likely the pre-edge feature observed at 532 eV results from Co-O hybridisation in the charged state of $LiCoPO_4$ (in the presence of $CoPO_4$).

The O K-edge charged spectra were collected from aged $LiCoPO_4$, when this material was charged the EELS Co L-edge region contained modified edge features compared to the fresh $LiCoPO_4$ (Figure 5.26) (the aged standard has less intensity on the Co(II)-maximum side of the Co L_3 edge compared to the original standard). As the new Co(III) L-edge in Figure 5.26 also does not contain the Co(II) L_3 multiplet features, it is likely this aged Co L-edge has more Co^{3+} character.

Figure 5.27 shows the $Li_{2/3}CoPO_4 \rightarrow CoPO_4$ differential capacity peak occurred at a higher potential for the aged Co L-edge, compared to the fresh Co L-edge in Figure 5.26. The higher potential for the phase change may have resulted in a difference in the extent of Li diffusion out of the $LiCoPO_4$ particles, with local Co environment modifying the EELS Co L-edge, however further studies would be required to prove this was the cause of the Co L-edge having more Co^{3+} character.

The O K-edge experiment was the last to be performed in the PhD, so it is possible the powder had undergone some degradation, despite being stored in an Ar filled glove box. The experiment should be performed with fresher powder to ensure the pre-edge feature always occurs, and is not a result of ageing materials.

XRD (Figure 5.14) and SAED (Figure 5.16) of the 5.1 V vs. Li/ Li^+ showed the presence of $CoPO_4$ in the charged electrode. Given literature states that the O K-edge hybridisation pre-edge only

occurs in the presence of $CoPO_4$, or $FePO_4$, due to the available O2p states created by oxidation [1], [19], it is likely the pre-edge would have occurred in the fresh $LiCoPO_4$ samples as well.

Overall, for the later cycle experiments described in the lithiation mechanisms chapter, the O K-edge will be mapped to look for evidence of Co-O hybridisation by observing the pre-edge feature on the O K-edge.

5.5.3 Effects of air exposure

It has been previously reported that $CoPO_4$ amorphises on contact with air [11]. However, there are no previous reports on the effect of amorphisation on the Co L-edge. Figure 5.29 shows that on air exposure for 3 days the Co L-edge shifted by 0.3 eV to higher energy losses. 0.3 eV was a significant enough difference that the oxidised Co(III)-rich standard had to be used to accurately fit the Co(II), and Co(III)-rich regions using MLLS fitting on oxidised samples (Figure 5.30). Once fitting was complete, the MLLS fitting maps show that a higher proportion of the 5.1 V vs. Li/ Li^+ electrode is fitted to Co(III)-rich (Figure 5.31).

Without modelling the electrode transitions using, for example, density functional theory, it is not possible to determine why the Co L-edge shifts to higher energy losses when the sample is exposed to air. However, as amorphisation has been previously reported on exposure of $CoPO_4$ to air [11], it is likely the bond lengths change as a result of the amorphisation, leading to a difference in electron density of states and the shift in the Co L-edge position. The effect on Co(II) was not tested, but as $LiCoPO_4$ has not been reported to amorphise in air at room temperature and confirmed by XRD pattern collection in air in this project (results not shown), it was assumed the Co(II) L-edge would be unaffected. Future work should confirm the $LiCoPO_4$ Co L-edge does not shift as a result of air exposure for completeness.

However, as higher energy loss onsets are associated with higher oxidation states, it is possibly due to Co shifting to a higher energy loss.

For the purposes of this study, the effect of air on the MLLS fitting maps, and the Co L-edge spectra demonstrate that air contact must be minimised to remove errors resulting from air exposure.

5.5.4 Microtoming

For TEM samples made by spreading dry powder onto a TEM support grid, Figure 5.32 demonstrates that particle overlap causes the Co(II)-rich and Co(III)-rich regions to be less well defined. The consequence is that it is difficult to draw conclusions about the lithiation mechanisms within the individual particles, counter to the primary aim of developing the oxidation state mapping technique. Figure 5.37 demonstrates why particle overlap causes poor definition between Co(II) and Co(III)-rich areas. MLLS fitting relies on the features Co(II), and Co(III)-rich features of the Co L_2 and L_3 edges being clearly separated in the STEM projection direction. If the sample is too thick, electrons can undergo plural scattering, reducing the signal and causing the signal to noise ratio of the EELS Co-L edge to be too high to define the shape of the Co(II), and Co(III) edges. Alternatively, if the beam passes through both Co(II), and Co(III)-rich regions before hitting the detector due to overlapping particles, the Co-L edge will have mixed Co(II) and Co(III) characteristics.

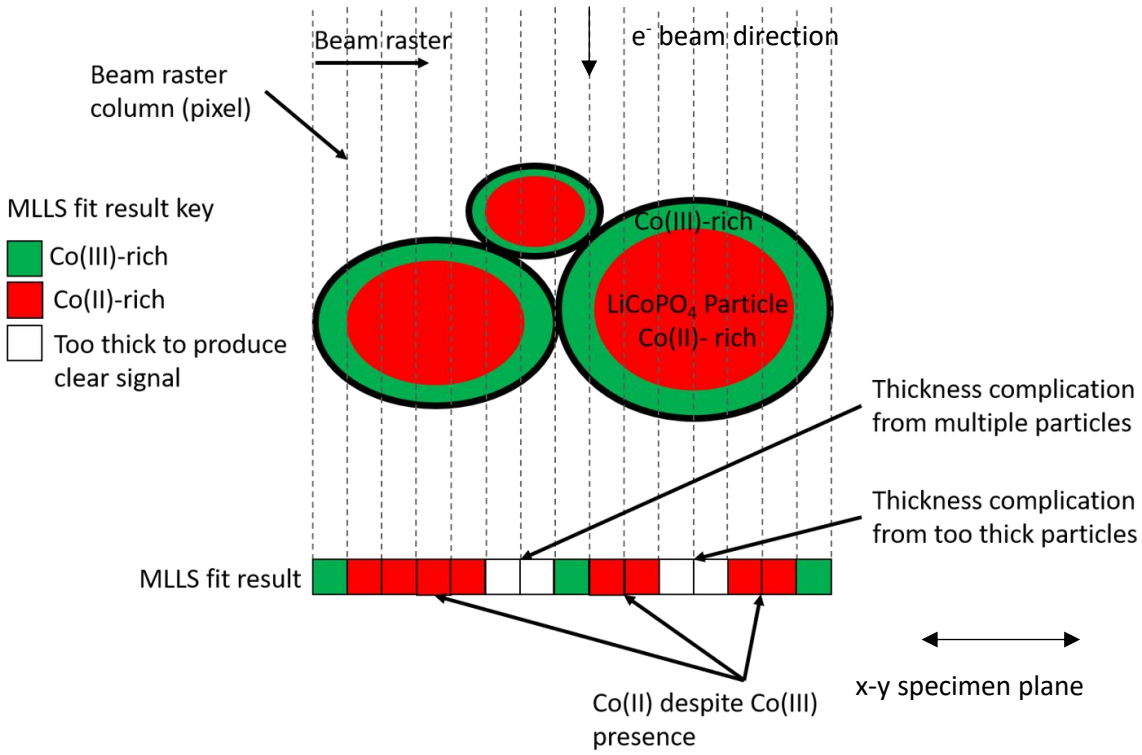

Figure 5.37: Schematic of the STEM electron beam rastering direction effects through dry mounted particle samples, and the effect on the MLLS fitting results on partially de-lithiated $LiCoPO_4$. Co(II)-rich is red, and Co(III)-rich is green. Thickness complication in the schematic is represented as white, although the program will attempt to assign red, or green.

Figure 5.33 demonstrated that by microtoming the particles, the particle overlap was reduced as the specimen thickness is smaller, more uniform, and contains fewer overlapping particles. This is demonstrated by the schematic in Figure 5.38 for partially de-lithiated $LiCoPO_4$ particles sliced by microtoming. However, thickness complications can still arise if the microtoming blade is not perfectly parallel to the sample. Moreover, Figure 5.33 demonstrates some 'blurring' of edges with small fragments visible, which suggests fracture damage from the microtome blade.

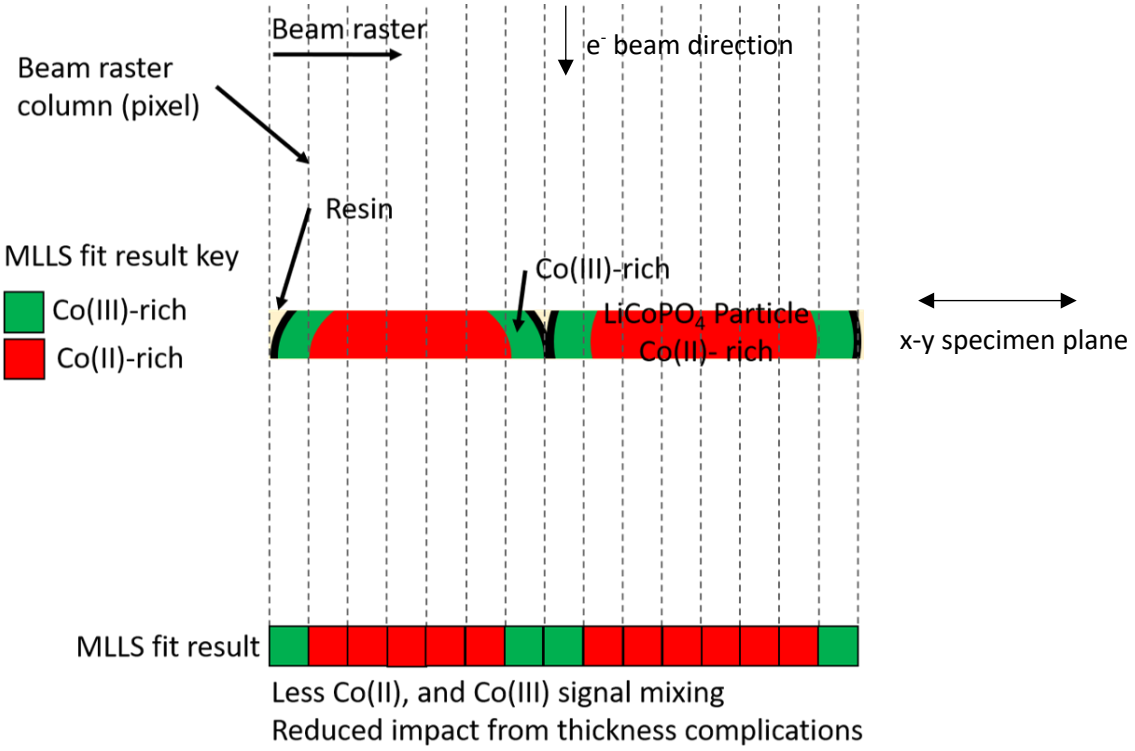

Figure 5.38: Schematic of the geometry as the STEM e- beam rasters across the micro-tomed sample, and the corresponding MLLS fit result.

A downside of microtoming is there is no control over the region of particle the blade sections, although within a given cross-section there will be a spread of particles sectioned differently. Therefore, if the section contains only the edge of a partially de-lithiated particle, the MLLS fitting may suggest that the particle is predominantly Co(II), when it may be predominantly Co(III)-rich. The issue is demonstrated in Figure 5.39, and may explain some of the presence Co(II)-rich particles in Figure 5.35. A solution to this error is to consider the size of the particle chosen for EELS analysis. Ideally analysed particle diameters should be 100-200 nm, as this is the diameter of a $LiCoPO_4$ particle and would suggest the section contains most of the original particle.

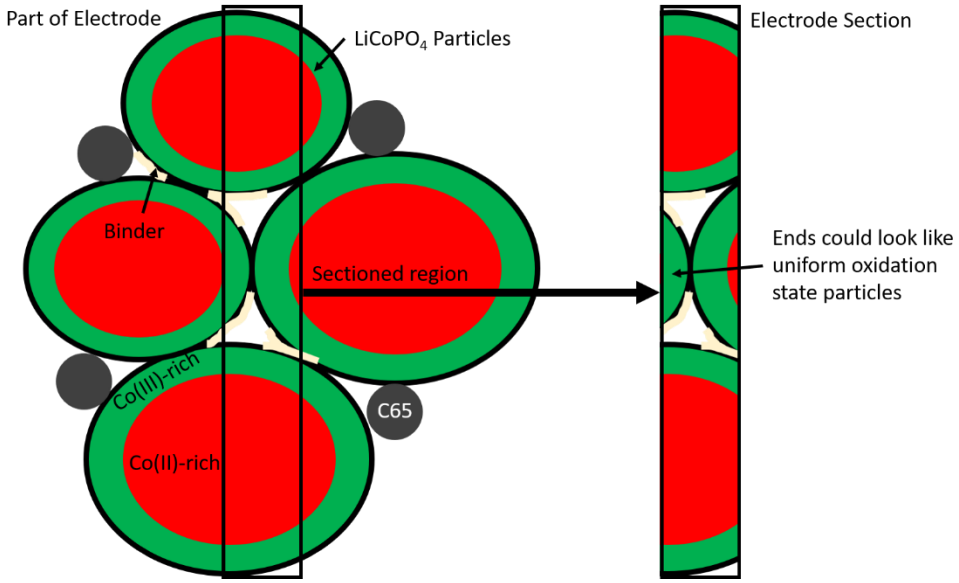

Figure 5.39: Schematic demonstrating how a microtomed electrode section does not contain the whole $LiCoPO_4$ particle, and can contain the sliced off edges of particles.

Investigations here suggest that the air exposure issue when microtoming is minimal, as the Co L-edge either did not shift, or only shifted slightly towards higher energy losses Figure 5.34. Air exposure of the particles can occur during resin mounting, and during sectioning. Slight variations in the oxidation of the particles may have been caused by sectioning, or resin mounting taking longer. To avoid further air exposure, the samples were stored in the glove box after sectioning. However, ideally the samples would be mounted in resin in the glove box, and sectioned under an inert atmosphere in the future. The Co(III)-rich standard for microtomed particles was also extracted from a microtomed sample.

Overall, microtoming demonstrated significant improvements in the mapping of $LiCoPO_4$ particles. Therefore, all the samples analysed for the lithiation mechanisms study have been microtomed.

5.6 Conclusion

A method of mapping the charged and discharged region of $LiCoPO_4$ has been developed for the first time. Mapping was achieved by MLLS fitting Co L-edge EELS spectra from spectrum images to a Co(II), and Co(III)-rich reference as the valence state of Co changes as $LiCoPO_4$ de-lithiates. Similar mapping was previously performed on $LiFePO_4$ samples [4], but this is the first demonstration in $LiCoPO_4$.

Standards for the O K-edge when $LiCoPO_4$ was de-lithiated, and lithiated were also collected. Similar to Lapping *et al.* it was found that at high levels of de-lithiation (as Co approaches Co(III)), O 2p hybridisation with the Co 3d states occurs, suggesting O is red-ox active at high potentials in $LiCoPO_4$ [1]. Collection of O K-edge standards should enable a comprehensive analysis of Co-O hybridisation during de-lithiation of $LiCoPO_4$.

Mapping of the Co L-edge, and O K-edge was improved by microtome sectioning the samples, allowing the phases present within individual $LiCoPO_4$ particles to be clearly distinguished.

The ability to map the lithiated and de-lithiated regions of $LiCoPO_4$ electrodes enabled greater understanding of the de-lithiation mechanisms, and electronic structure behaviour of $LiCoPO_4$

electrodes which may enable suggestions for performance improvement. The results for the de-lithiation mechanism are described in chapter 6.

5.7 REFERENCES

[1] J. G. Lapping, S. A. Delp, J. L. Allen, J. Allen, J. W. Freeland, M. D. Johannes, L. Hu, D. T. Tran, T. R. Jow, J. Cabana, "Changes in Electronic Structure upon Li Deintercalation from $LiCoPO_4$ Derivatives," *Chem. Mater.*, vol. 30, no. 6, pp. 1898–1906, 2018.

[2] R. F. Egerton, "An Introduction to EELS," in *Electron Energy-Loss Spectroscopy in the Electron Microscope*, Boston, MA: Springer US, 2011, pp. 1–28.

[3] "Lithium | EELS.info." [Online]. Available: http://www.eels.info/atlas/lithium. [Accessed: 30-Aug-2018].

[4] W. Sigle, R. Amin, K. Weichert, P. A. van Aken, and J. Maier, "Delithiation Study of $LiFePO_4$ Crystals Using Electron Energy-Loss Spectroscopy," *Electrochem. Solid-State Lett.*, vol. 12, no. 8, p. A151, 2009.

[5] S. Kobayashi, C. A. J. Fisher, A. Kuwabara, Y. Ukyo, and Y. Ikuhara, "Quantitative analysis of Li distributions in battery material $Li_{1-x}FePO_4$ using Fe M 2,3-edge and valence electron energy loss spectra," *Microscopy.*, vol. 66, no. 4, pp. 254–260, 2017.

[6] L. Laffont *et al.*, "Study of the $LiFePO_4$ /$FePO_4$ Two-Phase System by High-Resolution Electron Energy Loss Spectroscopy." *Chem. Mater.,* vol. 18, no. 23, pp. 5520-5529, 2006.

[7] J. H. Rask, B. A. Miner, and P. R. Buseck, "Determination of manganese oxidation states in solids by electron energy-loss spectroscopy," *Ultramicroscopy*, vol. 21, no. 4, pp. 321–326, 1987.

[8] L. Yedra, E. Xuriguera, M. Estrader, A. López-Ortega, M. D. Baró, J. Nogues, M. R. Gutierrez, M. Varela, S. Estradé, F. Peiró "Oxide Wizard: An EELS Application to Characterize the White Lines of Transition Metal Edges," *Microsc. Microanal*, vol. 20, pp. 698–705, 2014.

[9] R. F. Egerton, "TEM Applications of EELS," in *Electron Energy-Loss Spectroscopy in the Electron Microscope*, Boston, MA: Springer US, 2011, pp. 293–397.

[10] "Advanced SI | EELS.info." [Online]. Available: https://eels.info/how/spectrum-imaging/advanced-si. [Accessed: 24-Jun-2020].

[11] F. C. Strobridge, R. J. Clément, M. Leskes, D. S. Middlemiss, O. J. Borkiewicz, K. M. Wiaderek, K. W. Chapman, P. J. Chupas, C. P. Grey, "Identifying the Structure of the Intermediate, $Li_{2/3}CoPO_4$, Formed during Electrochemical Cycling of $LiCoPO_4$," *Chem. Mater.*, vol. 26, no. 21, pp. 6193–6205, 2014.

[12] J. Wolfenstine, B. Poese, and J. L. Allen, "Chemical oxidation of $LiCoPO_4$," *J. Power Sources*, vol. 138, no. 1–2, pp. 281–282, 2004.

[13] M. G. Palmer, J. T. Frith, A. L. Hector, A. W. Lodge, J. R. Owen, C. Nicklin, J. Rawle, "In situ phase behaviour of a high capacity $LiCoPO_4$ electrode during constant or pulsed charge of a lithium cell," *Chem. Commun. Chem. Commun*, vol. 52, no. 52, pp. 14169–14172, 2016.

[14] J. B. Goodenough and Y. Kim, "Challenges for Rechargeable Li Batteries," *Chem. Mater.*, vol. 22, no. 3, pp. 587–603, 2010.

[15] D. Su, S. Dou, and G. Wang, "Single Crystalline Co_3O_4 Nanocrystals Exposed with Different

Crystal Planes for Li-O_2 Batteries," *Sci. Rep.*, vol. 4, no. 1, p. 5767, 2015.

[16] L. Wheatcroft, N. Klingner, R. Heller, G. Hlawacek, J. Cookson, and B. J. Inkson, "Visualisation and Chemical Characterisation of the Cathode Electrolyte Interphase in High Voltage Li-ion Battery Material $LiCoPO_4$ using He-ion Microscopy and in-situ Time-of-Flight Secondary Ion Mass Spectroscopy," *Appl. Energy Materials,* 2020.

[17] J. K. Cockcroft, "Space Group 53: Pnma; P n m a." [Online]. Available: http://img.chem.ucl.ac.uk/sgp/large/062az2.htm. [Accessed: 27-Jun-2020].

[18] R. F. Egerton, F. Wang, M. Malac, M. S. Moreno, and F. Hofer, "Fourier-ratio deconvolution and its Bayesian equivalent," *Micron*, vol. 39, no. 6, pp. 642–647, 2008.

[19] J. Suntivich, W. T. Hong, Y-L. Lee, J. M. Rondinelli, W. Yang, J. B. Goodenough, B. Dabrowski, J. W. Freeland, Y. Shao-Horn, "Estimating hybridization of transition metal and oxygen states in perovskites from O k -edge X-ray absorption spectroscopy," *J. Phys. Chem. C*, vol. 118, no. 4, pp. 1856–1863, 2014.

[20] X. Liu, Y. J. Wang, B. Barbiellini, H. Hafiz, S. Basak, J. Liu, T. Richardson, G. Shu, F. Chou, T-C Weng, D. Nordlund, D. Sokaras, B. Moritz, T. P. Devereaux, R. Qiao, Y-D Chuang, A. Bansil, Z. Hussain, W. Yang, "Why $LiFePO_4$ is a safe battery electrode: Coulomb repulsion induced electron-state reshuffling upon lithiation †," *Phys. Chem. Chem. Phys*, vol. 17, p. 26369, 2015.

[21] X. Liu, J. Liu, R. Qiao, Y. Yu, H. Li, L. Suo, Y-S. Hu, Y-D. Chuang, G. Shu, F. Chou, T-C Weng, D. Nordlund, D. Sokaras, Y. J. Wang, H. Lin, B. Barbiellini, A. Bansil, X. Song, Z. Liu, S. Yan, G. Liu, S. Qiao, T. J. Richardson, D. Prendergast, Z. Hussain, F. M. F. de Groot, W. Yang, "Phase Transformation and Lithiation Effect on Electronic Structure of Li_xFePO_4 : An In-Depth Study by Soft X-ray and Simulations," *J. Am. Chem. Soc.*, vol. 134, no. 33, pp. 13708–13715, 2012.

[17] J. K. Cockcroft, "Space Group 53: Pmna; P m n a." [Online]. Available: http://img.chem.ucl.ac.uk/sgp/large/053az2.htm. [Accessed: 27-Jun-2020].

[18] R. F. Egerton, F. Wang, M. Malac, M. S. Moreno, and F. Hofer, "Fourier-ratio deconvolution and its Bayesian equivalent," *Micron*, vol. 39, no. 6, pp. 642–647, Aug. 2008.

[19] J. Suntivich *et al.*, "Estimating hybridization of transition metal and oxygen states in perovskites from o k -edge X-ray absorption spectroscopy," *J. Phys. Chem. C*, vol. 118, no. 4, pp. 1856–1863, Jan. 2014.

[20] X. Liu *et al.*, "Why LiFePO 4 is a safe battery electrode: Coulomb repulsion induced electron-state reshuffling upon lithiation †," *Phys. Chem. Chem. Phys*, vol. 17, p. 26369, 2015.

[21] X. Liu *et al.*, "Phase Transformation and Lithiation Effect on Electronic Structure of Li $_x$ FePO $_4$: An In-Depth Study by Soft X-ray and Simulations," *J. Am. Chem. Soc.*, vol. 134, no. 33, pp. 13708–13715, Aug. 2012.

6 DEGRADATION WITHIN $LiCoPO_4$ PARTICLES: UNDERSTANDING THE LITHIATION MECHANISMS OF $LiCoPO_4$

6.1 AIMS AND OBJECTIVES

$LiCoPO_4$ undergoes severe degradation during cycling , as has been shown previously in this thesis, and in literature, [1], [2]. To date most studies investigating the de-lithiation, and degradation mechanisms of $LiCoPO_4$ have used bulk techniques which do not spatially resolve changes in crystal, or electronic structure of the material [3]–[6]. Spatially resolving the phases formed during de-lithiation could be used to find the de-lithiation mechanisms of $LiCoPO_4$, and aid understanding of the contribution of proximity to electrolyte at high potentials, or instability of phases (such as $CoPO_4$) to the degradation of a$LiCoPO_4$.

The aim of this section of the thesis was to use the EELS Co L-edge, and O K-edge mapping techniques developed in the previous chapter to understand the de-lithiation mechanisms, and electronic structure changes of $LiCoPO_4$ electrodes during cycling. EELS Co L-edge valence state maps were used to identify Co(II), and Co(III)-rich regions of electrode, analogous to lithiated, and de-lithiated regions respectively. The O K-edge was mapped to understand Co-O hybridisation in $LiCoPO_4$ electrodes, found in chapter 5, and previously reported by [6].

The Co valence states were mapped at different potentials on the first cycle in order to understand the de-lithiation mechanism of $LiCoPO_4$. O K-edge mapping and extractions were also performed on electrodes charged on the first cycle to understand distribution of Co-O hybridisation, the presence of de-lithiated $LiCoPO_4$, and proximity to the $LiCoPO_4$- electrolyte interface.

The Co valence, and O K-edges were also extracted from electrodes cycled to the 5^{th}, and 10^{th} cycles to understand the effect of de-lithiation, and electronic structure change at later cycles when capacity has been lost. This work presents the first detailed crystallographic, and electronic structural study of $LiCoPO_4$ at later cycles.

X-ray diffraction (XRD), and selected area electron diffraction (SAED) were also performed to confirm the phases present on both the first cycle, and later cycle experiments.

Greater understanding of the degradation mechanisms of $LiCoPO_4$ could aid development of strategies to improve the cyclability of $LiCoPO_4$.

6.2 RESULTS: INVESTIGATING THE LITHIATION MECHANISMS OF $LiCoPO_4$

6.2.1 Experiments Performed

The scope of this section is to investigate the de-lithiation mechanisms of $LiCoPO_4$ in detail on the first cycle, and at later cycles. Co-O hybridisation was also investigated.

To investigate the first cycle de-lithiation mechanisms using the *ex-situ* EELS technique shown in chapter 5, potentials for *ex-situ* testing were chosen based on peaks in the differential capacity curve. EELS Co L-edge mapping was performed to identify the Co(II), and Co(III)-rich regions of electrodes charged to different potentials on the first cycle, analogous to the lithiated and de-lithiated regions of the electrodes. The potentials are shown in Table 6.1. XRD, and SAED were performed to identify the phases present in the electrodes at potentials corresponding to the EELS Co L-edge mapping potentials.

In a similar manner to the first cycle experiments, the de-lithiation mechanisms of electrodes at later cycles were assessed by performing EELS Co L-edge mapping on electrodes cycled to different cycles, and charged to 5.1 V vs. Li/ Li^+ (see Table 6.1). Electrodes were assessed in the charged state as this is where the most changes should be observed.

Co-O hybridisation was also assessed by mapping, and extracting the EELS O K-edge. Hybridisation experiments were performed on electrodes charged to 5.1 V vs. Li/ Li^+ at different cycles to assess whether hybridisation increased with increased cycle life. The experiment details are presented in Table 6.1.

The experiments in this section used the same methods described in 5.3 to prepare, and to characterise the samples using XRD, EELS, and SAED. Full details of the Co L-edge, and O K-edge mapping processes are detailed in 5.3, and 5.4, including the standards used for mapping. For STEM imaging, and EELS characterisation, the samples in this chapter were all microtomed to ensure changes could be resolved in each individual particle.

The full cell making, and cycling regimen is described in 5.3.1, but is summarised here. The electrodes consisted of 90 wt. % $LiCoPO_4$, 5 wt. % C65, and 5 wt. % PVDF. The electrode manufacturing, and cell making process are detailed in Chapter 3. The electrodes galvanostatically cycled at 0.1C between 2.5 V vs. Li/ Li^+ and 5.1 V vs. Li/ Li^+, unless otherwise stated. At the end of each charge, the electrodes were held at the final potential for 30 mins to ensure equilibrium. In between each cycle, the cells were rested for 1 hour. Table 6.1 shows the electrode cycling history for results presented in this chapter.

Table 6.1: Outline of the experiments performed in this chapter, the electrode cycling history, the characterisation techniques used, and the section where the results can be found. Whether the electrodes were fresh or aged as described in Chapter 5 is also stated.

Experiment	Electrode cycling history	EELS Co L-edge	EELS O K-edge	SAED	XRD	Section	Notes
De-lithiation mechanisms on the first cycle	Uncycled Electrodes charged on the first cycle to: 4.8 V vs. Li/ Li^+ 4.89 V vs. Li/ Li^+ 4.98 V vs. Li/ Li^+ 5.1 V vs. Li/ Li^+	Y		Y	Y	6.2.2	Fresh $LiCoPO_4$
De-lithiation mechanisms at later cycles	Uncycled Electrodes charged to 5.1 V vs. Li/ Li^+ on the: 1^{st} cycle 5^{th} cycle 10^{th} cycle	Y			Y	6.2.3	Aged $LiCoPO_4$
Understanding Co-O hybridisation	Uncycled Electrodes charged to 5.1 V vs. Li/ Li^+ on the: 1^{st} cycle 5^{th} cycle 10^{th} cycle		Y			6.2.3	Aged $LiCoPO_4$

6.2.2 Valence state and structural characterisation of the first cycle

Specific points during the $LiCoPO_4$ electrode cycling curve had to be chosen for electrode microstructural characterisation as the oxidation state mapping technique is an *ex-situ* characterisation technique.

Figure 6.1 shows a representative galvanostatic charge curve (a) and the associated differential capacity curve (b) of the first $LiCoPO_4$ charge cycle. The galvanostatic charge curve in Figure 6.1 (a) is plotted as voltage against specific capacity. The specific capacity was calculated by taking the integral under the current-time trace obtained during the galvanostatic charge and discharge testing.

2 voltage plateaus at 4.8 V and 4.9 V vs. Li/ Li^+ are visible on the galvanostatic charge curve in Figure 6.1 (a), similar to results observed by [7]. The total charging capacity for the sample represented in Figure 6.1 was 223 mAh g^{-1} which is greater than the theoretical capacity of $LiCoPO_4$ (167 mAh g^{-1}). The charging capacity being greater than the theoretical capacity is consistent with contributions from electrolyte degradation on the first cycle, or O-redox observed in the previous chapter.

The differential capacity is the first order differential of specific capacity (Q) against voltage (V) (dQ/dV). Peaks on a differential capacity curve correspond to physical processes occurring in a cell. Figure 6.1 (b) shows 3 peaks on the differential capacity curve, corresponding to 4.4 V, 4.8 V, and 4.9 V vs. Li/ Li^+ (the voltage plateau potentials on Figure 6.1 (a)). The integral of the differential capacity of the larger peaks (4.8 V and 4.9 V vs. Li/ Li^+) corresponds to the specific capacity

associated with the change creating the peak. The total integral of the 2 peaks in 154 mAh g^{-1} is 154 mAh g^{-1}, less than the theoretical capacity of $LiCoPO_4$ (167 mAh g^{-1}), consistent with the peaks arise due to physical changes within the $LiCoPO_4$ particles.

The $LiCoPO_4$ cells were charged to voltages after the peaks in the galvanostatic charge curve, indicated by the coloured triangles in Figure 6.1, as the peaks are likely to represent structural changes in the $LiCoPO_4$ particles which can be examined by EELS mapping. As voltage control is less reliable than specific capacity control, the differential capacity curves were checked prior to *ex-situ* testing to ensure the peak had occurred.

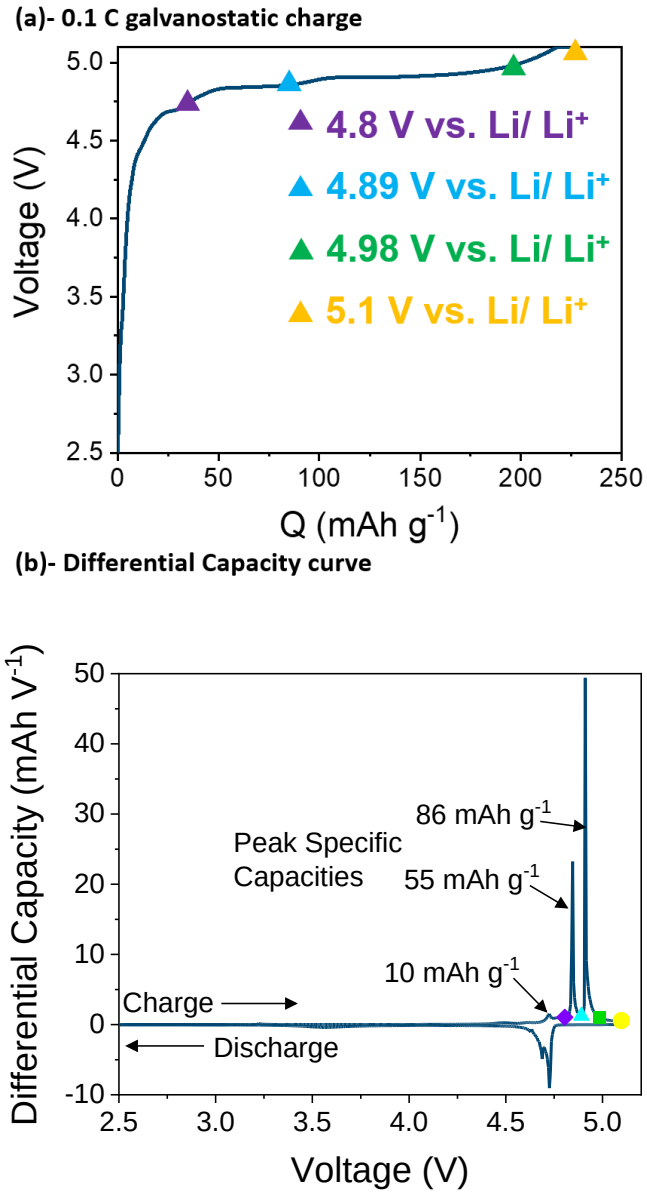

Figure 6.1: (a)- 0.1C galvanostatic charge curve of a $LiCoPO_4$ electrode, and (b) the corresponding differential capacity curve, showing the potentials where oxidation state mapping was performed on different electrodes: purple- 4.8 V, blue- 4.89 V, green- 4.98 V, and yellow- 5.1 V. Q- specific capacity.

After charging to each potential, XRD was performed on the electrodes to check the phases formed. Figure 6.2 shows Mo Kα XRD patterns collected on uncycled electrodes, and after electrodes were cycled to 4.89 V, 4.98 V, and 5.1 V vs. Li/ Li^+. The XRD patterns in Figure 6.2 have

been refined to $LiCoPO_4$, $Li_{2/3}CoPO_4$, and $CoPO_4$ using PDF cards 04-014-7339, 04-014-7340, and 04-014-7341 respectively.

Figure 6.2 shows that the uncycled electrode is 100 % $LiCoPO_4$, and the XRD peaks remain 100 % $LiCoPO_4$ until 4.89 V vs. Li/ Li^+ (after the second differential capacity peak in Figure 6.1). After charging to 4.98 V vs. Li/ Li^+, $LiCoPO_4$ peaks were undetectable.

$CoPO_4$ is present on the 4.98 V vs. Li/ Li^+, and the 5.1 V vs. Li/ Li^+ (Figure 6.2). This is consistent with 4.98 V vs. Li/ Li^+, and 5.1 V vs. Li/ Li^+ occurring after the final differential capacity peak in Figure 6.1 (b).

XRD shows that $Li_{2/3}CoPO_4$ is present at 4.98 V vs. Li/ Li^+, and remains present at 5.1 V vs. Li/ Li^+ (Figure 6.2). The presence of $Li_{2/3}CoPO_4$ in the 5.1 V vs. Li/ Li^+ sample indicates the examined electrodes were not fully charged.

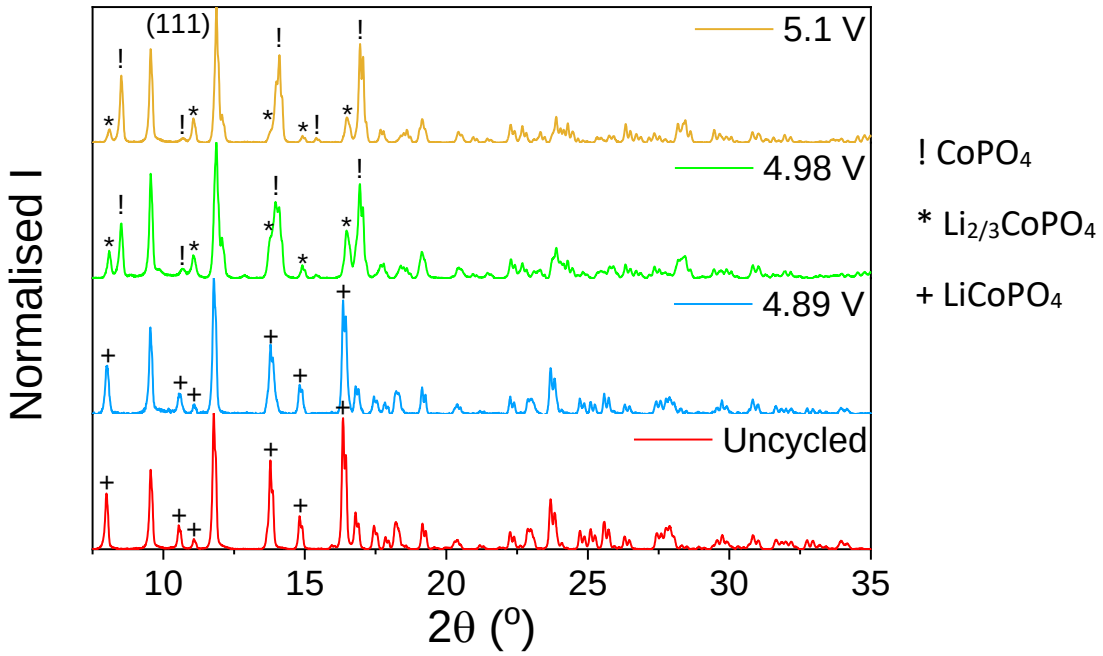

*Figure 6.2: Mo kα XRD patterns of electrodes cycled to 5.1 V, 4.98 V, 4.89 V vs. Li/ Li^+ on the first cycle, and an uncycled electrode. The XRD patterns have been normalised by the (111) reflection (labelled). The reflections corresponding to the different phases have been labelled as follows: !- $CoPO_4$, *- $Li_{2/3}CoPO_4$, +- $LiCoPO_4$.*

The phase proportions (weight fractions) in Table 6.2, and for all other XRD results tables, were calculated using Highscore plus using the same method as the previous chapter. Unfortunately, there was an issue with the focussing mirror for the Mo Kα source, which resulted in Si 640e standard peaks occurring in the wrong positions. Therefore the data in Figure 6.2 was not reliable enough for Rietveld refinement, or unit cell calculations. However, as the error was consistent between all the patterns, the phase proportions can be compared but the exact value is incorrect due to the reliance on unit cell volume for the weight fraction calculation. The error resulting from the Mo Kα source was not quantified. Calculated unit cell values can be found for Ag Kα XRD in Table 5.2 in Chapter 5.

Table 6.2 shows that the de-lithiated phases have formed at 4.98 V vs. Li/ Li^+. As the potential increased to 5.1 V vs. Li/ Li^+ the proportion of $Li_{2/3}CoPO_4$ decreases, and the proportion of $CoPO_4$

increases. However, the proportion of $CoPO_4$ never reaches 100 %, suggesting the 5.1 V vs. Li/ Li^+ electrodes in Figure 6.2 were not fully charged.

Table 6.2: Phase proportions and unit cell values calculated from the Mo kα XRD patterns in Figure 6.2 for each potential.

Potential (V vs. Li/ Li^+)	Phase	Phase Proportion (%)	R_{wp}
5.1	$CoPO_4$ $Li_{2/3}CoPO_4$	79.5(3) 20.5(2)	4.13
4.98	$CoPO_4$ $Li_{2/3}CoPO_4$	58.1(3) 41.9(3)	5.62
4.89	$LiCoPO_4$	100.0(2)	3.02
Uncycled	$LiCoPO_4$	100.0(1)	5.29

In order to understand the lithiation mechanisms occurring during the first charge cycle of $LiCoPO_4$, EELS Co oxidation state mapping was performed at the potentials marked by coloured triangles in Figure 6.1. Oxidation state maps of an uncycled sample, and samples charged to 4.8 V, 4.89 V, 4.98 V, and 5.1 V vs. Li/Li^+ are shown in Figure 6.3, along with the corresponding STEM-HAADF images. The Co(II)-rich standard used for mapping was extracted from uncycled $LiCoPO_4$ particles (Figure 5.9). The Co(III)-rich oxidation state mapping standard in Figure 6.3 was the microtomed electrode Co(III)-rich standard in Figure 5.34. As explained in 5.4.4 microtomed electrodes were exposed to air for 1 hour during the resin mounting, and sectioning processes, and when loading the sample into the TEM vacuum. The air exposure effects on the Co L-edge are shown in 5.4.3, and 5.4.4 in Chapter 5. The EELS experiments shown here were performed on non-aged (fresh) $LiCoPO_4$, therefore the galvanostatic profile shown in Figure 6.1 reflects the behaviour of the samples in Figure 6.4.

The uncycled Co-oxidation state map in Figure 6.3 (i) is mostly Co(II)-rich (red). XRD patterns in Figure 6.2 and Table 6.2 show that the bulk electrode consists of 100 % $LiCoPO_4$ in the uncycled state, which correlates with the Co(II)-rich mapping in Figure 6.3 (i).

Green Co(III)-rich regions are present on the uncycled oxidation state map, at the top of the imaged region in Figure 6.3 (i), despite no evidence of $CoPO_4$ being present on the XRD patterns in Figure 6.2. Comparison with the HAADF image in Figure 6.3 (j) shows that the green regions correspond to brighter contrast in the HAADF image, hence the region is thicker. It should be noted that the sample in Figure 6.3 (i), and (j) has not been microtomed.

4.8 V vs. Li/ Li^+ occurs after the first peak in the differential capacity curve in Figure 6.1 (b). The oxidation state map of the 4.8 V vs. Li/ Li^+ sample in Figure 6.3 (g) shows the sample is mostly Co(II) (red). Although no XRD patterns of a 4.8 V vs. Li/ Li^+ are presented in Figure 6.2, as the 4.89 V vs. Li/ Li^+ sample was 100 % $LiCoPO_4$, it can be assumed that a 4.8 V vs. Li/ Li^+ XRD pattern is also likely to be 100 % $LiCoPO_4$. The first peak at 4.4 V vs. Li/ Li^+ on the galvanostatic curve in Figure 6.1 could be from partially de-lithiated $LiCoPO_4$, or a result of electrolyte reaction at high potentials. The origin of the 4.4 V vs. Li/ Li^+ peak is discussed in 6.3.1.

4.89 V vs. Li/ Li^+ is after the second peak in the differential capacity curve in Figure 6.1 (b). The EELS oxidation state map of the 4.89 V vs. Li/ Li^+ charged particles in Figure 6.3 (e) shows that the majority of the particles are mixed Co(II), and Co(III) oxidation states as the map shows regions of

mixed red and green. Co(III)-rich regions (green) are also present on the 4.89 V vs. Li/ Li^+ sample and form on the edge of particles.

The 4.89 V vs. Li/ Li^+ XRD pattern in Figure 6.2 shows 100 % $LiCoPO_4$ which does not correlate to the localised particle oxidation states observed in Figure 6.3 (e). Given that the sample was stopped from charging after the second differential capacity peak, and the oxidation state map shows the presence of mixed oxidation states, it was expected the XRD pattern should show the presence of $Li_{2/3}CoPO_4$. It is unclear why the XRD pattern does not correlate with the observed oxidation state changes.

The 4.98 V vs. Li/ Li^+ Co-oxidation state map in Figure 6.3 (c) shows that the Co(III)-rich green regions on the edge of particles (visible on the 4.89 V vs. Li/ Li^+ sample in Figure 6.3 (e)) have either thickened to fill the entire particle, or have grown in towards the centre of the particle. Red Co(II)-rich regions remain in the centre of the particles where the Co(III)-rich regions have not penetrated the entire particle. Smaller particles (30 nm) are also red Co(II)-rich. This correlates with the XRD pattern in Figure 6.2 which shows 41.9 % $Li_{2/3}CoPO_4$, and 58.1 % $CoPO_4$, and with 4.98 V vs. Li/ Li^+ occurring after the second peak on the differential capacity curve in Figure 6.1 (b).

The 5.1 V vs. Li/ Li^+ sample has the highest state of charge, and occurs after the second peak in the differential capacity curve in Figure 6.1 (b). The particles in the 5.1 V vs. Li/ Li^+ oxidation state map in Figure 6.3 (a) are almost entirely Co(III)-rich (green). This correlates well with the XRD pattern result in Figure 6.2, which shows 79.5 % $CoPO_4$, and 20.5 % $Li_{2/3}CoPO_4$ present in a 5.1 V vs. Li/ Li^+ sample.

A particle in the top right hand corner of the oxidation state map in Figure 6.3 (a) is red, however comparison with the HAADF image in Figure 6.3 (b) shows that it is resting on some TEM carbon grid, creating thickness issues.

Red Co(II)-rich regions are visible on the surface of some particles in the 4.98 V vs. Li/ Li^+ sample in Figure 6.3 (c) and the 5.1 V vs. Li/ Li^+ sample in Figure 6.3 (a).

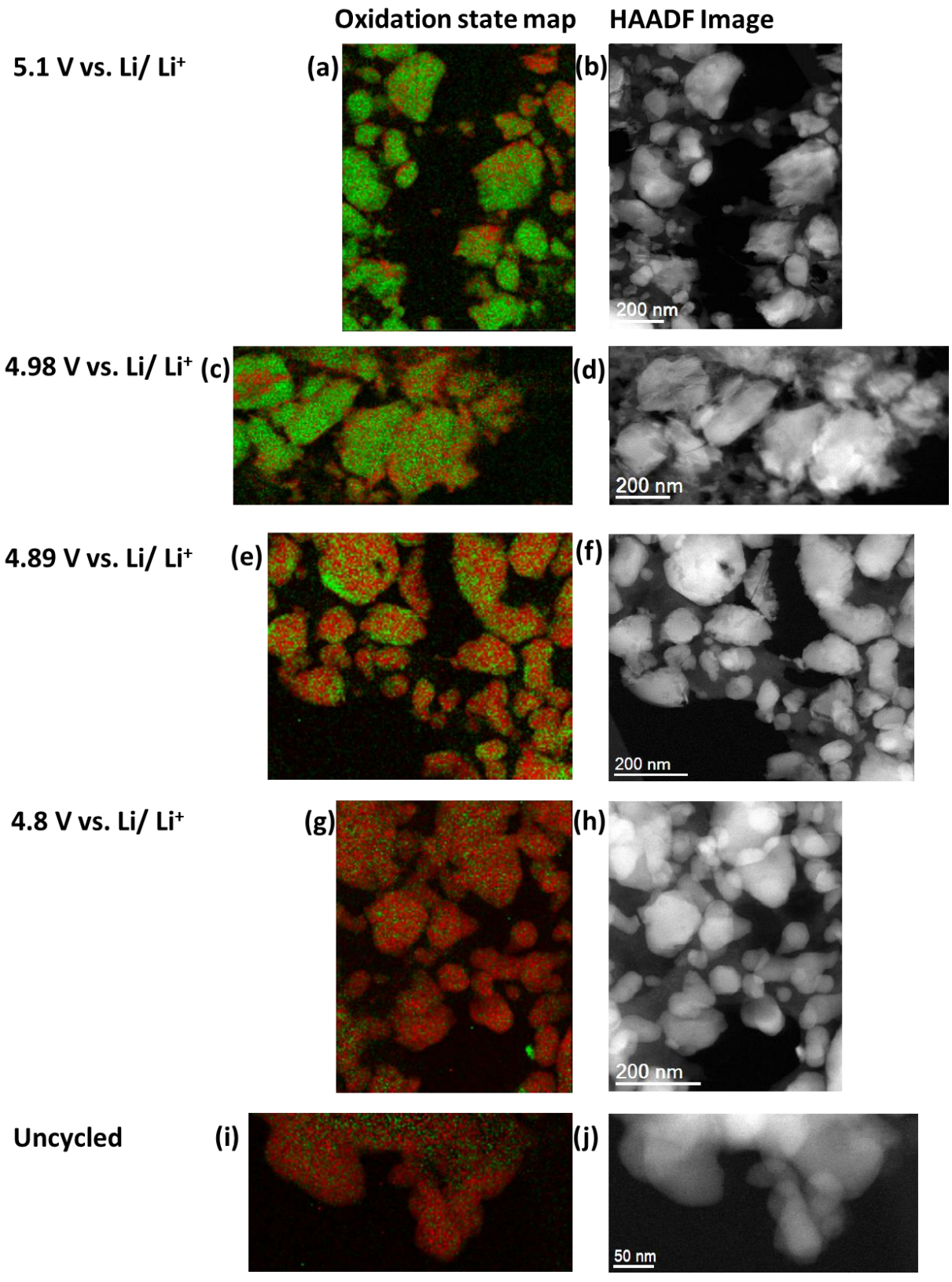

Figure 6.3: EELS Co L-edge oxidation state maps (a, c, e, g, and i), and the corresponding HAADF images (b, d, f, h, and j) for electrodes cycled to different potentials. Red regions are best fit to the Co(II)-rich standard; green regions are best fit to the Co(III)-rich standard. All samples are micro-tomed except for the uncycled sample (i, and j).

The EELS oxidation state maps in Figure 6.3 represent the Co(II)-rich and Co(III)-rich regions which form in particles during cycling of $LiCoPO_4$. Figure 6.4 shows a schematic summary of the

observations in Figure 6.3. Initially, when the sample is uncycled, the sample is Co(II)-rich. Charging past the first peak in the differential capacity curve in Figure 6.1 (b), retains the Co(II)-rich sample. Co(III)-rich regions start to form after the second peak in the differential capacity curve, at 4.89 V vs. Li/ Li^+ curve, and continue to grow towards the centre of the particles at 4.98 V vs. Li/ Li^+. Finally, at high potentials (4.98 V vs. Li/ Li^+, and 5.1 V vs. Li/ Li^+), a Co(II)-rich region begins to form on the surface of the particles.

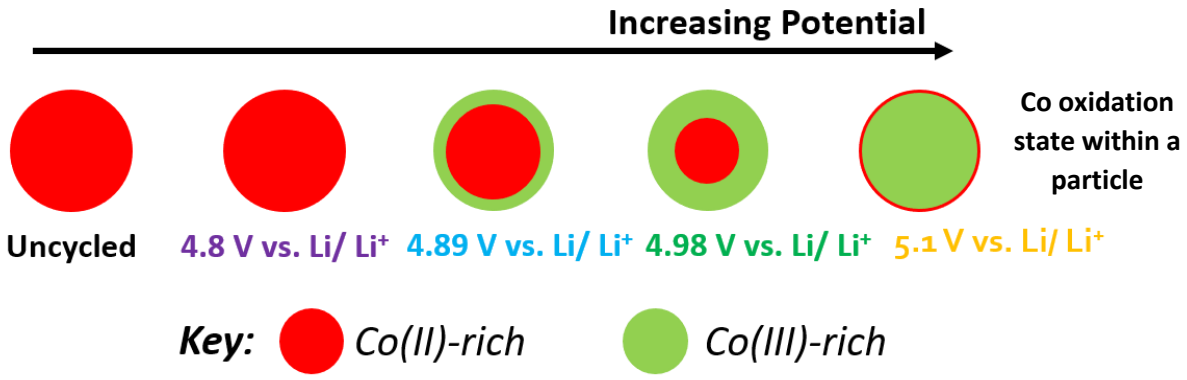

Figure 6.4: Schematic showing the lithiation mechanism trends shown by the EELS oxidation state maps in Figure 6.3. Green- Co(III)-rich (the charged state), red- Co(II)-rich (the discharged state).

Quantification of the Co(II) and Co(III)-rich regions was performed using the method described in 5.3.4 and is shown in Table 6.3. The averages shown in Table 6.3 were calculated across 3 areas of sample. Errors quoted in Table 6.3 are the standard deviations of the Co(II) %, Co(III) %, and average residual of the sampled regions. Only one region of uncycled electrode was analysed, hence standard deviation was not calculated for this sample. The average residual represents the unfitted signal, and represents the largest error produced by MLLS fitting. The average residuals in Table 6.3 are low, and have a low spread, indicating that the MLLS fitting results are reliable. Table 6.3 clearly shows that the proportion of Co(III)-rich areas increases with increasing charging potential.

Comparing the values in Table 6.3 to the XRD phase proportions in Table 6.2, the proportion of Co(III)-rich and Co(II)-rich areas are similar, and within the error limits. XRD is a bulk sample technique, therefore it is appropriate to use the standard deviation of the Co(III), and Co(II)-rich proportions calculated from different sample regions to aid comparison to XRD data as the standard deviation represents the spread across the sample. For example, 58.1(3) % of the sample was found to be $CoPO_4$ by XRD, whereas 55 ± 6 % of the sample was found to be Co(III)-rich using oxidation state mapping quantification for the 4.98 V vs. Li/ Li^+ sample.

Table 6.3: Quantification of the proportion of Co(II) and Co(III)-rich regions on EELS Co-oxidation state maps

Potential (V vs. Li/ Li^+)	Average Co(II)-rich (%)	Average Co(III)-rich (%)	Average Residual (%)
Uncycled	98	2	12
4.8	84 ± 2	16 ± 2	10 ± 1
4.89	74 ± 2	26 ± 2	3 ± 3
4.98	45 ± 6	55 ± 6	4 ± 1
5.1	38 ± 10	62 ± 10	7 ± 1

As there were dissimilarities between the XRD data in Figure 6.2, and the EELS oxidation state mapping data in Figure 6.3, SAED was performed to better correlate microstructural changes with

the observed oxidation state changes. As shown by Figure 6.2, no new XRD reflections occur for the $Li_{2/3}CoPO_4$, and $CoPO_4$ phases compared with $LiCoPO_4$, therefore different phases indexed using SAED were indexed based on lattice parameter changes. The phases will be referred to as $LiCoPO_4$, $Li_{2/3}CoPO_4$, and $CoPO_4$, but as the pdf cards refinements were performed with corresponded to these phases, (explained in 5.4.2.3), Li occupancy was not refined. The crystallographic phase was identified using the lattice parameter method described in 5.4.2.3.1.

Figure 6.5 (a) shows a TEM image of the uncycled electrode on the [-1 2 -1] zone axis. The planes associated with the diffraction spots in Figure 6.5 (b) are labelled. The planes were labelled by measuring the interplanar distances in Figure 6.5 (a), and comparing them to the d-spacings measured on the SAED pattern in Figure 6.5 (b). This method was repeated for the images in Figure 6.6, and Figure 6.7.

Figure 6.5 (a) shows the amorphous carbon coating on the outside of the $LiCoPO_4$ particles. The SAED pattern in Figure 6.5 (b) has been indexed to $LiCoPO_4$ [-1 2 -1] zone axis. 3 other SAED patterns taken on the sample were also indexed to $LiCoPO_4$. The result correlates with the XRD pattern in Figure 6.2 uncycled electrode being 100 % $LiCoPO_4$. The presence of $LiCoPO_4$ confirms the red Co(II)-rich oxidation state mapping in Figure 6.3 (g), is due to $LiCoPO_4$. The interplanar distance (0.42 nm, d_{hkl} (-1 0 1)) measured in the TEM image in Figure 6.5 (a) remain constant across the crystal, indicating the particle is a single crystal of $LiCoPO_4$, with a carbon coating.

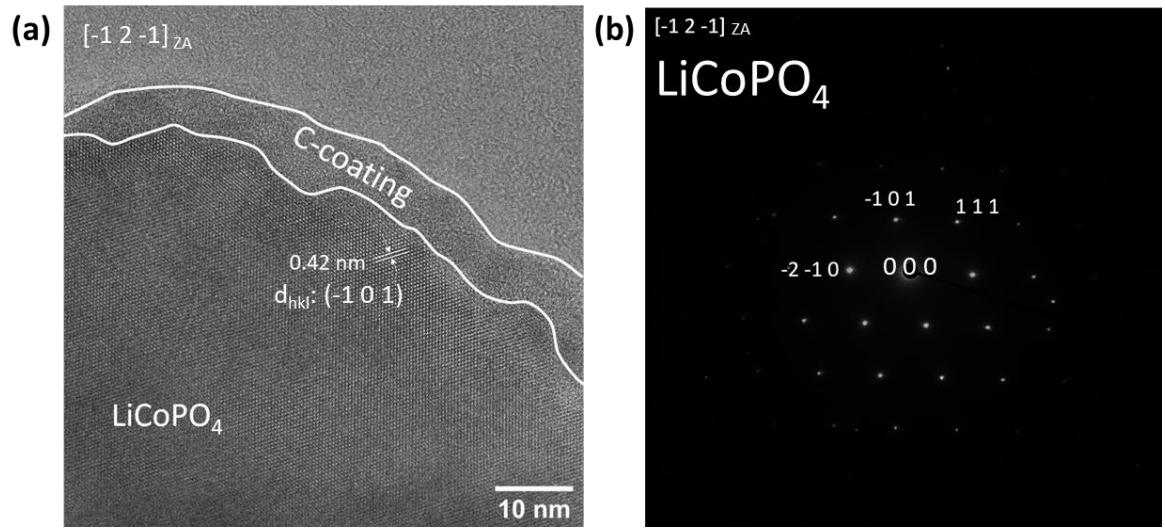

Figure 6.5: (a)- High resolution TEM image of an uncycled $LiCoPO_4$ electrode particle, and (b) the indexed SAED associated with (a). Images reproduced with permission from [8]*. Copyright, 2020, the American Chemical Society.*

A TEM image of a 4.89 V vs. Li/ Li^+ charged particle is shown in Figure 6.6 (a). The particle was indexed using the fast fourier transform (FFT) in Figure 6.6 (b) to the $[2\ -5\ 1]_{ZA}$ zone axis, and identified as $LiCoPO_4$, agreeing with the XRD pattern in Figure 6.2 which shows 100 % $LiCoPO_4$ reflections.

Indexing using the FFT can be unreliable as any astigmatism in the image can cause the d-spacings calculated from the FFT to be incorrect as the FFT is stretched. The FFT in Figure 6.6 (b) is slightly stretched (shown by the central ring being oval-shaped), so it is likely there is some error in the d-spacings. The zone axis is likely to be correct as the pattern correlated with crystal maker modelling of the expected $[2\ -5\ 1]_{ZA}$ SAED pattern.

Figure 6.6 (d) shows a SAED pattern taken from a different region of the 4.89 V vs. Li/ Li^+ charged particle, indexed to the $[-2\ 4\ 6]_{ZA}$ zone axis and identified as $Li_{2/3}CoPO_4$. Figure 6.6 (e) shows a SAED pattern of a 4.91 V vs. Li/ Li^+ indexed to the $[-2\ 0\ 4]_{ZA}$, and also identified as $Li_{2/3}CoPO_4$. Although not shown in Figure 6.2, XRD patterns collected at 4.91 V vs. Li/ Li^+ contained 100 % $LiCoPO_4$ reflections.

The presence of $Li_{2/3}CoPO_4$ is in disagreement with the XRD pattern in Figure 6.2 which shows 100 % $LiCoPO_4$ reflections. However, the 4.89 V vs. Li/ Li^+ oxidation state map in Figure 6.3 (e) shows a mixed oxidation state for the bulk of the particles imaged. The results suggest trace amounts of $Li_{2/3}CoPO_4$ were present at 4.89 V vs. Li/ Li^+, and 4.91 V vs. Li/ Li^+, but the proportion of $Li_{2/3}CoPO_4$ was not high enough to be reflected in the XRD patterns.

Figure 6.6 (b) is a blown up TEM image of the edge of the $LiCoPO_4$ particle in the TEM image in Figure 6.6 (a) (from an electrode charged to 4.89 V vs. Li/ Li^+). The blown-up image shows the carbon coating, and a layer with a slightly different contrast to the bulk. The structure is less well defined in the layer (Figure 6.6 (b)). Figure 6.3 (e) shows a Co(III)-rich layer on the outside of the 4.89 V vs. Li/ Li^+ particles, although the lattice spacing does not vary across the particle. It is possible less well defined structure is evidence of a new phase forming, correlating with the Co(III)-rich layer in Figure 6.3 (e), and the presence of extra spots in the FFT pattern (circled red in Figure 6.6 (c)) which do not index to the $[2\ -5\ 1]_{ZA}$ suggests a different sub-structure within the particle. However, the recombination of elastically scattered beams to form TEM images can result in contrast changes due to thickness variation, so the layer may result from the section being thinner at the edges.

The planar spacing (d_{hkl}: (2 1 1), 0.31 nm) does not change across the particle in Figure 6.6. Table 5.4 shows that for some planes, the difference in d-spacing between the 3 phases, $LiCoPO_4$, $Li_{2/3}CoPO_4$, and $CoPO_4$ can be as low as 0.001 nm for the $LiCoPO_4$ to $Li_{2/3}CoPO_4$ transition, depending on the plane. 0.001 nm is smaller than the resolution of the TEM images shown here. Therefore, it is difficult to discern crystallographic structure changes based on the TEM images.

The presence of extra spots in the SAED patterns in Figure 6.6 (d), (e), and the FFT in Figure 6.6 (c) suggests a lack of long range order in particles charged to 4.89 V vs. Li/ Li^+, and 4.91 V vs. Li/ Li^+. The majority of the spots could not be indexed, however, a forbidden reflection (0 1 0) is present in the $[-2\ 0\ 4]_{ZA}$ in Figure 6.6 (e), suggesting incomplete destructive interference, or vacancies in the Li positions due to a partially de-lithiated sample (the Li de-lithiation direction is the [0 1 0] direction).

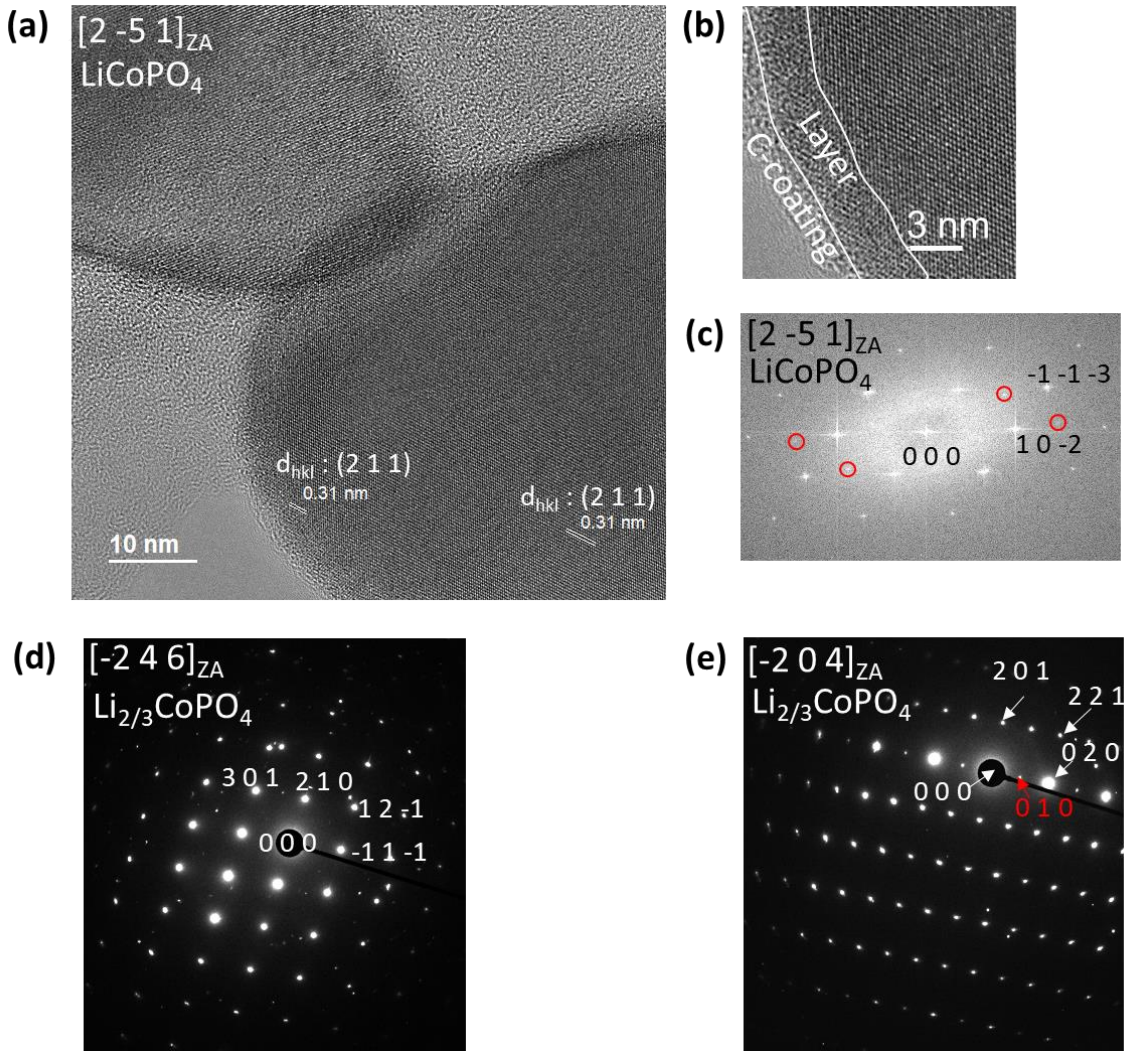

Figure 6.6: (a)- High resolution TEM image of 4.89 V vs. Li/ Li^+ $LiCoPO_4$ electrode particle, (b) blown up portion of (a), showing the edge of the particle, the carbon coating, and a layer showing poor definition of crystal structure at the surface, and (c) the fast fourier transform of the particle in the bottom right of (a) indexed to $[2\ -5\ 1]_{ZA}$, the FFT spots circled in red are not part of the $[2\ -5\ 1]_{ZA}$ pattern. (d) SAED pattern of a 4.89 V vs. Li/ Li^+ particle indexed to the $[-2\ 4\ 6]_{ZA}$ and identified as $Li_{2/3}CoPO_4$. (e) SAED pattern of a 4.91 V vs. Li/ Li^+ indexed to the $[-2\ 0\ 4]_{ZA}$. Forbidden reflections are labelled in red.

The SAED patterns in Figure 6.7 (b) and (d) show particles charged to 5.1 V vs. Li/ Li^+ are $Li_{2/3}CoPO_4$, and $CoPO_4$ respectively. This is in agreement with the XRD patterns in Figure 6.2, consistent with the green Co(III)-rich regions in Figure 6.7 (a) originating from $CoPO_4$.

The red 010 plane in Figure 6.7 (d) represents a forbidden reflection, suggesting incomplete destructive interference occurred during SAED collection.

The TEM image in Figure 6.7 (c) suggests that the $CoPO_4$ particles are uniform, with similar lattice spacings across the entire particle.

However, the TEM image in Figure 6.7 (a) shows some variation in contrast near the edge of the particle, which may indicate the formation of a surface phase, such as $CoPO_4$. At the magnifications imaged in Figure 6.7 (a), the difference between $d_{(2\ -1\ 0)}$ of $Li_{2/3}CoPO_4$, and $CoPO_4$ is too small (0.014 nm- see Table 5.4) to identify whether $CoPO_4$ is forming based on differences in lattice spacing.

The variation in intensity measurement requires the intensities to be reliable in the measurement region. As discussed above, where samples are thinner at the edge of particles, intensity can vary. Moreover, if 2 phases are present in the particle in Figure 6.7 (a), the corresponding diffraction pattern in Figure 6.7 (b) should contain secondary diffraction spots. Only one set of diffraction spots is visible on the [1 -2 3] diffraction pattern in Figure 6.7 (b).

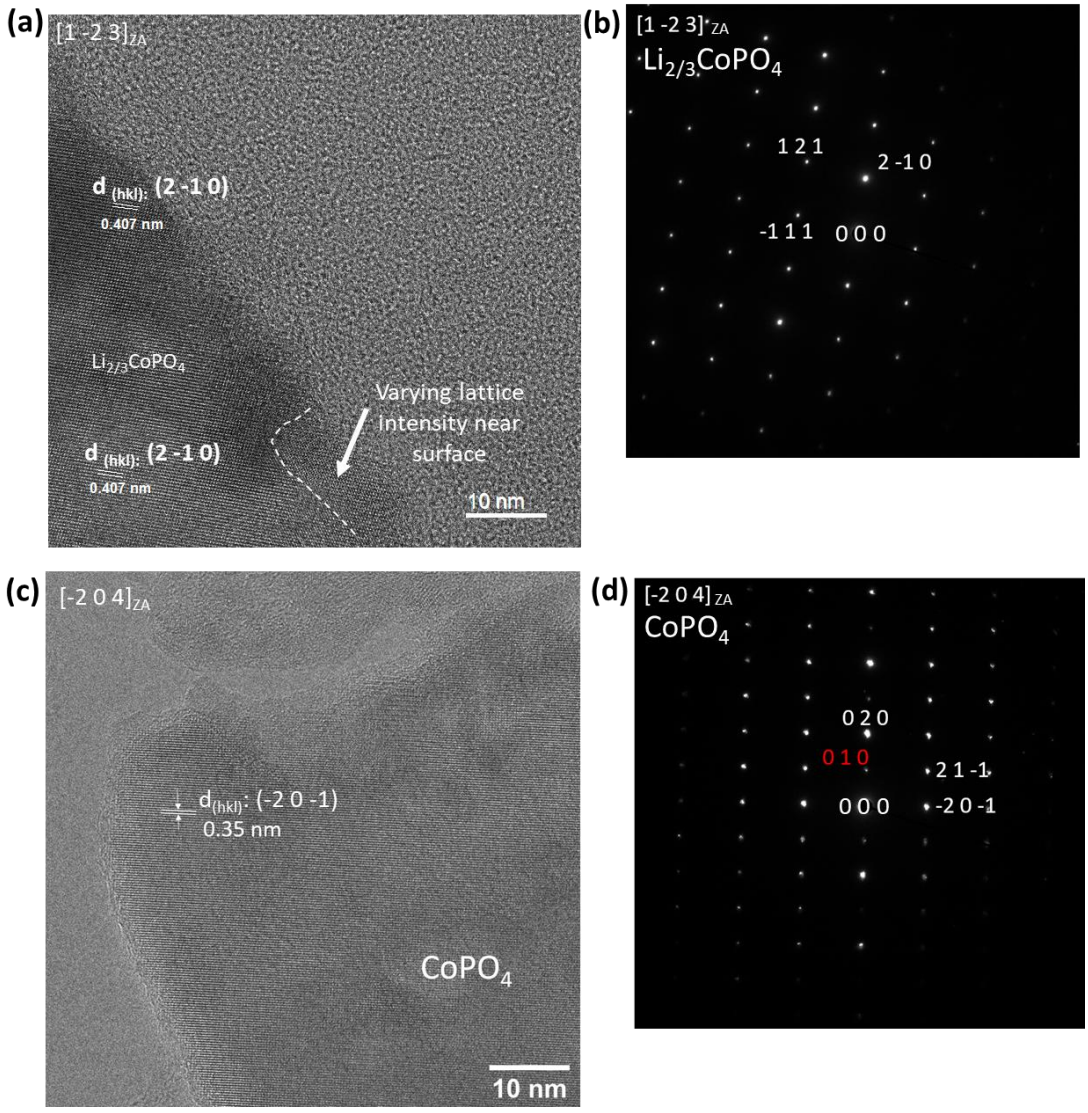

Figure 6.7: (a), and (c) High resolution TEM images of particles in a 5.1 V vs. Li/ Li^+ electrode, (b) the indexed SAED pattern associated with (a), and (c) the indexed SAED pattern associated with (c).

6.2.3 Valence state and structural characterisation of $LiCoPO_4$ at cycle 1-10

The previous results have considered the first charging cycle. However, Figure 6.8 (a) demonstrates that the gravimetric capacity of $LiCoPO_4$ cells drops significantly from 128 mAh g^{-1} to 14 mAh g^{-1} after 10 cycles. The purpose of this section is to use oxidation state mapping to establish why $LiCoPO_4$ experiences such a large drop in capacity after only 10 cycles.

Previously, the differential capacity curves were used to advise which potentials to halt charging at for EELS oxidation state mapping. To compare if the cells are undergoing similar phase transitions at later cycles, the differential capacity curves are compared (Figure 6.8 (b)).

Figure 6.8 (b) shows the differential capacity curves of the $LiCoPO_4$ samples used for oxidation state mapping. The first charge cycle on Figure 6.8 (b) has 2 clear peaks at 4.85, and 4.91 V vs. Li/ Li^+.

By the 5th charge cycle, 2 peaks occur on the charge differential capacity curve at 4.85, and 4.95 V vs. Li/ Li^+, however, the overall capacity is significantly lower. The area under peaks was found by integrating under the peaks, giving a gravimetric capacity of 23 mAh g^{-1} for the first peak, and 38 mAh g^{-1} for the second peak. The gravimetric capacities of the 5th cycle peaks are lower than the 1st cycle peaks (45 and 86 mAh g^{-1}).

Unlike the 1st cycle, and 5th cycle, the 2 peaks are not distinguishable on the 10th cycle gravimetric capacity curve. A small peak occurs at 5.0 V vs. Li/ $Li/^+$, however given the lack of peaks at 4.85, and 4.91 V vs. Li/ Li^+, it is unlikely this is a result of similar electrochemical processes.

(a)

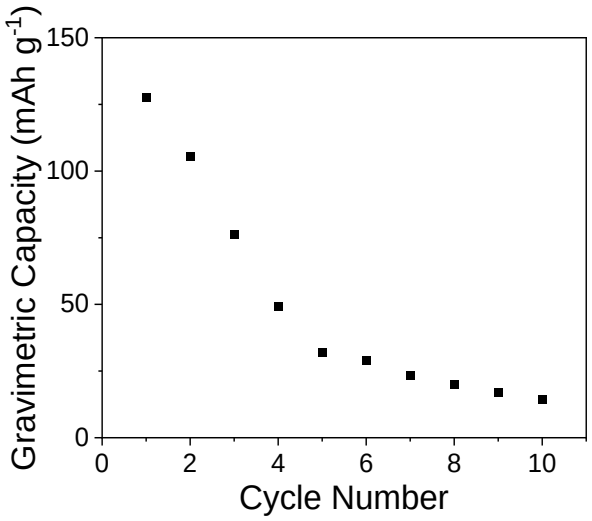

(b)

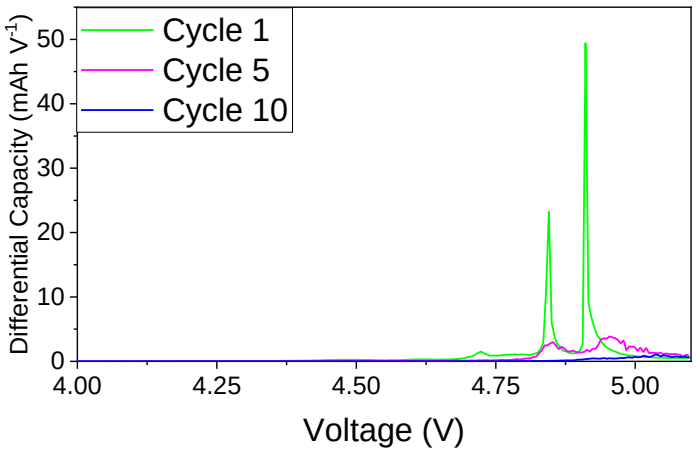

Figure 6.8: (a) Gravimetric capacity against cycle number, and (b) differential capacity curves for the samples mapped in Figure 6.10.

The changes in the differential capacity curves in Figure 6.8 imply the phases present at the end of charging may differ at longer cycle numbers. Ag Kα XRD patterns of uncycled electrodes, and electrodes charged to 5.1 V vs. Li/ Li^+ on the 1st, 5th, and 10th cycle (shown in Figure 6.9) were taken to investigate if the phases differ. The phases responsible for each reflection are marked on Figure 6.9, and the phase proportions are shown in Table 6.4.

Initially the uncycled electrodes are 100 % $LiCoPO_4$ (Figure 6.9). As the cycle number increases, the proportion of $CoPO_4$ (the de-lithiated phase), decreases until only $LiCoPO_4$ is present in the charged electrode. The observations in the XRD patterns correlate with the differential capacity curves in Figure 6.8 as the $CoPO_4$ transition peak isn't present in cycle 10, the $Li_{2/3}CoPO_4$, and $CoPO_4$ transition peaks have similar values for cycle 5, and the $CoPO_4$ transition peak is much larger in cycle 1.

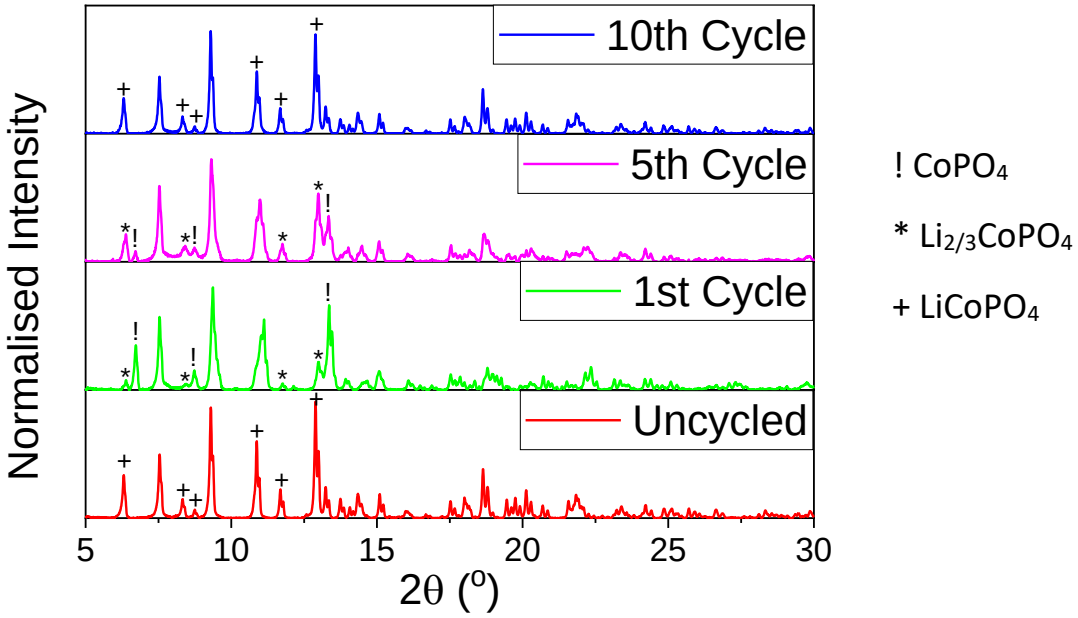

*Figure 6.9: Ag K-α XRD patterns of an uncycled electrode (red), and electrodes charged to 5.1 V vs. Li/ Li^+ on the 1st cycle, 5th cycle, and 10th cycle. + - reflections due to $LiCoPO_4$, * - reflections due to $Li_{2/3}CoPO_4$, ! – reflections due to $CoPO_4$.*

Table 6.4 shows the phase proportions, and unit cell dimensions calculated from the refinements of the XRD patterns in Figure 6.9. Errors were calculated using the methods described in 5.4.2.3. As stated above the uncycled, and 10th cycle electrodes diffraction peaks were 100 % $LiCoPO_4$. However, the unit cell of the 10th cycle electrode had longer unit cell dimensions in the a (0.03 %), and c (0.096 %) directions, and a slightly shorter b length (0.03 %). However, the changes are small.

$CoPO_4$, and $Li_{2.3}CoPO_4$ were present at the 1st and 6th cycles. The proportion of $Li_{2/3}CoPO_4$ increased from 41.9 % to 84.4 % from electrodes charged to 5.1 V vs. Li/ Li^+ on the 1st cycle to the 5th cycle. Similarly, the proportion of $CoPO_4$ decreased from 58.1 % on the 1st cycle, to 15.6 % on the 5th cycle electrode.

Similar to $LiCoPO_4$ from the uncycled electrode to the 10th cycle electrode, the unit cell dimensions increased for both $Li_{2/3}CoPo_4$ and $CoPO_4$ from the 1st cycle to the 5th cycle. The slight increase in unit cell volume may indicate an increase in defect formation, such as anti-site defects [9], atomic resolution STEM would be required to confirm this.

Table 6.4: Table showing the phase, phase proportions, and unit cell dimensions of phases in Figure 6.9.

Cycle	Phase	Phase Proportion (%)	Unit cell Dimensions (Å)			R_{wp} (%)
			a	b	c	
10th	$LiCoPO_4$	100.0(1)	10.206(2)	5.919(1)	4.703(1)	5.140
5th	$CoPO_4$ $Li_{2/3}CoPO_4$	15.6(3) 84.4(5)	9.57(2) 10.087(9)	5.78(1) 5.859(5)	4.76(2) 4.711(4)	6.74
1st	$CoPO_4$ $Li_{2/3}CoPO_4$	58.1(03) 41.9(3)	9.565(3) 10.07(1)	5.778(2) 5.853(7)	4.7597 4.704(6)	4.81
Uncycled	$LiCoPO_4$	100.0(1)	10.203(1)	5.9205	4.6985	5.049

To study the differences in lithiation mechanism between electrodes cycled to different cycle lives, EELS oxidation state maps were taken of electrodes charged to 5.1 V vs. Li/ Li^+ on the 1st, 5th, and 10th cycle (Figure 6.10). Green areas in Figure 6.10 are Co(III)-rich, whilst red are Co(II)-rich. The Co(III)-rich standard used was the Co(III)-rich oxidised standard in Figure 5.34 for the 1st cycle sample (Figure 6.10 (a)), and the Co(III)-rich new standard in Figure 5.26 for the 5th and 10th cycles. Different standards were used as the 5th cycle, and 10th cycle samples came aged samples made from older $LiCoPO_4$ powder. The XRD patterns collected in Figure 6.9 were also collected using electrode samples made from older $LiCoPO_4$ powder to ensure comparison.

Similar to Figure 6.3 (a) (an EELS oxidation state map of a different area, on the same sample), the oxidation state map of the electrode charged to 5.1 V vs. Li/ Li^+ on the first cycle shows a Co(III)-rich bulk, with red Co(II)-rich regions on the particle edges. A Co(III)-rich bulk is consistent with the XRD pattern in Figure 6.9 showing $CoPO_4$ present in a 1st cycle sample, and with the completion of the 2 differential capacity peaks in Figure 6.8.

The 5th cycle, and 10th cycle oxidation state maps in Figure 6.10 (d), and (f) are mostly red, indicating they are mainly Co(II)-rich. The presence of Co(II)-rich particles is consistent with the majority presence of $Li_{2/3}CoPO_4$ in the 5th cycle XRD pattern in Figure 6.9, and the presence of $LiCoPO_4$ in the 10th cycle XRD pattern, and with the lower capacity experienced by a 5th and 10th cycle electrode.

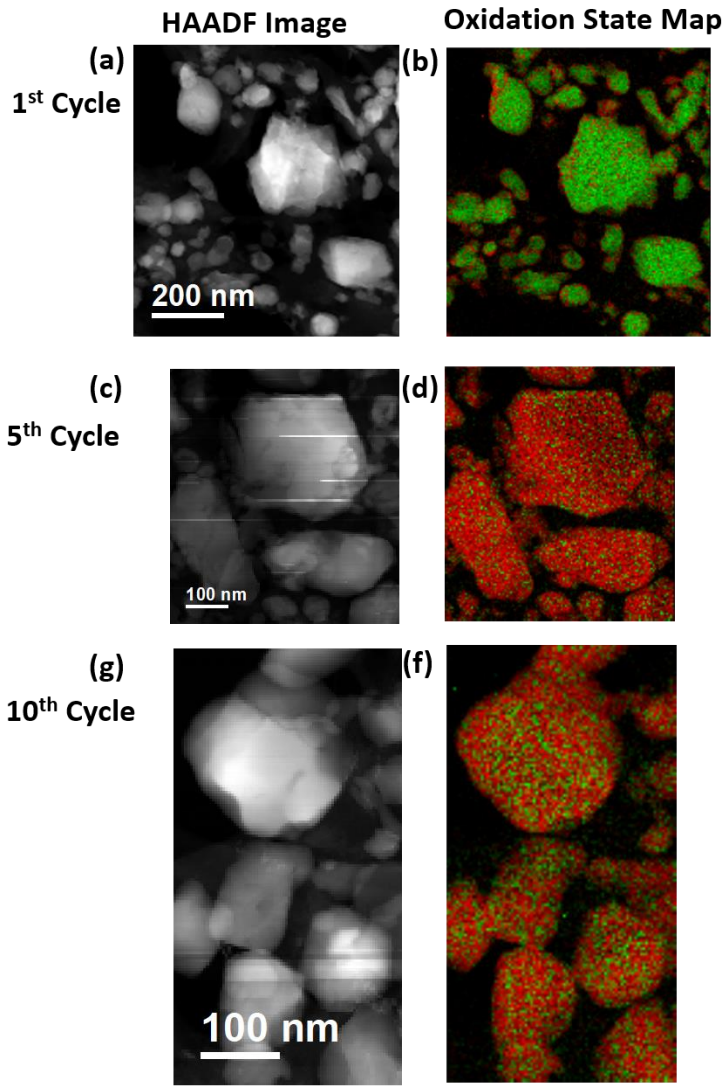

Figure 6.10: STEM HAADF images (a, c, and e), and the corresponding Co L-edge oxidation state maps (b, d, f), for electrodes charged to 5.1 V vs. Li/ Li^+ on the 1st cycle (a, and b), the 5th cycle (c, and d), and the 10th cycle (g, and f). Green- Co(III)-rich, red- Co(II)-rich.

However, the particles examined in the 10th cycle electrode in Figure 6.10 (f) have a greater proportion of green Co(III)-rich mixing than the 5th cycle electrode in Figure 6.10 (d). To confirm the proportion mismatch was not isolated to one region of sample, EELS Co L-edge oxidation state maps were taken from 4 different regions of sample and the proportions of Co(II), and Co(III)-rich regions in each map averaged using the quantification method outlined in 5.3.4. The aged Co(III)-rich reference in Figure 5.26 was used for quantification in Table 6.5.

The residual for the 5th, and 10th electrodes in Table 6.5 is higher compared to the 1st cycle residuals in Table 6.3. This is likely because the Co(III)-rich aged reference did not cover the entire EELS spectra collected during mapping.

Quantification demonstrates the proportion of Co(III) was greatest for the 1st cycle (51 ± 32 %), consistent with XRD peaks in Figure 6.9. However, the Co(III) proportion is greater for the 10th cycle (9 ± 6 %), compared with the 5th cycle (15 ± 3 %). This is surprising as the XRD patterns in Figure 6.9 suggest the 5th cycle electrode should contain a greater proportion of Co(III)-richer compounds ($Li_{2/3}CoPO_4$, and $CoPO_4$) than the 10th cycle electrode ($LiCoPO_4$).

Quantification was done by averaging 3 different regions, and the errors calculated by finding the standard deviations of Co(III), and Co(II) percentages, and the average residual percentage calculated from the 3 different regions (as described in 5.3.3). The standard deviations represent the spread across different regions. A standard deviation of 32 % on the first cycle indicates a large variation in de-lithiation across the electrode analysed, which was made from aged $LiCoPO_4$. This is consistent with the poor cyclability of aged $LiCoPO_4$ (see Figure 6.8 and Figure 5.27). Depending on the proximity to the current collector, Li diffusion may have been poorer to some regions of the electrode resulting in a wide variation in lithiation.

The average residual represents the unfitted signal, and is therefore an indicator of the quality of the fit for the regions analysed. The average residuals are larger for the aged samples, compared with the un-aged samples in Table 6.3, suggesting the fitting was poorer for the aged samples. The larger fitting error for the aged samples suggests the standards used for fitting may have required improvement. For example, a fresh Co(II) standard should have been collected from an uncycled aged $LiCoPO_4$ electrode.

The Al foil on the 1st, 5th, and 10th cycle samples was not imaged as it was not contained in the microtomed section, so it is not possible to investigate if a lower proportion of Co(III)-rich areas in the 5th cycle electrode (9 %) compared with the 10th cycle electrode (15 %) in Table 6.5, is due to the position of the particles relative to the current collector. As demonstrated in Figure 5.35, the position of the particles can influence the oxidation state mapping.

Table 6.5: Table showing the proportions of Co(II), and Co(III) in oxidation state maps taken from the 1st, 5th and 10th cycle electrodes, and the residual, unfitted signal.

Cycle Number	Average Co(II)-rich (%)	Average Co(III)-rich (%)	Average Residual (%)
1st cycle	49 ± 32	51 ± 32	13 ± 5
5th cycle	91 ± 6	9 ± 6	23 ± 9
10th cycle	85 ± 3	15 ± 3	19 ±4

To check that the changes in Co oxidation state mapping were also associated with changes to the Co L-edge, Co L-edges were extracted from Co(III)-rich regions on the samples in Figure 6.10 (see Figure 6.11). Figure 6.11 also includes the uncycled, Co(II)-rich standard (red), and the Co(III)-rich standards, collected from electrodes charged to 5.1 V vs. Li/ Li^+ on the 1st cycle for comparison with the 5th, and 10th cycle Co L-edges. The 1C aged standard was used for mapping of Figure 6.10 (f), and (d), and 1C fresh was used to map Figure 6.10 (b). The 1C aged, 1C fresh, and the uncycled standards have been discussed previously in 5.4.2.5, and 5.4.2.2.

The Co L-edge onset of the Co(III)-rich area signals for the 5th cycle (5C) and 10th cycle (10C) charged samples occurs at the same energy loss as the uncycled Co(II)-rich reference (at 779 eV) (see Figure 6.11). Moreover, both the 5C, and 10C samples have the multiplet hips on the L_3, and L_2 edges, present in the uncycled Co(II)-rich Co L-edge signal.

Despite both the 10C, and 5C samples containing Co(II)-rich characteristics, the 5C Co L-edge in Figure 6.11 contains more Co(II)-rich character than the 10C sample. The 5C sample contains a greater amount of intensity on the Co(II) maximum side of the Co L_3-edge (at 781 eV), than the 10C sample in Figure 6.11. The 10C sample, in contrast, has a similar intensity to the 1C fresh standard (Co(III)-rich) at 781 eV.

The 5C, and 10C samples also have Co(III)-rich characteristics. The maximum on the Co L_3-edge occurs the same energy loss as the 1C standards (at 782 eV) for both the 5C, and 10C samples.

The mixture between Co(III), and Co(II)-rich characteristics is consistent with the presence of $Li_{2/3}CoPO_4$ in the 5C sample, found using XRD (Figure 6.9). However, it is surprising the analysed particles from the 10C sample do not appear fully red Co(II)-rich, as diffraction peaks from the XRD (in Figure 6.9) found 10C samples to be 100 % $LiCoPO_4$. Moreover, it is surprising that the 5C Co L-edge, appears closer to the Co(II)-rich standard as the $Li_{2/3}CoPO_4$, and $CoPO_4$ (found in the 5C XRD pattern in Figure 6.9), contain more Co(III) than $LiCoPO_4$ found in the 10C XRD pattern in Figure 6.9. The results indicate that XRD does not pick up small regions of de-lithiation due to averaging across the bulk. The STEM-EELS analysis allows for analysis of small regional variation in lithiation.

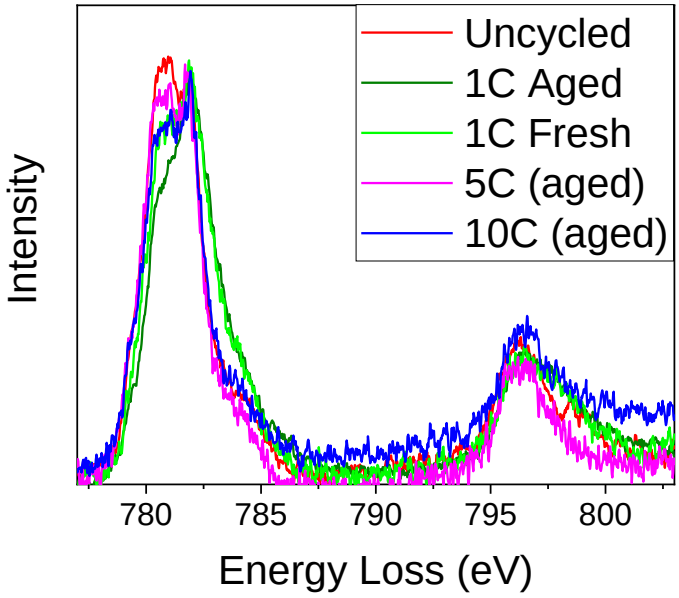

Figure 6.11: Co L-edge extractions from a Co(II)-rich area on an uncycled electrode (red), and Co(III)-rich areas of electrodes charged to 5.1 V vs. Li/ Li^+ on the 1st cycle (1C- dark green, and 1C- light green), the 5th cycle (5C- pink), and the 10th cycle (10C- blue). 1C new is the Co(III)-rich standard extracted from the sample made with older C-$LiCoPO_4$ powder sample in Figure 5.26, 1C old is the original Co(III)-rich edge in Figure 5.9. The samples mapped in Figure 6.10 required mapping with 1C new.

6.2.4 EELS O K-edge analysis

To confirm if Co-O bond hybridisation had occurred during cycling, the EELS O K-edge was also examined for the cycled electrodes. Figure 6.12 shows the O K-edge collected at 0.1 eV/ ch energy resolution across the entire spectrum image. The O K-edge intensities have been normalised to the 5C edge intensity (the least intense spectrum). As the O K-edges in Figure 6.12 are sum spectra over the entire spectrum images, they contain O K-edge signals from both Co(III)-rich and Co(II)-rich regions of sample.

Figure 6.12 shows that a pre-edge feature occurs before the O K-edge on the 1st cycle charged (1C) sample, which does not occur on any of the other charged samples. The pre-edge feature is also visible on the O K-edge standard collected from a first cycle Co(III)-rich area, shown in Figure 5.28.

The 5C, and 10C O K-edges appear identical to the uncycled electrode O K-edge. Unlike the O K-edge standard for the Co(II)-rich area in Figure 5.28, the uncycled, 5C, and 10C O K-edges in Figure 6.12 contain a shoulder at 541 eV. The shoulder at 541 eV was also observed on an uncycled electrode O K-edge in Figure 5.21 (b), where the particle was thicker.

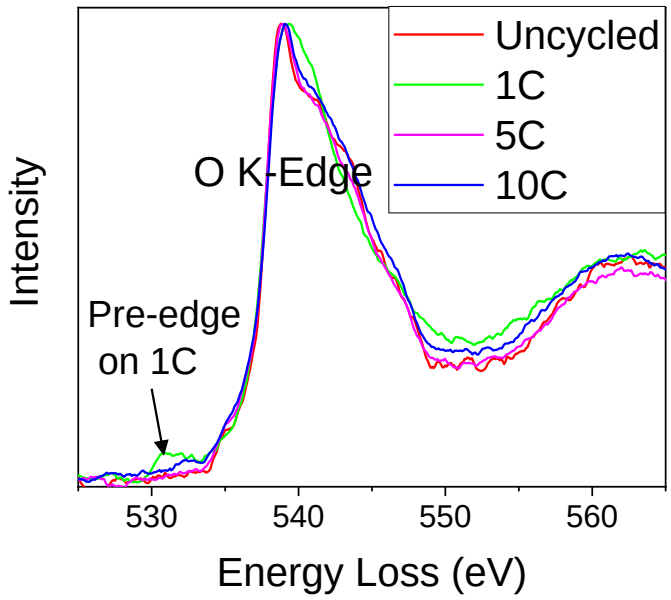

Figure 6.12: O K-edge spectra at 0.1 eV/ ch energy resolution extracted from an uncycled electrode, and electrodes charged to 5.1 V vs. Li/ Li^+ on the 1st cycle (1C- green), 5th cycle (5C- magenta), and the 10th cycle (10C- blue). The extractions were taken over the whole spectrum image so include signals from Co(II)-rich, and Co(III)-rich regions.

To check if the presence of the pre-edge feature on the O K-edge was exclusively associated with Co(III)-rich areas, O K-edge maps were generated and compared to Co L-edge maps (Figure 6.13). The Co L-edge standards used were the Co(III)-rich new standard, and the uncycled electrode Co(II)-rich standard in Figure 6.11. The O K-edge mapping was performed using the standards in Figure 5.28, where the green region represents a standard containing the pre-edge feature, and the red regions were better fit to a standard without the pre-edge feature shown in Figure 6.12, and Figure 5.28.

The maps in Figure 6.13 show that Co(III)-rich areas on different regions of a 5.1 V vs. Li/ Li^+ charged sample on the 1st cycle, correlate to regions which were fitted to an O K-edge standard containing the pre-edge peak. As the cobalt oxidation state in the samples in Figure 6.13 were fitted using the new Co(III)-rich standard (1C aged in Figure 6.11), it is unclear if the Co(III) match to the O K-edge pre-edge feature arises due to the greater Co(III) character of the new standard, or if the observation would have occurred for the older mapping shown in Figure 6.3. Previous literature modelling has found the available state for Co-O hybridisation to increase when Co is in the Co(III) valence state in $LiCoPO_4$ [6]. The green contrast in Figure 6.13 (b) appears darker due to the presence of one bright pixel. An X-ray spike on the EELS spectrum for the bright pixel caused a skew towards Co(III) for that pixel.

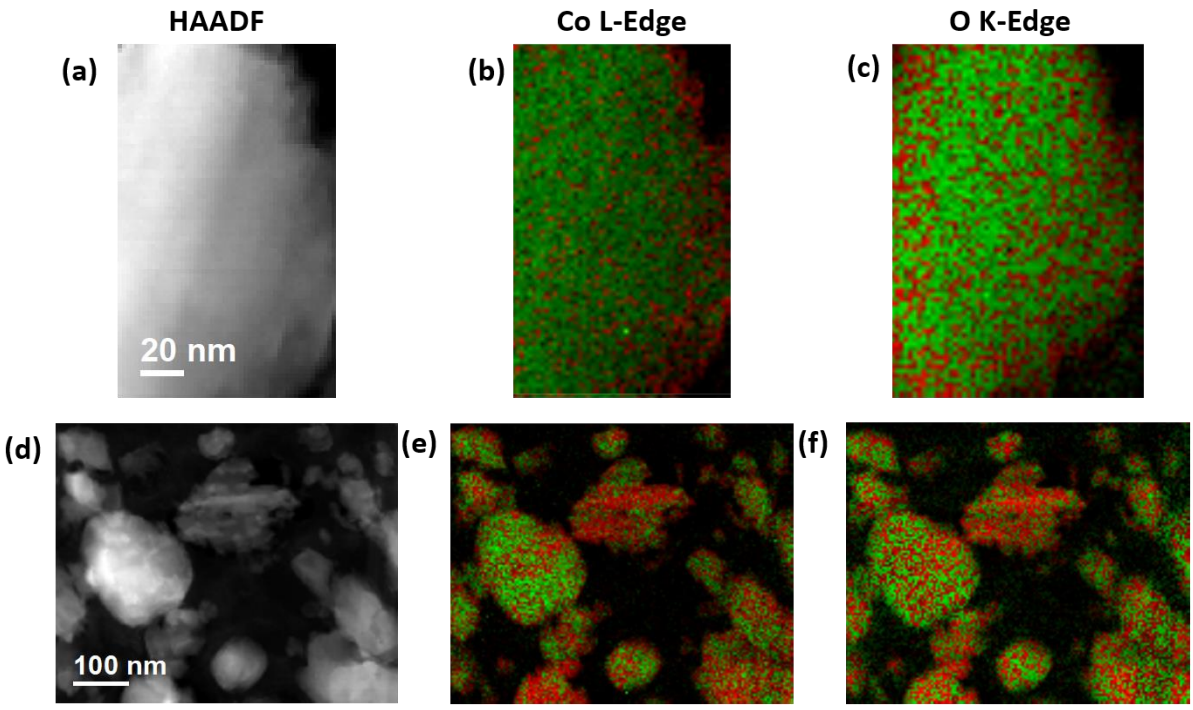

Figure 6.13: HAADF images (a, and d), and the corresponding Co L-edge maps (b, and e), and O K-edge maps (c, f), of different areas of an electrode charged to 5.1 V vs. Li/ Li^+ on the 1st cycle. On the Co L-edge maps: green- Co(III)-rich, red Co(II)-rich. On the O K-edge maps: green- O K-edge signal including the pre-edge feature extracted from Co(III)-rich regions of an electrode, red- O K-edge signal without the pre-edge feature extracted from Co(II)-rich regions of an electrode (standards in Figure 5.28).

As the EELS O K-edge pre-edge was not observed on the 5C, and 10C samples in Figure 6.12, it was expected that 5C O K-edge maps would appear entirely red. Figure 6.14 shows a Co L-edge map (b), and an O K-edge map of a region on the 5th cycle electrode (c). The maps were created using the same standards as the maps in Figure 6.13, hence green regions on the Co L-edge maps fit better to a Co(III)-rich standard, and green regions on the O K-edge maps fit better to an O K-edge standard containing the O K-edge pre-edge feature.

The green regions in the O K-edge map in Figure 6.14 (c), contains particles with a mixed green and red bulk, implying better fitting to a standard containing the O K-edge pre-edge feature. Comparing the O K-edge map to the Co L-edge map in Figure 6.14 (b), the green 'pre-edge' regions in Figure 6.14 (c), do not correlate to the green Co(III)-rich areas in Figure 6.14 (b).

The lack of correlation between the O K-edge, and Co(III)-rich maps may imply that mapping may be preferentially fitting to the larger O K-edge, rather than the pre-edge. O K-edge extractions from the greener regions in Figure 6.14 (c) show that the O K-edge pre-edge feature at 532 eV was not observed in any of the greener areas. Therefore the map in Figure 6.14 (c), was a poor fit to the O K-edge standards in Figure 5.28.

Despite the green occurring in the map in Figure 6.14 (c), the O K-edge signal correlates to the overall O K-edge signal for the 5C sample in Figure 6.12, which matches with the uncycled O K-edge signal.

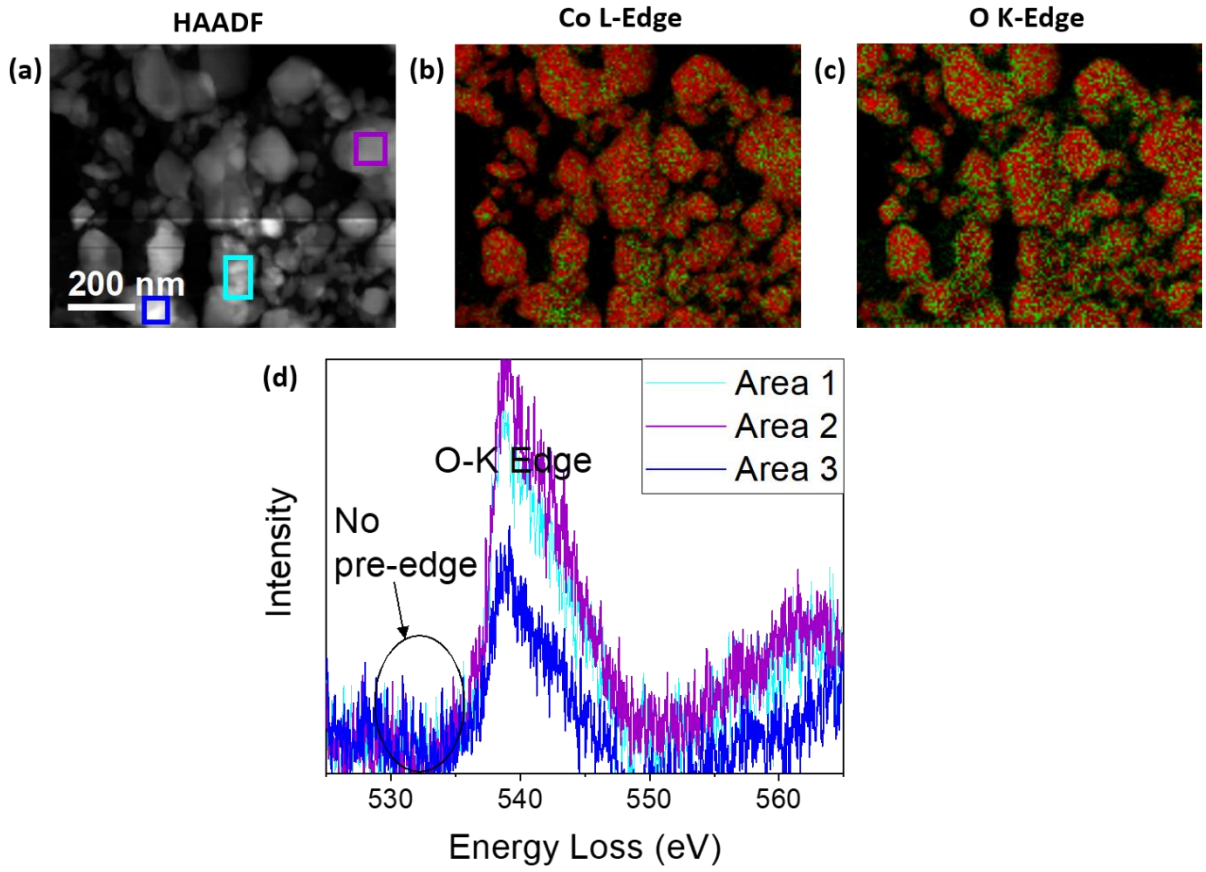

Figure 6.14: (a)- STEM-HAADF image, and the corresponding Co L-edge map (b), and O K-edge map (c) of a 5th cycle charged electrode. For the Co L-edge map: red- Co(II)-rich, and green- Co(III)-rich. O K-edge map uses the standards in Figure 5.28. Green- O K-edge signal extracted from a Co(III)-rich area, red- O K-edge signal extracted from a Co(II)-rich area. (d) the O K-edges extracted from the light blue, magenta, and dark blue regions in the HAADF image in (a).

To confirm the same mapping error did not occur for the first cycle O K-edge maps in Figure 6.13, O K-edge extractions are shown in Figure 6.15, and the pre-edge can be observed the regions corresponding to Co(III)-rich on the oxidation state maps. The extracted O K-edges are noisy, particularly in the region of the pre-edge. The sum spectrum in Figure 6.15 (b) is the sum of the O K-edge signals in the spectrum image in Figure 6.15 (a) which has been scaled to have the same intensity as the zone 2 O K-edge extraction. The O K-edge pre-edge is clearly visible on the sum spectrum, as well as the individual zone extractions in Figure 6.15 (b).

Compared to the pre-edge in Figure 5.28, the relative intensity of the pre-edge to the O K-edge is less in Figure 6.15 (b), indicating a lower degree of Co-O hybridisation in this region of sample. The O K-edge in Figure 5.28 was extracted from the region in Figure 6.13 (b). The proportion of Co(III) was higher in Figure 6.13 (b) (100 %, residual 19 %) compared with Figure 6.15 (a) (67 %, residual 9 %), suggesting the degree of Co-O hybridisation is associated with how Co(III)-rich a region is.

A split in the O K-edge peak at 542 eV energy loss is present on the extracted O-K edges from zones 1-4, resulting in a shoulder on the sum spectrum at 543 eV. It is not clear what the origin of the shoulder is, but literature has suggested that for octahedrally co-ordinated transmission metal ions, shoulders on the O K-edge in the 541-543 eV region can result from transitions to the unoccupied t_{1u} orbital [10]. Without further work modelling the O K-edge, and characterisation with XAS, or XANES it is not possible to confirm the origin of the shoulder. The focus here is on the presence of the pre-edge indicating Co-O hybridisation.

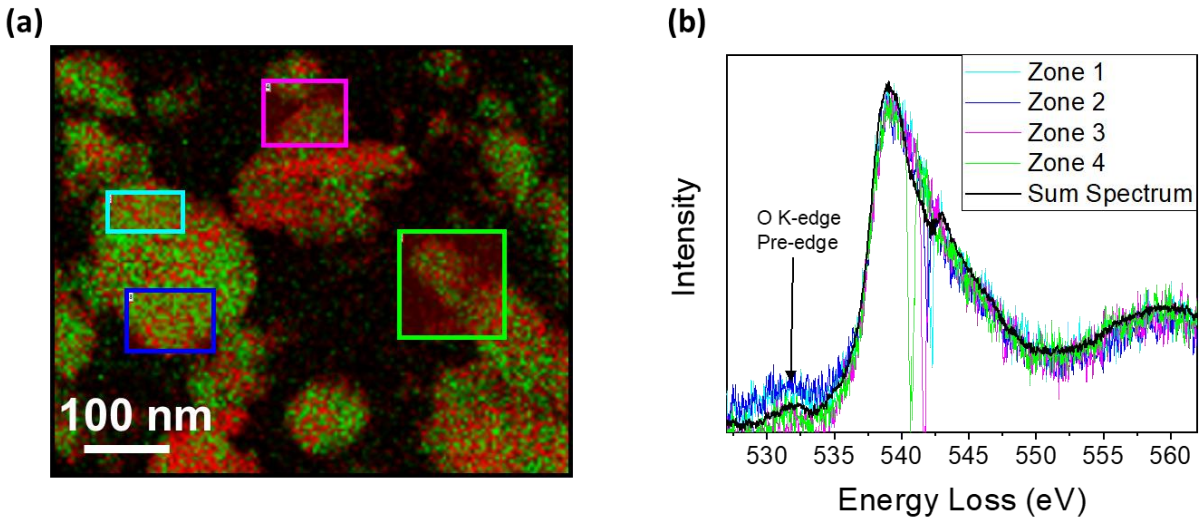

Figure 6.15: (a) Co L-edge map from Figure 6.13 (red- Co(II), green- Co(III)-rich), and the corresponding O K-edge extractions from the Co(III)-rich regions outlined in coloured boxes. The sum spectrum is the total O K-edge of the entire spectrum image.

Overall, if a pre-edge feature occurs in the O K-edge, the sample, and region of the sample, is more likely to be Co(III)-rich.

6.3 Discussion: Lithiation Mechanisms of $LiCoPO_4$

6.3.1 Phase Changes during the first cycle

The first cycle discharge capacity for the $LiCoPO_4$ electrodes was 128 mAh g^{-1} at 0.1C. 128 mAh g^{-1} is similar to capacities reported by [7], [11], [12].

In the first cycle 3 plateaus occur on the galvanostatic charge curve (Figure 6.1 (a)), accompanied by 3 peaks on the differential capacity curve (Figure 6.1 (b)). The peaks in Figure 6.1 (b) occurred at 4.4 V, 4.8, and 4.9 V vs. Li/ Li^+.

Peaks on differential capacity curves typically indicate electrochemical processes occurring in the cell, such as redox It is unlikely the first peak in the differential capacity curve in Figure 6.1 (b) contributes to the de-lithiation induced capacity change. The oxidation state map taken on electrodes charged to 4.8 V vs. Li/ Li^+ (a potential after the first peak in the differential capacity curve in Figure 6.1 (b)) is Co(II)-rich (Figure 6.3 (f)), suggesting that the electrode is either $LiCoPO_4$ or $Li_{2/3}CoPO_4$-rich. However, the XRD patterns show that electrodes charged to 4.89 V vs. Li/ Li^+, are have 100 % $LiCoPO_4$ diffraction peaks (Figure 6.2), suggesting that electrodes charged to lower potentials are also 100 % $LiCoPO_4$.

Strobridge et al. noticed a similar plateau on 0.1C $LiCoPO_4$ galvanostatic charge curves at 4.4-4.8 V vs. Li/ Li^+ [13]. Using *in-situ* XRD Strobridge et al. also noticed no obvious crystallographic change resulting from the plateau, suggesting that the plateau may result from slight de-lithiation, with no accompanying phase change, or from electrolyte reactions [13]. No crystallographic phase changes were noticed in this work (as shown by XRD in Figure 6.2). However, quantification of the Co L-edge signal extracted from oxidation state maps showed the Co L-edge at the 4.8 V vs. Li/ Li^+ was proportionally less Co(II)-rich (84 %) than the uncycled electrode (98 %) (Table 6.3). The Co L-edge shifting to slightly more Co(III)-rich character suggests some de-lithiation occurred by 4.8 V

vs. Li/ Li^+, without an accompanying crystallographic phase change, resulting in the peak in the differential capacity curve in Figure 6.1 (b) at 4.4 V vs. Li/ Li^+.

The specific capacity calculated by integrating under the 4.8 V, and 4.9 V vs. Li/ Li^+ differential capacity peaks in Figure 6.1 (b) was 154 mAh g^{-1}, near to the theoretical capacity of 167 mAh g^{-1} [2], indicating that the 2 peaks are likely to result from de-lithiation phase change mechanisms [13]. Palmer et al. Strobridge et al. and Bramnik et al. noticed plateaus in the charge curve at similar potentials to those observed in Figure 6.1 (a), and used *in-situ* XRD techniques to associate the plateaus with phase changes [7], [13], [14].

[7], [13], [14] suggested that the plateau at 4.8 V vs. Li/ Li^+ results from the $LiCoPO_4 \rightarrow Li_{2/3}CoPO_4$ phase transition. The oxidation state map of the electrode charged to 4.89 V vs. Li/ Li^+ in Figure 6.3 (e) shows that the bulk of the electrode have a mixed Co(III), Co(II) oxidation state (consistent with the formation of $Li_{2/3}CoPO_4$). Quantification of the Co L-edge extracted from 3 oxidation state spectrum images of different regions on the 4.89 V vs. Li/ Li^+ electrode showed the Co L-edge was 74 ± 2 % Co(II)-rich, with an average residual (representing un-fitted signal) of 3 ± 3 %. 66.6 % is the theoretical proportion of Co(II) in the $Li_{2/3}CoPO_4$ phase. 66.6 % is within the error margins of 74 ± 2 % when the residual unfit signal of 3 ± 3 %, which could be either Co(II), or Co(III), is considered. The quantification using EELS may be improved by not quantifying regions with negative fitting coefficients as either Co(II), or Co(III).

The discrepancy between the Co(II) proportion of $Li_{2/3}CoPO_4$, and the proportion calculated from the measured Co L-edges could be explained by uncertainty of the purity of the Co(III) reference discussed in 5.5.1. Moreover, potential partial discharging prior to cell disassembly (consequence of an *ex-situ* technique) may have resulted in the cell becoming more Co(II)-rich. Self-discharging of $LiCoPO_4$ electrodes has been previously noted in the literature [15], [14].

The XRD pattern of electrodes charged to 4.89 V vs. Li/ Li^+ shows that the electrodes are 100 % $LiCoPO_4$ (Table 6.2, and Figure 6.2). The SAED, and FFT patterns of electrodes charged to 4.89, and 4.91 V vs. Li/ Li^+ (after the 4.8 V specific capacity peak), are a mixture of $LiCoPO_4$, and $Li_{2/3}CoPO_4$ (Figure 6.6 (c), (d), and (e)) suggesting trace $Li_{2/3}CoPO_4$ is present after the 4.8 V vs. Li/ Li^+ peak.

The lack of $Li_{2/3}CoPO_4$ peaks in the XRD pattern in Figure 6.2 may also have been because the experiment was controlled by stopping the electrodes from charging once a specific potential was reached. However, comparison between the different *ex*-situ characterisation techniques used was difficult. As discussed in 5.5.1, stopping the electrodes once a specific lithium content (measured by specific capacity) had been reached may have resulted in more consistent results between the different *ex-situ* characterisation techniques, as self-discharge, and different cell resistances may have caused the lithium content to differ.

Refinement results presented in this theses show the $LiCoPO_4$ to $Li_{2/3}CoPO_4$ phase transition involves lattice parameter shrinkage in the a, and b direction of 1.3 %, and 1.1 % respectively, and a growth of 0.1 % in the c direction (Table 5.2). The calculated unit cell values in Table 5.2 were similar to those in literature [7], [14]. $LiCoPO_4$ maintained pnma symmetry throughout de-lithiation Figure 6.9. Li occupancy was not refined here, however Strobridge *et al.* presented detailed work identifying the structure of $Li_{2/3}CoPO_4$. Li in $Li_{2/3}CoPO_4$ is distributed among 2 Li sites in a superlattice (a x 3b x c), the 4 Liα sites are surrounded by 6 Co^{2+} ions, and the 8 Liβ sites are surrounded by 3 Co^{2+}, and $3Co^{3+}$ ions [13]. The stoichiometric composition is $Li_{2/3}Co(2/3\ Co^{2+}, 1/3\ Co^{3+})PO_4$ [13]. Li is distributed among the Li sites as a disordered sub-lattice of 6 different vacancy environments [13]. The presence of the forbidden reflection (0 1 0) in the $Li_{2/3}CoPO_4$ pattern in

Figure 6.6 (d) may be evidence of the disordered Li sub-lattice as Li diffuses out of the [0 1 0] direction, hence Li sites are present on the (0 1 0) plane.

The XRD patterns in Figure 6.2 showed that $Li_{2/3}CoPO_4$, and $CoPO_4$ were present in electrodes charged to 4.98 V vs. Li/ Li^+, and 5.1 V vs. Li/ Li^+. $Li_{2/3}CoPO_4$, and $CoPO_4$ were also found at 5.1 V vs. Li/ Li^+ using SAED (Figure 6.7 (b), and (d)). 4.98 V vs. Li/ Li^+, and 5.1 V vs. Li/ Li^+ occurs after the 4.9 V vs. Li/ Li^+ peak in the differential capacity curve in Figure 6.1 (b), suggesting the peak results from the $Li_{2/3}CoPO_4 \rightarrow CoPO_4$ phase transition. [7], [13], [14] also found the plateau at 4.9 V vs. Li/ Li^+ to result from the $Li_{2/3}CoPO_4 \rightarrow CoPO_4$ phase transition.

Table 6.2 shows that the proportion of $CoPO_4$ increases as at higher potentials (from 58.1 % at 4.98 V vs. Li/ Li^+ to 79.5 % at 5.1 V vs. Li/ Li^+). The oxidation state map in Figure 6.3 (a) shows Co(II)-rich regions on a 5.1 V vs. Li/ Li^+ electrode. The XRD, and oxidation state mapping results indicate the electrodes were not fully charged at 5.1 V vs. Li/ Li^+. Moreover, the increase in the proportion of $CoPO_4$ at higher potentials shown in Table 6.2 suggests that greater overpotentials help to drive the $Li_{2/3}CoPO_4 \rightarrow CoPO_4$ phase change. Similar results have been noted in literature. Lapping et al. found $LiCoPO_4$ had to be charged to 5.3 V vs. Li/ Li^+ for phase pure $CoPO_4$ [6], and Bramnik similarly noted that an overpotential had to be applied to achieve phase pure $CoPO_4$ [5].

Overall, the results indicate that phase transitions occur at the 4.8 V vs. Li/ Li^+, and the 4.9 V vs. Li/ Li^+. The results show the 4.8 V vs. Li/ Li^+ plateau resulted from the $LiCoPO_4 \rightarrow Li_{2/3}CoPO_4$ transition, and the 4.9 V vs. Li/ Li^+ plateau resulted from the $Li_{2/3}CoPO_4 \rightarrow CoPO_4$ phase transition.

XRD refinement of the charged phases ($Li_{2/3}CoPO_4$, and $CoPO_4$) was difficult as the overall intensity of the XRD patterns decreased for the charged phases. This may have occurred due to different packing densities in the XRD capillary tubes. [3] also noted a decrease in the intensity of charged phases of $LiCoPO_4$, causing refinement difficulties, and attributed the phenomenon to reduced long-range order. The presence of extra spots in the FFT, and SAED patterns in Figure 6.6 (c), (d), and (e) suggest a reduction in long-range order. For the SAED pattern, the extra spots may result from diffraction from more than one particle, however, the FFT in Figure 6.6 (c) was extracted from 1 particle specifically, with poor lattice contrast at the edges in Figure 6.6 (b). The TEM images of the charged particles in Figure 6.7 (a), and (c) show poor lattice contrast at the particle surfaces, possibly resulting from reduced long-range order within the particles, but more likely a result of thinner sample at the electrode surface.

Indexing the SAED patterns in Figure 6.7 (b), and (d), was also challenging due to the existence of forbidden reflections in the SAED patterns, for example the 010 spot in Figure 6.7 (d). Crystal maker modelling showed the presence of more, or less, lithium does not influence the appearance of the forbidden reflections. The forbidden reflections likely occurred because SAED was performed on microtomed electrodes which were very thin (80 nm), and therefore may have caused double diffraction.

However, [13] suggested that Li in the partially de-lithiated states of $Li_{2/3}CoPO_4$ is distributed around a super-lattice, consistent with the presence of (0 1 0) on the $Li_{2/3}CoPO_4$ SAED pattern in Figure 6.6 (d). The 010 spot on the $CoPO_4$ SAED pattern in Figure 6.7 (b) is possibly the result of a super-lattice reflection due to Li remaining in the lattice [5], [6]. The alternating contrast may therefore be evidence of partial de-lithiation. Li occupancy was not refined here, so $CoPO_4$ (the fully de-lithiated phases) was identified purely based on lattice parameter changes.

As already discussed in 5.5.1, the phases were identified using SAED by comparing calculated d-spacings, which could be very small (for example, the 102 spot has a calculated d-spacing of 0.229,

0.229, and 0.231 nm for $LiCoPO_4$, $Li_{2/3}CoPO_4$, and $LiCoPO_4$ respectively) as Pnma symmetry was maintained throughout de-lithiation. The d-spacing similarity was particularly problematic for identifying $Li_{2/3}CoPO_4$ from $LiCoPO_4$ as the unit cell values are similar (Table 5.2). The SAED error may have led to difficulties identifying the $Li_{2/3}CoPO_4$ phase after the 4.8 V plateau on the differential capacity curve in Figure 6.1 (b).

6.3.2 First Cycle de-Lithiation Mechanisms

As the phase changes and electrochemistry correlated well with literature, the Co oxidation state maps in Figure 6.3 were used to investigate the $LiCoPO_4$ de-lithiation mechanisms during the first charge cycle.

For the first cycle oxidation state maps in Figure 6.3, red regions represent Co(II)-rich regions, and green regions represent Co(III)-rich regions. As $Li_{2/3}CoPO_4$ was confirmed as the only Co(II)-rich phase present in the 4.98 V, and 5.1 V vs. Li/ Li^+ charged samples, Co(II) regions (red) on the 4.98 V, and 5.1 V vs. Li/ Li^+ maps in Figure 6.3 (a), and (c), are likely to be $Li_{2/3}CoPO_4$. $Li_{2/3}CoPO_4$ could not be distinguished from $LiCoPO_4$ due to the Co L-edge (Figure 5.17) signal being too similar to $LiCoPO_4$ for accurate MLLS fitting (see section 5.4.2.4).

Figure 6.3 shows that Co(III)-rich regions form on the outside of particles from 4.89 V vs. Li/ Li^+ (Figure 6.3 (e)), and grows inward toward the centre of the particle (Figure 6.3 (c)), until the bulk of the particle is Co(III)-rich at 5.1 V vs. Li/ Li^+ (Figure 6.3 (a)). This implies lithium is leaving the particles from the outside of the particles, leaving a Li-rich centre.

To check changes in Co oxidation state, mapped in Figure 6.3, correlated with structural changes, TEM images of the charged particles were taken. The TEM image of a 4.89 V vs. Li/ Li^+ charged particle indexed to $LiCoPO_4$ in Figure 6.6 (a) shows a region of differing contrast on the outside of particle, accompanied by extra spots on the fast fourier transform Figure 6.6 (b). Differing contrast on the edges of particles can be due to recombination of the elastically scattered electron beam in thinner regions of sample. However, the presence of extra spots in the FFT suggests a separate crystal structure, although they could not be indexed to confirm the phase, and the TEM image was not at high enough resolution to determine differences in lattice spacing. If the area of differing contrast is an extra phase in Figure 6.6 (b), the presence of an extra phase on the outside of particles correlates with Figure 6.3 (e) which suggests the outside of 4.89 V vs. Li/ Li^+ particles should be Co(III)-rich, and therefore have smaller lattice spacings. Further high resolution imaging and nano-diffraction would be required to confirm if an extra phase is forming on the outside of particles.

The 5.1 V vs. Li/ Li^+ charged particles are identified as $Li_{2/3}CoPO_4$ (Figure 6.7 (c)), or $CoPO_4$ ((Figure 6.7 (a)). The 100 % $Li_{2/3}CoPO_4$ particle is surprising as the oxidation state map of the 5.1 V vs. Li/ Li^+ electrode in Figure 6.3 (a) has a green Co(III)-rich bulk. The microtoming technique does mean there is uncertainty over whether particles have been fractured into smaller pieces, or the position of the particle- particles nearer the current collector have been shown to be more Co(II)-rich on 5.1 V vs. Li/ Li^+ electrodes (Figure 5.35), which may explain the discrepancy.

The TEM image in Figure 6.7 (a) of a $Li_{2/3}CoPO_4$ particle with smaller lattice spacing on the outside of the particle, 0.39 nm is the d-spacing d_{hkl}(2 -1 0) of $Li_{2/3}CoPO_4$, and 0.37 nm is the d-spacing d_{hkl}(2 -1 0) of $CoPO_4$, suggesting further de-lithiation from the edges of the particle. Further de-lithiation on the edges of the particle is consistent with Co(III)-rich regions forming on the edges of particles, shown by the oxidation state maps in Figure 6.3. However, the lattice spacings were measured based on the distance between intensity maxima. As explained, at edges of particles in

TEM images contrast variations can occur due to the recombination of elastically scattered electron beam which may have led to errors in lattice spacing measurement. Given the spacing difference is 0.02 nm the error is likely. Nano-diffraction would be required to confirm the presence of $CoPO_4$ on the outside of particles.

Anti-site defects could not be imaged (known to form in $LiCoPO_4$ [16]). Atomic resolution may help identify the structural changes causing shifts in Co oxidation state, particularly if it could be correlated with the oxidation state maps by performing both spectroscopy, and imaging in the same area.

Strobridge et al. reported that the $LiCoPO_4$/ $Li_{2/3}CoPO_4$/ $CoPO_4$ interface was coherent, suggesting the de-lithiation mechanism was a 2-phase formation mechanisms, along a coherent interface within a single $LiCoPO_4$ particle [3], rather than a domino cascade mechanism like in $LiFePO_4$ [17]. In a domino cascade model, the whole primary particle would be expected to rapidly shift from Co(II) to Co(III)-rich [3]. The existence of Co(III)-rich regions, and Co(II)-rich regions within the same particle, suggest the 2-phase coherent interface mechanism has also occurred in this study.

As the Co(III)-rich region forms on the edge of the particle, forming a lithium-rich region in the middle of the particle Figure 6.3, the $LiCoPO_4$ particles are de-lithiating with a shrinking-core mechanism with a coherent interface between the phases. Palmer et al. also proposed a shrinking-core mechanism for $LiCoPO_4$ using measurements with *in-situ* XRD [7]. However, this study presents direct imaging of the shrinking-core mechanism for the first time.

Figure 6.16 compares the shrinking-core mechanism proposed by Palmer et al. [7] with the de-lithiation trends observed using EELS oxidation state mapping in Figure 6.3. Figure 6.16 shows that for lower potentials, the shrinking-core mechanism proposed by Palmer is similar to that proposed in this study- lithium leaves from the outside of the particles causing them to transition from $LiCoPO_4$ to $Li_{2/3}CoPO_4$. However, at higher potentials, Palmer et al. propose that phase C ($CoPO_4$) nucleates in the $Li_{2/3}CoPO_4$ particles, forming a core of $CoPO_4$, as Li^+ migrates to the edge of the particle. *In-situ* XRD data from Palmer *et al.* suggested a $CoPO_4$ core nucleates, rather than forming on the edge as Li diffuses out of the particle because Vegard shifts (changes in lattice constant proportional to changes in composition) are consistent with a phase conversion mechanism, rather than a concentration polarisation [7]. A concentration polarisation mechanism would have resulted in $CoPO_4$ forming from the outside of a single particle.

The lithiation mechanism observed in the oxidation state maps in Figure 6.3, however show that $CoPO_4$ forms on the outside of the particles along a coherent interface, as a result of de-lithiation from the outside into the electrolyte. XRD is a bulk technique, therefore, although it can detect the formation of $CoPO_4$, the phases cannot be spatially resolved. Co L-edge mapping enables the phases to be spatially resolved, leading to a difference in the proposed mechanisms.

Li^+ in $LiCoPO_4$ diffuses along [010] [13] so differences in crystallographic direction may also have caused the discrepancy. XRD is a bulk averaging technique, and EELS was not done on zone axis oriented crystals so it is not possible to comment on the effect of crystallographic direction here.

(a) Shrinking Core de-lithiation mechanims proposed in this study

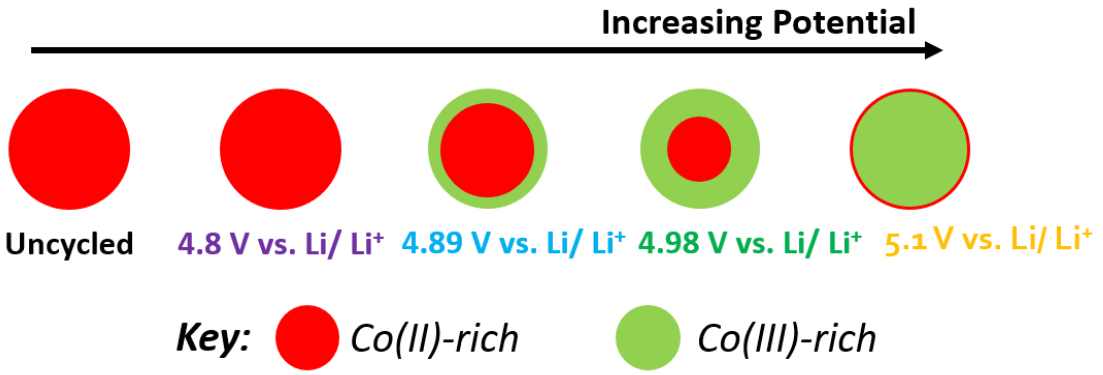

(b) Shrinking Core de-lithiation mechanism proposed by Palmer et al.

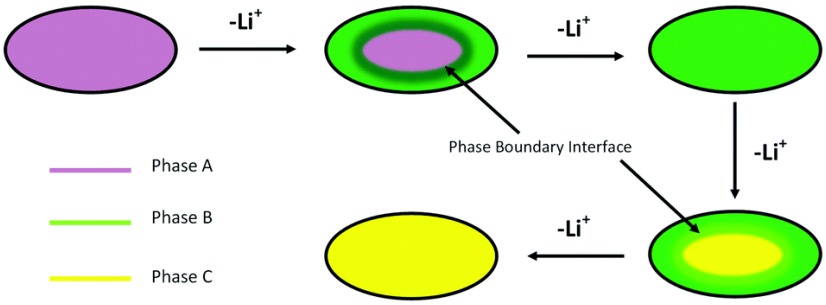

Figure 6.16: Comparison between the de-lithiation mechanisms proposed in this study using EELS Co L-edge oxidation state mapping (a), and by Palmer et al. using in-situ XRD. Adapted from Chem. Commun., 2016, 52, 14169, [7]*- Published by The Royal Society of Chemistry. In (b) Phase A- $LiCoPO_4$, Phase B- $Li_{2/3}CoPO_4$, and Phase C- $CoPO_4$.*

Figure 6.3 (a) also shows that a red Co(II)-rich region forming on the surface of the $CoPO_4$ particles at 5.1 V vs. Li/ Li^+. This is represented in Figure 6.16 (a) as a thin red region on the surface of the particle at 5.1 V vs. Li/ Li^+. SIMS depth profiling work in Figure 4.20 also shows a region of uncycled Li on the surface of charged particles which correlates to the presence of Co(II) on the surface of 5.1 V vs. Li/ Li^+ particles. SAED and TEM imaging do not identify if the Co(II) region on the surface results from the re-formation of $Li_{2/3}CoPO_4$. Manzi et al. noted in a study using XRD and fast fourier transform infra-red spectrometry (FTIR), that at high voltages, reaction with the electrolyte causes spontaneous re-incorporation of Li into the $LiCoPO_4$ lattice. Spontaneous reincorporation is likely in this case as the Co(II) surface feature is only observed at electrodes charged to 4.98 V, and 5.1 V vs. Li/ Li^+, around the breakdown potential of the $LiPF_6$ in EC/ DMC electrolyte [18].

Figure 4.20 also suggested Co diffusion into the C-coating. The presence of the Co(II)-rich band at the surface may also be further evidence for diffusion of Co into the C-coating, although it is unknown what valence state Co would take in this case.

Overall, Co L-edge mapping has, for the first time, spatially resolved the phases formed during de-lithiation of $LiCoPO_4$, demonstrating the material undergoes a shrinking-core de-lithiation mechanism. At high voltages, electrolyte degradation can cause re-incorporation of Li into the lattice, causing the Co oxidation state to shift from Co(III)-rich to Co(II)-rich.

6.3.3 Cycles 2- 10 De-lithiation Mechanisms

$LiCoPO_4$ underwent severe gravimetric capacity loss from 128 mAh g^{-1} to 14 mAh g^{-1} after 10 cycles at 0.1C (Figure 6.8 (a)). Severe capacity loss has also been previously reported in literature by [7],

[19]. The aim of the later cycles oxidation state mapping was to establish a cause for the severe capacity loss using oxidation state mapping.

The gravimetric capacity loss in demonstrated Figure 6.8 (a) was also associated with a loss of capacity under both peaks in the differential capacity curves in Figure 6.8 (b). By the fifth cycle, the gravimetric capacity contributed by the $LiCoPO_4 \rightarrow Li_{2/3}CoPO_4$ had dropped from 45 mAh g^{-1} to 23 mAh g^{-1}, whilst the $Li_{2/3}CoPO_4 \rightarrow CoPO_4$ peak had dropped from 86 mAh g^{-1} to 38 mAh g^{-1}. Moreover, by the 10th cycle, Figure 6.8 (b) shows that the 2 differential capacity peaks no longer occur. The loss of capacity by both differential capacity peaks over 10 cycles indicates that microstructural changes may have blocked phase transitions from occurring causing the capacity drop.

XRD showed that the capacity drop over 10 cycles was associated with a drop in the proportion of $CoPO_4$ present at 5.1 V vs. Li/ Li^+ (Figure 6.9, and Table 6.4). $CoPO_4$, and $Li_{2/3}CoPO_4$ were found at 5.1 V vs. Li/ Li^+ after charging for 1 cycle, and charging for 5 cycles, however the proportion of $CoPO_4$ dropped from 58.1 % to 15.6 %. This correlates with the presence of 2 smaller differential capacity peaks in Figure 6.8 (b), and the loss of capacity described above.

After 10 cycles XRD found that $CoPO_4$ and $Li_{2/3}CoPO_4$ no longer formed after charging to 5.1 V vs. Li/ Li^+ as the diffraction peaks were 100 % $LiCoPO_4$. This correlates with the lack of differential capacity peaks for the 10th cycle electrode in Figure 6.9 (b). Overall, the XRD results suggest a mechanism which prevents phase changes occurring in the material during cycling.

Comparison of the unit cell parameters of the phases after different cycles (1, 5, and 10) in Table 6.4 shows that the unit cell parameters increase at later cycles. The volume of $CoPO_4$ increased from 263.1 Å^3 to 263.5 Å^3, whilst the $Li_{2/3}CoPO_4$ cell volume increased from 277.4 Å^3 to 278.4 Å^3. There is some uncertainty in the unit cell values as a Si standard was not used during the XRD pattern so there is uncertainty about the refinement of the displacement parameter, which would impact the unit cell parameter values. The volume expansion of the individual phases was very small, potentially indicating the formation of defects, consistent with the formation of anti-site defects described in [9], [20].

The slight volume expansion of $CoPO_4$, and $Li_{2/3}CoPO_4$ in the charged samples may indicate slightly greater Li content in the charged state after 5 cycles, as higher lithium content results in larger unit cell parameters [7], [14]. This is evidenced by the lower gravimetric capacity in Figure 6.8 (a), and the red, Co(II)-rich oxidation state map in Figure 6.10 (d) for the 5th cycle.

The Co L-edge extractions from Co(III)-richer regions of the oxidation state maps show that the Co L-edges extracted from the 5th, and 10th cycle charged electrodes, have more Co(II) character than the 1st cycle charged electrode Co L-edge. The greater Co(II)-rich character is evidenced by the multiplet shoulder feature at 784 eV, which is present on the uncycled electrode Co L-edge, and by the Co L-edge onsets occurring at the same energy loss as the uncycled electrode (779 eV). The greater Co(II)-rich character of the 5th and 10th cycle electrodes Co L-edges are consistent with the XRD pattern and capacity results, and suggests issues with Li diffusion out of the particles.

The Co L-edge oxidation state maps of the 5th and 10th cycle charged electrodes in Figure 6.10 also agree with the XRD, and galvanostatic capacity loss results, as the Co oxidation state maps of the 5th and 10th electrodes are red Co(II)-rich. This implies either the presence of $LiCoPO_4$, or $Li_{2/3}CoPO_4$ in both cases as $Li_{2/3}CoPO_4$ contributions cannot be separated from $LiCoPO_4$ using oxidation state mapping.

It should be noted that the 5th cycle oxidation state map in Figure 6.10 (d) is more red Co(II)-rich than the 10th cycle oxidation state map in Figure 6.10 (f). Moreover, the 5th cycle Co L-edge has more Co(II) character than the 10th cycle Co L-edge in Figure 6.11. It is unclear why this occurred given XRD suggests the 5th cycle electrode should contain $CoPO_4$, whilst the 10th cycle electrode should only contain $LiCoPO_4$ (Figure 6.9). However, the oxidation state maps for the 5C sample may have been taken closer to the current collector (Figure 5.37).

Overall, the presence of $LiCoPO_4$ in 10th cycle electrodes shown by XRD in Figure 6.10, and decreased proportion of Co(III)-rich regions in later cycle electrodes (Figure 6.10 and Table 6.5) suggests the amount of active material is decreasing with increased cycles. Active material decreasing with increased cycles explains the drop in specific capacity shown in Figure 6.8.

Active material may have decreased due to damage from the electrolyte, and thickening of the CEI decreasing the Li diffusion kinetics. HIM imaging of the CEI layer shows thickening of the CEI in Figure 4.17 at the 5th and 10th cycles, and depth profiling in Figure 4.20 shows uncycled Li at the surface of 10th cycle charged electrode, consistent with the presence of Li in the CEI and CEI thickening, or Li in the active material at the surface, suggesting damage from the electrolyte. Given the CEI was no more than a few nm thick, it is unlikely CEI thickening was the cause of severe active material loss.

An alternative explanation for the loss of active material, is structural degradation of the active material preventing Lithiation. The XRD patterns (Figure 6.9), and Co L-edge oxidation state mapping quantification Table 6.5 show the proportion of $CoPO_4$, and Co(III)-rich regions decrease with increased cycling. The oxidation state maps of the 5th and 10th cycles (Figure 6.10) show the entire particles have shifted to be more Co(II)-rich, this was consistent across multiple areas of sample although not shown, hence unlike in the 1st cycle, Co(II)-rich regions are not isolated to the surface. If the decrease in active material was purely due to electrolyte induced decomposition it would be expected that the Co(II)-rich regions would be isolated to the surface. Evidence for electrolyte surface decomposition was present by the Co(II)-rich region on the surface of first cycle electrodes charged to 5.1 V vs. Li/ Li^+ (Figure 6.3 (a)), however by the 5th and 10th cycle, all of the particles are Co(II)-rich (Figure 6.10). The results therefore suggest degradation in $LiCoPO_4$ is a result of both electrolyte surface decomposition, and structural changes in the material preventing de-lithiation.

Literature has shown that degradation in $LiCoPO_4$ can occur due to the formation of anti-site defects when $LiCoPO_4$ is in the charged state [16]. Anti-site defects were not imaged here, however, the decrease in unit cell evidenced by XRD in Table 6.4 may be evidence of defect formation. High resolution TEM would be required to image the anti-site defects.

Overall, the results show that a process had occurred in the electrodes which caused the phase changes to not occur during cycling, and/ or due to prolonged exposure to electrolyte at high potentials causing Co dissolution and Li reincorporation into the lattice [15].

6.3.4 Cycling behaviour of the O K-edge

The O K-edge was assessed in order to confirm whether Co-O hybridisation had occurred, as proposed by Lapping et al. using XAS [6], and to consider the effects of cycle life on Co-O hybridisation. Section 5.5.2 discusses the origin of the features of the O K-edge in Figure 6.12 in detail.

The O K-edge pre-edge feature associated with Co-O hybridisation occurs at 5.1 V vs. Li/ Li^+ the 1st cycle (Figure 6.12). Comparing Co L-edge mapping of the 1st cycle charged electrode with O K-edge

mapping, using standards with and without the pre-edge feature shows that Co(III)-rich regions matched better with the O K-edge containing the pre-edge feature (Figure 6.13). The mapping result suggests that Co-O hybridisation occurs when the Co is in the Co(III) oxidation state ($CoPO_4$). The Co-O hybridisation result is consistent with hybridisation [8], and [19].

For the sample charged to 5.1 V vs. Li/ Li^+ on the first cycle, Figure 6.13 (c), and (f) show that the MLLS fitting is closer to the pre-edge standard within the bulk of the particles, rather than the edge of the particles. This indicates Co-O hybridisation in the bulk. As stated above, the hybridisation correlates with the presence of Co(III)-rich regions. Lapping et al. found that hybridisation occurred on the surface of electrode particles using XAS [6], and therefore associated the hybridisation with oxygen loss. The discrepancy is unclear, however, Lapping et al. did not spatially resolve the Co(III)-rich and Co-O areas of the particles using XAS [6], as done in this study.

Comparison of the pre-edge feature in Figure 5.27 (extracted from the 5.1 V vs. Li/ Li^+ 1^{st} cycle charged sample in Figure 6.13 (c)), and the pre-edge feature in Figure 6.15 (c) (extracted from the 5.1 V vs. Li/ Li^+ 1^{st} cycle charged sample in Figure 6.13 (f)) show the relative intensity of the O K-edge pre-edge can differ across the sample. The specific proportions of Co(II), and Co(III)-rich regions were calculated for spectrum images of the same region as O K-edge mapping (averaged in Table 6.5). The Co L-edge of the spectrum image in Figure 6.13 (f), where the hybridisation pre-edge intensity was less contained less Co(III)-rich character (68 %) than the region where the hybridisation pre-edge was more intense (100 %) Figure 6.13 (c). The intensity of the O K-edge pre-edge has previously been shown to represent the degree of covalency with hybridised transition metals [22], therefore the results indicate hybridisation increases with increased Co(III)-rich character. This is consistent with Co-O hybridisation occurring in $CoPO_4$ due to an increase in the unoccupied density of states in the O2p band above the Fermi level in $Co(III)PO_4$ [6].

Strobridge and Manzi found that spontaneous reincorporation of the Li from the electrolyte is caused by the instability of the octahedrally co-ordinated Co^{3+} in the $CoPO_4$ crystal structure [13], [15]. As Co(II)-rich regions were also found on the surface of 5.1 V vs. Li/ Li^+ charged electrodes in this study (Figure 6.3 (a) and Figure 6.13 (b) and (d)), it was suggested in 6.3.2 that a similar mechanism may be occurring in this study. Spontaneous reincorporation of Li would cause the density of states available for Co-O hybridisation to decrease, as the Co oxidation state decreases, leading to a less hybridisation on the surface. DFT modelling would be needed to confirm the density of states theory.

The Co-O hybridisation pre-edge did not occur at 5.1 V vs. Li/ Li^+ on the 5^{th} or the 10^{th} cycles (Figure 6.12). Moreover, the 5^{th} and 10^{th} cycle O K-edges were almost identical to the uncycled electrode O K-edge (Figure 6.12). The Co L-edges in Figure 6.11 show that the 5^{th} and 10^{th} cycle Co L-edges have more Co(II) character than the 1^{st} cycle Co L-edge, indicating a higher Li occupancy and lower Co oxidation state. The lack of O K-edge pre-edge feature on the 5^{th} and 10^{th} cycled electrodes in Figure 6.12 is consistent with the lack of Co(III)-rich regions, and hence further evidence of Co-O hybridisation being a feature of $CoPO_4$.

It was expected from XRD in Figure 6.9 that the 5^{th} cycle electrode would contain $CoPO_4$, and therefore would show Co-O hybridisation. However, the 5^{th} cycle electrode in Figure 6.12 did not demonstrate this, potentially due to the location of the TEM sample cut by microtome, and self-discharge issue discussed in 6.3.3.

O K-edge extractions (Figure 6.14 (d)) from the 'hybridised' regions of the spectrum image in Figure 6.14 (c) show that a pre-edge feature was not present, indicating that the mapping in Figure 6.14 was inaccurate. It should be noted that the pre-edge hybridisation feature was present in the Co-O hybridised regions of the 1st cycle maps in Figure 6.13. MLLS fitting works by summing the standards until they fit the collected signal (as shown by Figure 5.2). As the pre-edge signal is comparatively less intense to the main O K-edge feature, it is likely the mapping over-fit the O K-edge feature. This was not a problem for the 1st cycle maps as the O K-edge feature also changed slightly in the presence of the pre-edge (Figure 5.28), and the standard was extracted from a 1st cycle 5.1 V vs. Li/ Li^+ sample.

Overall, the EELS maps of the 2-10 later cycles, and the extracted EELS edges show no evidence of Co-O hybridisation at later cycles. The results indicate that Co-O hybridisation occurs in the presence of Co(III), and therefore can be used as an additional marker for the presence of $CoPO_4$. Similar to the Co L-edge oxidation state mapping, the O K-edge mapping did not offer any addition information regarding the degradation mechanisms of $LiCoPO_4$ other than offering further proof of $CoPO_4$ not forming at later cycles.

6.4 CONCLUSION

A Co L-edge valence state EELS technique has been developed, enabling mapping of Co(II)-rich and Co(III)-rich across $LiCoPO_4$ for the first time. XRD and SAED proved that the Co(II), and Co(III)-rich regions were representative of lithiated and de-lithiated regions of the electrode.

MLLS fitting to Co(II), and Co(III)-rich standards was used to fit collected EELS spectra from spectrum images of $LiCoPO_4$ to enable Co oxidation state mapping. Microtoming the electrode enabled differentiation of the Co(II), and Co(III)-rich regions of the electrode particles, with minimal damage to the electrode as a result of the sample preparation and mapping.

Overall, the EELS Co L-edge valence state mapping technique enabled the lithiated, and de-lithiated regions of the electrode to be spatially resolved allowing studies of the de-lithiation mechanisms. The statistical fitting uncertainties were not calculated as the residual, un-fitted, signal was the largest source of error. However, fitting was performed across all spectra with an average residual of 12 ± 6 %.

Galvanostatic charging, in combination with XRD revealed that $LiCoPO_4$ undergoes 2 phase changes during charging: $LiCoPO_4 \rightarrow Li_{2/3}CoPO_4$, and $Li_{2/3}CoPO_4 \rightarrow CoPO_4$, in agreement with a number of literature studies [3], [7], [13], [14].

The de-lithiation mechanisms of the first charge cycle were studied using the oxidation state mapping technique. Oxidation state mapping revealed a shrinking-core de-lithiation mechanism. Lithium diffused out of the edges of the $LiCoPO_4$ particles with increasing potential, shrinking a lithium-rich core with increased charging.

Palmer et al. previously reported a shrinking-core mechanism based on *in-situ* XRD [7], but suggested the Li-poor phase, $CoPO_4$, nucleates in the centre of the particles. This study represents the first direct visualisation of the shrinking-core mechanism in $LiCoPO_4$, where the de-lithiated phases form along the outside of the particles as the state of charge increases.

Direct visualisation of the Co oxidation states, also showed Co(II)-rich regions forming on the edge of the particles at potentials above 4.98 V vs. Li/ Li^+. It was concluded that this was evidence of spontaneous re-incorporation of Li into the lattice from the electrolyte.

O K-edge analysis revealed Co-O hybridisation in the Co(III)-rich phase $CoPO_4$, suggesting O is partially re-dox active in $LiCoPO_4$.

Further cycling of the $LiCoPO_4$ up to 10 cycles revealed severe capacity fade, consistent with previous studies [7], [19]. Oxidation state mapping revealed the electrodes remained Co(II)-rich after charging to 5.1 V vs. Li/ Li^+ at later cycles, correlating with the decrease in $CoPO_4$ phase formation detected by XRD in particles charged to 5.1 V vs. Li/ Li^+ at later cycles. O K-edge characterisation revealed a lack of Co-O hybridisation at later cycles, indicating $CoPO_4$ had not formed. Overall, the later cycles results indicate a mechanism blocking the phase changes required for charging of $LiCoPO_4$.

Overall, the EELS oxidation state mapping technique proved a powerful technique for visualising the Co(II) and Co(III)-rich regions of $LiCoPO_4$, allowing direct visualisation of the de-lithiation mechanism. The technique could be further applied to later cycles of $LiCoPO_4$ to understand why the de-lithiation mechanism is breaking down, and hence reasons for severe capacity fading.

6.5 Further Work

Although the EELS oxidation state mapping technique was able to visualise the lithiation mechanism in $LiCoPO_4$, the technique could be refined.

There was uncertainty about the identity of the Co(III)-rich phase due to a lack of a pure Co(III) standard. XAS could be used to help quantify the Co(III)-rich phase. Knowing the true oxidation state of the Co(III)-rich standard would help accurately quantify the Co L-edges, and enable improved conclusions about the phases present.

The MLLS fitting method used in this study was unable to differentiate the $Li_{2/3}CoPO_4$ phase from $LiCoPO_4$. If the two phases could be differentiated, this would enable conclusions to be drawn about the Co(II)-rich layer which forms on the surface of the particles at 5.1 V vs. Li/ Li^+.

Mapping of $Li_{2/3}CoPO_4$ couldn't be performed because the Co L-edge was too similar to the $LiCoPO_4$ Co L-edge for MLLS fitting to differentiate the signals. Principal component analysis (PCA) is a technique which finds significant features in the spectrum [23] (for example the high maximum at 782 eV for the $Li_{2/3}CoPO_4$). PCA could be attempted in the future to help map $Li_{2/3}CoPO_4$.

There were some issues regarding air contamination causing the Co L-edges of the Co(III)-rich phase to shift to higher energy losses. To completely eliminate the contribution from air, the technique should be completed in an air proof environment, using a vacuum transfer TEM holder, and microtoming in an inert atmosphere.

For the lithiation mechanism study, atomic resolution images, and nano diffraction could help identify the phase transitions better than the TEM images presented, as the lattice spacing changes were small between the different phases. This was particularly true for $LiCoPO_4$, and $Li_{2/3}CoPO_4$.

The oxidation state mapping of the 5^{th} and 10^{th} cycles revealed that the charged electrodes were entirely Co(II)-rich. The advantage of oxidation state mapping over other techniques is being able to spatially resolve the Co(II), and Co(III)-rich areas in individual particles. As the particles were uniformly Co(II)-rich it was difficult to gain extra conclusions, using the mapping technique, about reasons for capacity fade other than it is caused by structural degradation within the particle, and electrolyte interactions with the sample. The technique should ideally be applied to earlier cycles

(eg. cycle 2, and 3), to understand how the shrinking-core mechanism, and electrolyte induced lithiation of the lattice at high potentials is influenced by the capacity fade.

Overall, the oxidation state mapping technique could be further applied to $LiCoPO_4$ of different shapes, such as the hedgehog shaped particles by [19], with different coatings [2], or doping materials [6], to understand why the different techniques improved capacity fade.

6.6 REFERENCES

[1] E. Markevich, R. Sharabi, H. Gottlieb, V. Borgel, K. Fridman, G. Salitra, D. Aurbach, G. Semrau, M. A. Schmidt, N. Schall, and C. Bruenig, "Reasons for capacity fading of $LiCoPO_4$ cathodes in $LiPF_6$ containing electrolyte solutions," *Electrochem. commun.*, vol. 15, no. 1, pp. 22–25, 2012.

[2] M. Zhang, N. Garcia-Araez, and A. L. Hector, "Understanding and development of olivine $LiCoPO_4$ cathode materials for lithium-ion batteries," *Journal of Materials Chemistry A*, vol. 6, no. 30., pp. 14483–14517, 2018.

[3] F. C. Strobridge, H. Liu, M. Leskes, O. J. Borkiewicz, K. M. Wiaderek, P. J. Chupas, K. W. Chapman, and C. P. Grey, "Unraveling the Complex Delithiation Mechanisms of Olivine-Type Cathode Materials, $LiFe_xCo_{1-x}PO_4$," *Chem. Mater.*, vol. 28, no. 11, pp. 3676–3690, 2016.

[4] H. Ehrenberg, N. N. Bramnik, A. Senyshyn, and H. Fuess, "Crystal and magnetic structures of electrochemically delithiated $Li_{1-x}CoPO_4$ phases," *Solid State Sci.*, vol. 11, no. 1, pp. 18–23, 2009.

[5] N. N. Bramnik, K. Nikolowski, C. Baehtz, K. G. Bramnik, and H. Ehrenberg, "Phase Transitions Occurring upon Lithium Insertion−Extraction of $LiCoPO_4$," *Chem. Mater.*, vol. 19, no. 4, pp. 908–915, 2007.

[6] J. G. Lapping, S. A. Delp, J. L. Allen, J. L. Allen, J. W. Freeland, M. D. Johannes, L. Hu, D. T. Tran, T. R. Jow, and J. Cabana, "Changes in Electronic Structure upon Li Deintercalation from $LiCoPO_4$ Derivatives," *Chem. Mater.*, vol. 30, no. 6, pp. 1898–1906, 2018.

[7] M. G. Palmer, J. T. Frith, A. L. Hector, A. W. Lodge, J. R. Owen, C. Nicklin, and J. Rawle, "In situ phase behaviour of a high capacity $LiCoPO_4$ electrode during constant or pulsed charge of a lithium cell," *Chem. Commun*, vol. 52, no. 52, pp. 14169–14172, 2016.

[8] L. Wheatcroft, N. Klingner, R. Heller, G. Hlawacek, J. Cookson, and B. J. Inkson, "Visualisation and Chemical Characterisation of the Cathode Electrolyte Interphase in High Voltage Li-ion Battery Material $LiCoPO_4$ using He-ion Microscopy and in-situ Time-of-Flight Secondary Ion Mass Spectroscopy," *Appl. Energy Materials*, 2020.

[9] Y. H. Ikuhara, X. Gao, C. A. J. Fisher, A. Kuwabara, H. Moriwake, K. Kohama, H. Iba, and Y. Ikuhara, "Atomic level changes during capacity fade in highly oriented thin films of cathode material $LiCoPO_4$," *J. Mater. Chem. A*, vol. 5, no. 19, pp. 9329–9338, 2017.

[10] R. Brydson, H. Sauer, W. Engel, J. M. Thomass, E. Zeitler, N. Kosugi, and H. Kuroda, "Electron energy loss and X-ray absorption spectroscopy of rutile and anatase: a test of structural sensitivity Related content Electron energy loss and x-ray absorption spectroscopy of rutile and anatase: a test of structural sensitivity," *J. Phys. Condens. Matter.*, vol. 1, No. 4, pp. 797–812, 1989.

[11] S. M. G. Yang, V. Aravindan, W. I. Cho, D. R. Chang, H. S. Kim, and Y. S. Lee, " Realizing the Performance of $LiCoPO_4$ Cathodes by Fe Substitution with Off-Stoichiometry ," *J.*

Electrochem. Soc., vol. 159, no. 7, pp. A1013–A1018, 2012.

[12] I. C. Jang, H. H. Lim, S. B. Lee, K. Karthikeyan, V. Aravindan, K. S. Kang, W. S. Yoon, W. I. Cho, and Y. S. Lee, "Preparation of $LiCoPO_4$ and $LiFePO_4$ coated $LiCoPO_4$ materials with improved battery performance," *J. Alloys Compd.*, vol. 497, no. 1–2, pp. 321–324, 2010.

[13] F. C. Strobridge, R. Clément, M. Leskes, D. S. Middlemiss, O. J. Borkiewicz, K. M. Wiaderek, K. W. Chapman, P. J. Chupas, and C. P. Grey, "Identifying the Structure of the Intermediate, $Li_{2/3}CoPO_4$, Formed during Electrochemical Cycling of $LiCoPO_4$," *Chem. Mater.*, vol. 26, no. 21, pp. 6193–6205, 2014.

[14] N. N. Bramnik, K. Nikolowski, C. Baehtz, K. G. Bramnik, and H. Ehrenberg, "Phase transitions occurring upon lithium insertion-extraction of $LiCoPO_4$," *Chem. Mater.*, vol. 19, no. 4, pp. 908–915, 2007.

[15] J. Manzi, F. M. Vitucci, A. Paolone, F. Trequattrini, D. Di Lecce, S. Panero, and S. Brutti, "Analysis of the self-discharge process in $LiCoPO_4$ electrodes: Bulks," *Electrochim. Acta*, vol. 179, pp. 604–610, 2015.

[16] A. Boulineau, and T. Gutel, "Revealing Electrochemically Induced Antisite Defects in $LiCoPO_4$: Evolution upon Cycling," *Chem. Mater.*, vol. 27, no. 3, pp. 802–807, 2015.

[17] C. Delmas, M. Maccario, L. Croguennec, F. Le Cras, and F. Weill, "Lithium deintercalation in $LiFePO_4$ nanoparticles via a domino-cascade model," *Nat. Mater.*, vol. 7, no. 8, pp. 665–671, 2008.

[18] J. B. Goodenough and Y. Kim, "Challenges for Rechargeable Li Batteries," *Chem. Mater.*, vol. 22, no. 3, pp. 587–603, 2010.

[19] F. Wang, J. Yang, Y. Nuli, and J. Wang, "Novel hedgehog-like 5 v $LiCoPO_4$ positive electrode material for rechargeable lithium battery," *J. Power Sources*, vol. 196, no. 10, pp. 4806–4810, 2011.

[20] S. Brutti, J. Manzi, D. Meggiolaro, F. M. Vitucci, F. Trequattrini, A. Paolone, and O. Palumbo, "Interplay between local structure and transport properties in iron-doped $LiCoPO_4$ olivines," *J. Mater. Chem. A*, vol. 5, no. 27, pp. 14020–14030, 2017.

[21] J. Suntivich, W. T. Hong, Y-L. Lee, J. M. Rondinelli, W. Yang, J. B. Goodenough, B. Dabrowski, J. W. Freeland, and Y. Shao-Horn, "Estimating hybridization of transition metal and oxygen states in perovskites from O K-edge X-ray absorption spectroscopy," *J. Phys. Chem. C*, vol. 118, no. 4, pp. 1856–1863, 2014.

[22] G. S. Henderson, F. M. F. De Groot, and B. J. A. Moulton, "X-ray absorption near-edge structure (XANES) spectroscopy," *Reviews in Mineralogy and Geochemistry*, vol. 78, no. 1. Mineralogical Society of America, pp. 75–138, 2014.

[23] S. Jesse, M. Chi, A. Belianinov, C. Beekman, S. V. Kalinin, A. Y. Borisevich, and A. R. Lupini, "Big Data Analytics for Scanning Transmission Electron Microscopy Ptychography," *Sci. Rep.*, vol. 6, no. 1, pp. 1–8, 2016.

7 TIME DEPENDENT DEGRADATION CHARACTERISATION: DEVELOPMENT OF AN *IN-OPERANDO* TEM TECHNIQUE FOR STUDYING $LiCoPO_4$ DEGRADATION

7.1 AIMS AND OBJECTIVES

This chapter presents work performed to set-up an *in-operando* transmission electron microscopy (TEM) method of characterising Li-ion battery electrodes. An *in-operando* set-up, cycling active material within a TEM, could avoid the sample contamination, and the loss of transient information experienced by the *ex-situ* characterisation techniques presented in previous chapters.

The objective was to set-up a Li-ion half-cell in the TEM using a Protochips P-500 liquid stage. The Protochips set up consists of 2 silicon chips with electron transparent windows. A counter, reference and working electrode are patterned onto one of the chips. Liquid electrolyte can be flowed in-between the chips creating a 3 electrode electrochemical cell in the TEM. The aim was to create $LiCoPO_4$ Li-ion half-cell by positioning Li on the counter electrode, and $LiCoPO_4$ on the working electrode, whilst flowing electrolyte through the cell.

However, the set-up is challenging as the electrode array is very small (with electrodes ranging from 2500 μm^2 to 260000 μm^2), and the entire thickness of the cell is 500 nm at room pressure. Moreover, the electron beam itself causes damage to the materials *in-situ* TEM, potentially causing erroneous observations for an *in-operando* set-up.

As the work is very different to the other *ex-situ* characterisation methods used to explore lithiation mechanisms, the chapter begins with a literature review on *in-situ* TEM methods for battery research. After this, methods to set-up the *in-operando* TEM set-up are demonstrated.

A method to position $LiCoPO_4$ onto the working electrode is demonstrated by microtoming the $LiCoPO_4$ and positioning it with nano-manipulators. The success was evaluated using SEM. A method plating Li from the electrolyte onto the electrodes is demonstrated and assessed using cyclic voltammetry (CV), and post-mortem SEM.

The effects of electron beam damage on the electrolyte are assessed by performing an *in-situ* TEM experiment on $LiPF_6$ in EC DMC, and imaging the effects post-mortem in SEM.

Unfortunately, during the work to set-up the *in-operando* TEM system, the TEM holder required by the experiment suffered a severe breakage resulting in an extended period of down time. The work presented in this chapter is the work completed up until the breakage. The final section suggests some improvements to the approach attempted here which could be attempted in the future.

7.2 LITERATURE REVIEW

So far this thesis has demonstrated that $LiCoPO_4$ is a complex system which suffers from multiple degradation mechanisms during operation. Degradation mechanisms occur within the crystal structure, including bond hybridisations and phase changes (see the 'degradation within $LiCoPO_4$ particles' chapter), and as a result of electrolyte breakdown and surface reaction leading to the formation of CEI layers (see the 'degradation at the electrode surface' chapter).

The previous characterisation techniques demonstrated in this thesis have been *ex-situ* techniques. A common theme with both the EELS technique ('degradation within $LiCoPO_4$ particles' chapter), and the HIM SIMS technique ('degradation at the electrode surface' chapter) has been the potential for errors resulting from sample handling and air exposure. Both techniques provide a snapshot of the state of degradation in a given moment, requiring the assembly and disassembly of multiple cells to understand the changes that take place across a single cycle, and over the lifetime of the cell. This is not only inefficient, but may also have resulted in the loss of information on transient processes, such as detailed structural changes, or intermediate phases [1] [2].

In-situ and *in-operando* techniques can avoid the issues associated with *ex-situ* techniques [2], namely that cycled cells are dismantled and then their evolved microstructures characterised post-mortem. *In-situ* techniques refer to the characterisation of the material in the original place, under the reaction conditions, or conditions relevant to reaction conditions [1], [3]. For a battery system, *in-situ* characterisation may be in the presence of electrolyte, or under biasing conditions. *In-operando* refers to techniques which characterise a 'working' material [3], for batteries this would involve charge and discharge of the material in the presence of an electrolyte and anode.

In-situ and *in-operando* techniques provide a potential route to avoid the issues associated with *ex-situ* techniques, and aid understanding of the system as a whole [2], as they avoid changes to the system from post-mortem sample handling, and allow observation of transient processes. For $LiCoPO_4$, a system which could combine observation of electrolyte effects with crystallographic changes could be useful as there is some evidence of dependence between the two degradation mechanisms.

A range of *in-situ/ in-operando* techniques have been developed for battery research, depending on the length scale, or chemical or physical nature of the degradation mechanism. *In-situ* Atomic force microscopy (AFM) has been used for studies on the morphology of SEI layer formation in the $LiNi_{0.5}Mn_{1.5}O_4$ system [4]. Structural and chemical changes to electrode phases have been studied through the development of *in-situ*/ *in-operando* XRD, and X-ray absorption spectroscopy (XAS) [1]. All the *in-operando* techniques require the development of specific cells to allow the material to be charged or discharged within the confines of the experimental set-up [1], [2].

This study focusses on the development of an *in-operando* TEM technique to study Li-ion battery degradation. TEM provides site-specific high-resolution imaging and diffraction on features down to the atomic scale, allowing analysis of phase changes, and electrode/ electrolyte interface studies as demonstrated *ex-situ* earlier in this thesis (see 'degradation within $LiCoPO_4$ particles' chapter). Chemical changes can also be analysed with high spatial resolution in the TEM using electron energy loss spectroscopy (EELS) and energy dispersive X-ray spectroscopy (EDS). The <1 nm spatial resolution of TEM microstructural analysis is ideal for studying battery processes such as charge/ discharge mechanisms and cathode/ solid electrolyte interphase formation [5].

This review focusses on *in-operando* cell design and challenges associated with performing *in-operand/ in-situ* TEM experiments on battery materials.

7.2.1 *In-operando* TEM techniques for Li-ion Battery Research

TEM requires electron transparent samples (typically <200 nm thick), is performed under high vacuum, and the high energy electron beam itself can cause sample damage. *In-operando*/ *in-situ* cells must address these limitations for effective operation.

To date, most *in-operando* TEM techniques for battery studies can be split into 3 categories, based on the *in-situ* cell configuration: (1)- solid-state battery configurations, (2) closed liquid cell configurations, and (3) open cell configurations [1]. Schematics of the configurations are shown in Figure 7.1.

(1) The solid state battery configuration typically consists of a focussed ion beam (FIB) section of a thin film consisting of layers of electrode and solid electrolyte [6]. Electrical connections to an external galvanostat are created using a Pt metal contact with an *in-situ* biasing holder [6].
(2) The open cell configuration is completely exposed to the vacuum. The cell consists of an anode and cathode (typically nanowires) with either a low vapour pressure or solid LiO_2 electrolyte making point contact between the nano-wire electrodes [7], [8].
(3) The closed liquid cell consists of enclosed cells where the cell is isolated from the vacuum, allowing high vapour pressure electrolytes to be used. Often the system consists of 2 chips, one with electrodes patterned on it, with a thin liquid layer compressed between them. The electrodes are fully immersed in electrolyte [9]–[11].

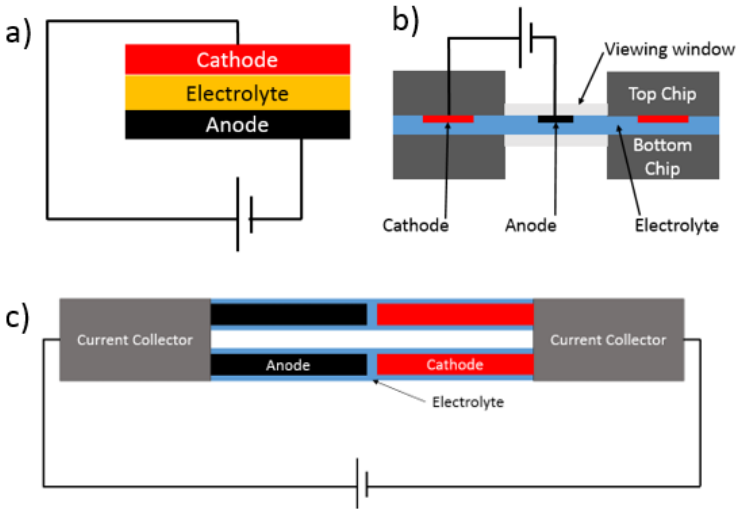

Figure 7.1: (a)- Solid state battery configuration (adapted from [6]*), (b) Closed liquid cell configuration (adapted from* [11]*), (c) Open-cell configuration (adapted from* [7]*)*

The first example of a Li-ion electrochemical cell in a TEM was in 2010 by Huang et al. using the open cell configuration. SnO_2 nanowires were grown on an *in-situ* TEM electrical biasing holder, separated from bulk $LiCoO_2$ by an ionic liquid electrolyte and biased to induce charge and discharge, allowing the lithiation mechanisms to be observed [8].

The open-cell set-up allows for good spatial resolution (atomic scale) and the ability to perform chemical characterisation using EELS, due to the electron beam predominantly interacting with the sample of interest rather than the electrolyte in the closed cell configuration. More recently Niu et al. have taken advantage of this to observe the formation of a random solid solution zone in $LiFePO_4$ during the cycling by biasing pre-cycled $LiFePO_4$ nanowires, against a Si nanowire *in-situ* TEM [7]. Residual $LiPF_6$ in the binder covering the $LiFePO_4$ nanowire was used as an electrolyte/ separator in the *in-situ* set-up. Chen et al. studied the lithiation and de-lithiation of FeS nanosheets using FeS nanowires cycled against metallic lithium with a Li_2O layer as a solid electrolyte to create

an *in-operando* set-up [12]. The open cell configuration allowed for electron diffraction and high resolution imaging.

The point contact set-up shown in Figure 7.1(c) can modify the diffusion pathways and does not mimic a real cell. To compensate for this, and to investigate novel solid state battery systems, the solid-state battery configuration was developed (Figure 7.1(a)). Wang et al. created a nano battery by focus ion beam (FIB) milling a slice of $LiCoO_2$/ LiPON/ Si and galvanostatically charging the sample *in-situ* TEM [13]. Using EELS they mapped Co(III), and Co(II) rich regions allowing lithiation mechanisms to be assessed, similar to work presented in this thesis. However, this approach only allows for the use of weak currents due to the sample dimensions, and gallium contamination can occur from the FIB [13], [14].

Overall there are limitations to open-cell set-up- (1) the set-up is exposed to the 10^{-4} -10^{-7} Pa vacuum, limiting electrolytes to low vapour pressure liquids excluding most standard battery electrolytes such as LiPF6 in ethylene carbonate and dimethyl carbonate [15]. (2) there is only point contact between the anode, electrolyte, and cathode (see Figure 7.1(c)), potentially changing the charging mechanisms. (3) If ionic liquids are used they can polymerise under the electron beam, and (4) the use of solid electrolytes can create large overpotentials [1].

In terms of *in-situ* characterization of phenomena presented in this thesis (oxidation state mapping for lithiation mechanisms, and CEI formation), the open-cell configuration could provide the best environment for an *in-situ* lithiation mechanism study, but CEI layer growth would not be possible. Aside from the solid-state battery system, most open-cell configurations do not mimic a real cell. $LiCoPO_4$ experiments typically use liquid electrolytes ($LiPF_6$ in EC and DMC in this thesis) which cannot be exposed to a TEM vacuum, so the open-cell configuration would not suit studies involving CEI layer formation.

The closed liquid-cell set-up (Figure 7.1(b)) was first developed by Ross and co-workers in 2003 who combined the electrical biasing technique with *in-situ* liquid TEM to image the electrochemical deposition of copper from copper sulfate solution [9]. This technique has since been expanded to Li-ion battery based systems by using battery electrolytes (such as $LiPF_6$ in EC/ DMC [16]) as the liquid. Sacci et al. achieved direct visualization of initial SEI morphology when plating Li onto Au from $LiPF_6$ in EC/ DMC by running cyclic voltammetry with Au pseudo electrodes [16]. Mehdi et al. observed the morphology of plated and stripped Li onto patterned Pt from $LiPF_6$ solutions [17].

Since the earlier plating systems, current research has developed to better mimic 'real' battery systems by depositing anode and cathode materials onto the patterned current collectors within the sealed liquid cells. Using this technique, Unocic and co-workers observed SEI formation on graphite [18]. Holtz et al. used valence energy loss spectroscopy to observe phase contrast between $LiFePO_4$ and $FePO_4$, using deposited activated carbon as the anode and deposited $LiFePO_4$ particles on the working electrode [11]. Systems such as these would be ideal for studying the CEI formation on $LiCoPO_4$ and the phase distribution of $LiCoPO_4$, and $CoPO_4$ to compare *in-situ* work with *ex-situ* work.

However, compared to the open-cell configuration, the sealed liquid-cell also has a few limitations. Firstly, the spatial resolution is significantly lower due to the presence of the liquid

layer and the SiN_x membrane in the electron path reducing the electron transparency, limiting the ability to perform structural and chemical evolution studies [15], [19]. In terms of mimicking a real cell, despite the ability to precisely coat nano-scale electrodes [11], [18] with anode and cathode materials, the electrolyte must still be flowed around the system in order to prevent the non-infinite diffusion issue caused by having a nano-scale thin layer of liquid electrolyte. The rest of this review will consider the challenges associated with sealed-liquid cell *in-situ* TEM configurations.

7.2.2 Challenges *in-operando* TEM

7.2.2.1 Electron Beam Effects

One of the key challenges in liquid cell TEM is the effect of the high energy electron beam (typically 200 keV) on the sample. It is important to quantify the effects of beam damage, as it can affect the interpretation of results, cause interference with lithium exchange at the electrode/ electrolyte interface, and the electrolyte stability [20].

Electron beam damage is a well-documented phenomenon in electron microscopy. In general S/TEM, beam damage can occur via 3 main mechanisms:

- *Radiolysis*
  Breaking of chemical bonds caused by inelastic scattering of electrons (typically via electron-electron mechanisms such as ionisation).
- *Knock-on damage or sputtering*
  Creation of point defects via the displacement of atoms from their lattice positions (knock-on damage) and the ejection of atoms from the sample surface (sputtering). The effect is induced by inelastic scattering of electrons.
- *Heating*
  Heat is generated by phonons in the sample [21].

Battery cathode materials are predominantly ionic crystals and therefore typically undergo radiolysis. Inelastic scattering electron-electron interactions can cause the formation of new compounds [21], which may have adverse effects on the operation of the material *in-operando*. Lin et al. found that a 300 keV STEM beam decomposed $LiNi_{0.4}Mn_{0.4}Co_{0.18}Ti_{0.02}O_2$ to a phase with a higher impedance structure [22]. No literature could be found on the decomposition of $LiCoPO_4$ during electron beam irradiation. It is possible Li and O could be removed by interaction with the electron beam, similar to other Li and O containing compounds. Moreover, the behaviour of post-cycled $LiCoPO_4$ could be different as surface reaction layers can react differently under irradiated conditions [21].

For liquid cell TEM, phonon generation can be mitigated due to heat dissipation by the liquid [23]. Battery electrolytes tend to be a lithium containing salt dissolved in a solvent. The electron beam has previously been shown to cause radiolysis in salt solutions [20], [24]–[26]. Woehl and co-workers observed the electron beam induced nucleation of Ag nanoparticles from silver salts in water [25], whilst Jungjohann and co-workers observed the growth on Pd on Au seeds in water to form Au-Pd [26]. Aqueous electrons generated by electron beam radiolysis of water caused metal ions in the solution to reduce and nucleate as metal nanoparticles.

Similar phenomena have been observed in battery electrolytes. Abellan et a. conducted a study of the behaviour of a number of electrolyte solutions irradiated by a 300 kV electron beam. The solutions tested included common salts such as $LiAsF_6$, $LiPF_6$, and LiTf in carbonate solvents such

as DMC, EC, 1,3-dioxolane (DOL) and dimethyl sulfoxide (DMSO) [24]. Initial electron irradiation of $LiAsF_6$ in EC and DMC caused the formation of LiF particles (see Figure 7.2(a)) followed by the formation of carbonates (the large darker particles in Figure 7.2(a)).

The proposed mechanism for radiolysis induced electrolyte damage was the formation of highly reactive lewis acids (AsF_6^-) due to the reduction of $LiAsF_6$ by solvated electrons [24]. Recombination of the Li^+ and F^- ions led to the formation of LiF, followed by polymerisation of the organic solvents [24]. $LiPF_6$ in EC and DMC (the electrolyte system used in this thesis) decomposed in a similar way to $LiAsF_6$ [24].

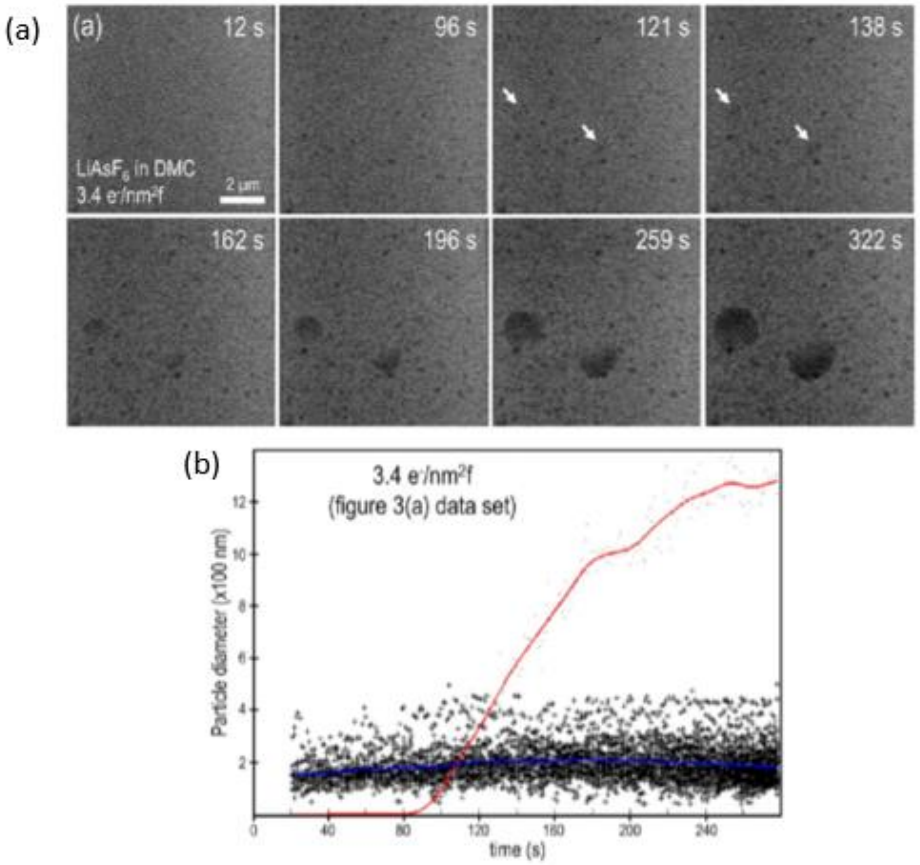

Figure 7.2: Electron beam induced electrolyte breakdown. (a) Formation of particles formed by irradiation of $LiAsF_6$ in DMC using a 300 kV STEM beam. Small primary particles are visible in all images. The white arrows in 121 s and 138 s indicate the seeding of larger secondary particles visible in 162 s – 322 s. (b) growth of primary and secondary particles with increasing electron dose time. Reprinted with permission from Nano Lett. 2014, 14,3, 1293-1299. Copyright 2014, the American Chemical Society [24].

The effects of beam damage can be mitigated by changing microscope parameters, as well as the solvent-salt system.

Microscope Parameters

- *Accelerating voltage:* Increasing the accelerating voltage (beam energy) increases the volume of elastic scattering and hence decreases inelastic scattering. Radiolysis is induced by inelastically scattered electrons, so radiolysis can be reduced if the sample volume is small, or the accelerating voltage is increased, although other knock-on effects such as sample damage events and heating may be increased. Abellan conducted beam induced effect experiments on nucleated Ag nanoparticles from Ag salt ($Ag^+ \rightarrow Ag^0$). The expectation was that the increase in acceleration voltage would decrease the number of nucleated Ag nanoparticles, however,

an increase in nucleated Ag nanoparticles was observed [20]. This was likely due to the formation of other radicals. As demonstrated above, battery electrolytes are more complex, so the accelerating voltage and would need to be optimised. Magnification and electron flux have minimal effect on the inelastic and elastic cross-section, however knock-on effects may be effected by these factors as well [27].

- *Electron Dose:* In Ag^+ and Au^+ solution nanoparticle nucleation experiments, it has been found that a threshold does is required to induce nucleation of metal nanoparticles [25], [28], [29]. This is likely due to an activation energy requirement for nucleation of metal nanoparticles [27]. However, if the electron dose can be kept under the threshold for a particular system, electrolyte beam damage may be mitigated. Currently lowering the electron flux to the order of less than 1 $e^-/ Å^2s$ is seen as a method of reducing radiolysis damage [30].
- *Imaging Mode (STEM or TEM):* The electron beam in STEM mode is a focussed beam ~1 Å scanned across the sample with a pixel dwell time of 0.5 – 5 µs, leading to a total exposure time of ~500 ms per image. The high dose rate can lead to supersaturation of electrons needed for nucleation, leading to increased nucleation [20], [27]. However, the scanning ability allows for greater control over where the dose is delivered to the sample [28]. TEM imaging in contrast, can have less exposure (25 ms or greater), but the overall higher beam dose per second can lead to gas bubble formation due to increased reduction of solvents in a liquid (causing electrochemistry issues, and potential breakage of the window). The parallel beam can also result in sample region irradiation outside of the viewing frame, leading to less controlled radiolysis [20], [27].

Solution Composition

The stability of a solution undergoing radiolysis is determined by the number of radicals that form, and the stability of any solvated electrons, e_s^- that form [30]. One method of reducing the effect of radicals and e_s^- is to flow fresh electrolyte or solution into the system, but the timescale which radiolysis can occur can be as short as 10^{-12} s, mitigating the benefit of electrolyte flow as a preventative measure [30], [31]. A method of reducing the number of radicals that form is to introduce radical scavenging species to the solution, such as isopropanol to scavenge $OH^·$ radicals [32]. However, given the purpose of the *in-situ* TEM experiments is to replicate the bulk Li-ion cell system as closely as possible, adding scavengers is not ideal.

Some solvents are more likely to generate e_s^- than other systems. e_s^- species are generated when a beam driven ionisation event liberates an electron. Immediately after ionisation, the solvent does not immediately polarise in response to the increased charge density, creating a 'dry' electron- which is highly unstable and likely to recombine with surrounding solvent molecules [30]. If the solvent molecules reorient to compensate for the increased charge density created by the electron, a potential well is created, stabilising the electron to create a solvated electron. Solvated electrons are more stable, hence have longer lifetimes and can cause more damage compared to the dry electron state [30].

The ability of a solvent to stabilise solvated electrons is determined by the dielectric constant of the solvent, and the kinetic ability, and the energy barrier required of the solvent molecules to re-orientate to charge compensate for the electron beam liberated electrons [30]. Highly polarisable solvents, such as water, have a high reorganisation energy barrier, so are less able to stablilise solvated electrons, whilst low polarising solvents such as ammonia are able to re-orient and stabilise e_s^- [30].

For battery electrolytes previous work by Abellan and co-workers has observed the addition of EC to DMC reduced the number of precipitates formed [24], this is likely due to EC having a higher dielectric constant than DMC (89 compared to 3.107 [33]). Moreover, LiTf in highly polarisable DMSO was found to be stable under the electron beam for up to 7 minutes [24].

However, Abellan et al. also found that EC and DMC without the presence of a salt were stable under the electron beam, indicating the need for a salt for the cascading process to occur [24], moreover the damage was less using $LiPF_6$ as a salt, compared with $LiAsPF_6$.

It has been proposed the increased stability of $LiPF_6$ was due to a $LiPF_6$ having a lower bimolecular rate constant K_e (rate constant of e^-_s + electron scavenger → product [34]) than $LiAsF_6$. Therefore, for beam damage to occur in battery electrolytes, the critical step appears to be the formation of the lewis acid PF_6^- as a result of reaction with solvated electrons. The bimolecular rate constant effects the kinetics of this occurring for a particular salt, whilst the ability to stabilise the solvated electrons by the solvent system to allow the reaction to occur will also effect degradation.

Overall, the beam damage phenomenon is not ideal for replicating battery systems as either the beam dosage must be lowered to levels where resolution can be compromised (1 $e^-/ Å^2s$) [30], or the electrolyte system must be adjusted to increase stability from radiolysis [24]. For the $LiCoPO_4$ experiments, the *in-situ* results need to reflect observations found *ex-situ* therefore, the electron beam control method will be employed in this set-up to reduce electrolyte damage.

The formation of SEI layers in standard LP30 electrolyte is instigated by the decomposition of the electrolyte to form LiF and $LiPF_x$ followed by further decomposition resulting in the formation of $LiCO_3$ [35], similar to the beam damage radiolysis mechanisms suggested for liquid cell TEM [24]. Liquid cell TEM presents an interesting opportunity to control the electron dose acting on the electrolyte, and therefore investigate the specific mechanisms forming SEI layers in anodes, and CEI layers in cathodes.

7.2.2.2 Setting up the cell to mimic real cell processes: Protochips Liquid Cell Set-up

The electrochemical biasing holder available at the University of Sheffield is a sealed liquid cell set-up (Figure 7.1(b)). A diagram of the set-up is shown in Figure 7.3. As the set-up is a sealed liquid cell, the goal would be to understand how $LiCoPO_4$ reacts under biasing conditions in the presence of electrolyte, preferably in a similar way to work performed by [11], essentially creating a Li-ion half-cell in the TEM.

This section discusses literature methods of setting up the sealed liquid cell to be a Li-ion half-cell in a TEM.

The sealed liquid cell set-up used in this project is a Poseidon P500 liquid stage designed by Poseidon Protochips. A schematic of the cell is shown in Figure 7.3. The cell consists of a thin film layer of liquid electrolyte ($LiPF_6$ in EC and DMC) (~500 nm) sandwiched between 2 silicon chips. The silicon chips both contain a SiN_x surface coating, allowing an electron transparent SiN_x viewing window which enables material to be imaged using transmission electron microscopy. An electrolyte reservoir, external to the TEM, is connected to a syringe pump and allows electrolyte to be flowed into the cell.

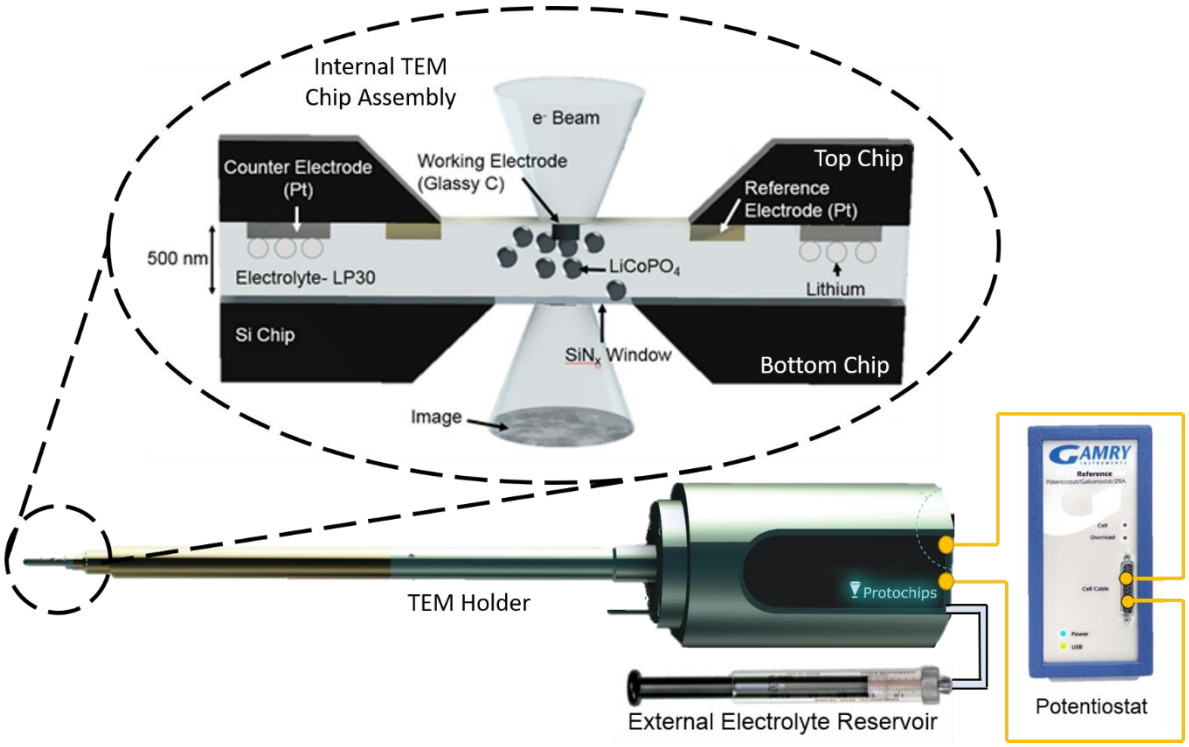

Figure 7.3: Schematic of the Protochips liquid cell set-up.

The top chip contains patterned electrodes- platinum counter (CE) (260000 μm^2), and reference (RE) (7500 μm^2) electrodes, patterned on the Si chip, and a glassy carbon working electrode (WE) (2500 μm^2), patterned onto the SiN_x window. The electrode arrangement is shown in Figure 7.4. The electrodes are connected to an external Gamry potentiostat which is used for cycling or electrochemical impedance spectroscopy.

There are experimental conditions where the function of the electrodes is switched (eg. the CE will act as a WE). For clarity, throughout this chapter of the thesis, the large Pt circular electrode will be referred to as the counter electrode (CE), the Pt smaller oval electrode the reference electrode (RE), and the glassy carbon electrode on the SiN_x as the working electrode (WE). Where relevant, if the function has been switched this will be made clear.

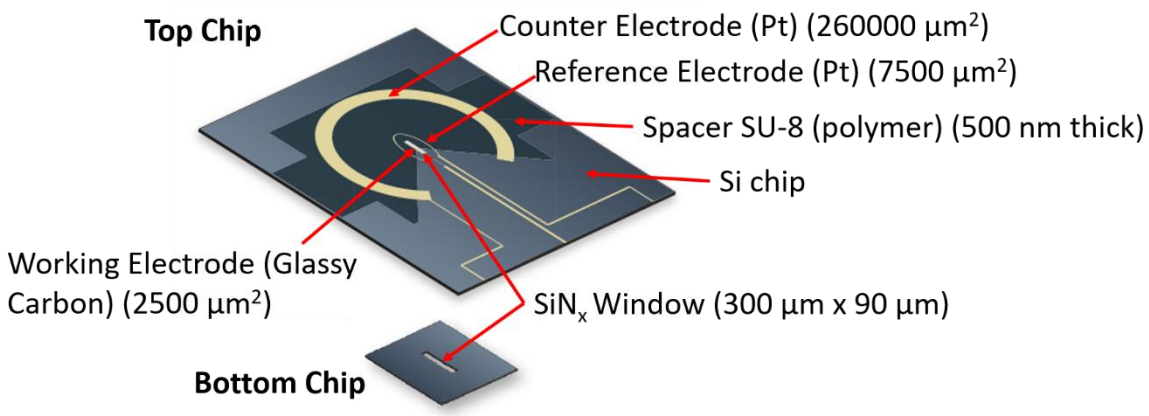

Figure 7.4: Schematic of the electrode array on the top chip of the liquid cell, showing the electrode materials and areas, and the bottom chip showing the SiN_x window dimensions. Top and bottom have been labelled as the set-up is assembled. In the microscope, the chips will reverse [36].

In order to create a half-cell, $LiCoPO_4$ would need to be cycled against Li in the presence of electrolyte. Therefore, Li would need to be positioned on the counter electrodes, whilst $LiCoPO_4$ would need to be positioned on the working electrode. For the *in-situ* work to be comparable to bulk cell work shown earlier in this thesis, the electrochemistry must be quantifiable. The exact area of electrode material on any electrode must be known in order to calculate current densities. Given the small size of the electrodes in Figure 7.4 attaching material to the electrodes in a controlled manner is challenging.

A number of different methods have been used in literature to position active material onto the working electrode. The simplest method is to drop suspended particles in a solvent onto the electron transparent window and hope some of the particles touch the working electrode. This method was demonstrated by Unocic et al. who dropped suspended graphite onto the electrodes [18]. There are a few issues with this method, (1) the particles may fall off the electrode when the cell is flooded with electrolyte, (2) it is not possible to control the amount of particles dropping onto the electrode, making the electrochemistry difficult to quantify.

More recently, authors have worked towards deposition methods with greater precision. Holtz et al. used a Dimatrix printer to print a suspension of $LiFePO_4$ in isopropanol onto the working electrode [11], whilst Leenheer et al. used dielectrophoresis to deposit $LiFePO_4$, where an 8V AC voltage was applied between electrodes submerged in a suspension of $LiFePO_4$ [37]. Both of these methods still have an adhesion problem. In order to help improve adhesion onto the electrodes Zeng et al. heated the chip to 80 °C for 20 mins [38].

A final method that has been used to deposit and attach precise volumes of active material to the electrodes is to take a focus ion milled slice of active material and attach it to the electrode on the *in-situ* cell. This method has been demonstrated by Protochips [39] and Fawey et al. [40]. The precise active material volumes and areas achievable by this method improves the control over the electrochemistry. However, the method is difficult and time consuming as the active material would need to be deposited without breaking the SiN_x window, which involves careful tilting in order to avoid ion milling a hole through the SiN_x window when the sample is attached.

Earlier in this thesis, microtoming was demonstrated as a method to thinly slice active material. The active material could then be precisely positioned using a nanomanipulator. This method could decrease the complications experienced by the FIB slicing method.

In order to act as a half cell, the deposited active material on the working electrode would need to be cycled against metallic Li. This would involve positioning Li onto the counter electrode. Unocic et al. circumvented this challenging by attaching metallic Li to a Ni wire submerged in electrolyte external to the *in-situ* cell. Tubing was used to allow flow of electrolyte between the *in-situ* cell and Li. This method is advantageous as it avoids the complication of having to attach Li to the small electrode on the *in-situ* cell. However, the cell resistance is likely to increase.

An alternative method is to not use Li as the counter electrode at all, but use the Pt metal as a pseudo-electrode, whilst flowing electrolyte around the circuit to provide sufficient Li^+ for lithiation, delithiation and any SEI formation. This method was demonstrated by Mehdi et al. [10], but it is difficult to control the voltage and it is not directly comparable to a bulk half-cell.

A final option is to directly plate Li onto the counter electrode from the electrolyte solution. Li plating from the electrolyte was demonstrated *in-situ* TEM by Mehdi et al. [17] and Sacci et al. [41] directly onto the working electrode. Although the plated Li in these experiments were not intended to be used as half-cell counter electrodes, it demonstrates the possibility of plating Li directly from the $LiPF_6$ in EC/ DMC solution. The advantage of this method is that the system would be completely sealed prior to Li deposition, avoiding any issues associated with air contact. This method was attempted for this set-up.

The limited *in-situ* TEM battery studies so far have used constant potentials potential sweeps or cyclic voltammetry using potentials of known electrochemical processes to link the *in-operando* observations to bulk electrochemical cells [11], [17]. So far in this review, the bulk coin cell half-cell has been treated as being directly comparable to the *in-situ* TEM geometry. This is incorrect as the nature of the *in-situ* thin film electrolyte and electrode geometry used will change the electrochemistry as the diffusion processes change. The infinite diffusion assumptions required by bulk electrochemistry are no longer valid in this case.

Unocic et al. used the $[Fe(CN)_6]^{3-/4-}$ system to study the impact of a thin film electrochemical cell on the electrochemistry [42]. In order to prevent complete electrolysis of the system, electrolyte had to be flowed around the system for sufficient Li^+ ions. Moreover, for the experiments to be repeatable, the precise electrochemically active area had to be known for quantification.

Overall, for repeatable experiments, and comparison with bulk coin-cell behaviour, it is important to set-up the *in-situ* cell so that active material is adhered, and electrically connected, to the working electrode, and the precise amount of active material on the working electrode is known

7.2.2.3 In-situ TEM Set-up Strategy

The overall aim on the *in-situ* TEM set-up is to create a reliable method of setting up a Li-ion half-cell in the TEM using $LiCoPO_4$ as the working electrode, and Li as the counter. Once the half-cell was set-up, the aim was to use the system to explore the effects of CEI formation and the electrode/ electrolyte interface on the $LiCoPO_4$ system. Theoretically the system could also be used to study other battery systems. The set-up strategy is detailed in Table 7.1.

Table 7.1: In-situ TEM Set-up Strategy

Goal	Justification	Experiments
Understanding electron beam effects on the electrolyte	It is known that $LiPF_6$ in EC and DMC undergoes electrolyte degradation [24]. The precise electron dose threshold where degradation will start must be known to prevent interference from radiolysis induced beam damage on the experiment.	Irradiate electrolyte *in-situ* TEM using the electron beam.
Positioning material onto the working electrode	A precise amount of active material must be positioned onto and adhered to the working electrode for quantitative electrochemistry.	Attempt cryo microtoming of $LiCoPO_4$ electrodes, and positioning with a nanomanipulator.
Positioning Li onto the counter electrode	Li is needed on the counter electrode for the *in-situ* cell to act as a Li-ion half-cell *in-situ* TEM.	Investigate the plating potentials of Li from $LiPF_6$ in EC/ DMC using the *in-situ* TEM cell set-up.

7.3 INFLUENCE OF THE ELECTRON BEAM ON THE ELECTROLYTE

7.3.1 Experimental

Preparation of the E-chips and holder loading

Poseidon Protochips top and bottom E-chips (ECT-24CO, and ECB-39A- shown in Figure 7.4) were cleaned of photoresist (the E-chips are shipped with a layer of photoresist to protect the surface) by swirling in acetone for 2 mins, followed by 2 mins in methanol. After removal of the photoresist, the E-chips were plasma cleaned for 13 s at 6540 W to ensure complete removal of photoresist, and complete wetting of the SiN_x windows by electrolyte.

The E-chip array was loaded onto the tip of a Poseidon Protochips P500 sealed liquid cell electrochemical TEM holder inside an Ar glovebox, to ensure no contamination from air. The TEM holder was connected to a syringe containing $LiPF_6$ in a 50/ 50 volume ratio of EC and DMC (Sigma Aldrich) using PEEK tubing and IDEX PEEK fittings. Using the syringe, electrolyte was flooded into the TEM holder tip. To ensure the tip region was fully flooded with electrolyte, tubing was connected to the exit port and electrolyte flooded into the holder until electrolyte could be seen coming out of the exit port. After flooding with electrolyte, the tubing was disconnected and the holder tubing capped. The irradiation experiment was performed in static mode (no electrolyte flowing around the circuit whilst the holder was in the TEM).

Electrolyte Irradiation

Prior to loading into the TEM the holder was vacuum leak checked using a pumping station. The holder had to achieve 10^{-5} mbar in the pumping station, to ensure proper assembly of the tip prior to insertion into the TEM.

Electrolyte irradiation experiments were performed in a JEOL 3010 at 300 keV beam energy in TEM mode. Due to the presence of liquid, the TEM could not be aligned independent of the sample prior to imaging, limiting the resolution and magnifications available. Focussing was performed with the objective lens.

Different regions of the electrolyte filled cell were irradiated and images taken at a beam current density of 1.5 pA cm^{-2}.

Post-mortem Analysis

After imaging, the Poseidon Protochips set-up was flooded with DMC to ensure complete removal of electrolyte. The E-chips were removed from the tip and washed further with DMC. The disassembly process was performed in an Ar filled glove box. The TEM holder was further cleaned with ethanol outside the glovebox.

Post-mortem SEM imaging of the was performed using an FEI Helios NanoLab G3 UC in secondary electron mode at 5 keV beam energy with an Everhart Thornley detector. Energy Dispersive X-ray Spectroscopy (EDS) was also performed using an Oxford Instruments EDS detector.

7.3.2 Results

Electrolyte Electron Beam Irradiation

Figure 7.5 shows the effects of electron beam irradiation at 1.5 pA cm^{-2} with a 300 kV beam. Within the first 10 s of irradiation, no visible precipitation of particles occurs (Figure 7.5 (f)). It should be noted that precipitation may have occurred, but deeper in the liquid than the focus region, although nucleation is more likely on the SiN_x window.

Figure 7.5 (f) is of a different region of sample than Figure 7.5 (a)- (e). Figure 7.5 (a)- (e) were not taken as a video so a delay occurred in taking the first image allowing some precipitation, however, no nucleation was observed at the start of electron beam irradiation.

After 20 s of irradiation (Figure 7.5 (a)), small particles with light contrast (100- 200 nm diameter) nucleate, as well as the nucleation of some larger particles with darker contrast (600 – 800 nm diameter). The imaging was performed in TEM mode, darker contrast typically results from thicker particles, however, in liquid cell microscopy contrast interpretation is more difficult as particles which form deeper in the solution typically appear lighter than those closer to the focal plane. In this case the boundary of the 100-200 nm particles is in focus so the lighter contrast is more likely due to the particles being thinner.

The region of slightly darker contrast on Figure 7.5 (a) occurred due to the beam drifting across the same area of sample prior to the image being taken. Therefore, the region within the slightly darker contrast on the left hand side of Figure 7.5 (a) had slightly higher beam dose than the right hand side of the image. The electron beam irradiation times recorded are the highest beam dose experienced by regions of the images in Figure 7.5 (a)-(e).

The darker strip on the left hand side of (Figure 7.5 (a), (b) and (c)) is the glassy carbon electrode. Nucleation and growth of particles is clearly visible on the edge of the electrode.

Particle growth of all the nucleated particles occurs between Figure 7.5 (a) and (Figure 7.5 (b)) and continues until 196 s (Figure 7.5 (c)).

After 309 s of electron beam irradiation (Figure 7.5 (d)), the particles continue to increase in diameter, with the lighter contrast particles forming a film. The film visible in (Figure 7.5 (d)) has a round edge as it is the edge of the electron beam from (Figure 7.5 (c)), so regions which have formed a film will have experienced greater electrolyte irradiation. Electron beam (focal) drift resulted in the beam moving between Figure 7.5 (c), and Figure 7.5 (e). After 391 s (Figure 7.5 (e)), the film regions form darker contrast, potentially because it is thickening.

It should be noted that a faint round region of darker contrast is visible in Figure 7.5 (a), a similar shape to the film in Figure 7.5 (d), but with lighter contrast. The nucleated particles within the slightly dark region of contrast are larger (100 – 800 nm) than those which have nucleated outside of the slightly dark region of contrast (60 – 80 nm). This implies some beam drift prior to imaging, hence the electrolyte on the left hand side of Figure 7.5 (a), is likely to have experience more irradiation than the region on the right. It is not possible to quantify the degree of extra irradiation.

In order to track the rate of particle growth with increased electron beam irradiation, the area of particles labelled 1 and 2 on Figure 7.5 (a)- (e) were measured using ImageJ, and plotted against irradiation time (Figure 7.5 (g)). Particles 1 and 2 were chosen as they remained within the irradiation zone throughout imaging. The growth rates were calculated by drawing a line of best fit (shown by the dotted lines on Figure 7.5 (g)), and calculating the gradient.

Figure 7.5 (g) shows that particle 1 is smaller than particle 2 throughout the growth period, however, both particle 1 and particle 2 experience similar changes in growth rate. From 20 s to 196 s the growth rate for particle 1 was 1180 $nm^2\ s^{-1}$, and for particles 2 was 1860 $nm^2\ s^{-1}$. After 309 s of irradiation there was an acceleration in particle growth rate to 4610 $nm^2\ s^{-1}$ for particle 1, and 5910 $nm^2\ s^{-1}$ for particle 2.

It should be noted the particle diameters measured in Figure 7.5 are larger than the nominal thickness of the liquid cell spacer (500 nm). Under the TEM vacuum the SiN windows bow, hence the thickness between the windows is thicker than 500 nm.

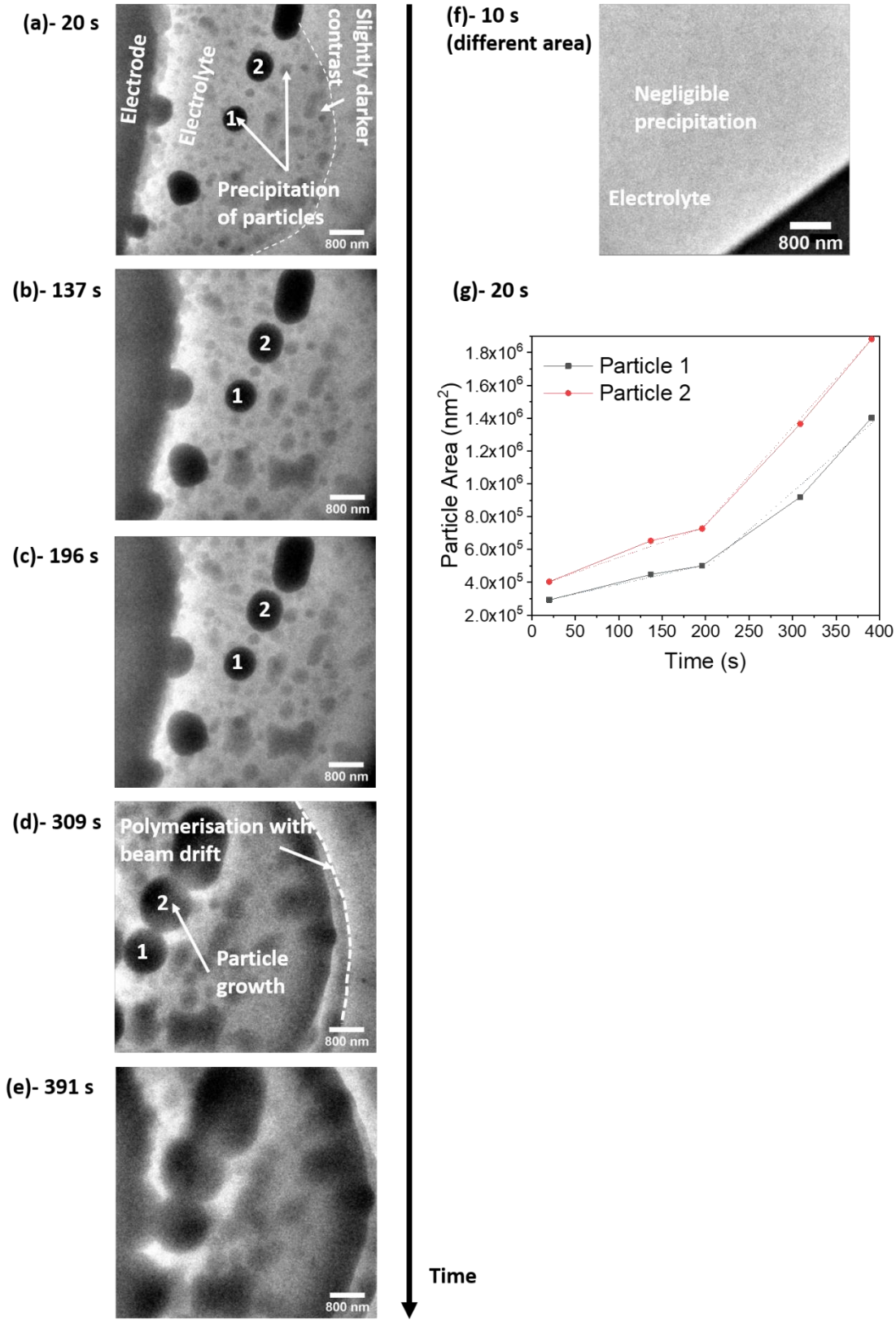

Figure 7.5: (a)-(e) in-situ electron beam irradiation TEM images of $LiPF_6$ in EC/ DMC electrolyte from (a) 20 s, (b) 137 s, (c) 196 s, (d) 309 s, and (e) 391 s irradiation using a 300 kV e-beam. (f) in-situ TEM image of a different region of electrolyte after 10 s. (g) particle area variation with electron irradiation time of the particles marked 1, and 2.

It was not possible to perform any *in-situ* chemical characterisation in the TEM due to a lack of EELS, EDS, and STEM capability in the JEOL 3010. Therefore, in order to study any chemical changes, the top (electrode) E-chip was examined post-TEM electron beam irradiation in a scanning electron microscope using secondary electron imaging (Figure 7.6) and EDS (Figure 7.7). As noted in 7.3.1, the E-chip was washed with DMC prior to SEM imaging.

Figure 7.6 (a) is a low magnification image of the SiN_x window and the glassy carbon electrode. It should be noted that the SiN_x window in the secondary electron images has very dark contrast because it is electron transparent. The large trapezium shaped region to the left of the image is part of the electrode insulation (SU-8 polymer), patterned onto the E-Chips.

Figure 7.6 (a) clearly shows two circular regions of differing morphology (material deposition) on the surface of the glassy carbon electrode and the SiN_x window. These are the residual films deposited by the electron irradiation of the electrolyte imaged in Figure 7.5. The electron beam has a circular projection through the sample, and hence the films have a similar shape to those imaged in Figure 7.5 (d) and (e). Evidence of a third irradiation region is present on the upper ring (as an arc of thicker deposition). It is likely the third deposition was short as the film does not extend, hence during the third deposition, the beam enhanced deposition from the top film, but the dose was not high enough to nucleate material in other areas.

As this is a post-mortem experiment, the effects of multiple irradiation events undergone by the E-chip during the TEM experiment are present. Movement of the irradiation area due to beam drift, or sample drift, observed in Figure 7.5, and movement of the sample to look at different areas likely caused the differences in electron beam irradiation, and hence differences in material deposition.

The lower residual e^- beam damage region is not as round because there is a crack in the SiN_x window which occurred post-TEM and has resulted in the spalling of part of the SiN membrane and attached deposited film.

Higher magnification images of the residual e^- beam damage regions show the morphology of the electron beam induced film Figure 7.6 (b) and (c). The films are not uniform, containing particle ridges and tooth-like particle structures. It should be noted that the thicker regions are in an arc shape, or where the two beam-damage regions have overlapped, implying that these areas may have experienced a greater degree of electrolyte damage due to experiencing a higher electron dose because of the reasons stated above. The e^- dose can also be enhanced at the perimeter of the beam spot, leading to thicker regions at the edges of the films. In the TEM the glassy carbon electrode is not electron transparent so it is possible to overlap previously irradiated regions of electrolyte without realising.

Figure 7.6 (c) shows a higher magnification image of the right hand side of the upper round region in Figure 7.6 (b). The thicker arc region is visible, however the film also consists of smaller spherical particles (150 – 200 nm), the same size as the initial nucleated particles in Figure 7.5 (a). The larger bulbous type structures consist of particles ranging from 600 – 1000 nm), similar to the large dark particles in Figure 7.5 (e). The remainder of the film is relatively featureless, similar to the background film visible on Figure 7.5 (d) and (e).

Small salt crystals (30- 80 nm) are visible on the surface of the glassy carbon electrode (Figure 7.6 (c)). The small crystals are also visible on the surface of the e^- beam induced film, implying they are likely a drying effect.

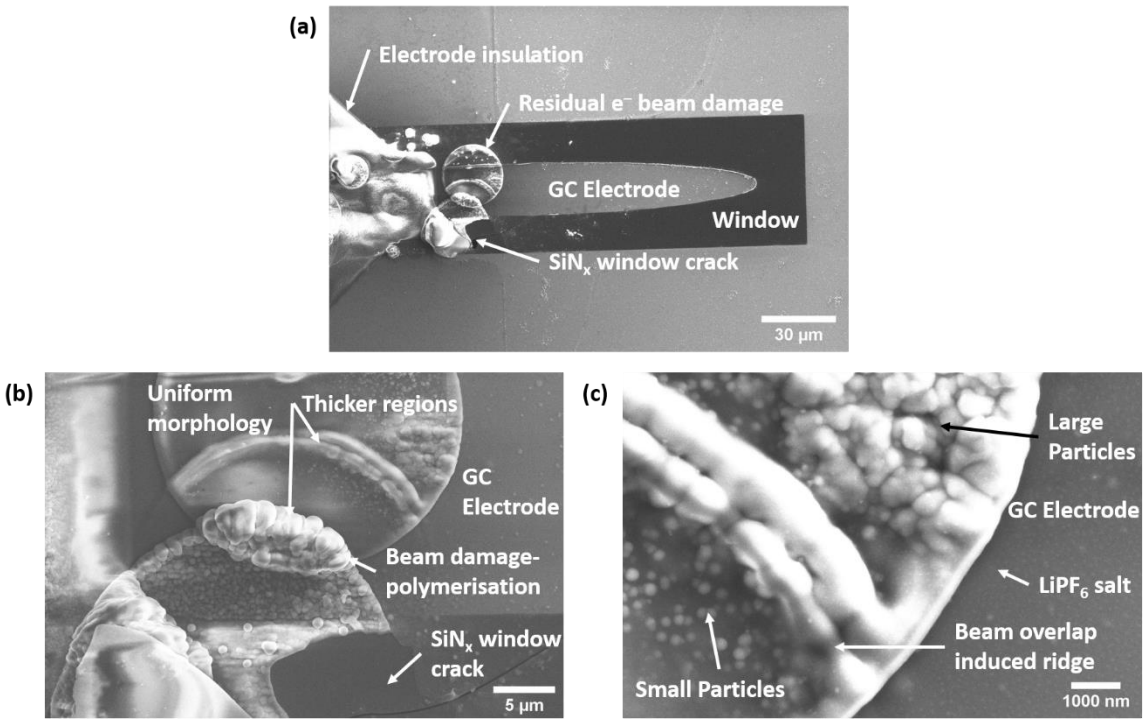

Figure 7.6: SEM images of the electrode chip post-electrolyte electron beam irradiation. (a)- overview of the electron transparent window with a central glassy carbon electrode, (b)- magnified image of the TEM electron beam damage region, (c)- further magnified image of the TEM electron beam damage region.

In order to chemically characterise the e^- induced film EDS was performed (Figure 7.7 (b)). Figure 7.7 (b) shows the EDS map corresponding to the secondary electron image in Figure 7.7 (a). P is present all over the sample, but particularly concentrated on the surrounding glassy carbon electrode, and SiN_x window regions. This implies the salt crystals visible on Figure 7.6 (c) are likely residual $LiPF_6$ salt.

The e^- beam damage residue regions are rich in C and O, with some P present as well. F is detected across the sampling area, likely due to the salt crystals shown in Figure 7.6 (c). This implies the e^- beam damage residue regions are likely polymerised solvent (DMC and EC). EDS cannot detect Li so it was not possible to detect any Li salts. In order to make more deductions about the surface chemistry, backscattered imaging at low potentials should have been performed.

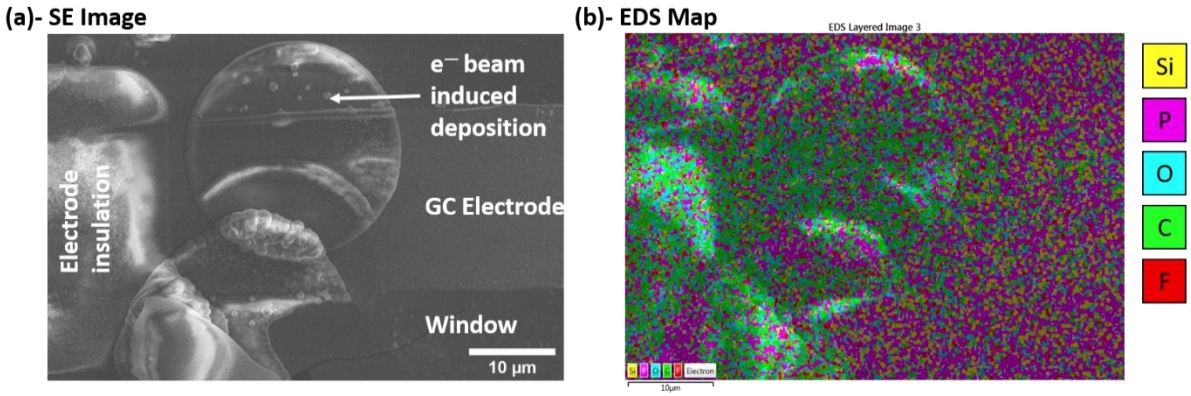

Figure 7.7: SEM image (a), and corresponding EDS map (b) of the TEM electron beam deposition onto the electrode chip after irradiation of $LiPF_6$ in DMC/ EC.

7.3.3 Discussion

The results of the electron irradiation of $LiPF_6$ in EC and DMC electrolyte experiment in Figure 7.5 show that above a threshold dose, precipitation of particles ranging from 100- 800 nm occurs, followed by an increased growth rate in particles and the formation of films after 391 s irradiation at 1.5 pA cm^{-1}. The films remained on the electrode after the experiment (Figure 7.6), with EDS confirming they are rich in carbon and oxygen (Figure 7.7). Abellan et al. in their experiment irradiating $LiPF_6$ in EC and DMC, noted similar results, identifying initial 100 nm precipitates as LiF, formed from nucleophilic attack on $LiPF_6$, followed by the precipitation and growth of carbonate due to decomposition of the electrolyte solvents [24]. As in Abellan et al. the precipitates in Figure 7.5 (a)-(d) also grew in a bulbous manner suggesting similar chemistry.

Figure 7.5 (f) indicates there is an electron dose under which no damage to the electrolyte will be visible (after 10 s irradiation at 1.5 pA cm^{-1}). It is possible the nucleated particles are too thin to give detectable contrast in Figure 7.5 (f). However, a lack of nucleated particles is similar to other work, suggesting a threshold activation energy, and minimum electron dose is required to begin nucleation of precipitates from electron beam irradiation[24], [43]. 1.5 pA cm^{-1} was the current density measured on the CCD detector during data collection, however it is not necessarily the electron dose received by the electrolyte as scattering mechanisms, such as scattering by the SiN window, occur before the electrons hit the detector.

Conclusions around activation energy for precipitation, and comparison with literature and future experiments are not possible without knowing the electron dose. Silver nanoparticle formation can be used as a method of calibrating dose as recombination of silver ions in solution with a solvated electron results in the formation of silver nanoparticles [20]. The effect of dose can then be visualised. Further work would require calibration of the dose to be able to compare to literature, and to control the dose for future experiments.

After 20 s of electron beam irradiation, precipitates of 100- 800 nm formed Figure 7.5(a). Due to a lack of EELS equipment available in the JEOL 3010, it was not possible to chemically characterise the precipitates in this experiment. However, the smaller precipitates in Figure 7.5(a) were the same size as those measured by Abellan et al. (100 nm) [24], suggesting these are likely to be LiF.

As the liquid thickness is at least 500 nm thick (the spacer thickness, not accounting for the window bowing thickness [19]) it is possible the smaller particles are deeper in the solution, presenting focussing issues as the particles may be out of the focal plane, leading to an error in the particle size due to poor resolution [43]. Given the particles in Figure 7.5 don't move relative to the electrode, it is likely they are attached to the SiN window. Examples of the precipitates growing on the windows are shown in Figure 7.6.

The larger particles in Figure 7.5 (d), and (e) have diameters larger than 500 nm. Window bowing likely provided more room for particle growth. The precipitates may also have touched the bottom window constraining growth towards the other chip. In practical terms, this behaviour is risky as the SiN windows could fracture, exposing electrolyte to the TEM, if precipitate growth is too large.

Figure 7.5 (g) shows that there is a rapid change in growth rate of the precipitates after 196 s of irradiation, coupled with the formation of a film in the area of electron beam irradiation (Figure 7.5 (d) and (e)). This suggests the possibility of a two-step damage mechanism, in agreement with Abellan et al. [24]. Initially $LiPF_6$ forms LiF due to the recombination of Li^+ and F^- following on from the e_s^- formation of PF_5^- lewis acid. The lewis acid attacks solvent molecules, leading to the precipitation of polycarbonate films (such as the film visible in Figure 7.5 (d) and (e)).

Post-mortem EDS of the residual film in Figure 7.7 (b) shows that residual films on the electrode surface contain C and O, supporting the identity of the film in Figure 7.5 (d) and (e) as polycarbonate resulting from solvent breakdown. Moreover, charging was evident by the bright streaking on the residual film in the SEM images in Figure 7.6, implying an insulating layer and further supporting the polycarbonate film argument. It should be noted that it is not clear if the region imaged in the SEM images in Figure 7.6 was the same as the region imaged using *in-situ* TEM in Figure 7.5 as multiple irradiations were run on the same sample.

The post-mortem SEM images in Figure 7.6 show that the film grown is not uniform. The arc shaped ridge and the thicker bulbous region Figure 7.6 (a) is likely due the region being irradiated by the TEM beam for longer periods of time. The round shape of the arc suggests this is the edge of the electron beam, and the bulbous region is where the two films overlap. This is in agreement with prolonged exposure to the electron beam, causing further damage to the electrolyte [24].

Given the precipitate formation sequence shown in Figure 7.5 (a)- (e), it is likely the nucleated particles coalesce into a film. The larger bulbous regions are potentially nucleation regions which have yet to coalesce into the film. Further work is required to clarify this.

The higher magnification images in Figure 7.6 (b) and (c) show that the film on the E-chip surface also consists of small spherical particles (150- 200 nm), and larger bulbous type particles (600 – 1000 nm). The sizes are similar to the sizes of the particles precipitated in Figure 7.5, suggesting they might be residual particles left on the electrode surface. As discussed above, the particles could be LiF. F was found all over the surface of the E-chip by EDS (Figure 7.7 (b)), and attributed to residual electrolyte salt. In order to fully identify the particles on Figure 7.6 (b) and (c), EDS should have been performed at higher magnifications, coupled with backscattered imaging.

Overall, the initial electrolyte beam irradiation tests indicate that there is a threshold electron beam dose under which electrolyte damage would be minimal. For experiments involving *in-operando* cycling of $LiCoPO_4$ imaging would need to be performed under this dose. As the electron dose itself was not calibrated, currently the suggested imaging conditions would be 1.5 pA cm^{-1} for 10 s. The electron beam dose would need to be calibrated for greater accuracy and control.

7.4 Setting up the Protochips Cell as a 3 Electrode Cell

7.4.1 The Ideal Set-Up

The aim of this section is to detail the different methods attempted to position $LiCoPO_4$ (active material) on the working electrode, and Li on the counter electrode (as shown in Figure 7.8).

It should be noted that Figure 7.8 shows $LiCoPO_4$ as particles on the working electrode. In the initial stages of the process, a powder suspension drop method was attempted, which resulted in powder on the working electrode, isolated from the counter electrode. Unfortunately, this process also resulted in contamination of the reference electrode with $LiCoPO_4$ powder, which would lead to inaccurate potential readings, so a more precise method was attempted. The more precise method developed here is a microtoming method.

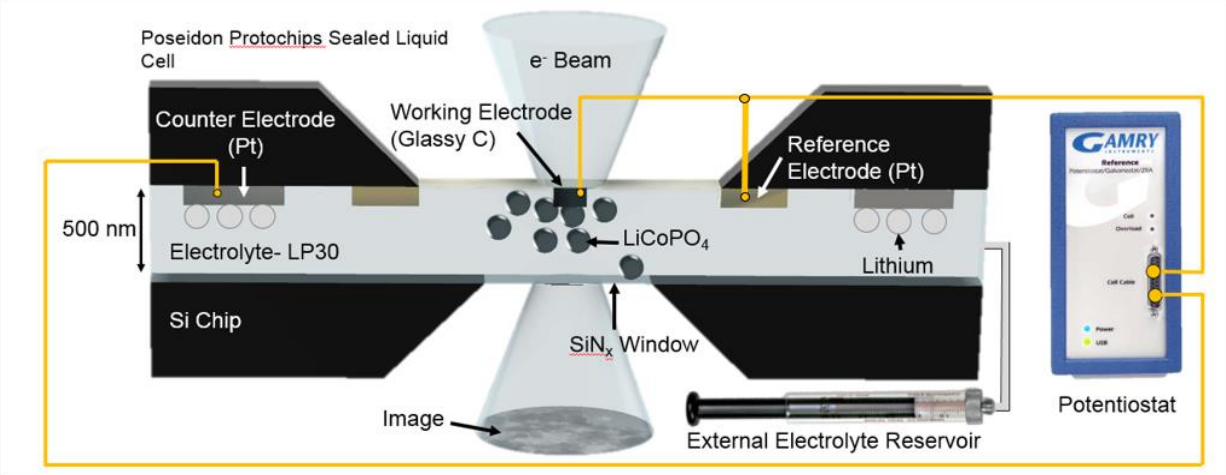

Figure 7.8: Schematic of the initially targeted nano-cell set-up. Lithium is plated onto the Pt counter electrode, and $LiCoPO_4$ is isolated on the glassy carbon working electrode.

7.4.2 Placing Electrode Active Materials on the Working Electrode

7.4.2.1 Experimental

Electrodes of composition 0.9 wt. % C-$LiCoPO_4$, 0.05 wt. % C65, and 0.05 wt. % PVDF were manufactured using the slurry tape casting method described in the previous two chapters of this thesis. The electrodes were calendared to between 1.8 g cm^{-3} and 2 g cm^{-3} density.

The electrodes were cryo-microtomed onto a Si wafer to 100 nm thickness. Cryo microtoming was performed using a Leica EM UC6 microtome. In order to cryo-microtome the electrodes, the electrodes were cut into a small 2 mm x 2 mm triangles and mounted onto a stub using Tissue-Tek glue. Hexanol was dropped onto the tip of the triangle, and the temperature of the cryo-microtome dropped until the hexanol froze. The previous microtoming work in this thesis mounted the electrodes in resin so that the slices would not crumple during microtoming. The hexanol was intended to act in a similar way, except melt and eventually evaporate so only the electrode was left on the E-chip electrode.

The electrode slices were positioned onto the working electrode of the E-chip from the Si collection wafer using bench top micromanipulators. The micromanipulators transferred the $LiCoPO_4$ section from the Si collection wafer to the E-chip using electrostatic forces. An optical microscope enabled accurate position of the $LiCoPO_4$ section.

After positioning the electrode slices onto the working electrode, the samples were imaged using a Helios Nanolab G3 UC FIB-SEM, and a Pt tab deposited to attach the slices to the working electrode, using electron beam ion beam deposition (EBID).

7.4.2.2 Results and Discussion

Figure 7.9 (a) shows that electrode slices were successfully sliced from the main electrode and positioned onto the glassy carbon working electrode of the *in-situ* cell. However, there was a risk that the slices could move off the electrode prior to transfer into the SEM, and during imaging (Figure 7.9 (b)).

In terms of viability for an *in-situ* TEM experiment, the sample in Figure 7.9 (a) would not have worked in a TEM imaging experiment as no part of the sample is sitting over the electron transparent window. However, the sample could have been viable for *ex-situ* testing.

The SEM imaging of the slices in Figure 7.9 (a) show that the electrode slice had curled. The electrodes were microtomed to 100 nm set thickness, because the spacer on the top chip is 500 nm thick. Any sample positioned into the *in-situ* TEM holder has to be less than 500 nm thick, or risk breaking the SiN_x windows when the E-chips are assembled into the TEM holder. The thickness tolerance increases during TEM imaging as the TEM vacuum causes the SiN_x windows to bow, however, sample loading occurs at room pressure so the bowing advantage is not available. Curling electrode pieces risked the electrodes becoming greater than 500 nm thick, and breaking the SiN_x windows.

Additionally, Figure 7.9 (a) shows that the slices of electrode positioned onto the working electrode were different sizes. This reduces the ability to repeat the experiment and quantify any electrochemistry, as the active material area is not known. If the slice is adjacent to the glassy carbon electrode, the section size could be measured during the *in-situ* TEM experiment. However, the experiment would not be repeatable as micro-toming does not allow for repeatable section sizes.

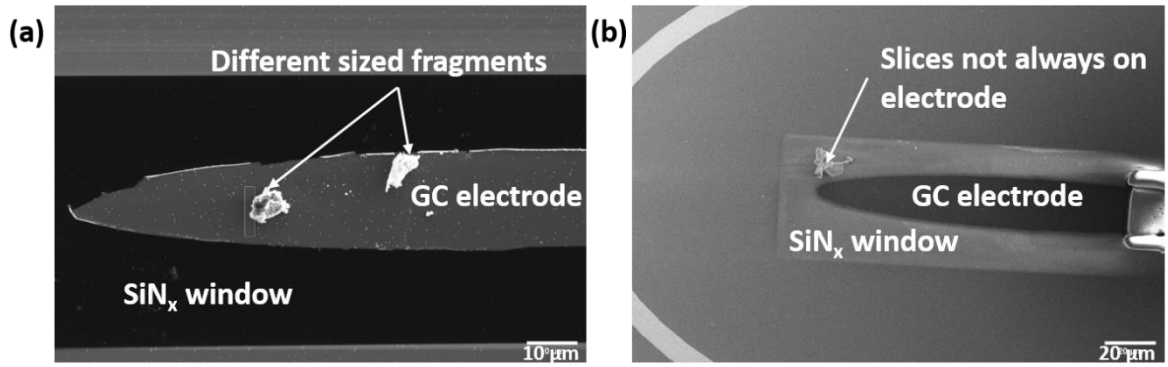

Figure 7.9: SEM images of microtomed electrode sections positioned (a) onto the working electrode (GC electrode) or (b) near the working electrode.

The SEM images in Figure 7.9 demonstrate a few problems with the microtoming method. However, there is a further electrical contact problem detailed in the schematic in Figure 7.10. Microtoming was performed on electrodes containing binder, conductive additive, and $LiCoPO_4$. In a bulk electrode, the particles are randomly distributed in a 3D array, creating many different conduction pathways, in spite of using an electrically insulating binder to hold the electrode together. When the electrode is microtomed to 100 nm thickness, there are fewer electrical conduction pathways, within the limited volume, to the $LiCoPO_4$. In the microtomed section the binder can act as an insulating barrier between the $LiCoPO_4$ particles and the working electrode. Therefore, knowledge and the control over the volume of active material being used and hence the current density is lost.

To circumvent the binder induced conductive pathway issue, a green body of compressed $LiCoPO_4$ particles should have been microtomed. Alternatively, the FIB sectioning method should have been used on a $LiCoPO_4$ green body as this would have allowed greater control over the volume and dimensions of $LiCoPO_4$ positioned onto the E-chip. However, the FIB slice would likely be contaminated with Ga.

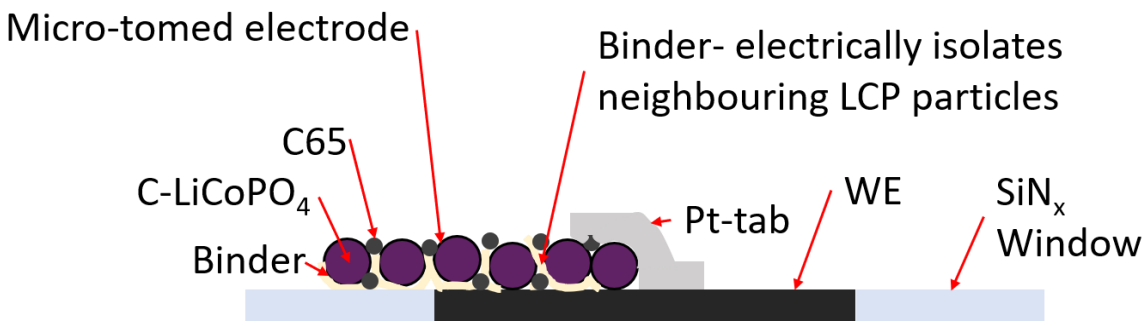

Figure 7.10: Schematic outlining the problem of electrical isolation associated with microtoming composite electrodes, and positioning the slices onto the working electrode (WE).

7.4.3 Plating Li onto the Counter electrode

7.4.3.1 Experimental

Lithium Plating on to the counter electrode

The goal of the plating experiments was to understand how to plate Li from $LiPF_6$ in EC and DMC on to the Pt counter electrode of the top chip (Figure 7.4), with the aim to create Li-ion half-cell in the TEM.

The Poseidon Protochips P500 TEM holder tip assembly was set-up using the dry loading method described in 7.3.1 in an Ar filled glove box using $LiPF_6$ in 50/ 50 volume ratio of EC and DMC (Sigma Aldrich).

Unlike the experiment described in 7.3.1, the plating experiment required electrolyte flow through the E-chip array (see Figure 7.3). A syringe of electrolyte was attached to a Harvard syringe pump connected to the TEM holder inlet tube using PEEK tubing and IDEX fittings. The outlet tube led into a beaker sealed with parafilm. After assembly in the Ar filled glove box, the TEM holder rig was removed from the glove box and placed on the lab bench for electrochemistry experiments outside of the TEM.

Work by Mehdi et al. showed that Li can be plated onto Pt electrodes from $LiPF_6$ in propylene carbonate (PC) electrolyte [10] using the Poseidon *in-situ* TEM holder (see Figure 7.11). The parameters in [10] were used as initial starting parameters for finding the plating potential of Li from $LiPF_6$ in 50/ 50 EC and DMC.

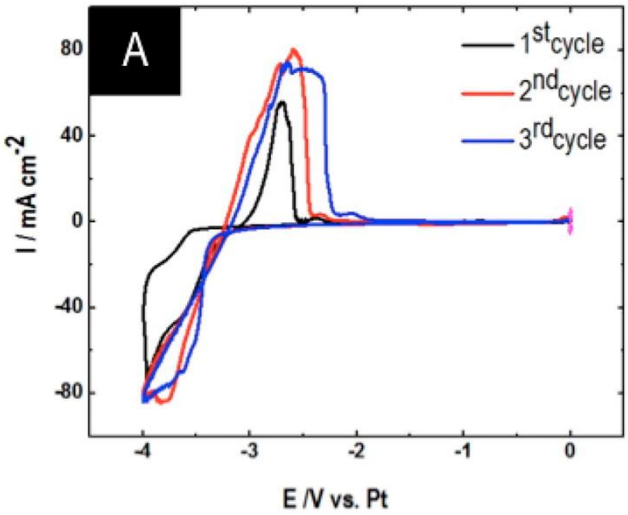

Figure 7.11: Literature example cyclic voltammetry (CV) plating Li onto Pt electrodes using Poseidon in-situ TEM cell. Reprinted with permission from *Nano Lett. 2015, 15, 3, 2168-2173.* Copyright 2015, the American Chemical Society [10]

For cyclic voltammetry (CV) experiments, the Poseidon P500 holder was connected to a Gamry Reference 600 potentiostat using the connections shown in Figure 7.12. It should be noted that the plating electrode (the Pt counter electrode) is referred to as the Pt counter electrode in this section, although it is acting as a working electrode in this experiment.

Cyclic voltammetry was performed from 0 V vs. Pt to different potentials (-4.3 V vs. Pt, -4.7 V vs. Pt, and -5 V vs. Pt) to 0 V vs. Pt at 5 mV s^{-1}. The end potential was dropped to lower potentials from -4.3 V vs. Pt until plating was evident from the cyclic voltammetry curve (when the voltage sweep to positive potentials overlapped the voltage sweep to negative potentials in the negative current density regime). To prevent the solution from fully electrolysing, the electrolyte was flowed at a rate of 600 µL h^{-1} using a Harvard syringe pump to refresh the electrolyte through the cell.

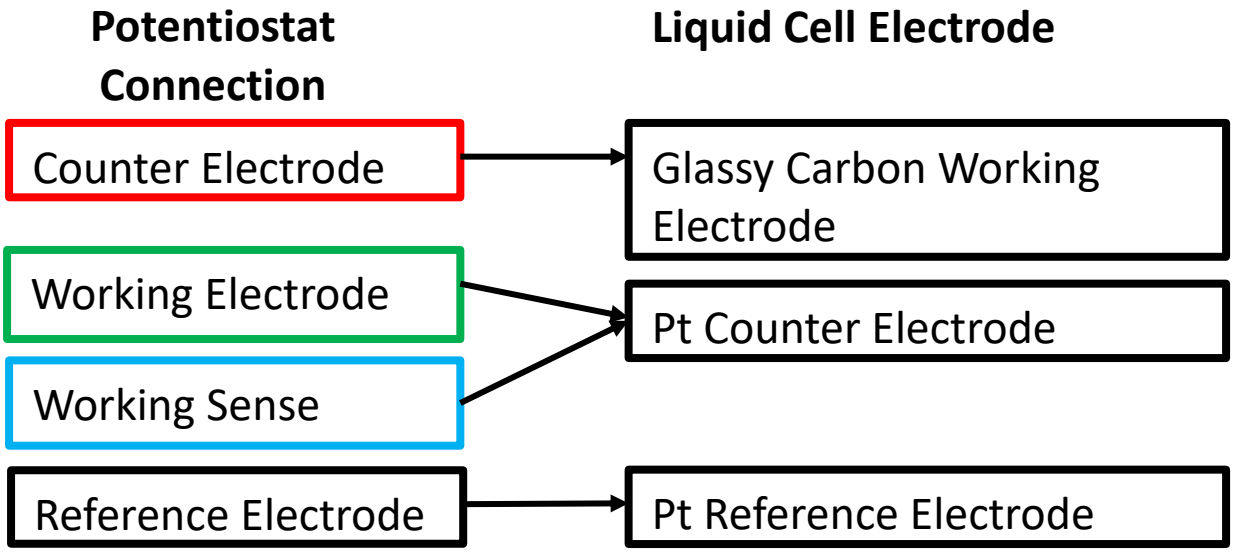

Figure 7.12: Gamry potentiostat Electrode connection to the Liquid cell electrodes for the Li and Cu plating experiments. The liquid cell electrode array is shown in Figure 7.4.

Once Li plating was evident on the cyclic voltammetry curve, a linear sweep potential at 5 mV s^{-1} to the plating potential (-5 V vs. Pt) was performed in order to plate the Pt counter electrode with Li.

After plating the Pt counter electrode, the TEM holder assembly was taken back into an Ar filled glove box, and the E-chip array disassembled and cleaned with DMC using the method described in 7.3.1. After cleaning the E-chips were removed from the glove box and imaged using an Inspect F SEM using both secondary electron imaging, and backscattered electron imaging.

$CuSO_4$ Solution Plating Experiment

In order to test the metal plating without the air exposure issues associated with Li electrolytes, the plating experiment was also performed with copper sulphate solution, aiming to plate copper onto the counter electrode via the half-cell reaction:

$Cu^{2+} + 2e^- \rightarrow Cu$

A solution of 0.1 M $CuSo_{4(aq)}$ in 0.1 M $H_2SO_{4(aq)}$ was made up for plating.

In order to estimate the voltage window required to plate copper in the liquid cell, initially Cu plating was performed using a benchtop 3 electrode cell, where the solution was placed into a beaker. The electrode array used was a Pt working electrode, a Pt reference electrode, and a glassy carbon electrode. This set-up is referred to as the bulk cell.

Different maximum potentials were applied using a 20 mV s^{-1} voltage sweep, until Cu plating was achieved. Plating was checked visually by inspecting to see if the silver coloured Pt working electrode had a layer of Cu.

The liquid cell E-chip array was dry assembled as described above, and $CuSO_4$ solution flooded into the cell at 600 µL h^{-1} using a Harvard syringe pump.

Cyclic voltammetry was performed on the $CuSO_{4(aq)}$ solution using the electrode connections shown in Figure 7.12. Cyclic voltammetry from 0 V to -1 V, to 0.5 V to 0 V vs. OCP (open circuit potential) was performed at a scan rate of 5 mV s^{-1}.

$CuSO_4$ was flowed at 600 µL h^{-1} during CV to prevent total electrolysing of the solution. Lower flow rates were attempted, but cell overload occurred.

In order to leave Cu on the counter electrode for inspection with the SEM, a linear sweep voltammetry at 5 mV s^{-1} from 0 V to -1V vs. OCP was carried out.

The E-chip assembly was disassembled and the top E-chip imaged using an SEM (Inspect F) to look for evidence of Cu plating on the Pt electrode.

7.4.3.2 Results and Discussion: Li Plating onto in-situ *chips*

Figure 7.13 shows the cyclic voltammetry (CV) curves acquired when attempted to plate Li onto the Pt counter electrode from $LiPF_6$ in 50/ 50 EC and DMC, and a linear sweep voltammetry (LSV) curve used to plate Li onto the large Pt counter electrode in Figure 7.4 (a) for post-mortem SEM. The CV and LSV curves in Figure 7.13 are plotted against current density, calculated by dividing the measured current by the counter electrode area (260000 μm^2).

The light blue dash-dot curve in Figure 7.13 is a cyclic voltammetry curve swept to -4.3 V vs. Pt. The curve is a banana shape, with no observable reduction or oxidation peaks observed. The

banana shape of the CV is likely due to capacitive behaviour of the electrolyte. Minimal noise was recorded on the -4.3 V vs. Pt curve.

The -4.7 V vs. Pt sweep curve (dark blue dotted) has a similar shape to the -4.3 V vs. Pt (light blue dash-dot), indicating some capacitive behaviour. However, unlike the -4.3 V vs. Pt curve, some small reduction and oxidation peaks are observed at -4.25 V vs. Pt, -4.58 V vs. Pt, and -2.08 V vs. Pt respectively. It is unclear what is causing the small oxidation and reduction peaks, however the lack of sudden increase in negative current density (as seen on the pink curve), the associated overlap, and the dissimilarity between the shape of the dark blue dotted curve and the CV curves in [10] (Figure 7.11) suggests this is not Li plating.

The -5 V vs. Pt curve in Figure 7.13 (pink solid line) has a significantly different shape to the -4.3, and -4.7 V vs. Pt curves. Firstly, as the cell is taken to negative potentials, a sudden negative increase in current is observed at -4.3 V vs. Pt, with a reduction peak occurring at -4.76 V vs. Pt. An oxidation peak was observed at -2.14 V vs. Pt. Significant noise was also observed at -4.8 V vs. Pt which is discussed later. Ignoring the significant noise evident at -4.8 V- 5 V vs. Pt, the shape of the -5 V vs. Pt curve is similar to the Li plating curves in [10] (Figure 7.11), with observable oxidation and reduction peaks, and overlap of the trace on current reversal in the reduction region. This suggests that Li plating occurred on the -5 V vs. Pt sweep.

The slight difference in reduction and oxidation peak between the measured data in Figure 7.13, and the literature example in Figure 7.11 may have occurred as the counter electrode in this experiment was glassy carbon, whereas all the electrodes reported in [10] were Pt. Changes in the H_2O content of the electrolyte, which was not measured here, may also influence the oxidation and reduction potentials due to increased HF presence.

The -5 V vs. Pt sweep was the final CV performed in this set of experiments. The variations in the -4.7 V vs. Pt sweep curve (Figure 7.13 dark blue dotted line) suggest the potential for some changes to the Pt electrode surface prior to the eventual plating observed on the -5 V vs. Pt sweep (Figure 7.13 solid pink line), hence the plating may not have been directly onto a Pt surface. Mehdi et al. noted the observation of solid electrolyte interphase on the surface of the Pt electrodes during the plating process. SEI layers should theoretically form before Li plating [44], so it is also possible that Li plating is occurring onto an SEI layer.

Despite plating being achieved on the -5 V vs. Pt sweep, significant noise occurred at between -4.8 and 5 V vs. Pt (Figure 7.13 solid pink line). It is unclear what caused this noise to occur. The noise only occurred when the voltage sweep was greater than -4.8 V vs. Pt (Figure 7.13), so it is unlikely to be an earthing problem. Given the very small current measured in the experiment (µA), it is possible that external vibrations, may have caused a degree of noise. Bubble formation in the electrolyte may also cause noise.

The noise occurred after plating, and stopped when the potential is shifted towards 0 V vs. Pt, suggests the cause may be electrochemical in nature. Further breakdown of the electrolyte may have started causing gas bubbles to form, particularly if any water was present in the electrolyte [45]. It is likely moisture contamination of the electrolyte occurred as the electrolyte outflow was into a beaker, sealed with parafilm, opening the system to atmosphere. The electrolyte injected into the cell was uncycled prior to being flowed into the cell. Electrolyte also contains trace amounts of water.

In terms of repeating experiments in the TEM, bubbles create a large risk to the experiment. The TEM requires a high vacuum to operate, and bubble formation inside the liquid cell could risk breaking the SiN_x window and hence loss of vacuum in the TEM.

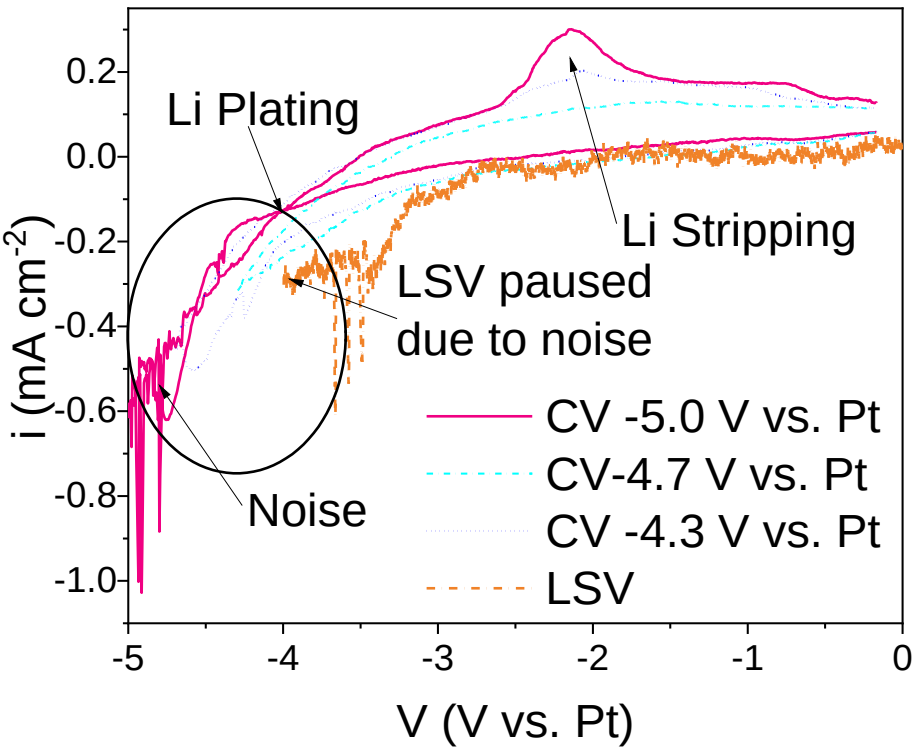

Figure 7.13: Cyclic voltammagrams plating Li onto the large, liquid cell counter electrode. The CVs were run to -4.3 (light blue dash-dot), -4.7 (dark blue dots), and -5.0 V vs. glassy carbon (GC) (pink solid line). The linear sweep voltammetry (LSV) (orange dash-dot) was run to -5.0 V vs. Pt, but was paused at -3.8 V vs. Pt due to noise. Plating occurred on the -5.0 V vs. Pt cycle, circled on the graph.

To confirm whether Li plating had occurred, SEM was performed on the E-chip after a linear sweep voltammetry (LSV) to -5 V vs. Li/ Li^+. The linear sweep voltammetry was performed after the cyclic voltammetry experiments in Figure 7.13, therefore the SEM images in Figure 7.14 and Figure 7.15 are of plating onto an already contaminated Pt surface. The samples were also exposed to air prior to insertion into the SEM, so any Li which did form is likely to have oxidised.

The LSV in Figure 7.13 was originally programmed to sweep to -5 V vs. Pt to ensure Li plating. Figure 7.13 shows the LSV was stopped at -3.8 V vs. Pt due to noise being recorded and worries over damaging the *in-situ* TEM cell if the sweep was completed. Given the drop to more negative current densities at -3 V vs. Pt, it is likely a reduction process occurred, however, given the sweep did not continue to the full plating potential, it is unclear if the reduction process was due to Li plating.

Figure 7.14 shows SEM images of the surface of the electrode array using (a) secondary electrons, and (b) backscattered electrons. The secondary electrode image shows an in-homogenous distribution of surface deposits on the surface of the E-chip. The deposits are not isolated on the Pt counter electrode, but extend across the surface of the electrode region. The deposits are mostly contained within the spacer defined electrode array region, however, some deposits can be seen on the spacer surface. This is indicative of some leaking of the electrolyte between the edges of the two chips.

Comparing the secondary electron image Figure 7.14(a) to the backscattered electron image Figure 7.14(b), shows that the deposit regions have a comparatively low Z to the platinum and the SU-8 spacer. SU-8 is an epoxy based photoresist, consisting of carbon and oxygen chains. The average Z number of the deposits is therefore likely to be lower, suggesting the deposits are either Li, or lithium based salts. Li is not detectable using EDS, so EDS could not be performed to confirm the presence of Li.

The backscattered electron image in Figure 7.14(b) shows that there is less coverage by the Li based deposit on the Pt reference electrode compared to other areas. This is likely due to the Pt reference electrode, acting as the reference electrode in the experiment (see Figure 7.12), and therefore having minimal current. In terms of SEM imaging, the underlying Pt may contribute to a higher yield of backscattered electrodes on the electrode, compared to the SU-8.

The secondary electron image in Figure 7.14(a) shows a 500 µm dendrite shape extending across the surface of the electrode array. It is possible that this is a Li dendrite growing in the direction of the electric field (towards the centre). However, it is surprising that the dendrite does not touch the Pt electrode which should be where the electric field is strongest. Finite element modelling of the electric fields on the electrode set-up was not performed, so it is difficult to draw conclusions from this.

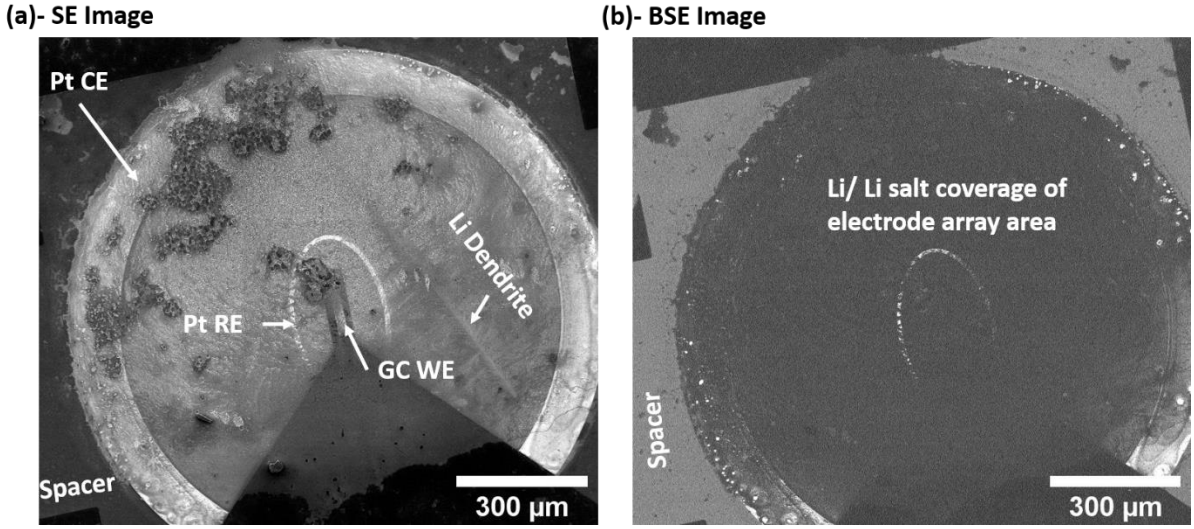

Figure 7.14: (a)- secondary electron image of the electrode array post-Li plating, (b)- the corresponding backscattered electron image of the area. Both images were taken at 5 kV.

Higher magnification images of the electro-deposits on the Pt electrode are shown in Figure 7.15(a), (c), and (d). It is clear that the deposits consist of spheres covering the surface of the electrode array. Initially it was thought that the spheres were a result of dried electrolyte salt. However, closer inspection of regions away from the electrode array Figure 7.15(b) revealed salt crystals of a different shape to the spheres in Figure 7.15(a). The salt crystals in Figure 7.15(b) are likely to be dried $LiPF_6$ salt, hence the spheres in Figure 7.15(a) likely result from electrochemical activity.

Figure 7.15(a) shows that the spherical formations are not distributed evenly across the surface. Some of the gaps are random shapes, however, some gaps are circular. The circular gaps are likely evidence of bubble formation from electrolyte reduction, potentially shown by the noise in the LSV curve in Figure 7.13 (orange). The gaps may also have arisen from cracking as the surface dried post-mortem.

Figure 7.15(c) and (d) show higher magnification images of the spheres. Figure 7.15(c) shows that as the nanoparticle layer thickens the spherical formations form a crust and can coalesce into a film. The film contains dots of darker contrast on the surface. Figure 7.15(c) is a secondary electron image, so the dots on the surface are likely a result of surface topology.

Figure 7.15(c) also shows a distinct circular gap in the film. Within the hole globule type shapes on the surface suggest there is a layer on the surface, before reaching the underlying Pt electrode. This is likely originates because the multiple cycling of the TEM chip cell left residue on the surface of the Pt electrode (such as SEI layer), similar to results observed in [10].

Figure 7.15(d) shows that the deposited nano-spheres are very uniform, and approximately 160 nm in diameter.

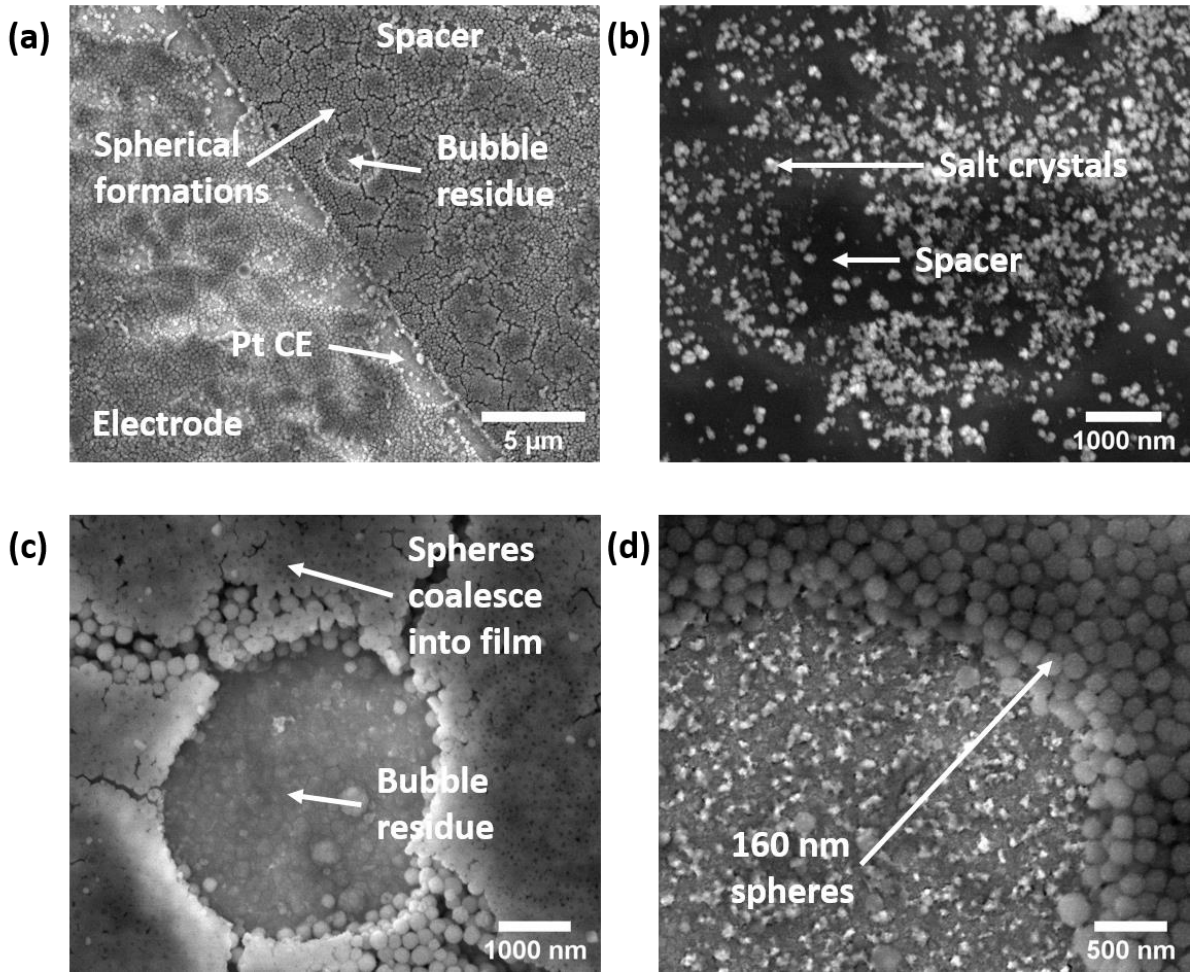

Figure 7.15: Secondary electron 5 kV images of (a) the Pt CE electrode/ spacer interface, (b)- a region on the spacer away from the electrode array showing residual salt crystals, (c)- Region of the Pt CE electrode surface with spheres coalescing into a film, (d)- high magnification image of the spheres.

The chemical composition of the spheres cannot be identified by SEM. As discussed above the backscattered image (Figure 7.14(b)) suggests that they are either Li, or Li containing salts. Further work involving chemical characterisation techniques, such as SIMS or XPS would be required to fully identify the nano-spheres. Without further testing, it is not possible to identify the origin of the nano-spheres in Figure 7.15, however there are a few possibilities for the identity of the nano-spheres:

(1) Plated Li

(2) SEI layer formation nano-particles, similar to the *in-situ* TEM experiment in Figure 7.5.

In both cases, the morphology, and chemistry, has likely been changed by oxidation of the electro-deposits by air prior to loading into the SEM.

There are several different types of Li dendrite morphologies observed in literature, whiskers, moss, dendrites, globules, trees, and cracks (where Li forms on cracks in the electrode) [46]. The closest morphology the spheres in Figure 7.15 resemble is the moss morphology which is electrodeposited lithium presented as solid, interconnected pebbles. However, none of the standard morphologies in [46] show spherical formations of Li. Air exposure may have changed the morphology of the electro-deposit due to oxidation.

The LSV in Figure 7.13 did not sweep to the Li plating potential over concerns of damage to the cell due to the noise. The formation of nano-spheres due to reduction of $LiPF_6$ in 50/ 50 EC and DMC is similar to the formation of spheres by electrolyte irradiation by the electron beam in Figure 7.5, and [24]. [24] noted the nucleation of LiF nano-spheres of 100 nm upon electron beam irradiation of the electrolyte. The LSV to low potentials here is also induces reductive processes (shown by the drop to more negative current densities at -3 V vs. Pt in Figure 7.13). In this instance the spheres are 160 nm, the discrepancy between the measured 160 nm and 100 nm diameter nano-spheres measured by [24] could have occurred due to oxidation of the layer. Figure 7.15 (c) also shows the nano-spheres coalescing into a film, which also occurred *in-situ* TEM in Figure 7.5, suggesting similar processes.

In terms of using this electrochemical method to plate Li onto the Pt counter electrode for use as a half cell, given the coverage of the entire electrode array by deposits (shown in Figure 7.14), it is likely the uncontrolled plating technique would contaminate any sample of interest positioned on the working electrode. Therefore, greater control is needed for the Li plating method to be a viable method of position Li onto the Pt electrodes.

7.4.3.3 Results and Discussion: Cu Plating onto in-situ chips

Plating Li from electrolyte had many uncontrollable variables, such as the effect/ stability of the solvent, and air exposure during and after the plating experiment. To try to gain a better understanding of the system, plating was attempted using a simpler, and better understood system Cu from aqueous $CuSO_4$ solution.

Initially Cu plating was performed using a bulk cell to find the Cu plating potentials (the blue dashed line in Figure 7.16. The bulk cell showed a Cu plating reduction peak at -0.67 V vs Pt, and a stripping oxidation peak at -0.27 V vs. Pt. After a linear sweep voltammetry to 0.8 V vs. Pt, Cu was visually observed on the Pt CE electrode.

Bulk electrochemical cell cycling was performed to estimate a voltage window for cycling the nano-cell. A recording error meant the area of the Pt electrode was not recorded, so the Cu-bulk cell CV is plotted against measured current in Figure 7.16. Due to the lack of known current density, the bulk-cell results are only used to compare plating potentials with the nano-cell set-up.

The nano cell CV curves are plotted against current density. Current density was calculated by diving the measured current by the area of the electrode (260000 μm^2). When applying the same CV voltage sweep limits in the TEM set-up (Figure 7.16 nano cell solid red curve), the Cu plating reduction peak was observed at similar potentials (-0.64 V vs. Pt) to the bulk cell.

A second potential sweep to -0.9 V vs. Cu caused the plating reduction peak to be observed at -0.73 V vs. Pt. The shift in plating potential may have been caused by changes to the Pt surface after the first plating event.

The oxidation stripping potential occurred at a higher potential in the nano-cell (0.13 V vs. Pt for the Figure 7.16 orange and red lines) compared to the bulk cell electrochemistry (-0.27 V vs. Pt for the dark blue dashed line in Figure 7.16). Moreover, the signal is noisier for the nano cell CVs (solid red, and orange dash-dot) compared with the bulk cell (blue dashed line).

It is not clear why the nano cell CVs are so noisy in Figure 7.16. Some of the noise may be due to bubble formation, as discussed regarding the Li plating noise observed after the plating potential in Figure 7.13. Unlike the Li CV curves in Figure 7.13, noise was recorded on every Cu CV curve performed in the nano-cell in Figure 7.16.

Bubble formation would not explain the reduction peak at -0.08 V vs. Pt, observed on both the -0.8 V and -0.9 V vs. Pt CV traces in Figure 7.16. The smoothness of the bulk electrochemical cell trace, and the consistent noise recorded during Cu plating in Figure 7.16, and not Li plating in Figure 7.13 suggests the noise issue is related to the nano cell set-up rather than the solution. It is possible contamination was present on the liquid cell array, such as polymer in proper removal of the SU-8 polymer.

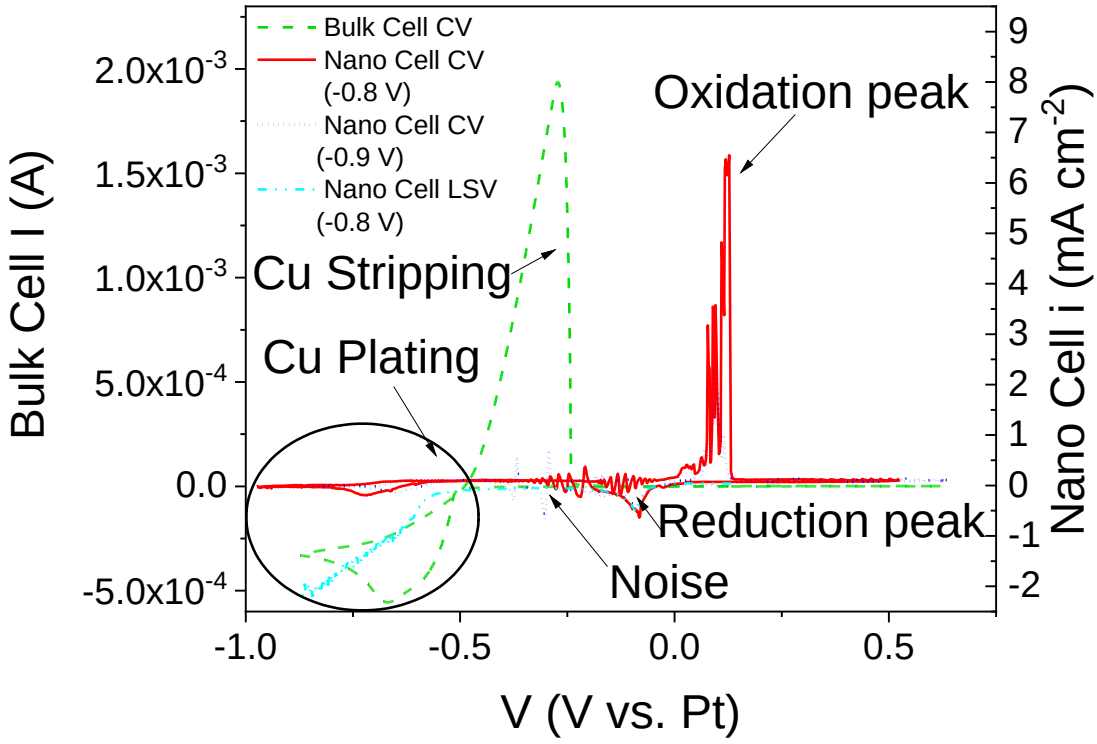

Figure 7.16: Cyclic voltammagrams plating Cu onto: green dash- bulk Cu electrode, red solid line- liquid cell Pt counter electrode to -0.9 V vs. Pt, and blue dashed line- liquid cell counter electrode to -0.8 V vs. Pt. The nano cell LSV to -0.8 V vs. Pt (light blue dash-dot) was used to coat the platinum electrode for SEM. The Cu plating potential is marked on the CV curves. Nano cell CV and LSV curves are plotted against current density (i). The bulk cell is plotted against measured current (I).

To check whether Cu plating had occurred at -0.64 V vs. Pt, the E-chip was imaged using an SEM after a linear sweep voltammetry to -0.8 V vs. Pt. (see Figure 7.16). The LSV was done to -0.8 V vs. Pt as Cu plating was recorded when the CV was performed to -0.8 V vs. Pt, with less noise than the CV to -0.9 V vs. Pt.

The LSV to -0.8 V vs. Pt in Figure 7.16 drops to more negative current densities at -0.55 V vs. Pt, indicating the start of a reductive process such as Cu plating.

Figure 7.17 shows images of the Pt counter electrode after the linear sweep voltammetry. It is clear from both Figure 7.17 (a), and (b) that Cu coverage of the Pt counter electrode was incomplete. However, unlike the Li plating experiment (Figure 7.14), there deposits did not fully cover the electrode array (Figure 7.17).

Figure 7.17 (a) shows the formation of dendrites on the inner edge of the counter electrode, along with an unidentified film. The dendrites are likely Cu formed from nucleation during electroplating. Cu formed on the edges of the counter electrode, either because this is where the electric field is strongest, or because edges provided a nucleation point for Cu as heterogeneous nucleation has a lower energy cost than homogenous nucleation.

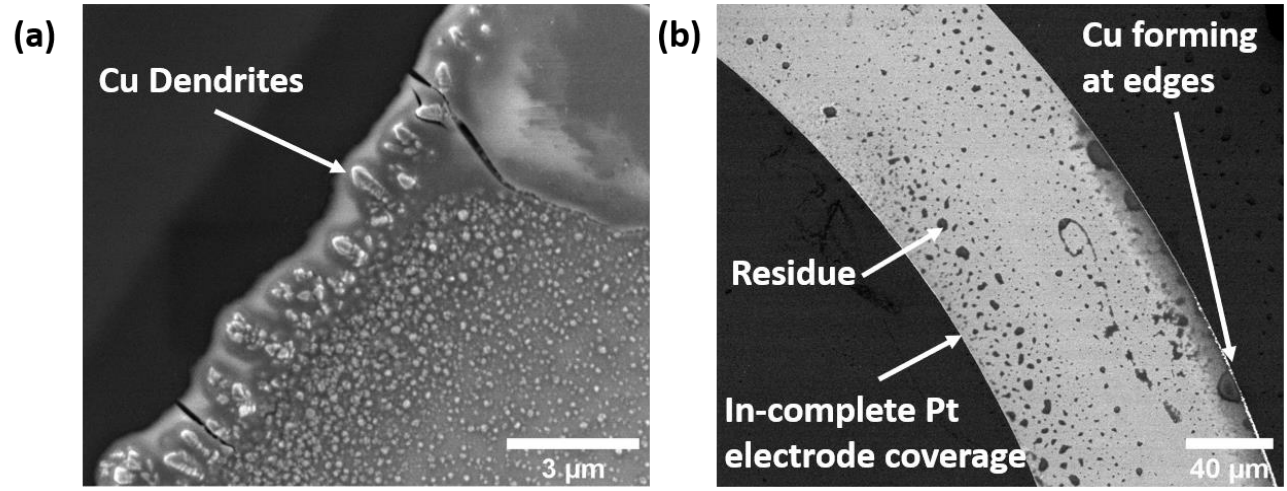

Figure 7.17: SEM (secondary electron) images of the Pt electrode, post-Cu plating. (a)- corner of the Pt electrode showing Cu dendrite formation on the edges. (b)- larger field of view image showing in complete Cu coverage and drying residue on the Pt electrode. Images were taken at 5 kV.

7.4.3.4 Summary of Benchtop Electroplating

Overall, the electroplating of Li onto the electrode experiment succeeded in plating Li onto the *in-situ* cell counter electrode. However, the process resulted in complete coverage of deposits across the electrode array region (including non-electrode regions), which would be detrimental to any *in-operando* experiments. For accurate electrochemical readings, the counter electrode, reference electrode, and working electrode must be electrically isolated from each other. If any deposition resulted in Li dendrite formation, the circuit would be shorted, and *in-operando* results invalidated.

Moreover, a large amount of noise was noted on the CV traces, potentially due to bubble formation, or contamination of the *in-situ* cell prior to cycling. Greater control would be required to make the plating work as a method to position Li on the counter electrode. Modelling of the electric field induced by the electrodes may aid future experiment design, as the Cu electroplating

results suggest the field is stronger, particularly on the edges, which may affect the uniformity of any successful plating attempt.

7.5 Perspectives on *in-operando* TEM for structural degradation studies on Li-ion batteries: Suggestions for a Better Approach

As demonstrated by the above results and discussion sections, attempts to set-up the *in-situ* TEM rig for *in-operando* TEM came across a number of issues. As the *in-situ* cell required major repairs during the PhD process, unfortunately these issues could not be resolved in the PhD. This section of the report serves to suggest a better approach to the *in-situ* TEM set-up, informed by the issues found by our attempt.

The electron beam irradiation experiments demonstrated that there is a threshold beam dose where no electrolyte damage would occur or be measurable here for $LiPF_6$ in EC and DMC. This beam dose would need to be fully calibrated and imaging performed under the threshold for any *in-operando* experiments.

The ultimate goal of the *in-operando* TEM set-up was to create a Li-ion half-cell in the TEM. This would involve having a controlled volume of $LiCoPO_4$ (active material) attached to the working electrode of the top E-chip (see Figure 7.4). A number of techniques were attempted to isolate $LiCoPO_4$ onto the working electrode. Drop casting resulted in $LiCoPO_4$ being located on both the working electrode and the reference electrode, which would have caused issues measuring the voltage *in-operando*.

The $LiCoPO_4$ attachment method presented here demonstrates the methodology of microtoming electrodes and positioning the sections onto the working electrodes with nano-manipulators. However, because the microtoming was performed on electrodes containing binder, neighbouring particles could become electrically isolated, affecting the quantification of electrochemistry (Figure 7.10). If the microtoming could be performed on a non-binder containing $LiCoPO_4$, this issue could be reduced.

Microtome sectioning is typically used for soft materials; as hard materials can blunt the diamond knife. However, microtoming of a green body of $LiCoPO_4$ powder (compressed in a pellet die) could be attempted. Alternatively, microtoming a sintered pellet could also be attempted, although this would risk blunting the diamond blade.

Little control over the volume and area of the microtomed sections has been achieved so far with the preliminary microtoming work in this thesis. Therefore, it may be better to use a method such as FIB sectioning and positioning to achieve precise area and volume sections required for quantitative electrochemistry.

The initial goal of this work was to create a Li-ion half-cell in the TEM, requiring Li plating onto the counter electrode of the *in-situ* TEM chip. This was attempted by plating Li directly from $LiPF_6$ in EC and DMC, as demonstrated in 7.4.3. The plating demonstrated here was uncontrolled, however, modelling of the electric fields, and careful experiments adjusting the plating times, improved electrode design, and methods could control this. However, there are a couple of fundamental issues regarding plating Li from electrolyte onto the counter electrodes:

(1) It is unlikely that pure Li will ever be plated onto the *in-situ* chip electrode, as Li in the presence of electrolyte will form a SEI layer, which on the scale of the E-chip set-up, will cause resistance issues. The results in 7.4.3 suggest the nano-spheres formed may be electrolyte reduction

products, which may lead to SEI formation, however full analysis was difficult because air exposure damaged would affect any SEI layer that may have formed.

(2) Plating Li onto the counter electrode would be unlikely to aid the electrochemistry as the potential difference of the working electrode is measured against the Pt reference electrode. Applying Li to the counter electrode would in theory provide an infinite source of Li ions for diffusion, however, given the constrained nature of the *in-situ* set-up it is unlikely Li plated on the counter electrode would provide an 'infinite' source of Li.

Previous authors have noted that an SEI layer forms on Li in the presence of electrolyte [17], [18]. Using the Li as a counter electrode may cause resistance issues, as compared to the very thin Li plating, the SEI layer may be comparatively thick. However, SEI layers form on Li in bulk Li-ion half-cells, so the issue could increase the similarity between the *in-situ* TEM set-up and bulk Li-ion half cells.

Bulk $LiCoPO_4$ Li-ion half cells consist of a $LiCoPO_4$ electrode cycled against metallic Li. The $LiCoPO_4$ is the working electrode, whereas the metallic Li acts as both the counter electrode, and the reference electrode. Voltage is measured against the $LiCoPO_4$ working electrode, and the Li metal counter/ reference electrode. The use of lithium metal provides a stable voltage to measure the potential difference at the working electrode against. As shown by Figure 7.4, the electrode array on the E-chip consists of a 3 electrode array, so potential difference at the working electrode is measured against the reference electrode, not the counter electrode. For electrochemistry experiments, Li should be positioned onto the reference electrode, not the counter electrode.

It should be noted that the Protochips array has a counter sense (voltage measuring cable for the counter electrode) connection, so it is possible to set-up the *in-situ* TEM cell as a 2 electrode Li-ion half-cell.

The area of the counter electrode (260000 μm^2) is much larger than the working electrode, which likely led to issues with the plating in 7.4.3. The reference electrode is 7500 μm^2, which is closer to the 2500 μm^2 working electrode, so Li plating onto the reference electrode may be more controlled as the working electrode could act as a more appropriate counter electrode to plating on the reference electrode.

However, given the SEI layer issues, it may be a better approach to simplify the experiment and use the Pt reference electrode as the reference electrode, instead of plating Li onto it, as done by Mehdi et al. [17]. Therefore, the Pt electrode would act as a pseudo reference electrode. Flowing electrolyte around the system would provide a constant supply of Li^+ ions for reactions at the $LiCoPO_4$ interface, and the Pt counter electrode interface.

The *in-situ* set-up is difficult to compare to bulk cell electrochemistry as the system is small. The infinite diffusion assumptions, which form the basis of electrochemistry, are no longer valid [47]. In this work initial attempts at CV were made without flowing electrolyte through the cell (results are not presented). The CV traces were not measured until electrolyte was flowed around the cell so the fresh electrolyte could act as an infinite source of new Li^+ ions. Instead of trying to completely replicate a bulk electrochemical cell, the *in-situ* cell should be set-up to optimise electrochemistry in a nano-volume environment.

A schematic showing the proposed improved set-up, including the FIB sectioned $LiCoPO_4$ on the working electrode, and the use of the patterned Pt electrodes as pseudo-electrodes is shown in Figure 7.18.

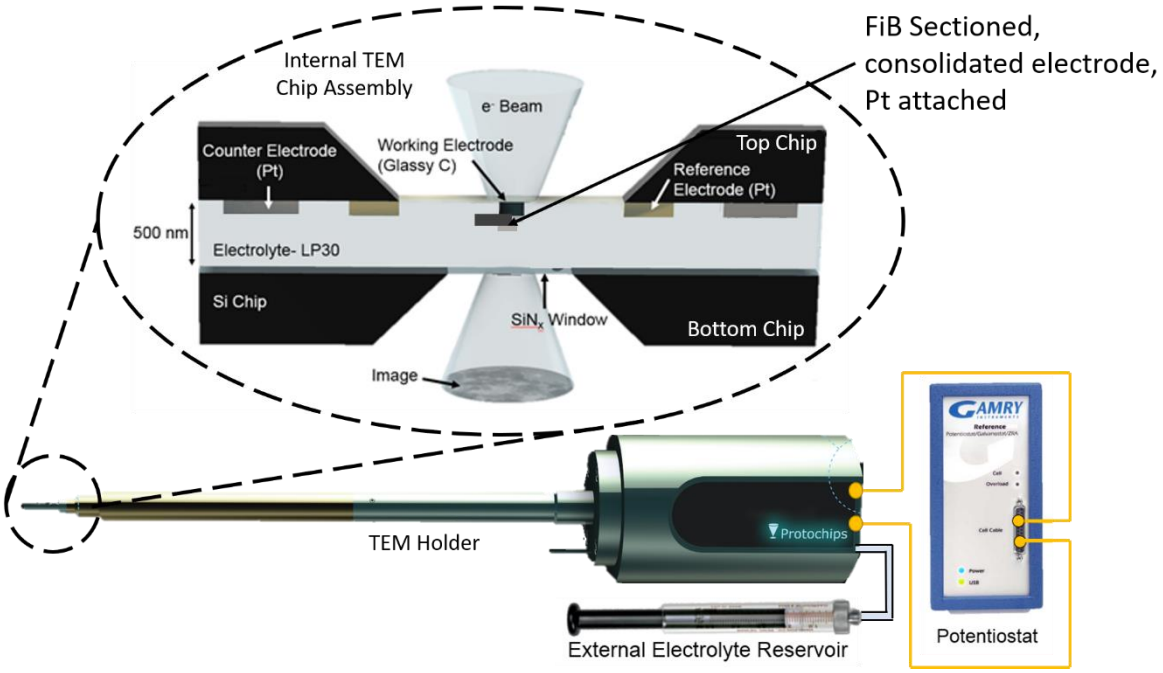

Figure 7.18: Schematic of a potentially improved in-operando TEM set-up. Li is not plated onto the counter electrode. Pt electrodes are used as a pseudo-reference electrode, whilst electrolyte is flowed through the cell. Consolidated (e.g. Sintered) $LiCoPO_4$ is FIB sectioned and attached with a Pt tab.

So far the discussion has involved attempts to set-up an *in-operando* TEM experiment to image materials and their microstructural changes while cycling in the TEM. As discussed, *in-operando* TEM of cathode/ anode materials involves a number of set-up challenges. The *in-situ* imaging of the formation and post-mortem imaging of the residual polycarbonate film on the E-chip after electron beam irradiation presents an interesting opportunity to study CEI/ SEI formation mechanism.

As discussed in the previous thesis chapter, CEI layers form as a result of breakdown of the electrolyte due to reduction induced by the potential [44]. The *in-situ* TEM environment is similar in that the solvated electrons are causing reduction of the electrolyte, analogous to reduction of electrolyte, resulting in the formation of thin polycarbonate films, observed in the electron beam irradiation experiments in 7.3.. The fact that the polycarbonate layer formed by electron beam damage remained on the window surface post-mortem (Figure 7.6), suggests the polycarbonate films are similar to a CEI/ SEI layer.

A disadvantage of using the *in-situ* TEM set-up to study C/SEI formation mechanisms by electron beam irradiation would be that it ignores the potential for involvement by other cell components, such as the active material and conductive additives. The results in the degradation at the electrode surface chapter suggested Co involvement from the $LiCoPO_4$. Moreover, the kinetics may differ as the electron energy delivered by the beam may be different to the electron energy delivered by cycling.

The TEM set-up is unique as the electron dose can be tightly controlled, and the effects imaged and characterised. Therefore, the *in-situ* TEM set-up presents an interesting opportunity to study the mechanisms of electrolyte reduction, analogous to SEI formation. The experiment shown in 7.3, could be expanded (once the dose rate is calibrated), to electrolyte solutions containing different additives. This experiment would avoid the complicated set-up involved in creating a half-cell in the TEM, but still gaining interesting information, unique to a TEM set-up.

Overall, although the work on the liquid cell was halted due to equipment failure, the results found present a number of avenues to investigate battery materials *in-situ* TEM.

7.6 REFERENCES

[1] D. Liu, Z. Shadike, R. Lin, K. Qin, H. Li, K. Li, S. Wang, Q. Yu, M. Liu, S. Ganapathy, X. Qin, Q-H. Yang, M. Wagemaker, F. Kang, X-Q. Yang, and B. Li, "Review of Recent Development of In Situ/Operando Characterization Techniques for Lithium Battery Research," *Advanced Materials*, vol. 31, no. 28., p. 1806620, 2019.

[2] P. Harks, F. M. Mulder, and P. H. L. Notten, "In situ methods for Li-ion battery research: A review of recent developments," *J. Power Sources*, vol. 288, pp. 92–105, 2015.

[3] A. Gurlo and R. Riedel, "In situ and operando spectroscopy for assessing mechanisms of gas sensing," *Angewandte Chemie - International Edition*, vol. 46, no. 21., pp. 3826–3848, 2007.

[4] R. R. Liu, X. Deng, X. R. Liu, H. J. Yan, A. M. Cao, and D. Wang, "Facet dependent SEI formation on the $LiNi_{0.5}Mn_{1.5}O_4$ cathode identified by in situ single particle atomic force microscopy," *Chem. Commun.*, vol. 50, no. 99, pp. 15756–15759, 2014.

[5] D. N. Qian, C. Ma, K. L. More, Y. S. Meng, and M. F. Chi, "Advanced analytical electron microscopy for lithium-ion batteries," *Npg Asia Mater.*, vol. 7, p. 10, 2015.

[6] Y. S. Meng, T. McGilvray, M-C. Yang, D. Gostovic, F. Wang, D. Zeng, Y. Zhu, and J. Graetz, "In Situ Analytical Electron Microscopy for Probing Nanoscale Electrochemistry," *Electrochem. Soc. Interface*, vol. 20, pp. 49–53, 2011.

[7] J. J. Niu, A. Kushima, X. Qian, L. Qi, K. Xiang, Y-M. Chiang, and J. Li, "In Situ Observation of Random Solid Solution Zone in $LiFePO_4$ Electrode," *Nano Lett.*, vol. 14, no. 7, pp. 4005–4010, 2014.

[8] J. Y. Huang, L. Zhong, C. M. Wang, J. P. Sullivan, W. Xu, L. Qiang Zhang, S. X. Mao, N. S. Hudak, X. H. Liu, A. Subramanian, H. Fan, L. Qi, A. Kushima, and J. Li, "In situ observation of the electrochemical lithiation of a single SnO_2 nanowire electrode.," *Science*, vol. 330, no. 6010, pp. 1515–20, 2010.

[9] M. J. Williamson, R. M. Tromp, P. M. Vereecken, R. Hull, and F. M. Ross, "Dynamic microscopy of nanoscale cluster growth at the solid–liquid interface," *Nat. Mater.*, vol. 2, no. 8, pp. 532–536, 2003.

[10] B. L. Mehdi, J. Qian, E. Nasybulin, C. Park, D. A. Welch, R. Faller, H. Mehta, W. A. Henderson, W. Xu, C. M. Wang, J. E. Evans, J. Liu, J-G. Zhang, K. T. Mueller, and N. D. Browning, "Observation and Quantification of Nanoscale Processes in Lithium Batteries by Operando Electrochemical (S)TEM," *Nano Lett.*, vol. 15, no. 3, pp. 2168–2173, 2015.

[11] M. E. Holtz, Y. Yu, D. Gunceler, J. Gao, R. Sundaraman, K. A. Schwartz, T. A. Arias, H. D. Abruña, and D. A. Muller, "Nanoscale Imaging of Lithium Ion Distribution During In Situ Operation of Battery Electrode and Electrolyte," *Nano Lett.*, vol. 14, no. 3, pp. 1453–1459, 2014.

[12] K. J. Chen, K. Cao, C. Xing, Y. Hu, J. Liu, Y. He, J. Wang, A. Li, and H. Qin, "In-situ TEM study of the lithiation and delithiation of FeS nanosheets," *J. Alloys Compd.*, vol. 688, pp. 946–952, 2016.

[13] Z. Wang, D. Santhanagopalan, W. Zhang, F. Wang, H. L. Xin, K. He, J. Li, N. Dudney, and Y.

S. Meng, “In situ STEM-EELS observation of nanoscale interfacial phenomena in all-solid-state batteries,” *Nano Lett.*, vol. 16, no. 6, pp. 3760–3767, 2016.

[14] Z. Z. Yang, Z. Zhu, J. Ma, D. Xiao, X. Kui, Y. Yao, R. Yu, X. Wei, L. Gu, Y-S. Hu, H. Li, and X. Zhang, “Phase Separation of Li_2S/S at Nanoscale during Electrochemical Lithiation of the Solid-State Lithium-Sulfur Battery Using In Situ TEM,” *Adv. Energy Mater.*, vol. 6, no. 20, p. 5, 2016.

[15] C. M. Wang, “In situ transmission electron microscopy and spectroscopy studies of rechargeable batteries under dynamic operating conditions: A retrospective and perspective view,” *J. Mater. Res.*, vol. 30, no. 3, pp. 326–339, 2015.

[16] R. L. Sacci, N. J. Dudney, K. L. More, L. R. Parent, I. Arslan, N. D. Browning, and R. R. Unocic, “Direct visualization of initial SEI morphology and growth kinetics during lithium deposition by in situ electrochemical transmission electron microscopy,” *Chem. Commun.*, vol. 50, no. 17, pp. 2104–2107, 2014.

[17] B. L. Mehdi, A. Stevens, J. Qian, C. Park, W. Xu, W. A. Henderson, J-G. Zhang, K. T. Mueller, and N. D. Browning, “The Impact of Li Grain Size on Coulombic Efficiency in Li Batteries,” *Sci. Rep.*, vol. 6, no. 1, p. 34267, 2016.

[18] R. R. Unocic, X-G. Sun, R. L. Sacci, L. A. Adamczyk, D. H. Alsem, S. Dai, N. J. Dudney, and K. L. More, “Direct Visualization of Solid Electrolyte Interphase Formation in Lithium-Ion Batteries with In Situ Electrochemical Transmission Electron Microscopy,” *Microsc. Microanal.*, vol. 20, no. 4, pp. 1029–1037, 2014.

[19] N. de Jonge and F. M. Ross, “Electron microscopy of specimens in liquid,” *Nat. Nanotechnol.*, vol. 6, no. 11, pp. 695–704, 2011.

[20] P. Abellan, T. J. Woehl, L. R. Parent, N. D. Browning, J. E. Evans, and I. Arslan, “Factors influencing quantitative liquid (scanning) transmission electron microscopy,” *Chem. Commun.*, vol. 50, no. 38, pp. 4873–4880, 2014.

[21] C. C. B. Williams D B., “Inelastic Scattering and Beam Damage,” in *Transmission Electron Microscopy A Textbook for Materials Science*, vol. 2, C. C. B. Williams D B., Ed. Springer, 2009, p. 66.

[22] F. Lin, I. M. Markus, M. M. Doeff, and H. L. L. Xin, “Chemical and Structural Stability of Lithium-Ion Battery Electrode Materials under Electron Beam,” *Sci. Rep.*, vol. 4, p. 6, 2014.

[23] F. M. Ross, *Liquid Cell Electron Microscopy*. New York, NY: Cambridge University Press, 2017.

[24] P. Abellan, B. L. Mehdi, L. R. Parent, M. Gu, C. Park, W. Xu, Y. Zhang, I. Arslan, J-G. Zhang, C-M. Wang, J. E. Evans, and N. D. Browning, “Probing the Degradation Mechanisms in Electrolyte Solutions for Li-Ion Batteries by in Situ Transmission Electron Microscopy,” *Nano Lett.*, vol. 14, no. 3, pp. 1293–1299, 2014.

[25] T. J. Woehl, J. E. Evans, L. Arslan, W. D. Ristenpart, and N. D. Browning, “Direct in Situ Determination of the Mechanisms Controlling Nanoparticle Nucleation and Growth,” *ACS Nano*, vol. 6, no. 10, pp. 8599–8610, 2012.

[26] K. L. Jungjohann, S. Bliznakov, P. W. Sutter, E. A. Stach, and E. A. Sutter, “In Situ Liquid Cell Electron Microscopy of the Solution Growth of Au-Pd Core-Shell Nanostructures,” *Nano Lett.*, vol. 13, no. 6, pp. 2964–2970, 2013.

[27] T. J. Woehl and P. Abellan, “Defining the radiation chemistry during liquid cell electron microscopy to enable visualization of nanomaterial growth and degradation dynamics,” *J. Microsc.*, vol. 265, no. 2, pp. 135–147, 2017.

[28] T. J. Woehl, K. L. Jungjohann, J. E. Evans, I. Arslan, W. D. Ristenpart, and N. D. Browning, “Experimental procedures to mitigate electron beam induced artifacts during in situ fluid imaging of nanomaterials,” *Ultramicroscopy*, vol. 127, pp. 53–63, 2013.

[29] J. H. Park, N. M. Schneider, J. M. Grogan, M. C. Reuter, H. H. Bau, S. Kodambaka, and F. M. Ross, “Control of Electron Beam-Induced Au Nanocrystal Growth Kinetics through Solution Chemistry,” *Nano Lett.*, vol. 15, no. 8, pp. 5314–5320, 2015.

[30] S. M. Rehn and M. R. Jones, “New Strategies for Probing Energy Systems with In Situ Liquid-Phase Transmission Electron Microscopy,” *ACS Energy Lett.*, vol. 3, no. 6, pp. 1269-1278, 2018.

[31] N. Hodnik, G. Dehm, and K. J. J. Mayrhofer, “Importance and Challenges of Electrochemical in Situ Liquid Cell Electron Microscopy for Energy Conversion Research,” *Acc. Chem. Res.*, vol. 49, no. 9, pp. 2015–2022, 2016.

[32] G. V. Buxton, C. L. Greenstock, W. P. Helman, and A. B. Ross, “Critical Review of rate constants for reactions of hydrated electrons, hydrogen atoms and hydroxyl radicals (·OH/·O− in Aqueous Solution,” *J. Phys. Chem. Ref. Data*, vol. 17, no. 2, pp. 513–886, 1988.

[33] A. Ponrouch, E. Marchante, M. Courty, J. M. Tarascon, and M. R. Palacín, “In search of an optimized electrolyte for Na-ion batteries,” *Energy Environ. Sci.*, vol. 5, no. 9, pp. 8572–8583, Sep. 2012.

[34] E. Peled, D. Golodnitsky, C. Menachem, and D. Bar-Tow, “An advanced tool for the selection of electrolyte components for rechargeable lithium batteries,” *J. Electrochem. Soc.*, vol. 145, no. 10, pp. 3482–3486, 1998.

[35] S. J. Rezvani, R. Gunnella, A. Witkowska, F. Mueller, M. Pasqualini, F. Nobili, S. Passerini, and A. Di Cicco, “Is the Solid Electrolyte Interphase an Extra-Charge Reservoir in Li-Ion Batteries?,” *ACS Appl. Mater. Interfaces*, vol. 9, no. 5, pp. 4570–4576, 2017.

[36] “Advanced Transmission Electron Microscopy Solutions | Protochips.” [Online]. Available: https://www.protochips.com/. [Accessed: 02-Jul-2020].

[37] A. J. Leenheer, J. P. Sullivan, M. J. Shaw, and C. T. Harris, “A Sealed Liquid Cell for In Situ Transmission Electron Microscopy of Controlled Electrochemical Processes,” *J. Microelectromechanical Syst.*, vol. 24, no. 4, pp. 1061–1068, 2015.

[38] Z. Y. Zeng *et al.*, “In Situ Study of Lithiation and Delithiation of MoS_2 Nanosheets Using Electrochemical Liquid Cell Transmission Electron Microscopy,” *Nano Lett.*, vol. 15, no. 8, pp. 5214–5220, 2015.

[39] “Sample Prep: FIB Sample Preparation” [Online]. Available: http://www.protochips.com/wp-content/uploads/2017/10/prep-fib-samples.pdf. [Accessed: 26-Feb-2020].

[40] M. Hammad Fawey, V. S. K. Chakravadhanula, M. A. Reddy, C. Rongeat, T. Scherer, H. Hahn, M. Fichtner, and C. Kübel, “In situ TEM studies of micron-sized all-solid-state fluoride ion batteries: Preparation, prospects, and challenges,” *Microsc. Res. Tech.*, vol. 79, no. 7, pp. 615–624, 2016.

[41] R. L. Sacci, J. M. Black, N. Balke, N. J. Dudney, K. L. More, and R. R. Unocic, "Nanoscale Imaging of Fundamental Li Battery Chemistry: Solid-Electrolyte Interphase Formation and Preferential Growth of Lithium Metal Nanoclusters," *Nano Lett.*, vol. 15, no. 3, pp. 2011–2018, 2015.

[42] R. R. Unocic, R. L. Sacci, G. M. Brown, G. M. Veith, N. J. Dudney, K. L. More, F. S. Walden 2nd, D. S. Gardiner, J. Damiano, and D. P. Nackashi, "Quantitative Electrochemical Measurements Using In Situ ec-S/TEM Devices," *Microsc. Microanal.*, vol. 20, no. 2, pp. 452–461, 2014.

[43] N. de Jonge, L. Houben, R. E. Dunin-Borkowski, and F. M. Ross, "Resolution and aberration correction in liquid cell transmission electron microscopy," *Nature Reviews Materials*, vol. 4, no. 1., pp. 61–78, 2019.

[44] J. B. Goodenough and Y. Kim, "Challenges for Rechargeable Li Batteries †," *Chem. Mater.*, vol. 22, no. 3, pp. 587–603, 2010.

[45] B. Michalak, H. Sommer, D. Mannes, A. Kaestner, T. Brezesinski, and J. Janek, "Gas Evolution in Operating Lithium-Ion Batteries Studied in Situ by Neutron Imaging," *Sci. Rep.*, vol. 5, Oct. 2015.

[46] L. Frenck, G. K. Sethi, J. A. Maslyn, and N. P. Balsara, "Factors That Control the Formation of Dendrites and Other Morphologies on Lithium Metal Anodes," *Front. Energy Res.*, vol. 7, p. 115, 2019.

[47] R. Rousseau, M. L. Délia, and A. Bergel, "A theoretical model of transient cyclic voltammetry for electroactive biofilms," *Energy Environ. Sci.*, vol. 7, no. 3, pp. 1079–1094, 2014.

8 CONCLUSIONS

This PhD project had two aims. (1) Develop new electron and ion microscopy techniques to characterise degradation in high voltage Li-ion battery materials, enabling understanding of the impact of local environment, and correlation of chemical and structural changes with electrochemical history. (2) Apply the techniques to $LiCoPO_4$ to investigate cathode degradation processes, and use successful investigations to validate the efficacy of the techniques developed.

Ex-situ He-ion microscopy and Ne-ion ToF SIMS, was successfully developed to image and chemically characterise CEI layers. *Ex-situ* EELS Co valence state electron energy loss spectroscopy electron microscopy was successfully developed to identify the lithiated, and de-lithiated regions within individual $LiCoPO_4$ primary particles.

He-ion microscopy and *in-situ* Ne-ion ToF SIMS have been shown, for the first time, to be capable of imaging and chemically characterising CEI layers on $LiCoPO_4$ electrodes. He-ion microscopy enabled imaging of CEI layers on the electrode scale, allowing the CEI morphology and thickness to be correlated with the underlying electrode microstructure, thus enabling the impact of local environment on CEI layer formation to be understood. In HIM iSE imaging, the CEI layers appear as regions of dark contrast on electrodes due to charge build-up of the He-ion beam on the non-conducting CEI layer, with variations in contrast indicating local CEI thickness variations.

In-situ Ne-ion ToF SIMS allowed chemical mapping of the electrode surface, and depth profiling of the primary particles from the surface CEI layers and carbon coating down into the internal structure of the particle. Comparison with HIM imaging enabled correlation of CEI chemistry and morphology with the underlying electrode microstructure. The location of the SIMS spectrometer on the HIM also prevented further sample degradation generated by moving between equipment for imaging and chemical characterisation.

He-ion microscopy was shown to provide higher resolution imaging of the CEI compared with SEM. He-ion microscopy ion-induced secondary electron imaging uses predominantly surface sensitive SE1 electrons to form the image, and the smaller spot size allowed higher resolution imaging of the CEI layers. The ability of ToF SIMS to detect Li in combination with the advantages of HIM imaging made the HIM-SIMS technique a powerful new method of characterising CEI layers in high voltage Li-ion battery materials.

An EELS Co L-edge mapping technique was applied to $LiCoPO_4$ electrodes to map the Co(II), and Co(III)-rich regions within single particles of $LiCoPO_4$. Co(II), and Co(III) are analogous to the lithiated and de-lithiated regions of $LiCoPO_4$. Microtome sectioning was shown to improve the resolution of the Co(II), and Co(III)-rich regions of electrode as slices through large particles can be obtained, and the overall sample thickness uniformity improves on sectioning. In a given slice, microtome sectioning maintained electrode particles within their original position in the electrode, thus enabling further information of local environment within the electrode to be obtained during S/TEM imaging. However, retaining the soft Al current collector within the section proved difficult.

Development of an *in-operando* TEM technique to image microstructural changes in Li-ion battery materials primary particles during cycling was attempted by forming a Li-ion half-cell within the TEM. $LiCoPO_4$ was successfully isolated on the working electrode. However, efforts to develop the *in-operando* technique showed that plating Li from the electrolyte onto the micron-sized electrodes within the *in-operando* cell to form the half-cell was an uncontrolled method of forming

a half-cell. It is suggested that a better approach would be to use the already patterned Pt as a pseudo electrode.

Electrolyte irradiation experiments to understand the influence of the electron beam on the electrolyte, and to find a safe electron dose threshold, indicated that irradiation of $LiPF_6$ in EC and DMC by a 300 kV beam electrolyte beam resulted in the formation of precipitates. Precipitate formation indicates electrolyte breakdown which would make *in-operando* analysis difficult. However, as irradiation by the electron beam is analogous to electrolyte reduction, the study presents an interesting opportunity to study the reduction processes within Li-ion battery electrolytes.

$LiCoPO_4$ in this study was found to undergo severe capacity loss over the course of 10 cycles. To validate the efficacy of the techniques developed, the techniques were used to study the degradation processes of $LiCoPO_4$ during cycling.

Post-mortem XRD, and SAED on cycled cathodes, found that $LiCoPO_4$ de-lithiated with a 3 phase de-lithiation mechanism: $LiCoPO_4 \rightarrow Li_{2/3}CoPO_4 \rightarrow CoPO_4$, consistent with previous studies [1]–[3]. EELS Co L-edge mapping was used to image and quantify the shrinking-core de-lithiation mechanism of $LiCoPO_4$ for the first time. EELS Co L-edge mapping found that $LiCoPO_4$ de-lithiates first from the outside of the $LiCoPO_4$ particles, hence $CoPO_4$ first forms at the electrode/ electrolyte interface.

EELS O K-edge extraction and mapping indicated Co-O hybridisation when $LiCoPO_4$ was charged to 5.1 V vs. Li/ Li^+. The Co-O hybridised regions correlated with Co(III)-rich regions, indicating hybridisation occurs in $CoPO_4$. The presence of hybridisation in $CoPO_4$ indicates the instability of the phase during de-lithiation. By the 10^{th} cycle $CoPO_4$ no longer forms, and a lack of de-lithiation is evident across entire $LiCoPO_4$ particles. The results indicate severe structural degradation accompanying the electrochemical degradation during cycling.

The formation of $CoPO_4$ on the outside of particles caused the unstable $CoPO_4$ to be exposed to degradation from the electrolyte. Active material dissolution had previously been reported by [4] at high potentials. At high potentials (5.1 V vs. Li/ Li^+), a Co(II)-rich layer formed on the outside of particles indicating partial re-lithiation at the electrode/ electrolyte interface, consistent with [5]. This was supported by SIMS depth profiling indicating surface Li rich regions at the electrode surface.

HIM-SIMS imaging and characterisation of CEI layers on $LiCoPO_4$ showed formation of CEI layers at 5.1 V vs. Li/ Li^+. The CEI layers consisted of Li and oxyfluoro phosphates consistent with [4], [6], suggesting they were reduction products of $LiPF_6$ in EC and DMC electrolyte.

CEI layer formation can be passivating, helping to reduce electrolyte surface degradation. However, HIM imaging of $LiCoPO_4$ electrodes at different cycle numbers, and at different states of charge showed partial dissolution of the CEI when the electrodes are discharged to 2.5 V vs. Li/ Li^+ for the first time. Partial dissolution of the CEI indicated that the CEI forming on $LiCoPO_4$ was not passivating, thus exposing the unstable $CoPO_4$, which forms on the surface of particles during de-lithiation, to continued degradation from the electrolyte.

Across the $LiCoPO_4$ electrode, HIM-SIMS characterisation showed that the partial CEI dissolution was most significant on larger agglomerates, resulting in an inhomogenous CEI layer. The result indicates that the local electrode environment influences CEI formation.

The use of HIM-SIMS and EELS techniques provide a comprehensive picture of degradation within $LiCoPO_4$ particles, and electrodes by correlating electrochemically driven chemical changes with specific features of the underlying cathode microstructure at different length scales. The techniques show how the local environment is linked to specific degradation mechanisms. The results from the project indicate that methods to stabilise the $CoPO_4$ phase, stabilisation of the CEI layer, methods to protect the particles from degradation from the electrolyte, and control of the electrode microstructure, could improve capacity fade in $LiCoPO_4$ electrolytes. The techniques applied developed here could be expanded to other materials to gain an understanding of degradation mechanisms in Li-ion battery materials.

8.1 REFERENCES

[1] F. C. Strobridge, R. J. Clément, M. Leskes, D. S. Middlemiss, O. J. Borkiewicz, K. M. Wiaderek, K. W. Chapman, P. J. Chupas, and C. P. Grey, "Identifying the Structure of the Intermediate, $Li_{2/3}CoPO_4$, Formed during Electrochemical Cycling of $LiCoPO_4$," *Chem. Mater.*, vol. 26, no. 21, pp. 6193–6205, 2014.

[2] N. N. Bramnik, K. Nikolowski, C. Baehtz, K. G. Bramnik, and H. Ehrenberg, "Phase Transitions Occurring upon Lithium Insertion−Extraction of $LiCoPO_4$," *Chem. Mater.*, vol. 19, no. 4, pp. 908–915, 2007.

[3] H. Ehrenberg, N. N. Bramnik, A. Senyshyn, and H. Fuess, "Crystal and magnetic structures of electrochemically delithiated $Li_{1-x}CoPO_4$ phases," *Solid State Sci.*, vol. 11, no. 1, pp. 18–23, 2009.

[4] E. Markevich, R. Sharabi, H. Gottlieb, V. Borgel, K. Fridman, G. Salitra, D. Aurbach, G. Semrau, M. A. Schmidt, N. Schall, and C. Bruenig, "Reasons for capacity fading of $LiCoPO_4$ cathodes in $LiPF_6$ containing electrolyte solutions," *Electrochem. commun.*, vol. 15, no. 1, pp. 22–25, 2012.

[5] J. Manzi, F. M. Vitucci, A. Paolone, F. Trequattrini, D. Di Lecce, S. Panero, and S. Brutti, "Analysis of the self-discharge process in $LiCoPO_4$ electrodes: Bulks," *Electrochim. Acta*, vol. 179, pp. 604–610, 2015.

[6] J. Manzi and S. Brutti, "Surface chemistry on $LiCoPO_4$ electrodes in lithium cells: SEI formation and self-discharge," *Electrochim. Acta*, vol. 222, pp. 1839–1846, 2016.

9 FURTHER WORK

The results in this thesis present a number of interesting opportunities for future work.

Chapter 4 presents a novel methodology for imaging and chemically characterising CEI layers on $LiCoPO_4$ using He-ion microscopy, and *in-situ* ToF SIMS. The HIM SIMS technique could be applied to other lithium ion battery materials which form organic C/ SEI layers to understand how the electrode microstructure affects C/ SEI formation. For $LiCoPO_4$ degradation studies, the results in chapter 4 showed that the size of the agglomerates affects the dissolution of CEI layer and that no CEI layer was observed on the conductive additive particles. The effects of cathode microstructure on CEI formation, such as particle/agglomerate size and cohesion, or binder type, and the efficacy of CEI passivation, could be further studied on $LiCoPO_4$, and other Li-ion battery materials.

A particularly interesting future avenue for the HIM SIMS technique would be to create an *in-operando* HIM SIMS technique, potentially using similar methodologies to *in-operando* SEM [1]. An *in-operando* HIM-SIMS technique would remove sample transfer contamination issues, although outgassing from ionic liquid electrolytes may cause contamination. An *in-operando* HIM-SIMS technique could also potentially provide the opportunity to study S/CEI formation and dissolution across an electrode.

Chapter 5 and 6 presented a STEM-EELS study of the de-lithiation mechanisms of $LiCoPO_4$, directly imaging the shrinking-core de-lithiation mechanism by spatially resolving the Co(II), and Co(III)-rich regions of $LiCoPO_4$. Ideally the technique should be refined to spatially resolve the 3 phases which form during cycling of $LiCoPO_4$ ($LiCoPO_4$, $Li_{2/3}CoPO_4$, and $CoPO_4$) potentially by using nano diffraction to identify the phases in the TEM. In terms of understanding the degradation mechanisms of $LiCoPO_4$, earlier cycle numbers could be investigated to determine if the surface degradation from electrolyte reactions, or structural degradation within the primary particles were the overriding factor leading to capacity loss.

In terms of the STEM-EELS technique, using microtomed prepared electrode cross-sections could potentially be applied to any other transition metal containing Li-ion battery electrode material to study de-lithiation, as has been previously demonstrated using $LiFePO_4$ [2].

Chapter 7 presented routes to setting up an *in-operando* TEM set-up by setting up a Li-ion half-cell in the TEM. The microtome method of positioning $LiCoPO_4$ onto the working electrode could be improved by microtoming consolidated $LiCoPO_4$. The cell should also use the pre-patterned Pt as a pseudo reference electrode for cycling in order to simplify the set-up. However, as outlined in the perspectives section, based on electrolyte electron beam irradiation results an interesting avenue for the closed-liquid-cell TEM set-up could be to use it as a method of understanding the reduction mechanisms of electrolyte solutions containing different electrolyte additives. C/ SEI layers form on electrodes as a result of reduction and oxidation of electrolyte [3], so the *in-situ* electrolyte irradiation experiment provides an opportunity to control the electron dose in the electrolyte and study reduction mechanisms which would be relevant to C/ SEI formation.

9.1 REFERENCES

[1] H. Shi, X. Liu, R. Wi, Y. Zheng, Y. Li, X. Cheng, W. Pfleging, and Y. Zhang, “In Situ SEM Observation of Structured Si/C Anodes Reactions in an Ionic-Liquid-Based Lithium-Ion Battery,” *Appl. Sci.*, vol. 9, no. 5, p. 956, 2019.

[2] X. Mu, A. Kobler, D. Wang, V. S. K. Chakravadhanula, S. Schlabach, D. V. Szabó, P. Norby,

and C. Kübel, “Comprehensive analysis of TEM methods for LiFePO4/FePO4 phase mapping: spectroscopic techniques (EFTEM, STEM-EELS) and STEM diffraction techniques (ACOM-TEM),” *Ultramicroscopy*, vol. 170, pp. 10–18, 2016.

[3] J. B. Goodenough and Y. Kim, “Challenges for Rechargeable Li Batteries,” *Chem. Mater.*, vol. 22, no. 3, pp. 587–603, 2010.